

GRADUATE COURSE IN PHYSICS
UNIVERSITY OF PISA

The School of Graduate Studies in Basic Sciences “Galileo Galilei”



Angela Papa

**Search for the lepton flavour violation in
 $\mu^+ \rightarrow e^+ \gamma$.**

**The calibration methods for
the MEG experiment**

Ph.D. Thesis XX cycle

Advisor
Prof. Carlo Bemporad

April 2009

Foreword

The MEG experiment gathers about sixty physicists from Italy, Japan, Russia, Switzerland, United States. The list of the institutions involved:

Italy:

Genova University and INFN
Lecce University and INFN
Pavia University and INFN
Pisa University and INFN
Roma University and INFN

Japan:

KEK, Tsukuba
Osaka University
Tokyo University
Waseda University

Russia:

BINP, Novosibirsk
JINR, Dubna

Switzerland:

PSI, Villigen

United States:

California University and DOE, Irvine

Contents

| | | |
|-----------|---|-----------|
| I | Theory and phenomenology | 11 |
| 1 | The rare muon decays in the Standard Model and beyond | 13 |
| 1.1 | The Standard Model as a gauge theory | 13 |
| 1.1.1 | Abelian gauge theories | 13 |
| 1.1.2 | Non-Abelian gauge theories | 14 |
| 1.1.3 | Spontaneous Symmetry Breaking | 15 |
| 1.1.4 | The Lagrangian of the Standard Model | 16 |
| 1.2 | The muon decay in the Standard Model | 19 |
| 1.2.1 | Muon mass and lifetime | 19 |
| 1.2.2 | The muon decay modes | 20 |
| 1.3 | Neutrino mass and mixing | 20 |
| 1.4 | Muon decay and neutrino mass | 22 |
| 1.5 | Beyond the Standard Model | 23 |
| 1.5.1 | Grand Unified Theories | 23 |
| 1.5.2 | Supersymmetry | 24 |
| 1.6 | SUSY-GUT theories | 25 |
| 1.7 | Muon decay in SUSY-GUT theories | 27 |
| 2 | The $\mu \rightarrow e\gamma$ decay. A survey | 33 |
| 2.1 | The search for $\mu^+ \rightarrow e^+\gamma$ | 33 |
| 2.2 | Event signature and backgrounds | 37 |
| 2.2.1 | Correlated background | 37 |
| 2.2.2 | Accidental background | 38 |
| 2.3 | $\mu^+ \rightarrow e^+\gamma$ decay NOW | 40 |
| II | The MEG experiment and the LXe calorimeter | 41 |
| 3 | The MEG experiment | 43 |
| 3.1 | Principles of measurement | 43 |
| 3.2 | The μ^+ -beam and the target | 45 |
| 3.2.1 | The MEG beam line | 47 |
| 3.2.2 | The target | 47 |
| 3.3 | The positron spectrometer | 48 |
| 3.3.1 | The COBRA magnet | 49 |
| 3.3.2 | The Drift Chambers | 52 |
| 3.3.3 | The Timing Counter | 52 |
| 3.4 | The γ calorimeter | 55 |
| 3.5 | The Trigger and DAQ systems | 57 |
| 3.5.1 | The Trigger system | 57 |
| 3.5.2 | Front-end electronics and DAQ | 60 |

| | | |
|------------|--|------------|
| 4 | Liquid xenon as a scintillating medium | 63 |
| 4.1 | Rare gas liquid scintillation detectors | 63 |
| 4.2 | Liquid Xenon properties as a scintillating medium | 64 |
| 4.2.1 | The scintillation process | 64 |
| 4.2.2 | Scintillation photon yield | 67 |
| 4.2.3 | Decay times | 69 |
| 4.2.4 | The attenuation length | 70 |
| 4.3 | The absorption length | 70 |
| 4.4 | The Rayleigh scattering length | 72 |
| 4.4.1 | Theoretical models for the optical properties of non-polar rare gases | 76 |
| 4.4.2 | Experimental measurements performed in Xe | 77 |
| 4.4.3 | The Clausius-Mossotti relation from the Xe gas phase to the Xe liquid phase in the VUV | 81 |
| 4.5 | The relation between the Rayleigh scattering length and the refractive index | 86 |
| 5 | The liquid xenon calorimeter | 95 |
| 5.1 | The Xe cryostat and the cryogenic equipment | 95 |
| 5.1.1 | The Xe cryogenic circuit | 95 |
| 5.1.2 | The cryostat | 98 |
| 5.2 | The Xe purification system | 98 |
| 5.3 | The photomultipliers for the LXe calorimeter | 100 |
| 5.3.1 | Physics of PMTs at low temperature | 100 |
| 5.3.2 | The bialkali photocatode resistivity at low temperature | 101 |
| 5.3.3 | The first PMT version: instabilities at high background rates and at cryogenic temperatures. The test in the Large Prototype | 103 |
| 5.3.4 | The PMT cryogenic facility in Pisa | 106 |
| 5.3.5 | The second PMT version: the R9288 PMT series and the results at the Cryo-Facility | 106 |
| 5.3.6 | The final PMT version: the R9869 PMT series | 109 |
| 6 | The expected LXe calorimeter performance | 113 |
| 6.1 | The LXe calorimeter geometry | 113 |
| 6.2 | The shower development | 116 |
| 6.3 | The γ energy estimate | 116 |
| 6.4 | The estimate of the event time | 119 |
| 6.4.1 | The evaluation of the average impact time | 121 |
| 6.4.2 | The result | 121 |
| 6.5 | The evaluation of the γ entrance coordinates | 121 |
| III | Calibration and monitoring of the MEG experiment | 125 |
| 7 | Calibration and monitoring methods | 127 |
| 7.1 | Motivations | 127 |
| 7.2 | The LXe calibrations | 127 |
| 7.3 | The LXe calorimeter and Timing Counter synchronization | 129 |
| 7.4 | The Drift Chamber calibration | 129 |
| 7.5 | The muon beam intensity measurement | 129 |
| 8 | PMT characteristics and Xe optical properties | 131 |
| 8.1 | LED | 131 |
| 8.2 | Americium wire sources | 133 |
| 8.2.1 | The leakage tests for the ^{241}Am -sources | 133 |
| 8.2.2 | The method for determining the relative QE of all PMTs | 134 |
| 8.2.3 | The results | 136 |

| | | |
|-----------|---|------------|
| 8.2.4 | The absorption length determination | 138 |
| 9 | The 9 MeV γ-line from thermal neutron capture by Ni | 139 |
| 9.1 | The 9 MeV γ generator | 139 |
| 9.2 | The γ -lines from thermal neutron capture | 140 |
| 9.2.1 | Capture on nickel | 140 |
| 9.2.2 | Capture on Xenon, Iodine and other elements | 141 |
| 9.3 | The neutron sources | 145 |
| 9.3.1 | The radioactive neutron sources | 145 |
| 9.3.2 | The neutron generator | 145 |
| 9.4 | The neutron moderator | 147 |
| 9.5 | The results of the 9 MeV γ generator test | 149 |
| 9.6 | The neutron capture time in a polyethylene/nickel assembly | 155 |
| 9.6.1 | The experimental set-up and the results | 156 |
| 9.7 | The 9 MeV γ generator set-up | 158 |
| 9.8 | Prevention against the possible neutron activation of materials | 159 |
| 10 | The 17.6 MeV γ-line by the ${}^7_3\text{Li}(p, \gamma){}^8_4\text{Be}$ reaction | 161 |
| 10.1 | The nuclear reactions excited by protons | 161 |
| 10.1.1 | ${}^7_3\text{Li}(p, \gamma){}^8_4\text{Be}$ | 161 |
| 10.1.2 | ${}^{11}_5\text{B}(p, \gamma){}^{12}_6\text{C}$ | 168 |
| 10.1.3 | Towards a proton accelerator | 171 |
| 10.2 | The Cockcroft-Walton accelerator | 174 |
| 10.2.1 | The RF ion source | 174 |
| 10.2.2 | The electrode cascade | 175 |
| 10.2.3 | The accelerator driver | 177 |
| 10.2.4 | The acceptance test | 177 |
| 10.2.5 | The C-W installation at PSI | 182 |
| 10.2.6 | The energy stability | 183 |
| 10.3 | The proton beam line | 183 |
| 10.3.1 | Mechanics of the proton beam line | 184 |
| 10.3.2 | The beam diagnostics | 185 |
| 10.3.3 | The proton beam optics and the beam alignment. | 191 |
| 10.4 | The target support; heat production and cooling; the targets | 193 |
| 11 | π^- CEX reaction | 195 |
| 11.1 | The kinematics of the π^- charge exchange reaction | 195 |
| 11.2 | The π^- capture on hydrogen and hydrogenous compounds | 196 |
| 11.3 | The first CEX reaction measurement | 199 |
| 11.3.1 | The experimental set-up | 199 |
| 11.3.2 | The results | 199 |
| 11.4 | The experimental set-up for the CEX reaction in MEG | 204 |
| 11.4.1 | The liquid hydrogen target | 204 |
| 11.4.2 | The NaI tagging detector | 204 |
| 11.5 | Conclusions | 207 |
| 12 | Timing counter tuning with the proton accelerator | 209 |
| 12.1 | Introduction | 209 |
| 12.2 | The PMT gain equalization | 211 |
| 12.3 | The PMT time fine-tuning | 213 |
| 12.4 | The timing of all MEG detector elements and plans for a new hardware | 219 |

| | |
|---|------------|
| 13 LXe-TC time fine-tuning | 223 |
| 13.1 The boron thick-target excitation curve and the γ spectra | 223 |
| 13.2 Boron targets | 224 |
| 13.3 Lithium+boron targets | 226 |
| 13.4 The predictions of Monte Carlo method | 228 |
| 14 Calibration method based on PIXE | 233 |
| 14.1 The particle induced X-ray emission | 233 |
| 14.1.1 The ionization cross section | 235 |
| 14.1.2 The X-ray production cross section | 235 |
| 14.1.3 The X-ray rate emission | 236 |
| 14.2 The X-ray fluorescence measurements | 239 |
| 14.2.1 The experimental set-up | 240 |
| 14.2.2 The detector calibration | 240 |
| 14.2.3 The results | 242 |
| 14.3 The measurements of proton induced X-ray | 246 |
| 15 Muon Beam monitoring and diagnostics | 251 |
| 15.1 Introduction | 251 |
| 15.2 Muon induced X-ray emission (MIXE) | 252 |
| 15.2.1 MIXE simulation | 252 |
| 15.2.2 MIXE measurement | 252 |
| 15.3 A He Ionization Chamber | 254 |
| 15.3.1 Ion motion in crossed E and H fields | 255 |
| 15.3.2 Test of the first prototype | 257 |
| 15.4 Muon beam diagnostics by luminescence | 258 |
| 15.4.1 Muon beam diagnostics by CsI(Tl) light emission | 260 |
| 15.5 Conclusion | 261 |
| IV MEG Run | 263 |
| 16 MEG Autumn 2008 Run | 265 |
| 16.1 The LXe calorimeter | 265 |
| 16.1.1 The monitoring of the LXe calorimeter | 265 |
| 16.1.2 The LXe calorimeter linearity and energy resolution | 271 |
| 16.1.3 The time resolution of the LXe calorimeter | 271 |
| 16.2 TC detector | 273 |
| 16.2.1 The time resolution of the TC | 273 |
| 16.2.2 LXe-TC timing | 273 |
| 16.3 The DC system | 274 |
| 16.4 The MEG detector efficiencies | 274 |
| 16.4.1 The positron detection efficiency | 274 |
| 16.4.2 The efficiency of γ detection | 277 |
| 16.5 The MEG sensitivity for the $\mu^+ \rightarrow e^+\gamma$ decay | 279 |
| 16.6 The muon radiative decay signal | 283 |

Introduction

The search for $\mu^+ \rightarrow e^+\gamma$ decay began 10 years after the discovery of the muon (1937) and after sixty years this process continues to play a fundamental role in physics, although the motivations for its study have changed over the time.

Today $\mu^+ \rightarrow e^+\gamma$ decay is an important tool for investigating physics beyond the Standard Model. Fundamental theories such as supersymmetric unification predict that $\mu^+ \rightarrow e^+\gamma$ decay should occur with a branching ratio that should be above 10^{-14} . The MEG experiment was designed to measure a branching ratio of $\approx 10^{-13}$, if no event is observed. The experiment has therefore a real chance of making a discovery, which would provide very clear evidence for new physics beyond the Standard Model.

Even a non-observation of decay at the predicted level of sensitivity would place a very tight constraint on these theories and on the general nature of the new physics, and will thus be of crucial importance in pointing out the future direction of particle physics, though with the evidence provided by neutrino oscillations the importance of such a search is greatly enhanced.

To reach this ambitious goal the experiment must use the most intense continuous beam available and rely on advanced technology (LXe calorimetry, a specially designed superconduction spectrometer, a flexible and powerful trigger system, etc.). The energy, time and space resolutions are the highest reachable to-day. The data collection will last about three years. On those terms, the only way to ensure that the required performances are reached and maintained in time is to use several complementary and redundant methods to calibrate and monitor the behaviour of all detectors.

This thesis deals with the design and the assembly of the calibration methods of the MEG experiment, their testing, to verify their reliability, their coupling to the MEG experiment, and the analysis of the acquired calibration data, during the MEG run 2008.

After a brief introduction to the Standard Model, its possible extensions and the phenomenology of the lepton flavour violation (chapter 1), an historical overview of the role of the $\mu^+ \rightarrow e^+\gamma$ decay is given (chapter 2).

The MEG experiment is described (chapter 3).

A discussion of the liquid xenon as a scintillating medium is given in chapter 4. The LXe calorimeter, the Xe cryostat, the cryogenic equipment, the purification system, the photomultipliers are the subject of chapter 5. The expected LXe calorimeter performance and the reconstructed event algorithms are described in chapter 6.

An introduction to all the calibration methods is given in chapter 7.

Liquid scintillator calorimeters and in particular liquid cryogenic noble gas detectors can be calibrated and monitored by the use of multiple α -sources distributed in the detector sensitive volume. LXe PMT equalization and the Xe optical properties can be measured by means of this method, as described in chapter 8.

The PMT behaviour, in conditions of high background induced by the muon beam, can be

monitored by means of 9 MeV γ 's, produced by neutron thermal capture in Nickel. A neutron generator will be the neutron source (chapter 9).

The LXe calorimeter energy resolution and linearity, the light yield and Xe purity are monitored by means of the 17.6 MeV γ -line from the ${}^7_3\text{Li}(p, \gamma){}^8_4\text{Be}$ nuclear reaction. A C-W accelerator is used for this purpose (chapter 10).

γ 's at 54.9 MeV, with an energy very close to that of the expected signal, are obtained from the π^0 decay, produced from the π^- charge exchange reaction at rest in liquid hydrogen (chapter 11).

The PMT TC equalization and the LXe-TC time fine-tuning are performed by using coincident γ 's from the ${}^{11}_5\text{B}(p, \gamma){}^{12}_6\text{C}$ nuclear reaction. The C-W accelerator is used for this method again (chapter 12 and 13).

Independent measurement of the muon beam intensity is proposed by using muon induced X-ray emission and/or a He ionization chamber (chapter 14 and 15).

The last chapter deals with the detector performances achieved during the MEG run autumn 2008, measured by using the discussed methods (chapter 16). The achieved single event sensitivity of the MEG experiment is given and a clear evidence of the radiative muon decay signal is shown.

Part I

Theory and phenomenology

Chapter 1

The rare muon decays in the Standard Model and beyond

In this chapter we will discuss the predictions for $\mu^+ \rightarrow e^+\gamma$ decay, as a tool for investigating the new physics. These are given in the framework of the Standard Model and beyond.

The Standard Model (SM) describes all observed interactions between elementary particles with high precision. It represents our starting point. Nevertheless this model has many unanswered fundamental questions which justify the attempts to develop a more general theory. $\mu^+ \rightarrow e^+\gamma$ decay, a fundamental process, plays a useful role in this respect.

1.1 The Standard Model as a gauge theory

The Standard Model is a description of the building blocks of matter (quarks and leptons) and their interactions (strong, weak and electromagnetic interactions) in terms of certain symmetries (*gauge symmetries*). A gauge theory is one that possesses invariance under a set of *local transformations* i.e. transformations whose parameters are space-time dependent. The matter fields are organized in families. The interactions are described in terms of vector bosons, which mediate them. A scalar field, the Higgs boson, is added to generate the vector-boson and fermion masses. All things are given in a gauge invariant way.

In the following subsection we recall the fundamental ingredients that are needed to build the SM as a gauge theory.

1.1.1 Abelian gauge theories

We start our consideration from the Lagrangian density for a free Dirac field ψ (because the matter building blocks are fermions):

$$\mathcal{L} = \bar{\psi}(i\gamma^\mu\partial_\mu - m)\psi. \quad (1.1)$$

This lagrangian is invariant (i.e. $\mathcal{L}(\psi') = \mathcal{L}(\psi)$) under the transformation:

$$\psi \rightarrow e^{-i\omega}\psi = \psi', \quad \bar{\psi} \rightarrow e^{i\omega}\bar{\psi} = \bar{\psi}', \quad (1.2)$$

where ω is a real parameter and $\bar{\psi}$ is the conjugate field. The set of the numbers $e^{-i\omega}$, which commute between them, form the abelian group $U(1)$ (unitary 1×1 matrices, i.e. $U^\dagger U = 1$, with U^\dagger is the adjoint matrix). The Lagrangian is then called invariant under *global* $U(1)$ transformations.

If ω depends on the space-time point $\omega(x^\mu)$ the Lagrangian is no longer invariant under this *local* transformations, because of the derivative between $\bar{\psi}$ and ψ :

$$\delta\mathcal{L} = \bar{\psi}(x)\gamma^\mu[\partial_\mu\omega(x)]\psi. \quad (1.3)$$

The gauge invariance can be restored if we assume that the fermion field interacts with a vector field A_μ , called a ‘‘gauge field’’, with an interaction term:

$$-e\bar{\psi}\gamma^\mu A_\mu\psi \quad (1.4)$$

added to the lagrangian density, where A_μ changes as:

$$A_\mu \rightarrow A_\mu + \delta A_\mu(x) = A_\mu + \frac{1}{e}[\partial_\mu(\omega(x))] \quad (1.5)$$

under a gauge transformation.

In order to have a complete description, we need a kinetic term also for the A_μ field without spoiling the invariance under gauge transformations. This is achieved by defining the field strength $F_{\mu\nu}$ as:

$$F_{\mu\nu} = \partial_\mu A_\nu - \partial_\nu A_\mu. \quad (1.6)$$

This is an example of an abelian gauge theory, in which there is only one gauge field.

1.1.2 Non-Abelian gauge theories

Let us restrict ourselves to the transformations coming from the group $SU(n)$ (unitary $n \times n$ matrices, with determinat equal to 1). A $SU(n)$ matrix is completely specified by $n^2 - 1$ real parameters. An arbitrary $SU(n)$ matrix is written as:

$$e^{-i\omega^a \mathbf{T}^a} \quad (1.7)$$

where ω^a , $a \in \{1 \dots n^2 - 1\}$ are the real parameters and \mathbf{T}^a are the $n^2 - 1$ generators of the group. Two general elements of $SU(n)$ do not commute (non-abelian group). The commutation rules are following the ones of the generators:

$$[\mathbf{T}^a, \mathbf{T}^b] = if^{abc}\mathbf{T}^c \neq 0. \quad (1.8)$$

These relations define the group algebra and f^{abc} are the structure constants of the group.

Consider again the free fermion lagrangian density:

$$\mathcal{L} = \bar{\psi}^i (i\gamma^\mu \partial_\mu - m)\psi_i \quad (1.9)$$

where the index i is summed over 1 to n , where ψ_i make up the multiplet ψ .

Under $SU(n)$ gauge transformations:

$$\psi_i \rightarrow (e^{-i\omega^a \mathbf{T}^a})^j_i \psi_j \quad (1.10)$$

if ω^a are constant numbers the lagrangian density eq. (1.9) is invariant; if ω^a is function of the space-time points $\omega^a(x)$ the eq. (1.9) changes to:

$$\delta\mathcal{L} = \bar{\psi}^i (T^a)^j_i \gamma^\mu (\partial_\mu \omega^a(x)) \psi_j \quad (1.11)$$

as observed in the abelian case.

The local gauge symmetry can again be restored by introducing interactions with vector (spin-one) gauge bosons. We need $n^2 - 1$ such gauge bosons, W_μ^a , one for each generator of $SU(n)$, which transform as:

$$\delta W_\mu^a(x) = -f^{abc} A_\mu^b(x) \omega^c(x) + \frac{1}{g} [\partial_\mu \omega^a(x)], \quad (1.12)$$

under gauge transformations.

The interaction with these gauge bosons is encoded by replacing the ordinary partial derivative in the lagrangian density with a covariant derivative, which in this case is a $n \times n$ matrix defined by:

$$\mathbf{D}_\mu = (\partial_\mu \mathbf{I} + ig\mathbf{T}^a W_\mu^a) \quad (1.13)$$

where \mathbf{I} is the unit matrix.

The kinetic term for the gauge bosons is again constructed from the field strengths $F_{\mu\nu}^a$:

$$\mathbf{F}_{\mu\nu} = -\frac{i}{g}[\mathbf{D}_\mu, \mathbf{D}_\nu] \quad (1.14)$$

or:

$$F_{\mu\nu}^a = \partial_\mu W_\nu^a - \partial_\nu W_\mu^a - gf^{abc}W_\mu^b W_\nu^c. \quad (1.15)$$

The kinetic term for the gauge bosons of a non-abelian theory contains terms which show that these gauge bosons are mutually interacting. This is a very important difference between abelian and non-abelian gauge theories.

1.1.3 Spontaneous Symmetry Breaking

Until now all particles, matter building blocks and gauge bosons, are massless. It is possible to generate masses dynamically through the interaction with a scalar field, which represents a spontaneously broken gauge mechanism. The vacuum may have a non-zero (scalar) field value represented by $\Phi = ve^{i\phi}$; v is called the vacuum expectation value (vev). The same minimum is reached for an arbitrary value of the phase ϕ : the ground state is degenerate. Once a particular value of the phase is chosen, it cannot change locally. The new feature is that the ground state is not invariant under gauge transformations. In the framework of $SU(n)$ this means that:

$$e^{-i\omega^a \mathbf{T}^a} |0\rangle \neq |0\rangle, \quad (1.16)$$

which entails

$$\mathbf{T}^a |0\rangle \neq 0 \text{ for some } a. \quad (1.17)$$

The theory is spontaneously broken if there exists at least one generator that does not annihilate the vacuum.

Consider the SM case (discussed in the next section), where one needs to break the $SU(2)_L \otimes U(1)_Y$ symmetry to the $U(1)_{em}$ symmetry. This can be achieved by choosing Φ to be a complex $SU(2)$ doublet, with the following Lagrangian density (for a scalar field):

$$\mathcal{L} = \frac{1}{4} F_{\mu\nu}^a F^{a\mu\nu} + |\mathbf{D}_\mu \Phi|^2 - V(\Phi) \quad (1.18)$$

where:

$$\mathbf{D}_\mu \Phi = \partial_\mu \Phi + igW_\mu^a \mathbf{T}^a \Phi, \quad (1.19)$$

and

$$V(\Phi) = -\mu^2 \Phi^+ \Phi + \lambda(\Phi^+ \Phi)^2. \quad (1.20)$$

This potential has a minimum at $\Phi^+ \Phi = \frac{1}{2}\mu^2/\lambda$. We can choose the vev to be:

$$\langle \Phi \rangle = \frac{1}{\sqrt{2}} \begin{pmatrix} 0 \\ v \end{pmatrix}, \quad (1.21)$$

where $v = \mu/\sqrt{\lambda}$. We expand Φ about its vev:

$$\Phi = \frac{1}{\sqrt{2}} \begin{pmatrix} \phi_1 + i\phi_2 \\ v + \phi_3 + i\phi_4 \end{pmatrix}. \quad (1.22)$$

If we insert this expansion into the potential eq. (1.20) we get only a mass term for the ϕ_3 component, which we call the physical Higgs scalar H ($m_H = \sqrt{2}\mu$).

If we use the eq. (1.21) in the kinetic term of the eq. (1.18), we can see that some of the bosons physical fields (a linear combination of the W_μ^a) have acquired mass (terms like $\frac{1}{2}m_\phi\phi^2$, where ϕ here indicates our physical field, are present).

The introduction of the scalar field Φ is also fundamental for generating the fermion mass. We shall see in the next section that the left-handed and right-handed fermions are assigned to different multiplets of weak isospin (doublets and singlets, respectively). As a consequence we cannot have an explicit mass term for them.

However we can have an interaction between the left-handed doublet, the right-handed singlet and the scalar doublet Φ . This is again an invariant gauge term, called the Yukawa interaction term, written as:

$$\mathcal{L}_{Yukawa} = -\frac{G_e}{\sqrt{2}} \begin{pmatrix} \bar{\nu}_L \\ \bar{e}_L \end{pmatrix}^T \begin{pmatrix} 0 \\ v + H \end{pmatrix} e_R + h.c. \quad (1.23)$$

where here we consider an example with only one lepton family. The part proportional to the vev v is simply:

$$-\frac{G_e}{\sqrt{2}}(\bar{e}_L e_R + \bar{e}_R e_L) = -\frac{G_e}{\sqrt{2}}\bar{e}e. \quad (1.24)$$

In this particular case the electron has acquired a mass, which is proportional to the vev v of the scalar field.

1.1.4 The Lagrangian of the Standard Model

Combining the previous information we can select the gauge group and the matter content of the SM.

Experimental observation helps in defining the gauge group. The result, achieved with various theoretical and experimental efforts, is the *Standard Model*. The SM is based on the *gauge principle*, according to which all forces of Nature are mediated by an exchange of gauge fields of the corresponding symmetry group. The symmetry group of the SM is

$$SU(3)_{Color} \otimes SU(2)_{Left} \otimes U(1)_{Hypercharge} \quad (1.25)$$

with the following field content:

Gauge sector: Spin 1 The gauge bosons are spin 1 vector particles, which are listed as:

| | | | |
|----------------------|-----------|---------------|------------|
| <i>gluons</i> | G_μ^a | for $SU_C(3)$ | with g_s |
| <i>weak bosons</i> | W_μ^i | for $SU_L(2)$ | with g |
| <i>abelian boson</i> | B_μ | for $U_Y(1)$ | with g' |

where g_s , g and g' are the coupling constants for $SU_C(3)$, $SU_L(2)$ and $U_Y(1)$.

Fermion sector: Spin 1/2 The matter fields are fermions belonging to the fundamental representation of the gauge group. These are believed to be quarks and leptons of at least three generations. The SM is left-right asymmetric. Left-handed and right-handed fermions have different quantum numbers:

quarks:

$$Q_{\alpha L}^i = \begin{pmatrix} U_\alpha^i \\ D_\alpha^i \end{pmatrix}_L = \begin{pmatrix} u^i \\ d^i \end{pmatrix}_L, \quad \begin{pmatrix} c^i \\ s^i \end{pmatrix}_L, \quad \begin{pmatrix} t^i \\ b^i \end{pmatrix}_L \quad (1.26)$$

$$U_{\alpha R}^i = u_{iR}, \quad c_{iR}, \quad t_{iR} \quad (1.27)$$

$$D_{\alpha R}^i = d_{iR}, \quad s_{iR}, \quad b_{iR} \quad (1.28)$$

leptons:

$$L_{\alpha L} = \begin{pmatrix} N_{\alpha} \\ E_{\alpha} \end{pmatrix}_L = \begin{pmatrix} \nu_e \\ e \end{pmatrix}_L, \quad \begin{pmatrix} \nu_{\mu} \\ \mu \end{pmatrix}_L, \quad \begin{pmatrix} \nu_{\tau} \\ \tau \end{pmatrix}_L \quad (1.29)$$

$$E_{\alpha R} = e_R, \quad \mu_R, \quad \tau_R \quad (1.30)$$

with $i = 1, 2, 3$ - color, and $\alpha = 1, 2, 3$ - generation.

Higgs Sector: Spin 0 In the minimal version of the SM there is one doublet of Higgs scalar fields

$$H = \begin{pmatrix} \phi^+ \\ \phi^0 \end{pmatrix} \quad (1.31)$$

which is introduced in order to give mass to quarks, leptons and intermediate weak bosons via spontaneous breaking of the electroweak symmetry.

The SM lagrangian, in the framework of the Quantum Field Theory, is:

$$\mathcal{L} = \mathcal{L}_{gauge} + \mathcal{L}_{Higgs} + \mathcal{L}_{Yukawa} \quad (1.32)$$

The lagrangian for the gauge interaction, \mathcal{L}_{gauge} , is given by:

$$\mathcal{L}_{gauge} = \sum_{SU(3)_C, SU(2)_L, U(1)_Y} F_{\mu\nu}^a F^{a\mu\nu} + \sum_{quarks, leptons} i\bar{\psi}_{iL(R)} \gamma^{\mu} D_{\mu} \psi_{iL(R)} + |D_{\mu} H|^2 \quad (1.33)$$

$$(1.34)$$

where $F_{\mu\nu}^a$ is the gauge-field strength for the considered group:

$$F_{\mu\nu}^a = G_{\mu\nu}^a, \quad W_{\mu\nu}^i, \quad B_{\mu\nu}, \quad (1.35)$$

listed as:

$$\begin{aligned} G_{\mu\nu}^a &= \partial_{\mu} G_{\nu}^a - \partial_{\nu} G_{\mu}^a - g_s f^{abc} G_{\mu}^b G_{\nu}^c, \\ W_{\mu\nu}^i &= \partial_{\mu} W_{\nu}^i - \partial_{\nu} W_{\mu}^i - g \epsilon^{ijk} W_{\mu}^j W_{\nu}^k, \\ B_{\mu\nu} &= \partial_{\mu} B_{\nu} - \partial_{\nu} B_{\mu}, \end{aligned} \quad (1.36)$$

with f^{abc} and ϵ^{ijk} structure constants for $SU(3)$ and $SU(2)$ respectively (for $U(1)$ the structure constants are zero because the group is abelian). $\psi_{iL(R)}$ are the matter fields as listed in the Fermion Sector; D_{μ} is the covariant derivative defined as:

$$D_{\mu} = \partial_{\mu} + ig_s \frac{\lambda^a}{2} G_{\mu}^a + ig \frac{\tau^a}{2} W_{\mu}^a + ig' Q_Y B_{\mu} \quad (1.37)$$

The term λ^a ($a = 1-8$) is the Gell-Mann matrix for a $SU(3)$ group, and τ^a ($a = 1-3$) is the Pauli matrix for a $SU(2)$ group. The terms of the singlet representation, for either the $SU(3)_C$ or $SU(2)_L$ gauge groups, are absent in the definition of D_{μ} .

The Higgs lagrangian, \mathcal{L}_{Higgs} , is given by:

$$\mathcal{L}_{Higgs} = -\mu^2 |H|^2 + \lambda |H|^4 \quad (1.38)$$

where μ is the Higgs mass parameter and λ is the Higgs coupling parameter. For $\mu^2 > 0$ all the particles obtain their masses due to the spontaneous breaking of $SU(2)_L$ symmetry group via a non zero vacuum expectation value (v.e.v.) of the Higgs field:

$$\langle H \rangle = \begin{pmatrix} 0 \\ v/\sqrt{2} \end{pmatrix}, \quad v = \mu/\sqrt{\lambda}, \quad (1.39)$$

with the physical Higgs mass given by:

$$m_H = \sqrt{2\lambda}v. \quad (1.40)$$

As a result, the gauge group of the SM is spontaneously broken down into:

$$SU(3)_C \otimes SU(2)_L \otimes U(1)_Y \Rightarrow SU(3)_C \otimes U(1)_{EM}. \quad (1.41)$$

The $SU(3)$ gauge bosons, the gluons, remain massless. The physically weak intermediate bosons are linear combinations of the gauge ones:

$$W_\mu^\pm = \frac{W_\mu^1 \mp iW_\mu^2}{\sqrt{2}}, \quad Z_\mu = -\sin\theta_W B_\mu + \cos\theta_W W_\mu^3 \quad (1.42)$$

with masses:

$$m_W = \frac{1}{2}gv, \quad m_Z = \frac{m_W}{\cos\theta_W}, \quad \tan\theta_W = \frac{g'}{g}, \quad (1.43)$$

while the photon field:

$$A_\mu = \cos\theta_W B_\mu + \sin\theta_W W_\mu^3 \quad (1.44)$$

remains massless.

The Yukawa lagrangian, \mathcal{L}_{Yukawa} is given by:

$$\mathcal{L}_{Yukawa} = \bar{L}_\alpha y_{\alpha\beta}^L E_\beta H + \bar{Q}_\alpha y_{\alpha\beta}^D D_\beta H + \bar{Q}_\alpha y_{\alpha\beta}^U U_\beta \tilde{H} + h.c., \quad (1.45)$$

where $h.c.$ means hermitian conjugate, $y_{\alpha\beta}^L$, $y_{\alpha\beta}^D$ and $y_{\alpha\beta}^U$ are the Yukawa coupling matrices for the charged leptons, the down-type quarks and the up-type quarks respectively, and $\tilde{H} = i\tau_2 H^\dagger$. After substituting the vacuum expectation value for the Higgs field, the Yukawa interaction generates the mass terms of quarks and leptons, proportional to the Yukawa matrices:

$$\mathcal{L}_{mass} = -(\bar{E}_{\alpha R} M_{\alpha\beta}^L E_{\beta L} + \bar{D}_{\alpha R} M_{\alpha\beta}^D D_{\beta L} + \bar{U}_{\alpha R} M_{\alpha\beta}^U U_{\beta L} \tilde{H}) + h.c., \quad (1.46)$$

with

$$M_{\alpha\beta}^L = y_{\alpha\beta}^L \cdot v, \quad M_{\alpha\beta}^D = y_{\alpha\beta}^D \cdot v, \quad M_{\alpha\beta}^U = y_{\alpha\beta}^U \cdot v. \quad (1.47)$$

Each mass matrix is diagonalized by unitary transformations for the left-handed fermions and the right-handed fermions with the same charge. Since the unitary matrices for the left-handed up-type quark and the left-handed down-type quark are generally different, flavour mixing is induced in the charged weak-current interaction for quarks. It is given by:

$$\mathcal{L}_{W\bar{q}q} = -\frac{g}{\sqrt{2}}[\bar{U}_{iL}\gamma^\mu(V_{CKM})_{ij}D_{jL}W_\mu^+ + \bar{D}_{iL}\gamma^\mu(V_{CKM})_{ji}^*U_{jL}W_\mu^-] \quad (1.48)$$

where $(V_{CKM})_{ij}$ is the Cabibbo-Kobayashi-Maskawa matrix.

On the other hand, the charged-lepton mass matrix in eq. (1.46), which is proportional to the lepton Yukawa coupling-constant matrix, is fully diagonalized by unitary transformations on the lepton doublet fields and the lepton singlet fields. In the mass-eigenstate basis, the charged weak-current interaction for leptons remains diagonal as follows:

$$\mathcal{L}_{W\bar{\nu}e} = -\frac{g}{\sqrt{2}}(\bar{N}_{iL}\gamma^\mu E_{iL}W_\mu^+ + \bar{E}_{iL}\gamma^\mu N_{iL}W_\mu^-). \quad (1.49)$$

For every global phase transformation of the field $\psi \rightarrow \psi e^{iL\theta}$ a corresponding quantum number is conserved. The SM lagrangian is invariant under four such global symmetries. Since these symmetries are not dictated by gauge invariance, they are called *accidental* and correspond to the conserved quantum numbers B (the baryon number) and to the lepton family number of each generation (the electron number L_e , the muon number L_μ and the tau number L_τ).

1.2 The muon decay in the Standard Model

The muon interactions in the SM are mediated by the A_μ , the W_μ^\pm and the Z_0 fields. The coupling with the Higgs bosons is also present. The lagrangian associated with these interactions is:

$$\begin{aligned} \mathcal{L} = & e\bar{\mu}\gamma^\mu\mu A_\mu \\ & -\frac{g}{\sqrt{2}}(\bar{\nu}_{\mu L}\gamma^\mu\mu_L W_\mu^+ + \bar{\mu}_L\gamma^\mu\nu_{\mu L}W_\mu^-) \\ & -\sqrt{(g^2 + g'^2)}\left[\bar{\mu}_L\gamma^\mu\left(-\frac{1}{2} + \sin^2\theta_W\right)\mu_L + \bar{\mu}_R\gamma^\mu\sin^2\theta_W\mu_R\right]Z_\mu^0 \\ & -\frac{m_\mu}{v}\bar{\mu}\mu H. \end{aligned} \quad (1.50)$$

The muon decays, $\mu^+ \rightarrow e^+\nu_e\bar{\nu}_\mu$ and $\mu^- \rightarrow e^-\bar{\nu}_e\nu_\mu$, are described by the charged weak-current interaction mediated by the W_μ^\pm gauge boson, the second line of the eq. (1.50). Due to the large mass, the W_μ^\pm will propagate a finite, very small distance (≈ 0.0025 fm). Thus the decay can be described by the *point-like* four-fermion interaction, given by:

$$\mathcal{L}_{Fermi} = -\frac{G_F}{\sqrt{2}}[\bar{\mu}\gamma^\mu(1 - \gamma_5)\nu_\mu\bar{e}\gamma_\mu(1 - \gamma_5)\nu_e + \bar{\nu}_e\gamma^\mu(1 - \gamma_5)e\bar{\mu}\gamma_\mu(1 - \gamma_5)\nu_\mu] \quad (1.51)$$

where G_F is the Fermi coupling, connected with the weak constant by the relation:

$$G_F = \frac{g^2}{4\sqrt{2}m_W^2} \quad (1.52)$$

Eq. (1.51) describes the *standard* muon decay, which represents the main muon decay mode (Branching Ratio B.R. = $\Gamma_i/\Gamma \approx 100\%$).

1.2.1 Muon mass and lifetime

The muon mass and the lifetime are two parameters of the Standard Model. The muon mass was obtained from the ratio of the muon mass to the electron mass, m_μ/m_e , in a muonium atom ($\mu^+ e^-$). The measured value is:

$$m_\mu = 106.658389(34) \text{ MeV}, \quad (1.53)$$

where QED corrections are taken into account.

The measured lifetime time is:

$$\tau_\mu = 2.19703(4) \times 10^{-6} \text{ s}. \quad (1.54)$$

The lifetime is connected with the Fermi coupling constant which can therefore be determined from τ_μ . The relation, where QED corrections are included, is:

$$\tau_\mu^{-1} = \frac{G_F^2 m_\mu^5}{192\pi^3} F\left(\frac{m_e^2}{m_\mu^2}\right) \left(1 + \frac{3}{5}\frac{m_\mu^2}{m_W^2}\right) \left[1 + \frac{\alpha(m_\mu)}{2\pi} \left(\frac{25}{4} - \pi^2\right)\right]. \quad (1.55)$$

F is defined as:

$$F(x) = 1 - 8x + 8x^3 - x^4 - 12x^2 \cdot \ln x, \quad (1.56)$$

and the electromagnetic coupling constant $\alpha(m_\mu)^{-1}$ is given by:

$$\frac{1}{\alpha(m_\mu)} = \frac{1}{\alpha} - \frac{2}{3\pi} \ln\left(\frac{m_\mu}{m_e}\right) + \frac{1}{6\pi} \approx 136. \quad (1.57)$$

The Fermi constant obtained from the measurement of τ_μ , by using (1.55), is:

$$G_F = 1.16639(1) \times 10^{-5} \text{ GeV}^{-2}. \quad (1.58)$$

Table 1.1: μ -decay modes.

| Decay mode | Branching Ratio | Reference |
|---|---|-----------|
| $\mu^+ \rightarrow e^+ \nu_e \bar{\nu}_\mu$ | $\approx 100\%$ | |
| $\mu^+ \rightarrow e^+ \nu_e \bar{\nu}_\mu \gamma$ | $1.4 \pm 0.4\%$ (for $E_\gamma > 10$ MeV) | [1] |
| $\mu^+ \rightarrow e^+ \nu_e \bar{\nu}_\mu e^+ e^-$ | $(3.4 \pm 0.4) \times 10^{-5}$ | [2] |
| $\mu^+ \rightarrow e^+ \bar{\nu}_e \nu_\mu$ | 1.2% | [3] |
| $\mu^+ \rightarrow e^+ \gamma$ | $< 1.2 \times 10^{-11}$ | [4] |
| $\mu^+ \rightarrow e^+ e^+ e^-$ | $< 1.2 \times 10^{-12}$ | [5] |
| $\mu^+ \rightarrow e^+ \gamma \gamma$ | 7.2×10^{-13} | [6] |

1.2.2 The muon decay modes

The measured decay modes of the muon are:

- $\mu^+ \rightarrow e^+ \nu_e \bar{\nu}_\mu$ (Michel decay);
- $\mu^+ \rightarrow e^+ \nu_e \bar{\nu}_\mu \gamma$ (radiative decay);
- $\mu^+ \rightarrow e^+ \nu_e \bar{\nu}_\mu e^+ e^-$.

The measured branching ratios and the upper bounds (90% of C.L.) for the exotic ones are reported in Tab. 1.1.

1.3 Neutrino mass and mixing

Lepton flavour is preserved in the SM because of the vanishing neutrino masses. How does this compare with the evidence for the neutrino oscillations, which represent indirect evidence for massive neutrinos? How do we explain the neutrino mass? What are the predictions for $\mu \rightarrow e \gamma$, in this scenario?

In this and in the following paragraphs we answer these questions.

If we include a ν_R in the model, nothing prevents us from writing a mass term for neutrinos. In a way similar to the up-type quarks in eq. (1.45), we can add the following term:

$$\mathcal{L}_{\nu_R} = \bar{\nu}_{\alpha R} y_{\alpha\beta}^\nu l_{\beta L} \tilde{H}^\dagger + h.c., \quad (1.59)$$

where $y_{\alpha\beta}^\nu$ is the Yukawa coupling matrix for neutrinos. Once one has a mass term one has to carefully distinguish between mass eigenstates and interaction eigenstates, because we can have a mixing similar to that of the quark sector. We indicate with ν_i the mass eigenstates, $\tilde{\nu}_i$ the interaction eigenstates and V ($\tilde{\nu}_i = V_{ij} \cdot \nu_j$) the mixing matrix. If one considers only three neutrinos, V is a unitary 3×3 matrix: the Pontecorvo-Maki-Nakagawa-Sakata matrix, V_{PMNS} .

In the mass-eigenbasis one writes the Schrödinger equation as:

$$i \frac{d}{dt} \tilde{\nu} = H \cdot \tilde{\nu} \quad (1.60)$$

where H is the diagonal Hamiltonian.

The time evolution of the mass-eigenstates is:

$$\tilde{\nu}_i(t) = e^{-i(E_i t - p_i L)} \tilde{\nu}_i(0) \approx e^{-i(m_i^2/2E_i)L} \tilde{\nu}_i(0), \quad (1.61)$$

where E_i (eigenvalues of H), p_i and m_i are the energy, momentum and rest mass of neutrinos. If momenta and energies are assumed to be larger than the neutrino masses, the approximation $L = vt = ct = t$ on the eq. (1.61) is valid. Let us now consider the time evolution of a propagating

neutrino created at $t = 0$ (or $L = 0$) as an interaction eigenstate; at time t (or distance L) this state is described by:

$$\tilde{\nu}_j(t) = \sum_i V_{ji} e^{-i(m_i^2/2E_i)L} \nu_i(0) \approx \sum_k \sum_i V_{ji} e^{-i(m_i^2/2E_i)L} V_{ki} \tilde{\nu}_i(0). \quad (1.62)$$

Using the previous relation, the probability that a neutrino of flavour l acquired components corresponding to other flavours l' is simply the absolute squared value of the amplitude:

$$\mathcal{P}_{\nu_l \rightarrow \nu_{l'}} = |\langle \nu_{l'} | \nu_l \rangle|^2 = \left| \sum_i V_{li} V_{l'i}^* e^{-i(m_i^2/2E_i)L} \right|^2 = \sum_i |V_{li} V_{l'i}|^2 + \mathcal{R} \sum_i \sum_{j \neq i} V_{li} V_{l'i}^* V_{lj}^* V_{l'j} e^{i(|m_i^2 - m_j^2|L/2p)}. \quad (1.63)$$

The necessary and sufficient conditions for the existence of neutrino oscillations are: (a) the non-vanishing value of at least one neutrino mass m_i ; (b) the non-vanishing value of at least one nondiagonal matrix element of the mixing matrix V .

In this scenario, the total lepton number is preserved, whereas the conservation of the individual lepton flavours is violated.

Before discussing the $\mu \rightarrow e\gamma$ decay, we examine the problems relative to the neutrino mass values.

The experimental results confirmed the evidence for neutrino oscillations ([7, 8, 9, 10, 11, 12, 13, 14, 15, 16, 17]). Hence neutrinos have mass. Neutrino oscillations are only sensitive to mass differences and nothing is learned about the absolute neutrino masses. Some experimental upper limits are available for neutrino masses: $2 \text{ eV}/c^2$ for ν_e , $190 \text{ keV}/c^2$ for ν_μ and 18.2 MeV for ν_τ , very small masses compared to that of other leptons [18, 19, 20, 21, 22].

A natural explanation for the smallness of neutrino masses is provided by the *see-saw* mechanism. We already added a (Dirac) mass term in the lagrangian, similar to the the one of the quark sector:

$$m_D \bar{\nu} \nu = m_D (\bar{\nu}_L \nu_R + \bar{\nu}_R \nu_L) \quad (1.64)$$

In fact, since ν_R is a singlet under gauge transformations, if one wants the most general gauge invariant lagrangian, one has also to add the term:

$$M \nu_R \nu_R + h.c. \quad (1.65)$$

Note that for this term to be gauge invariant it is mandatory that $Y(\nu_R) = 0$ and that ν_R neither couples to the $SU(2)$ nor to the $SU(3)$ gauge bosons. Such a right-handed neutrino is said to be sterile. The mass term present in eq. (1.65) is the Majorana mass. Whereas m_D is expected to be of the same size as charged lepton masses (due to the fact that the Yukawa couplings of all fermions are roughly the same), the most natural value for M is much greater. Ultimately one expects that, at a high energy scale (at $M \approx 10^{15} \text{ GeV}$, the GUT scale) there is a theory that explains all fermion masses. Then, the natural value for the fermion masses is of the order M . Consider the neutrino matrix for (ν_L, ν_R) :

$$\begin{pmatrix} 0 & m_D \\ m_D & M \end{pmatrix} \quad (1.66)$$

The physical particle masses are the eigenstates of the mass matrix:

$$\frac{m_D^2}{M} \quad \text{and} \quad M. \quad (1.67)$$

Since $m_D \approx m_{leptons}$ and $M \gg m_D$ this provides an explanation for the smallness of the left-handed neutrino masses relative to the mass of the other leptons.

The consistence between neutrino oscillations and small neutrino masses being recovered, we can proceed to the correlation between neutrino masses and muon decay.

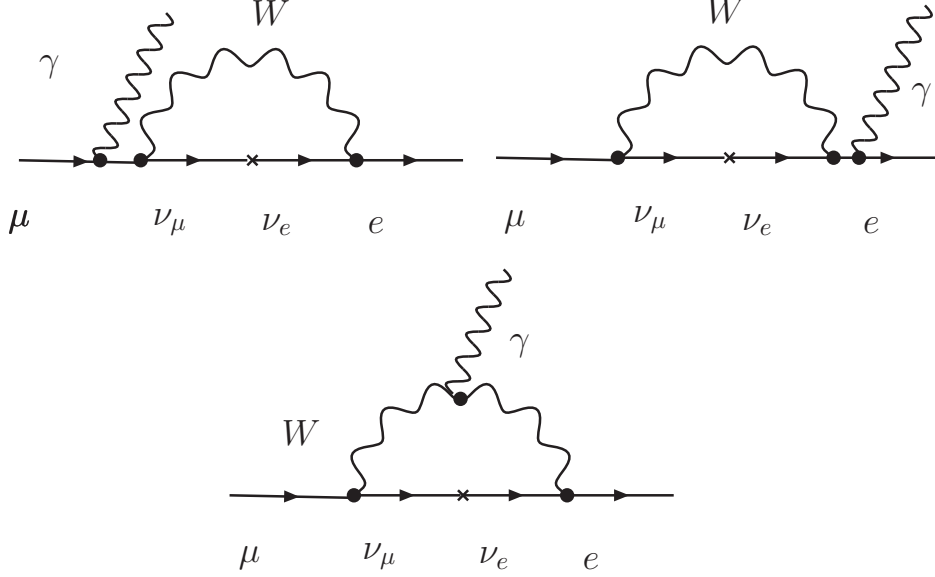


Figure 1.1: *Feynman diagrams for the $\mu^+ \rightarrow e^+ \gamma$ decay in the Standard Model, extended to massive neutrinos.*

1.4 Muon decay and neutrino mass

The Lagrangian with massive and mixed neutrinos leads to the Feynman diagrams for $\mu \rightarrow e \gamma$ decay shown in Fig. 1.1. The expected muon decay rate is:

$$\Gamma(\mu \rightarrow e \gamma) = \frac{G_F^2 m_\mu^5}{192\pi^3} \frac{3\alpha}{32\pi} \left| \sum_i (V_{PMNS}^*)_i (V_{PMNS})_i \frac{m_{\nu_i}^2}{m_W^2} \right|^2 \quad (1.68)$$

If we assume that only ν_e and ν_μ are mixed, the mixing matrix simplifies:

$$\begin{pmatrix} \cos \theta & -\sin \theta \\ \sin \theta & \cos \theta \end{pmatrix}, \quad (1.69)$$

and the oscillation probability becomes:

$$\mathcal{P}_{\nu_e \rightarrow \nu_\mu}(L) = \sin^2 2\theta \sin^2(\Delta m^2 L/4E). \quad (1.70)$$

The rate of the $\mu \rightarrow e \gamma$ can be written as:

$$\begin{aligned} \Gamma(\mu \rightarrow e \gamma) &\approx \frac{G_F^2 m_\mu^5}{192\pi^3} \frac{\alpha}{2\pi} \sin^2 2\theta \sin^2 \left(\frac{\Delta m^2 L}{4E} \right) \\ &\approx \frac{G_F^2 m_\mu^5}{192\pi^3} \frac{\alpha}{2\pi} \sin^2 2\theta \left(\frac{\Delta m^2}{m_W^2} \right)^2 \end{aligned} \quad (1.71)$$

where one can recognize the standard muon amplitude $\Gamma(\mu \rightarrow e \nu \bar{\nu})$, a γ -vertex, and the contribution of the neutrino oscillations (one assumes that the oscillation $\nu_e \rightarrow \nu_\mu$ should take place over a distance of $L \approx 1/m_W$ and the energy which flows in the energy loop is of the order m_W).

The Branching Ratio, normalized to the standard muon decay and including the measured oscillation parameters, becomes:

$$\begin{aligned}
 B(\mu \rightarrow e\gamma) &= \frac{\Gamma(\mu \rightarrow e\gamma)}{\Gamma(\mu \rightarrow e\nu\bar{\nu})} \approx \frac{\alpha}{2\pi} \sin^2 2\theta (\Delta m^2/m_W^2)^2 \\
 &\approx \frac{1}{2 \times 137 \times \pi} \left(\frac{7 \times 10^{-5} \text{ eV}^2}{80 \text{ GeV}^2} \right)^2 \\
 &\approx 10^{-55}.
 \end{aligned} \tag{1.72}$$

This extremely small Branching Ratio is not presently measurable.

In conclusion, the Standard Model correctly describes the observed elementary particle phenomenology and the different forces of nature (similarly treated, i.e.: as gauge theories). It can be extended to include massive neutrinos, but in this case the lepton flavour violation is extremely small.

1.5 Beyond the Standard Model

Despite its success in describing the particle phenomenology, the Standard Model is unsatisfactory since it is founded on many assumptions and leaves many fundamental questions unanswered. For example:

- the origin of the three constant couplings is not given;
- flavour mixing and the number of generations are arbitrary;
- the origin of the mass spectrum is unclear;
- the Higgs boson has not yet been observed and it is not clear whether it is fundamental or composite;
- the quantization of the electric charge is not explained;
- gravity is not included in this framework;
- the hierarchy problem and the fine-tuning problem are unresolved;
- etc.

These facts lead to the conclusion that the SM is only a low-energy effective theory of a yet-more-fundamental theory, where these problems can be resolved. This assumption guides us towards Supersymmetry and Grand Unification.

1.5.1 Grand Unified Theories

Since the main motivation for SUSY is related to the unification theory, let us briefly recall the main points of Grand Unification. The idea behind Grand Unification is based on the hypothesis that gauge symmetry increases with energy. All known interactions are different branches of a unique interaction associated with a simple gauge group. Unification occurs at high energy:

$$\begin{aligned}
 \text{LOW ENERGY} &\Rightarrow \text{HIGH ENERGY} \\
 SU(3)_C \otimes SU(2)_L \otimes U(1)_Y &\Rightarrow G_{GUT} \\
 g_s \quad g \quad g' &\Rightarrow g_{GUT}
 \end{aligned} \tag{1.73}$$

In the SM the strong and the weak couplings, associated with non-Abelian gauge groups, decrease with energy, while, the electromagnetic one, associated with the Abelian group, increases. It becomes then possible that at some energy scale they become equal. According to the GUT

idea, this equality is not occasional, but is a manifestation of the unique origin of these three interactions. As a result of spontaneous symmetry breaking, the unifying group is broken and the unique interaction is split into three branches which we call strong, weak and electromagnetic interactions. The coupling constant unification at a single point is impossible within the SM, while it is possible in the SUSY framework, since new physics enters between the electroweak and the Planck scale. This take place at a very high energy level, of the order of $10^{15\div 16}$ GeV.

SU(5) model

The smallest group G which embeds the symmetry group $SU(3)_C \otimes SU(2)_L \otimes U(1)_Y$ is the $SU(5)$ group, so the minimal extension of the SM towards a GUT is based on the $SU(5)$ group [23]. In the $SU(5)$ group the 15 particles and antiparticles of the first generation can be fitted into $\bar{5}$ -plet and 10-plet (the bar indicates the complementary of the fundamental representation).

In the minimal $SU(5)$ the neutrino is massless. It is of course possible to put a right-handed neutrino into a singlet representation.

$SU(5)$ rotations can be represented by 5×5 matrices. Local gauge invariance requires the introduction of $N^2 - 1 = 24$ gauge fields (the mediators), which cause the interactions between the matter fields. New gauge bosons add to the gluons and to the weak bosons and new transitions, mediated by the new gauge bosons, can occur.

According to this simple group it is possible to unify the coupling constants and explain the charge quantization. This model unfortunately predicts a proton decay rate which is in conflict with the experiment. As a consequence, the minimal $SU(5)$ model is not a viable GUT. As will be later discussed, the supersymmetry extension of $SU(5)$ gets over this conflict.

SO(10) model

The $SO(10)$ group was independently proposed by Georgi and Fritzsch&Minkowski.

From the theoretical point of view, the main criticism of $SU(5)$ is that it did not unify all the fermions of a given generation into a single irreducible representation, together with its dual for antiparticles. $SO(10)$ solves this problem, and contains $SU(5)$ as a subalgebra, with $SU(5) \times U(1)$ being the maximal subalgebra. $SU(5)$ is in a class of groups that admits spinor representations of dimension 15. The $SO(10)$ group admits a representation of dimension 16. This additional 16th state can accommodate the right-handed neutrino. This means that one can easily give masses to neutrinos, an obvious benefit to the theory. The advantage of $SO(10)$ over $SU(5)$, as the group for grand unification, is a 16-dimensional spinor representation of $SO(10)$ having the right quantum numbers to accommodate all fermions of one generation, including the right-handed neutrino.

Although the GUT theories address some critical points of the Standard Model, others appear, such as the hierarchy problem. We discuss this point after introducing Supersymmetry.

1.5.2 Supersymmetry

Supersymmetry is introduced to unify all the forces of nature (including gravity).

The graviton has spin 2, while the other gauge bosons have spin 1. They correspond to different representations of the Poincaré algebra. Attempts to unify all four forces within the same algebra face a problem. Unification of spin 2 and spin 1 gauge fields is allowed in supersymmetry algebra. The *uniqueness* of SUSY is due to a strict mathematical statement: the algebra of SUSY is the *only* graded (i.e. containing anticommutators as well as commutators) Lie algebra possible within a relativistic field theory.

If Q is a generator of SUSY algebra, then

$$Q|boson\rangle = |fermion\rangle \quad Q|fermion\rangle = |boson\rangle. \quad (1.74)$$

Hence, starting with the graviton state of spin 2 and acting by a SUSY generator we get the following chain of states:

$$spin\ 2 \rightarrow spin\ 3/2 \rightarrow spin\ 1 \rightarrow spin\ 1/2 \rightarrow spin\ 0. \quad (1.75)$$

Table 1.2: Particle content of the MSSM.

| Superfield | Bosons | Fermions | $SU_C(3)$ | $SU_L(2)$ | $U_Y(1)$ |
|------------|---|--|-----------|-----------|----------|
| Gauge | | | | | |
| G^a | gluon g^a | gluino \tilde{g}^a | 8 | 0 | 0 |
| V^k | Weak W^k (W^\pm, Z) | wino, zino \tilde{w}^k (\tilde{w}^\pm, \tilde{z}) | 1 | 3 | 0 |
| V' | Hypercharge $B(\gamma)$ | bino $\tilde{b}(\tilde{\gamma})$ | 1 | 1 | 0 |
| Matter | | | | | |
| L_i | sleptons $\left\{ \begin{array}{l} \tilde{L}_i = (\tilde{\nu}, \tilde{e})_L \\ \tilde{E}_i = \tilde{e}_R \end{array} \right.$ | leptons $\left\{ \begin{array}{l} L_i = (\nu, e)_L \\ E_i = e_R \end{array} \right.$ | 1 | 2 | -1 |
| E_i | | | 1 | 1 | 2 |
| Q_i | squarks $\left\{ \begin{array}{l} \tilde{Q}_i = (\tilde{u}, \tilde{d})_L \\ \tilde{U}_i = \tilde{u}_R \\ \tilde{D}_i = \tilde{d}_R \end{array} \right.$ | quark $\left\{ \begin{array}{l} Q_i = (u, d)_L \\ U_i = e_R^c D_i = d_R^c \end{array} \right.$ | 3 | 2 | 1/3 |
| U_i | | | 3^* | 1 | -4/3 |
| D_i | | | 3^* | 1 | 2/3 |
| Higgs | | | | | |
| H_1 | Higgsess $\left\{ \begin{array}{l} H_1 \\ H_2 \end{array} \right.$ | higgsinos $\left\{ \begin{array}{l} \tilde{H}_1 \\ \tilde{H}_2 \end{array} \right.$ | 1 | 2 | -1 |
| H_2 | | | 1 | 2 | 1 |

A partial unification of matter (fermions) with forces (bosons) naturally arises from an attempt to unify gravity with other interactions.

A symmetry between fermions and bosons is obtained. The symmetry can be realized in nature only if one assumes that each particle with spin j has a supersymmetric partner with spin $j-1/2$. This leads to a doubling of the particle spectrum (introducing a superpartner for each particle) and adding another Higgs doublet (with its superpartner). The symmetry between fermions and bosons is important to solve the naturalness and hierarchy problems, as discussed in the next section.

This supersymmetry cannot however be an exact symmetry of nature. In a theory with an exact symmetry, fermions and their bosonic superpartners must be degenerate in mass. The Standard Model spectrum clearly does not satisfy this requirement. If supersymmetry is realized in nature, it must be broken. Supersymmetry-breaking terms can be included in the theory. The simplest model of this type is called the Minimal Supersymmetric Standard Model MSSM ([25], [26], [27], [28]). Its particle content is given in table 1.2.

If we take into account the evolution of the coupling constants in the supersymmetric extension of the SM, unification is obtained. The SUSY particles are assumed to contribute only above the effective SUSY scale M_{SUSY} (of about 1 TeV); this causes a change of slope in the evolution of the coupling constants.

1.6 SUSY-GUT theories

The GUT theory introduces two energy scales, associated with the m_W and m_{GUT} , leading to the *hierarchy problem*. There are three aspects of this problem.

The first is the existence of a hierarchy. To get the desired spontaneous symmetry breaking pattern, one needs:

$$\begin{aligned}
m_H &\approx v \approx 10^2 \text{ GeV} \\
m_\Sigma &\approx V \approx 10^{16} \text{ GeV} \\
\frac{m_H}{m_\Sigma} &\approx 10^{-14} \ll 1,
\end{aligned} \tag{1.76}$$

where H and Σ are the Higgs fields respectively responsible for the spontaneous breaking of the $SU(2) \times U(1)$ and of the GUT groups. In this context, it is a mystery why the ratio m_H/m_Σ is so small. The problem remains even in the absence of grand unification of strong and electroweak

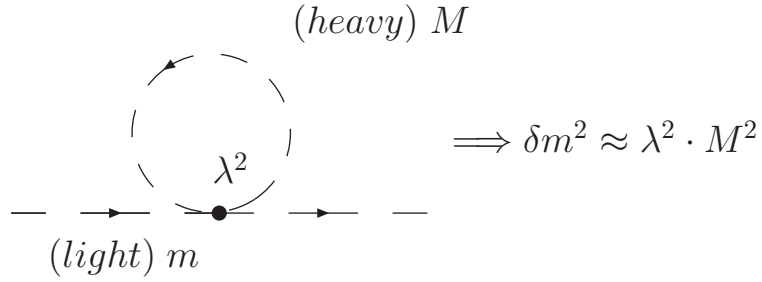


Figure 1.2: Radiative corrections to the light Higgs boson mass.

forces at a very high energy scale, where the SM must be modified to incorporate the effects of gravity at the Planck scale ($M_P \approx 10^{19}$ GeV).

The second aspect of the hierarchy problem has to do with its consequences at low energy (naturalness problem). If one couples a theory of scalar particles to new physics at some arbitrarily high scale Λ , radiative corrections to the scalar squared-mass are of order $\mathcal{O}(\Lambda^2)$. Thus the natural mass for any scalar particle is Λ . As an example let us consider the radiative corrections to the light Higgs mass. They are given by the Feynman diagram shown in Fig. 1.2 and they are proportional to the mass squared of the heavy particle. As a consequence, in order to have a successful electroweak theory, the Higgs mass must be of the order of the electroweak scale, but radiative corrections shift the mass to the Λ scale.

The third aspect is connected with the preservation of a given hierarchy (fine-tuning problem). Even if we choose the hierarchy like in eq. (1.76), the radiative corrections will destroy it, and it need to be cancelled. A Higgs mass of order the electroweak scale can be obtained only if the bare Higgs squared mass is of $\mathcal{O}(\Lambda^2)$. This very accurate cancellation, with a precision of $\approx 10^{-28}$, needs a fine tuning of the coupling constants.

A way of achieving this kind of cancellation of quadratic terms is to adopt supersymmetry.

This is due to the superpartners of ordinary particles. The contribution by the boson loops cancels those from the fermion loops because of an additional factor (-1) coming from Fermi statistics, as shown in Fig. 1.3. One can see the two types of contribution. The upper part of the figure represents the contribution of the heavy Higgs boson and its superpartner; the strength of the interaction is given by the Yukawa coupling λ . The bottom part of the figure represents the gauge interaction from the heavy gauge boson and heavy gaugino, proportional to the gauge coupling constant g .

In both cases the quadratic term cancellation takes place. The cancellation is true, in the case of an unbroken supersymmetry, due to the following sum rule relating the masses of the superpartners:

$$\sum_{bosons} m^2 = \sum_{fermions} m^2 \quad (1.77)$$

and is violated when SUSY is broken. The cancellation is then true up to the SUSY breaking scale, m_{SUSY} , since

$$\sum_{bosons} m^2 - \sum_{fermions} m^2 = m_{SUSY}^2, \quad (1.78)$$

which should not be very large (≤ 1 TeV) to make the fine-tuning natural. Let us consider the Higgs boson mass. If one requires, for the perturbation theory to be consistent, that the radiative corrections to the Higgs boson mass do not exceed the mass itself, one obtains:

$$\delta m_H^2 \approx g^2 m_{SUSY}^2 \approx m_H^2. \quad (1.79)$$

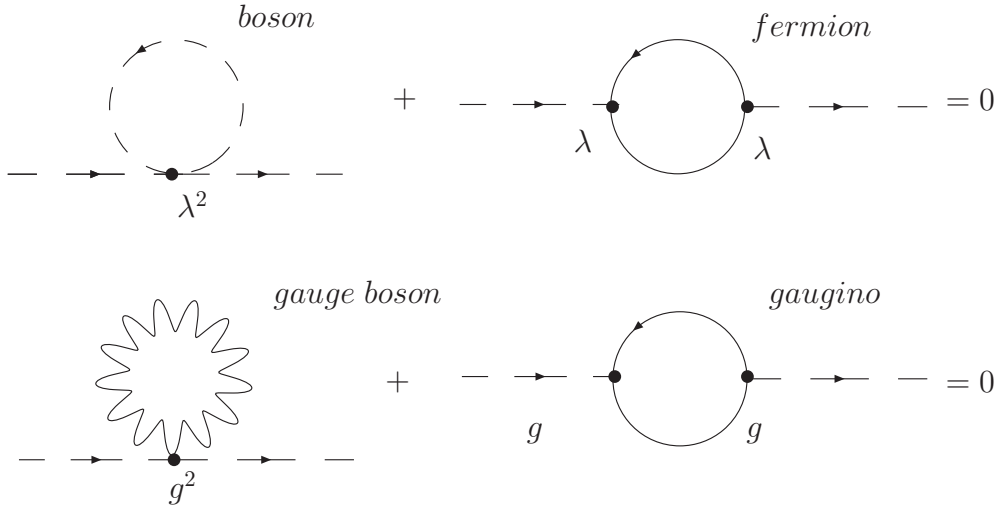
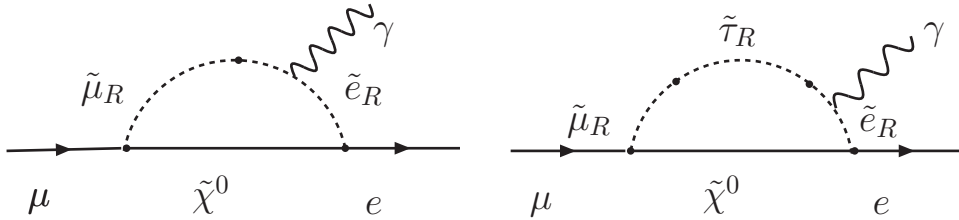


Figure 1.3: Cancellation of quadratic terms (divergencies).

Figure 1.4: Feynman diagrams for the $\mu^+ \rightarrow e^+ \gamma$ decay in the $SU(5)$ SUSY – GUT model. The closed lines represent the flavour transitions due to the off-diagonal terms of the slepton mass matrices.

So, if $m_H^2 \approx 10^2$ GeV and $g \approx 10^{-1}$, one needs $m_{SUSY} \approx 10^3$ GeV for eq. (1.79) to be valid. One obtains again the same rough estimate of $m_{SUSY} \approx 10^3$ GeV, as from the gauge coupling unification already examined; the two requirements are well matched.

That is the reason why it is usually said that supersymmetry solves the hierarchy problem (*There is no GUT without SUSY*).

1.7 Muon decay in SUSY-GUT theories

In this paragraph we present the predictions of the $SU(5)$ SUSY – GUT and $SO(10)$ SUSY – GUT models on the $\mu^+ \rightarrow e^+ \gamma$ decay. Starting from the pionier work on $\mu^+ \rightarrow e^+ \gamma$ decay as a significant signature of supersymmetric unification [29, 30], this process attracted the attention of both experimentalists and theorists ([31, 32] and references therein). The models we selected are consistent with the fact that the three gauge coupling constants determined at LEP and SLC agree with $SU(5)$ GUT predictions and with the predictions of the other embedding groups as $SO(10)$ GUT. The three coupling constants are unified at 2×10^{16} GeV. The contributions from SUSY particles play a relevant role in the renormalization-group evolution of the coupling constants, as discussed in the previous paragraph. For this reason the $SU(5)$ or $SO(10)$ SUSY – GUT groups appear to be well-based extensions of the Standard Model.

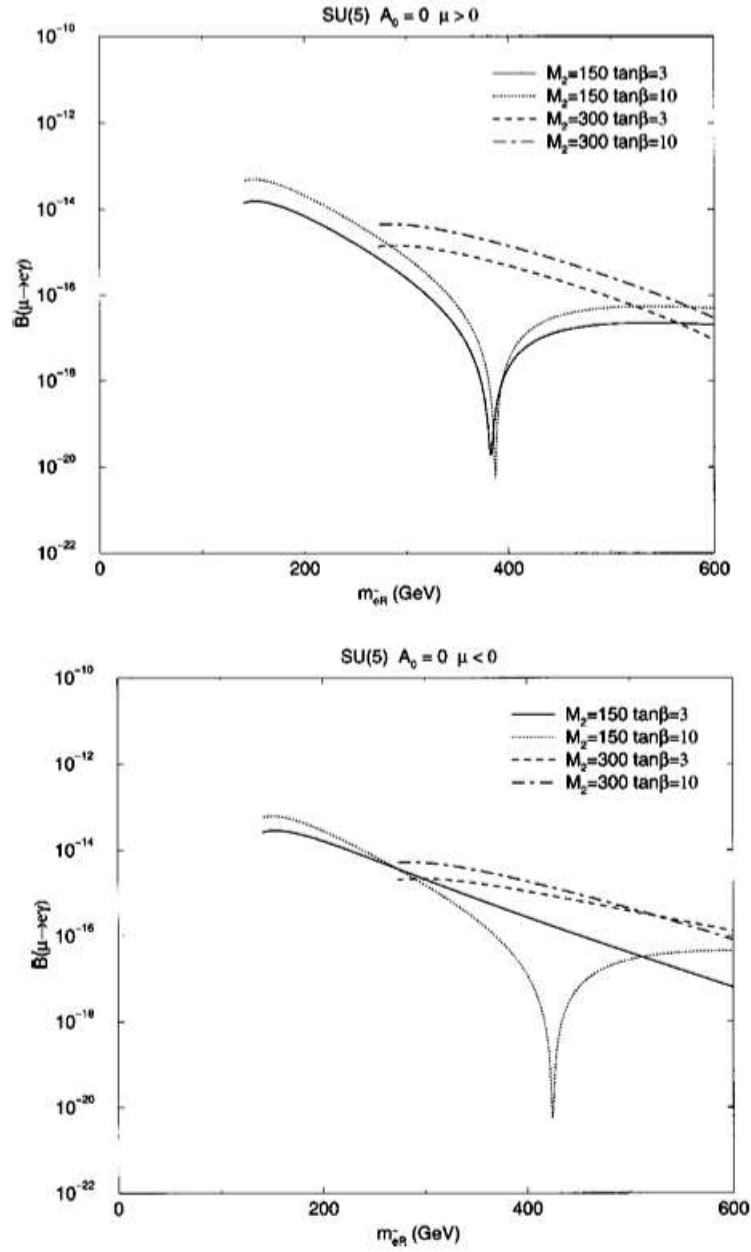


Figure 1.5: Predicted branching ratios for the $\mu^+ \rightarrow e^+\gamma$ decay in the SU(5) SUSY – GUT model [31].

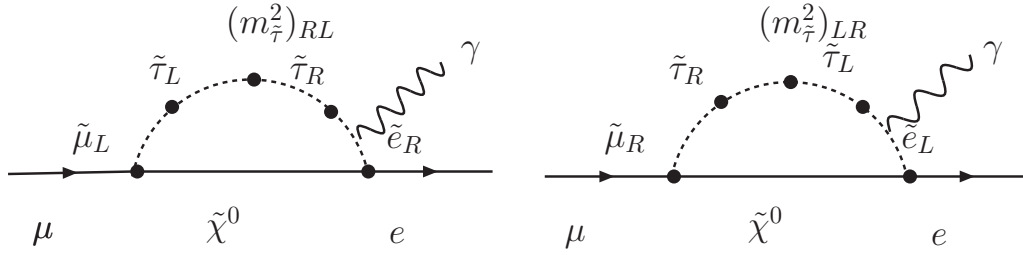


Figure 1.6: Dominant Feynman diagrams in the $SO(10)$ SUSY – GUT model for the $\mu^+ \rightarrow e^+\gamma$ decay.

In the $SU(5)$ SUSY – GUT framework, LVF is induced by a mismatch of the lepton and slepton diagonalization. The diagonal terms of the slepton mass matrix can be examined on the basis where the Yukawa coupling constant for lepton is diagonalized. The off-diagonal elements of the right-handed slepton mass matrix on this basis become a source of LVF through the diagrams in Fig. 1.4. The predictions for the branching ratio of $\mu^+ \rightarrow e^+\gamma$ decay are presented in Fig. 1.5. The branching ratio reaches about 10^{-14} for slepton mass of few hundred GeV/c^2 . The plot shows the branching ratio of the $\mu^+ \rightarrow e^+\gamma$ decay as a function of the right-handed slepton mass matrix element. Some parameters of the theory are fixed. In particular the figure refers to a set of the SUSY input parameters: the $SU(2)$ gaugino mass, indicated as M_2 and the ratio of the two Higgs vacuum expectation values, $\tan \beta$.

Large LVF are expected in the $SO(10)$ SUSY-GUT model. In the minimal $SO(10)$ SUSY-GUT both the left-handed and the right-handed sleptons are subject to LVF effects. A large contribution is from the diagrams shown in Fig. 1.6, where the m_τ is involved. In this case, the prediction for the branching ratio of $\mu^+ \rightarrow e^+\gamma$ decay is enhanced by $(m_\tau/m_\mu)^2$ compared to the predictions of the minimal $SU(5)$ SUSY-GUT. The branching ratio of the muon LFV processes as a function of the right-handed slepton mass is shown in the Fig. 1.7. The SUSY input parameters are the same as in Fig. 1.5. The branching ratio becomes comparable to the present experimental upper bounds.

Finally, in the $SO(10)$ SUSY-GUT framework, Fig. 1.8 shows the branching ratio for the $\mu^+ \rightarrow e^+\gamma$ decay as a function of the $M_{1/2}$ parameter, scanning the LHC accessible SUSY-GUT parameter space at a fixed values of $\tan \beta$ and for two theoretical cases (see [33]). The horizontal lines are the present (MEGA) and the MEG experimental sensitivities.

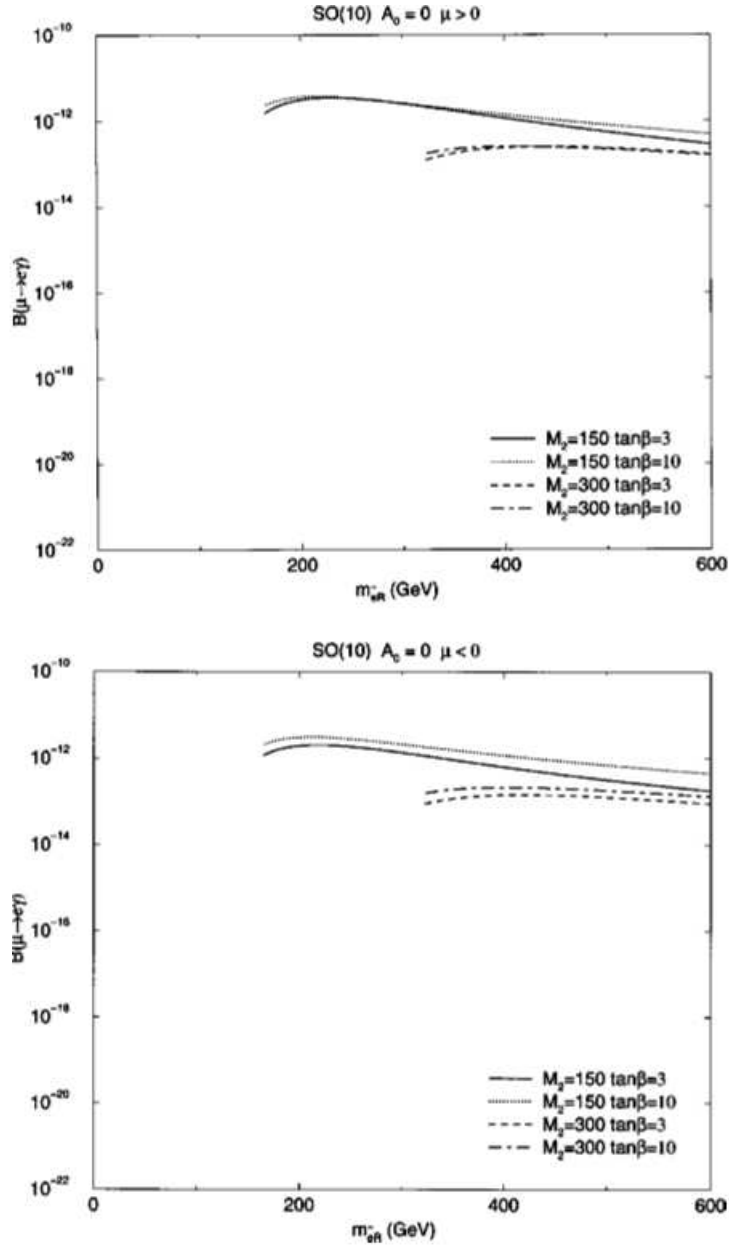


Figure 1.7: Predicted branching ratios for the $\mu^+ \rightarrow e^+ \gamma$ decay in the $SO(10)$ $SUSY - GUT$ model [31].

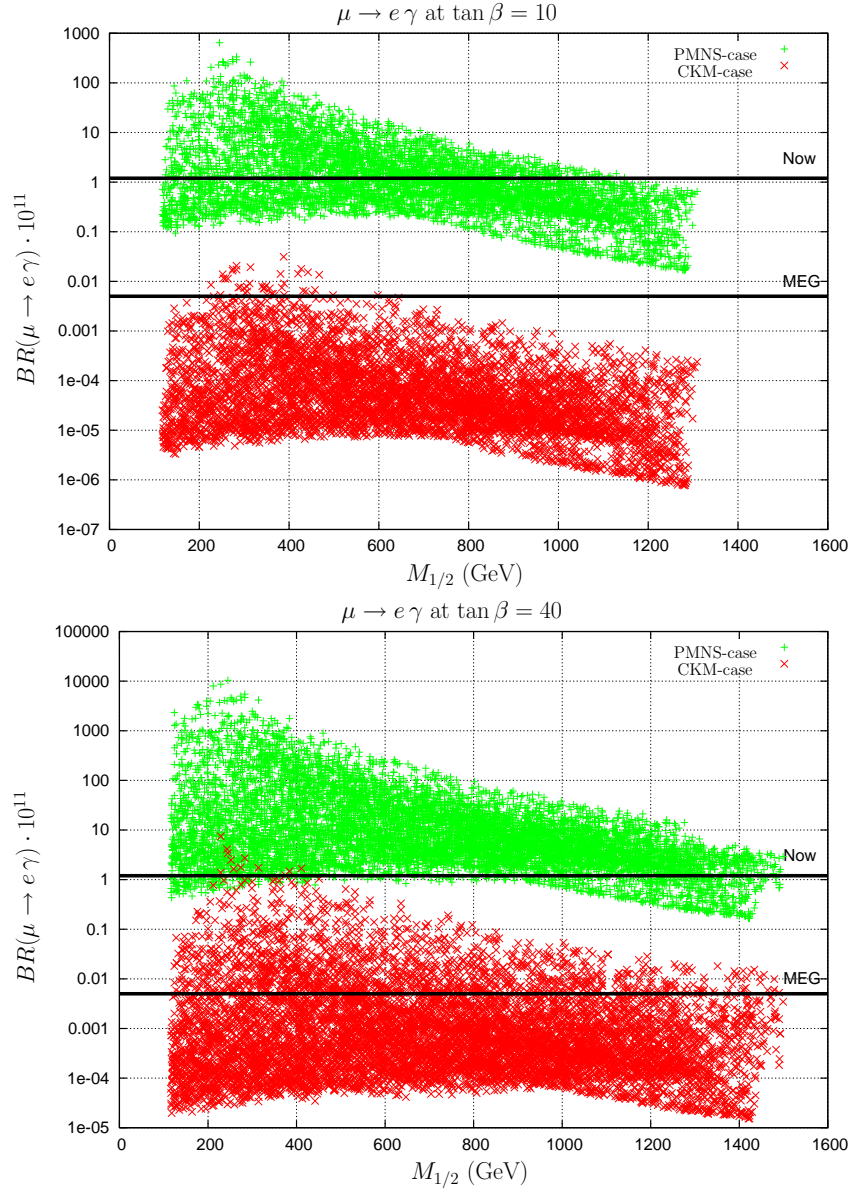


Figure 1.8: $BR(\mu \rightarrow e \gamma)$ vs. $M_{1/2}$ for the $SO(10)$ SUSY – GUT model. The plots refer to the LHC accessible SUSY-GUT parameter space at fixed values of $\tan \beta$. The horizontal lines are the present (MEGA) and the future (MEG) experimental upper limit [33].

Chapter 2

The $\mu \rightarrow e\gamma$ decay. A survey

This chapter presents a survey of $\mu \rightarrow e\gamma$ decay as a fundamental physical process and as an important tool for investigating crucial theoretical issues. The repeated experiments, performed over the years, were characterized by the use of muon beams of increasing intensity and by the use of detectors with increasingly improved performances. This allowed an increasing sensitivity in the search for the rare decay under study and an effective background rejection.

The various background sources affecting the $\mu \rightarrow e\gamma$ decay are discussed in connection with the characteristics of previous experiments. The properties of our experiment are then examined. The potentialities of MEG emerge by comparison.

2.1 The search for $\mu^+ \rightarrow e^+\gamma$

The motivations for a research into $\mu^+ \rightarrow e^+\gamma$ decay changed in the course of time, but the process always maintained a fundamental role.

The muon was discovered in 1937 by Neddermeyer and Anderson in cosmic ray cloud chamber pictures [173]. The particle had both positive and negative charge and a mass approximately 200 times that of the electron. It was thought to coincide with the one predicted by Yukawa as the short-range strong force mediator.

Conversi, Pancini and Piccioni later proved this to be untrue [35]. The muon was a baffling discovery as it seemed to have no particular purpose. It behaves exactly like a heavy electron and it decays into an electron in 2.2×10^{-6} s [36, 37] (and so is not found in ordinary matter).

Pontecorvo was the first to raise the question: “*is the electron emitted by the meson with a mean life of about 2.2 microseconds accompanied by a γ of about 50 MeV?*” [38].

The search for the $\mu^+ \rightarrow e^+\gamma$ decay starts in 1947 [39, 40] and a first upper limit was reached: $B(\mu^+ \rightarrow e^+\gamma) < 10\%$ [41]. The experiment used Geiger-Muller counters to detect the meson and the decay particles. The result also excluded the emission of a new type of meson in the muon decay and it supported the evidence for a muon decay to an electron and two neutrinos (requiring $1/2$ spin for the μ -meson).

The assumption was at the same time made of a universal interaction acting among spin- $\frac{1}{2}$ particles and, as a consequence, what was known of the β decay applied also to the muon process [42, 43].

The hypothesis that two like neutrinos were ejected in μ decay had now a theoretical support. The observable secondary electron spectrum was predicted by Michel [44]. Data on which to fit the Michel theory were soon available [45]. The annihilation of the charged particle emitted by the μ^+ decay identified it as a positron.

Although the theory could adequately explain the experimental observations, it could not equally well explain what was not observed. In particular the decay of a muon into an elec-

tron and a γ was not observed despite being a perfectly valid electromagnetic transition. The $\mu^+ \rightarrow e^+\gamma$ search went on and a new upper limit, four orders of magnitude better, was achieved [46]. The π^+ mesons were stopped in a carbon target and two detectors, one for the 50 MeV electrons and the other for the γ rays after conversion in a lead layer, were placed at the opposite sides of the target. The system was calibrated with electrons from the normal μ decay. An upper limit of 2×10^{-5} was reached for the $\frac{\mu^+ \rightarrow e^+\gamma}{\mu^+ \rightarrow \text{tot}}$ branching ratio.

This result and the prediction of $B(\mu^+ \rightarrow e^+\gamma) \approx 10^{-4}$ [47], based on the hypothesis of a universal Fermi interaction mediated by a charged vector boson, proposed by Feynman and Gell-Mann [48], seemed inconsistent. However, the fashionable intermediate vector boson of the weak interaction is not ruled out if some selection rules apply forbidding $\mu^+ \rightarrow e^+\gamma$. Such selection rules were first proposed by Konopinski and Mahmoud, supposing that μ and e have opposite quantum numbers [42]. Later on, additive or multiplicative conservation laws were proposed involving two sorts of neutrinos: one associated with electrons, the other with muons [49]. The electron-type neutrinos ν_e can never transform into muons, nor muon-type neutrinos ν_μ into electrons. The neutron β -decay only involves electron-type antineutrinos and the muon decay of the negative pion only involves muon-type antineutrinos. All this means that the lepton conservation law is associated with that of the lepton type (flavour) conservation; both the electron number and the muon number must be separately conserved in each reaction.

Meanwhile a new upper limit was achieved: $B(\mu^+ \rightarrow e^+\gamma) < 6 \times 10^{-8}$ at 90% C.L. ([50]), supporting the idea that some selection rule prevents the unobserved $\mu^+ \rightarrow e^+\gamma$ decay.

As written by Feinberg, Kabir and Weinberg “*the absence of such transformation does not constitute a paradox, there being no compelling reason why muons should transform into electrons, but it seems a mystery that processes which are allowed energetically and in every other known respect do not occur*” [51].

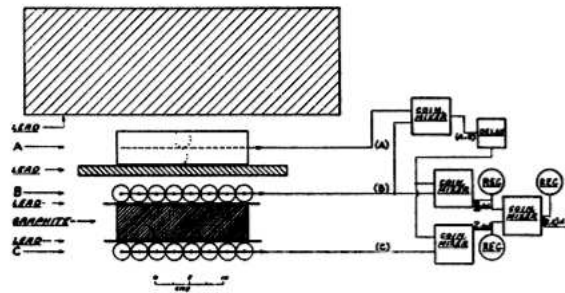
The distinction between electron- and muon-neutrinos was confirmed at Brookhaven in (1962) [52], by using the first source of high-energy neutrinos, following the original idea for an accelerator experiment, independently proposed by Pontecorvo and Schwartz.

A new upper limit: $B(\mu^+ \rightarrow e^+\gamma) < 3.6 \times 10^{-9}$ at 90% C.L. [53] was obtained at TRIUMF, using two large NaI(Tl) crystals viewing the pion stopping target and detecting the positron and the γ from the $\mu^+ \rightarrow e^+\gamma$ decay at rest. The experiment had improved energy resolutions, checked by measurements of the positron Michel spectrum and by measuring the π^0 decay into two γ 's ($\pi^0 \rightarrow 2\gamma$).

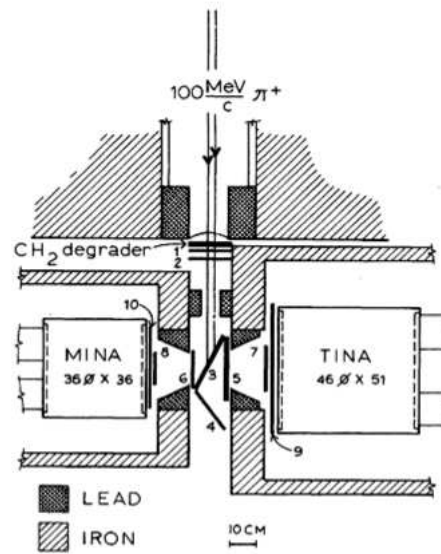
A new generation of $\mu^+ \rightarrow e^+\gamma$ decay experiments started in the eighties, using muon beams instead of pion beams. A new upper limit was obtained: $B(\mu^+ \rightarrow e^+\gamma) < 1 \times 10^{-9}$ [54].

Another order of magnitude was gained at LAMPF [55] by improving the selection of collinear events. The apparatus measured energy, direction, relative timing and origin of both positron and γ . The magnetic spectrometer was equipped with multiwire proportional chambers (MWPC's) and plastic-scintillators. A segmented array of NaI(Tl) crystals was used for the γ ray measurement. A large-gap sweeping magnet, placed between the NaI(Tl) array and the target, protected the former from the flux of charged particles. An upper limit: $B(\mu^+ \rightarrow e^+\gamma) < 1.7 \times 10^{-10}$ at 90% C.L. was obtained.

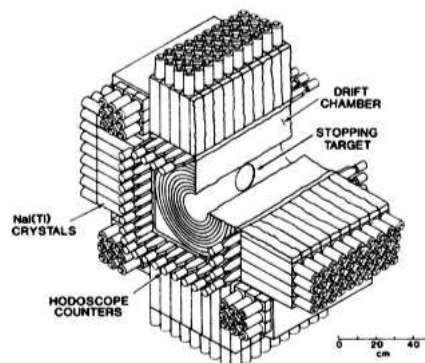
Again in the eighties the Standard Model predictions were thoroughly studied at CERN. Vector bosons were discovered (1982) and all SM predictions were confirmed at a high level of precision. The model had nevertheless no explanation for the replication of fermion families and had no prediction for fermion masses and weak mixings, etc. In this framework, the conservation of lepton flavour appeared as an accidental conservation law, not associated with either a space-time symmetry or with the existence of a massless gauge boson[57]. On the experimental side, the Crystal Box experiment, a general-purpose detector, reached new standards of sophistication and precision.



(a) The first $\mu^+ \rightarrow e^+\gamma$ experiment (1948). Cosmic rays are the source of muons [41]



(b) The TRIUMF experiment (1977). A pion beam is the source of muons [53];



(c) The Crystal Box experiment (1988). The experiment simultaneously search for $\mu \rightarrow e\gamma$, $\mu \rightarrow e\gamma\gamma$ and $\mu \rightarrow eee$ [56];

Figure 2.1: Set-up of some $\mu^+ \rightarrow e^+\gamma$ experiments.

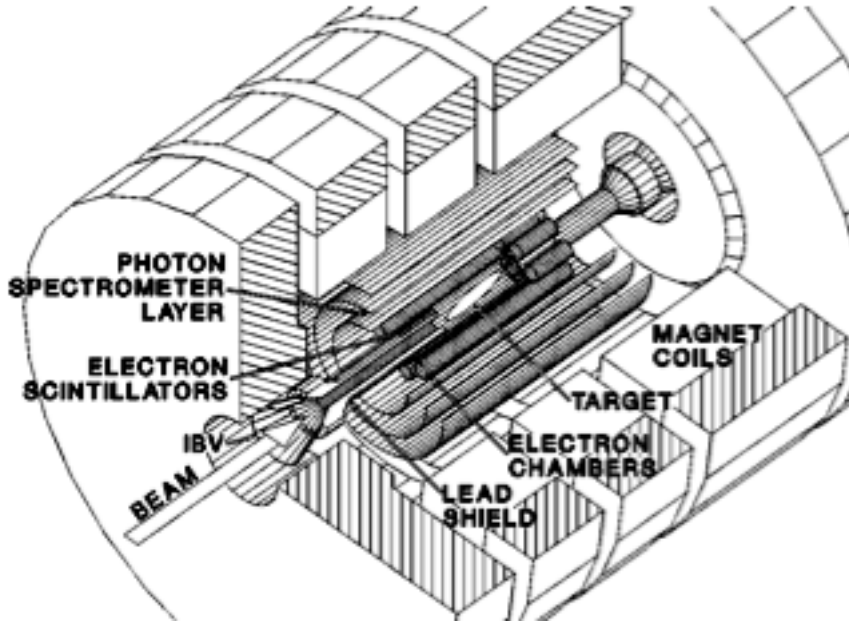


Figure 2.2: The MEGA experiment (2002). The most recent $\mu^+ \rightarrow e^+\gamma$ experiment [4].

The beam was a so-called “surface muon beam”, the angular acceptance of the set-up was very wide. An array of 396 NaI(Tl) crystals surrounded the polystyrene target and a cylindrical drift chamber was used as the central tracking device. Precise measurements of the energy, direction and timing of the decay products were effective in rejecting unwanted backgrounds. An upper limit: $B(\mu^+ \rightarrow e^+\gamma) < 4.9 \times 10^{-11}$ was established [56].

A general-purpose detector is, however, not optimized for any single channel. The following MEGA experiment was intended to be more specialized and optimized for detecting the $\mu^+ \rightarrow e^+\gamma$ decay in a background-free environment, if its branching ratio was greater than 10^{-13} .

The MEGA goal was to obtain a more precise measurement of the γ and positron momentum. A high precision, two-section magnetic spectrometer was assembled: (1) a low-mass multiple-wire proportional chamber system (MWPC’s) for tracking the positron plus a series of plastic scintillators for timing, (2) a pair spectrometer to convert and detect the γ ’s and measure their characteristics.

The replacement of the total absorption calorimeter, used in previous experiments, with a pair spectrometer was a trade-off between detection efficiency and momentum resolution. A new upper limit: $B(\mu^+ \rightarrow e^+\gamma) < 1.2 \times 10^{-11}$ at 90% C.L. was established [4].

Fig. 2.1 and Fig. 2.2 show the set-up of some of previous $\mu^+ \rightarrow e^+\gamma$ experiments and Fig. 2.3 shows the improvements of the 90% C.L. upper limits for the $\mu^+ \rightarrow e^+\gamma$ decay branching-ratio as the years go by.

The $\mu^+ \rightarrow e^+\gamma$ chronicle stops here, having reached the birth of the MEG experiment. Before describing MEG, it is convenient to discuss signal and background in detail. The latter must be efficiently rejected and therefore affect the design of the MEG set-up.

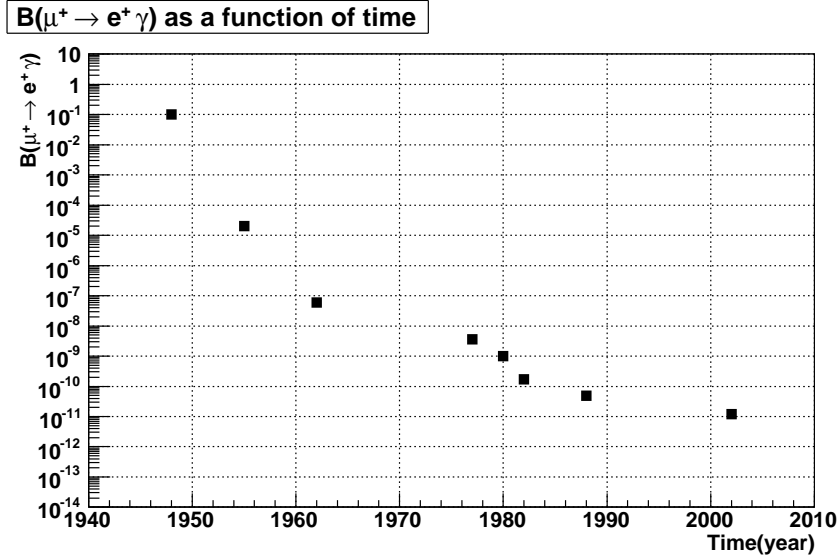


Figure 2.3: The improvement of the 90% C.L. upper limit on the $\mu^+ \rightarrow e^+ \gamma$ decay branching ratio as a function of the time.

2.2 Event signature and backgrounds

The event signature of $\mu^+ \rightarrow e^+ \gamma$ decay at rest is a positron and a γ in coincidence, moving collinearly back-to-back with their energies equal to half the muon mass ($m_\mu/2 = 52.8$ MeV). If we assume CPT invariance, this decay is equivalent to $\mu^- \rightarrow e^- \gamma$, but the former is more convenient from the experimental point-of-view, because of μ^+ can be stopped without being captured by a nucleus of the target.

Two kinds of background are present.

The correlated background from the radiative muon decay, $\mu^+ \rightarrow e^+ \nu_e + \bar{\nu}_\mu \gamma$, when the positron and the γ are emitted in the opposite directions and the two neutrinos take away a small amount of energy.

The accidental background due to an accidental coincidence between a positron from the normal muon decay, $\mu^+ \rightarrow e^+ \nu_e \bar{\nu}_\mu$, and a high energy γ from the radiative muon decay $\mu^+ \rightarrow e^+ \nu_e \bar{\nu}_\mu \gamma$, annihilation in flight, or external bremsstrahlung of positrons from normal muon decay.

2.2.1 Correlated background

The correlated background, from the radiative muon decay, $\mu^+ \rightarrow e^+ \nu_e \bar{\nu}_\mu \gamma$ (branching ratio = 1.4 % for $E_\gamma > 10$ MeV), when the positron and the γ are emitted in opposite directions and the two neutrinos take away a small amount of energy, is an important background for the $\mu^+ \rightarrow e^+ \gamma$ decay. The differential decay width was calculated as a function of the positron energy (E_e) and the γ energy (E_γ) normalized to their maximum energies, namely, $x = 2E_e/m_\mu$ and $y = 2E_\gamma/m_\mu$ [58, 59]. The variables x and y vary between $0 \leq x, y \leq 1$. The dangerous region is for $x \approx 1$ and $y \approx 1$ and the angle between the positron and the γ directions, $\theta_{e\gamma}$ almost 180° . The differential decay width of $\mu^+ \rightarrow e^+ \nu_e \bar{\nu}_\mu \gamma$ was computed as a function of x , y and $z = \pi - \theta_{e\gamma}$ and expanded in the region $x \approx 1$, $y \approx 1$ and $z \approx 0$.

When $x = 1$ and $y = 1$ exactly, the decay width vanishes. However, in an actual experiment, finite detector resolutions would produce the acceptance of background events limiting the sensitivity of a $\mu^+ \rightarrow e^+ \gamma$ search. This can be estimated by integrating the differential decay width over the signal box:

$$\begin{aligned}
dB(\mu^+ \rightarrow e^+\nu_e\bar{\nu}_\mu\gamma) &= \\
&= \frac{1}{\Gamma(\mu^+ \rightarrow e^+\nu_e\bar{\nu}_\mu)} \int_{1-\delta x}^1 dx \int_{1-\delta y}^1 dy \int_0^{\min[\delta z, 2\sqrt{(1-x)(1-y)}]} dz \frac{d\Gamma(\mu^+ \rightarrow e^+\nu_e\bar{\nu}_\mu\gamma)}{dxdydz} \\
&= \frac{\alpha}{16\pi} [J_1 \cdot (1 - P_\mu \cos\theta_e) + J_2 \cdot (1 + P_\mu \cos\theta_e)] d(\cos\theta_e), \tag{2.1}
\end{aligned}$$

where δx , δy and δz are half-widths of the $\mu^+ \rightarrow e^+\gamma$ signal region. $\Gamma(\mu^+ \rightarrow e^+\nu_e\bar{\nu}_\mu)$ is the total muon decay width, and J_1 and J_2 are:

$$J_1 = (\delta x)^4 (\delta y)^2 \quad \text{and} \quad J_2 = \frac{8}{3} (\delta x)^3 (\delta y)^3 \quad \text{for } \delta z > 2\sqrt{\delta x \delta y}. \tag{2.2}$$

or

$$\begin{aligned}
J_1 &= \frac{8}{3} (\delta x)^3 (\delta y) \left(\frac{\delta z}{2}\right)^2 - 2(\delta x)^2 \left(\frac{\delta z}{2}\right)^4 + \frac{1}{3} \frac{1}{(\delta y)^2} \left(\frac{\delta z}{2}\right)^8 \\
J_2 &= 8(\delta x)^2 (\delta y)^2 \left(\frac{\delta z}{2}\right)^2 - 8(\delta x)(\delta y) \left(\frac{\delta z}{2}\right)^4 + \frac{8}{3} \left(\frac{\delta z}{2}\right)^6 \\
&\text{for } \delta z \leq 2\sqrt{\delta x \delta y}. \tag{2.3}
\end{aligned}$$

Fig. 2.4 shows the accepted fraction of the $\mu^+ \rightarrow e^+\nu_e\bar{\nu}_\mu\gamma$ decay for given δx and δy values, with unpolarized muons in case of $\delta z \leq 2\sqrt{\delta x \delta y}$. It can be seen that both δx and δy of about 0.01 are needed to achieve a sensitivity limit around 10^{-15} .

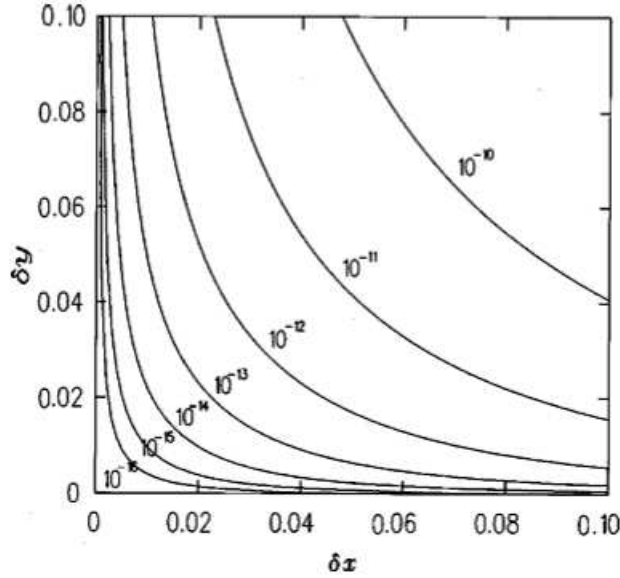


Figure 2.4: Branching ratio due to the background from the radiative decay. The variables are the relative e^+ energy resolution δx and the γ energy resolution δy [31].

2.2.2 Accidental background

The reaching of the greatest possible sensitivity in a reasonable time requires an intense muon beam. In this case, as for the MEG experiment, the accidental background is more important than the correlated background.

The rate of the accidental background normalized to the total decay rate, B_{acc} , is:

$$B_{acc} = R_\mu \cdot f_e^0 \cdot f_\gamma^0 \cdot \Delta t_{e\gamma} \cdot \left(\frac{\Delta\omega_{e\gamma}}{4\pi} \right), \quad (2.4)$$

where R_μ is the muon rate. f_e^0 and f_γ^0 are the integrated fractions of the positron and γ spectrum in normal muon decay ($\mu^+ \rightarrow e^+ \nu_e \bar{\nu}_\mu$) and in muon radiative decay ($\mu^+ \rightarrow e^+ \nu_e \bar{\nu}_\mu \gamma$), within the signal region. They include their corresponding branching ratios. The terms $\Delta t_{e\gamma}$ and $\Delta\omega_{e\gamma}$ refer to the full widths of the signal regions for the timing coincidence and for the angular constraint on the e^+ and γ collinearity.

B_{acc} can be evaluated once the size of the signal region is defined. δx , δy , $\delta\theta_{e\gamma}$, and $\delta t_{e\gamma}$ are, the half-widths of the relative positron energy, relative γ energy, $\theta_{e\gamma}$ collinearity angle, and relative e^+ and γ timing.

f_e^0 can then be estimated by integration of the Michel spectrum of normal over $1 - \delta x \leq x \leq 1$, yielding: $f_e^0 \approx 2(\delta x)$.

The angular resolution $\delta\theta_{e\gamma}$ on the collinearity angle gives $\Delta\omega_{e\gamma}/4\pi = (\delta\theta_{e\gamma})^2/4$.

f_γ^0 is related to the radiative muon decay $\mu^+ \rightarrow e^+ \nu_e \bar{\nu}_\mu \gamma$ or to e^+ annihilation from the normal muon decay $\mu^+ \rightarrow e^+ \nu_e \bar{\nu}_\mu$. As an example, in the first case, the differential branching ratio must be integrated over 2π for θ_γ , and then over the γ energy within the width of the signal region ($1 - \delta y \leq y \leq 1$). For unpolarized muons, one obtains:

$$\begin{aligned} f_\gamma^0 &= \int_{1-\delta y}^1 dy \int d(\cos\theta_\gamma) \frac{dB(\mu^+ \rightarrow e^+ \nu_e \bar{\nu}_\mu \gamma)}{dy d(\cos\theta_\gamma)} \\ &\approx \left(\frac{\alpha}{2\pi} \right) (\delta y)^2 [\ln(\delta y) + 7.33]. \end{aligned} \quad (2.5)$$

Eq. (2.5) shows that f_γ^0 is roughly proportional to $(\delta y)^2$.

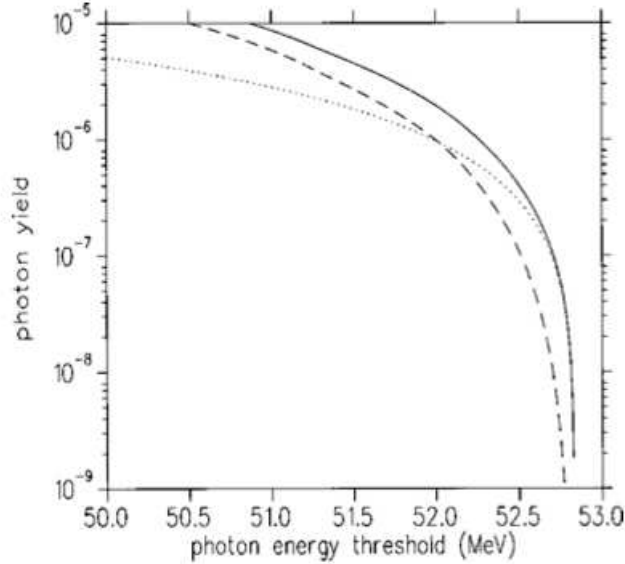


Figure 2.5: Integrated background rates as a function of the γ energy. Dotted line: e^+ annihilation in flight; dashed line: radiative muon decay. The solid line is the sum of the dotted and dashed line [31].

Positron annihilation in flight (or external bremsstrahlung) in normal muon decay gives contributions which depend on the amount of material along the positron path. Fig. 2.5 shows the

Table 2.1: Progress in the search for $\mu^+ \rightarrow e^+\gamma$ decay. Resolutions: (FWHM).

| Laboratory | Year | ΔE_e | ΔE_γ | $\Delta t_{e\gamma}$ (<i>ns</i>) | $\Delta\theta_{e\gamma}$ (<i>mrاد</i>) | Upper Limit. | Ref |
|------------|------|--------------|-------------------|---------------------------------------|---|-----------------------|------|
| TRIUMF | 1977 | 10% | 8.7% | 6.7 | | 3.6×10^{-9} | [53] |
| SIN | 1980 | 8.7% | 9.3% | 1.4 | | 1.0×10^{-9} | [54] |
| LANL | 1982 | 8.8% | 8% | 1.9 | 37 | 1.7×10^{-10} | [55] |
| LANL | 1988 | 8% | 8% | 1.8 | 87 | 4.9×10^{-11} | [56] |
| LANL | 2002 | 1.2% | 4.5% | 1.6 | 15 | 1.2×10^{-11} | [4] |
| PSI | 2008 | 0.7 – 0.9% | 4% | 0.15 | 17 – 20.5 | $\approx 10^{-13}$ | [60] |

contribution of the annihilation in flight for positrons passing through a muon-stopping target of 50-mg thickness. The contribution from the target is normally smaller than the muon radiative decay, being important only if the γ energy resolution is extremely good. This point will be fully discussed in the last chapter, keeping track of all the materials present in the experiment.

In summary the effective branching ratio of the accidental background is:

$$B_{acc} = R_\mu \cdot (2\delta x) \cdot \left(\frac{\alpha}{2\pi} (\delta y)^2 [\ln(\delta y) + 7.33] \right) \cdot \left(\frac{\delta\theta_{e\gamma}^2}{4} \right) \cdot (2\delta t_{e\gamma}). \quad (2.6)$$

For some realistic values: 1% (FWHM) for the positron energy resolution, 5% (FWHM) for the γ energy resolution, $\Delta\omega_{e\gamma} = 3 \times 10^{-4}$ steradian, $\Delta t_{e\gamma} = 1$ ns and $R_\mu = 3 \times 10^8 \mu^+/s$, B_{acc} is 2.5×10^{-13} .

Further considerations are contained in the last chapter of this thesis, in connection with the resolutions achieved during the engineering run.

2.3 $\mu^+ \rightarrow e^+\gamma$ decay NOW

One can treasure what one obtained from the study of previous experiments to optimize the search for $\mu \rightarrow e\gamma$ with the MEG experiment.

The ability of an experiment to identify the signal and to reject background depends on the detector resolutions in measuring the relevant four-momenta, in our case: those of the positron and of the γ .

A precise measurement of the positron relies on a magnetic spectrometer (drift chambers + superconducting magnet). This is similar to what MEGA did, but MEG has a magnet with an additional field gradient to get rid of low momentum positrons and to reduce the number of unwanted hits in the drift chambers. Good timing is obtained by fast scintillation counters.

Standard γ calorimetry, based on NaI(Tl) crystal arrays, provides a good energy measurement, but poor timing. MEG decided to develop an innovative calorimetry based on the use of liquid xenon. The new detector combines a good γ energy determination with an optimum timing resolution.

In the two following chapters the MEG detectors are described, in particular focusing on the new liquid xenon calorimeter.

Tab. 2.1 summarizes the upper limits on the $\mu^+ \rightarrow e^+\gamma$ branching ratio, obtained by the last experiments. The associated experimental resolutions and the expected MEG resolutions are also reported.

Part II

The MEG experiment and the LXe calorimeter

Chapter 3

The MEG experiment

In this chapter the principles of the measurement of the $\mu^+ \rightarrow e^+\gamma$ decay at rest are discussed. The MEG detectors and their expected performances are presented. The trigger system and the data acquisition are described.

3.1 Principles of measurement

The aim of the MEG experiment [60] is to measure the branching ratio of the rare muon decay $B = \frac{\mu^+ \rightarrow e^+\gamma}{\mu^+ \rightarrow \text{TOT}}$ with a sensitivity of $\approx 10^{-13}$, two orders of magnitude lower than the last measurement by the MEGA collaboration [4].

The signature for a $\mu^+ \rightarrow e^+\gamma$ decay at rest is the simultaneous emission of the two daughter particles, in opposite directions and with the same energies $E_\gamma = E_{e^+} = m_\mu/2 = 52.8$ MeV. In order to identify the $\mu^+ \rightarrow e^+\gamma$ decay, one has to precisely measure the energies of the two particles, their relative angle and time coincidence.

The sensitivity of an experiment searching for rare muon decays improves linearly with the number of observed muons, if the background is lower than the possible signal.

For a muon beam intensity of $R_\mu \approx 10^7 - 10^8 \mu^+/\text{sec}$, an observation period equivalent to one year (10^7 sec) and a total detection efficiency of 10%, $\approx (10^{13} - 10^{14})\mu^+$ decays can be observed, and a branching ratio sensitivity ($10^{-14} - 10^{-13}$) is reached.

The MEG experiment was built at PSI, in Switzerland, the laboratory hosting the world's most intense continuous muon beam ($3 \times 10^8 \mu^+/\text{s}$).

The positron trajectory and momentum are measured by the magnetic spectrometer COBRA, consisting of a superconducting magnet (1.24 T at the center) and by a set of 16 drift chambers.

The positron timing is measured by a timing counter, two arrays of 30 plastic scintillator bars, one at each side of the target, and two sets of scintillating optical fibers, one for each array.

The γ energy, direction and timing are measured by the liquid xenon calorimeter.

A schematic layout of the MEG detector is shown in the Fig. 3.1 and Fig. 3.2 [60]. The coordinate system is such that the z-axis lies along the incoming beam direction. The plane orthogonal to this direction is called the r- ϕ plane, and we will use rectangular (x, y, z), cylindrical (r, z, ϕ) or spherical (ρ , θ , ϕ) coordinates. The origin of the reference system is the target center which is also the center of experiment ($x = y = z = 0$).

Tab. 3.1 summarizes the expected resolutions of the MEG detector. They will be described in more details in the following sections.

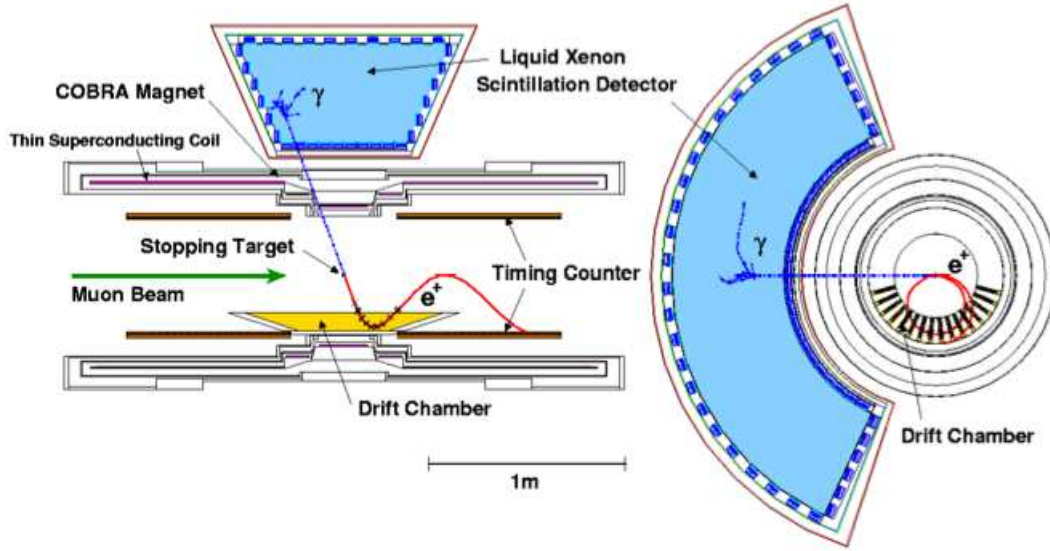


Figure 3.1: *Schematic view of the MEG detector.*

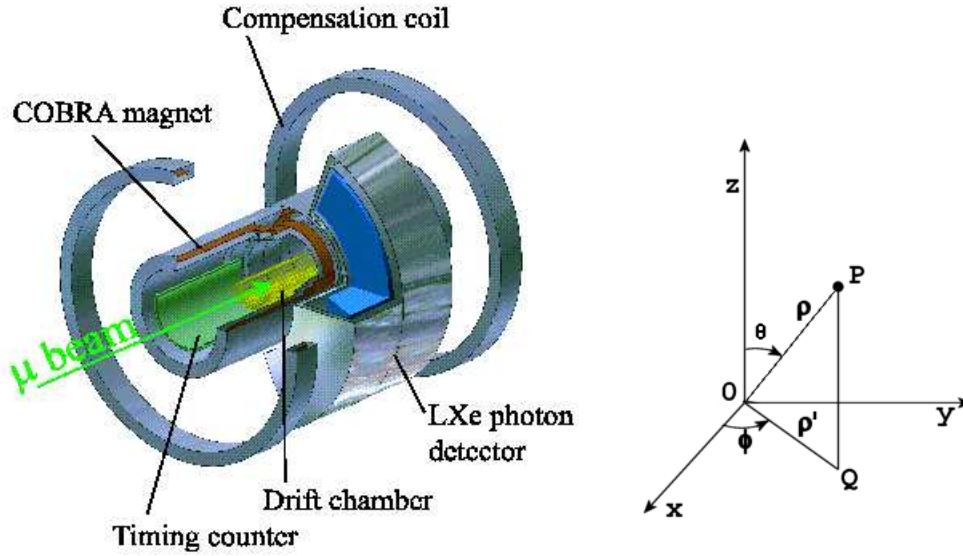


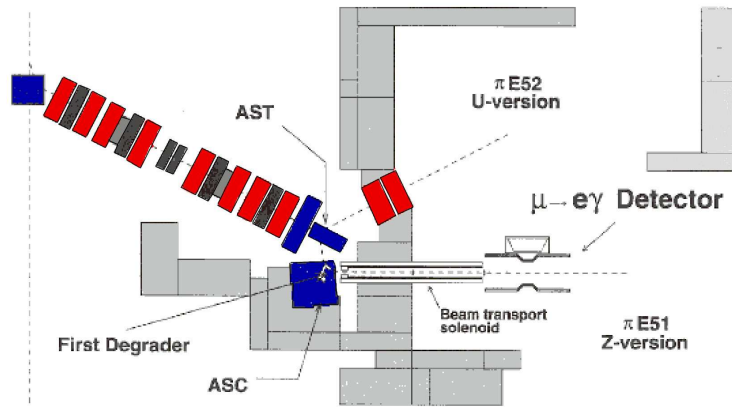
Figure 3.2: *3D view of the MEG detector. Coordinate system.*

Table 3.1: MEG expected resolutions and upper limit on the branching ratio.

| $\Delta E_\gamma / E_\gamma$ | $\Delta p_e / p_e$ | $\Delta t_{e\gamma}$ | $\Delta \theta_{e\gamma}$ | Upper Limit BR($\mu \rightarrow e\gamma$) |
|------------------------------|--------------------|----------------------|---------------------------|---|
| 4.5 % | 0.7=0.9 % | 150 ps | 17-21 mrad | 1.2×10^{-13} |

Table 3.2: Main properties of the PSI cyclotron proton beam.

| | |
|-------------------------------|--|
| Injection energy | 72 MeV |
| Extraction energy | 590 MeV |
| Extraction momentum | 1.2 GeV/c |
| Relative energy spread (FWHM) | ca. 0.2% |
| Beam emittance | ca. $2 \text{ mm} \times \pi \text{ mrad}$ |
| Beam current | 1.8 mA DC |
| Accelerator frequency | 50.63 MHz |
| Time between pulses | 19.75 ns |
| Bunch width | ca. 0.3 ns |

Figure 3.3: The $\pi E5$ beam and the MEG experimental hall.

3.2 The μ^+ -beam and the target

Two types of muon beam operation are present in muon factories: a pulsed or a continuous (DC) operation. In a pulsed beam the muons are grouped into bunches of definite time width, separated by time intervals with no muon present. The ratio of the bunch width to the total period is the *duty cycle* of the beam. In a DC operation the muons are continuously generated and the duty cycle is approximately one. For a given muon flux, the peak rate is higher in a pulsed beam. The dominant background source, the accidental coincidence of a high energy γ and a high energy positron from two different muon decays in a $\mu^+ \rightarrow e^+\gamma$ search experiment, quadratically increases as a function of the *instantaneous* muon rate, since each daughter particle comes from a different muon. The $\mu^+ \rightarrow e^+\gamma$ signal and the background from prompt coincidences, grow instead only linearly, since the two daughter particles originate from the same muon. A continuous muon beam is therefore preferable to a pulsed beam.

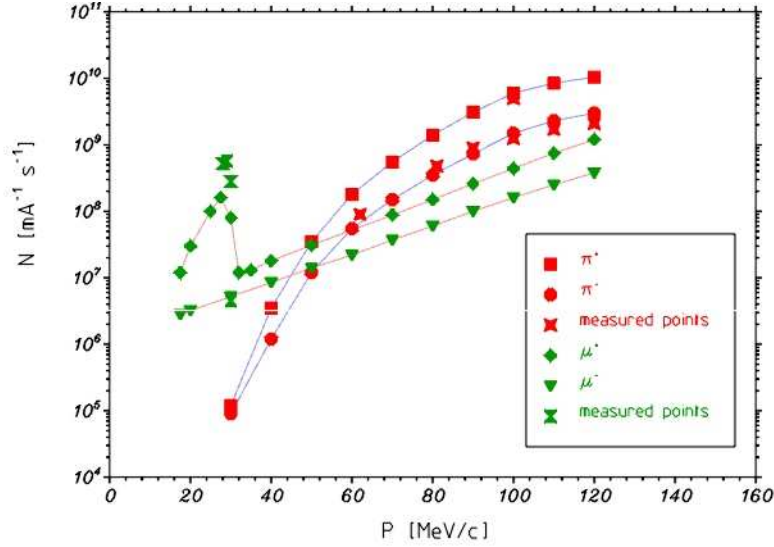
The PSI cyclotron accelerates protons (current 1.8 mA) to an energy of 590 MeV. Secondary beams of pions are generated at two target stations. The main properties of the proton beam are listed in the Tab. 3.2. Past the meson production targets, the beam is either stopped in a beam dump or refocused on the target of a high flux spallation neutron source (SINQ).

The two target stations feed seven secondary pion and muon beam-lines. The $\pi E5$ channel is the one dedicated to the MEG experiment (with two possible configurations U and Z (Fig. 3.3)). $\pi E5$ is the highest flux pion and muon beam.

Pions and muons at low energy are extracted from a thick primary target (40 mm or 60 mm

Table 3.3: Main properties of the $\pi E5$ beam-line.

| | |
|-------------------------------------|---------------------|
| Solid angle acceptance | 150 msr |
| Momentum range | 20-120 MeV/c |
| Length | 10.4 m |
| Relative momentum band (FWHM) | 10% |
| Relative momentum resolution (FWHM) | 2 % |
| Horizontal emittance | 15.3 cm· rad |
| Vertical emittance | 3.6 cm· rad |
| Spot size | 4×4 cm ² |

Figure 3.4: The $\pi E5$ beam line. Muon and pion fluxes, as a function of momentum.

thick in the direction of the proton beam), at an angle of 175° with respect to the primary proton beam. The main characteristics of the beam are listed in the Tab. 3.3. The muons for MEG are the so-called *surface-muons* [61], [62] and [63] i.e.: muons from pions decaying at rest in the primary target. The kinetic energy and the momentum of these surface-muons are ≈ 3.6 MeV and 29 MeV/c respectively. Their range in graphite is ≈ 1 mm; the surface-muons are therefore produced only by π^+ -pion decaying close to the target surface.

Fig. 3.4 shows the different particle measured fluxes, as a function of the momentum, in the $\pi E5$ beam line. The higher μ^+ -flux around 29 MeV/c is associated with surface-muons and is an effect due to the pion decay kinematics. The use of a low momentum muon beam when searching for muon decaying at rest in a target offers the advantage of a very thin muon stopping region. The range straggling is given by the expression:

$$\Delta R = a \left\{ \left[\left(\frac{200m_e}{M} \right)^{1/2} f \left(\frac{E}{Mc^2} \right) \right]^2 + \left(3.5 \frac{\Delta p}{p} \right)^2 \right\}^{1/2} \cdot p^{3.5} \quad (3.1)$$

where the first term is associated with the statistic nature of the particle slowing-down [209], and the second term is associated with the initial beam momentum width (the empirical 3.1 is only valid for $p < 100$ MeV/c).

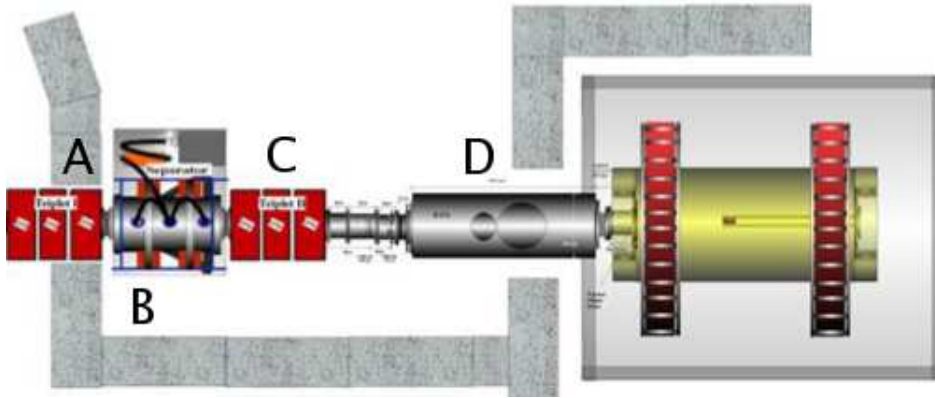


Figure 3.5: $\pi E5$ area. End elements of the muon beam line.

3.2.1 The MEG beam line

The last part of the beam line, inside the $\pi E5$ area, is optimized according to the following needs:

- reduction of the spurious particles in the beam;
- coupling of the μ^+ -beam-line with the high field COBRA magnet;
- reduction of the muon momentum for stopping the beam in a thin target.

Studies were made with several moderators and particle selecting devices. The final beam design contains the following elements, shown in Fig. 3.5:

- a quadrupole triplet to re-focus the beam after the ASC bending magnet, the one in the wall separating the $\pi E5$ area from the rest of the remaining part of the experimental hall (item A);
- an electrostatic separator (a Wien filter) to reduce the positron content of the μ^+ -beam. After the separator, the positrons in the μ^+ -beam are less than 1% (item B). The positrons are dumped on a collimator, far from the Cobra target. The positrons and muons separation, shown in Fig. 3.6, is equal to 7.2σ , where σ quadratically combines the separated σ 's of the muon and positron beams;
- a second quadrupole triplet refocuses the muon beam after the positron separation (item C);
- a transport solenoid (BTS) for coupling the beam to the COBRA magnet. In the middle of the transport solenoid, at a beam focus, a μ^+ -momentum degrader (Mylar sheet of $300 \mu\text{m}$ of thickness) is inserted (item D).

The corresponding muon beam has an intensity of $3 \times 10^8 \mu^+/\text{sec}$, with transverse dimensions at the COBRA center: $\sigma_x = 10 \text{ mm}$ and $\sigma_y = 11 \text{ mm}$.

3.2.2 The target

The target is an elliptical shaped CH_2 sheet of $210 \times 70 \text{ mm}^2$, a thickness of $175 \mu\text{m}$, mounted at an angle of 22° relative to the muon beam direction. This choice of angle maximizes the CH_2 thickness crossed by the beam and minimizes the outgoing positron energy loss. The target is in an atmosphere of He. The ensemble degrader+target corresponds to the best choice of materials (high radiation length) for background suppression and beam quality. Finally, the target

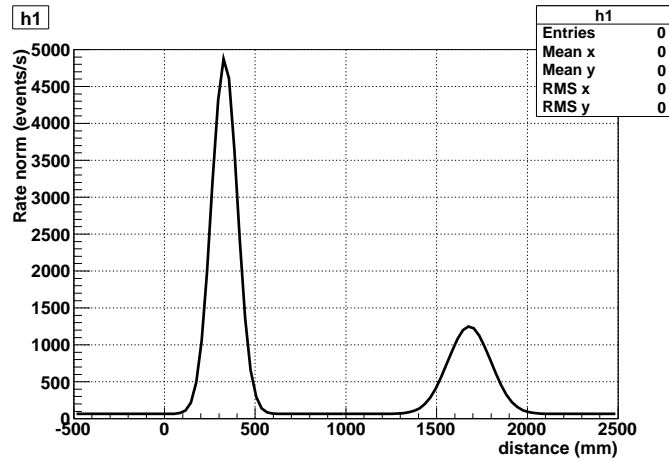


Figure 3.6: Muon (right) and positron (left) separation by an electrostatic Wien filter.

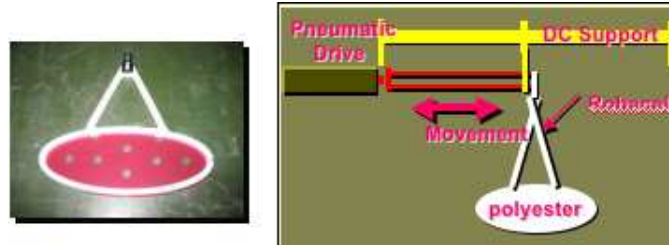


Figure 3.7: Muon target and the He pressurized insertion system.

depolarizes the muon beam, which is originally highly polarized, due to the $\pi^+ \rightarrow \mu^+ \nu_\mu$ decay at rest.

The target is handled by a He pressurized insertion system capable of moving the target from the parking position (upstream along the beam line, at ≈ 20 cm from the COBRA center, allowing the introduction of the target for the CW proton beam) to the normal position, at the COBRA center.

The Fig. 3.7 shows a scheme of the target and of the pneumatic insertion system.

3.3 The positron spectrometer

The positron momentum and direction are measured by means of the COBRA spectrometer, composed of the COBRA superconducting magnet and by 16 Drift Chambers (see Fig. 3.8); the time of flight is measured by a scintillation counter system, called the Timing Counter.

The magnetic field map, the positions of the Drift Chamber and Timing Counter were chosen to satisfy these requirements (with the following properties):

- the abundant low momentum positrons from muon decays (the Michel's positrons) are swept away from the MEG target, without hitting the chambers and the counters. The COBRA disuniform magnetic field is so shaped as to make the projected (in the x-y plane) radius of the positron trajectory depend only on the modulus of the momentum, whatever the positron direction. Low momentum trajectories are confined to a small radius cylindrical region. Rates remain low in the drift chamber system;

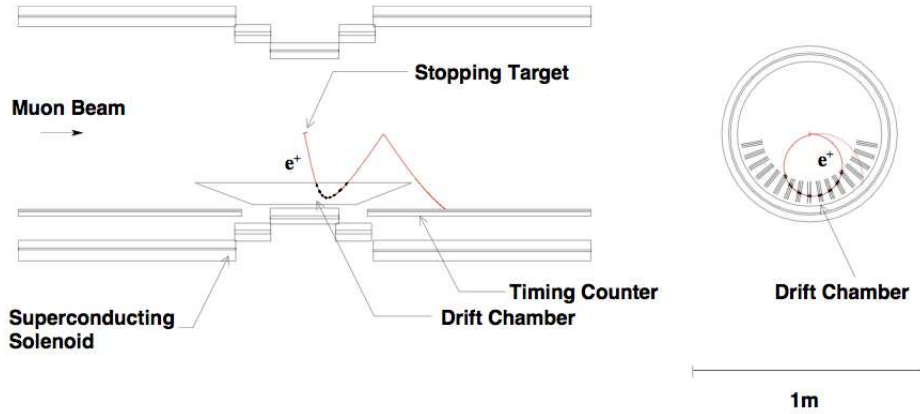


Figure 3.8: Schematic view of the positron spectrometer.

Table 3.4: Parameters of the COBRA magnet

| Coil | Central | Gradient | Inner end | Outer end | Compensation |
|-----------------|---------|----------|-----------|-----------|--------------|
| Conductivity | Super | Super | Super | Super | Resistive |
| Inner dia. (mm) | 700 | 810 | 920 | 920 | 2210 |
| Outer dia. (mm) | 712.4 | 820.6 | 929.5 | 929.5 | 2590 |
| Length (mm) | 240.3 | 110.4 | 189.9 | 749.2 | 265 |
| Layers | 4 | 4 | 3 | 3 | 14 |
| Inductance (H) | 1.64 | 0.62 | 0.35 | 2.29 | 0.54 |
| I (A) | 360 | 360 | 360 | 360 | 360 |
| Energy E (kJ) | 106 | 40 | 23 | 148 | 35 |
| Weight M (Kg) | 9 | 4 | 7 | 28 | 1620 |
| E/M (KJ/Kg) | 11.8 | 10.0 | 3.3 | 5.3 | 0.02 |

- positrons emitted at large angles relative to the magnet axis are rapidly removed from the target region in the case of the COBRA disuniform field. The number of multi-turn trajectories crossing the chambers is minimized and the reconstruction of the higher momentum trajectories is greatly simplified.

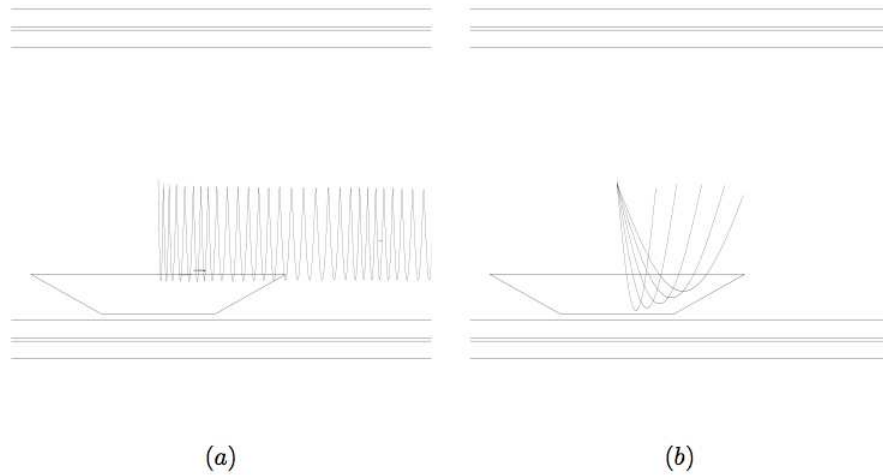
Fig. 3.9 illustrates the behaviour of the positron trajectories in the case of a uniform solenoidal magnetic field and in the case of the COBRA disuniform magnetic field.

3.3.1 The COBRA magnet

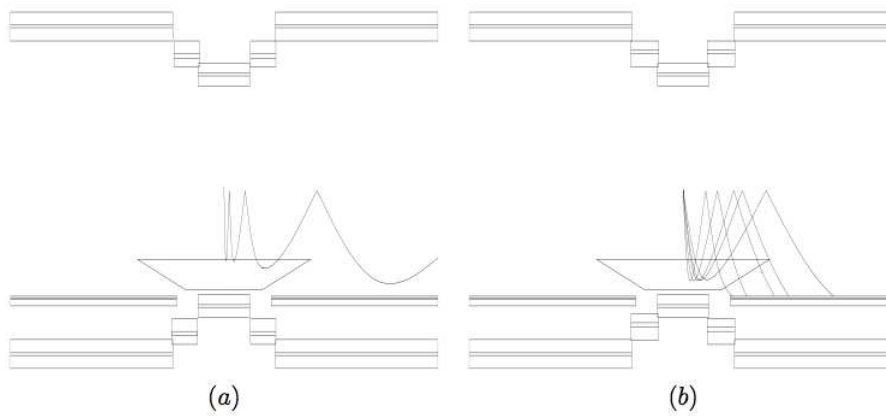
The COBRA (COntant Bending RAdius) magnet consists of a main superconducting magnet and a pair of compensation (non superconductive) coils.

The main magnet is designed to generate a gradient magnetic field; this optimizes the behaviour of the tracking system, as previously discussed. It consists of five coils with three different radii: one central, two gradient, and two end coils. Their parameters are listed in Tab. 3.4. The field profile along the magnet axis is shown in Fig. 3.10. The disuniform field has a central 1.24 T maximum and decreases as it moves towards the spectrometer limits.

The compensation coils were introduced to reduce the stray magnetic field in the region of the γ detector, a necessity for its proper operation. The stray field might degrade the performance of the liquid xenon detector because of the fast PMT gain reduction as a function of the magnetic



(a) Problems with a uniform solenoidal magnetic field: (a) r-z view of the solenoid with the trajectory of a positron emitted at 88° crossing several times the DC system. (b) Trajectories relative to a fixed momentum positron with various angles of emission. The bending radius depends on the angle of emission.



(b) Advantages present in the case of a disuniform magnetic field: (a) r-z view of the COBRA spectrometer with the trajectory of a positron emitted at 88° . The particle is swept away much more quickly than in the previous case. (b) Trajectories relative to a fixed momentum positron with various angles of emission. The bending radius is independent of the angle of emission.

Figure 3.9: Comparison between a uniform and a disuniform magnetic field.

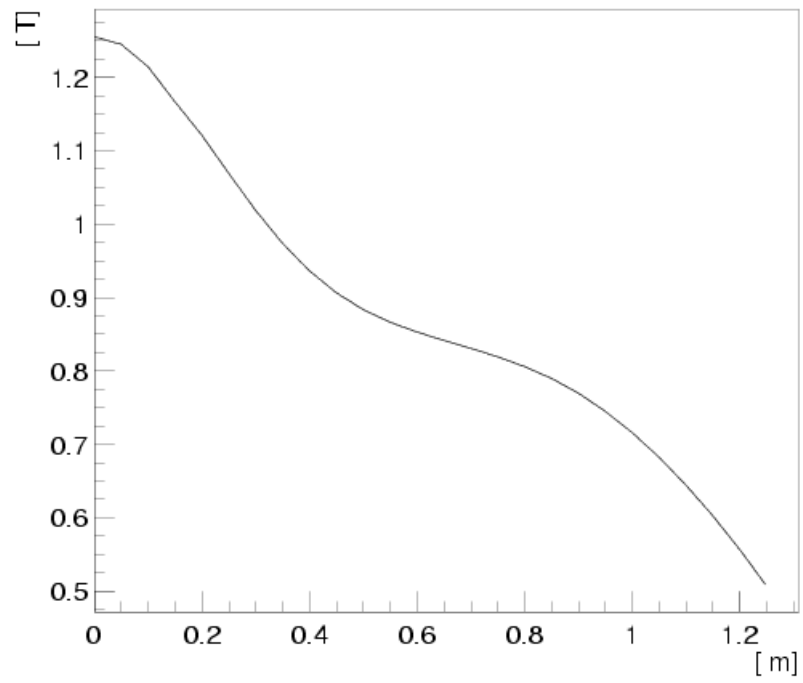


Figure 3.10: *Magnetic field intensity along the magnet axis.*

field intensity [65]. Fig. 3.11 (on the top) shows the relative outputs of the PMT HAMAMATSU R6041Q, as a function of the magnetic field intensity and field orientation, where the z-axis is the one of the PMT axis. The tolerance to the magnetic field of the PMT depends strongly on the direction of the applied magnetic field compared to the tube axis.

Fig. 3.11 (on the bottom) shows the contour plot of the magnetic field intensity produced by the COBRA spectrometer. The stray field intensity is small over the LXe detector region.

3.3.2 The Drift Chambers

Positron trajectories are determined with 16 drift chamber sectors radially aligned at 10.5° intervals in azimuth (see Fig. 3.12). Each sector is made up of two staggered trapezoidal arrays of drift cells. The sensitive area of the chamber extends from a radius of 19.3 cm to a radius of 27.0 cm. The active region extends up to $z = \pm 50$ cm at the inner radius and $z = \pm 21.9$ cm at the outer radius. 29 MeV/c positrons emitted from the target with $|\cos\theta| < 0.35$ and $|\phi| < 60^\circ$ are accepted by the system.

The resolutions on the measurements of momentum and angle are primarily limited by multiple scattering in the chamber materials and gas. Particular care was paid to reduce this effect.

Fig. 3.13 shows the structure of a chamber sector and gives some information about the method of the measurement. The chamber wall, working as a cathode, is made of an extremely thin, $12.5 \mu\text{m}$ thick polyamide foil, with a 250 nm aluminum coating. An array of sense (anode) and potential wires, fixed to a carbon fiber frame, is mounted inside the chambers. The carbon frame has only three sides and it is open towards the target. This *open-frame* makes wire and foil stretching more challenging, but keeps the amount of material to a minimum; the overall material crossed by the typical trajectory of a 52.8 MeV/c positron corresponds to $0.002 X_0$.

The drift chamber system is filled with a 50% He - 50 % C_2H_6 gas mixture and is surrounded by 100 % pure He at 1 atm. Such a choice corresponds to a sufficient ionization loss in the chamber gas ($\approx 65 \text{ e}^-/\text{cm}$ for minimum ionizing particles) and to the minimization of multiple Coulomb scattering effects on trajectories.

The staggered-cell configuration allows the simultaneous measurement of the r-coordinate and of the absolute time of a chamber-sector positron crossing. The difference between the drift times $t_1 - t_2$ in two adjacent cells gives the r-coordinate of the track with 100-200 μm accuracy, while the mean time $(t_1 + t_2)/2$ gives the absolute time of the sector crossing with $\approx 5 \text{ ns}$ accuracy. This excellent timing resolution is important for the pattern recognition.

The z-coordinate (muon beam direction) along the wire is determined by the ratio of the charges observed at both ends of the sensitive wire, with an accuracy of $\approx 1 \text{ cm}$. The thin layer of aluminum deposit on the four cathode foils is patterned to make a 5 cm period *Zig-Zag-strip*, called *Vernier pattern* as shown in Fig. 3.13. Consequently, the ratio of charges induced on each pad gives the z-coordinate precisely to an accuracy of 300-500 μm .

The results from the first prototype (with a square-framed support), tested in Tokyo with β -particles from a ^{90}Sr source, are shown in Tab. 3.5. The second prototype, built at the PSI (with an open-frame support), confirmed the results of the first prototype, and it was successfully operated in a 1 Tesla magnetic field using beam particles (electrons, pions and muons).

Predictions for the spectrometer resolutions were obtained by a GEANT simulation taking into account the characteristics and the distribution of all materials. 52.8 MeV positrons were generated and their trajectories were reconstructed using several methods. The resulting momentum resolution is in the range 0.7-0.9 % (FWHM) and the angular resolution is in the range 9-12 mrad (FWHM). The positron origin can be reconstructed with a resolution in the range 2.1-2.5 mm.

3.3.3 The Timing Counter

The Timing Counter (TC) was designed to measure the positron timing with a resolution of 100 ps (FWHM). This fast detector is used, at the trigger level, for selecting events in which a positron is

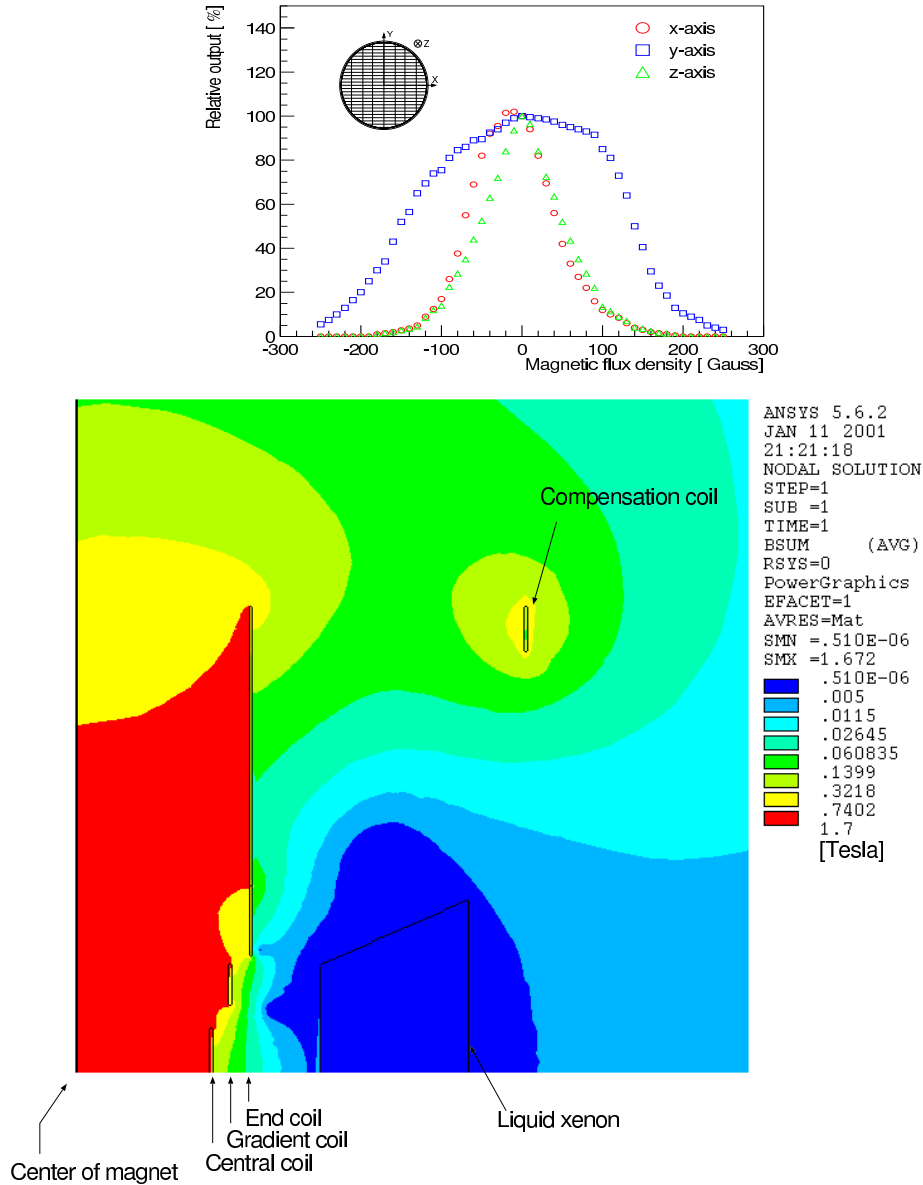


Figure 3.11: *LXe* calorimeter relative PMT outputs, as a function of the magnetic field intensity (top). Contour plot of the residual magnetic field intensity (bottom).

Table 3.5: The resolutions achieved in the test of the first drift chamber prototype.

| Method | | Resolution |
|------------|-------------------------------|-----------------------|
| σ_r | drift time measurement | 100-150 μm |
| σ_z | Vernier cathode measurement | 425 μm |
| σ_z | charge division measurement | 2 cm |
| σ_t | drift velocity and drift time | 4-12 ns |

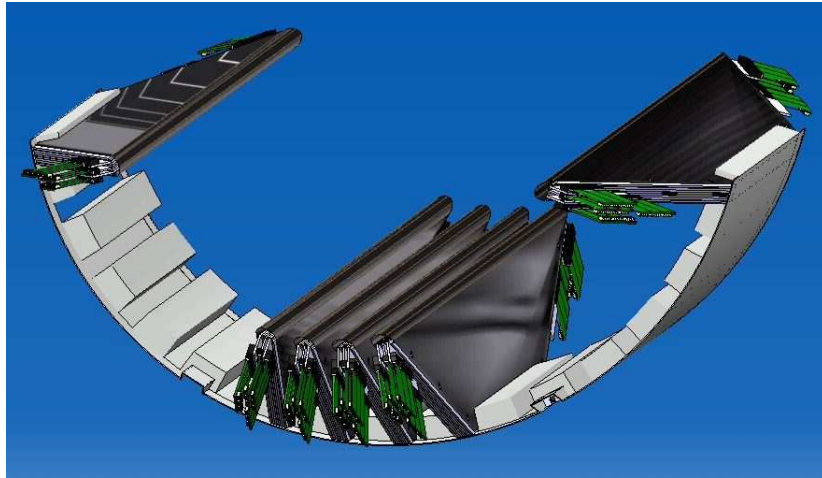


Figure 3.12: Schematic view of the drift chamber system.

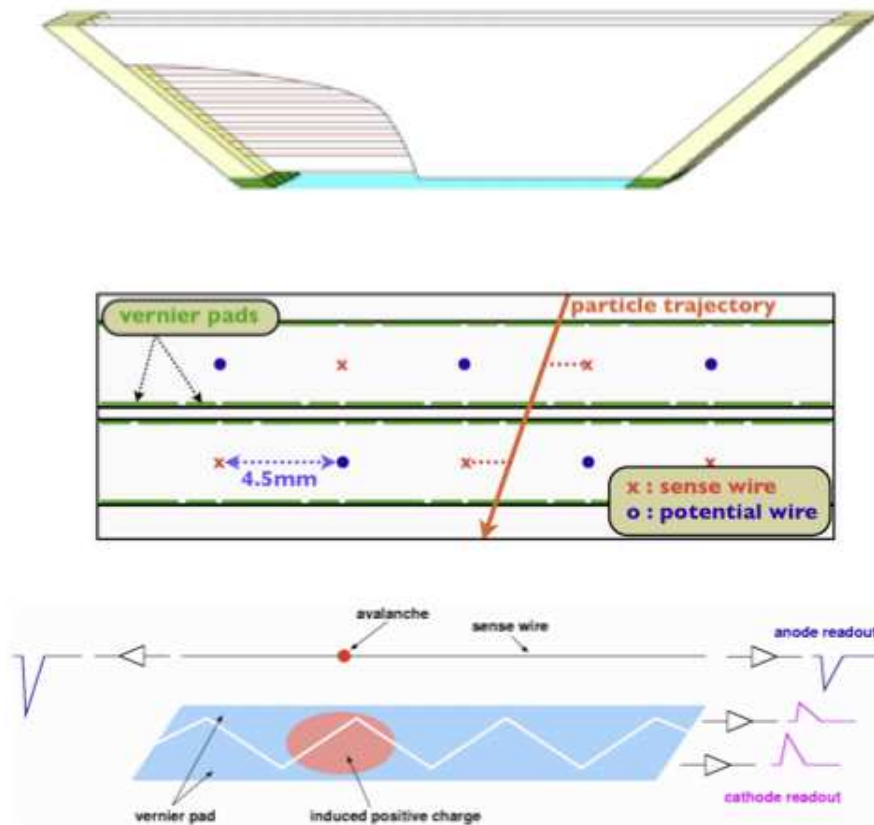


Figure 3.13: (Top) side view of a drift chamber sector. The frames stretching wires and foils are shown schematically. (Middle) a cross-section view of a chamber sector. One can see two layers of drift cells, staggered by half a cell. (Bottom) a schematic view of the Vernier pad system.

coincident in time and collinear in direction, with a γ detected in the electromagnetic calorimeter.

Two plastic scintillator hodoscopes, half cylinders coaxial with COBRA (made up of 15 scintillator bars) are placed on both side of the positron spectrometer to detect positrons and provide timing and trigger signals. The timing counter layout is shown in Fig.3.14. One can see the z-oriented scintillator bars with their PMTs and the tranverse detector made of scintillating fibers with their APDs. The counter arrays are at a 29.5 cm radius, their acceptance in ϕ and z are 145° and $25 < |z| < 95$ cm. The $\mu^+ \rightarrow e^+\gamma$ positrons emitted in the angular range $0.08 < |\cos\theta| < 0.35$ strike the timing counter after completing ≈ 1.5 turns in the r- ϕ plane. The timing counter, the drift chamber system and the LXe calorimeter have equal and correponding acceptances, as derived from kinematics and positron trajectories in COBRA.

The layer of the z-oriented scintillator bars provides an accurate timing of the positron hit, as well as a rough, but fast determination of the corresponding ϕ . Each timing counter scintillator bar (BC404 plastic scintillator, $40 \times 40 \times 780$ mm³) is equipped with two Hamamtsu 2" fine mesh R5924 PMTs. This PMT type can properly operate at high magnetic field ($B \approx 1.5$ T). The PMT axis is not aligned with the field, but has a slant angle of 11° corresponding to an optimized performance (see Fig. 3.15).

The PMT at each bar end measures the pulse height and the arrival time associated with the scintillation light (t_L and t_R). The mean time gives the impact time. The time difference $t_R - t_L$ and the pulse-height ratio give the z-coordinate of the impact point with an accuracy of ± 1 cm.

The transverse detector is made up of two layers of 128 scintillating fibers (BCF20) with square cross-section (5×5 mm²), equipped at both ends with Avalanche Photo Diode (APDs) practically insensitive to the magnetic field. The transverse module provides the z-coordinate of the positron impact point, used to constrain the reconstruction of the positron trajectory and allowing a fast rejection of events with unmatched kinematic parameters.

The timing resolution is mainly limited by the photo-electron statistics and therefore it depends on the path length of a positron crossing the scintillator, which should then be maximized. A detailed Monte Carlo simulation advised an optimized position for the bar, corresponding to a 20° rotation around its axis.

The first test of the finalized TC detector was made in Frascati at the beam test facility. The results are summarized in Fig. 3.16.

3.4 The γ calorimeter

The MEG γ detector is a C-shaped homogeneous Liquid Xenon calorimeter, which represents the most innovative part of the experiment. Its characteristics will be discussed in detail in the following chapters. A first general survey will be given here.

A schematic layout of the γ detector is shown in Fig. 3.17. The detector is entirely outside COBRA. The liquid Xenon starts at 65 cm from the target center and its thickness is 47 cm, sufficient to contain 52.8 MeV γ 's. The fiducial volume of the detector corresponds to a solid angle $\Delta\Omega/4\pi \approx 12\%$ ($|\cos\theta| < 0.35$ and 120° in ϕ).

The LXe calorimeter determines the energy, the timing and the impact point of the γ from the $\mu^+ \rightarrow e^+\gamma$ decay. The detector contains 800 liters of pure liquid xenon. The LXe scintillation light is measured by 846 photomultipliers, immersed in the liquid. A R&D was necessary to ensure that these photomultipliers (Hamamatsu R9869) correctly work at LXe temperature ($\approx -108^\circ\text{C}$), in the vacuum ultra-violet region (Xenon emission line $\lambda_{\text{scin}} = 178$ nm), at high pulse rate (photomultiplier anodic current ≈ 4 μA) (see chapter 5).

The high number of scintillation photons (40000 ph/MeV), the fast time constant (three components $\tau_1 = 4$ ns, $\tau_2 = 22$ ns and $\tau_3 = 45$ ns), the high atomic number ($Z = 54$), the high density (2.95 g/cm³) are desirable characteristics for a calorimeter (see chapter 4).

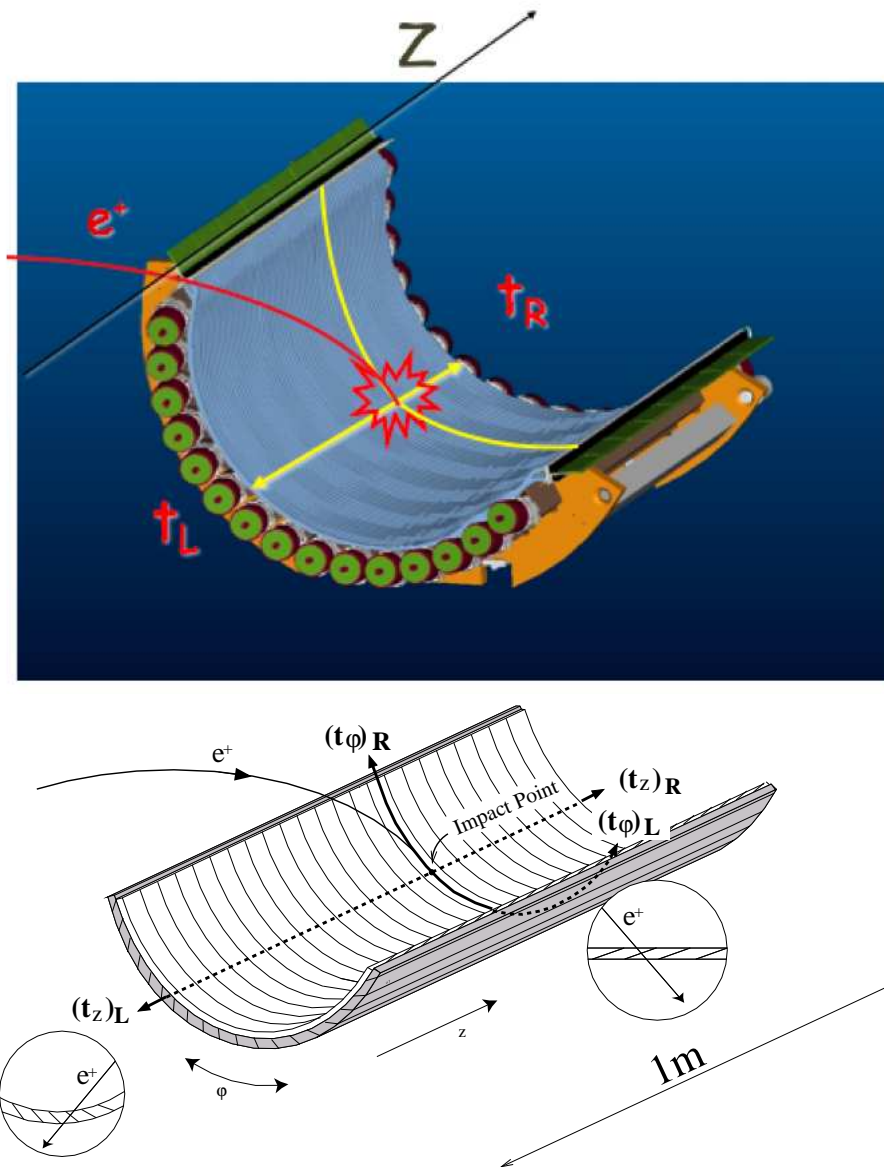


Figure 3.14: *The Timing counter layout and its working principle. The TC bars and the scintillator fibers are shown.*

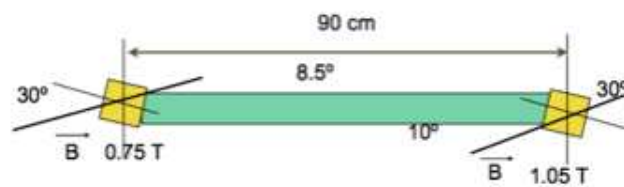


Figure 3.15: *The Timing Counter PMT orientation relative to the magnetic field.*

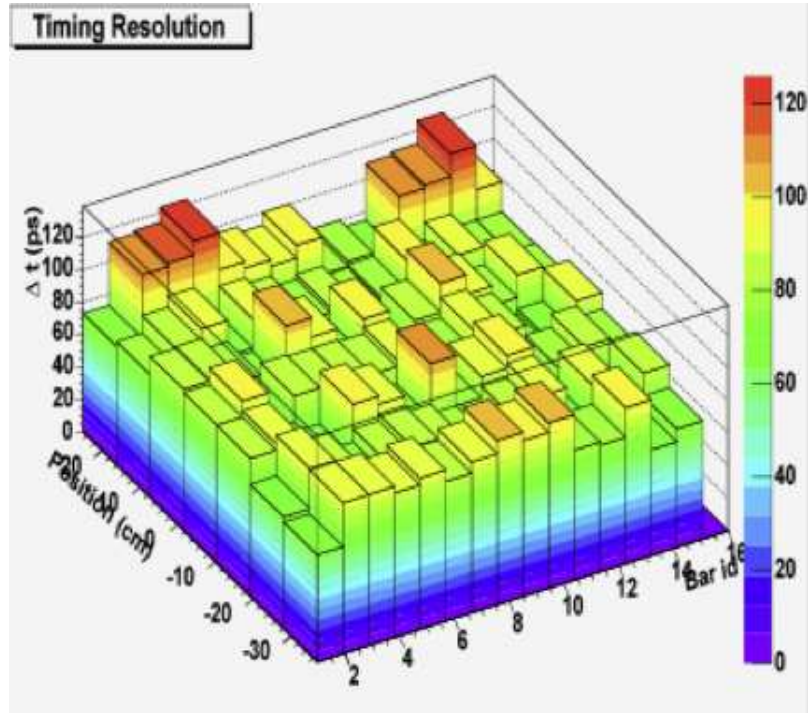


Figure 3.16: *The timing resolution of the scintillator bars along the bar.*

The γ -energy is directly related to the light intensity measured by the PMTs. The γ is supposed to come from the vertex of a companion positron at the target, and its direction is defined once the γ impact point is determined. The information from all PMTs is used to extract the timing of the γ interaction.

Since the calorimeter corresponds to a large volume single vessel, we expect a high rate of low energy γ 's. The waveforms of all PMTs are therefore registered to identify the events in which the accidental pile-up of γ -rays occurs (see section 3.5.2).

The performance of this large volume calorimeter depends largely on the knowledge of the LXe optical properties, in particular, on its transparency (as discussed in detail in the next chapter).

A study based on a detailed Monte Carlo simulation gives the following predictions: an energy resolution $\Delta E_\gamma/E_\gamma(\text{FWHM}) = 4.5\%$, a time resolution $\Delta t_\gamma(\text{FWHM}) \approx 120$ ps and a position resolution $\Delta x(\text{FWHM}) = \Delta y(\text{FWHM}) \approx 1.5$ cm (see Chapter 6).

3.5 The Trigger and DAQ systems

3.5.1 The Trigger system

The trigger system uses the signals coming from the fast detectors (Liquid Xenon calorimeter and Timing Counter) to select, with the great efficiency, the $\mu^+ \rightarrow e^+\gamma$ candidate events, and effectively reject background.

In the following, a short presentation of the trigger algorithm for $\mu^+ \rightarrow e^+\gamma$ is given.

We recall the $\mu^+ \rightarrow e^+\gamma$ signature: a back-to-back γ -positron pair, coincident in time, each particle of energy half of the muon mass. The measurement of the positron momentum by the drift chambers is not used, being too slow. As a consequence, the useful quantities for triggering are:

- the γ energy, time and direction from the LXe calorimeter;

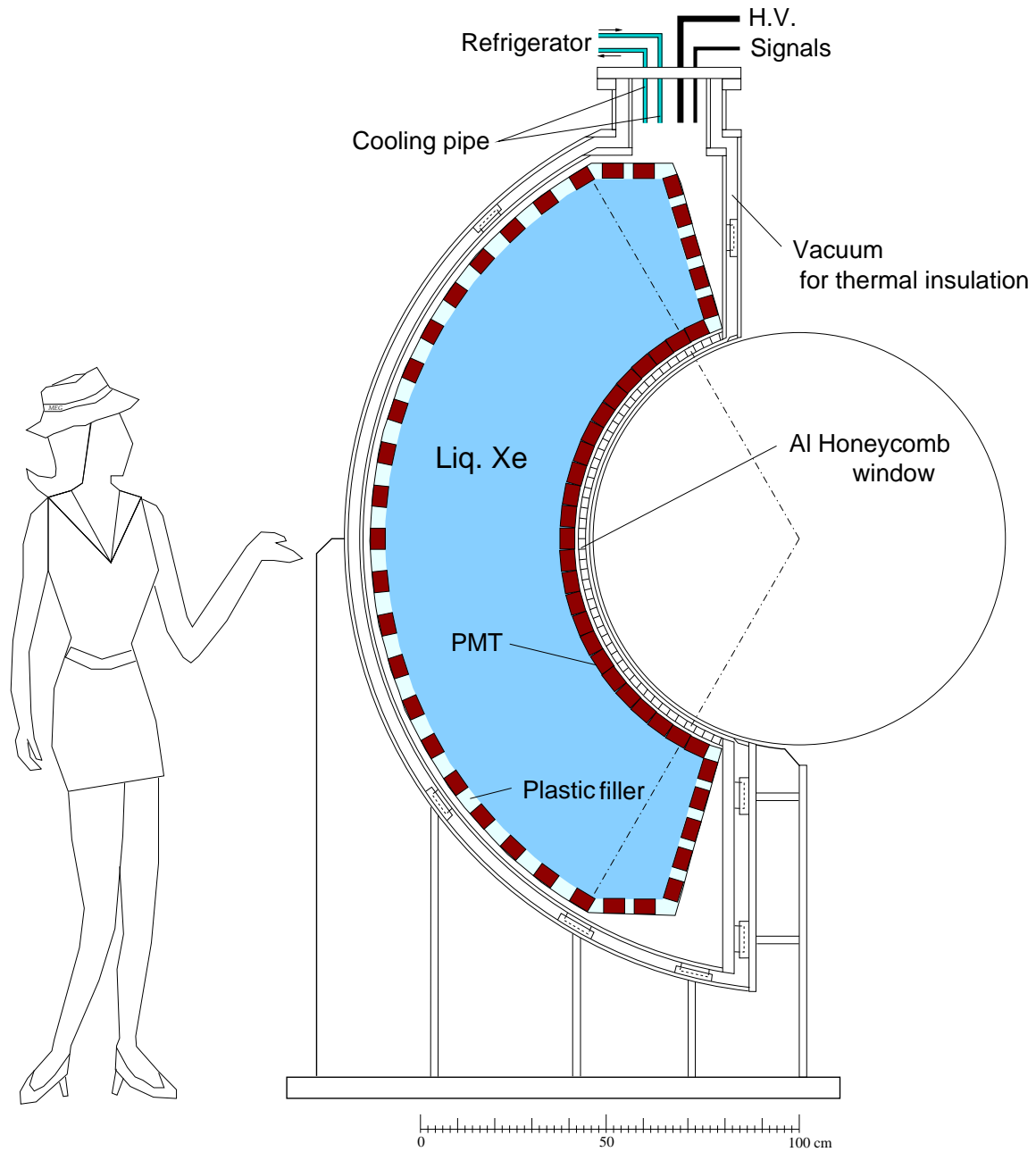


Figure 3.17: Schematic view of the Liquid Xenon calorimeter.

- the positron time and impact point from the Timing Counter.

We discuss the signal selection efficiency for each quantity, the background rejection and the expected trigger rate, as evaluated by a Monte Carlo simulation.

The γ energy is measured adding all PMT charges, weighed with the gains and the quantum efficiency of the PMTs and with the PMT photocathode coverage. The selected trigger threshold corresponds to $E_\gamma \geq 45$ MeV. The efficiency for detecting the γ signal is $\epsilon_\gamma = 98\%$. The γ -background in the LXe calorimeter comes from the positron annihilation in flight and from the muon radiative decay. The background rejection, normalized to the number of muon radiative decays with $E_\gamma > 10$ MeV, is $f_\gamma = 8 \times 10^{-3}$.

The γ direction is given, by definition, by the (θ, ϕ) coordinates of the PMT with the largest signal. It is assumed that the γ comes from the target center. The following efficiencies are obtained: $\epsilon_\gamma(\theta) = 99\%$ and $\epsilon_\gamma(\phi) = 99\%$.

The positron direction is derived from the (z, ϕ) coordinates of the impact point measured by the TC fiber system and the TC bar system. The fiber hit gives the z-coordinate with an accuracy of 10 cm; the bar hit gives the ϕ -coordinate with an accuracy of 10° .

The positron- γ direction is obtained combining the previous angular selections. The efficiency is $\epsilon_{e\gamma} = 99\%$ and the ϕ and θ rejection are: $f_\theta = 0.2$ and $f_\phi = 0.5$.

The γ time is evaluated from the rise time of the PMT waveform associated with the PMT with the maximum signal.

The positron time is evaluated from the arithmetic mean of the waveforms measured from the two PMTs mounted at the ends of the bar.

The positron- γ coincidence time window is $|\Delta T| < 10$ ns, with an efficiency $\epsilon_t = 99\%$.

One can now evaluate the trigger rate.

The expected γ rate is given by the expression:

$$R_\gamma = R_\mu P(\mu^+ \rightarrow e^+ \nu_e \bar{\nu}_\mu \gamma, \text{ with } E_\gamma \geq 10 \text{ MeV}) f_\gamma \frac{\Omega}{4\pi} = 2.2 \times 10^3 \text{ events/s} \quad (3.2)$$

where $R_\mu = 3 \times 10^8 \mu^+ / s$ is the muon rate stopped on the target, $P(\mu^+ \rightarrow e^+ \nu_e \bar{\nu}_\mu \gamma) = 1.4\%$ is the probability that the γ from the muon radiative decay has $E_\gamma > 10$ MeV and $\frac{\Omega}{4\pi} = 12\%$ is the LXe calorimeter solid angle acceptance.

The expected positron rate is:

$$R_{TC} = 2 \times 10^6 \text{ events/s} \quad (3.3)$$

Using R_γ and R_{e^+} we expect a trigger rate of:

$$R_{trigger} = R_\gamma R_{TC} f_\theta f_\phi 2\Delta T \approx 10 \text{ events/s} \quad (3.4)$$

The hardware of the trigger system is based on two different electronics boards.

A first board (Type 1, with 16 FADCs and 1 FPGA) receives the analog signal and digitizes it by a 100 MHz Flash Analog-to-Digital Converter (FADC). The digitized signals can then be used by the Fast Programmable Gate Array (FPGA) (part of the Type 2 board), which operates according to different algorithms, programmable in a simple and flexible way (see Fig. 3.18).

The system allows individual corrections to each PMT signal: the different PMT gain and quantum efficiency can be taken into account and the baseline of each signal can be subtracted (the latter feature is essential for correctly evaluating the energy deposited in the LXe calorimeter).

Preparatory operations like: the equalization of the PMT gains, the PMT baseline subtraction, the evaluation of the maximum PMT signal, the sum of the PMT charges, etc., are all performed in Type 1 Boards.

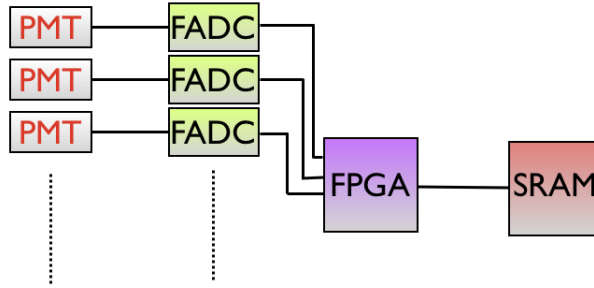


Figure 3.18: *The trigger system hardware.*

The functions of the second board (Type 2, with 2 FPGAs) are to combine the information provided by the Type 1 boards and to perform more complex algorithms.

The boards are organized in a tree structure as shown in Fig. 3.19.

The trigger signal is delivered by the final Type 2 board, which receives all previous information, which is also recorded by a Static Random Access Memory (SRAM).

Finally, a third board (the Ancillary) is added to the trigger system to provide the clock and the synchronization signals to all other boards.

3.5.2 Front-end electronics and DAQ

The signal digitization is obtained by a 2 GHz waveform which samples a CMOS chip. The waveform sampling was adopted to cope better with a possible event pile-up at the high MEG rates. The adopted solution is based on a capacitor sampling chip, previously developed at PSI [69].

Our Domino Sampling Chip is characterized by a sampling speed of 2 GHz (500 ps bin width; necessary to obtain a timing resolution of 50 ps), with the domino wave permanently circulating until stopped by the trigger. This new chip is called the Domino Ring Sampler [70], [71]. The number of storage capacitors is 1024, and the readout speed, via the shift register, is 40 MHz.

Eight data channels and two auxiliary channels are integrated on a single chip, which is housed and read out by a custom VME board using 12 bit flash ADCs and FPGAs. Thanks to the FPGAs, the algorithms of the data acquisition can be changed and optimized during the set-up of the experiment. A simplified schema of the DRS chip is shown in Fig.3.20. The data flux is shown in Fig. 3.21.

The DAQ system of the MEG experiment uses the DRS chip on all 1000 PMT channels (LXe calorimeter and TC) at a sampling speed of 2 GHz and on all 3000 drift chamber channels (cathodes and anodes) at a sampling speed of 500 MHz. A timing calibration signal is distributed and sampled in all DRS chips, meeting the requirement for a 100 ps timing accuracy.

A cluster of about 10 PC's is used for the on-line waveform processing. This corresponds to a resulting data rate below 2 MB/s for an event rate of 100 Hz. A schematic view of the data acquisition system is shown in Fig. 3.22.

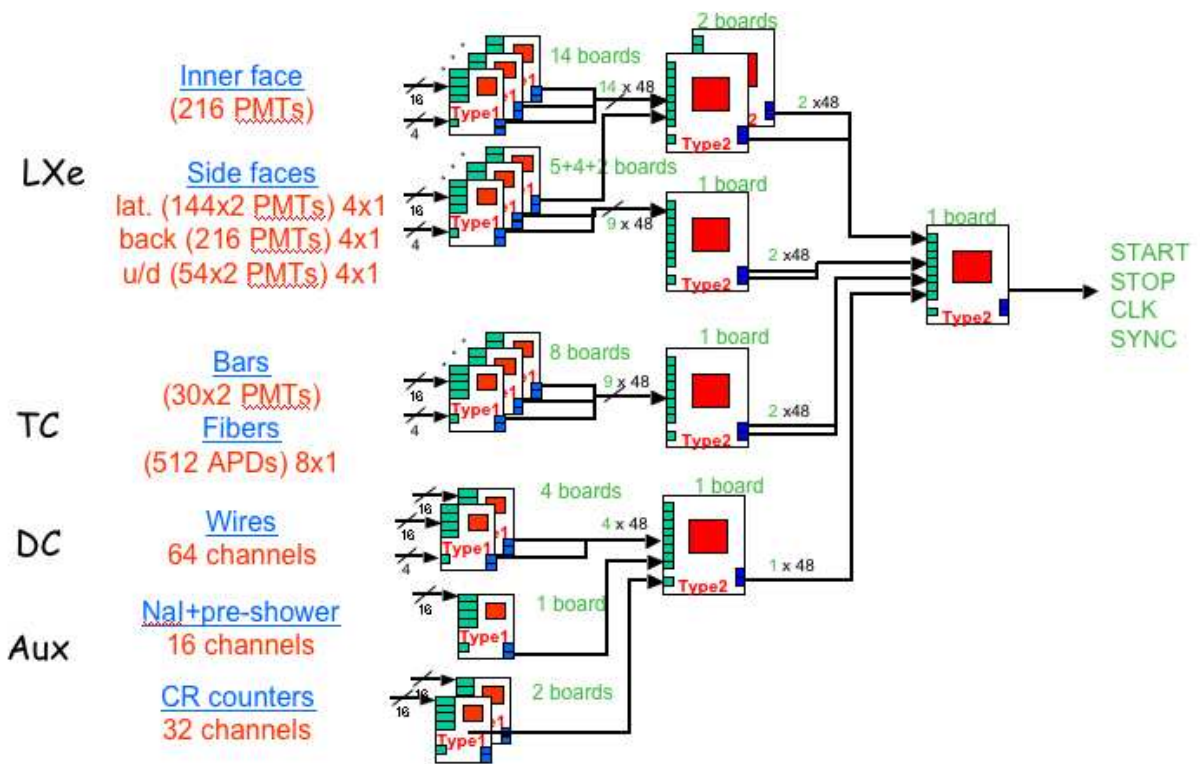


Figure 3.19: The structure of the trigger system: the two board types are used for the γ calorimeter and for the positron tracker. The boards are arranged in a tree-like structure.

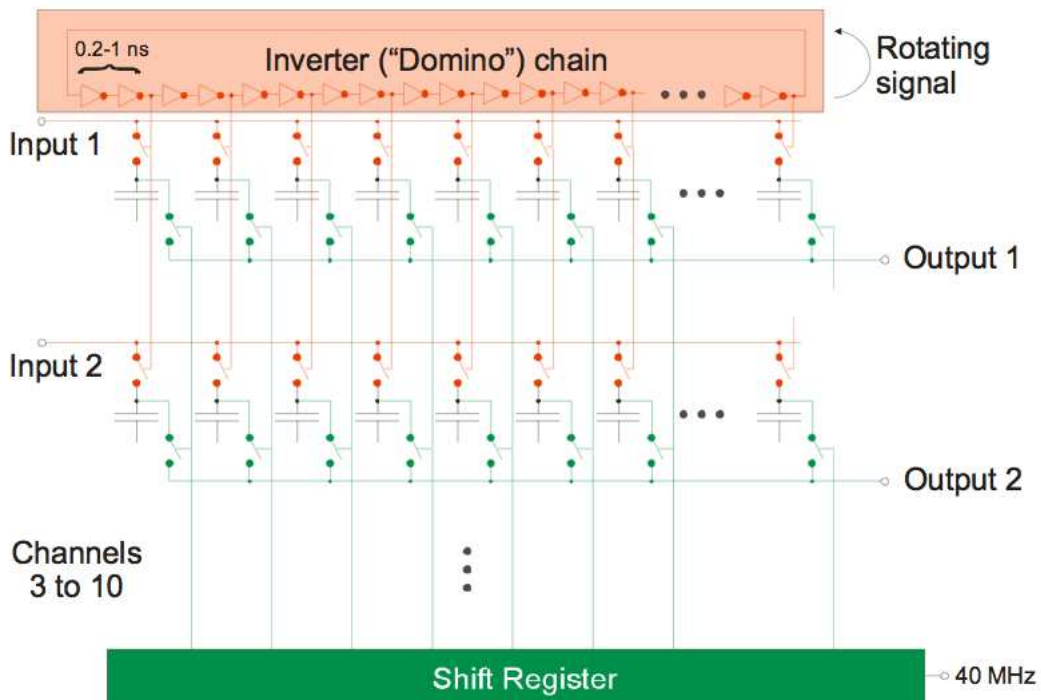


Figure 3.20: A simplified layout of the Domino Ring Sampler chip.

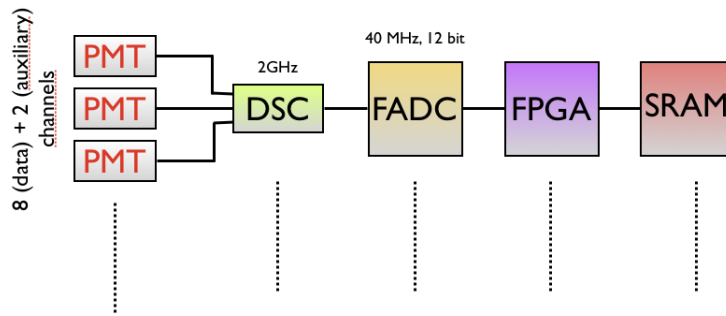


Figure 3.21: *The data flux through the DRS chip.*

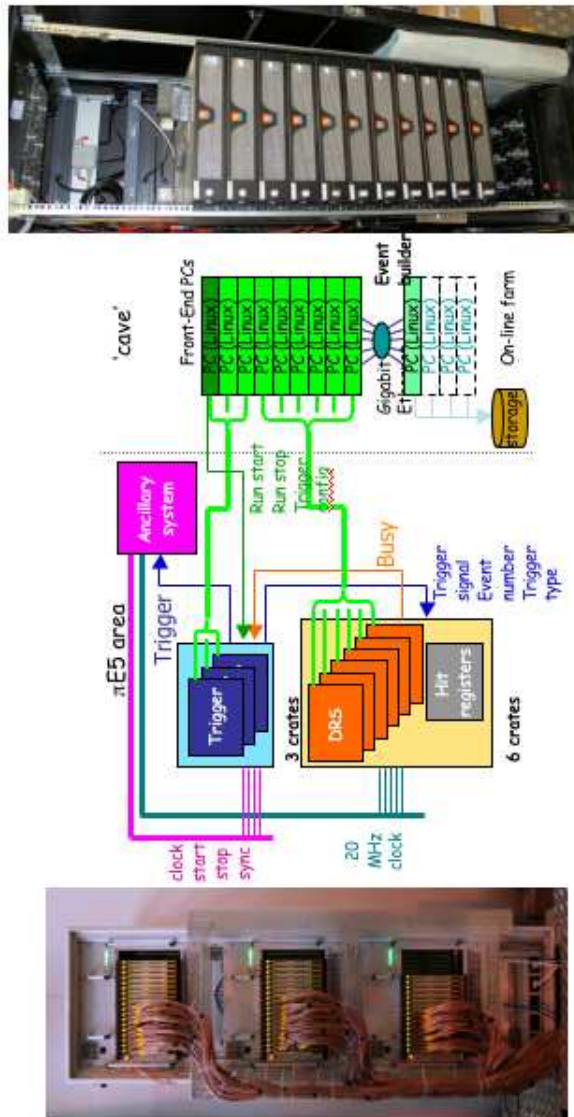


Figure 3.22: *Schematic view of the acquisition data system.*

Chapter 4

Liquid xenon as a scintillating medium

Since 1974, year of the first successful application of a the liquid Ar sampling calorimeter, there has been great progresses in the field of rare gas liquid detectors. The high light yield and the fast decay times are the two appealing characteristics of liquid rare gases as scintillating media, although the emission is in the vacuum ultraviolet (VUV): 128 nm for liquid Ar, 147 nm for liquid Kr, and 178 nm for liquid Xe. The VUV light is one of the problems one must cope with, requiring R&D for developing special photomultipliers (PMTs) working in this spectral region. Other aspects must also be considered when dealing with large detectors: the scintillator optical properties (refractive index, absorption length, attenuation length, scintillator purity), which influence the light propagation and thus the detector performance.

In this chapter we discuss the LXe optical properties. We studied Xe as a scintillator, trying to improve the determination of poorly known parameters.

We first describe the LXe scintillation mechanism and examine the light emission yield, the decay time constants and the required Xe purity. Measurements of these quantities are presented and discussed. We then present a novel and original method for obtaining the poorly known LXe refractive index and diffusion length (the Rayleigh scattering length), from the abundant information available in the visible and VUV spectral regions of gaseous Xe. A useful relation is established between the refractive index and the diffusion length. All experimental data are critically examined. The physical expressions valid for generic fluids are discussed. Simpler relations for LXe are then derived, together with their region of validity in terms of the thermodynamical variables (temperature, pressure, density, etc.).

4.1 Rare gas liquid scintillation detectors

Two kinds of rare gas liquid detectors have been developed up to now: the liquid Ar time projection chamber (TPC), originally proposed by Rubbia, or the homogeneous rare gas liquid calorimeters (Ar, Xe, Kr) [72, 73, 74, 75, 76, 77, 78, 79]

The homogeneous calorimeters can be divided into two groups, according to their mode of operation: (i) based on the measurement of ionization and (ii) based on the measurement of scintillation light. In both cases an excellent energy resolution is expected. Our LXe calorimeter is the first large scale Xe detector exclusively based on scintillation light. An excellent timing resolution is guaranteed by the short scintillation decay times.

Homogeneous calorimeters of type (i) have already been developed and successfully applied to

several elementary particle experiments [80].

Hybrid (scintillation+ionization) noble gas liquid detectors were proposed and studied for dark matter experiments.

The characteristics of Ar, Kr and Xe are presented in Tab. 4.1. Among the liquid rare gases Xe is particularly interesting, because of the higher light emission wavelength, the fast response and the short radiation length. Scintillation based cryogenic calorimeters do not need the segmentation normally required in inorganic crystal detectors.

Table 4.1: The main characteristics of Ar, Kr and Xe as scintillators.

| | Ar | Kr | Xe |
|-------------------------|------|-------|-------|
| $\rho(g/cm^3)$ | 1.39 | 2.45 | 2.98 |
| Z | 18 | 36 | 54 |
| $\lambda_{scint}(nm)$ | 128 | 147 | 178 |
| Boiling T(K) | 87.3 | 119.9 | 167.1 |
| dE/dx (m.i.p.) (MeV/cm) | 2.11 | 3.45 | 3.89 |
| $X_0(cm)$ | 14.0 | 4.76 | 2.87 |
| Moliere radius (cm) | 7.3 | 4.7 | 4.1 |
| $\tau_1(ns)$ | 6 | 2 | 4 |
| $\tau_3(ns)$ | 1000 | 91 | 22 |
| $\tau_r(ns)$ | - | - | 45 |

4.2 Liquid Xenon properties as a scintillating medium

In this section we discuss only the Xe properties relevant for a detector. Thanks to its high atomic number and density, one can design a compact and self-shielding liquid Xe electromagnetic calorimeter. Cryogenic and vacuum facilities are associated with it (Fig. 4.1). Xe is rare and very expensive. Commercial Xe is not at the purity level adequate to a detector use ($O_2 < 5ppm$ and $H_2O < 5ppm$, see section 4.3). A Xe purifier can remove contaminants and guarantee the transparency to VUV radiation.

Tab. 4.2 summarizes the main properties of Xe. The isotopic abundance is shown in Tab. 4.3.

4.2.1 The scintillation process

The luminescence process of Xe is shown in Fig. 4.2. It is similar to those of the other rare gas liquids.

The scintillation process occurs via the formation of excited dimers (excimers, formed by two species with at least one in an electronic excited state). Dimers radiatively decay to two ground state unbound xenon atoms [95, 96].

Ionizing particles produce excitons and electron-ion pairs. In the case of excitation a neutral excimer Xe_2^* is produced:



The radiative decay proceeds from the lowest excited molecular state $^1\Sigma_u^+$ or $^3\Sigma_u^+$ to the repulsive ground state $^1\Sigma_g^+$ (Fig. 4.3). Two decay constants are expected. A fast one, associated with the singlet transition $^1\Sigma_u^+ \rightarrow ^1\Sigma_g^+$ and a slow one, corresponding to the triplet transition $^3\Sigma_u^+ \rightarrow ^1\Sigma_g^+$.

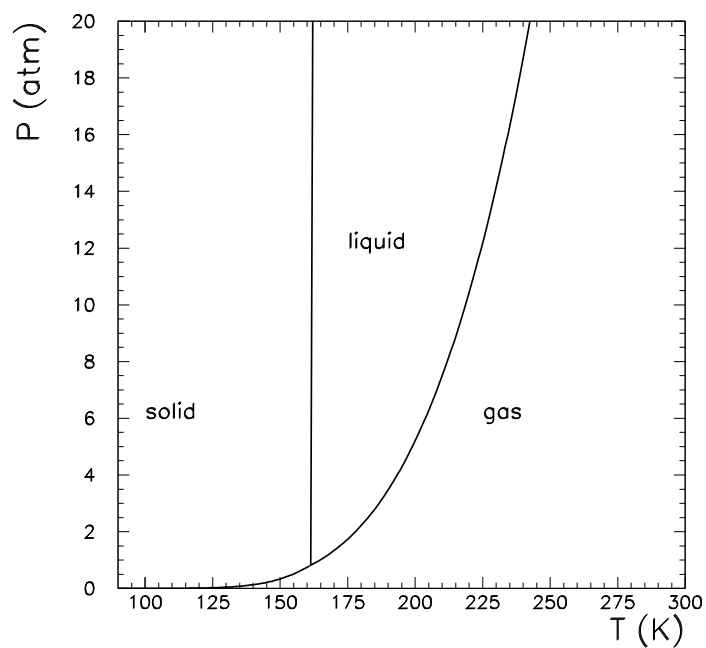
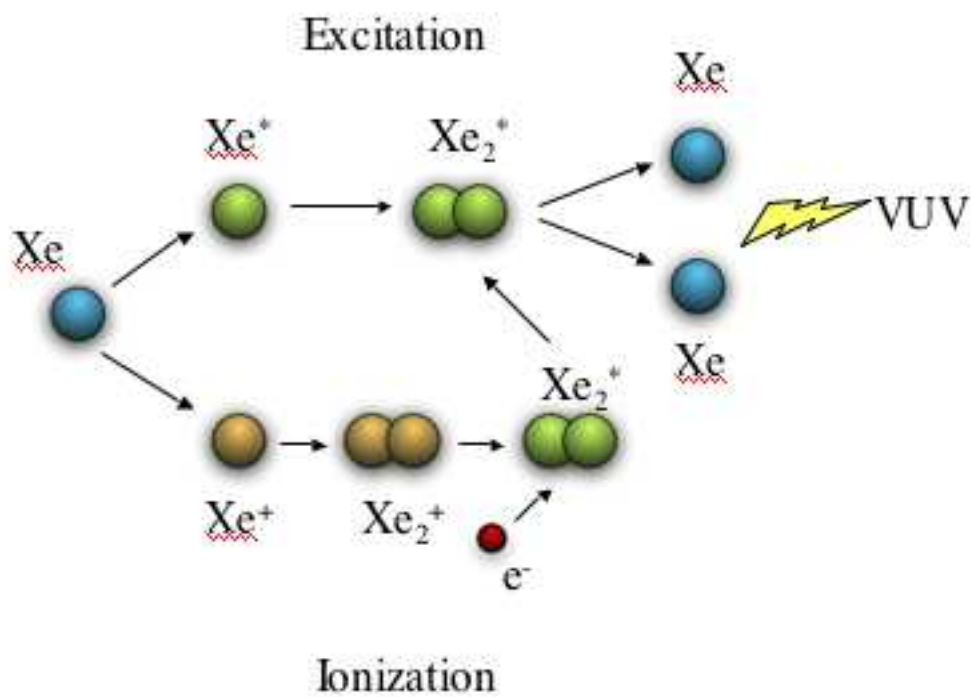
Figure 4.1: *The Xe phase diagram.*Figure 4.2: *The two processes leading to the Xe emission of scintillation photons at 178 nm.*

Table 4.2: Liquid Xe properties.

| | Value & Unit | Condition | Ref. |
|--|------------------------------|----------------------------|------------------------------|
| Atomic number Z | 54 | | |
| mass A | 131.29 g/mole | | [81] |
| Boiling point T_b | 165.1 K | 1 atm | [81] |
| Fusion point T_m | 161.4 K | 1 atm | [81] |
| Density ρ_{liq} | 2.98 g/cm ³ | 161.35 K | [82] |
| Molar fraction $\rho_{\text{gas}}/\rho_{\text{liq}}$ | 550 | 15 °C, 1 bar | [83] |
| Critical point T_c, P_c | 289.7 K, 58.4 bar | | [83] |
| Triplet point T_3, P_3 | 161.3 K, 0.816 bar | | [83] |
| Radiation length X_0 | 2.77 cm | in liquido | [18] |
| | 8.48 g/cm ² | | |
| Molière radius R_M | 5.6 cm | | [18] |
| Critical energy | 10.4 MeV | | [18] |
| $-(dE/dx)_{\text{mip}}$ | 1.255 MeV cm ² /g | | [18] |
| Refractive index | 1.6 ÷ 1.72 | for liquid phase at 178 nm | [133, 135, 136] ^a |
| Fano factor | 0.041 | theoretical | [87] |
| | not known | experimental | |
| Energy/scint. photon W_{ph} | (23.7 ± 2.4) eV | electrons | [88] |
| | (19.6 ± 2.0) eV | particles α | [88] |
| Decay constant τ_s | 22 ns | | [88] |
| Decay constant τ_t | 4.2 ns | | [88] |
| Recombination time τ_r | 45 ns | e, γ | [88] |
| Emission peak λ_{scint} | 178 nm | | [149, 90, 150] |
| Width emission spectrum (FWHM) | ~ 14 nm | | [149, 150] |
| Absorption length λ_{abs} | > 100 cm | | [92] |
| Rayleigh length λ_R | (29 ± 2) cm | | [93] |
| σ_{tot} for thermal neutron | (23.9 ± 1.2) barn | natural composition | [94] |

^aDiscrepancy between values. Refractive index in [133] at 180 nm.

Table 4.3: Natural Xe isotopic composition.

| | Relative abundance (%) |
|-------------------|------------------------|
| ¹²⁴ Xe | 0.096 |
| ¹²⁶ Xe | 0.090 |
| ¹²⁸ Xe | 1.92 |
| ¹²⁹ Xe | 26.44 |
| ¹³⁰ Xe | 4.08 |
| ¹³¹ Xe | 21.18 |
| ¹³² Xe | 26.89 |
| ¹³⁴ Xe | 10.44 |
| ¹³⁶ Xe | 8.87 |

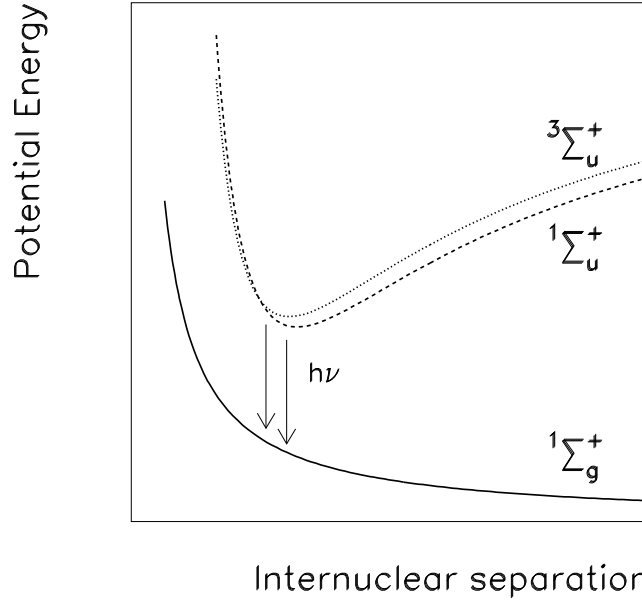
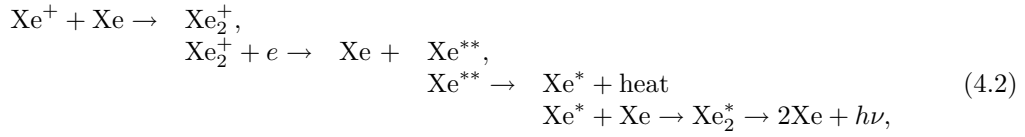


Figure 4.3: The photon emission by a Xe_2^* excimer, from the lowest state to the unbound ground state.

In the case of ionization charged excimers are formed. They are then neutralized by thermalized electrons (recombination luminescence):



4.2.2 Scintillation photon yield

The average energy needed to produce one photon by a ionizing radiation, W_{ph} , is one of the Xe important and not well-known parameters. Several measurements and estimates are available, which often disagree (Tab. 4.4). Xe is however a high light yield scintillator, comparable to NaI (Tab. 4.5).

As already said, photons are produced by excitation or ionization:

$$N_{ph} = N_i + N_{ex} = N_i \left(1 + \frac{N_{ex}}{N_i}\right) \tag{4.3}$$

where N_{ph} , N_i and N_{ex} indicate the number of scintillation photons, of ionized and excited scintillator atoms. The N_{ex}/N_i ratio depends on the projectile particle, and we expect different W_{ph} in case of different ionization densities (Tab. 4.5).

If E_0 is the energy deposited in the medium, a simple relation between W_{ph} and W_i , the average energy required to produce an electron-ion pair, can be derived from the eq. (4.3):

$$N_{ph} = N_i \left(1 + \frac{N_{ex}}{N_i}\right) = \frac{E_0}{W_i} \left(1 + \frac{N_{ex}}{N_i}\right) = \frac{E_0}{W_{ph}} \tag{4.4}$$

$$W_{ph} = \frac{W_i}{1 + \frac{N_{ex}}{N_i}} \tag{4.5}$$

W_{ph} depends on the physical state of the scintillating medium (Tab. 4.6, [98]), linked to the density and to the ionization energy. The density affects the N_{ex}/N_i -ratio (Xe liquid/gas density

Table 4.4: *Compilation of liquid Xe W_{ph} data.*

| W_{ph} | Comments | year | Ref. |
|-------------------------|----------------------|------|--------------|
| α -particles | | | |
| 19.6 ± 2.1 | Theoretical estimate | 1990 | [95], [96] |
| 40 ± 3.7 | | 1990 | [97] |
| 16.3 ± 0.3 | | 1992 | [98] |
| 16.4 ± 1.6 | | 1999 | [101] |
| 17.1 ± 1.4 | | 2005 | [102] |
| electrons | | | |
| 23.7 ± 2.4 | Theoretical estimate | 1990 | [95], [96] |
| 15.6 ± 0.3 | | 1975 | [103] |
| < 35 | | 1976 | [104] |
| 24.3 ± 2.0 | | 1987 | [105], [102] |
| 67 ± 27 | | 1992 | [106] |
| 14.2 | | 1992 | [107] |
| 29.6 ± 1.8 | | 1993 | [108] |
| 12.7 ± 1.3 | | 1995 | [109] |
| 42 ± 6 | | 1995 | [110] |
| 21.7 ± 2.2 | | 1999 | [101] |
| 20.6 ± 1.7 | | 2004 | [111], [102] |
| 18.3 ± 1.5 | | 2005 | [102] |
| Relativistic heavy ions | Theoretical estimate | | |
| 14.7 ± 1.5 | | 1990 | [95], [96] |

Table 4.5: The average energy needed to produce a scintillation photon in liquid Xe W_{ph} (eV) (theoretical estimate) [88] is compared with similar quantities for NaI(Tl) (measured) and Ar (theoretical estimate) [88].

| Scintillator | Relativistic electrons | α -particles | Relativistic heavy particles |
|--------------|------------------------|---------------------|------------------------------|
| Ar | $25.1^{+2.5}$ | $27.5^{+2.8}$ | $19.5^{+2.0}$ |
| Xe | $23.7^{+2.4}$ | $19.6^{+2.0}$ | $14.7^{+1.5}$ |
| NaI(Tl) | $17.2^{+0.4}$ | | |

Table 4.6: A compilation of W_{ph} data and its pressure dependence. Xe gas.

| W_{ph} | Comments | year | Ref. |
|---------------------|------------------------|------|-------|
| α -particles | | | |
| 49 ± 1.1 | $P = 1.01 \times 10^5$ | 1992 | [98] |
| 34.3 ± 1.6 | $P = 1.01 \times 10^5$ | 2002 | [112] |
| 27.5 ± 1.3 | $P = 2.03 \times 10^5$ | 2002 | [112] |
| 21.0 ± 0.8 | $P = 4.05 \times 10^5$ | 2002 | [112] |
| 17.5 ± 0.6 | $P = 6.08 \times 10^5$ | 2002 | [112] |
| 16.5 ± 0.5 | $P = 7.09 \times 10^5$ | 2002 | [112] |
| 15.6 ± 0.5 | $P = 8.10 \times 10^5$ | 2002 | [112] |
| 14.6 ± 0.5 | $P = 1.01 \times 10^6$ | 2002 | [112] |

ratio $\rho_{liq}/\rho_{gas} = 550$). The ionization energy depends on the atomic levels in gas or on valence and conduction bands in liquid (see Fig. 4.4).

We measured a LXe/GXe light yield ratio of about 2.7, for α -particles (see section 4.3). Our value agrees with the only one previously available: $W_{ph}(\alpha, GXe)/W_{ph}(\alpha, LXe) = 3.0 \pm 0.1$ [98].

We up to now assumed that all excited or ionized atoms generate a scintillation photon. This is not always the case and deviations from eq. (4.5) can occur. For instance: (i) some electrons might have very long recombination times with ions (of the order of milliseconds) and the radiation might then escape detection. (ii) Quenching effects might occur and this also reduces the photon yield. Recombination and quenching effects were experimentally studied [113], [114], [115] and [116]. The theoretical estimate of W_{ph} for Xe is compared with W_{ph} for Ar (theoretical estimate) and NaI (measured) in Tab. 4.5 .

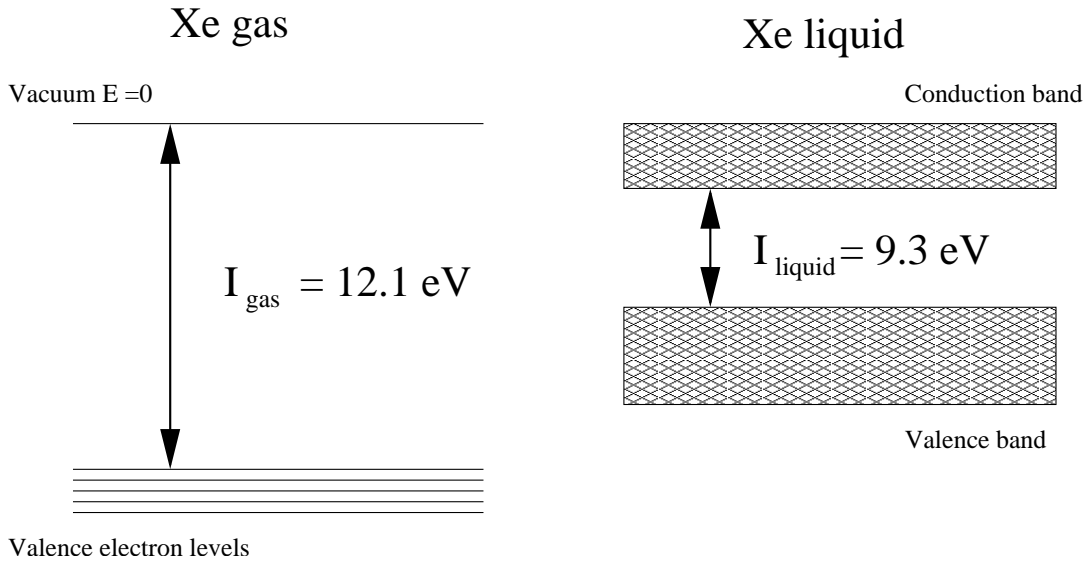


Figure 4.4: *Schematic energy level and band structure of gaseous and liquid Xe.*

4.2.3 Decay times

The waveforms corresponding to α and γ -events are shown in Fig. 4.5. They correspond to two different decay-times: $\tau_\alpha = 19.4 \pm 1.9$ ns and $\tau_\gamma = 50.9 \pm 4.0$ ns. The measured τ 's agree with what is available in the literature [88, 99, 100].

The reason for such a large difference between the γ - and α -event decay constants is not entirely clear at present. One notes that Xe dimers are produced via direct Xe excitation or via ionization. One also notes that longer decay constants are possibly associated with the contribution of electron diffusion times prior to recombination.

Experimental measurements tried to separate contributions of excitation and ionization to the scintillation light. Data are available for argon, krypton and xenon excited by α 's [99, 100, 113, 117, 118, 119, 120] and γ 's [121, 122, 123]. Separate and simultaneous measurements of scintillation light and ionization were performed as a function of an applied electric field, for different ions and energies. Both α and γ scintillation light decreases for increasing electric field, but the effect is more pronounced for γ 's. This indicates that slow recombination is the primary contribution to the γ scintillation light. Excitation and ionization are both contributing to the scintillation light, but it is possible that the higher ionization density associated with ions favours a fast recombination, while a slower recombination is present for γ 's. In other words, ions are associated with excitation, ionization and fast recombination (short decay times) while γ 's are associated with excitation,

ionization, electron diffusion and slow recombination (long decay times). A critical analysis of all available literature seems to be in agreement with the outlined scheme, but more complete and precise measurements are highly desirable. Since noble liquid detectors are more and more part of new experimental projects, laboratory investigations would be fully justified.

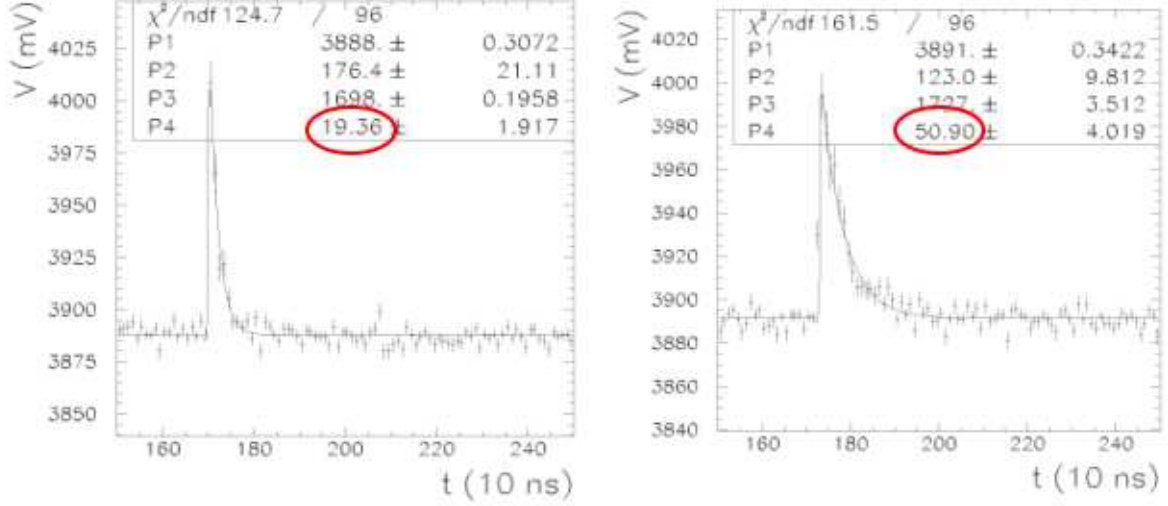


Figure 4.5: LXe waveform associated with an α -event (left) and a γ -event (right). $\tau_\alpha = 19.4 \pm 1.9$ ns, $\tau_\gamma = 50.9 \pm 4.0$ ns.

4.2.4 The attenuation length

The VUV light propagation affects the performance of a big calorimeter. The light intensity that reaches a PMT photocathode from an interaction at a distance x , obeys the expression:

$$I(x) = I_0 e^{-x/\lambda_{att}} \quad (4.6)$$

where λ_{att} is the light attenuation length. We assume that the attenuation is the result of light diffusion and of light absorption:

$$\frac{1}{\lambda_{att}} = \frac{1}{\lambda_{abs}} + \frac{1}{\lambda_{dif}} \quad (4.7)$$

where λ_{dif} is the diffusion length (photon elastic scattering) and λ_{abs} is the absorption length (photon disappearance).

The attenuation, absorption and diffusion lengths in liquid xenon are poorly known. The measurements in the VUV region are not easy and the results may strongly depend on experimental conditions (i.e. Xe purity, etc.).

4.3 The absorption length

Referring to the LXe scintillation processes already examined (via excimer states Xe_2^*), light absorption in pure LXe is impossible, i.e. $\lambda_{abs} \approx \infty$. Any light absorption is thus caused by VUV absorbing Xe contaminants.

Common substances like H_2O and O_2 have a high absorption cross section in this region. The H_2O and the O_2 absorption cross section are presented in Fig. 4.6 and Fig. 4.7 together with the Xe scintillation spectrum.

Absorption lengths can be derived from cross sections and from the amount of contaminants. The absorption lengths of Xe, for a 1 ppm impurity level of H_2O and O_2 , are presented in Fig. 4.8

and Fig. 4.9. These plots suggest that small amounts of contaminants, at a level of a few parts per million, can dramatically influence the LXe optical parameters.

A correct determination of the LXe optical parameters requires the monitoring of the xenon purity. A LXe volume of adequate linear size must be used for a reliable determination of the absorption length. The Large Prototype (LP, 100 l of LXe and 67 l of sensitive volume, 264 PMTs) was initially used. The purification system of the Large Prototype and the final LXe calorimeter

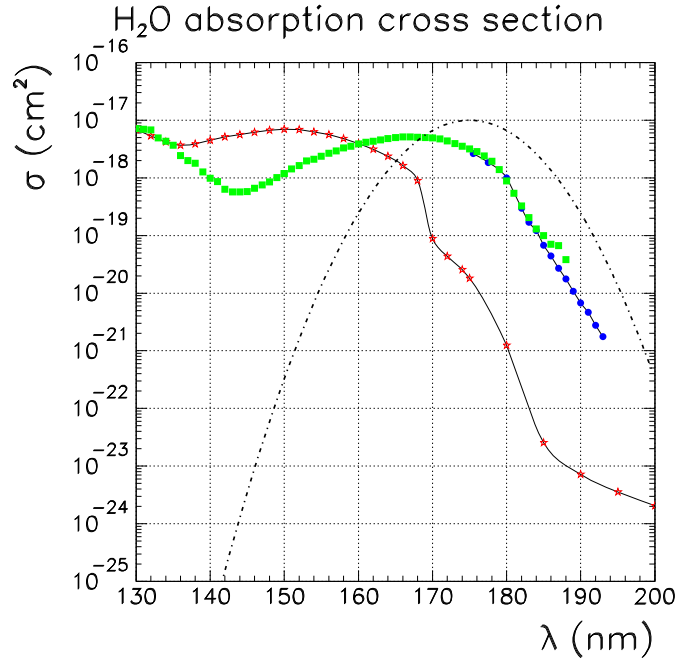


Figure 4.6: Absorption cross section of the H_2O (red stars = liquid phase, green and blue square = gas phase). The Xe scintillation spectrum is superimposed (dashed line, arbitrary units).

is described in section 5.2.

The first measurement of the liquid xenon absorption length was based on events due to cosmic rays and to α -sources.

The determination of λ_{abs} depends on the measurement of the total number of photoelectrons collected by all PMTs, N_{phe} . This number is only sensitive to the loss of the scintillation light, and is therefore a good estimator of the absorption length. The N_{phe} , associated with cosmic ray events, is plotted in Fig. 4.10 (a), as a function of time during the purification process. After about one month (≈ 700 hours), N_{phe} saturates, having increased by a factor of four relative to the initial value. A comparison with a Monte Carlo simulation indicates that λ_{abs} varied from ≈ 10 cm to over 1 m. The same result was obtained from α -events due to sources mounted on the walls of the LP. The signal recorded by PMTs at a known distance from a source, is shown as a function of time in Fig. 4.10 (b). To evaluate the absorption length by α -data, we compared the PMT signals in LXe to those in GXe (negligible light absorption and scattering) and to a Monte Carlo simulation with no absorption and variable λ_R . The PMT signals either normalized to those in GXe (in Fig. 4.11 (a)) or to the MC simulation with $\lambda_R = 45$ cm (see 4.11 (b)), are plotted against the source-PMT distance. The distributions at the start of the purification process (open circles) and at the saturation (closed circles) are compared. The exponential decrease present at the start of the purification process almost disappeared after purification.

These distribution were then fitted with exponential functions. From the comparison with the GXe data, an attenuation length of 54_{-9}^{+14} cm was obtained at the end of the purification process (we recall that the attenuation length combines both the absorption and the scattering (Rayleigh)

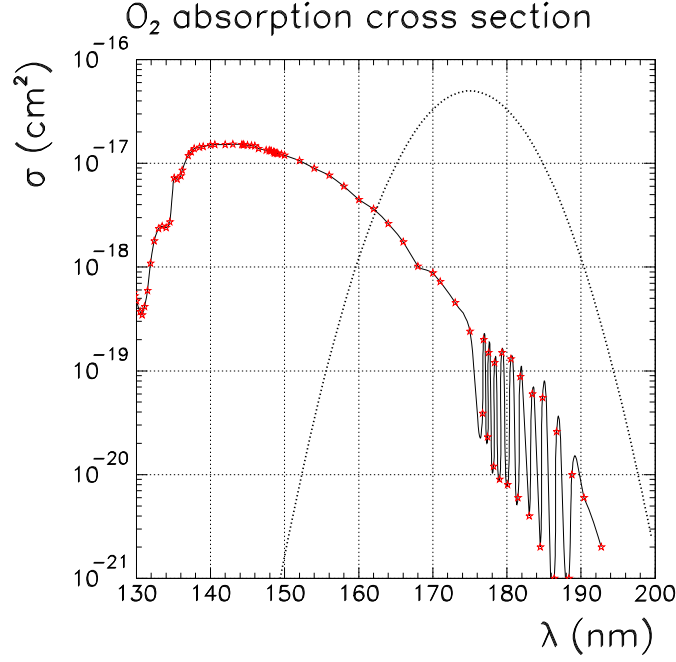


Figure 4.7: *Absorption cross section of O₂ (star). The Xe scintillation spectrum is superimposed (dotted line, arbitrary units).*

lengths).

Note that the LXe/GXe ratio is larger than unity (≈ 2.7), as previously discussed.

The comparison with the simulation does not show a significant slope as a function of source-PMT distance. We used this result to establish a lower limit on the absorption length λ_{abs} of 90 cm at 90% C.L., where λ_R was varied from 30 cm to 50 cm in the simulation [92]. Before the purification λ_{abs} was 12.0 ± 1.8 cm.

We conclude by stating that the level of water content after the purification was much lower than 100 ppb.

The subsequent improvement of the λ_{abs} lower limit was obtained by using α -source deposited on thin wires, immersed in the liquid xenon. The method is described in detail in chapter 8.

4.4 The Rayleigh scattering length

The Rayleigh scattering describes the light diffusion, when the size of the scattering center is smaller than the wavelength of the radiation and the scattered light is sufficiently far from the diffusion center; one can then rely on a plane wave approximation. The Rayleigh cross section is:

$$\begin{aligned} \sigma &= \frac{k^4}{6\pi N^2} |(\epsilon - 1)|^2 \\ &\simeq \frac{2k^4}{3\pi N^2} |(n - 1)|^2 \end{aligned} \quad (4.8)$$

where k is the wave number of the radiation, ϵ is the dielectric permeability of the medium, n is the refractive index and N is the number of molecules per unit volume. The second expression in eq. (4.8) follows from the condition $|(\epsilon - 1)| \ll 1$, valid for all rarified gas. From the eq. (4.8) the reciprocal of the Rayleigh length follows:

$$h = \frac{1}{\lambda_R} \equiv N\sigma \simeq \frac{2k^4}{3\pi N} |(n - 1)|^2 \quad (4.9)$$

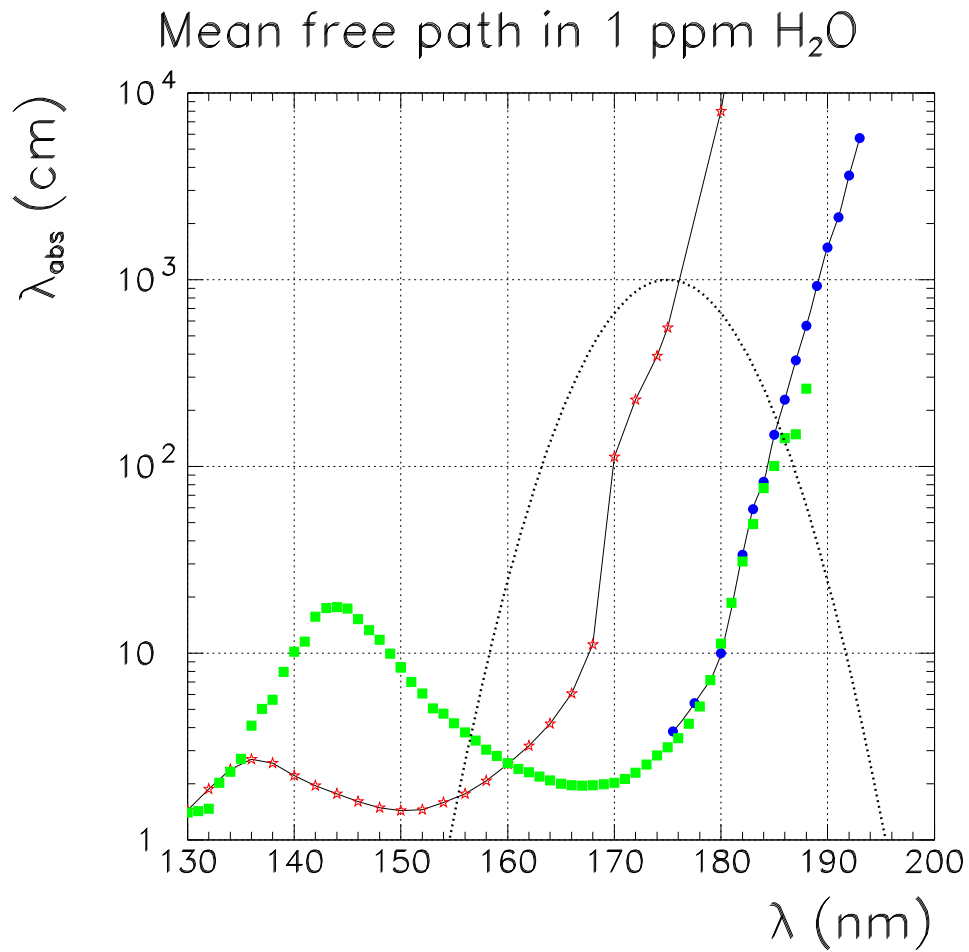


Figure 4.8: The Xe absorption length, doped with 1 ppm of H₂O (red stars = liquid phase, green and blue square = gas phase). The Xe scintillation spectrum is superimposed (dotted line).

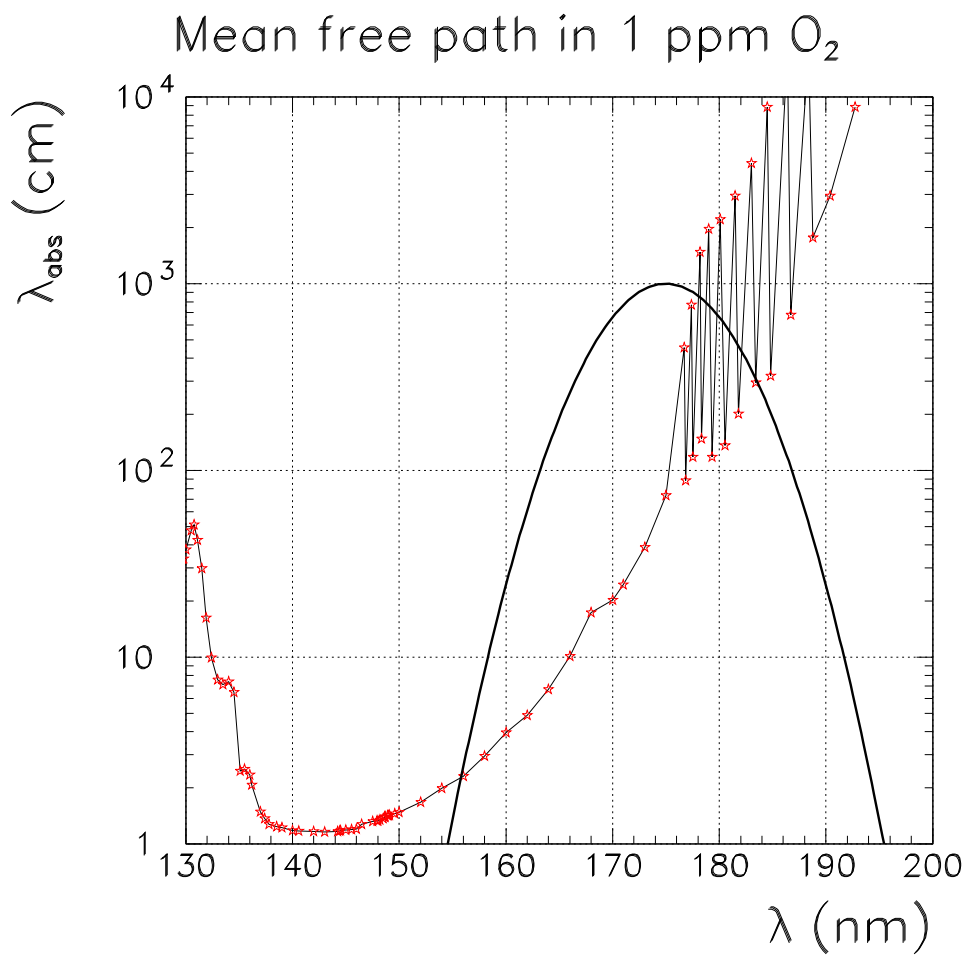


Figure 4.9: Xe absorption length, doped with 1 ppm of O₂. The Xe scintillation spectrum is superimposed (black line).

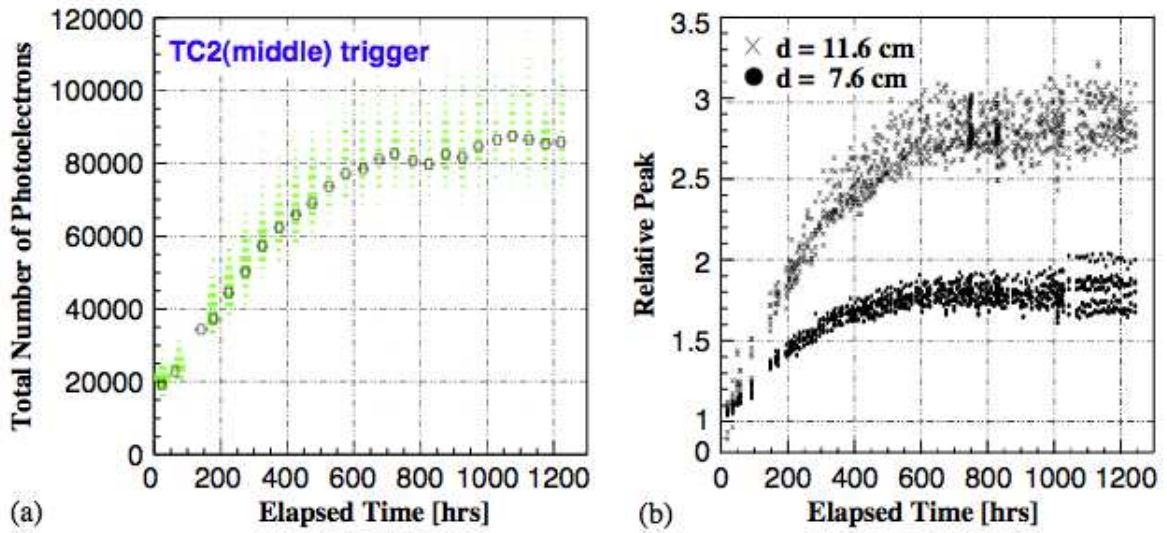


Figure 4.10: The total number of photoelectrons collected by all PMTs of the LXe LP, N_{phe} , for cosmic ray events (a), as a function of time, during the purification process. The variations of the maximum of the α -spectra for PMTs located at 7.6 cm and 11.6 cm from the α -source (b).

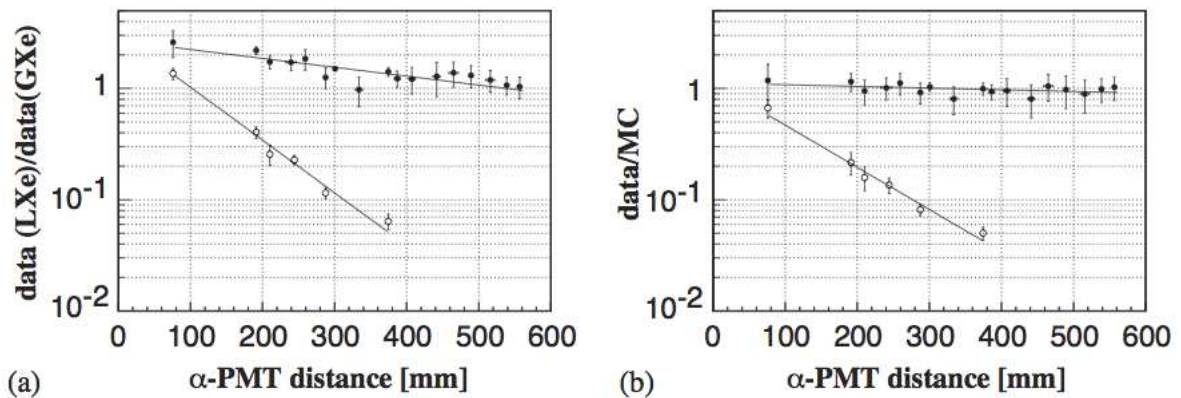


Figure 4.11: The PMT signals normalized to those in GXe (a) or normalized to the result of the MC simulation with $\lambda_R = 45$ cm (b), are plotted against the source-PMT distance. Beginning of the purification process (open circles). After purification (closed circles).

where h is the extinction coefficient.

For a dense fluid like LXe λ_R depends on density ρ and temperature T fluctuations of the medium, according to the Einstein's expression [125]:

$$\frac{1}{\lambda_R} = \frac{\omega^4}{6\pi c^4} \left[KT\rho^2 \kappa_T \left(\frac{\partial \epsilon}{\partial \rho} \right)_T^2 + \frac{KT^2}{\rho c_v} \left(\frac{\partial \epsilon}{\partial T} \right)_\rho^2 \right] \quad (4.10)$$

where c is the speed of light, κ_T is the isothermal compressibility, c_v is the specific heat capacity at constant volume, and K is the Boltzmann's constant. In the case of a rarified gas eq. (4.10) evolves to eq. (4.9).

In this section and in the following one, we try to answer the question: how does the LXe dielectric polarizability depend on density and temperature? Do we have some kind of analytical expression? What the available experimental data suggest?

4.4.1 Theoretical models for the optical properties of non-polar rare gases

In the case of a dilute non-polar gas, the Clausius-Mossotti relation answers our first question. However some extra considerations are necessary if deviation from this condition occurs.

The Clausius-Mossotti (as a function of dielectric constant ϵ) and the Lorentz-Lorentz equation (as a function of the refractive index n) provide a link between the microscopic and macroscopic fluid properties [125],[126] :

$$F_{LL} = \frac{n^2(\omega) - 1}{n^2(\omega) + 2} = \frac{\epsilon(\omega) - 1}{\epsilon(\omega) + 2} = \frac{4\pi}{3} \frac{N_A \alpha(\omega) \rho}{M} = A(\omega) \rho_m, \quad (4.11)$$

where N_A is the Avogadro's number, $\alpha(\omega)$ is the molecular polarizability, ρ (units: g cm^{-3}) is the density and M is the molecular weight. As we shall later see, $A(\omega)$ represents "the first virial coefficient".

This relation is valid for dilute non-polar gases. At higher gas densities and for the liquid and solid states, the simple eq. (4.11) are in general no longer valid and non-linear effects come into play due to interatomic interactions. In this case the Clausius-Mossotti and Lorentz-Lorentz equations must be generalized into:

$$F_{LL} \equiv \frac{n^2(\omega, T, \rho) - 1}{n^2(\omega, T, \rho) + 2} = \frac{\epsilon(\omega, T, \rho) - 1}{\epsilon(\omega, T, \rho) + 2} = \frac{4\pi}{3} N_A \alpha(\omega, T, \rho) \rho_m, \quad (4.12)$$

and one often uses a so called "virial expansion" of the type:

$$F_{LL} = [A_R(\omega, T) + B_R(\omega, T)\rho_m + C_R(\omega, T)\rho_m^2 + \dots]\rho_m \quad (4.13)$$

where the suffix R indicates that A_R, B_R, C_R are meant to be at optical and VUV wavelengths, unlike $A_\epsilon, B_\epsilon, C_\epsilon$ which are meant to be at the limit of very large wavelengths.

Here we study the Xe virial expansion. The aim is to evaluate the terms that follow the first virial coefficient for liquid Xe in the VUV region, using data in different physical conditions, from visible light to the VUV region.

The different terms of the virial expansion can be interpreted as follows: A_R represents the atomic polarizability, B_R represents the interactions of two atoms, C_R represents the interactions of three atoms, etc. If instead of dealing with optical properties, one deals with the fluid equation of state, one often uses the "compressibility":

$$Z = \frac{P}{RT\rho_m}, \quad (4.14)$$

where ρ_m is the molar density. For a perfect gas $Z = 1$. For a real gas Z measures the deviations from the perfect gas behaviour. A virial expansion can be introduced for Z :

$$Z = 1 + B_{2V}(T)\rho_m + B_{3V}(T)\rho_m^2 + B_{4V}(T)\rho_m^3 + \dots \quad (4.15)$$

Interatomic interactions are taken care of by the terms B_{2V}, B_{3V}, B_{4V} , etc. It is important to note that if the B 's are experimentally known for the fluid, one can use a F_{LL} virial expansion in terms of the perfect gas molar density:

$$\rho_0 = \frac{P}{RT}, \quad (4.16)$$

with coefficients which can be expressed in terms of those of eq. (4.13).

The expression eq. (4.13) becomes simpler for Xenon, taking into account the fact that this gas has no permanent dipole moment. It can be shown [127] that this reflects into an $A_R(\omega, T) \rightarrow A_R(\omega)$, no longer depending on temperature and:

$$F_{LL} = [A_R(\omega) + B_R(\omega, T)\rho_m + C_R(\omega, T)\rho_m^2 + \dots]\rho_m. \quad (4.17)$$

The question is: can one use for Xenon, whatever its pressure and state, the simple Clausius-Mossotti equation, so keeping only the first term of the virial expansion and a linear relation with density? We briefly discuss this point in section 4.4.3, after critically examining in section 4.4.2 the existing literature and the experimental measurements on the relevant Xenon properties.

4.4.2 Experimental measurements performed in Xe

Over the years, several measurements have been produced of quantities such as the real and imaginary parts of the dielectric constant (ϵ_1, ϵ_2), the real and the imaginary part of the refractive index (n, k), the molecular polarizability $\alpha(\omega, T, \rho)$, etc. over a large range of temperatures T and pressures P , from dilute gas to liquid and solid phases. We present and discuss the available data and papers.

The experimental determination of the dielectric virial coefficients of atomic gases as a function of temperature. J. Hout and T.K. Bose [128]

State: gas. Temperature: $T = 323.15$ K. Density: $0.13 < \rho < 0.79$ g cm⁻³ equivalent to $10^{-3} < \rho_m < 6.0 \cdot 10^{-3}$ mol cm⁻³. Method: Absolute measurement of the dielectric constant in capacitances (at low frequency).

Result: Determination of the first three virial coefficients $A_\epsilon, B_\epsilon, C_\epsilon$. At 323.15 K $A_\epsilon = 10.122 \pm 0.002$ cm³ mol⁻¹, $B_\epsilon = 32 \pm 2$ cm⁶ mol⁻², $C_\epsilon = -3482 \pm 310$ cm⁹ mol⁻³.

This measurement is made at very low frequency, hence very far from the visible and the VUV region, and at densities which are about one hundred times smaller than at LXe. Moreover, models were proposed for the dependence of B_ϵ and C_ϵ on the temperature T , which seem not to be confirmed by experimental data.

It is remarkable that, if one, somewhat arbitrarily, computes the Clausius-Mossotti relation in the visible and at densities up to a density $\rho_m = 0.016$ mol cm³ using $A_\epsilon, B_\epsilon, C_\epsilon$ of this paper, one finds that A is not very different from direct determinations closer to the specified region [129] and that B_ϵ and C_ϵ introduce terms which produce rather small deviations from the main A term.

The experimental determination of the refractivity virial coefficients of atomic gases. H.J. Achtermann et al. [129]

State: gas. Temperature: $T = 298 - 348$ K. Pressure: $p < 4 \times 10^2$ Atm. Density: $\rho_m < 0.016$ mol cm⁻³. Method: Measurement of the refractive index by a differential interferometric technique at $\lambda = 633$ nm.

Result: Determination of the first three virial coefficients A_R, B_R, C_R . $A_R = 10.344 \pm 0.002$ cm³ mol⁻¹, $B_R = 28.5 \pm 0.5$ cm⁶ mol⁻², $C_R = -1802.0 \pm 50.0$ cm⁹ mol⁻³ at $T = 348$ K.

The measurements were made in the visible region at densities close to the one of LXe. One observes that A_R is not very different from A_ϵ of the static measurement. The terms related to B_R and C_R are small in respect of the main A_R one at LXe densities.

The refractive index of the condensed rare gases, argon, krypton and xenon. A.C. Sinnock [130]

State: liquid and solid Xe. Temperature: $T = 30 - 178$ K. Pressure: $p \approx 1$ Atm. Density: $\rho_m = 0.0215 - 0.0280$ mol cm⁻³. Method: Measurement of the refractive index by a total reflection refractometer at $\lambda = 546.1$ nm. It studies Xe in the liquid and solid forms and in the visible region.

Result: Determination of the refractive index and determination of A from the Lorentz-Lorenz function F_{LL} . In LXe $n \approx 1.4$ and $A \approx 10.5 \pm 0.025$ cm³ mol⁻¹ at $\lambda = 546.1$ nm.

The value of A is remarkably similar to those in gas over a large density range. In a previous article [82], similar measurements were performed also at different wavelengths ($361.2 < \lambda < 643.9$ nm). The Lorentz-Lorenz function, hence A , only varies $\approx 3\%$ over the entire range studied; this implies that the variation of n is $\approx 1.5\%$ in the specified region.

The frequency-dependence of second refractivity virial coefficient of small molecules between 325 nm and 633 nm. U. Hohm [131]

State: gas. Temperature: Room temperature. Pressure: $p < 3$ Atm. Density: $\rho_m < 1.25 \cdot 10^{-4}$ mol cm³. Method: Measurement of the refractive index n as a function of the gas density by a Michelson interferometer between $325 < \lambda < 633$ nm.

Results: The first two virial coefficient A_R, B_R are derived from the measurements. $A_R(633) = 10.43$, $A_R(594) = 10.46$, $A_R(543.5) = 10.52$, $A_R(325.1) = 11.26$ cm³ mol⁻¹. $23.2 < B_R < 25.5$ cm⁶ mol⁻². Apart from the normal dispersion as a function of the wavelength, the values of A_R and B_R are remarkably stable whatever the Xe physical state.

The measurement of refractive index of Neon, Argon, Krypton and Xenon in the range 253.7-140.4 nm wavelength. Dispersion relations and estimated oscillator strengths of the resonance lines. A. Bideau-Mehu et al. [132]

State: gas. Temperature: $T = 290$ K. Pressure: $p \approx 1$ Atm. Density: $\rho_m = 4.49 - 5$ mol cm⁻³. Method: Measurement of the refractive index by a Fabry-Perot interferometer in the region $140.4 < \lambda < 253.7$ nm.

This is one of the few precise measurements of the refractive index in the VUV and close to the first Xe absorption line. We saw that in the visible region $A(\omega)$ is rather stable around 10.5 cm³ mol⁻¹ even for large density variations from dilute gas to the liquid and solid states. One can expect that in the VUV the same is true, although normal dispersion from the visible to the VUV region corresponds to a higher value for $A(\omega)$. From these measurements of the refractive index one can derive a $A(\omega) \approx 17.0$ cm³ mol⁻¹ at 175 nm. The LXe refractive index, in the approximation of a Lorentz-Lorenz function linear in the density ρ , is predicted to be $n \approx 1.69$ at 175 nm.

The measurement of refractive index of liquid Xenon for intrinsic scintillation light. L.M. Barkov [133]

State: liquid Xenon. Temperature: $T = 161.36$ K. Pressure: $p \approx 0.81$ Atm. Density: $\rho_m \approx 2.26 \cdot 10^{-2}$ mol cm⁻³. Method: Measurement of the refractive index by modification of the focalization of a lens when immersed in LXe, at $\lambda = 180$ nm.

Result: $n = 1.5655 \pm 0.0024 \pm 0.0078$. The quoted errors are probably underestimated.

The evolution of excitonic bands in gas and liquid xenon. P. Laporte and I.T. Steinberger [134]

State: gas under pressure and liquid Xenon. Temperature: gas $275 < T < 292.7$ K, liquid $T = 163$ K. Pressure: gas $61.0 < p < 82.3$ Atm, liquid $p = 0.79$ Atm. Density: gas $7.6 \cdot 10^{-3} < \rho_m < 1.45 \cdot 10^{-2}$ mol cm⁻³, liquid $\rho_m = 2.26 \cdot 10^{-2}$ mol cm⁻³. Method: Study of the real and

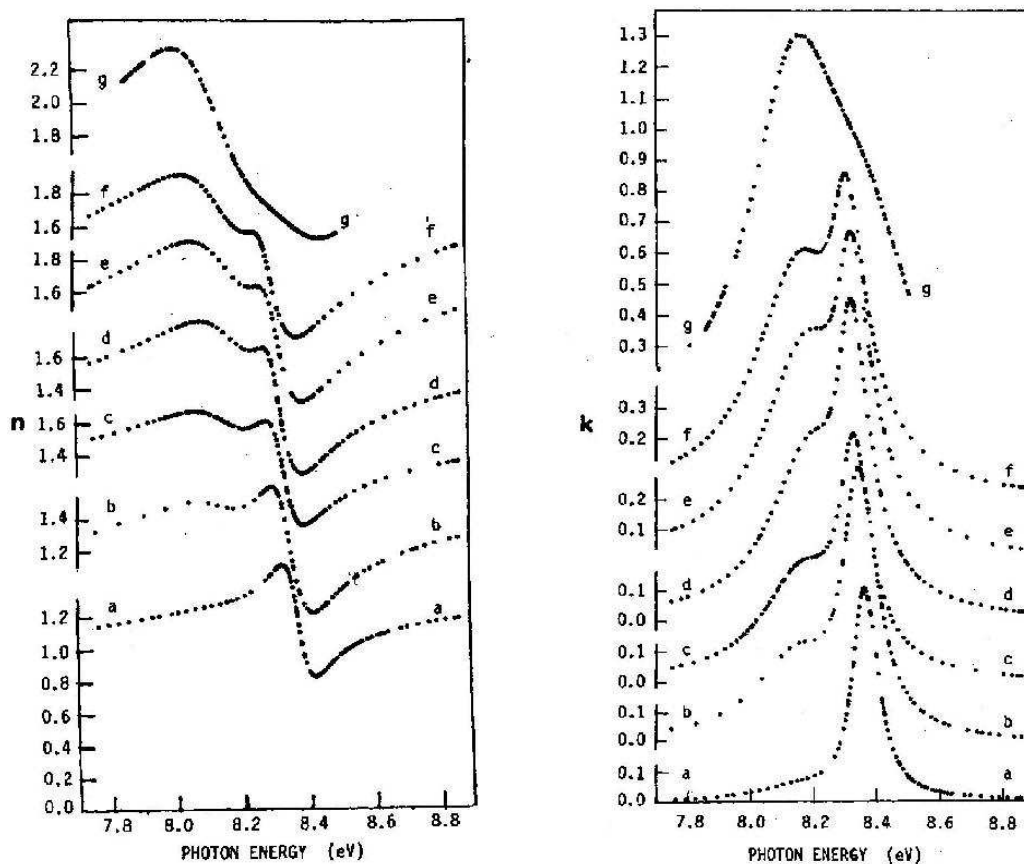


Figure 4.12: The real and the imaginary parts of the Xe refractive index vs photon energy in the region of the first Xe absorption line. Increasing densities from a to g (the LXe emission is at 7.1 eV) [134].

imaginary parts of the refractive index using the reflection method, in the VUV wavelength region $115 < \lambda < 165$ nm.

Result: An important and precise study of the characteristics of the first Xe absorption lines and of their evolution as a function of the density.

The appearance of new lines and the broadening and displacement of normal lines is interpreted as due to Wannier excitons (see at section 4.4.3). This can be clearly seen in Fig. 4.12 which shows the real and the imaginary parts of the Xe refractive index as a function of the photon energy and (from bottom to top) for increasing densities (the curves labelled from a to f; the curve g is for LXe).

The real part of n in the region of LXe emission at $\lambda = 175$ nm cannot be easily extrapolated from these measurements, since one would have to know the complex n both at lower and higher wavelengths.

The data are of sufficiently good quality to allow a test of the linearity on ρ of the Lorentz-Lorenz function on a large range of densities (but at smaller wavelengths than that of LXe emission).

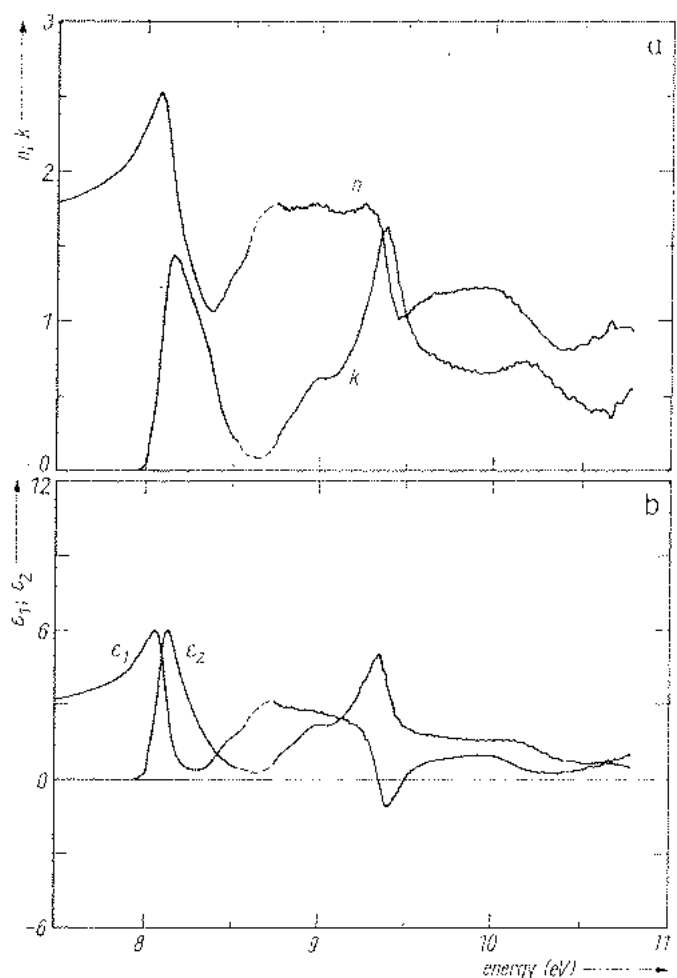


Figure 4.13: *The real and the imaginary parts of the Xe refractive index and dielectric constant vs photon energy [135].*

The VUV Optical Constants of Liquid and Solid Xenon at the Triple Point. J.L. Subtil et al. [135]

State: liquid and solid Xenon. Temperature: $161.2 < T < 163.2$ K. Pressure: $p \approx 1$ Atm. Density: $\rho_m = 2.27 \cdot 10^{-2}$ mol cm^{-3} . Method: Study of the real and imaginary parts of the refractive index by the reflection method, in the VUV wavelength region $112 < \lambda < 203$ nm.

Result: An important and precise study of the characteristics of the first Xe absorption lines and of their evolution in the passage from the liquid to the solid state.

A wider range of wavelengths was studied; the LXe emission wavelength $\lambda = 175$ nm (7.1 eV) is therefore included and the corresponding LXe refractive index is $n = 1.71$. It is interesting to note that $n = 1.69$ is the value extrapolated from the VUV gas measurements of Bideau-Mehu [132], assuming a linearity of the Lorentz-Lorenz function with the density. The passage from liquid to solid Xe in the absorption region shows effects due to the Wannier excitons (see at section 4.4.3). The real and the imaginary parts of the refractive index in LXe are shown in Fig. 4.13 over a wide range of photon energies.

Table 4.7: First virial coefficient as a function of the wavelength, for Xe gas, in different density and temperature conditions.

| A_R ($cm^3 mol^{-1}$) | T, P (K), (bar) | λ (nm) | level purity | Ref. |
|------------------------------|-------------------------------|-------------------|---------------------------------|-------|
| 10.122 ± 0.002 | T=323.15 $P < 13$ | - | - | |
| 10.40 ± 0.01 | $300 < T < 1100$ $P < 1.5$ | 632.99 | 99.95% | [127] |
| 10.427 ± 0.01 | T=293 $P < 3$ | 632.99 | - | [127] |
| 10.463 ± 0.01 | T=293 $P < 3$ | 594.096 | - | [127] |
| 10.524 ± 0.01 | T=293 $P < 3$ | 543.516 | - | [127] |
| 11.256 ± 0.01 | T=293 $P < 3$ | 325.139 | - | [127] |
| 10.345 ± 0.002 | T=303 $1 < P < 400$ | 632.99 | $H_2O < 5$ ppm $O_2 < 2$ ppm | [129] |
| 10.344 ± 0.002 | T=348 $1 < P < 400$ | 632.99 | $H_2O < 5$ ppm $O_2 < 2$ ppm | [129] |
| 12.06 ± 0.6 | T=298 P=0.81 | 253.7 | $Kr < 450$ vpm | [132] |
| 12.74 ± 0.6 | " | 228.8 | " | " |
| 13.27 ± 0.7 | " | 213.9 | " | " |
| 14.42 ± 0.7 | " | 194.2 | " | " |
| 15.29 ± 0.8 | " | 184.9 | " | " |
| 15.78 ± 0.8 | " | 180.7 | " | " |
| 17.61 ± 0.9 | " | 170.2 | " | " |
| 19.58 ± 1 | " | 164.1 | " | " |
| 30.70 ± 1.5 | " | 152.5 | " | " |
| 47.64 ± 2 | " | 149.5 | " | " |
| 75.56 ± 4 | " | 148.3 | " | " |
| 9.703 ± 0.5 | " | 140.4 | " | " |

4.4.3 The Clausius-Mossotti relation from the Xe gas phase to the Xe liquid phase in the VUV

The Tab. 4.7, Tab. 4.8, Tab. 4.9 and Tab. 4.10 summarize the measurements presented in the previous paragraph. The measurements associated with the first virial coefficient are tabulated in Tab. 4.7. The data are ordered as a function of the wavelength, in different conditions of pressure and temperature, for Xe gas. Where the purity of the sample is known, the level is reported. The same available information for the second virial coefficient is in Tab. 4.8. Tab. 4.9 shows also the temperature dependence of the coefficient. Finally the Tab. 4.10 shows the measurements about the third virial coefficient.

Only in the visible region we have simultaneously the measurements of the A_R , B_R and C_R in the same condition of pressure and temperature. Although for this set of data the temperature is not cryogenic, the pressure is very high and this data set allows us to verify that in the visible region and at high pressure the contribution of the second and third coefficient is negligible.

The data set of the first virial coefficient in the visible region supports also the statement that the dependence of A_R from the temperature is negligible for $T < 1100$ K.

Table 4.8: Second virial coefficient as a function of the wavelength, for Xe gas, in different density and temperature conditions.

| B_R cm ⁶ mol ⁻² | T, P (K), (bar) | λ (nm) | level purity | Ref |
|--|------------------------|-------------------|---------------------------------|----------------|
| 35 ± 2 | T=242.95 $P < 13$ | — | — | [128] |
| 32 ± 2 | T=323.15 $P < 13$ | — | — | [128] |
| 12 ± 2 | T=407.6 $P < 13$ | — | — | [128] |
| 28.5 ± 0.5 | T=348 $1 < P < 400$ | 632.99 | $H_2O < 5$ ppm $O_2 < 2$ ppm | [129] [129] |
| 25.5 ± 2.85 | T=293.60 $P < 3$ | 632.99 | — | [127] [127] |
| 25.5 ± 2.85 | T=294.05 | ” | — | ” |
| 24.58 ± 2.5 | T=293.6 | 543.516 | — | ” |
| 25.26 ± 2.5 | T=294.05 | ” | — | ” |
| 23.25 ± 2.5 | T=293.6 | 325.139 | — | ” |
| 23.25 ± 2.5 | T=294.05 | ” | — | ” |

Table 4.9: Second virial coefficient B_R as a function of temperature.

| T (K) | B_R cm ⁶ mol ⁻² |
|------------|--|
| 294.24 | 37.2 ± 8.9 |
| 387.27 | 34.8 ± 2.6 |
| 478.32 | 29.7 ± 2.0 |
| 564.46 | 27.1 ± 3.3 |
| 665.78 | 27.2 ± 1.8 |
| 762.24 | 27.3 ± 2.3 |
| 859.20 | 26.2 ± 1.3 |
| 965.03 | 24.6 ± 2.4 |
| 1079.69 | 24.2 ± 0.1 |

Table 4.10: Third virial coefficient C_R for Xe gas, in different density and temperature conditions.

| C_R cm ⁹ mol ⁻³ | T, P (K), (bar) | λ (nm) | Ref |
|--|----------------------|-------------------|-------|
| -3482 ± 310 | 323.15 $P < 13$ | ∞ | [128] |
| -1164 ± 437 | 407.6 $P < 13$ | ∞ | ” |
| -1802.0 ± 50.0 | 348 $1 < P < 400$ | 632.99 | [129] |

The conclusion of the first step of our analysis is that, in the visible region, the eq. (4.13) is:

$$F_{LL} = \frac{n^2(\omega) - 1}{n^2(\omega) + 2} = \frac{\epsilon(\omega) - 1}{\epsilon(\omega) + 2} = A_R(\omega)\rho_m. \quad (4.18)$$

Note that only the dependence on the wavelength remains and nothing else.

Eq. (4.18) appears to be a simple tool to derive the refractive index in liquid Xe, if the first virial coefficient was measured in gas.

We verified that the same equation is still valid in the VUV.

For this purpose we verified up to which photon energy eq. (4.18) is still valid, by plotting the quantity $F_{LL} = A(\omega)\rho$ versus the density ρ_m , at different photon energies. Fig. 4.14, 4.15, 4.16, 4.17 and 4.18 show the results.

One can observe that for energies up to 8.1 eV the F_{LL} data are well fitted by a linear dependence on the density, over quite a wide density range, from dilute gas to liquid. $A(\omega)$, the slope of the fitted lines, corresponds to a rather constant value, up to 8.1 eV, as it appears in Fig. 4.19. Note that the Xenon excited by ionizing radiation emits at $\lambda = 178$ nm, that is: photons with $\hbar\omega = 7.0$ eV.

It was observed that, when the density reaches high values, the absorption lines are distorted and broadened and a system of satellite lines appears, always at energies lower than the main lines.

This phenomenon is explained in terms of exciton formation¹ [134, 138, 139] and can be immediately related to higher density terms in the virial expansion. As a consequence we expect that the Clausius-Mossotti relation is no longer linear in ρ_m at photon energies close to the absorption lines. This is what we observed in our fits. At higher photon energies, hence closer to the Xe photon absorption lines, the fits become increasingly worse, the linear model is rejected (and the error on $A(\omega)$ is meaningless).

One can therefore conclude that, when ω is reasonably far from the absorption region, most of the information obtained for gaseous Xenon in various physical conditions can be used for predicting the optical properties of LXe at the emission wavelength [137].

The experimental determinations of the refractive index in LXe, at the Xe emission wavelength of 178 nm [135, 136] and at 180 nm [133], are presented in Fig. 4.20 (a) and (b). The errors on n are those quoted in the papers with the exception of [135], which has very small errors from point to point, but a systematic error on n which is not clearly stated; we assumed a systematic error of $\approx 3\%$.

The measured refractive index is compared with an extrapolated value we derived, based on the simple Clausius-Mossotti equation utilizing VUV data obtained in gas at low density [132].

One can observe a rather good agreement between the measured n and the extrapolated value. The measurement corresponding to [133] gives a n value at 180 nm which is somewhat low, but the experimental error, quoted in the paper, appears to us over-optimistic.

Since we assumed (and checked) the validity of the simple Clausius-Mossotti equation, the relation between $n(\omega)$ and $A(\omega)$ is fixed. We present in Fig. 4.21 the dispersive behaviour of $A(\omega)$ as a function of the photon energy $\hbar\omega$. The open circles are the VUV measurements [132] obtained at low density ($p \approx 1$ Atm). The dashed line is the fit to those points. The function used is:

$$A(E) \approx \sum_{i=1}^3 \frac{P_i}{E^2 - E_i^2} \quad (4.19)$$

with $E = \hbar\omega$, P_i the parameters resulting from the fit and E_i the absorption line positions ($P_1 = 71.23$ eV² cm³ mol⁻¹, $P_2 = 77.75$ eV² cm³ mol⁻¹, $P_3 = 1384.89$ eV² cm³ mol⁻¹, $E_1 = 8.4$

¹by Wannier-excitons one means Rydberg levels, at energies between the valence band and the conduction band, due to electron-hole bound states extending over ≈ 10 nm regions of the fluid.

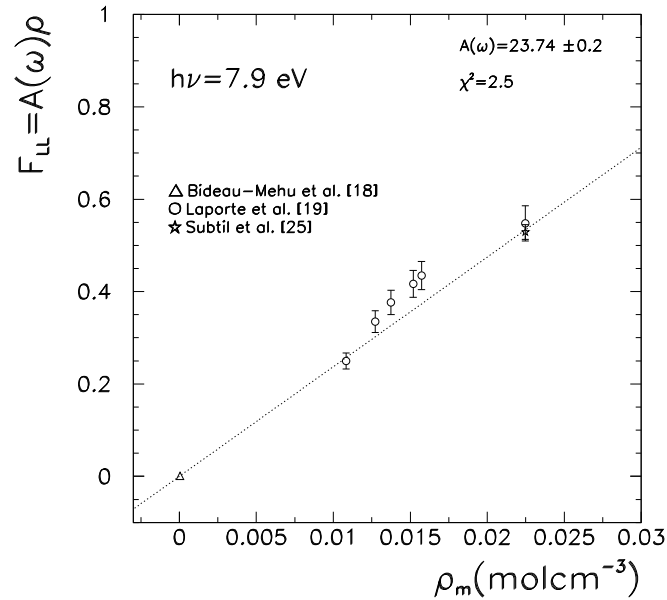


Figure 4.14: Check of the linearity of F_{LL} as a function of the density ρ_m , from the gas to the liquid phase at $h\nu = 7.9$ eV.

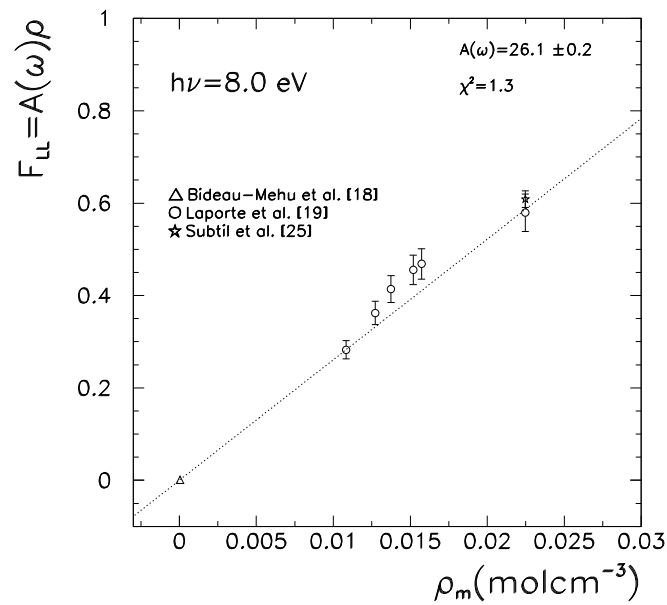


Figure 4.15: Check of the linearity of F_{LL} as a function of the density ρ_m , from the gas to the liquid phase at $h\nu = 8.0$ eV.

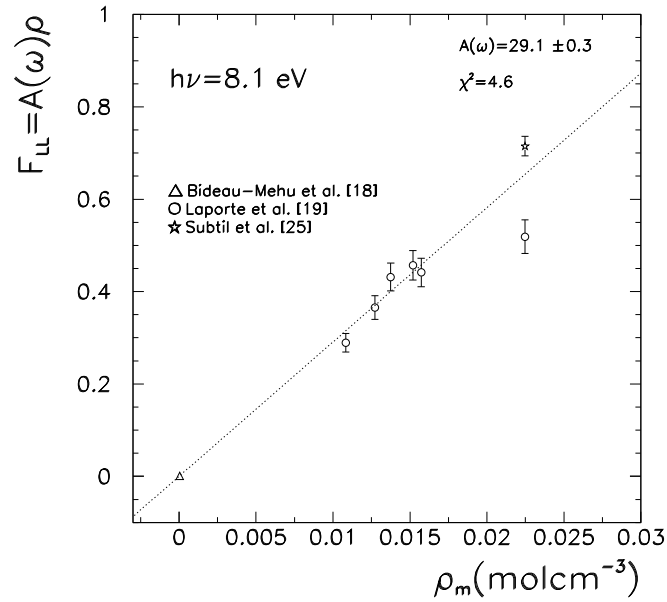


Figure 4.16: Check of the linearity of F_{LL} as a function of the density ρ_m , from the gas to the liquid phase at $h\nu=8.1 \text{ eV}$.

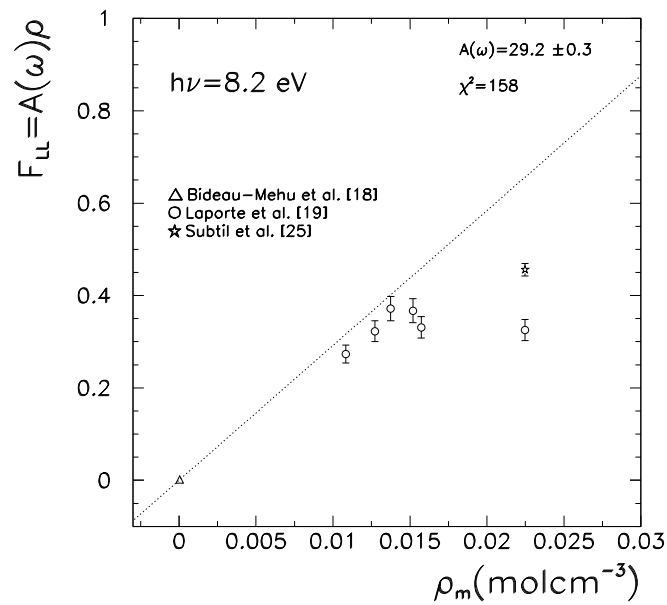


Figure 4.17: Check of the linearity of F_{LL} as a function of the density ρ_m , from the gas to the liquid phase at $h\nu=8.2 \text{ eV}$.

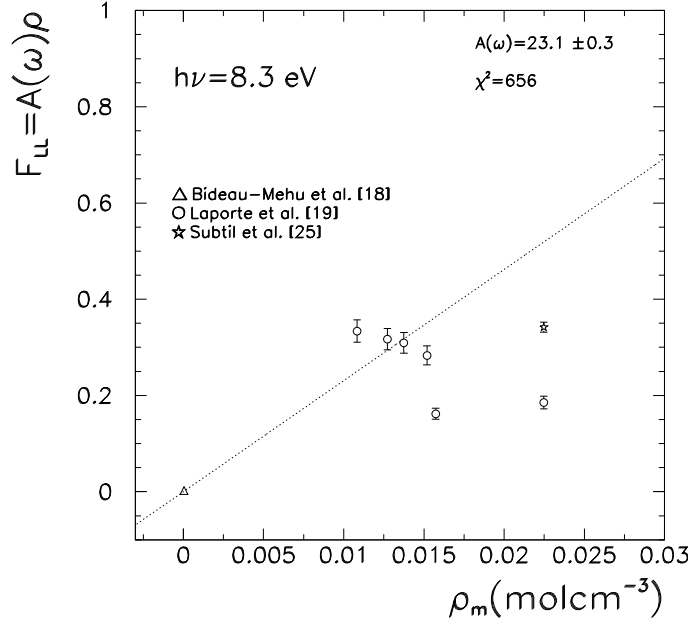


Figure 4.18: Check of the linearity of F_{LL} as a function of the density ρ_m , from the gas to the liquid phase at $h\nu = 8.3 \text{ eV}$.

eV $E_2 = 8.81 \text{ eV}$ and $E_3 = 13.2 \text{ eV}$). The star symbols are the values of $A(\omega)$ corresponding to the fits of Fig. 4.14, 4.15, obtained over the large density range from dilute gas to liquid Xe. The experimental measurements of the refractive index n in LXe at 178 and 180 nm [133, 135, 136] are also shown by their corresponding $A(\omega)$, as black symbols.

If we use eq. (4.19) in eq. (4.18) and we introduce the simplifications possible for rarified gas we obtain the Sellmeier equation, which describes the refractive index as a function of the wavelength (frequency):

$$n - 1 \propto \sum \frac{f}{\omega'^2 - \omega^2} \quad (4.20)$$

The refractive index data are well fitted by the expression with three parameters:

$$n - 1 = 1.2055 \times 10^{-2} \left(\frac{0.26783}{46.301 - \lambda^{-2}} + \frac{0.29481}{59.578 - \lambda^{-2}} + \frac{5.0333}{112.74 - \lambda^{-2}} \right) \quad (4.21)$$

The Fig. 4.22 shows the data with the fitted curve. We show also the the measurements of the refractive index in liquid xenon, where the gas data fitted curve is superimposed. The agreement is very good (Fig. 4.23).

4.5 The relation between the Rayleigh scattering length and the refractive index

We are ready to move again from Einstein's equation, which we rewrite here:

$$\frac{1}{\lambda_R} = \frac{\omega^4}{6\pi c^4} \left[KT\rho^2 \kappa_T \left(\frac{\partial \epsilon}{\partial \rho} \right)_T^2 + \frac{KT^2}{\rho c_v} \left(\frac{\partial \epsilon}{\partial T} \right)_\rho^2 \right] \quad (4.22)$$

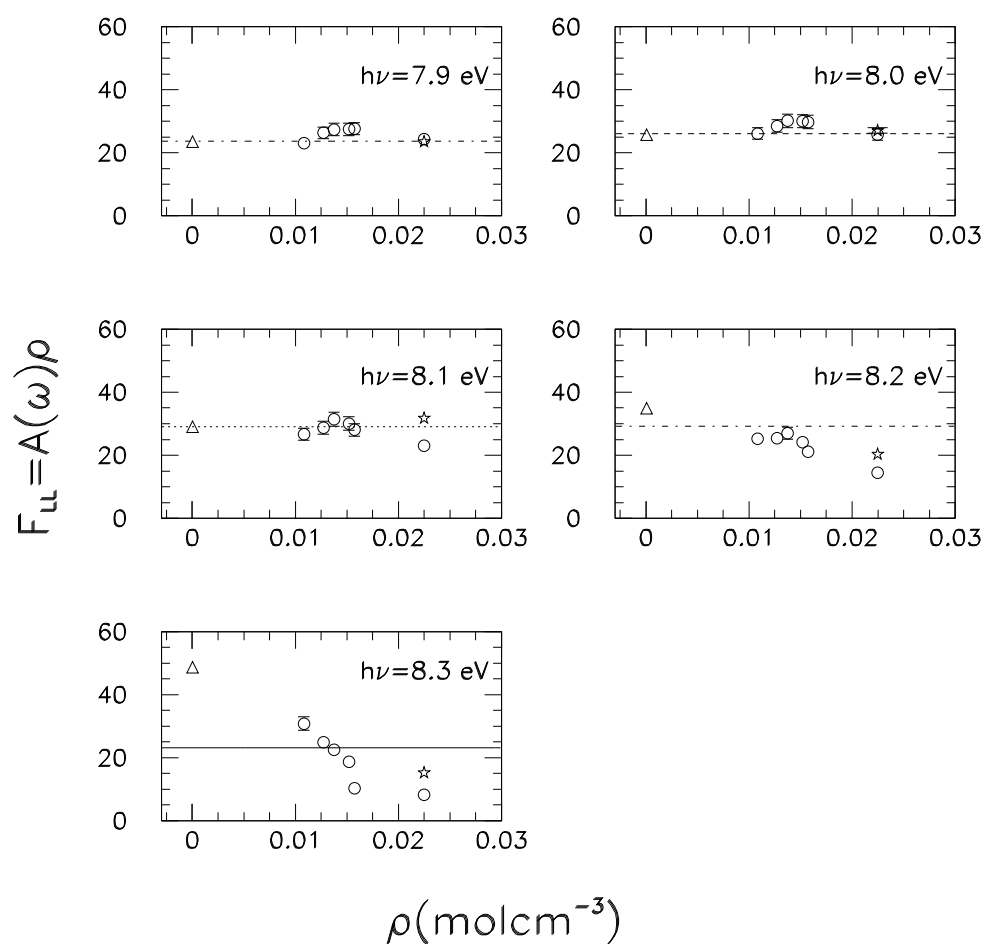


Figure 4.19: $A(\omega)$ as a function of the density ρ_m , at different photon energies. $A(\omega)$ approximately corresponds to a constant value up to $h\nu \approx 8.1 \text{ eV}$.

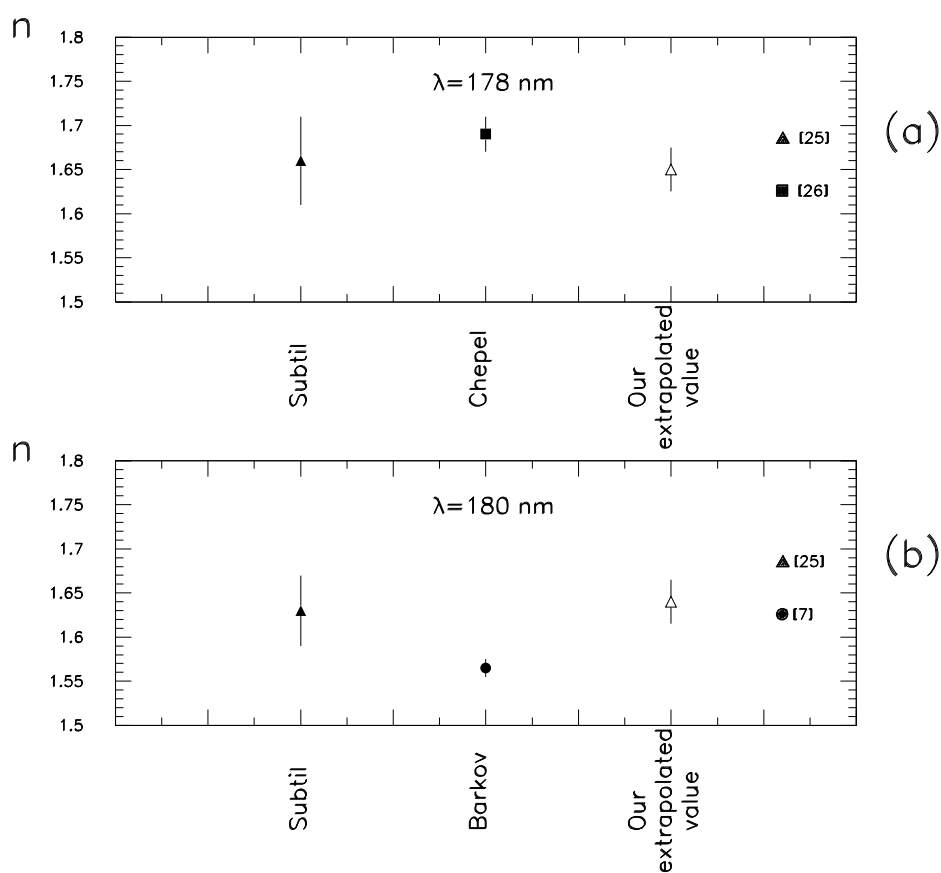


Figure 4.20: Measurements of the refractive index in LXe (black symbols) are compared with a value extrapolated from low densities (open triangle), at two different wavelengths.

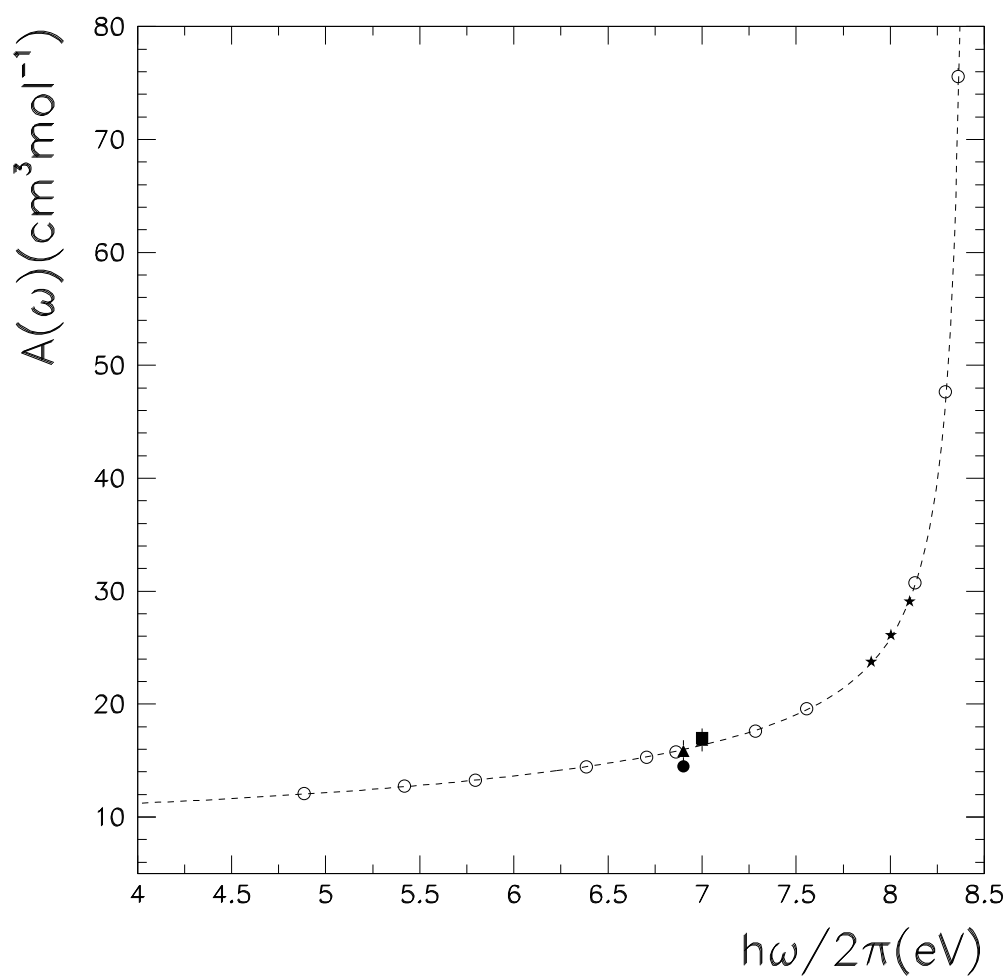


Figure 4.21: *The dispersive behaviour of $A(\omega)$ as a function of the photon energy $h\omega$. Experimental measurements at higher densities are also shown (see text).*

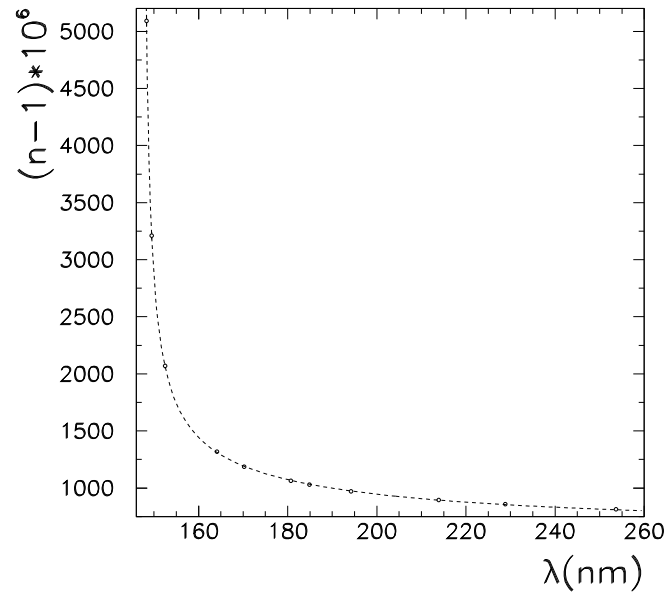


Figure 4.22: Measured refractive index in gas Xe (open circles) and result of a fit (dashed line) [132].

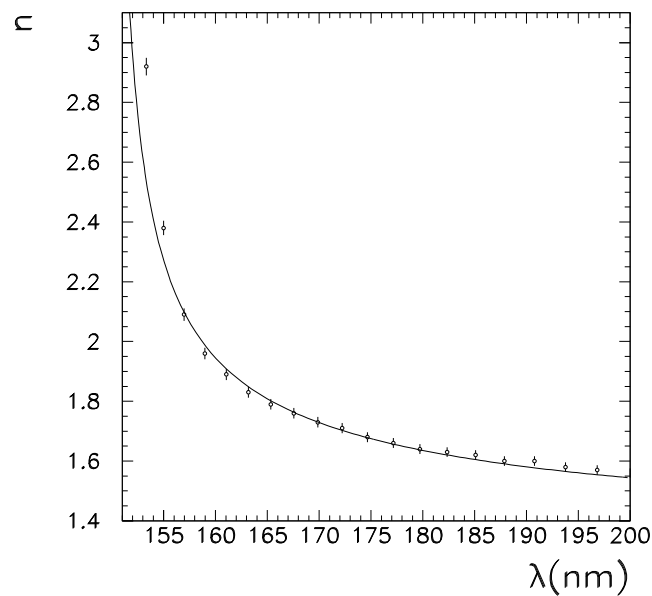


Figure 4.23: Measured refractive index in liquid Xe (open circles) [135], with the previous fit result on gas Xe data, after correcting for gas to liquid density variation [132].

Since Xenon is a non-polar fluid, the second part of eq. (4.22) turns out to be negligible [137, 127, 82]. The derivative appearing in the first part of eq. (4.22) can be computed from the Clausius-Mossotti equation eq. (4.11). Einstein's equation reduces to:

$$\frac{1}{\lambda_R} = \frac{\omega^4}{6\pi c^4} \left\{ K T \kappa_T \frac{[n^2(\omega) - 1]^2 [n^2(\omega) + 2]^2}{9} \right\}. \quad (4.23)$$

This equation establishes a useful relation between the refractive index in pure LXe and the Rayleigh scattering length, which can undergo an experimental test ². Due to the form of the relation and to error propagation, for a $n \approx 1.65$ in LXe at $\lambda \approx 178$ nm $\sigma_{\lambda_R}/\lambda_R \approx 8.6\sigma_n/n$.

λ_R vs n from equation eq. (4.23) (black circles) is shown in Fig. 4.24. The input values for the refractive index $n(\omega)$ are those obtained from a fit to the low pressure VUV measurements [132]. The simple Clausius-Mossotti relation eq. (4.11) (and its linearity as a function of ρ_m) is assumed to be valid.

There are only two published measurements of the Rayleigh scattering length in LXe at 178 nm which gave $\lambda_R = 29 \pm 2$ cm [93] and $\lambda_R = 36.4 \pm 1.8$ cm [136] (in this last case the refractive index was also measured); we note that the two values are far apart. These determinations were obtained for light produced by radioactive source excitation of LXe. This means that the measured λ_R is an average over the 14 nm (FWHM) LXe emission spectrum. In checking the validity of equation eq. (4.23) an average over the LXe emission spectrum must therefore be performed.

In Fig. 4.24 eq. (4.23) is also shown after averaging over the LXe emission spectrum (open circles); the differences between the two curves are small. In the same figure the only available experimental measurement of both n and λ_R [136] (black square) is compared with the extrapolated values for the same two quantities (open triangle) obtained, as already explained, from the low-pressure VUV data and the Clausius-Mossotti relation.

In the case of small amounts (ppm) of other rare gases, like Ar or Kr, added to Xe, eq. (4.23) preserves its validity and λ_R does not vary appreciably. This is not true in the case of absorbing contaminants, as was shown during the tests of the large prototype detector [60], and is discussed in the section 4.3.

If impurities are present, to the two terms in the eq. (4.22) another must be added [137]:

$$h_{imp} = \frac{8\pi^3\omega^4}{3c^4} \left[\frac{xM}{N_a} \left(\frac{\partial\epsilon}{\partial x} \right)^2 \right] \quad (4.24)$$

where x is the impurity level and M is its molecular mass. If we use the approximation:

$$\epsilon \approx x\epsilon_{imp} + (1-x)\epsilon_{Xe} \quad (4.25)$$

eq. (4.24) becomes:

$$h_{imp} = \frac{8\pi^3\omega^4}{3c^4} \frac{xM}{N_a} (\epsilon_{Xe} - \epsilon_{imp})^2 \quad (4.26)$$

Then, if the impurity level is low and $\epsilon_{Xe} - \epsilon_{imp} \approx 1$, the contribution of the eq. (4.26) is negligible:

$$h_{imp} \approx 10^{-8} \left(\frac{x}{1ppm} \right) cm^{-1}. \quad (4.27)$$

Then the presence of non-polar impurities at a level lower than 1 ppm (as required for a large absorption length), preserves the validity of eq. (4.22).

The α -sources on the walls allow a crude evaluation of the Rayleigh scattering length, by using the information of PMTs located on the same face as the source. We expect that what is collected

²To the best of our knowledge this relation was never previously applied to LXe.

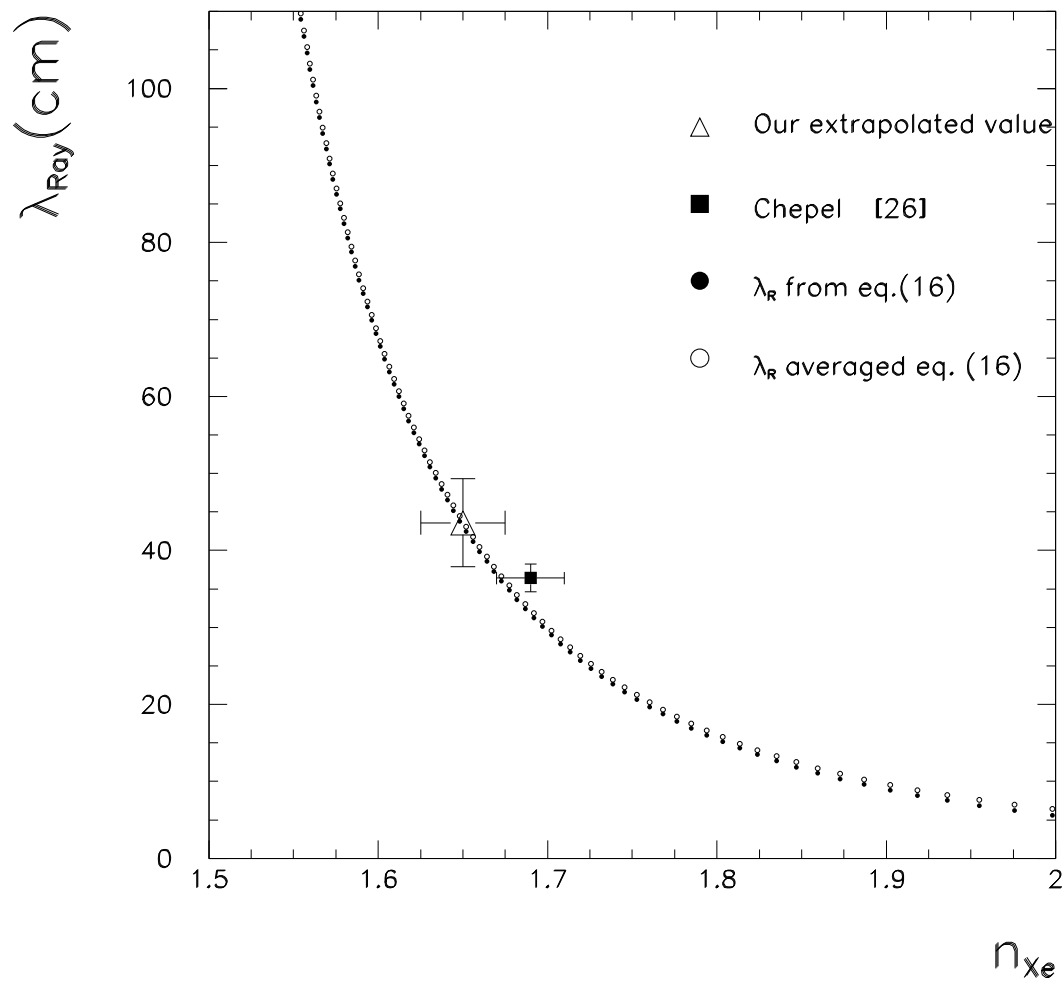


Figure 4.24: λ_{R} vs n from equation eq. 4.23 (black points). The average over the LXe emission spectrum is also shown (open points). The only available experimental measurement of both λ_{R} and n is compared with the prediction of our model.

Table 4.11: Measurements of λ_{att} for liquid Xe, in the VUV region.

| λ_{att} (cm) | Ref. |
|----------------------|---------------------|
| 29 ± 2 | Ishida et al. [93] |
| 36.4 ± 1.8 | Chepel et al. [136] |

by these PMTs comes from scattered light only. Our data prefer values of λ_R of the order of 40-50 cm, which is consistent with what is available in the literature, at present.

If we assume that λ_{abs} is greater than 1 m, as suggested by our measurements, λ_{att} is mainly determined by λ_R . Tab. 4.5 reports the two available measurements of λ_{att} . The λ_{att} extrapolated value, according to the method proposed by Lanou et al., is not far from the Chepel et al. ed Ishida et al. values.

Measurements of λ_{att} , λ_{abs} , λ_R and n are however required, to confirm our results. The measurement of the Xe purity is important if one has to compare results. Note that the impurities influence also the refractive index, and therefore λ_R .

From the optical theorem:

$$\Im f(0) = \frac{k}{4\pi} \sigma_{tot} \quad (4.28)$$

where $f(0)$ is the diffusion amplitude (for $\theta = 0$) and σ_{tot} :

$$\sigma_{tot} = \sigma_{abs} + \sigma_{dif}. \quad (4.29)$$

Also:

$$\lambda_{att} = \frac{1}{N\sigma_{tot}} \quad (4.30)$$

and:

$$\left(\frac{d\sigma}{d\Omega} \right)_{dif}(0) = |\Re f(0)|^2 + |\Im f(0)|^2 \quad (4.31)$$

This result underlines the fact that also in the Monte Carlo simulation the knowledge of the optical properties of the Xenon is relevant.

Chapter 5

The liquid xenon calorimeter

In this chapter we discuss the main components of the liquid xenon calorimeter:

- the cryostat and the cryogenic equipment;
- the Xe purification system;
- the photomultipliers.

The development of the photomultipliers for the LXe calorimeter, being particularly relevant, is presented in detail.

5.1 The Xe cryostat and the cryogenic equipment

5.1.1 The Xe cryogenic circuit

Xenon is kept liquid in the cryostat at 165 K and 0.12 MPa during normal operations. The LXe active volume is 800-liter (see Fig. 5.1), the total amount of LXe being approximately 850 liters.

A diagram of the liquid xenon cryogenic system is shown in Fig. 5.2.

Xe can be stored as a gas in eight tanks with a total volume of 2448 liters, at a pressure of 70 bar or, as a liquid, in a 1000 liter dewar using the cryogenic equipment in common with the cryostat. The two volumes are in a 650 ratio to compensate for the different density of LXe (at 1 atm and -108°C) and GXe (at 1 atm and 25°C).

Xe is liquified by cooling the cryogenic volume in which it is being collected. Both the cryostat and the dewar are equipped with a pulse tube cryocooler and liquid nitrogen LN₂ pipes. The pulse tube cryocoolers and the LN₂ pipes are placed at the top of both the cryostat and dewar. The cryostat is precooled to reduce the duration of the cooling phase, by LN₂ circulating in pipes attached to the lateral walls of its inner volume. During liquefaction the pulse tube cryocooler and the LN₂ circulation are switched on. At the end of the process the LN₂ flow is switched off, the pulse tube cryocooler alone being able to maintain Xe in the liquid state.

The time needed to liquefy fully Xe is about 1 month, a rather long time interval. The dewar was introduced into the cryogenic circuit because it allows the storage of LXe. If the cryostat has to be emptied, LXe can be transferred from the dewar to the cryostat (or vice versa) in approximately 3 days.

The level of LXe is monitored by a cylindrical capacitance following the C-shape of the inner vessel. Xe (liquid or gas) is the capacitor dielectric [142].

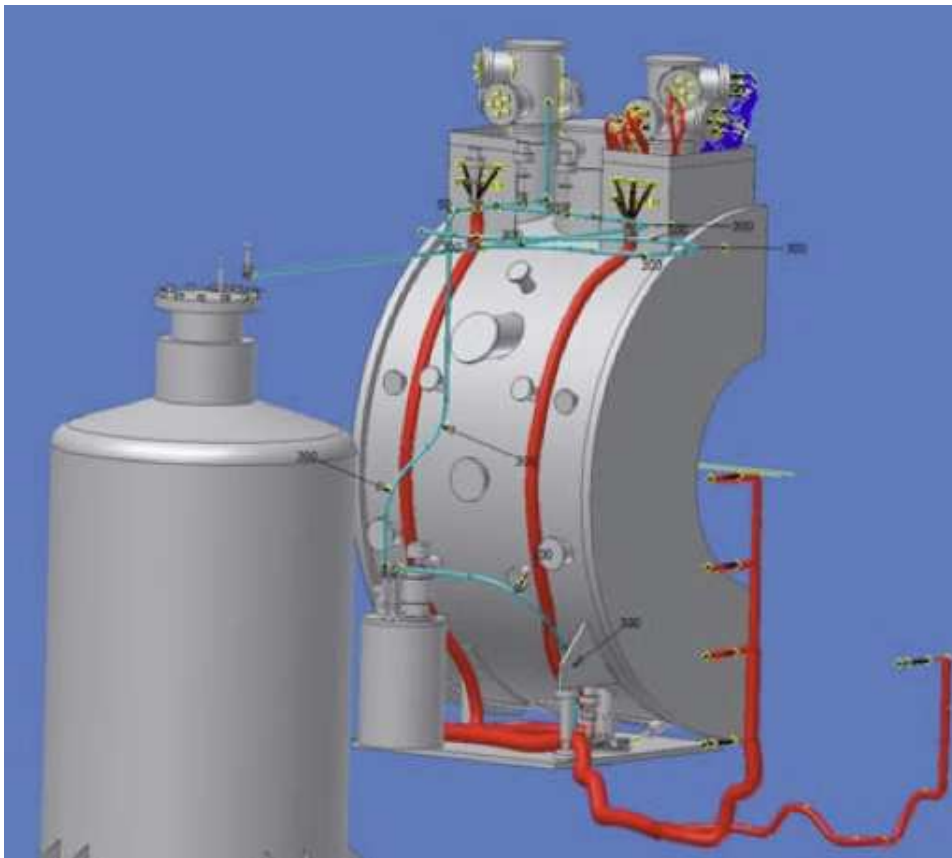


Figure 5.1: *The LXe cryostat and the LXe dewar.*

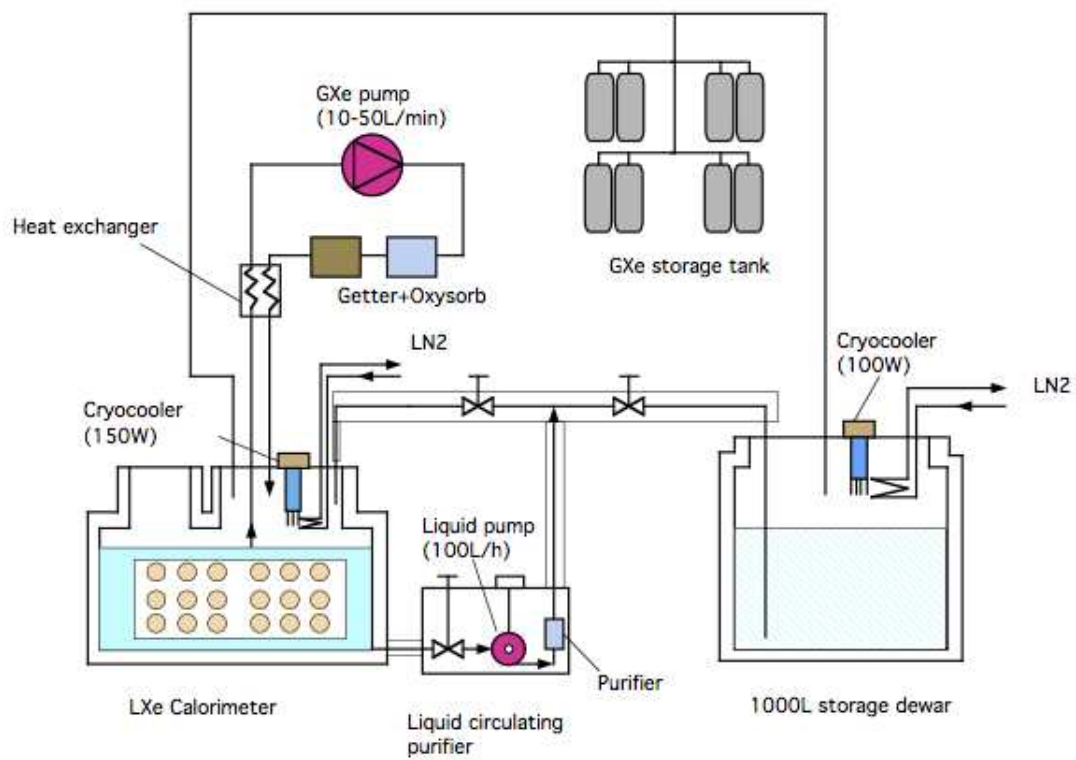


Figure 5.2: *Diagram of the MEG LXe cryogenic system.*

Table 5.1: Xenon main cryogenic properties.

| Property | Unit | Value |
|--|--|---------------|
| Saturation temperature | T(K) | 164.78 |
| Latent heat (boiling) | $L_v(\text{J/kg}) \times 10^3$ | 95.8 |
| Latent heat (melting) | $L_v(\text{J/kg}) \times 10^3$ | 1.2 |
| Specific heat | $C_p(\text{J/kg}) \times 10^3$ | 0.3484 |
| Density | $\rho(\text{Kg/m}^3) \times 10^3$ | 2.947 |
| Viscosity | $\mu(\text{Pa} \cdot \text{s}) \times 10^{-4}$ | 5.08 |
| Temperature/Pressure at the triple point | $T_t(\text{K})/P_t(\text{MPa})$ | 161.36/0.0815 |

5.1.2 The cryostat

The main cryogenic properties of Xe are shown in Tab. 5.1. The cryostat consists of two vessels, the inner one (the cold vessel), where Xe is liquid, and the outer one (the warm vessel), kept under vacuum.

The cryostat was carefully designed to reduce the heat transfer between the inner and outer vessel. To that end, the connections and the supports of the inner vessel are kept to a minimum and the heat convection is lowered by maintaining the outer vessel under vacuum, at the mbar level. The heat irradiation is suppressed by the use of super-insulation foils (about 20 layers).

If one considers the amount of heat transfer, which is minimized, but not zero, and the heat due to the photomultipliers mounted inside the inner vessel (PMT total emitted power: approximately 40 W), a pulse tube cryocooler with a power of 150 W to keep Xe liquid is needed.

The use of a pulse tube cryocooler is an important improvement in the cryogenic system [140], [141] since no moving part is in contact with the cold liquid, thus reducing the vibrations present in other commercial cryocoolers (of the order of $8 \mu\text{m}$ peak-to-peak). The cryogenic experts in MEG developed a new pulse tube cryocooler, with optimized performances and vibrations reduced by 96%.

The inner and outer vessels are C-shaped. This maximizes the accepted solid angle and minimizes the LXe volume. The photomultiplier support structure has the same C-shape (see Fig. 5.3). Particular care went into the design of the thin window of the inner vessel. Both the inner and the outer vessels have very thin steel windows (thickness about 3 mm) to minimize the interactions of γ 's from μ -decay. A honeycomb structure is fixed on the inner thin window to avoid its shape change, from concave to convex, when vacuum is created in the outer vessel and LXe is present in the inner one. The honeycomb is a thin carbon fiber structure characterized by a high mechanical rigidity.

Finally three large nozzles are placed at the top of the cryostat. They house the pulse tube refrigerator, the vacuum pump, feed-through connectors for temperature readout, HV supply and PMT signal cables, pressure/vacuum gauges, and various kinds of valves for the xenon transfer.

5.2 The Xe purification system

We already mentioned in the previous chapter that LXe is transparent to its own scintillation light, but possible contaminants, such as water and oxygen at the ppm level, might produce a considerable absorption.

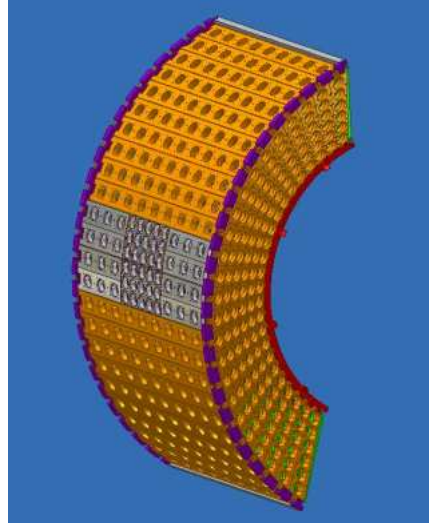


Figure 5.3: *The PMT support structure mounted inside the cryostat inner vessel.*

Table 5.2: Specifications of the purifier cartridge.

| | |
|-------------------------------|--|
| Purifier cartridge dimensions | 58 mm (diam.) 184 mm (height) |
| Absorbent | Molecular sieves (13 A) 1/16 inch, pellet type |
| Absorbent filling factor | 0.59 g/cm ³ |
| Water absorption capacity | > 24g |
| Design pressure | 0.4 MPa |
| Operation temperature | 165 K |

A preliminary study of the Large Prototype has shown that water is the dominant contaminant, while the oxygen concentration was of a smaller order of magnitude. The level of other VUV absorbing contaminants, such as the hydrocarbons, was more than two orders of magnitude smaller.

We know that G10, the material used for inner parts of the cryostat, can absorb and desorb water. The simplest way to remove water is to heat the cryostat while evacuating it. This is impossible, since the PMTs are internally mounted. Some water can therefore be trapped in the cryostat and then pass into LXe. Water is the contaminant, that must be removed.

Xe in the Large Prototype was purified as a gas; a Molecular Filter and a Gas Purifier were used. The gas was in equilibrium with the liquid and was continuously filtered.

The purification in the final calorimeter was improved, in efficiency and speed, by the use of a Molecular Filter and a Gas Purifier operating in the liquid phase. The coupling of a cryogenic centrifugal pump to the Filter and Purifier achieved a purification corresponding to 40 ppb from an initial water impurity of 250 ppb, in only 5 hours [144], [143].

A purifier cartridge of 500 cm³ filled with molecular sieves (MS13A), with a filling density of 0.59 g/cm³ was prepared. The cartridge is surrounded by a cylinder containing heaters, with a low emission rate of dust and impurities, produced by the Watlow Electric Manufacturing Company. The purifier cartridge can absorb more than 24 g of water after regeneration, although that depends on the water contamination level in LXe. The specifications of the purifier cartridge are summarized in Tab. 5.2.

The cryogenic centrifugal pump is produced by BarBer-Nichols Inc. At the normal working point (3175 rpm rotational speed of the pump head) the pump can move 100 liters of liquid Xe

Table 5.3: Normal operating conditions of the cryogenic centrifugal pump.

| Properties | Value |
|---------------------------|--------------|
| Fluid | Liquid Xenon |
| Inlet pressure (absolute) | 0.10 MPa |
| Inlet temperature | 165 K |
| Flow rate | 100 L/h |
| Differential pressure | 0.2 MPa |
| Operating speed | 3175 rpm |

per hour. In normal use, 5000 hours of operation are guaranteed by the manufacturer. This corresponds to 600 purification cycles for MEG. The specifications of this pump are summarized in Tab. 5.3.

5.3 The photomultipliers for the LXe calorimeter

The photomultipliers (PMTs) for the LXe calorimeter must satisfy conditions rarely met, associated with the use of Xenon as a scintillating medium. The most important are the following three. PMTs must work:

- in the vacuum ultra-violet (VUV) region. We recall that the Xe scintillation spectrum is centered at 178 nm (FWHM 14 nm). A quartz window must be used;
- at cryogenic temperature. The PMTs are immersed in liquid xenon ($T = -108^\circ\text{C}$) to guarantee an efficient and direct light collection;
- at high rates. Neutrons induced by the primary proton beam, and γ 's from radiative muon decays (we run at high muon intensity, $I_\mu \approx 6 \cdot 10^7 \mu/\text{s}$) are the main sources of background in the LXe calorimeter.

At a temperature lower than 0°C , alkali photocathodes can be used. High quantum efficiency and low dark current are two appealing characteristics. However (1) the producer guarantees their performance only over $T \geq -30^\circ\text{C}$; (2) the photocathode resistivity becomes very high at low temperatures.

A period of R&D was needed to develop photomultipliers working at $T = -108^\circ\text{C}$ and at high background rate. This then guaranteed the stability of the detector, the calorimeter behaviour being unaffected by considerable changes in the muon beam intensity. The PMTs were thoroughly studied under conditions similar to those expected during the experiment.

5.3.1 Physics of PMTs at low temperature

In this subsection we discuss the physics directly related to the PMTs performance at low temperature, skipping well known items to be found in PMTs data sheets and guides (such as: photoemission, photoabsorption, electron diffusion, surface barrier, photoelectron energy distribution, secondary emission mechanism, etc.) [145].

The photocathode response as a function of temperature is characterized by:

1. a photocathode resistivity increase at cryogenic temperature, later discussed;
2. a dark current reduction as the temperature decreases, whose main contribution is described by the Richardson's formula:

$$I = AT^2 \exp\left(\frac{-e\phi}{kT}\right) \quad (5.1)$$

where A is a constant, ϕ is the work function (it is the minimum energy needed to remove an electron from a solid), T is the temperature and k the Boltzmann constant;

3. variations in the photocatode spectral sensitivity;
4. gain changes, due to possible variations of the secondary emission coefficient.

The main limitation of the bialkali photocatode behaviour is the high photocatode resistivity at low temperature. We will try to explain the physical processes associated with this effect and the solution adopted to reduce the photocatode resistivity.

5.3.2 The bialkali photocatode resistivity at low temperature

A bialkali photocatode is made of alkali metals (K, Cs, Rb, etc.) and semiconductors (Sb). Metals and semiconductors are characterized by a resistivity ρ , which varies according to temperature in a different way. When the temperature decreases the metal conductivity ($\sigma = 1/\rho$) increases (for a pure metal at zero kelvin it becomes infinite), while the semiconductor conductivity decreases to zero (the semiconductor becomes an insulator). Experimentally we distinguish between metals and semiconductors by their conductivity temperature dependence.

The metal conductivity at high temperature is directly related to the electron diffusion while ions oscillate around their equilibrium positions. At low temperature the ion oscillations become negligible, the most important phenomenon remaining the electron diffusion on crystal impurities and defects.

The contributions of these two mechanisms are described by:

$$\rho \sim T \text{ for } T \geq \Theta_D \quad (5.2)$$

$$\rho \sim T^5 \text{ for } T \leq \Theta_D \quad (5.3)$$

where Θ_D is the Debye temperature, which separates the high and low temperature regions.

The semiconductor conductivity behaviour is different from that of metals.

Electrons in completely filled bands do not conduct current. An insulator in the ground state has all bands filled, while a metal has only one band partially filled. The energy difference between the lower level of the empty bands and the higher level of the full bands is the gap energy E_g . From the theoretical point of view, we distinguish between insulator, with $E_g \neq 0$, and metal, with $E_g = 0$. From the phenomenological point of view, we distinguish between insulator and conductor, if they respectively verify the conditions $E_g \gg k_B T$ or $E_g \sim k_B T$ (T is the room temperature).

At $T \sim 300 \text{ K}$:

- for metal: $10^4 \leq \sigma \leq 10^6 \text{ ohm}^{-1} \text{ cm}^{-1}$;
- for semiconductor: $10^{-10} \leq \sigma \leq 10^4 \text{ ohm}^{-1} \text{ cm}^{-1}$;
- for insulator $10^{-20} \leq \sigma \leq 10^{-10} \text{ ohm}^{-1} \text{ cm}^{-1}$.

As consequence a solid with $E_g \neq 0$ at $T = 0 \text{ K}$ does not conduct.

At $T \neq 0 \text{ K}$ there is a probability that some electrons, thermally excited, jump to the conduction bands from the valence bands. The induced conductivity crucially depends on the E_g -value.

The number of electrons so excited follows an exponential function and the resistivity is therefore given by:

$$\rho \sim e^{-\frac{E_g}{2k_B T}} \quad (5.4)$$

This clearly appears in Fig. 5.4 for a bialkali photocatode.

An solution to this problem is to deposit metal strips (aluminum strip in our case) on the photocatode. In the following sections we discuss the PMT behaviour observed at low temperature and in high background conditions and the final choices for MEG.

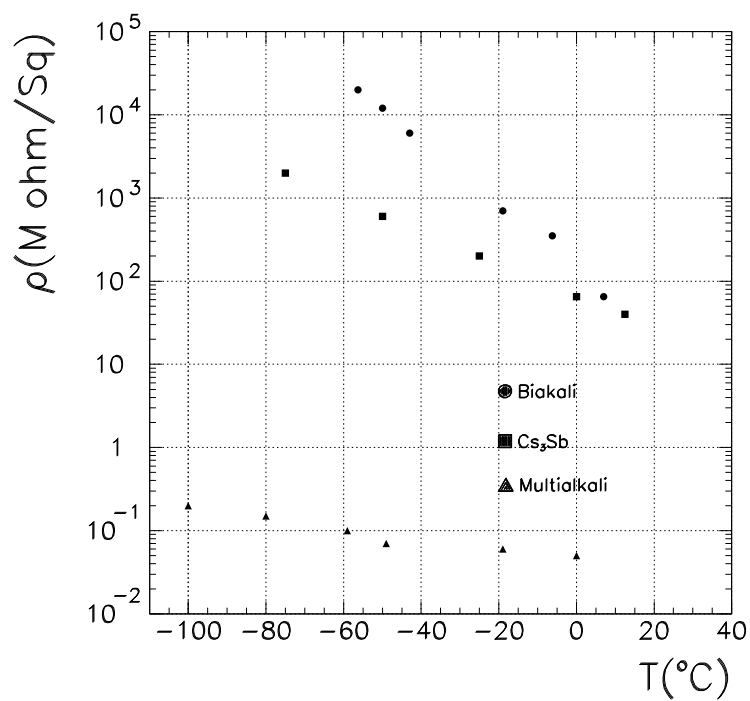


Figure 5.4: Photocathode resistivity as a function of temperature for different photocathode materials.

Table 5.4: The main PMT Hamamatsu R6041 properties.

| | |
|---------------------|---------------------------|
| Diameter | 57 mm |
| Photocathode | Rb-Cs-Sb |
| Sensitive area | 46 mm |
| QE at 165 K | $\approx 5\%$ (at 178 nm) |
| Dynode type | metallic channel |
| Multiplier stage | 12 |
| High voltage | 800 V |
| Typical gain | $\approx 10^6$ |
| Transit time spread | 750 ps (FWHM) |

5.3.3 The first PMT version: instabilities at high background rates and at cryogenic temperatures. The test in the Large Prototype

The first PMTs tested for the LXe calorimeter were the R6041. Their main characteristics are summarized in Tab. 5.4. The PMT has a Rb-Cs-Sb alkali photocathode and compact metallic channel dynodes (mesh PMT), to work in a magnetic field (up to ≈ 100 G). Unfortunately this PMT has a response which depends on the beam intensity, making it unsuitable for a MEG use.

The results of the first test of the Large Prototype, equipped with the R6041 PMT, using different signal sources are presented in this section (year 2003).

A schematic view of the Large Prototype is shown in Fig. 5.5. This is the first Large Prototype of a LXe calorimeter based on scintillation light, having dimensions second only to those of the final LXe MEG calorimeter. The active volume is ≈ 67 l (over a total requested filling of 120 l of LXe). 264 PMTs are used, corresponding to a photocathode coverage of about 40%. Although the LP active volume is smaller than the one of the final calorimeter ($V = 800$ l of LXe and 864 PMTs), its thickness is the same. The test of this detector was very important for understanding its calorimetric properties, at an energy close to that of γ 's from muon decay ($E_\gamma = 52.8$ MeV), and for studying LXe as a scintillating medium.

A total of four ^{241}Am α -sources and eight LEDs are mounted on the lateral walls of the LP. They were used to determine the PMT QEs and gains (see chapter 8).

The α -sources provide a well defined energy line. We monitored its energy with beam on or off (a negative pion beam). We used γ 's at an energy of $E_\gamma = 54.9$ MeV, produced by the exchange reaction $\pi^0(\pi^-, p)n$ followed by π^0 -decay $\pi^0 \rightarrow \gamma\gamma$ (see chapter 11). Fig. 5.6 shows the apparent variation of the α energy with beam on and off (about 16%).

The phenomenon of the PMT gain variation, in conditions of beam on and off, was reproduced with light signals from LEDs (in the visible region). Fig. 5.7 presents the results. The signal reduction has the same value $\approx 16\text{-}18\%$.

Finally Fig. 5.8 shows the same signal variation in the case of γ 's events. The two γ lines, at 54.9 MeV and 82.9 MeV, are clearly visible.

To better understand the phenomena, we simulated the beam generated background using LED signals (pulsed at a 50 kHz frequency and a pulse amplitude equivalent to a 5 MeV energy), and we monitored the α measured energy. During these measurements the anodic (I_a) and resistive divider (I_b) current of each PMT was about $I_a = 0.6 \mu\text{A}$ and $I_b = 70 \mu\text{A}$. We recorded the same signal reduction.

These results forced us to develop a cryogenic facility, to test and optimize the properties of PMTs for the LXe calorimeter.

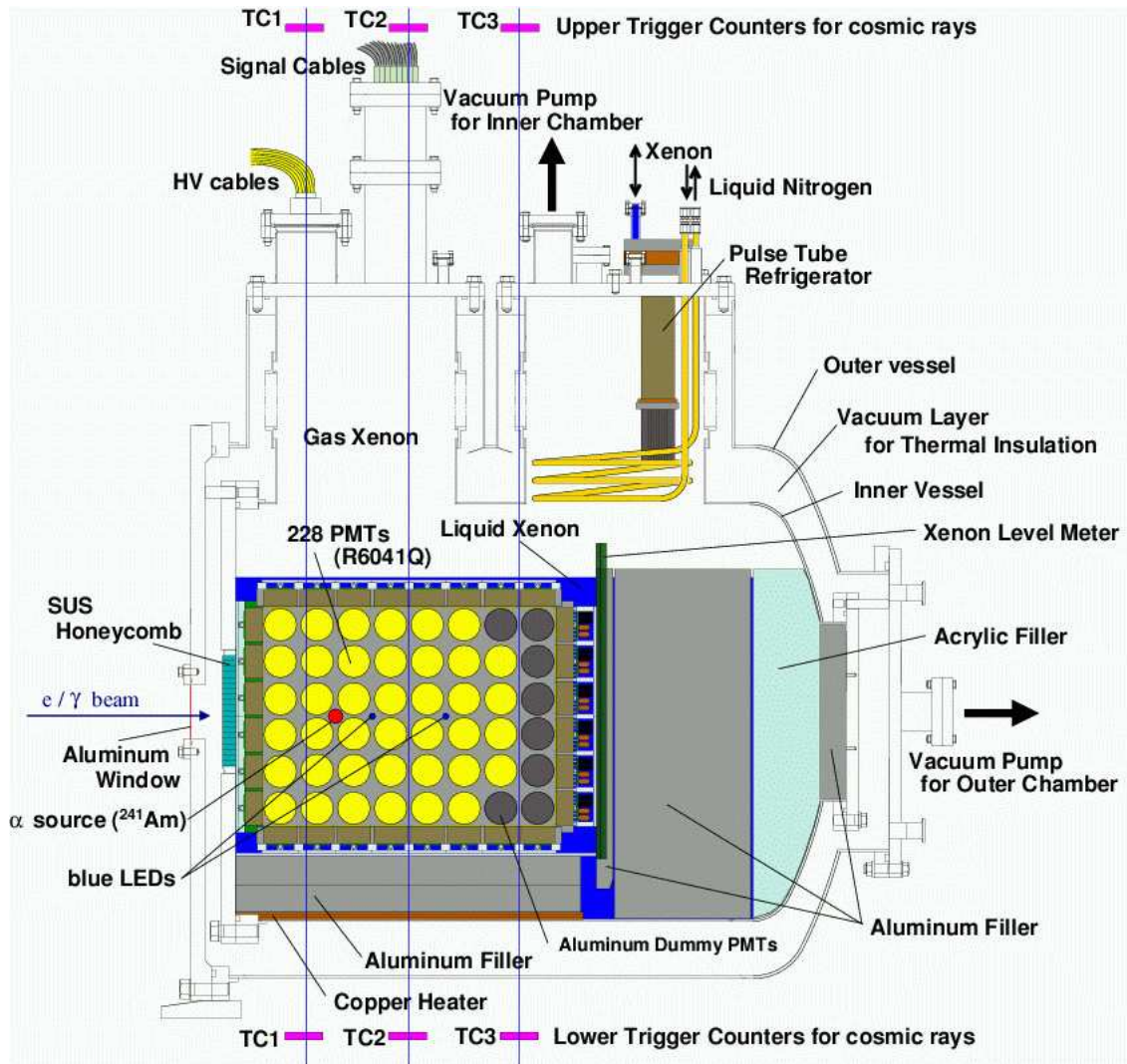


Figure 5.5: Schematic view of the Large Prototype.

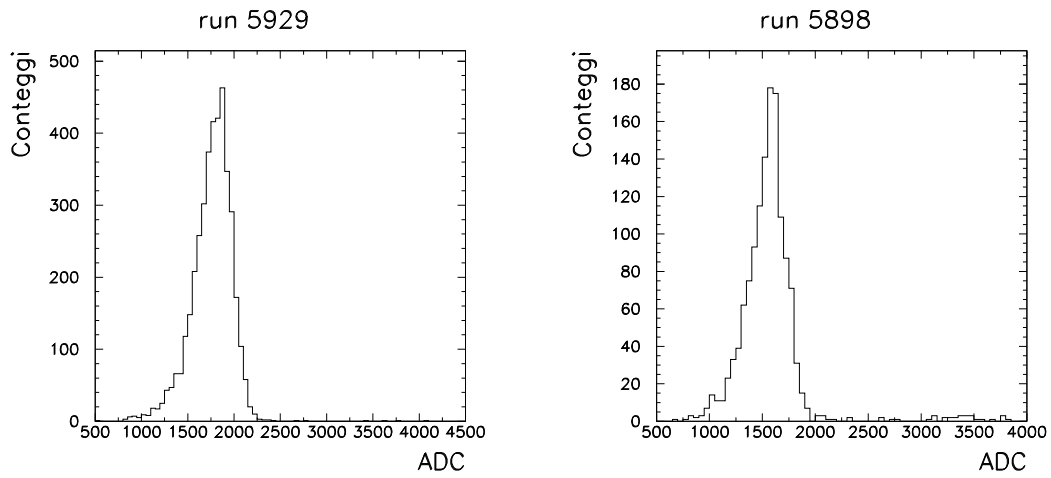


Figure 5.6: α -source energy spectrum (beam-off, left; beam-on, right).

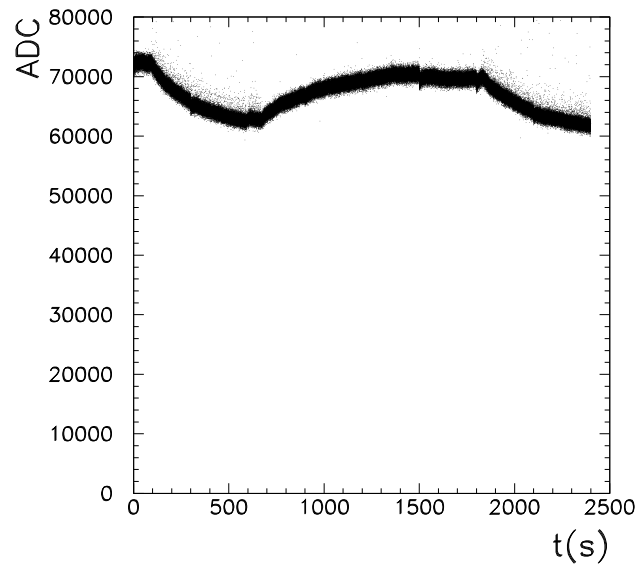


Figure 5.7: The PMT signal variation (beam on or off). The signal is induced by blue light LEDs.

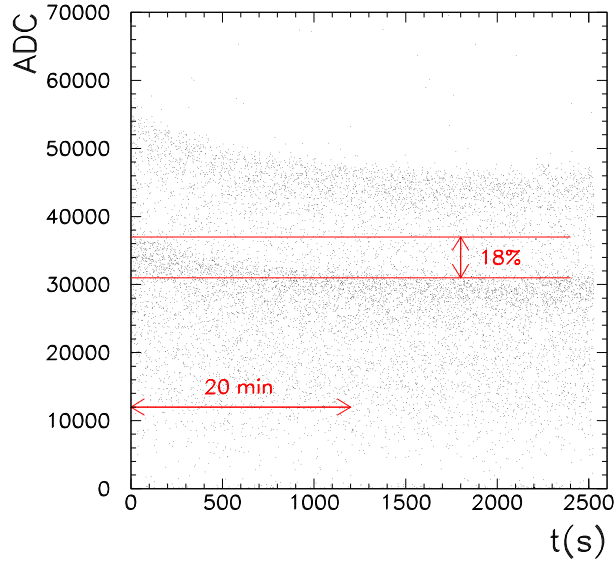


Figure 5.8: *The PMT signal reduction, induced by the beam. The signal is due to γ 's from the π^0 -decay.*

5.3.4 The PMT cryogenic facility in Pisa

The cryogenic facility [146] consists of a small cryostat (volume equal to 1 l of LXe), a 600 l stainless steel buffer and a cryogenic circuit (with vacuum pumps, purification system, vacuum leak detector, bottles, gate valves etc., see the scheme of Fig. 5.9). Two PMTs are immersed in LXe (see Fig. 5.10). One is the reference PMT, the other the PMT under test. Each PMT is independently tested.

The facility allows the replacement of the PMT under test, without Xe losses and without introducing impurities. All PMTs are immersed and extracted by means of a linear actuator and a gate valve system. Xe is permanently kept liquid in the test volume. When a PMT is extracted, the volume is insulated with the help of a gate valve. The gaseous Xe present in the volume where the PMT is parked before removal (called “gas volume”), is recovered in a coil and cooled by liquid nitrogen. 2.5 h are roughly needed to test one PMT. 3.5 PMTs are tested per day.

We simulate the PMT behaviour in a background environment by using two different blue LEDs at the same time. One induces the PMT signal, the other is used in a pulsed-mode at high frequency (4-40 KHz) to simulate the high background rate conditions.

The electronics consists of VME ADCs and TDCs, a CAMAC LED driver, and a VME/CAMAC interface to the same PC used for controlling the Cryo-Facility.

5.3.5 The second PMT version: the R9288 PMT series and the results at the Cryo-Facility

We were able to reproduce the R6041 PMT behaviour at the Pisa cryogenic facility. A signal reduction appears when an anode current $I_a = 0.8 \mu\text{A}$ is reached. At room temperature, the signal reduction is no longer present. We interpreted the signal reduction as caused by a charge accumulation at the photocathode, due to its increased resistivity at low temperature.

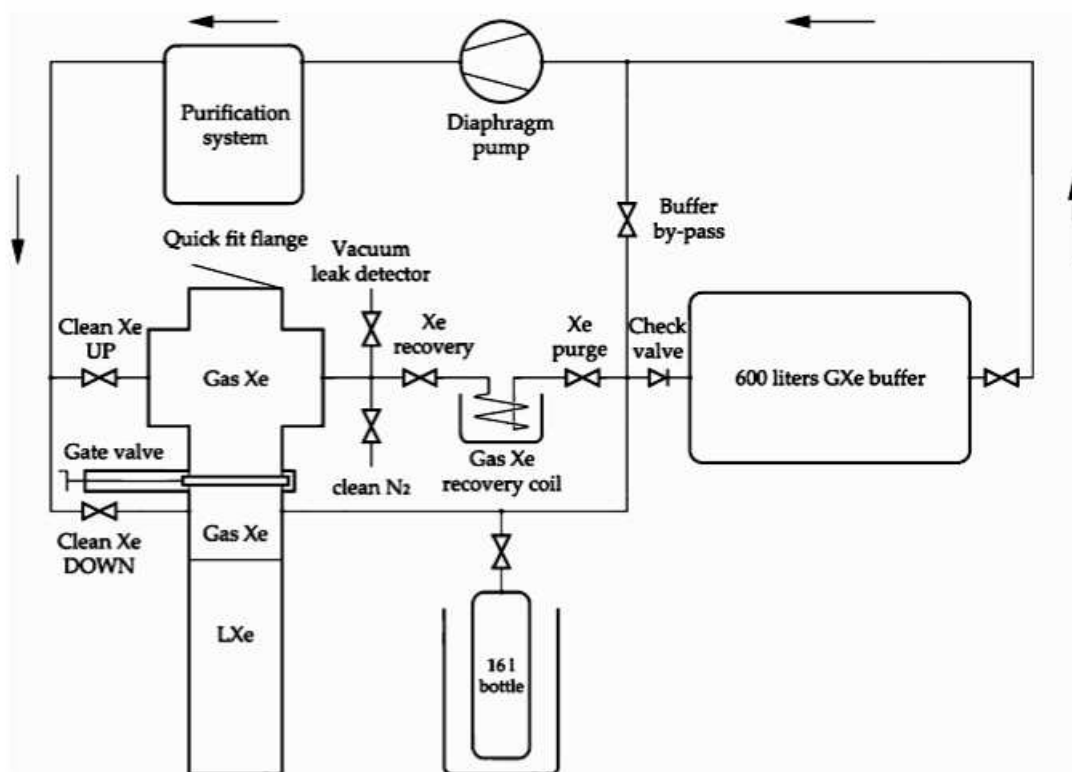


Figure 5.9: A schematic view of the cryogenic facility in Pisa.



Figure 5.10: A detail of the small cryostat in Pisa. One can see the internal volume, where the two PMTs are immersed. The reference PMT is mounted at the bottom of the cryostat, the PMT under test is in front of it, at the top of the cryostat.

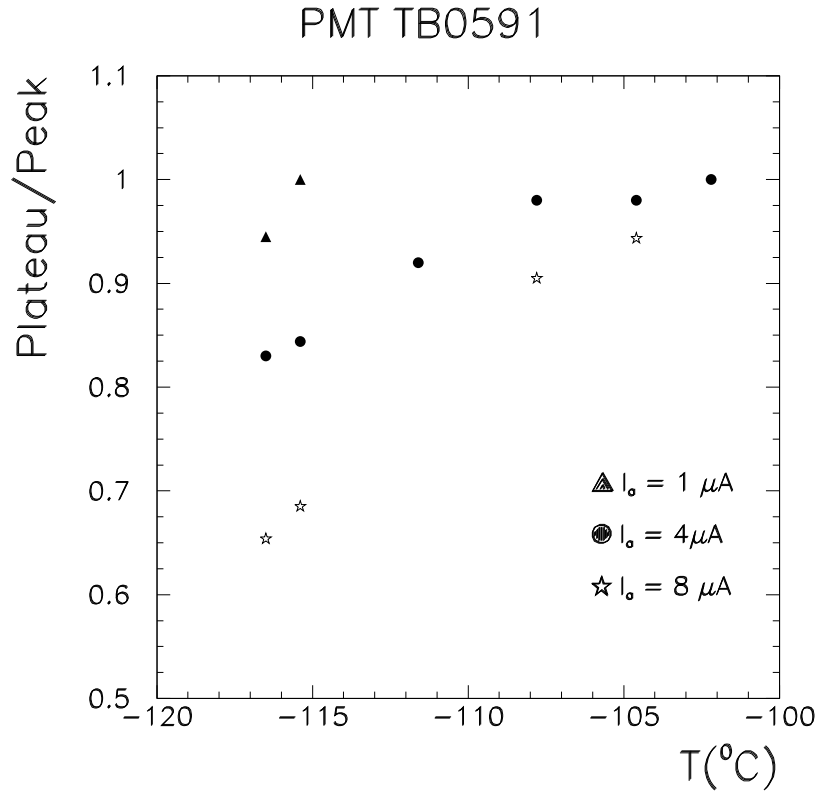


Figure 5.11: Signal reduction of the PMT R9288, as a function of temperature and for various anode current $I_a = 1, 4, 8 \mu\text{A}$.

This effect is greatly reduced for R9288 PMTs, since Al strips deposited on the photocathode reduce its resistivity at low temperature. At $I_a = 1 \mu\text{A}$, we did not observe any anomalous signal reduction. However, when the anode current increases, the signal reduction appears again (see Fig. 5.11).

We also observed the so called over-linearity effects coming out when the ratio of the anode current to the resistive divider current increases ($I_a/I_b \geq 0.01$ [145]), see Fig. 5.12 (left). The PMT works roughly at a resistive divider current of $I_b = 50 \mu\text{A}$ and for I_a of few μA this effect is present. The over-linearity effect can be separated from the effect due to the cathode resistivity. At room temperature only the over-linearity effect is present (see Fig. 5.12 (right)).

These results were not considered satisfactory. A third PMT generation was therefore developed.

5.3.6 The final PMT version: the R9869 PMT series

The new R9869 PMT improves the R9288 PMT by doubling the cathode Al strip density. This allowed the reaching of a sufficiently small photocathode resistivity. Fig. 5.13 compares the PMT second and third versions. The gain reduction is absent up to an anodic current $I_a = 6-7 \mu\text{A}$. This result guarantees an adequate PMT stability under high background conditions.

The over-linearity phenomenon is also present. We corrected this unwanted behaviour by adopting zener diodes in the resistive divider last two stages (see Fig. 5.14). The comparison of the two R9869 PMT response, with and without zener diodes, is shown in Fig. 5.15.

This PMT was used in the final LXe calorimeter. Note that, although the third PMT version corresponds to an cathode area reduction of about 8%, due to the Al strips, its QE improved by

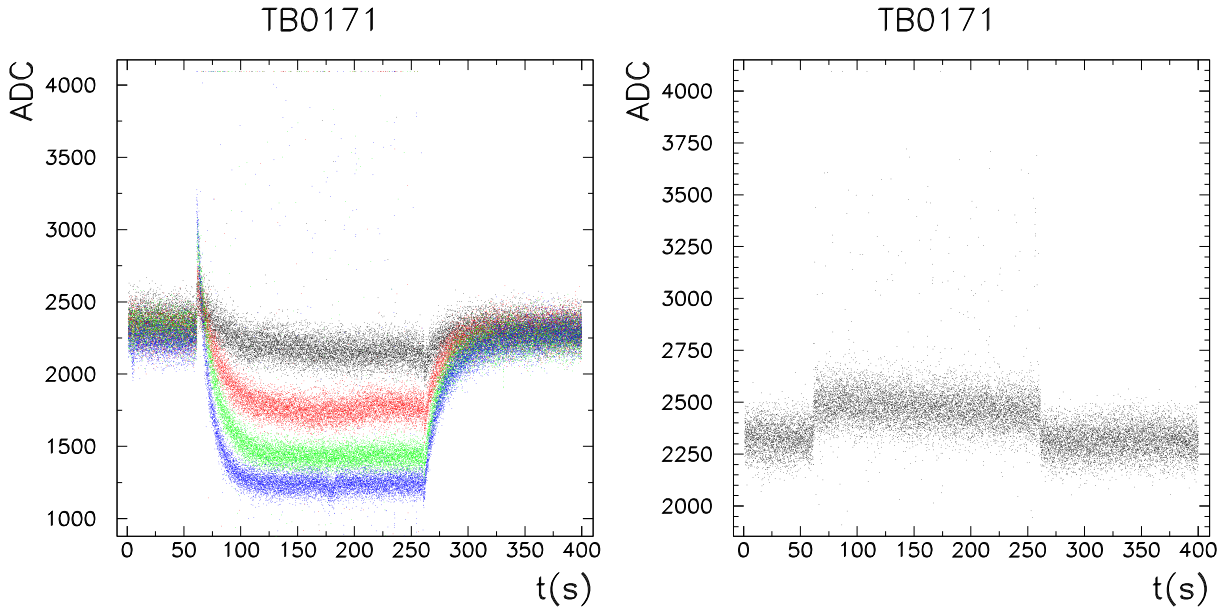


Figure 5.12: The PMT R9288 gain reduction for different anodic currents: $I_a = 4, 8, 12, 16 \mu\text{A}$ (black, red, green and blue; left). Over-linearity at room temperature for $I_a = 4\mu\text{A}$ (right).

a factor 3: from the previous QEs of 5-6% to the final QEs of 15-18% (see Tab. 5.5).

Table 5.5: The main PMT Hamamatsu R9869 properties.

| | |
|---------------------|----------------------------|
| Diameter | 57 mm |
| Photocathode | K-Cs-Sb |
| Sensitive area | 42 mm |
| QE at 165 K | $\approx 15\%$ (at 178 nm) |
| Dynode type | metallic channel |
| Multiplier stage | 12 |
| High voltage | 800 V |
| Typical gain | $\approx 10^6$ |
| Transit time spread | 750 ps (FWHM) |

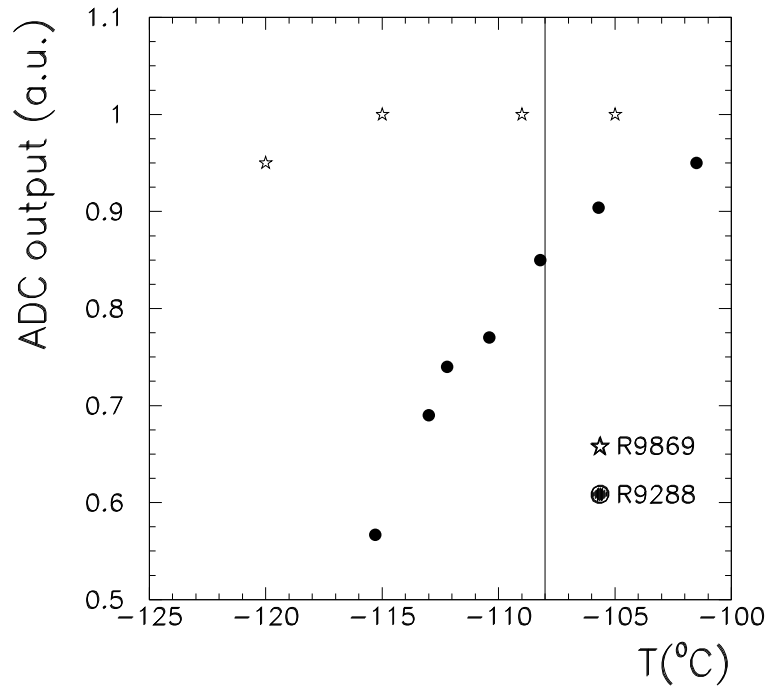


Figure 5.13: Gain reduction for PMT R9288 (circles) and PMT R9869, (triangle) as a function of temperature, at $I_a = 4\mu\text{A}$.

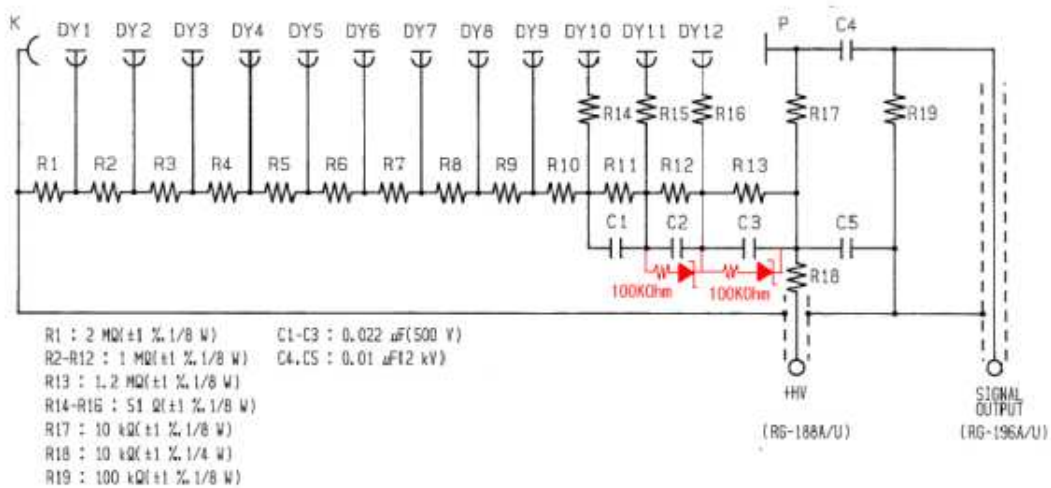


Figure 5.14: The PMT R9869 base circuit. The zener diodes are added at the last divider stages (red).

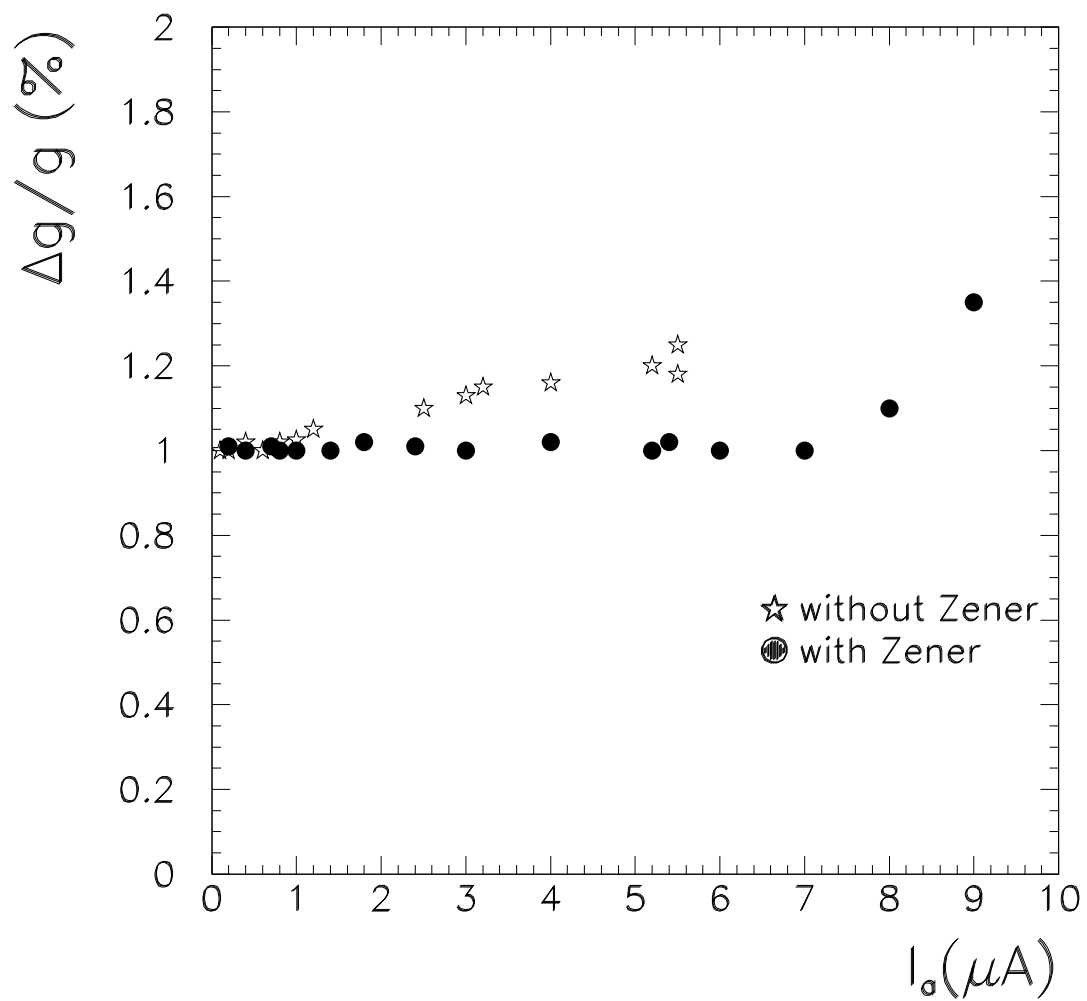


Figure 5.15: The over-linearity of PMT R9288 and PMT R9869 with/without the zener diodes in PMT base.

Chapter 6

The expected LXe calorimeter performance

In this chapter we discuss the LXe calorimeter performance and the method used for the event reconstruction. A full GEANT based Monte Carlo simulation was needed for obtaining results on the γ energy resolution and on the spacial and timing accuracy on the interacting γ . We describe the algorithms applied to the Monte Carlo data (later used on real data).

We consider 52.8 MeV γ 's coming from $\mu^+ \rightarrow e^+\gamma$ decays and γ 's coming from known background sources (radiative decay and positron annihilation in flight). We follow the shower development of any γ in the calorimeter, taking into account all relevant electromagnetic processes (pair production, bremsstrahlung, Compton scattering, photoelectric effect, ionization losses, multiple scattering and positron annihilation). Secondary particles are traced down to energies of 10 keV.

We generate the number of scintillation photons corresponding to any energy release in the calorimeter. Each scintillation photon is followed as far as the calorimeter walls. The liquid Xenon properties, discussed in chapter 4 (the light yield, emission spectrum, decay time constant, λ_{abs} , $\lambda_R = \lambda_R(n_{Xe})$) are taken into account. We record the number of scintillation photon reaching each photomultiplier and the number of corresponding photoelectrons, taking into account the PMT quantum efficiency and the time information.

An unformatted data stream is prepared for each γ -event, which contains the coordinates of the origin and the momentum of the primary γ , the energy released in all crossed materials, the coordinates of the first interaction point and the charge and time information recorded by each PMT.

The method used to determine the characteristics of the original γ -event from this set of data will be fully discussed.

The performance of the detector depends on LXe parameters such as the Rayleigh scattering length, the absorption length, etc. We therefore studied how the modification of these parameters affects the achievable calorimeter resolutions.

6.1 The LXe calorimeter geometry

The data on the detector geometry are given in Tab. 6.1. The μ -beam is oriented along the positive z axis. The calorimeter is contained in the $x < 0$ half-space; $y = 0$ and $z = 0$ are the symmetry planes of the detector. The curved surface next to the target is called the *inner* side and the outermost one the *outer* side; the calorimeter walls in the (x, y) planes are called the *left* and *right* sides and the limiting surfaces at fixed azimuthal (ϕ) angles are called the *up* and *down* plugs. The polar angles θ and ϕ are defined as usual.

The photomultipliers (their total number is 846) were distributed on the various surfaces according to the following criteria:

Table 6.1: LXe calorimeter dimensions.

| | |
|------------------------------|-------------------------------|
| Inner radius | 65 cm |
| Outer radius | 112 cm |
| Height | 80 cm |
| Angular coverage(θ) | $-0.35 < \cos \theta < 0.35$ |
| Angular coverage(ϕ) | $-60^\circ < \phi < 60^\circ$ |

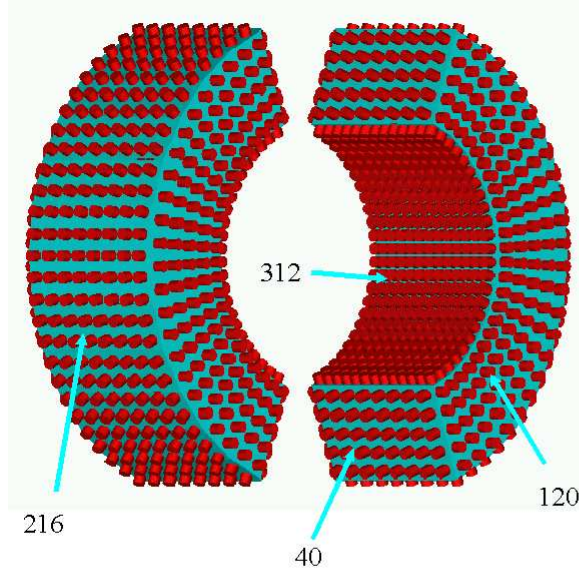


Figure 6.1: The LXe calorimeter PMT distribution.

- the PMT density is as high as possible, for optimizing the determination of energy, position and timing of γ -events. The PMT density is the highest on the inner side, as suggested by the characteristics of the shower development. A high density is also present in a small section of the outer side (for calibration purpose, see chapter 9);
- the PMTs are distributed on all sides along lines of constant cylindrical coordinate;
- the PMT distribution is equal on the *up* and *down* plugs and on the *left* and *right* sides.

Fig. 6.1 and Tab. 6.2 summarize the photomultiplier distribution on all calorimeter sides.

Table 6.2: PMT distribution on the LXe calorimeter side walls.

| Surface | PMT number |
|-------------------------------------|------------|
| Inner side | 312 |
| Outer side | 216 |
| Lateral sides ($\times 2$) | 240 |
| Top and bottom sides ($\times 2$) | 80 |
| Total | 846 |

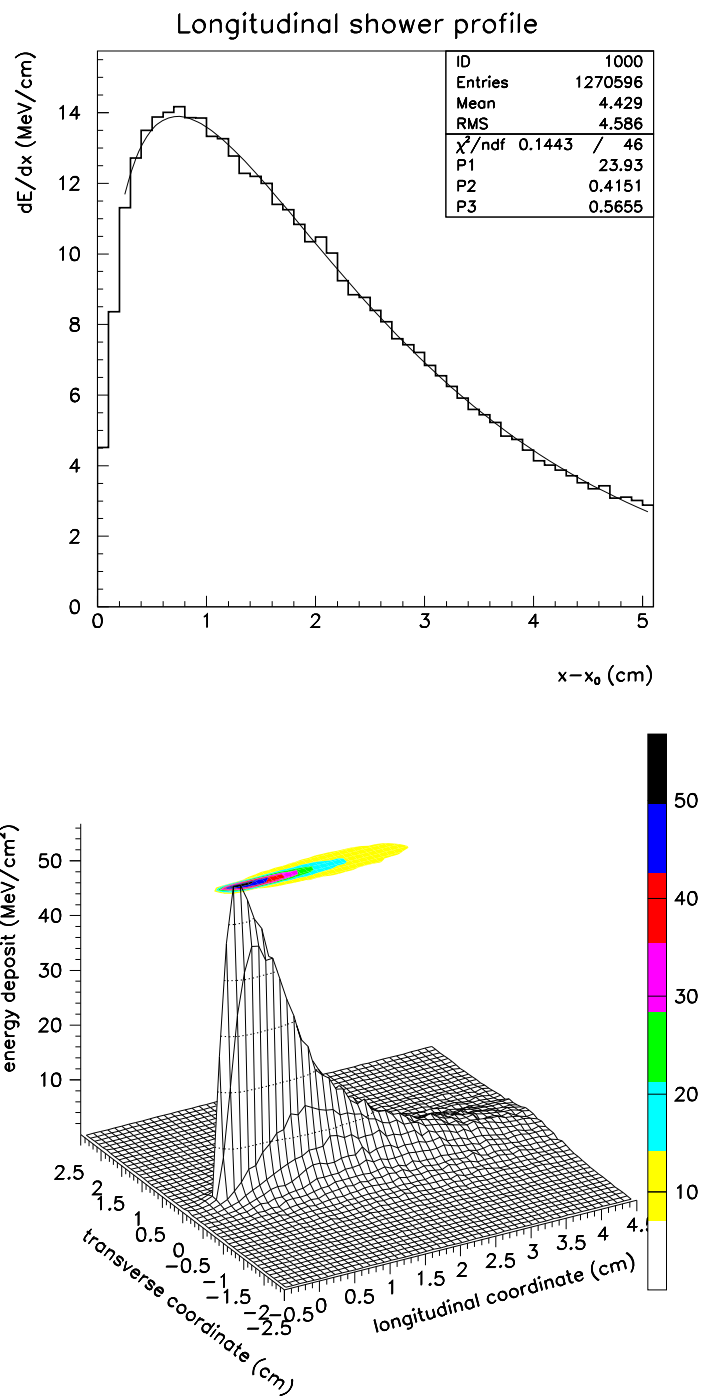


Figure 6.2: Longitudinal shower profile (top) and bidimensional shower profile (bottom).

6.2 The shower development

The longitudinal (top) and bi-dimensional profiles (bottom) of a sample of 10000 showers are shown in Fig. 6.2. In Fig. 6.2 x_0 is the coordinate of the γ interaction point, x is along the shower axis. The longitudinal spread is ≈ 5 cm and the transverse spread is ≈ 2 cm. The primary interaction point is closer to the “inner” calorimeter side; the inner side PMT density is accordingly higher.

The average shower development neglects however the large fluctuations present among different showers. This is particularly true at low γ -energies (MeV scale, not GeV scale). Fig. 6.3 shows in more detail for four shower events, how the energy releases occur at several positions (cm scale), with large fluctuations. The cross indicates the energy-weighted shower position. The color indicates the time of the energy release (blue = earlier times, red = later times).

6.3 The γ energy estimate

The simplest method for estimating the energy released by a γ -event in the LXe calorimeter is to sum the charges collected by all PMTs, scaling each charge by a numerical factor taking into account the PMT density (i.e. the different surface photocathode coverage), the different PMT gain and quantum efficiency:

$$E_{Qsum} = \sum_i c_i Q_i \quad (6.1)$$

where Q_i is the PMT output charge and c_i is the weighing factor. This method is also the most efficient, if the scintillation light absorption is negligible. Fig. 6.4 shows the energy resolution reached by this $Qsum$ -method in the absence of absorption and diffusion processes. At 52.8 MeV one obtains $\Delta E_\gamma/E_\gamma$ (FWHM) $\approx 4.2\%$.

The energy spectrum is asymmetrical. The tail at lower energies is due to γ interactions in materials preceding the LXe scintillator or to the shower leakage (mostly low-energy escaping γ 's). The spectrum was fitted with the following function:

$$f(x) = \begin{cases} C e^{-\frac{1}{2}(\frac{x-\mu}{\sigma})^2}, & \text{if } x > \mu; \\ C e^{-\frac{1}{2}(\frac{x-\mu}{s(x-\mu)})^2} & \text{if } x \leq \mu; \end{cases} \quad (6.2)$$

where $s(x - \mu)$ is defined as:

$$s(x - \mu) = s_0 + s_1(x - \mu) + s_2(x - \mu)^2. \quad (6.3)$$

The stated energy resolution corresponds to the σ right (for $x > \mu$).

These ideal conditions are unfortunately not met in reality. Absorption and diffusion must be taken into account. Fig. 6.5 shows the energy resolution derived by a Monte Carlo simulation corresponding to $\lambda_{abs} = 200$ cm and $\lambda_{Ray} = 45$ cm. At 52.8 MeV the γ -energy resolution for 52.8 MeV γ 's, by the $Qsum$ method, is $\Delta E_\gamma/E_\gamma$ (FWHM) $\approx 9\%$.

The $Qsum$ method is no longer the best for measuring γ -energies, when λ_{abs} and λ_{Ray} have finite values.

A finite λ_{abs} corresponds to a real photon absorption and it affects the energy resolution since it reduces the number of scintillation photons collected by the PMTs.

A small λ_{Ray} corresponds to a longer photon path, from the emission point to the PMT photocathode. The longer path increases the absorption probability for finite values of λ_{abs} .

While the weighing factors have a very simple form when the “Q-sum” method is applicable, this is no longer true for finite λ_{abs} and λ_{Ray} . The γ direction and the shower development are such that the *inner* side is normally closer to the bulk of the energy deposit; the *outer*, *top*, *bottom* and *lateral* sides are instead farther away. The light collected at the various sides is differently affected by scattering and absorption. A full Monte Carlo simulation must be used for predicting the photon distribution at each calorimeter side, for γ -events of known energy and calorimeter entrance coordinates.

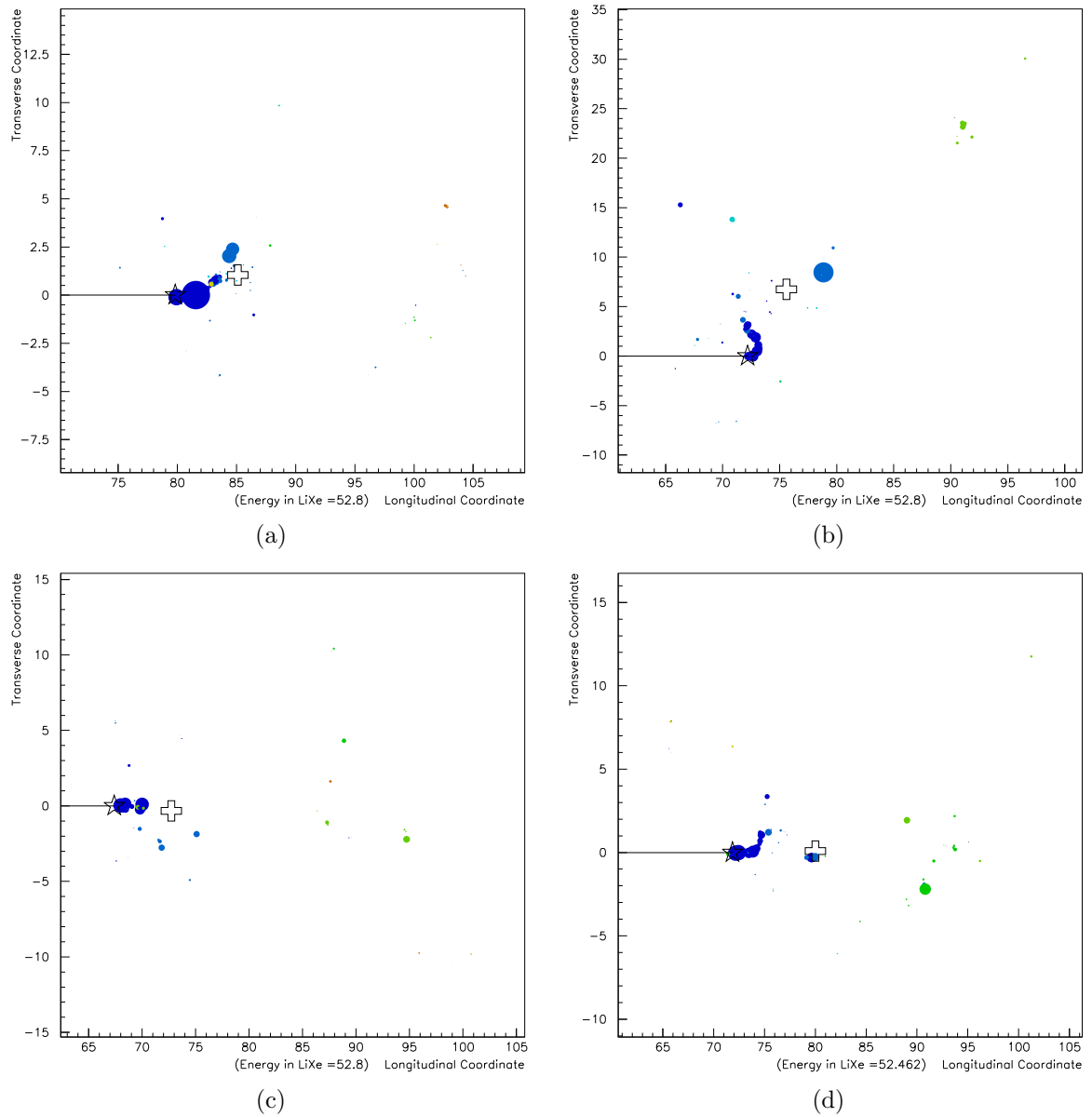


Figure 6.3: *Examples of the energy releases associated with different showers. The star indicates the first γ interaction point in the LXe detector; the cross is the weighted shower position; the spot dimensions are proportional to the released energy; the color corresponds to the shower time development (blu=before rosso=after).*

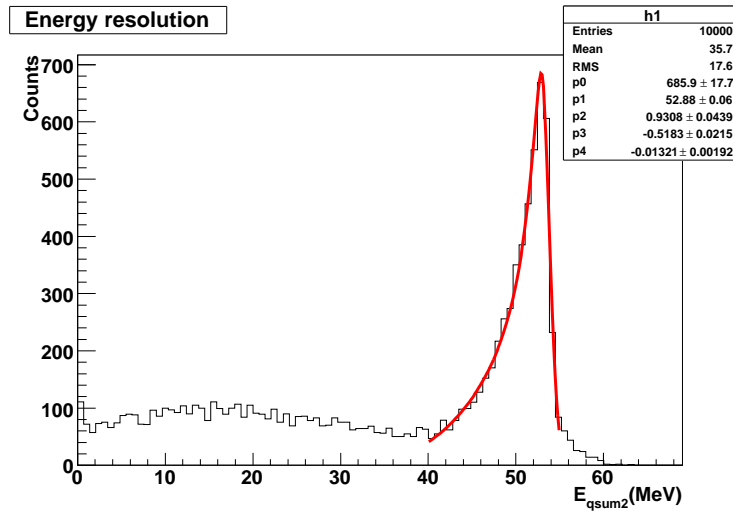


Figure 6.4: LXe calorimeter energy resolution for 52.8 MeV γ 's, by using the Q-sum method ($\lambda_{abs} = \infty$, $\lambda_{Ray} = \infty$).

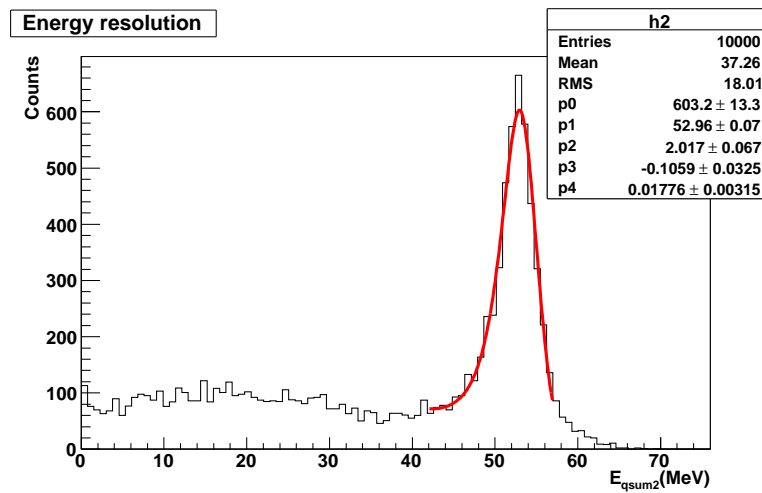


Figure 6.5: LXe calorimeter energy resolution for 52.8 MeV γ 's, by the Q-sum method ($\lambda_{abs} = 200$ cm, $\lambda_{Ray} = 45$ cm).

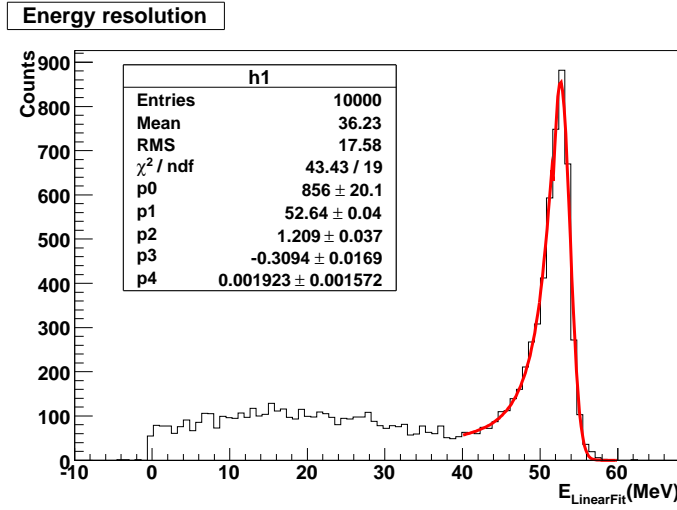


Figure 6.6: LXe calorimeter energy resolution for 52.8 MeV γ 's. Linear Fit method ($\lambda_{abs} = 200$ cm, $\lambda_{Ray} = 45$ cm).

The reconstructed γ -energy can be written as a linear sum of the PMT output charges Q_i with arbitrary coefficients c_i :

$$E_{LFit} = c + \sum_i c_i Q_i. \quad (6.4)$$

The coefficients c_i are then derived by minimizing the quantity:

$$\chi^2 = \langle (E_{LFit} - E_t)^2 \rangle \quad (6.5)$$

where E_t is the assumed γ -energy (the *true energy* of the event). In what follows $\langle A \rangle$ represents the average of any quantity A over all Monte Carlo generated events. The minimization yields the results:

$$c_i = \mathbf{M}^{-1} \left(\frac{\langle E_t Q_i \rangle - \langle E_t \rangle \langle Q_i \rangle}{\langle Q_i \rangle} \right)$$

$$c = \langle E_t \rangle - \left\langle \sum_j c_j Q_j \right\rangle. \quad (6.6)$$

\mathbf{M} is the covariance matrix of Q_i for all Monte Carlo generated events:

$$\mathbf{M}_{kl} \approx \frac{N}{N-1} \langle (Q_k - \langle Q_k \rangle)(Q_l - \langle Q_l \rangle) \rangle. \quad (6.7)$$

The procedure just outlined is conventionally called the *Linear Fit* method [147].

The linear fit method gives relative energy resolution $\Delta E_\gamma / E_\gamma$ (FWHM) is approximately equal to 5.4 % for 52.8 MeV γ 's, as shown in Fig. 6.6.

6.4 The estimate of the event time

In this section we describe the algorithm for the timing determination, applying it to the γ 's of the Monte Carlo simulation. The same procedure will be used for the experimental data.

The physical processes which must be taken into account in following the γ path are the electromagnetic shower development and the scintillation light propagation, from the γ interaction point to the PMTs.

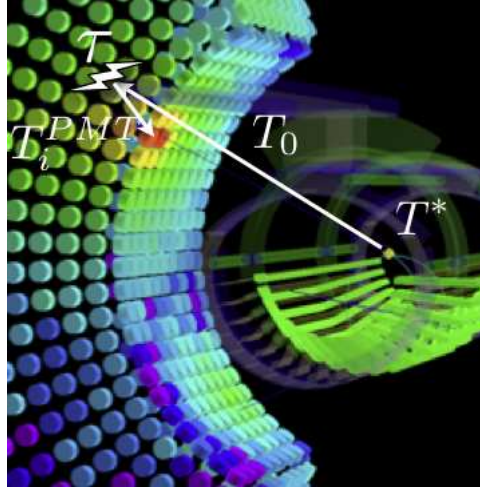


Figure 6.7: The γ travel time from the target to the i th PMT.

The γ is generated at the muon decay time T^* in the Monte Carlo simulation. T^* is also the quantity we want to measure when dealing with real events. γ 's within the calorimeter acceptance travel (at the speed of light c) towards the detector and interact with liquid xenon at different positions. For each energy release the corresponding scintillation photons travel (with speed c/n_{Xe}) to the PMTs on the calorimeter sides, subject to Rayleigh scattering, possible absorption, reflection at the PMT face, etc. Each i -th PMT is characterized by its photon arrival time T_i^{PMT} and its position \vec{X}_i . In the simplest model of the γ -shower detection in the calorimeter, the shower can be associated with an average position \vec{X}_0 and an average time T_0 , where the average is dependent on the characteristics of the energy release in the shower development.

Following this model (see fig. 6.7), the arrival time of the scintillation photon at the i -th PMT is approximated by the following expression:

$$T_i^{PMT} = \underbrace{T^* + T_0}_{\bar{T}} + \tau \cdot \log \left(\frac{N_i^{ph}}{N_i^{ph} - 1} \right) + d_{eff}(|\vec{X}_i - \vec{X}_0|) \frac{n_{Xe}}{c}. \quad (6.8)$$

The third term in eq. (6.8) takes into account the scintillation time distribution, where τ is the light decay-time constant and N_{ph} is the number of photons collected by the i -th PMT. The last term takes into account the effective path length d_{eff} of the photon, from the interaction point to the PMT photocathode. In eq. (6.8) T_0 and T^* are grouped into \bar{T} since, as explained in the following, one can determine \bar{T} as a first step and only later determine T^* , our goal.

Schematically the method is the following:

1. \vec{X}_0 is determined by using the Q_i , as described in section 6.5;
2. \bar{T} is determined by using \vec{X}_0 and T_i^{PMT} , as explained in subsection 6.4.1;
3. the μ -decay position \vec{X}_t is the extrapolating to the target of the positron trajectory tracked by the DC;
4. the T^* is extracted combining the previous information:

$$T^* = \bar{T} - \frac{|\vec{X}_0 - \vec{X}_t|}{c} \quad (6.9)$$

where one assumes that the γ -shower (not the photons of the scintillation light) propagates with speed c in LXe.

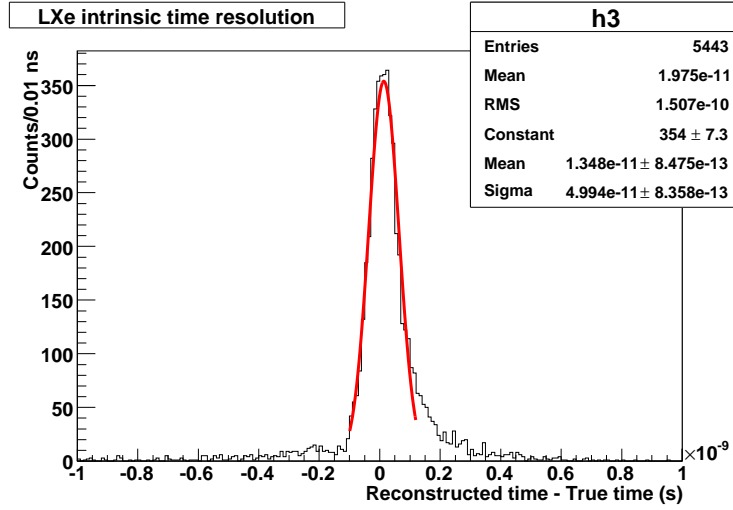


Figure 6.8: LXe time resolution at 52.8 MeV ($\lambda_{abs} = 200$ cm and $\lambda_{Ray} = 45$ cm).

6.4.1 The evaluation of the average impact time

We now deal with $\bar{T} = T_0 + T^*$. The procedure is called: determination of *the average interaction time* since, in the simple assumption $T^* = 0$, it follows that $\bar{T} = T_0$, where T_0 is the average shower time. We refer, for the moment, to events generated by the Monte Carlo simulation. To extract \bar{T} we minimize the χ^2 -function, as a function of \bar{T} :

$$\chi^2 = \sum_i^{PMT} \frac{(T_i^{CAL} - T_i^{MEA})^2}{\sigma_{T_i^{CAL}}^2 + \sigma_{T_i^{MEA}}^2} \quad (6.10)$$

where T_i^{CAL} is:

$$T_i^{CAL} = \bar{T} + \tau \cdot \log \left(\frac{N_i^{ph}}{N_i^{ph} - 1} \right) + d_{eff} (|\vec{X}_i - \vec{X}_0|) \frac{n_{Xe}}{c}; \quad (6.11)$$

with N_i^{ph} the number of photoelectron collected by each PMT, \vec{X}_i is the i -th PMT position, \vec{X}_0 , evaluated as described in section 6.5. T_i^{MEA} is the time of the first photon reaching the i -th PMT, as predicted by the Monte Carlo simulation. The method previously described can be equally applied to real data, as recorded by the waveform digitizers.

6.4.2 The result

The γ timing resolution, based on events generated by the Monte Carlo simulation, is the standard deviation σ of the distribution of the differences between the time T^* , determined according to eq. (6.9), and the true time T^* originally associated with each Monte Carlo generated event.

The result is shown in Fig. 6.8. The LXe γ timing resolution is ΔT_γ (FWHM) ≈ 117 ps, at $E_\gamma = 52.8$ MeV.

6.5 The evaluation of the γ entrance coordinates

Various algorithms were developed to determine the γ conversion point in the LXe calorimeter.

The simplest and fastest algorithm weighs the *inner* side PMT positions, with the corresponding output charges Q_i . A 52.8 MeV γ -shower has a complex and fluctuating shape. Its energy is

released at various positions in the LXe medium (as discussed in section 6.2). The first energy release has however a close memory of the interaction point and is, almost always, near to the *inner* side. The exclusive use of the *inner* side PMT information enhances the sensitivity to position of this first energy release. The output charges of PMTs on other sides are heavily affected by later and sparse energy releases; they are sensitive to the center of the shower energy, different from the conversion point we are trying to determine. We derive the conversion point from the expressions:

$$\begin{aligned}\bar{x} &= \frac{\sum_i x_i Q_i}{\sum_i Q_i} \\ \bar{y} &= \frac{\sum_i y_i Q_i}{\sum_i Q_i} \\ \bar{z} &= \frac{\sum_i z_i Q_i}{\sum_i Q_i}.\end{aligned}\tag{6.12}$$

where the i -index is restricted to the *inner* side PMTs.

The alternative MINUIT position method takes into account the solid angle subtended by each PMT at a point-like light source at a distance z_0 from the *inner* side. The output charge corresponding to the i -th PMT is proportional to:

$$Q_i \propto \frac{z_0}{(z_0^2 + (x_i - x_0)^2 + (y_i - y_0)^2)^{3/2}} \pi R^2\tag{6.13}$$

R being the PMT radius. The best x_0 , y_0 , z_0 values for each event is obtained by minimizing the function:

$$\chi^2 = \frac{Q_i^{EXP} - Q_i^{MES}}{(\sigma_i^{EXP})^2 + (\sigma_i^{MES})^2}\tag{6.14}$$

where Q_i^{EXP} is the expected charge, given by eq. (6.13), and Q_i^{MES} is the charge measured by each PMT (*inner* side only). Other improved variants of the method were studied, but will not be discussed here. rid of the tails of the light distribution on the front face.

As an alternative method, the Linear Fit algorithm can be used (see end of 6.3). The method obtains similar resolutions in the determination of cylindrical (ρ , θ and ϕ) and cartesian (X , Y and Z) coordinates and uses similar computer times.

We report the LXe angular resolutions for the θ and ϕ coordinates given by the Linear Fit method, as shown in Fig. 6.9 and Fig. 6.10, for events from the Monte Carlo simulation.

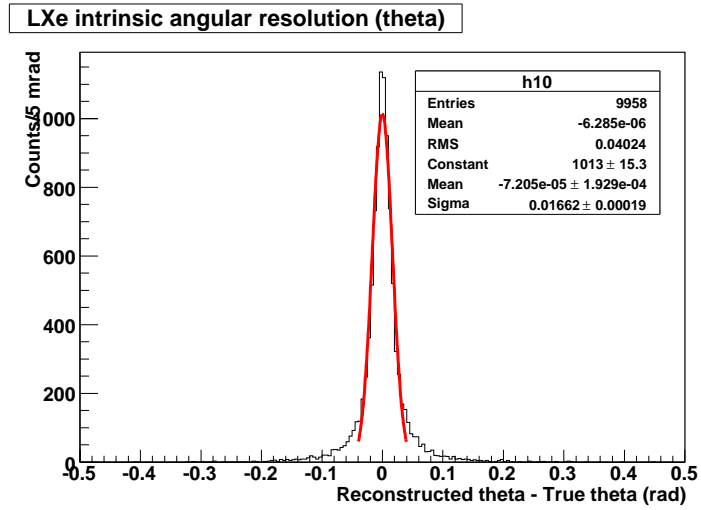


Figure 6.9: *LXe angular resolution (θ variable) at 52.8 MeV ($\lambda_{abs} = 200$ cm and $\lambda_{Ray} = 45$ cm).*

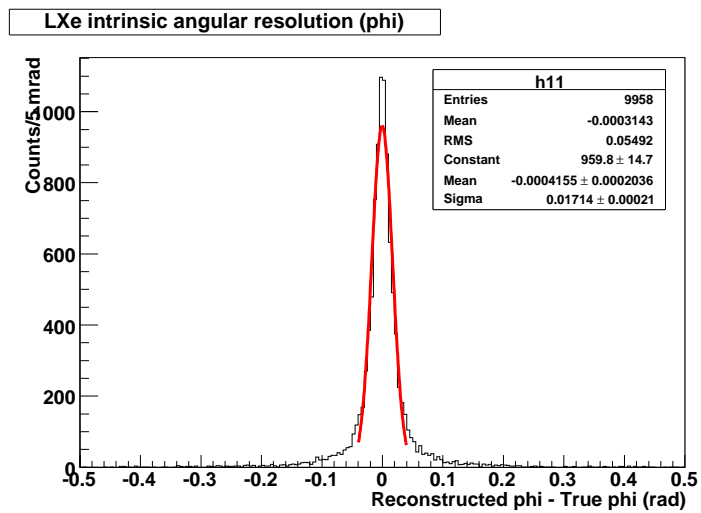


Figure 6.10: *LXe angular resolution (ϕ variable) at 52.8 MeV ($\lambda_{abs} = 200$ cm and $\lambda_{Ray} = 45$ cm).*

Part III

Calibration and monitoring of the MEG experiment

Chapter 7

Overview of the calibration and monitoring methods for the LXe calorimeter and for the MEG experiment

7.1 Motivations

The separation of a possible $\mu^+ \rightarrow e^+\gamma$ signal from background mainly relies on kinematics and on the highest precision in measuring the 4-vectors of the μ -decay products. At the same time one needs a considerable running stability of all detectors, under a high beam intensity and its possible time variations. These requirements were evident from the first planning of MEG. Time and effort were devoted to the development of several calibration and monitoring (C&M) methods and to experimentally demonstrate their potentialities.

This chapter briefly describes the C&M methods.

In the following chapters all methods are re-examined in more detail and their relative merits are discussed. The outcome is: a single method is not sufficient to solve all problems; complementary and redundant methods are needed to obtain MEG optimized performances.

7.2 The LXe calibrations

The liquid Xe and the photomultipliers are the two main components of a LXe calorimeter. The detector behaviour depends on the LXe scintillator light yield, on the light propagation in LXe and on the PMT characteristics.

The previous chapter discussed LXe scintillation and light propagation. Xe is an ideal scintillator, good for precise energy and time measurements. LXe is transparent to its scintillation light, at $\lambda = 178$ nm. However, common elements and compounds, such as oxygen and water, have a high light absorption cross section in the ultra-violet. Therefore a high degree of Xe purity is required.

The optimization of PMTs working at cryogenic temperatures and sensitive to the LXe ultra-violet emission was already described.

Different aspects of LXe calorimetry, like: LXe purity, LXe emission spectrum, refractive index, Rayleigh diffusion length, absorption length, PMT quantum efficiency, PMT gain, etc. must be known and kept under control.

By “calibration” one means the determination of the calorimeter energy resolution as a function of the γ -ray energy and of the γ impact point, the resolution in the determination of the γ impact point, the calorimeter capacity in separating two particles in time and in space etc.

By “monitoring” one essentially means the check of the time stability of all important quantities in conditions which are, as close as possible, similar to the normal MEG running conditions (Cobra magnet at full field intensity, high beam intensity etc.).

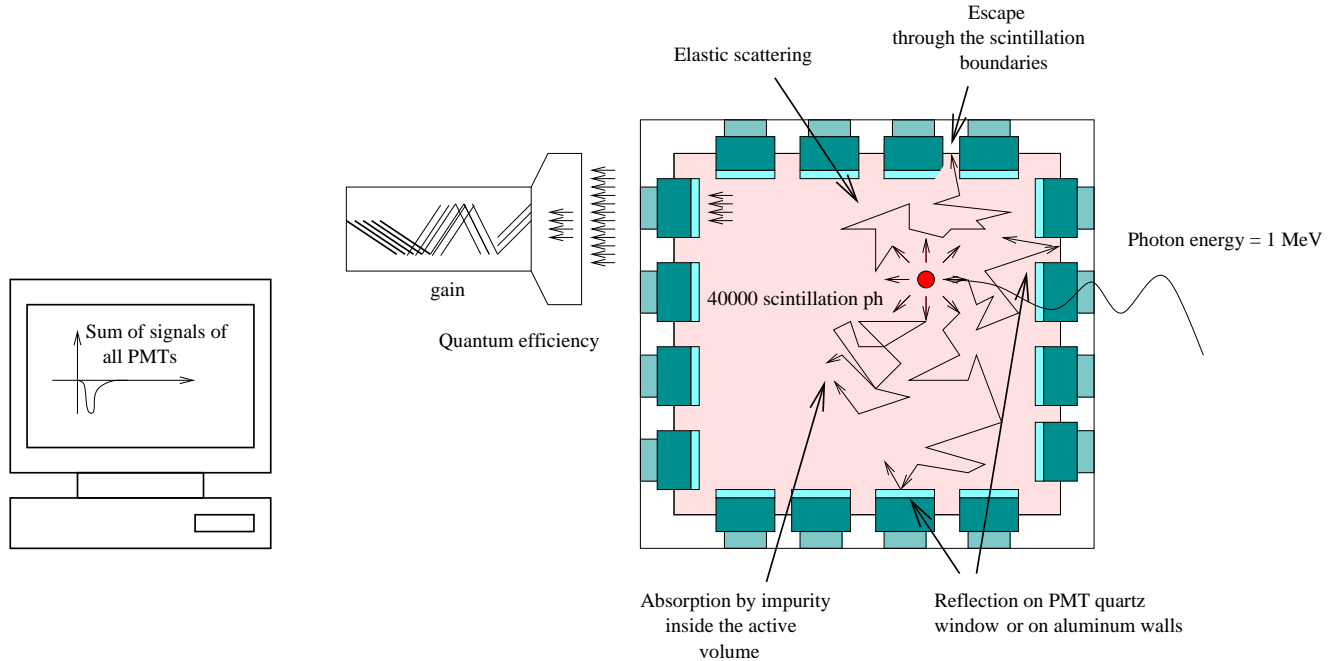


Figure 7.1: *Schematic view of some of the physical processes and PMT characteristics which determine the detector performance.*

Fig. 7.1 shows schematically the physical processes and the PMT characteristics which determine the detector performance.

The LXe optical properties were measured by the use of radioactive Am-sources mounted on tungsten wires (WS) immersed in the liquid. These were also used to evaluate the quantum efficiency (QE) of all PMTs. The gain equalization among the PMTs was obtained by using LEDs, mounted on the lateral faces of the detector (see chapter 8).

The simplest way to calibrate and monitor a calorimeter is to use γ 's, as similar as possible to those present in a normal run. γ -energies spanning a wide energy interval allow a test of the calorimeter linearity and uniformity as a function of energy.

We used 9 MeV γ 's from Am, Cf or neutron generator thermalized neutron capture on Ni (see chapter 9).

17.6 MeV γ 's were obtained by the reaction ${}^7_3\text{Li}(p, \gamma){}_4^8\text{Be}$. These γ 's, associated with a narrow resonance at $T_p = 440$ keV, are very useful in the study of the energy resolution, at an energy only a factor 3 lower than that of the expected signal (see chapter 10).

A study of the LXe detector at $E_\gamma = 54.9$ MeV, close to the γ -energy from muon decay, is obtained by the charge exchange reaction $p(\pi^-, \pi^0)n$, followed by the decay $\pi^0 \rightarrow \gamma \gamma$ (see chapter 11).

7.3 The LXe calorimeter and Timing Counter synchronization

The relative $e^+ - \gamma$ timing is one of the four quantities used to identify the $\mu^+ \rightarrow e^+ \gamma$ decay. The γ -time is measured by the LXe calorimeter and the e^+ -time is measured by the Timing Counter (TC).

Two simultaneous γ 's, at 4.4 MeV and 11.7 MeV, are emitted by the proton nuclear reaction ${}^{11}_5\text{B}(p, \gamma){}^{12}_6\text{C}$. We used these two γ 's to synchronize the LXe calorimeter and the timing counter (TC) (see chapter 13).

7.4 The Drift Chamber calibration

It is possible to study the DC system behaviour and tracking efficiency by using Michel positrons. We are investigating an alternative method based on the elastic and coherent scattering of monochromatic positrons (which can also be obtained in the MEG beam) by a low-Z element like carbon or CH_2 . The process corresponds to a perfectly known differential cross-section, allowing a direct measurement of the absolute DC tracking efficiency as a function of energy and positron emission angle.

7.5 The muon beam intensity measurement

The normalization of the experiment relies on the knowledge of the number of stopped muons, which is obtained from the measured number of secondary Michel positron tracks reconstructed in the drift chambers and timing counters. This method, on the assumption of equivalent acceptances and efficiencies for Michel positrons and positrons from a potential $\mu^+ \rightarrow e^+ \gamma$ signal, provides a self-normalization. However, a deeper understanding of various efficiencies and acceptances is advisable.

The muon stopping-rate, derived from the muon beam intensity, must also rely on knowledge of various factors like: beam momentum bite, beam size, beam energy-loss and stopping position.

It looks desirable to have a continuous and independent determination of the muon beam intensity. We present two methods, one based on X-rays and the other which uses a helium ionization chamber, that could provide a precise and continuous monitoring of the muon beam intensity (see chapter 15).

Chapter 8

PMT characteristics and Xe optical properties

The performances of the LXe calorimeter depend on: 1) the LXe properties: the LXe purity level, the intensity and spectral distribution of the light emission, the scintillation photon propagation (LXe optical parameters: refractive index, Rayleigh scattering and absorption length) and 2) the PMT response: the PMT amplification (gain g), the QE , the photocatode resistivity and their variations due to possible changes in the beam intensity.

We shall initially discuss how to measure the g and the QE for each PMT and then how to determine the LXe optical properties.

8.1 LED

The PMT gain is measured by light emitting LEDs. The method we are going to describe was first applied to the PMTs of the Large Prototype (LP). Its validity was fully confirmed.

The LP is the prototype of the final calorimeter, a parallelepiped box, containing 67 l of LXe and equipped with 264 PMTs (see Fig. 8.2, to the left).

Several LEDs were mounted on the calorimeter lateral walls (Fig. 8.2, to the right). They were pulsed at varying light intensities.

The PMT gain is determined as follows.

We assume that the number of the photoelectrons striking the first dynode following a light pulse is N and that the response of the PMT is linear in N . The anodic charge (ADC unit) will then be [148]:

$$q = gN + q_0 \quad (8.1)$$

where q_0 is the charge value corresponding to the pedestal and g is the PMT gain. The photoelectron distribution is poissonian (becoming gaussian for $N > 10$). Then, according to error propagation, we obtain:

$$\sigma^2 = g^2N + \sigma_0^2 \quad (8.2)$$

where σ_0 is the pedestal standard deviation. Combining equations (8.1) and (8.2) we obtain the useful result:

$$\sigma^2 = g(q - q_0) + \sigma_0^2 \quad (8.3)$$

g is obtained by a linear fit of σ^2 versus $q - q_0$ (ADC units) (see Fig. 8.1). An average PMT gain $g \simeq 10^6$ for $HV \simeq 800$ V was obtained.

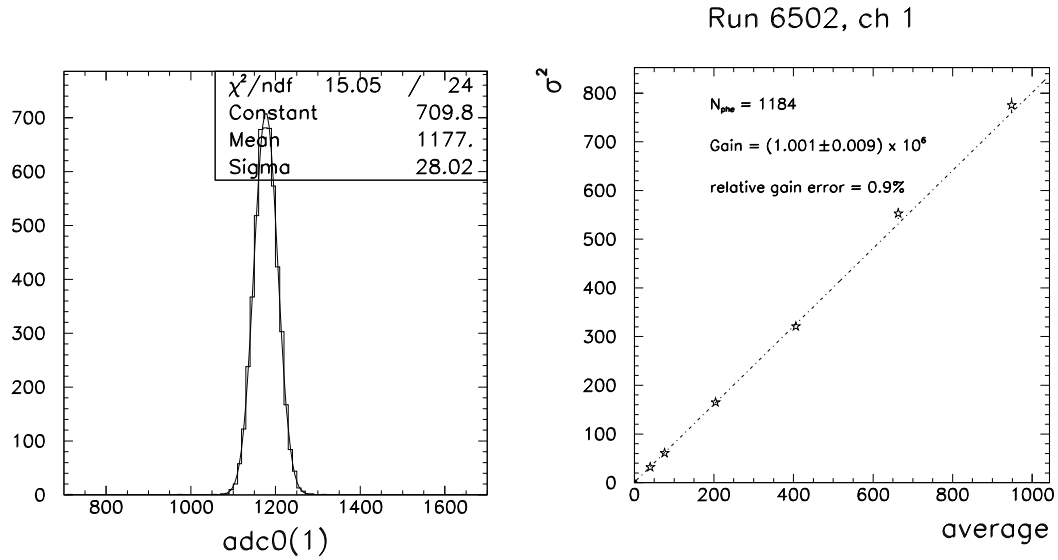


Figure 8.1: A gaussian fit to a PMT ADC spectrum (to the left). A linear fit to σ^2 versus $q - q_0$ for six different values of the LED intensity (to the right).

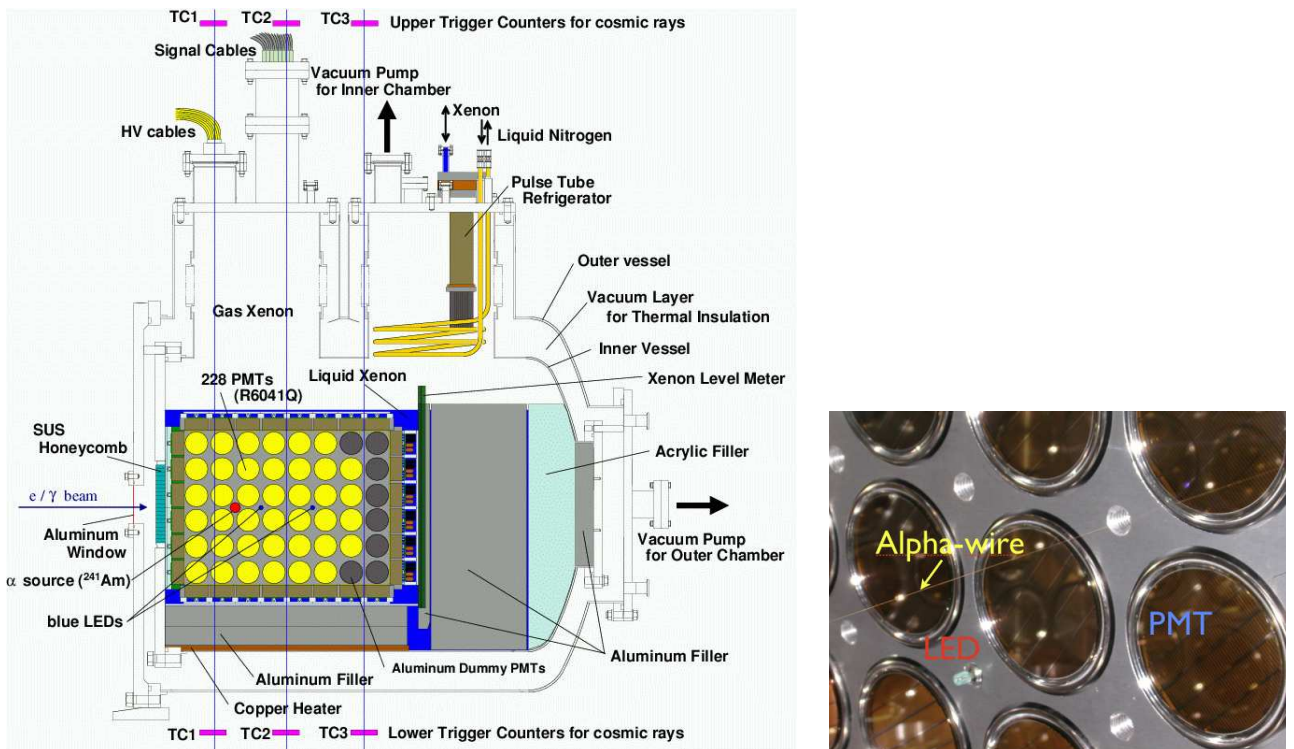


Figure 8.2: A schematic view of the LXe Large Prototype calorimeter (left). LEDs and a α -wire source inside the LP calorimeter (right).

8.2 Americium wire sources

The Americium α -sources on wire method (from now on: WS) is a beautiful and effective way to calibrate and monitor liquid detectors. It is based on a set of thin wires (diameter $100\ \mu\text{m}$) mounted inside the sensitive volume of the LXe calorimeter, in contact with, and at the same temperature as, LXe. The point-like ^{241}Am α -sources are bound to the wire (gold foil wrapped and thermocompressed). They are also protected by a thin gold layer ($\approx 1.5\ \mu\text{m}$) (see Fig. 8.3). The activity of each α -sources is $\approx 200\ \text{Bq}$.

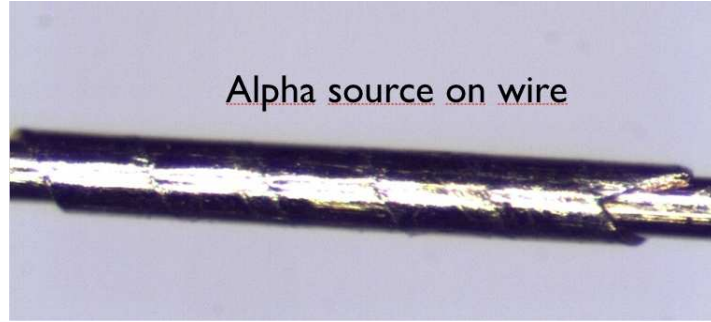


Figure 8.3: The ^{241}Am -source on wire. The picture was taken with the aid of a microscope. The longitudinal dimension is $\approx 2\ \text{mm}$.

8.2.1 The leakage tests for the ^{241}Am -sources

For this unusual application and to avoid possible contamination of the scintillator, it was important to carefully check the stability of the sources when immersed in a cryogenic fluid for long periods of time [153], [156]. Xenon is an expensive material and its purity should not be endangered. The α -sources are positioned at precise locations; a radioactive material dispersed into the LXe would however cause a disturbing diffused background.

Table 8.1: Characteristics of the tested sources.

| Source | (a) | (b) | (c) |
|--|--|--|---|
| Manufacturer | Sorad Ltd. [153] | AEA Technology QSA GmbH [154] | Sorad Ltd. [153] |
| Manufacturer product code | APZ-1-J | AMR01032-LW 516 | - |
| Manufacturer drawing code | EL 819 | VZ-1366 | - |
| Intended use | Smoke detector | Alpha wide area reference source | Specific for the MEG experiment |
| Nuclide | ^{241}Am | ^{241}Am | ^{241}Am |
| Nominal activity | 3 kBq | 3 kBq | 1 kBq |
| Leakage and contamination test performed by the manufacturer | [155], n. 5.1.4 | [155], n. 5.3.1 (wipe test) | - |
| Sealing technology | Covering foil | Incorporation in aluminium foil | Covering foil |
| Source geometry | Disk | Disk | thin wire |
| Diameter of active surface (mm) | n.a. | 16 | - |
| Source dimensions (mm) | 5.1 (diameter) 0.2 (thickness) | 25 (diameter) 3 (thickness) | 1000 (length) 0.2 (diameter) |
| Source construction | - Silver backing (0.2 mm) - Gold interface (0.001 mm) - Active matrix (0.001 mm) - Gold cover layer (0.0016 mm) | - Aluminium holder Anodised aluminium foil (0.3 mm thickness) with incorporated active layer (0.006 mm) | Gold-plated steel wire ^{241}Am dots mounted by thermocompression - Gold-cover layer |

The stability in cryogenic fluids of sources produced by different manufactures was investigated. The characteristics of the tested sources are shown in Tab. 8.1. Commercial α -sources are normally tested according to an international safety protocol [155]; in particular, they are tested at a minimum temperature of -40°C . There is no guarantee that commercial sources can be safely used at cryogenic temperatures. The additional tests, performed at ENEA-Casaccia, were:

1. Immersion test in acetone: the source was immersed in an acetone bath at 20°C for 6 hours. The removed activity was measured.
2. Wipe test: the source was wiped with a paper filter, moistened with water; the removed activity was measured.
3. Fast immersion in liquid nitrogen: the source was repeatedly immersed (5 times) in a liquid nitrogen bath at 77 K, for 3 minutes each time; the removed activity was measured.
4. Long immersion test in liquid nitrogen: the source was immersed in a liquid nitrogen bath at 77 K for 1 hour; the removed activity was measured.

The methods are described in detail in the ENEA internal note [156]. The results of the tests proved the stability of the sources and their safe use in LXe.

8.2.2 The method for determining the relative QE of all PMTs

The WS provide the most effective method for determining the relative QE of all PMTs and for monitoring the optical properties of LXe. The α -events are at known positions, the α -energy is known ($E_\alpha = 5.4$ MeV) and the Am-source is stable since its half-life is very long ($t_{1/2} = 432.7$ years).

Each PMT receives light from events due to sources at different positions. One can compute the number of expected photoelectrons (phe), taking into account the different distances and the solid angles subtended by each PMT at each source; a standard QE is assumed for all PMTs. The relative PMT QEs are obtained by plotting a graph of the measured vs the simulated number of photoelectrons, for the different sources. The slope of the interpolating linear fit directly gives the relative QE .

Fig. 8.4 shows an α -charge spectrum in GXe for one PMT. The number of photoelectrons is low, the charge distribution is therefore fitted by a Poisson distribution. This is characteristic of GXe, since its scintillation light intensity is a factor three lower than the one of LXe.

An example of a linear fit of the measured phe -number versus the MC simulation prediction is shown in Fig. 8.4 (right). The slope of the straight line fit is the measured PMT QE .

The method is based on the assumption that all physical processes considered in the reconstruction of the energy and position of α -events are correctly simulated.

In gas Xe (GXe) the simulation is much simpler than in LXe. One can assume that the absorption length λ_{abs} and the Rayleigh scattering length λ_{R} are very large ($\lambda_{\text{abs}} = \lambda_{\text{R}} \approx \infty$), and the refractive index is $n_{\text{Xe}} = 1$. The α -range in GXe is $R_\alpha \approx 7$ mm. The energy is lost far away from the wire and the wire-diameter can be neglected. The reconstructed events appear as spherical blobs, characterized by a gaussian distribution with $\sigma_{x,y,z} = 3$ mm. See Fig. 8.5 (to the left), where the predictions of the MC simulation and the data are completely superimposed.

The QE depends on the photocatode temperature and on the Xe emission spectrum. For these reasons the QEs in GXe were measured at a temperature as close as possible to the one of LXe (203 K). We verified that the gas and liquid xenon emission spectra are equal [149], [150], [151], [152]. The relative QEs in gas and in liquid are expected to be the same.

The same method was also applied to the LXe data. Note that, in this case, it is crucial to use the correct values of the LXe optical parameters (λ_{abs} , λ_{R} , n_{Xe}) which determine the light propagation inside the detector. The α -range in LXe is $R_\alpha \approx 40\mu\text{m}$, comparable to the supporting wire diameter ($d_{\text{wire}} = 100\mu\text{m}$). Each α -source can be assimilated to a small cylinder with axis along the wire. The short α -range causes part of the emitted light to be intercepted by the wire, therefore not reaching the photocatode of some PMTs behind the wire. As a consequence the reconstructed position (see chapter 6) is not the “true” position: all events are reconstructed at

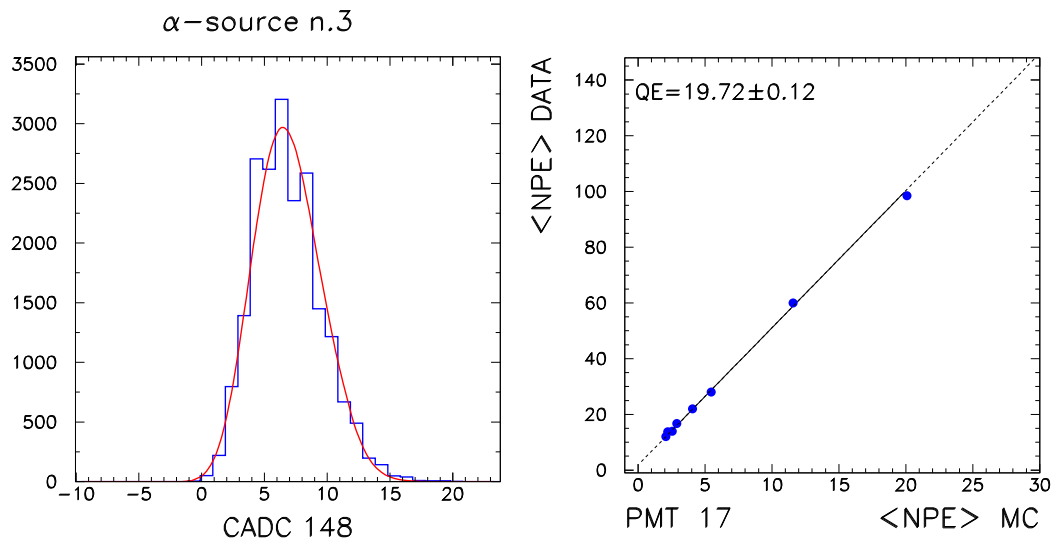


Figure 8.4: The charge α -spectrum of one PMT (left). The linear fit to the measured phe-number vs the MC simulation predictions (right). The slope of the fitted straight line is the measured QE.

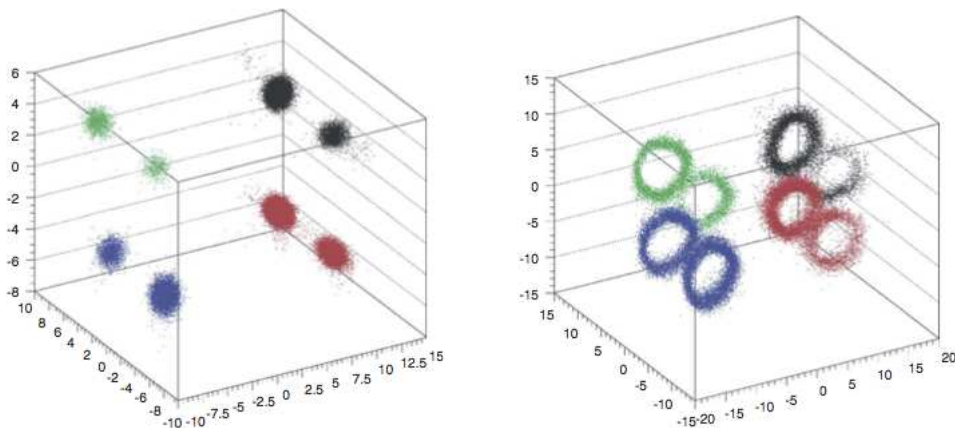


Figure 8.5: The measured and simulated position of the 8 sources inside the LXe large prototype: in gas Xe (left), in liquid Xe (right).

a distance from the wire. The result is a ring structure around the source position (see Fig. 8.5). This structure is well reproduced by the Monte Carlo simulation.

The size of the ring corresponds to a complex phenomenology and depends on many parameters: the Rayleigh scattering length, the LXe refractive index, the reflectivity of the calorimeter aluminum walls, the reflection and refraction of the PMT quartz windows, the light absorption in quartz, the PMT photocatode reflectivity, the wire diameter, the α -range etc.

While it is possible to obtain a satisfactory agreement between the measured characteristics of the rings and the predictions of the MC simulation, a separate determination of the various parameters is, at present, quite difficult and requires further studies. One hope for the future is to obtain a direct measurement of the Rayleigh scattering length in LXe, derived from a measurement of the ring diameter.

8.2.3 The results

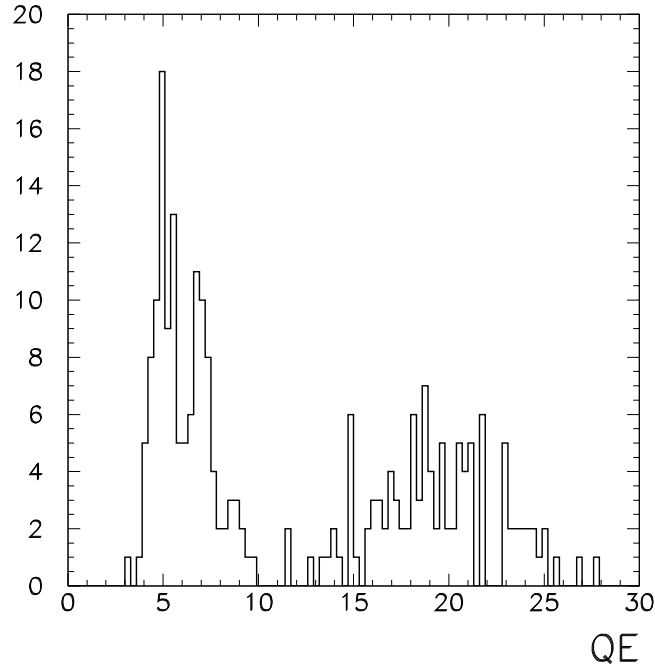


Figure 8.6: *QE distribution for all PMT. The QE were measured in gaseous Xe.*

The distribution of the measured QEs is shown in Fig. 8.6. The method allows the determination of the QEs at a 6 – 8% level. This precision is adequate, since, if the energy reconstruction depends on the information of N PMTs, then the associated error roughly scales as $1/\sqrt{N_{\text{PMT}}}$.

The correlation between the result of the measurement in gaseous and liquid Xe is shown in Fig. 8.7. The two data sets are in good agreement.

The LXe Large Prototype was used, after the determination of all PMT QEs , to measure γ 's from π^0 decays following the π^- -capture at rest by hydrogen (see chapter 11). Fig. 8.8 shows the

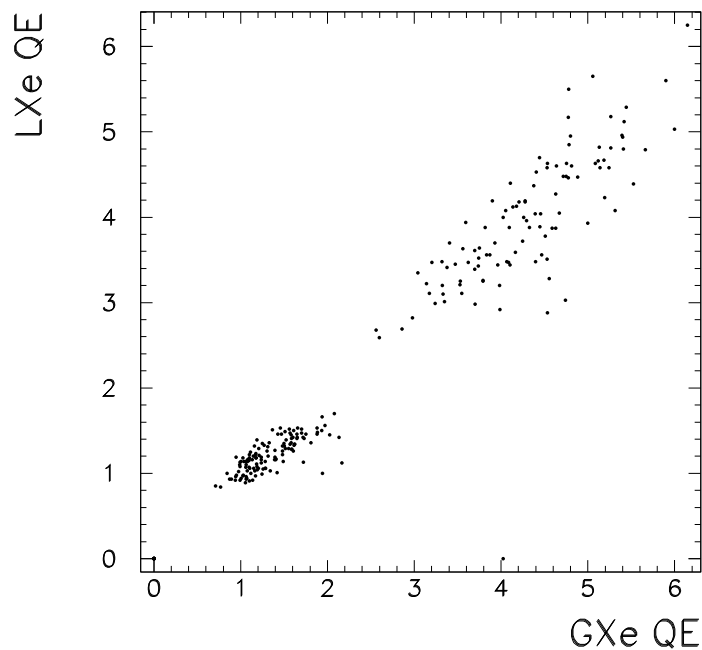


Figure 8.7: Correlation between the QE measured in liquid and gaseous Xe.

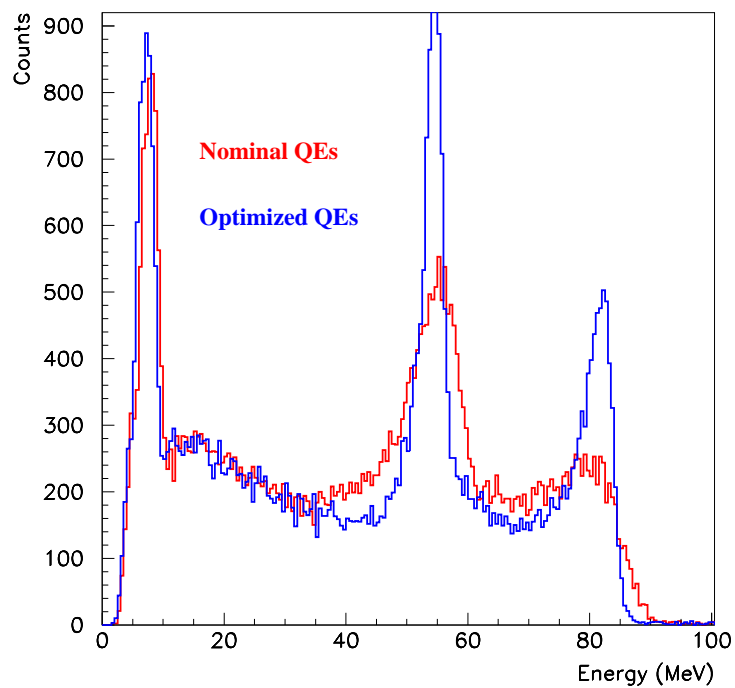


Figure 8.8: The γ -energy spectrum from π^0 -decay, in the LXe detector, with and without applying the correcting factors associated with the measured PMT QEs.

improvement in the γ -line widths, associated with the use of the QE measured values.

8.2.4 The absorption length determination

In chapter 4 we previously introduced the attenuation length λ_{att} , the absorption length λ_{abs} and the diffusion length λ_{diff} .

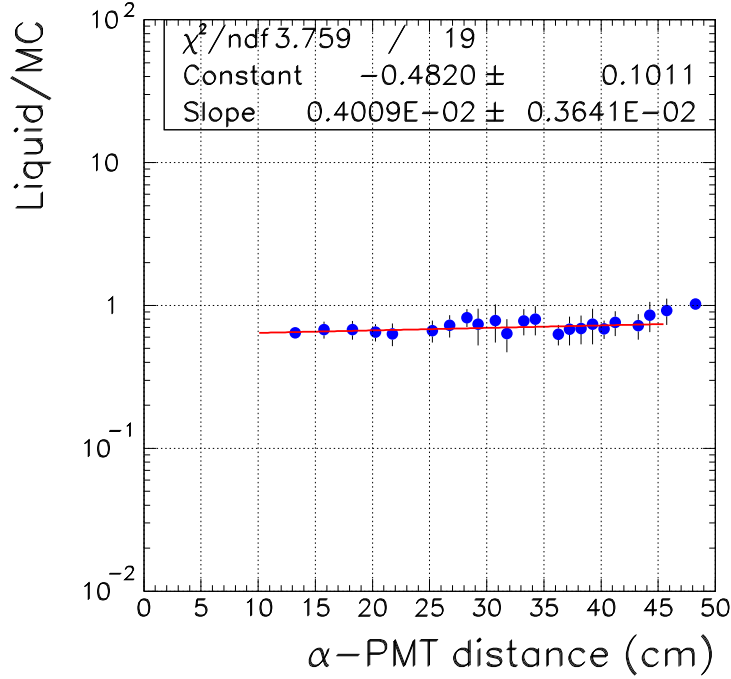


Figure 8.9: Comparison of the light yield measured by each PMT and the predictions of a Monte Carlo simulation, as a function of the PMT- α -source distance.

The use of the α -source improved our first lower limit of λ_{abs} for LXe (see chapter 4, [92], [124]). The result is a first measurement of this quantity for a large size detector.

To evaluate the λ_{abs} the light yield measured by each PMT is compared with the predictions of a Monte Carlo simulation, as a function of the PMT- α -source distance (see Fig. 8.9). In the MC simulation the absorption length is assumed to be $\lambda_{abs} \approx \infty$, λ_R really is $\lambda_R(n_{Xe}, h\nu_{Xe})$, where $h\nu_{Xe}$ indicates that the dependence of the Xe scintillation spectrum is included. The absorption length resulting from the measurements is $\lambda_{abs} \gg 3$ m at 90% C.L. and $\lambda_R \approx 45$ cm.

Chapter 9

The 9 MeV γ -line from thermal neutron capture by Ni

In this chapter we discuss in detail the method based on thermal neutron capture on nickel and its subsequent emission of a 9 MeV γ -ray. While other methods might possibly be more precise and complete, the neutron capture method is the only one which can be rapidly and frequently operated (several times a day), also when the μ -beam and its associated background are present. It is therefore promising for checking the stability of the calorimeter behaviour in case of variable μ -beam intensity.

Stability problems are present, to various extents, in all the experiments. MEG couples a high precision γ -energy measuring device to the use of the highest intensity μ -beam. The intrinsic precision of the LXe calorimeter can only be exploited if its stability is guaranteed for the whole duration of the experiment.

9.1 The 9 MeV γ generator

The 9 MeV γ generator (from now on: G9G) is based on a neutron source, a neutron moderator, and a nickel absorber. We describe each of these components: the properties of Ni, which has a high thermal-neutron capture cross-section and a high probability of emission of a 9 MeV γ -ray, the possible neutron sources, which can be a radioactive (Am/Be or Cf) source or a D-D or D-T neutron generator, and then the moderator, which thermalizes the neutrons emitted in the MeV energy range.

The criteria we adopted in selecting the source/moderator/geometry combination are the following:

1. a neutron source of moderate intensity to avoid the activation of materials and unwanted backgrounds;
2. good thermalization properties of the moderator;
3. large thermal neutron capture by nickel, low thermal neutron capture in the moderator;
4. low unthermalized neutron flux out of the moderator, to avoid the background from fast neutron interactions in the detector;
5. compactness of the moderator/nickel assembly;
6. easy and remote control of the γ -generator during a calibration.

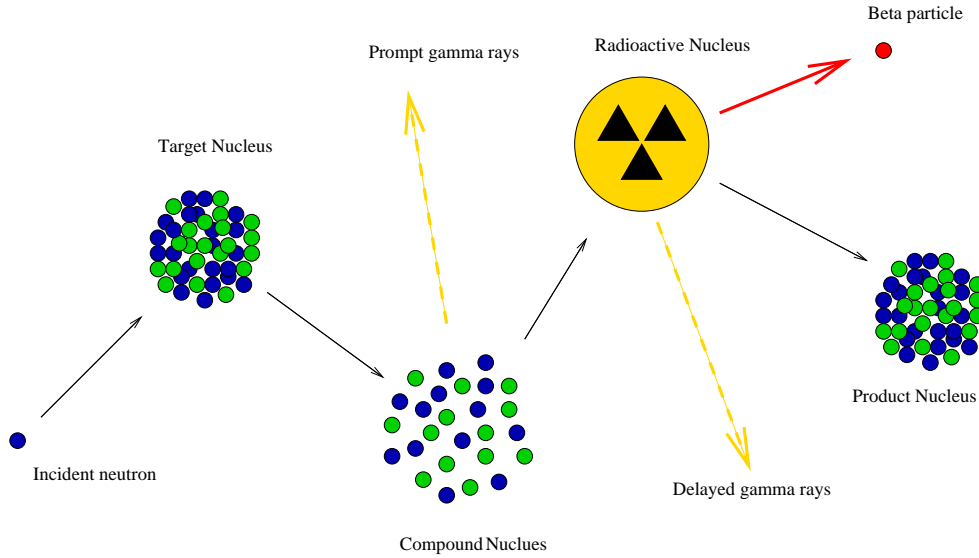
Figure 9.1: *Sequence of processes following neutron capture.*

Table 9.1: Ni isotopes, atomic weight, thermal neutron capture cross-section, isotope percentage, number of emitted gammas.

| Isotope | At.Wt.(amu) | σ_{γ} (b) | % | N_{γ} |
|---------|-------------|-----------------------|-------------|--------------|
| Ni | 58.6934(2) | 4.39(15) | 100. | 525 |
| Ni-58 | 58 | 4.5(2) | 68.0769(89) | 236 |
| Ni-60 | 60 | 2.9(2) | 26.2231(77) | 137 |
| Ni-61 | 61 | 2.5(8) | 1.1399(6) | 64 |
| Ni-62 | 62 | 14.5(3) | 3.6345(17) | 53 |
| Ni-64 | 64 | 1.63(7) | 0.9256(9) | 35 |

9.2 The γ -lines from thermal neutron capture

9.2.1 Capture on nickel

The thermal neutron nuclear capture usually produces a compound nucleus which soon de-excites by multiple gamma emission. This might sometimes be followed by the daughter nucleus β -decays (see Fig. 9.1). The transitions correspond to a rather complex and multiple path scheme. The energy released in the form of γ -rays amounts approximately to 8 MeV. One or more γ 's may be emitted.

Nickel is particularly convenient for two reasons:

- it emits γ 's for a large total energy of ≈ 9 MeV;
- in $\approx 34\%$ of the cases a single 9 MeV γ is emitted.

Since the solid angle at which the detector sees the moderator is normally rather small, multiple γ detection is unlikely and single intense γ -lines tend to emerge. The 9 MeV γ -line was previously used to calibrate the SuperKamiokande detector [157].

The relevant information on thermal neutron interactions, such as the elemental isotopic composition, the value of the thermal capture cross-section σ_{γ} , the energy and intensity of the emitted γ -lines, can be retrieved on-line [158]. Tab. 9.1 and Tab. 9.2 summarize the information in the

Table 9.2: Nickel. The most intense thermal neutron capture γ -lines (over 5 MeV and for $\sigma_\gamma > 0.04$ b). # is the number identifying the line.

| # | E_γ | Isotope | σ_γ (b) |
|-----|--------------|---------|---------------------|
| 464 | 5312.674(24) | Ni-58 | 0.0536(13) |
| 480 | 5695.80(3) | Ni-60 | 0.0416(12) |
| 484 | 5817.219(20) | Ni-58 | 0.1090(22) |
| 510 | 6837.50(3) | Ni-62 | 0.458(8) |
| 516 | 7536.637(25) | Ni-60 | 0.190(4) |
| 518 | 7819.517(21) | Ni-60 | 0.336(6) |
| 519 | 8120.567(16) | Ni-58 | 0.133(3) |
| 521 | 8533.509(17) | Ni-58 | 0.721(13) |
| 523 | 8998.414(15) | Ni-58 | 1.49(3) |

Table 9.3: Xe isotopes, atomic weight, thermal capture cross-section, isotope percentage, number of emitted gammas.

| Isotope | At.Wt.(amu) | σ_γ (b) | % | N_γ |
|---------|-------------|---------------------|-----------|------------|
| Xe | 131.29(2) | 24(3) | 100. | 268 |
| Xe-124 | 124 | 165(11) | 0.09(1) | 4 |
| Xe-128 | 128 | 5.2(13) | 1.92(3) | 7 |
| Xe-129 | 129 | 21(7) | 26.44(24) | 59 |
| Xe-130 | 130 | 4.8(12) | 4.08(2) | 13 |
| Xe-131 | 131 | 85(10) | 21.18(3) | 72 |
| Xe-132 | 132 | 0.40(6) | 26.89(6) | - |
| Xe-134 | 134 | 0.265(20) | 0.09(1) | - |
| Xe-136 | 136 | 0.26(2) | 8.87(16) | 113 |

most important Ni isotopes and the most intense Ni γ -lines. All γ -lines emitted from the different isotopes are shown in Fig. 9.2.

9.2.2 Capture on Xenon, Iodine and other elements

The nickel generated γ -lines will be detected by the MEG LXe calorimeter. Thermal neutrons from the moderator might directly reach the calorimeter and be captured by LXe. This can be strongly reduced by interposing a boron absorber between the neutron moderator and the calorimeter. A discussion on thermal neutron capture by Xe is nevertheless of some interest, because an appreciable neutron background is associated with $\pi E5$ when the beam is in operation [159]. Tab. 9.3, Tab. 9.4, and Fig. 9.3 refer to thermal neutron capture by Xe.

Note that Xe is also characterized by a sum of the emitted γ 's-energies equal to ≈ 9.3 MeV, but single lines at high energy have a low probability.

We also show nuclear data for iodine and aluminum, because we will show results on Ni-neutron capture studied by a NaI detector, and aluminum is largely present close to the calorimeter (Tab. 9.5, Tab. 9.6, Tab. 9.7, Fig. 9.4).

Iodine has no intense single γ -line for $E_\gamma > 5$ MeV and for $\sigma_\gamma > 0.06$ b. A very large number of closely spaced γ -lines is concentrated in the region from 0.45 to 0.6 MeV.

Aluminum has a large γ -line spectrum with an end-point at 7.7 MeV. The σ_γ is low.

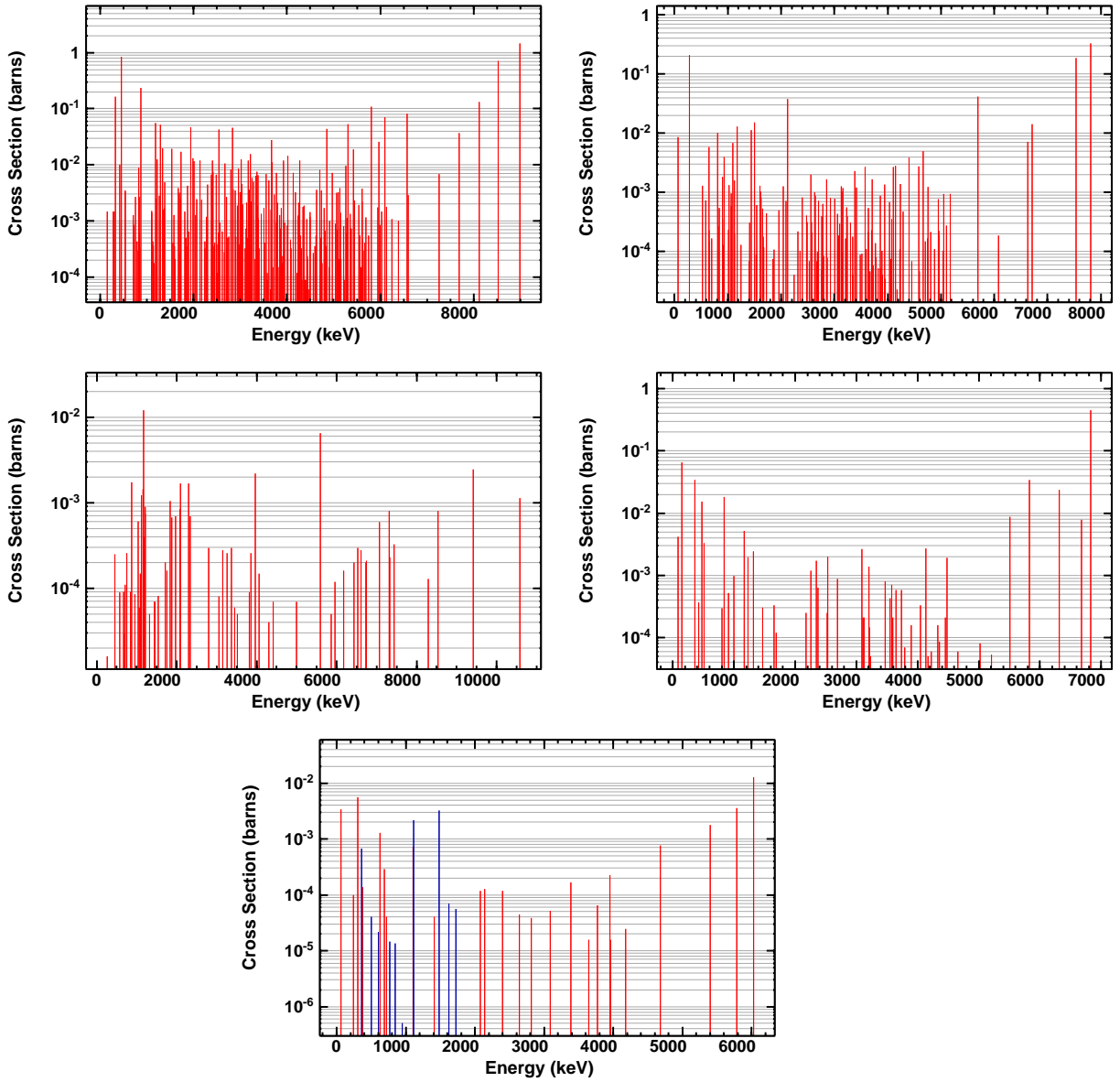


Figure 9.2: The spectra of the neutron capture γ -lines from the nickel isotopes. From top-left: *Ni-58, Ni-60, Ni-61, Ni-62, Ni-64.*

Table 9.4: Xenon. The most intense thermal neutron capture γ -lines (over 5 MeV and for $\sigma_\gamma > 0.2$ b.) # is the number identifying the line.

| # | E_γ | Isotope | σ_γ (b) |
|-----|-------------|---------|---------------------|
| 256 | 6380.62(13) | Xe-131 | 0.21(3) |
| 257 | 6467.09(12) | Xe-131 | 1.33(19) |

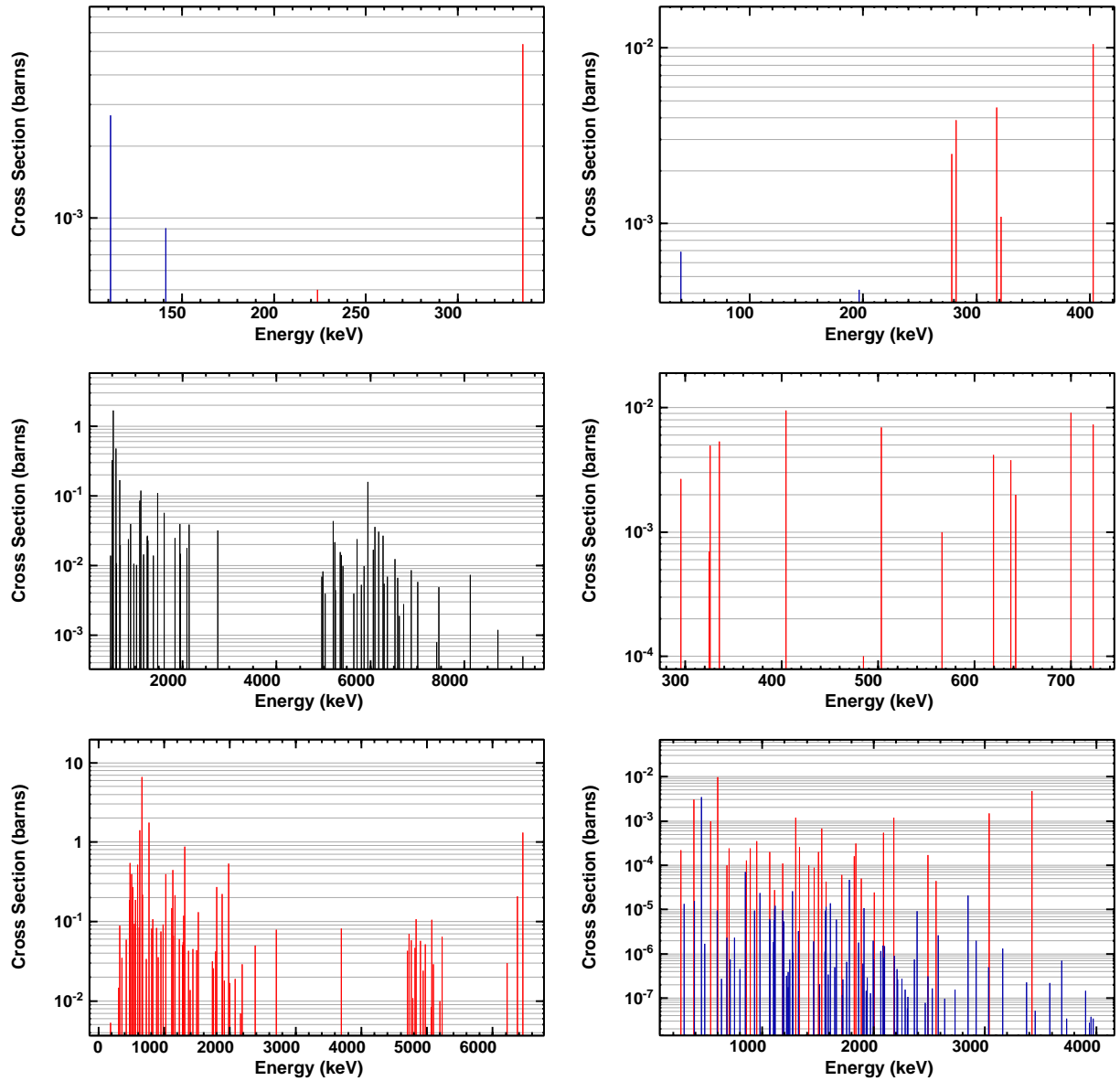


Figure 9.3: The spectra of the neutron capture γ -lines from the Xe isotopes. From top-left: Xe-124, Xe-128, Xe-129, Xe-130, Xe-131, Xe-136.

Table 9.5: I isotopes, atomic weight, thermal capture cross-section, isotope percentage, number of emitted gammas.

| Isotope | At.Wt.(amu) | σ_γ (b) | % | N_γ |
|---------|---------------|---------------------|------|------------|
| I | 126.904468(4) | 6.2(2) | 100. | 348 |
| I-127 | 127 | 6.2(2) | 100. | 348 |

Table 9.6: Al isotopes, atomic weight, thermal capture cross-section, isotope percentage, number of emitted gammas.

| Isotope | At.Wt.(amu) | σ_γ (b) | % | N_γ |
|---------|--------------|---------------------|------|------------|
| Al | 26.981538(2) | 0.231(3) | 100. | 216 |
| Al-27 | 27 | 0.231(3) | 100 | 216 |

Table 9.7: Aluminum. The most intense thermal neutron capture γ -lines (over 5 MeV and for $\sigma_\gamma > 0.002$ b). # is the number identifying the line.

| # | E_γ | Isotope | σ_γ (b) |
|-----|--------------|---------|---------------------|
| 181 | 5411.077(8) | Al-27 | 0.00481(19) |
| 187 | 5585.651(11) | Al-27 | 0.00279(12) |
| 197 | 6101.529(18) | Al-27 | 0.00570(21) |
| 199 | 6198.143(11) | Al-27 | 0.00210(14) |
| 201 | 6440.650(11) | Al-27 | 0.00147(8) |
| 208 | 6710.699(10) | Al-27 | 0.00220(12) |
| 215 | 7693.397(4) | Al-27 | 0.0081(3) |
| 216 | 7724.027(4) | Al-27 | 0.0493(15) |

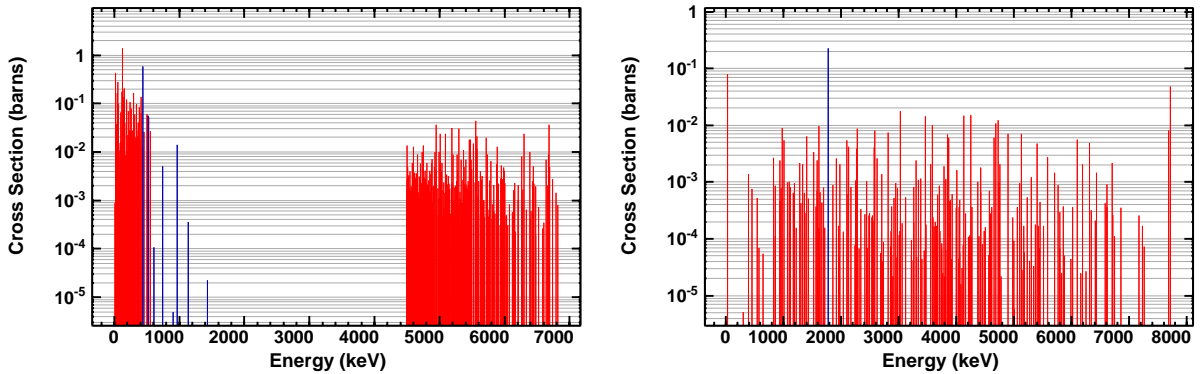


Figure 9.4: The spectra of the neutron capture γ -lines from I (left) and Al (right).

9.3 The neutron sources

The usual ways to produce neutrons are based on spontaneous fission (as for the ^{252}Cf -source), on (α, n) -reactions (as for the $^{241}\text{AmBe}$ -source). Such a source is made by mixing the target material with a strong α emitter, or on nuclear fusion reactions D-D or D-T (as for neutron generators) (see Fig. 9.5).

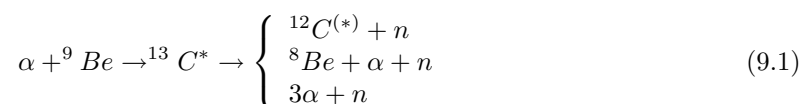
The preliminary tests, to verify that the nickel method is applicable to MEG, used AmBe- and Cf-sources. The advantage of a radioactive source is in its simplicity, but being a continuous emitter, its intensity must be limited to 20-70 kBq for safety reasons. If on the other hand a high and pulsed neutron emission is needed, a D-D neutron generator can be used (up to 10^8 n/s, at a 10 Hz typical frequency, with a pulse width of $1\mu\text{s}$). Stricter safety controls must in this case be satisfied.

9.3.1 The radioactive neutron sources

(α, n) sources are a mixture of a long-lived α -emitting actinide and of a low-Z target material. A clean neutron spectrum depends on a properly prepared mixture. ^{241}Am is commonly adopted as α -emitter because of its long half-life and its low γ emission. Be is used as a target because of its high neutron yield. Commercial AmBe sources are an homogeneous mixture of finely divided $^{241}\text{AmO}_2$ and finely powdered Be, compressed into a cylindrical pellet [161].

Fig. 9.6 shows the neutron energy spectrum of an Am-Be source [160] and of a Cf source [162].

The first is a complex spectrum, due to the neutron production mechanism:



where ${}^{13}\text{C}^{(*)}$ is the compound nucleus, which decays through a variety of channels, depending on the excitation energy.

The second spectrum exhibits a Maxwellian shape, typical of spontaneous nuclear fission.

Both spectra are continuous up to about 10 MeV. For capture by nickel, neutrons must be slowed-down. The Cf spectrum has a lower average energy than that of a AmBe-source. The first is therefore preferable for a faster thermalization.

However the AmBe is characterized by a 4.4 MeV γ -line emission, coming from the de-excitation of the ${}^{12}\text{C}^{(*)}$ nucleus (see eq. (9.1)) after part (60%) of the neutron emissions. The process can be useful for triggering, the γ being a signal of neutron emission. The Cf-source also emits γ 's but with a broad γ -spectrum.

9.3.2 The neutron generator

A neutron generator operates according to the two following reactions:

- $\text{D} + \text{T} \rightarrow {}^4\text{He} + \text{n}$ (Q-value = 17.59 MeV, neutron energy = 14 MeV)
- $\text{D} + \text{D} \rightarrow {}^3\text{He} + \text{n}$ (Q-value = 3.27 MeV, neutron energy = 2.45 MeV).

A generator offers several advantages: it only emits neutrons when necessary for a calibration and the neutron flux is adjustable. Neutrons can be emitted in pulses of $\approx 20 \mu\text{s}$. If one considers that the thermalization/capture time is $\approx 50 - 100 \mu\text{s}$, one can fix the number of neutrons/pulse to make the nickel γ -line (emitted during the $100 \mu\text{s}$) dominant relative to the background present in that energy region. The background is associated with the ^{241}Am α -sources on wires, and with events due to the μ -beam. The pulsed operation improves the signal/noise ratio and makes it possible to perform the nickel calibration even during the normal data taking. This is an important way to keep under control, by a physical signal, the shifts in the calorimeter response due to μ -beam intensity variations.

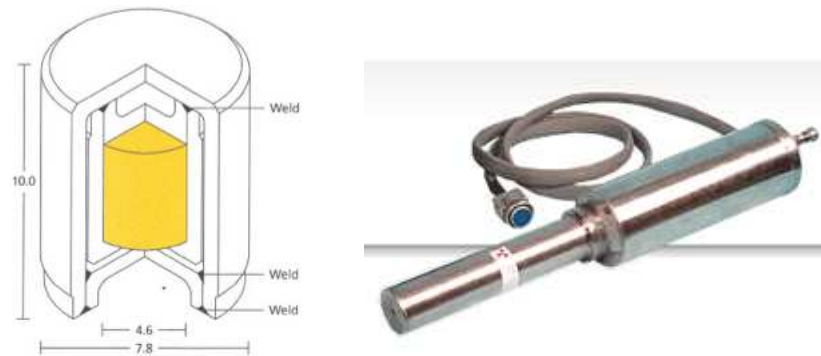


Figure 9.5: The two possible neutron sources: 1) a radioactive neutron source (a californium source is shown in the picture, with dimensions in mm); 2) a neutron generator (by Sodern, the GENIE 16c).

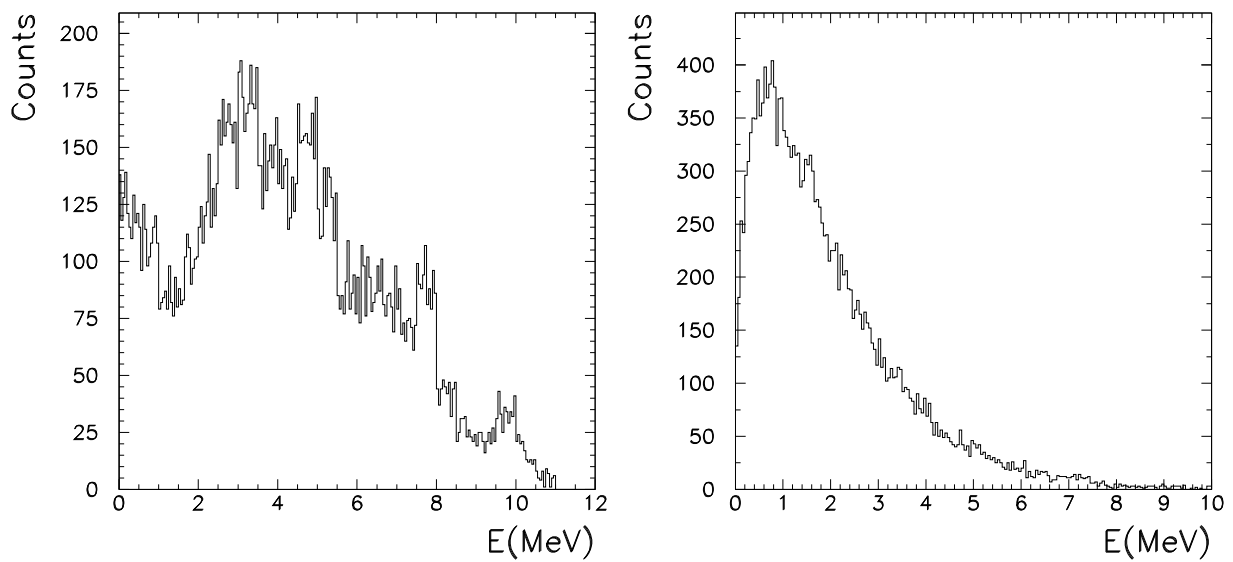


Figure 9.6: The neutron energy spectrum from an AmBe-source and a Cf-source.

Table 9.8: Some properties of the materials used for moderating neutrons.

| Material | A | $\rho(g/cm^3)$ | $\sigma_s(b)$ | $\sigma_\gamma(b)$ | $\Sigma_s(cm^{-1})$ | ξ | SDP(m^{-1}) | n |
|------------------|--------|----------------|---------------|-----------------------|---------------------|-------|-----------------|-----|
| H ₂ | 1.008 | 0.0708 | 20.49 | 0.33 | 0.87 | 1 | 87 | 20 |
| D ₂ | 2.014 | 0.169 | 3.39 | 0.52×10^{-3} | 0.171 | 0.725 | 12.4 | 27 |
| C | 12.001 | 2.265 | 4.74 | 3.5×10^{-3} | 0.538 | 0.158 | 8.5 | 125 |
| CH ₂ | 14.027 | 0.920 | 45.72 | 0.66 | 1.81 | 0.913 | 165 | 22 |
| H ₂ O | 18.015 | 1 | 44.74 | 0.66 | 1.49 | 0.92 | 138 | 22 |
| D ₂ O | 20.027 | 0.169 | 10.54 | 1.23×10^{-3} | 0.137 | 0.509 | 16 | 39 |

9.4 The neutron moderator

Neutrons must be slowed-down to be efficiently captured by nickel. At the same time the moderator should be of moderate size, the neutron capture from other elements than nickel should be small and the number of fast neutrons leaking out of the moderator should be minimized.

The quantities characterizing a moderator are:

- the σ_s scattering cross section;
- the value of σ_γ (i.e.: the n- γ thermal neutron absorption cross section);
- the average lethargy ξ (i.e.: the energy independent, average logarithmic loss of energy per collision, $\xi = \langle \log(E_0/E) \rangle$), hence $\log E = \log E_0 - n\xi$);
- the SDP slowing-down power ($SDP = \xi \Sigma_s$);

where Σ_s is the macroscopic scattering cross section, i.e.: $\Sigma_s = \sigma_s \cdot N$, where N is the number of target nuclei per cm^3) and n is the average number of collisions to reach thermalization [163]. Tab. 9.8 shows these quantities for common moderators.

A “good” moderator should have a high scattering cross section, or equivalently a small $\lambda_s = 1/(\sigma_s \cdot n)$, to increase the number of collisions for unit length. It should also have a high lethargy, to increase the energy loss for each collision. These two parameters appear in the definition of the SDP, which should then be maximized.

We also required a small absorption cross section by the moderator material, to increase the thermal neutron capture by the nickel target.

Polyethylene meets these requirements. Tab. 9.8 points to it as the best material, although its σ_γ is rather high (D₂O would be better, but exceedingly expensive). A Monte Carlo calculation was used to optimize a multilayer arrangement of moderator slabs and Ni target plates, according to the previously listed requirements.

The results for one of the best configurations are presented in Fig. 9.7. One can see a cloud of neutron capture events on CH₂ (predominantly on hydrogen) around the AmBe-source and the neutron capture events on the various nickel plates. Note that, although the plate on the right is less productive, it is closer to the calorimeter and therefore seen under a favourable solid angle. The γ 's from the plate closer to the source suffer from a higher energy degradation than those further away. This is shown in Tab. 9.9 where the rates γ_{cal} of the unmodified 9 MeV γ -rays coming out of the moderator front face and originating from the different nickel plates are presented; γ_{tot} are instead the rates of the 9 MeV γ -rays produced in the different nickel plates. The rates of the total number of non-thermal n_{nth} and thermal n_{th} neutrons coming out of the moderator (Tab. 9.10) are also presented. The results refer to the AmBe and the Cf neutron sources, in the so called “standard configuration”. The Monte Carlo simulation predicts that another configuration, corresponding to thinner moderator plates, gives a somewhat larger rate of 9 MeV γ -rays. It was not possible to experimentally check this prediction and we preferred to stick to the “standard configuration” which had been fully checked.

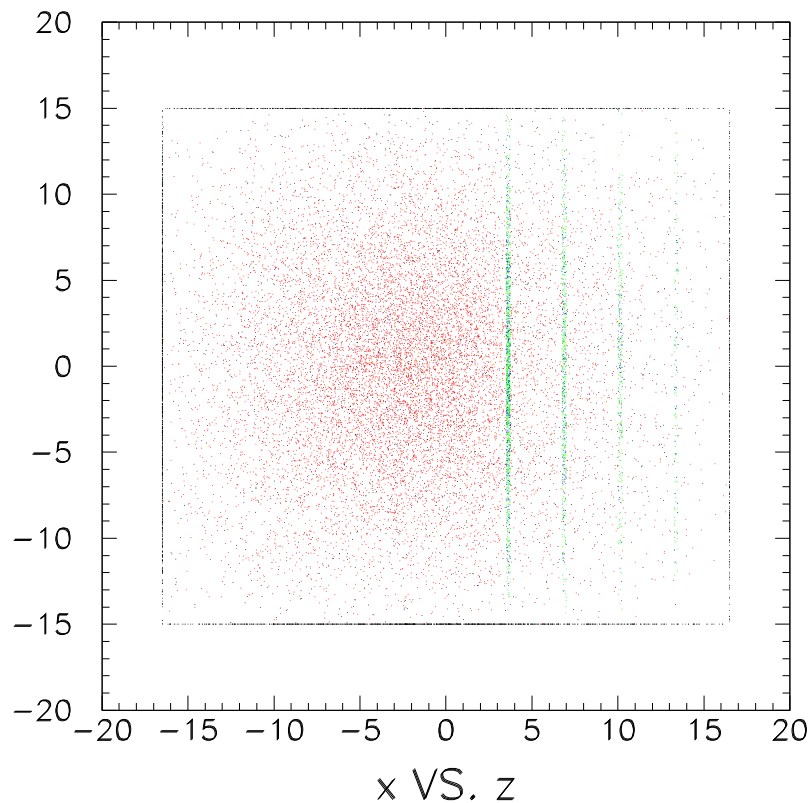


Figure 9.7: *Spatial distribution of the neutron captures in CH₂ and Ni.*

Table 9.9: The rates of the 9 MeV γ -rays coming out of the moderator front face and originating from each nickel plate. γ_{tot} are the rates of γ -rays produced in the same nickel plates. Neutron source rate: $70000 \text{ n} \cdot \text{s}^{-1}$.

| Plate | γ_{cal} | γ_{tot} |
|-------|-----------------------|-----------------------|
| NIC1 | 116 | 3378 |
| NIC2 | 88 | 1610 |
| NIC3 | 76 | 914 |
| NIC4 | 46 | 322 |

Table 9.10: Rate γ_{cal} of the 9 MeV γ 's coming out of the moderator front face. Rates of the non-thermal and thermal neutrons coming out of the moderator. Neutron source rate: $70000 \text{ n} \cdot \text{s}^{-1}$.

| Source | Configuration | γ_{cal} | n_{nth} | n_{th} |
|--------|---------------|-----------------------|------------------|-----------------|
| AmBe | std | 326 | 18638 | 5325 |
| Cf | std | 326 | 8439 | 2411 |

9.5 The results of the 9 MeV γ generator test



Figure 9.8: *The experimental set-up for the test of the 9 MeV γ -generator. A large NaI detector was used.*

The 9 MeV γ -generator was first tested in front of a large NaI detector ($28 \times 28 \times 35 \text{ cm}^3$). The experimental set-up is shown in Fig. 9.8. We used an AmBe-source (activity 20 kBq), several polyethylene slabs and several Ni-plates, to reproduce different configurations studied with the MC simulations. The NaI signal, obtained by adding up the signals of 4 PMTs (equalized by the AmBe 4.4 MeV γ -line), was fed into MCA analyzer. The experimental results confirmed the predictions of the MC studies. We only present the best result, associated with the so called “standard configuration” (see Fig. 9.9).

The γ -ray spectrum is shown in Fig. 9.10. One can clearly see the Ni 9 MeV γ -line, accompanied by the 8.54 MeV γ -line superimposed to the first escape peak of the 9 MeV γ -line. One can also see a weak 7.7 MeV γ -line from aluminum, material contained in the moderator stand and also associated with the NaI detector. The iodine of the NaI detector is visible as an intense 6.8 MeV γ -line. At 4.4 MeV one detects the usual γ -line associated with part of the AmBe neutron emission, accompanied by its first escape peak. At still lower energies, one can see the 2.2 MeV γ -line from neutron capture in CH_2 and some natural radioactivity γ -lines. It is worth noting that the right shoulder of the 9 MeV line is rather sharp and provides a reliable energy calibration reference (see, in a linear scale, the Ni 9 MeV γ -line in Fig. 9.11).

Two other energy spectra are shown in Fig. 9.10: one corresponding to the removal of the AmBe-source (some cyclotron generated neutrons are still present) and the other corresponding to the removal of the source and of the nickel contained in the moderator. Note that a weak nickel signal is still visible also for this condition. The signal is due to the cyclotron generated neutrons captured on the nickel parts of the COBRA magnet. With the cyclotron beam off, the Cobra related signal disappeared.

These tests confirmed that the 9 MeV γ -line is clearly visible with a NaI detector.

We repeated the tests by using the LXe Large Prototype Detector. Unfortunately the quality of the data in this last detector is inferior for two reasons:

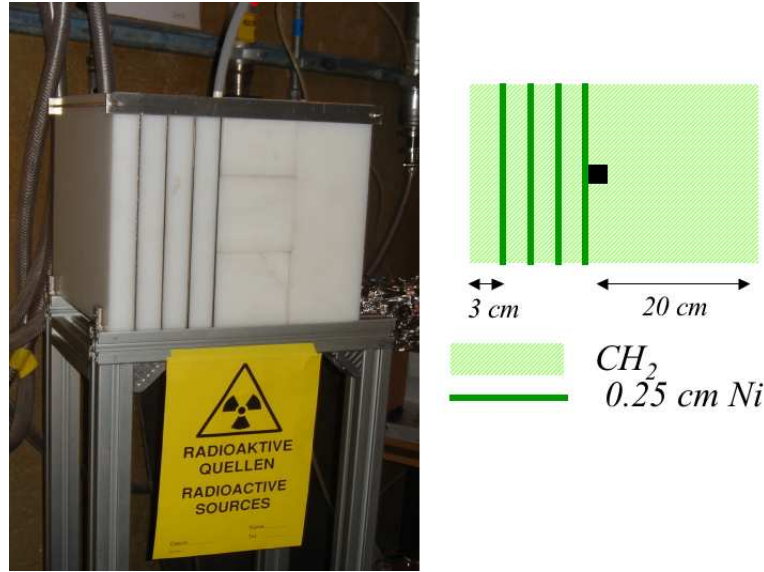


Figure 9.9: *The best moderator/nickel geometry for the 9 MeV γ -generator.*

- the γ -spectra are partially superimposed on the α energy spectra of several ^{241}Am -sources contained in the Large Prototype for calibration purposes;
- the neutron induced background in Xe is much more important than in NaI.

We discuss these two problems in more detail and propose solutions.

The first problem is related to the scintillation properties of Xe (see chapter 4). Fig. 9.12 shows the pulse-shapes of a cosmic muon event and of an α event, normalized in amplitude. α -particles are associated with a shorter scintillation time ($\tau = 4$ ns and $\tau = 22$ ns) relative to muons, electrons and γ s (associated with a $\tau = 45$ ns). The two kinds of events are also characterized by different W-values ($W_\alpha = 19.6 \pm 2.0$ and $W_\gamma = 23.7 \pm 2.4$). As a consequence, α -events at ≈ 5 MeV are equivalent to γ -events at ≈ 12 MeV. This makes their separation by a charge threshold impossible.

However if one plots the charge as a function of the amplitude for α - and γ -events, one obtains the result shown in Fig. 9.13. It is evident that the two types of events can be separated by pulse-shape analysis. This can be used, at the trigger level, during the neutron calibration.

The second problem is associated with the fast and thermal neutron backgrounds which we carefully measured both with the AmBe and the Cf source and their different neutron energy spectra.

The thermal neutron background can be suppressed by flexboron sheets in front of the detector. Flexboron is a flexible boron compound, characterized by a very high thermal capture cross section (boron $\sigma_\gamma = 3840$ barn), and useful around irregular shapes. We verified that a few mm of flexboron in front of the NaI detector reduced the thermal contribution to a negligible level and made the iodine peak disappear. The Large Prototype was unfortunately unprotected by flexboron and was therefore efficiently detecting thermal neutrons out of the moderator (with the rather high Xenon thermal neutron capture cross-section).

The fast neutron background cannot be suppressed. The moderator was therefore optimized to maximize the ratio of thermal against fast neutrons. Cf, which has a lower fast neutrons flux than AmBe, is the best source.

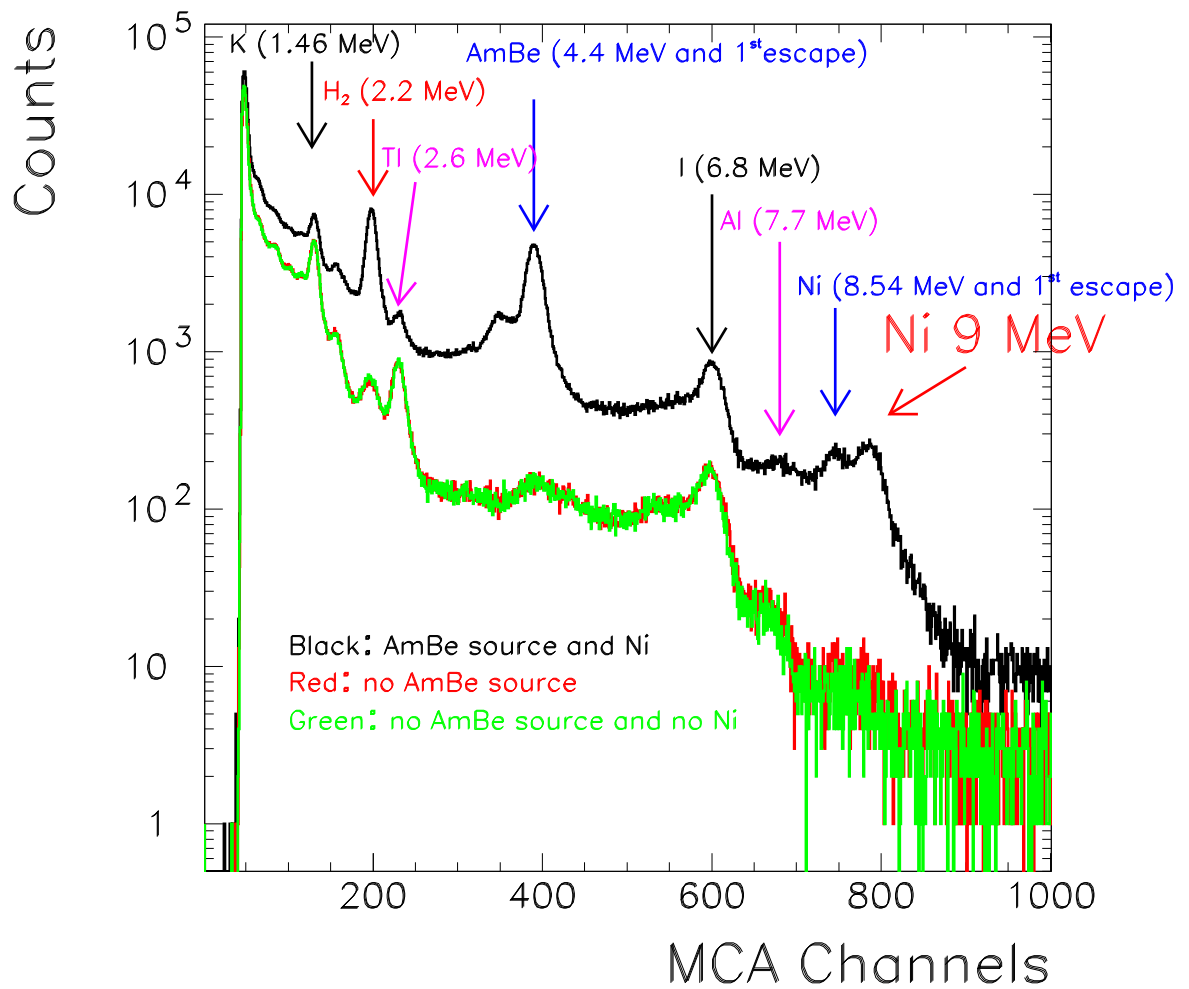


Figure 9.10: γ -energy spectrum from the 9 MeV γ -generator. NaI detector.

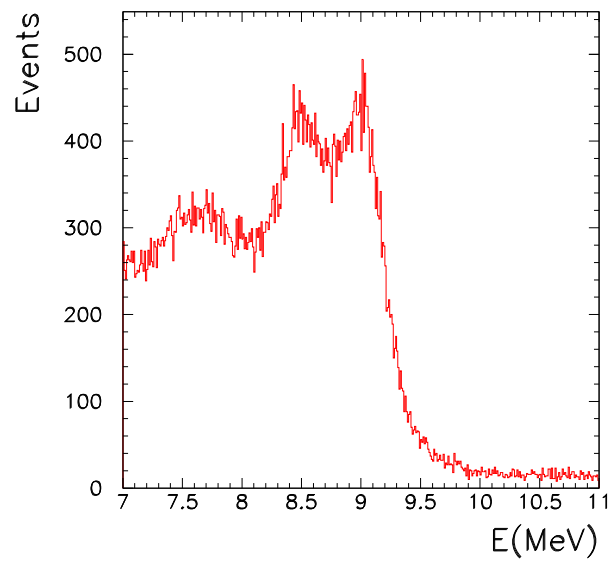


Figure 9.11: *The 9 MeV γ -line in a linear scale. NaI detector.*

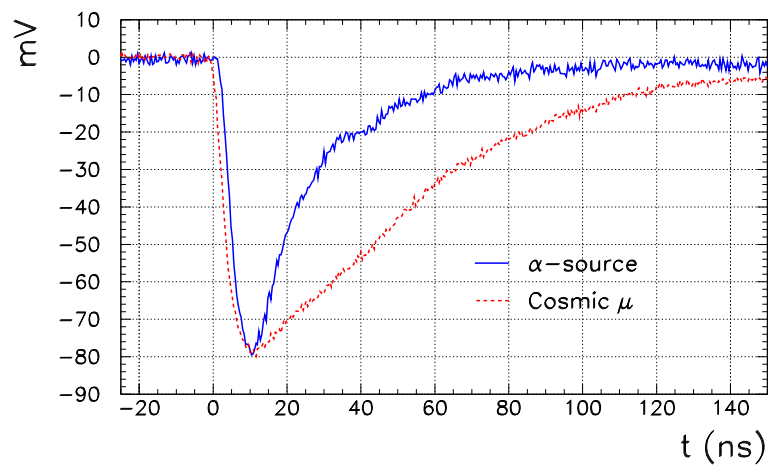


Figure 9.12: *The pulse-shape for α - and γ -events, normalized in amplitude.*

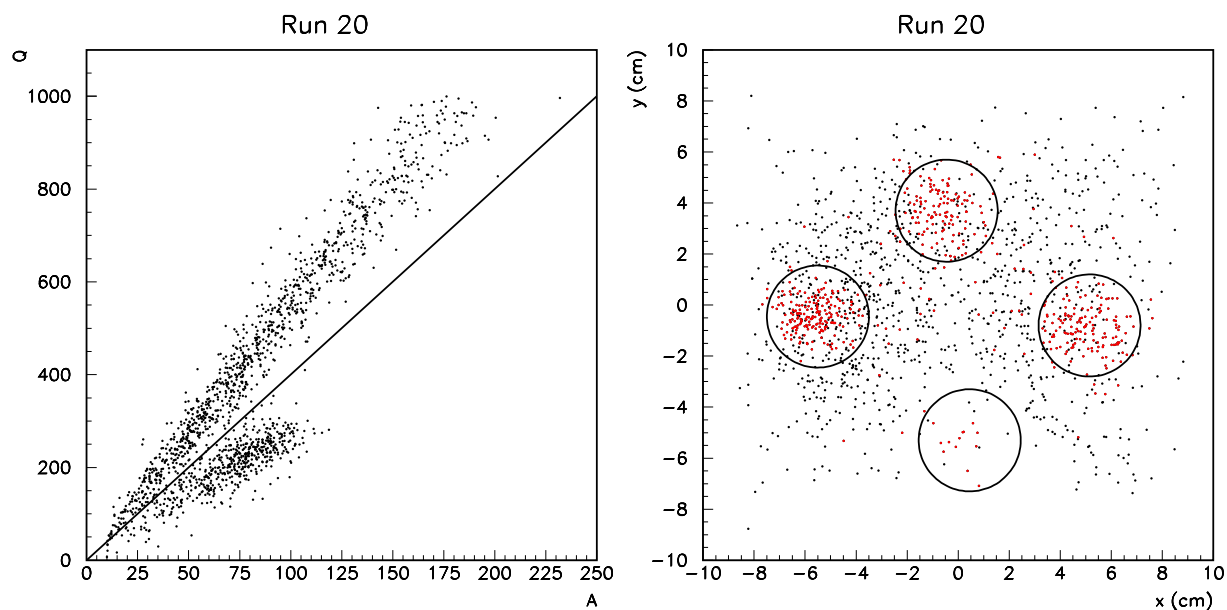


Figure 9.13: *The charge as a function of the amplitude for α - and γ -events (left). Measured positions of the two types of events on a X-Y projection, red: α -events; black: γ -events (right).*

This point is a crucial one since fast neutrons enter the calorimeter and generate a prompt background interfering with the detection of the 9 MeV γ -rays. As already said, this problem is reduced if, instead of a neutron source, a pulsed neutron generator is used.

The mechanism by which fast neutrons generate a signal in the calorimeter is rather complex. It first proceeds by $(n, 2n)$ reactions and then by $(n, n'\gamma)$ reactions, which effectively transform the neutron kinetic energy into detectable electromagnetic energy (scattering and nuclear recoils give much smaller contributions).

This background is present in any γ detector. It was present both in the NaI detector and in the LXe Large Prototype. Some detailed studies were performed for NaI crystals [164]. Typical energy spectra, measured by a 3 inch. \times 3 inch. NaI crystal at various incident neutron energies, were analysed.

We present in Fig. 9.14 the typical cross-sections for $(n, 2n)$ and $(n, n'\gamma)$ reactions for one of the Xe isotopes.

At the end of this section we report the rate we measured for the final configuration of the moderator/nickel assembly: $R_{\gamma 9} = 36$ Hz (Cf-source) and $R_{\gamma 9} = 30$ Hz (AmBe-source), for a source activity of 20 kBq. The expected rate in the LXe calorimeter is ≈ 80 kHz using a neutron generator which produces 10^5 n/pulse, at a pulse rate of 20 Hz, mounted in front of the LXe calorimeter, behind the Cobra coil. The expected background in the 9 MeV energy region is about 45 kHz when the MEG muon beam is on.

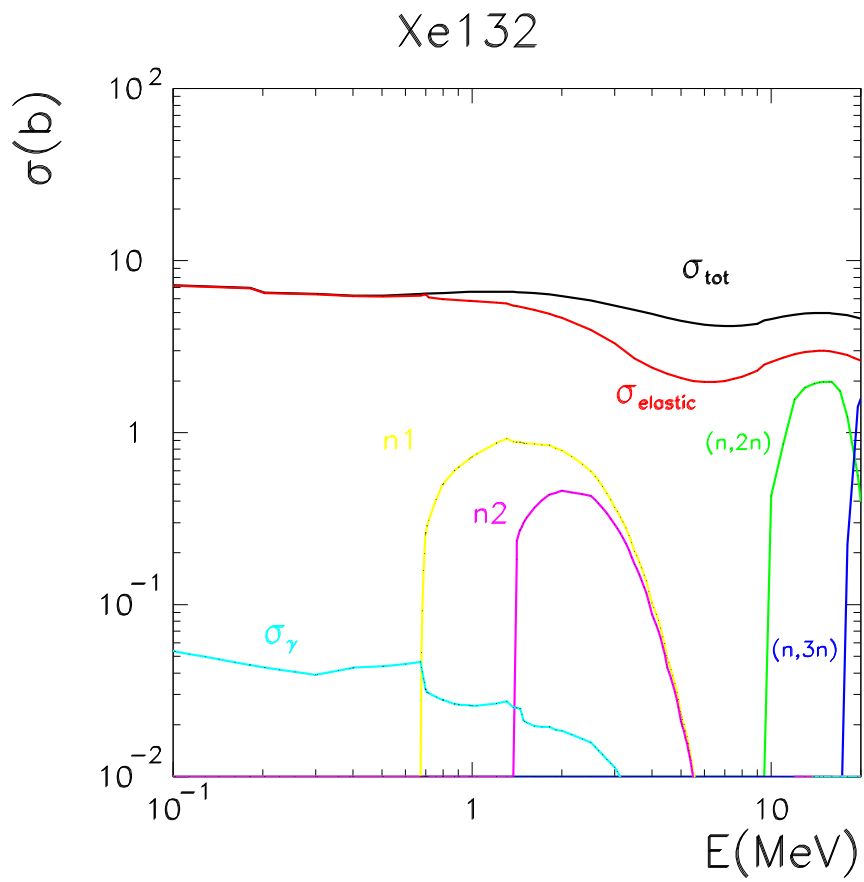


Figure 9.14: Xenon 132. The $(n, 2n)$ and $(n, 3n)$ cross-sections are shown; the cross-section for the excitation of the nuclear levels 1-2 is superimposed. The total, elastic and thermal capture cross sections are also plotted.

9.6 The neutron capture time in a polyethylene/nickel assembly

In section 9.3.2 the use of a pulsed neutron generator for selecting delayed neutron capture events and improving the signal/noise ratio was discussed.

It is therefore useful to measure the sum of the thermalization and capture times in the polyethylene/nickel assembly adopted for MEG.

The mean time $\bar{t}(E_0, E)$ for passing from a neutron energy E_0 down to E is given by the integral:

$$\bar{t}(E_0, E) = \int_0^{t^*} dt = \int_{E_0}^{E^*} \left(\frac{dt}{dE} \right) dE, \quad (9.2)$$

where $\left(\frac{dE}{dt} \right)$ is the neutron mean energy loss rate during thermalization.

If the neutron energy decreases from $E + \Delta E$ to E in a time interval $(t, t + \Delta t)$, the mean number of collision in that time interval is

$$\overline{\Delta n}(E + \Delta E, E) = \frac{1}{\xi} \ln \frac{E + \Delta E}{E} \approx \frac{1}{\xi} \frac{\Delta E}{E}. \quad (9.3)$$

where ξ is the lethargy of the material.

The time between two successive collisions is, on average, λ_s/v , where λ_s is the mean free path between two collisions and $v = \sqrt{2E/m_n}$ is the neutron velocity. The mean time interval for a neutron to pass from $E + \Delta E$ to E is therefore:

$$\Delta t = \frac{\lambda_s}{v} \overline{\Delta n}(E + \Delta E, E) = \frac{\lambda_s}{v} \frac{1}{\xi} \frac{\Delta E}{E}. \quad (9.4)$$

We have thus found the neutron mean energy loss rate, $dE/dt = (v/\lambda_s)\xi E$, from which the integral (eq. (9.2)) can be computed. Under the hypothesis of a constant neutron free path length λ_s in the energy interval (E_0, E) , one obtains:

$$\bar{t}(E_0, E) = \frac{2\lambda_s}{\xi} \left(\frac{1}{v} - \frac{1}{v_0} \right), \quad (9.5)$$

where v_0 and v are the neutron velocities at the beginning and the end of the thermalization time interval. Since $E_0 \gg E$, the mean stopping time depends very weakly on the initial neutron velocity (energy) and the total stopping time depends only on the final average thermal velocity. In Tab. 9.12 the neutron stopping parameters are presented for water, heavy water and graphite.

Table 9.11: Parameters for the slowing-down of neutrons in water, heavy water, and graphite.

| Material | Lethargy ξ | Mean free path λ_s (cm) | Slowing time t_s (s) |
|------------------|----------------|---------------------------------|------------------------|
| H ₂ O | 1 | 1.1 | 1×10^{-6} |
| D ₂ O | 0.73 | 2.6 | 4.6×10^{-5} |
| graphite | 0.16 | 2.6 | 1.5×10^{-4} |

After the slow-down and thermalization processes, the neutrons can be captured during the diffusion process. The diffusion equation is:

$$\frac{\partial n(r, t)}{\partial t} = -divj(r, t) + q(r, t) - N\sigma_{abs}vn, \quad (9.6)$$

where $n(r, t)$ is the neutron density in space, $j(r, t)$ is the neutron current density, $q(r, t)$ is the neutron source, N is the density of atoms in the medium, v is the neutron velocity. The first

term is related to the outgoing neutron flux, the two last terms respectively describe, the inflow of neutrons due to distributed sources and the loss of neutrons due to nuclear absorption reactions.

In the special condition in which the diffusion is extremely slow and the source is only “switched on” for a very short time, the first and the second terms of eq. (9.6) are negligible. The equation becomes simpler:

$$\frac{\partial n(r, t)}{\partial t} = -\frac{1}{T}n(r, t), \quad (9.7)$$

where $T = 1/(N\sigma_{abs}v)$ is the capture or diffusion time. The diffusion time is always greater than

Table 9.12: Diffusion parameters of thermal neutrons in water, heavy water, and graphite.

| Substance | Diffusion length L_s (cm) | Diffusion time t_s (s) |
|------------------|-----------------------------|--------------------------|
| H ₂ O | 2.7 | 2×10^{-4} |
| D ₂ O | 160 | 0.15 |
| graphite | 54 | 1.2×10^{-2} |

the thermalization time in the same material. Since the two times differ by orders of magnitude, when one measures their sum one is really measuring only the diffusion time. This is what we obtained for nickel.

9.6.1 The experimental set-up and the results

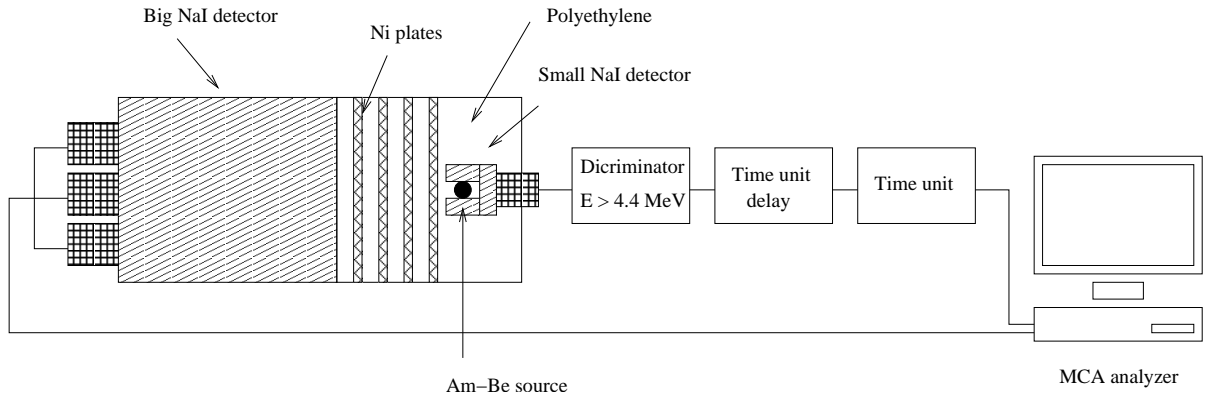


Figure 9.15: *The experimental set-up for the determination of neutron capture time in Ni.*

The experimental set-up is schematically shown in Fig. 9.15. A small and a big NaI detectors were used. The small detector was of the well type for housing the AmBe-source. Since a 4.4 MeV γ from AmBe is always associated with a neutron emission, a delayed coincidence was required between the small and the big NaI. We recorded the big NaI spectra for different delay times and selected the 9 MeV events from the neutron-capture by Ni.

Dead time corrections must be found and applied as a function of the delay time according to the equation:

$$n = \frac{m}{1 - m\tau} \quad (9.8)$$

where n is the true events rate, m is the acquired events rate and τ is the dead time. The effects due to the dead time appear in Fig. 9.16, where the ratio of the recorded events and of the number of triggers as a function of the delay time is shown. The true event rate can be derived from a fit to the data: $R = 4 \pm 0.1$ kHz, consistent with the value that was measured using a single detector ($R = 3.89 \pm 0.03$ kHz). The dead time corrected data are presented in Fig. 9.17

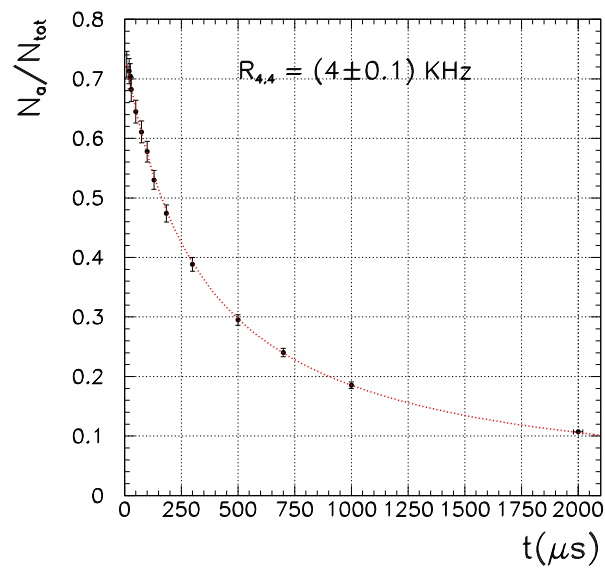


Figure 9.16: The ratio of the recorded events and of the number of triggers, as a function of the delay time.

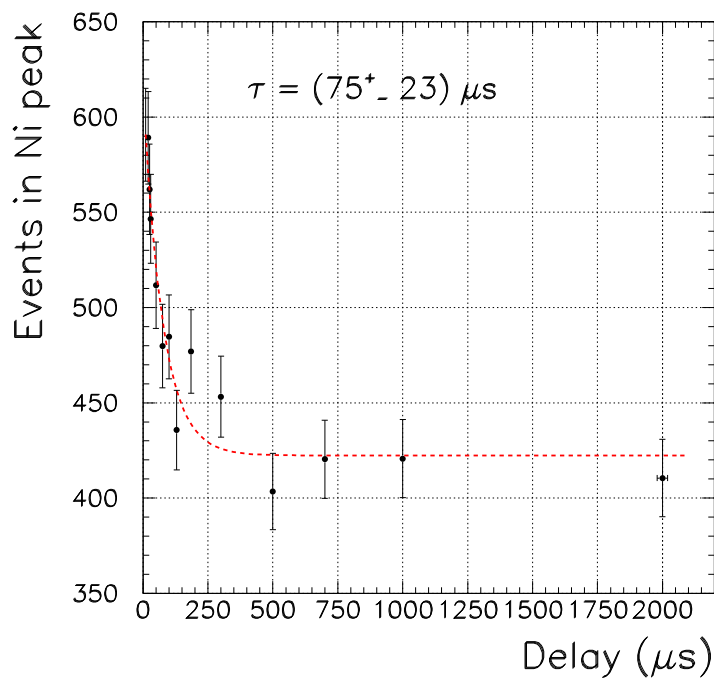


Figure 9.17: The neutron capture time in Ni.

as a function of the delay time. The measured diffusion time is $t_s = 75 \pm 23 \mu\text{s}$. This value is consistent with the diffusion time calculated by a Monte Carlo simulation of our experimental set-up: $t_s = 85 \pm 5 \mu\text{s}$. Note that this diffusion time is lower than that of water (similar to polyethylene) due to the presence of nickel with its high neutron capture cross-section within a hydrogen compound ($\sigma_\gamma(\text{Ni}) = 4.39 \text{ barn} \gg \sigma_\gamma(\text{H}) = 0.33 \text{ barn}$).

9.7 The 9 MeV γ generator set-up

We describe a 9 MeV γ generator associated with a Cf-source, which we intend to use until a neutron generator is finally available. The system will also be available for simpler calibrations when the pulsed generator cannot be operated.

The neutron moderator and nickel plate assembly is a parallelepiped of dimensions $30 \times 30 \times 33 \text{ cm}^3$ weighing $\approx 20 \text{ Kg}$. It sits on a aluminum Bosch stand fastened to the MEG calorimeter movable platform. The position and height of the stand can be varied. The system is normally positioned at the back of the calorimeter and in front of a special thin and flanged calorimeter window (see Fig. 9.18). The energy deposit of the 9 MeV γ 's takes place within a few centimeter from the back face. The calorimeter back and the front face are characterized by two different photocatode coverages. To optimize the reconstructed energy of the 9 MeV-line, the area associated with the flange window has the same photocatode coverage as that the front face.

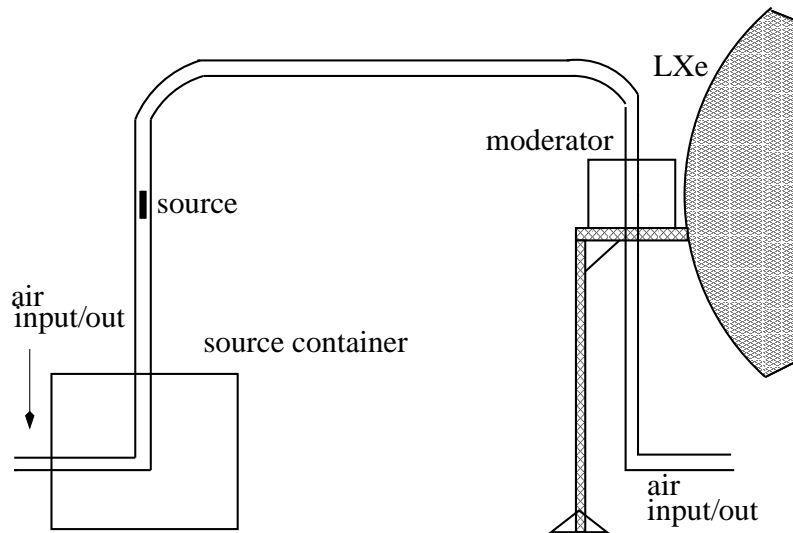


Figure 9.18: A schematic view of the moderator/nickel assembly positioned at the back of the calorimeter, and of the compressed air system for the Cf source movement.

The 70 kBq californium source is normally kept in a shielded deposit far from the experiment and is introduced in the moderator/nickel assembly only when calibrating. The shielded deposit is a large polyethylene moderator of dimensions $50 \times 50 \times 50 \text{ cm}^3$ surrounded by a 2.5 cm thick lead shield; the total weight is $\approx 600 \text{ Kg}$. The deposit sits on ground and is positioned against the concrete wall of the MEG experimental area. The total residual flux of neutrons and γ 's out of the deposit is of the order of 1 Hz. The LabView controlled movement of the source, from the deposit to the moderator/nickel assembly (and back), is based on a compressed air system. It includes a pressure regulation and a series of remote-control valves for inverting the air flux. The source travels along a plastic pipe (diameter 10 mm, length 10 m). The pipe makes a circular path from the deposit to the moderator/nickel assembly and back, passing through the deposit and the assembly. The source stops at two preset positions (two pipe narrow passages at the centre of the deposit and of the moderator/nickel assembly). An electrical contact, which is closed by the

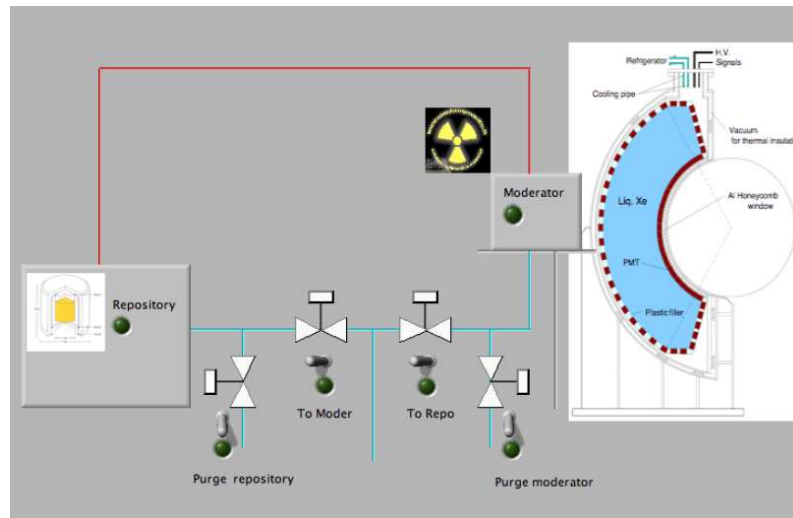


Figure 9.19: A schematic view of the Labview based control system.

Table 9.13: Activation of Al and Xe isotopes by thermal neutrons from a 5×10^4 Bq source at a distance of 30 cm from a 1 Kg sample. Exposure duration: 1 day.

| Isotope | weight | activity | new element | half-life |
|---------|----------|----------------|-------------|-----------|
| Al-27 | 1.0 Kg | 22.78 Bq | Al-28 | 2.240 m |
| Xe-124 | 943.8 mg | 2.102 Bq | Xe-125 | 16.8 h |
| Xe-124 | 943.8 mg | 14.02 mBq | I-125 | 60.15 d |
| Xe-126 | 959.0 mg | 1.338 mBq | Xe-127 | 36.40 d |
| Xe-132 | 270.2 g | 303.7 mBq | Xe-133 | 5.245 d |
| Xe-134 | 106.0 g | 468.7 mBq | Xe-135 | 9.110 h |
| Xe-136 | 92.12 g | 469.1 mBq | Xe-137 | 3.830 m |
| Xe-136 | 92.12 g | 29.41 μ Bq | Cs-137 | 30.17 a |
| Xe-136 | 92.12 g | 27.75 μ Bq | Ba-137m | 2.551 m |

source, signals that the source has reached the correct position. A view of the Labview control system is presented in Fig. 9.18.

9.8 Prevention against the possible neutron activation of materials

Several materials of the experiment will be exposed to the neutron flux from the source-moderator-nickel assembly during the calibrations.

Most of the possible activations are due to thermal neutrons. The ones coming out of the moderator can be stopped by a layer of flexboron, but fast neutrons can escape the moderator, can be thermalized elsewhere and can finally activate materials.

Since we are using a rather weak neutron source, the related activation turns out not to be a problem (more relevant are the neutrons associated with the beam). We examined the possible activation of several materials (carbon compounds, aluminum, iron, nickel, xenon).

We evaluated the activation of Al and Xe isotopes by a 50 kBq thermal neutron source at a distance of 30 cm from a 1 Kg material sample and for an exposure duration of 1 day (Tab. 9.8). The element with the highest activity is aluminum, decaying in a few minutes.

Chapter 10

The 17.6 MeV γ -line by the ${}^7_3\text{Li}(p, \gamma){}^8_4\text{Be}$ reaction

We describe in detail the calibration method based on the Cockcroft-Walton (C-W) accelerator, the most important and versatile calibration and monitoring method for the MEG experiment.

Short calibrations are performed daily. γ 's impinge on the calorimeter front face and illuminate the LXe almost isotropically.

We discuss the characteristics of the nuclear reactions used and the results of some preliminary tests to verify the proposed methods. We then discuss the characteristics of the accelerator and its integration into the MEG experiment. We describe the proton beam line, from the accelerator to the center of the COBRA magnet, and all the items needed to control the beam and to study its properties.

The results of the LXe calorimeter calibration are presented in chapter 16. We also examine the C-W accelerator safety issues associated with the radiation from nuclear reactions and from X-ray production.

10.1 The nuclear reactions excited by protons

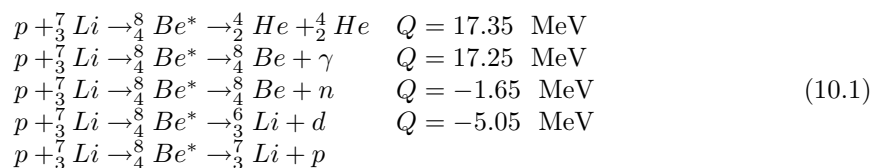
10.1.1 ${}^7_3\text{Li}(p, \gamma){}^8_4\text{Be}$

The 17.6 MeV γ 's are emitted by the resonant reaction ${}^7_3\text{Li}(p, \gamma){}^8_4\text{Be}$ (natural Li isotopic composition: ${}^6\text{Li} = 7.59\%$, ${}^7\text{Li} = 92.41\%$). MEG must detect the 52.8 MeV γ 's from the decay $\mu^+ \rightarrow e^+ \gamma$. The 17.6 MeV γ is close enough in energy to allow a useful, frequent and fast calibration.

The lithium nuclear reaction is the most exothermic, producing a single γ . The narrow resonance at $T_p = 440 \text{ keV}$ has $\sigma_R \approx 5 \text{ mbarn}$ and $\Gamma_R \approx 12.5 \text{ keV}$ (see Fig. 10.1) [165].

Protons can induce (p, α), (p,n), (p, γ), (p,p) reactions and very rarely (p,d). The probability of emission of charged particles by a compound nucleus is usually much higher than the probability of γ emission. Neutron emission takes place on the other hand only over rather high energy thresholds. A (p, γ) reaction normally has a very low yield and becomes competitive only if selection rules suppress the other reaction channels. This is the case of the Li-p reaction.

All the above-mentioned reactions occur when protons interact with lithium:



At proton energies lower than 1 MeV, only the (p, α), (p,p) and (p, γ) reactions take place, the (p,n) and the (p,d) being endoenergetic, with a threshold greater than 1.5 MeV. The (p,p) reaction is always allowed, but the scattered protons cannot leave the beam line and its vacuum pipes.

The (p, α) reaction on lithium has a high yield, while one expects a very low yield for the (p, γ) reaction. It was on the other hand experimentally shown that the (p, γ) reaction has an appreciable yield. (p, α) is associated with a wide resonance centered at $T_p = 3$ MeV; (p, γ) is associated with the very narrow resonance at $T_p = 440$ keV. The explanation is that two compound nuclei are produced in the reaction, $({}^8\text{Be}^*)_{\text{I}}$ and $({}^8\text{Be}^*)_{\text{II}}$, different in angular momentum and parity.

Let us call $N + p$ our system (where N is the lithium nucleus and p the proton). Let us call L the total angular momentum of the system, obtained by adding three quantum-mechanical vectors: the nuclear spin, the proton spin and the orbital angular momentum ($L = s_N + s_p + \ell$). The parity P of the system is obtained by multiplying the intrinsic N and p parities and taking into account the contribution of the orbital angular momentum ($P = P_N \cdot P_p \cdot (-1)^\ell$). We restrict our assumptions to $P_N = -1$ and $\ell = 0$ or 1 . We also assume that the transition of the compound nucleus (Be) * is to the ground state. From $s_N = 3/2$ and $s_p = 1/2$ we obtain the Tab. 10.1.

Consider the case of the two α in the final state. The total angular momentum of the two α

Table 10.1: Angular momentum and parity conservation for the (p, α) and (p, γ) reactions.

| l | $s_N + s_p + \ell = L$ | $P_N \cdot P_p \cdot (-1)^\ell = P$ |
|---|--|-------------------------------------|
| 0 | $3/2 + 1/2 + 0 = \begin{cases} 2 \\ 1 \end{cases}$ | $-1 \times 1 \times (-1)^0 = -1$ |
| 1 | $3/2 + 1/2 + 1 = \begin{cases} 3 \\ 2 \\ 1 \\ 0 \end{cases}$ | $-1 \times 1 \times (-1)^1 = +1$ |

coincides with their relative orbital angular momentum ℓ (the spin of the α -particles being zero), which also coincides with the spin of the disintegrating nucleus ${}^8_4\text{Be}^*$. The parity of the system of the two α is $P_{2\alpha} = P_\alpha^2 \cdot (-1)^\ell = (-1)^\ell = +1$, being a system of bosons (quantum statistics). Only even ℓ -values are allowed. Thus α -particles can be emitted from the states 2^+ and 0^+ . Similarly, only two states of the ${}^8_4\text{Be}^*$, 1^+ and 1^- , are responsible for the gamma transition to the ground state.

The γ energy E_γ is related to the reaction Q -value and to the proton LAB kinetic energy T_p ; $Q = 17.254$ MeV at the resonance [166], [167], [168], [169], [170], [171]. The γ -ray energy can be computed in a non-relativistic approximation (valid at a $3 \cdot 10^{-3}$ level around $T_p = 500$ keV):

$$E_\gamma^{(1)} \approx T_p + Q \quad (10.2)$$

$$E_\gamma^{(2)} \approx T_p + Q - \frac{(T_p + Q)^2}{2M_{\text{Be}}} \quad (10.3)$$

where $E_\gamma^{(1)}$ and $E_\gamma^{(2)}$ are a first and second order approximation. At the the resonance energy $T_p = 440$ keV, the last term is a 0.1% correction.

We also report the relevant transformation between the CM system kinematical variables (starred)

Table 10.2: Kinematical variables and cross-section

| T_p (keV) | T_p^* (keV) | T_{IN}^* (keV) | σ (mbarn) | $E_\gamma(0^\circ)$ MeV | $E_\gamma(90^\circ)$ MeV |
|-------------|---------------|------------------|------------------|-------------------------|--------------------------|
| 100.0 | 76.46 | 87.44 | 0.001 | 17.35 | 17.32 |
| 200.0 | 152.92 | 174.88 | 0.009 | 17.46 | 17.41 |
| 300.0 | 229.38 | 262.32 | 0.023 | 17.55 | 17.50 |
| 350.0 | 267.61 | 306.04 | 0.070 | 17.60 | 17.54 |
| 400.0 | 305.84 | 349.76 | 0.175 | 17.65 | 17.58 |
| 420.0 | 321.13 | 367.25 | 0.504 | 17.67 | 17.60 |
| 430.0 | 328.78 | 375.99 | 1.398 | 17.68 | 17.61 |
| 440.0 | 336.42 | 384.74 | 5.567 | 17.69 | 17.62 |
| 450.0 | 344.07 | 393.48 | 2.011 | 17.70 | 17.63 |
| 460.0 | 351.72 | 402.22 | 0.629 | 17.71 | 17.64 |
| 470.0 | 359.36 | 410.97 | 0.311 | 17.72 | 17.65 |
| 480.0 | 367.01 | 419.71 | 0.197 | 17.73 | 17.65 |
| 500.0 | 382.30 | 437.20 | 0.116 | 17.74 | 17.67 |
| 550.0 | 420.53 | 480.92 | 0.062 | 17.79 | 17.72 |
| 600.0 | 458.76 | 524.64 | 0.068 | 17.84 | 17.76 |
| 700.0 | 535.22 | 612.08 | 0.067 | 17.93 | 17.85 |
| 800.0 | 611.68 | 699.52 | 0.076 | 18.03 | 17.93 |
| 900.0 | 688.14 | 786.96 | 0.091 | 18.12 | 18.02 |
| 1000.0 | 764.60 | 874.40 | 0.102 | 18.21 | 18.11 |

and the LAB system kinematical variables (unstarred):

$$M_p = 938.27945 \quad M_{Li7} = 6533.88453 \quad M_{Be9} = 7454.90885 \text{ MeV} \quad (10.4)$$

$$Q = E_\gamma + T_{Be} - T_p = E_\gamma^* + T_{Be}^* - T_{Li}^* - T_p^* = M_{Li} + M_p - M_{Be} = 17.2551 \text{ MeV} \quad (10.5)$$

$$T_{IN}^* = T_p^* + T_{Li}^* \quad T_{OUT}^* = E_\gamma^* + T_{Be}^* \quad T_{OUT} = T_{IN}^* + Q \quad (10.6)$$

$$T_{IN} = T_p \quad T_{OUT} = E_\gamma + T_{Be} \quad T_{OUT} = T_{IN} + Q \quad (10.7)$$

$$T_{IN}^* = T_p \frac{M_{Li}}{M_p + M_{Li}} = 0.8744 T_p \quad (10.8)$$

$$T_p^* = T_p \left(\frac{M_{Li}}{M_p + M_{Li}} \right)^2 = 0.7646 T_p \quad (10.9)$$

$$T_{Li}^* = T_p \frac{M_{Li} M_p}{(M_p + M_{Li})^2} = 0.10980 T_p \quad (10.10)$$

$$E_\gamma^* + T_{Be}^* = E_\gamma^* + \frac{E_\gamma^2}{2M_{Be}} = 0.8744 T_p + 17.2551 \quad (10.11)$$

The exact relativistic expressions are:

$$E_{CM}^2 = M_p^2 + M_{Li}^2 + 2M_{Li}(M_p + T_p) \quad (10.12)$$

$$\beta_{CM} = \frac{p_p}{E_p + M_{Li}} = \frac{\sqrt{T_p^2 + 2M_p T_p}}{T_p + M_p + M_{Li}} \quad (10.13)$$

$$E_\gamma^* = \frac{E_{CM}^2 - M_{Be}^2}{2E_{CM}} \quad (10.14)$$

$$E_\gamma = E_\gamma^* \gamma_{CM} (1 + \beta_{CM} \cos \theta^*) \quad (10.15)$$

$$E_\gamma = \frac{E_\gamma^*}{\gamma_{CM} (1 - \beta_{CM} \cos \theta)} \quad (10.16)$$

At $T_p = 440$ keV, $\beta_{CM} = 3.8458 \cdot 10^{-3}$.

The Doppler shift effects appear in the Tab. 10.2, for the two angles 0° and 90° . We also report the values of the kinematical variables in the LAB and CM systems and the value of the total cross-section. When protons of energy much greater than that corresponding to the resonant energy are slowed-down in a thick target, the γ -line is shifted and becomes broader and somewhat deformed.

The characteristics of the lithium reaction were first studied at the Legnaro National Laboratory. The results of these preliminary measurements (discussed in the next section) clearly proved the reliability and effectiveness of this calibration method.

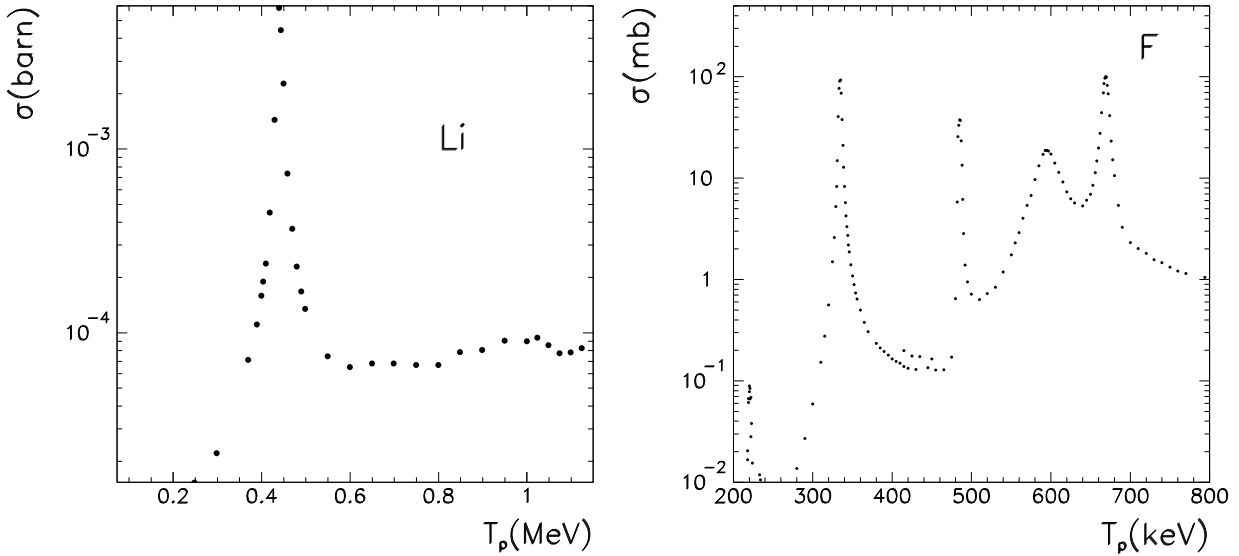


Figure 10.1: ${}^7\text{Li}(p,\gamma){}^8\text{Be}$ cross section as a function of the proton energy (left). ${}^{19}\text{F}(p,\gamma){}^{20}\text{Ne}$ cross section as a function of the proton energy (right).

The 17.6 MeV γ -line measured by a big NaI detector

The experimental set-up. The experimental set-up is shown in the Fig. 10.3. Protons hit a LiF target, mounted at 45° relative to the beam direction. A big NaI detector (28 cm \cdot 28 cm \cdot 35 cm, an assembly of four crystals, each separately coupled to a PMT) is mounted with its entrance window facing the target.

We used the intense proton beam of a Van de Graaff accelerator over a wide energy interval (typical characteristics: $N_p = 6 \cdot 10^{12}$ p/s at a current of $I_p = 1 \mu\text{A}$ and at an energy of $E_p = 500$ keV). Targets of various thicknesses were prepared by depositing LiF on copper disks. Thin and thick Li target excitation curves (reaction yield Y as a function of T_p) were measured.

Let us consider a resonant nuclear reaction, with resonance energy E_R and resonance width Γ_R , as for $\text{Li}(p,\gamma)\text{Be}$ (see Fig. 10.2). The cross-section is described by the Breit-Wigner formula:

$$\sigma = \frac{2\lambda^2(2J+1)}{(2s_a+1) \cdot (2s_b+1)} \frac{\Gamma^2/4}{[(E-E_R)^2 + \Gamma^2/4]} \quad (10.17)$$

where λ is the de Broglie wavelength, s_a and s_b are the spins of the incident and target particles and J is the spin of the resonant state (all in unit of \hbar).

If the target thickness t is equal or lower than the proton range interval corresponding to the resonance width, the target is considered “thin”, otherwise the target is considered “thick”. The thin target excitation curve follows the resonance profile, since the yield Y is proportional to it. The thick target excitation curve (with a thickness greater than the range of the highest energy protons $t \geq R$) corresponds to a yield monotonically increasing as a function of T_p , up to a plateau where T_p is well beyond the resonance energy, but protons are still stopping in the target.

The beam position at the target was initially checked by a CsI crystal, mounted on a plexiglass flange at the end of the beam line. The CsI crystal emits a visible light when bombarded by protons; this is detected by a TV camera. A system of aperture stops, at a distance of ≈ 15 cm

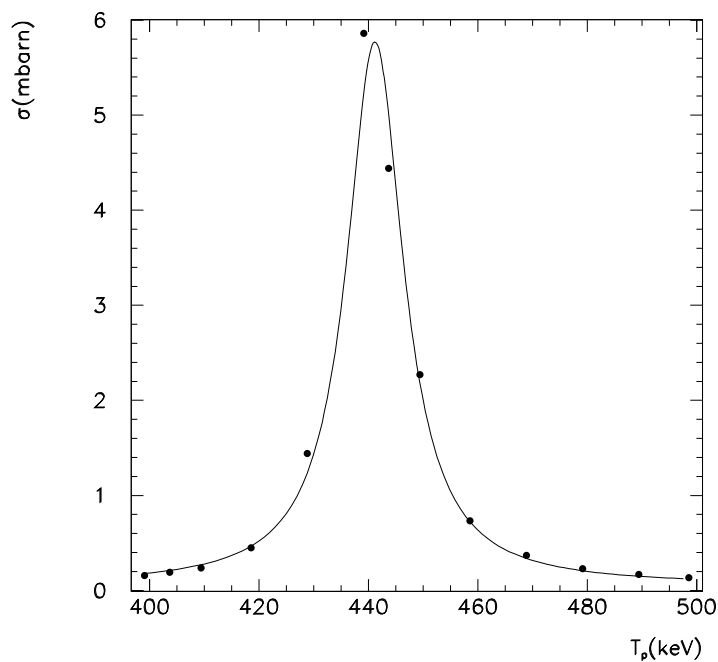


Figure 10.2: Resonance for ${}^7\text{Li}(p, \gamma){}^8\text{Be}$ as a function of T_p . $T_R = 440$ keV and $\Gamma_R \approx 12.5$ keV.

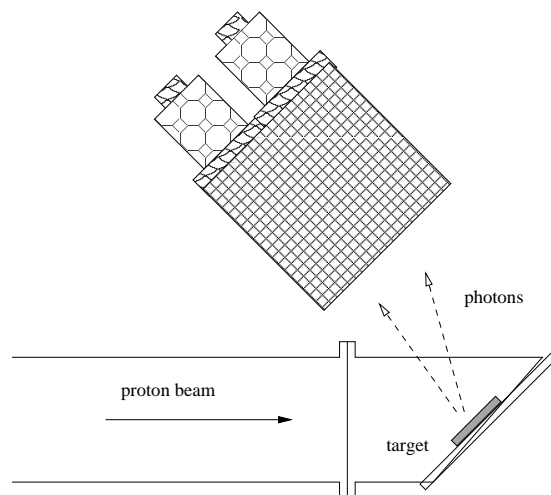


Figure 10.3: Experimental set-up. A big NaI detector was used to study the γ emission from the ${}^7\text{Li}(p, \gamma){}^8\text{Be}$ reaction.

from the target, allows a final check of the beam optimization, by comparing the value of the beam current measured on the aperture stop with the beam current measured at the target. The NaI spectra were registered with a multichannel analyzer (MCA).

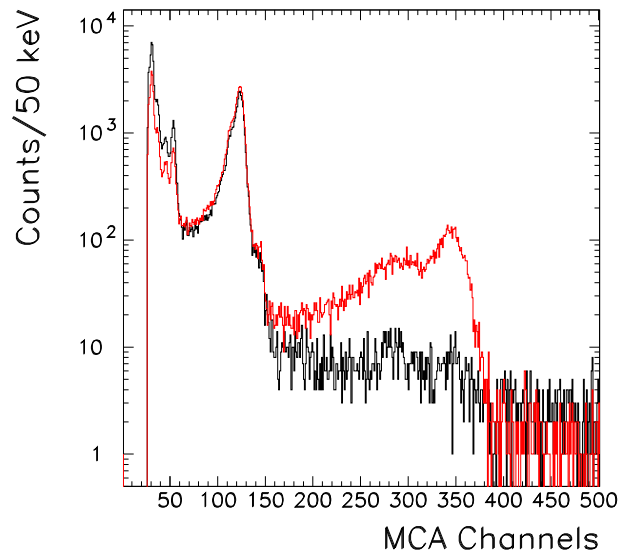


Figure 10.4: *The LiF spectrum close to the resonant proton energy. $T_p = 450$ keV (red) and $T_p = 400$ keV (black).*

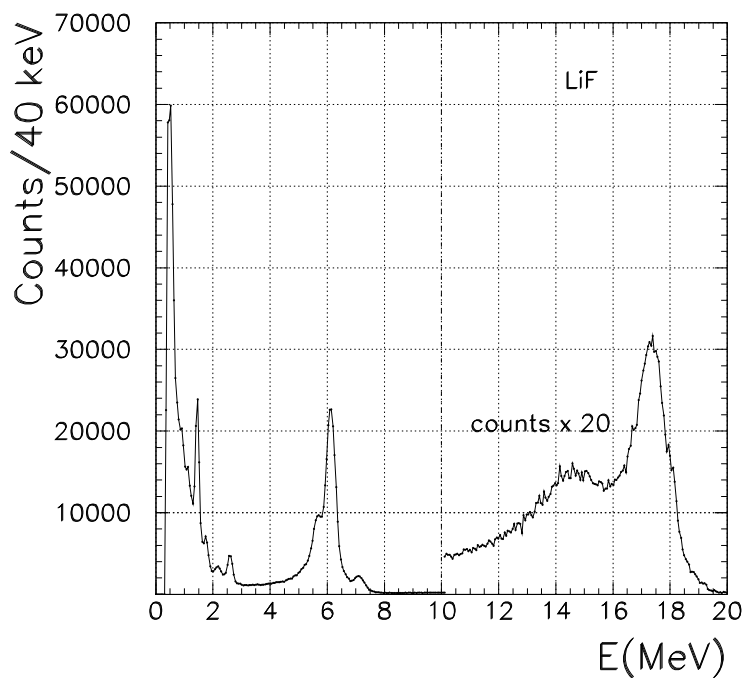


Figure 10.5: *The LiF spectrum from protons hitting a LiF target at $T_p = 500$ keV. The 17.6 MeV and 14.6 MeV γ -lines are clearly visible. Also visible are the 6.13 MeV, 6.92 MeV and 7.13 MeV γ -lines from fluorine. Natural radioactivity lines appear at low energies.*

The targets. All targets were home-made by thermal evaporation techniques. Thermal evaporation is accomplished by using vacuum pumps to reduce the pressure inside a deposition chamber to $10^{-4} \leftrightarrow 10^{-6}$ mbar, and by heating the material to be evaporated as a filament or inside a *boat* made of a high melting-point material. Both metals and thermally stable compounds, such as metal oxides, can be deposited. Films produced by evaporation are relatively pure. The properties of evaporated films are dependent on the film structure and also on the interaction of the film with its substrate. To obtain the most durable and adherent coatings on different substrates, the support surface must be free from contaminant films such as grease, absorbed water etc. The degree of durability and adhesion of a condensed deposit is dependent on many factors, other than surface cleanliness alone, but this is the basic requirement for obtaining a good target. We prepared several oxygen-free copper disks. Their intended use was as substrates for other deposited materials. Copper is cheap and easily available, it improves the heat dissipation and minimizes the deterioration of the target during bombardment [174]. The disks were obtained with a *wire erosion technique* [175] and have a 50 mm diameter and a 2 mm thickness. The disks were then polished by grade 1000, 2400 and 4000 abrasive papers (Silicon Carbide) and, as a final polishing, by a colloidal silica suspension. Before the target material deposition on the copper disks, an acetone ultrasonic cleaning of the disks was performed.

We prepared lithium fluoride targets since metallic lithium is more difficult to handle and to store, due to the high Li chemical reactivity.

The proton range in LiF at $T_p = 500$ keV is $R_{LiF} = 4.73 \mu\text{m}$. We succeeded in depositing three LiF targets: a thin target ($\approx 1\Gamma_R = 0.12 \mu\text{m}$), a thick target ($\approx 10\Gamma_R = 1.41 \mu\text{m}$) and a very thick target ($\approx 4.76 \mu\text{m}$).

Due to the Boron high evaporation temperature, the boron targets were deposited by using an electron beam evaporation technique [176] with a carbon crucible (1797 °C at 10^{-4} mbar). We obtained two targets of similar thickness: 1.78 ± 0.21 and $1.84 \pm 0.22 \mu\text{m}$, thinner than the ones originally envisaged for the Legnaro test.

The results. A ^{60}Co -source and natural radioactivity γ -lines (^{40}K , at 1.46 MeV; ^{208}Tl , at 2.61 MeV) were used for a preliminary calibration of the NaI detector.

Fig. 10.4 shows that the γ -line only appears at T_p greater than the resonant energy. The two spectra (logarithmic scale) were measured at $T_p = 400$ keV and at $T_p = 450$ keV. Fig. 10.5 shows the LiF spectrum at $T_p = 500$ keV, in a linear scale. The sharp $17.3 + T_p$ MeV γ -line, corresponding to the ^8Be transition to the ground state (γ_0), is clearly visible. Also visible is the broad $14.3 + T_p$ MeV γ -line, corresponding to the $^8\text{Be}^*$ transition to the first excited state of ^8Be (γ_1). The subsequent transition to the ground state is via an α -decay. The branching ratio, $x = \frac{\gamma_0}{\gamma_0 + \gamma_1} = 0.72 \pm 0.07$, was measured at $T_p = 441$ keV [169]. The MEG calorimeter calibration is based on the very sharp γ_0 -line.

Addition lines from fluorine are seen at $E_{\gamma_1} = 6.13$ MeV, $E_{\gamma_2} = 6.92$ MeV and $E_{\gamma_3} = 7.12$ MeV. They originate from the $^{19}\text{F}(p, \alpha\gamma)^{16}\text{O}$ reaction, having resonances at different proton energies (see Fig. 10.1) [165], [177], [178], [179], [180], [181], [182]. The well-known fluorine lines provide extra checks of the energy calibration. At a fixed proton energy, the time integrated fluorine rate can be used as an alternative to a beam charge normalization for the Li reaction measurement. The Fig. 10.6 shows the correlation between the fluorine γ integrated rates and the beam charge. The thin target excitation curve ($\approx 0.12 \mu\text{m}$ target thickness) is shown in Fig. 10.7 (left). It reproduces the shape of the resonant cross section, centered at 452 ± 2 keV. The data were fitted by a Breit-Wigner curve, whose measured width $\Gamma = 18 \pm 0.5$ keV combines the intrinsic resonance width and the energy width corresponding to the target thickness. The nominal accelerator energy appears to be shifted by ≈ 5 keV. This result is better confirmed by the thick target excitation curve measurement, which will be discussed later.

Fig. 10.7 (right) presents the thick target excitation curve ($\approx 1.41 \mu\text{m}$ target thickness). It is centered at 445 ± 1 keV with a resonance width $\Gamma_R = 14 \pm 2$ keV, as expected ($\Gamma_R = 10\text{--}15$ keV).

At this point it is important to discuss the frequency and the duration of each calorimeter calibration during the experiment, starting from the measured reaction rates. The γ_0 -rate was, as expected, $R_{\gamma_0} \simeq 100$ Hz, at $T_p = 440$ keV with a $I_p = 92 \pm 10$ nA (in this case the solid angle accepted by the NaI detector was $\Delta\Omega/\Omega \approx 6.35\%$). Taking into account the LXe calorimeter solid angle ($\approx 12\%$), at a $I_p \approx 200$ nA, we expect a $R_{\gamma_0} \simeq 200$ Hz, which is enough to saturate the acquisition rate (100 Hz).

One important point to recall is that both the MEG μ -beam and the C-W proton beam must cross an intense magnetic field region before reaching the target at the center of the COBRA spectrometer. The proton momentum at $T_p = 440$ keV is $p_p = 28.74$ MeV/c, very similar to the one of the surface muons: $p_\mu = 29.3$ MeV/c. The beam optics optimization similarly concerns both beams. For instance: problems like the behaviour of low momentum beams in a non homogeneous magnetic field and the need to avoid reflections, as in a magnetic bottle. A preliminary study of the proton trajectory envelope is presented in Fig. 10.8, on the assumption that the proton beam divergence is $\approx 0.1^\circ \approx 2$ mrad, at the distance of 300 cm from the Cobra center (as expected for the beam of the MEG C-W accelerator). The radius of the envelope is $\rho < 2$ cm in the high field region while the beam diverges when reaching the low magnetic fields. At the Cobra center the beam is focused onto a spot with $\rho < 0.8$ cm if $|z| < 2$ cm. More studies were performed for other initial beam characteristics, confirming a non-critical beam behaviour.

10.1.2 ${}^{11}_5\text{B}(p, \gamma){}^{12}_6\text{C}$

Another proton induced nuclear reaction useful for MEG is the ${}^{11}_5\text{B}(p, \gamma){}^{12}_6\text{C}$ (natural boron isotopic composition: ${}^{10}\text{B} = 19.9\%$, ${}^{11}\text{B} = 80.1\%$). The reaction is resonant at $T_p = 163$ keV ($\Gamma_R \simeq 5.3$ keV), with $Q = 15.956$ MeV (Fig. 10.9) [165], [170], [172], [173]. A $E_{\gamma_0} = 16.1$ MeV γ is emitted in the transition directly reaching the ${}^{12}\text{C}$ ground state. A $E_{\gamma_1} = 11.7$ MeV γ is emitted when the ${}^{12}\text{C}$ nucleus is left in the first excited state at 4.44 MeV, whose transition to the ground state produces an additional γ -line. The γ_0 has a low branching ratio $\frac{\gamma_0}{\gamma_0 + \gamma_1} = (3.5 \pm 0.07) \times 10^{-2}$, the γ_1 is much more frequently emitted. The precise position of the γ_0 and γ_1 lines depend on the incident proton energy. This is not the case for the 4.44 MeV γ -line, since it corresponds to a nuclear level de-excitation.

It is interesting to note that the 11.7 MeV and 4.44 MeV γ s are emitted in coincidence and this provides a unique opportunity for the relative timing of the Xe calorimeter vs the timing counter (although at low γ energies). The ${}^{11}_5\text{B}(p, \gamma){}^{12}_6\text{C}$ is the only proton-induced exothermic reaction, associated with the emission of two coincident γ -rays both at MeV energies. The timing calibration will be discussed in chapter 13. Here we present only the preliminary studies confirming the feasibility of what was proposed. It is also worth noting that the boron reaction, used at high rates, will test the capability of the calorimeter to distinguish double- γ 's entering this detector.

The 16.1 MeV, 11.7 MeV and 4.4 MeV γ -lines, detected by two NaI detectors

Experimental set-up. We used an experimental set-up similar to that of Fig. 10.3. The original set-up, using the big NaI, was modified (see Fig. 10.10) to allow for γ 's coincident measurement. The small NaI detector is a $4'' \times 4''$ cylindric crystal, coupled to a single PMT. A thick boron target was used (thickness $\approx 1.84\mu\text{m}$).

Results. Fig. 10.11 shows the boron γ -spectrum obtained by the big NaI detector at $T_p = 600$ keV. The three line at 16.1 MeV, 11.7 MeV and 4.4 MeV are clearly visible. Natural radioactivity γ -lines are seen at low energies. Since T_p was greater than the one of the resonance, the measured rate is the sum of two different contributions: one corresponding to the integrated cross section of the resonance, the other due to the integrated direct cross section. The histograms in Fig. 10.12 (left) were recorded at different energies and show how important the direct production is. They refer to the B γ_1 -line. We measured $R_{600} = 16$ Hz, $R_{500} = 5$ Hz, $R_{400} = 3$ Hz at $T_p = 600$ keV, $T_p = 500$ keV and $T_p = 400$ keV. At proton energies higher than the resonance energy the γ -lines are somewhat spoiled. This is not relevant if the γ 's are only used for time measurements.

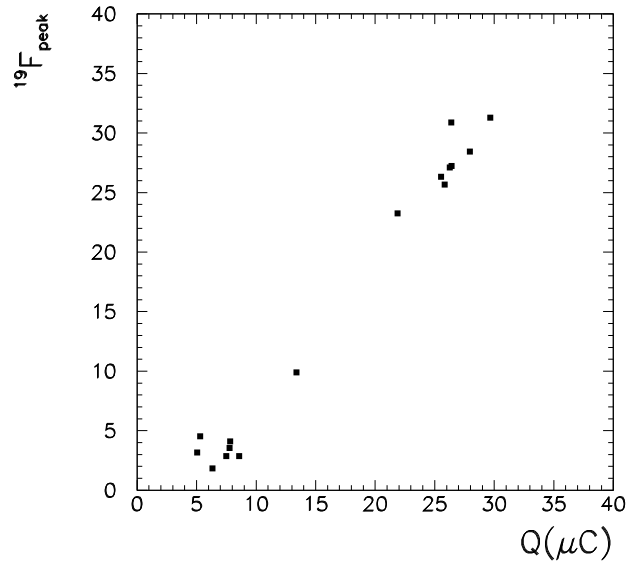


Figure 10.6: Correlation between the fluorine integrated γ -rates and the beam charge.

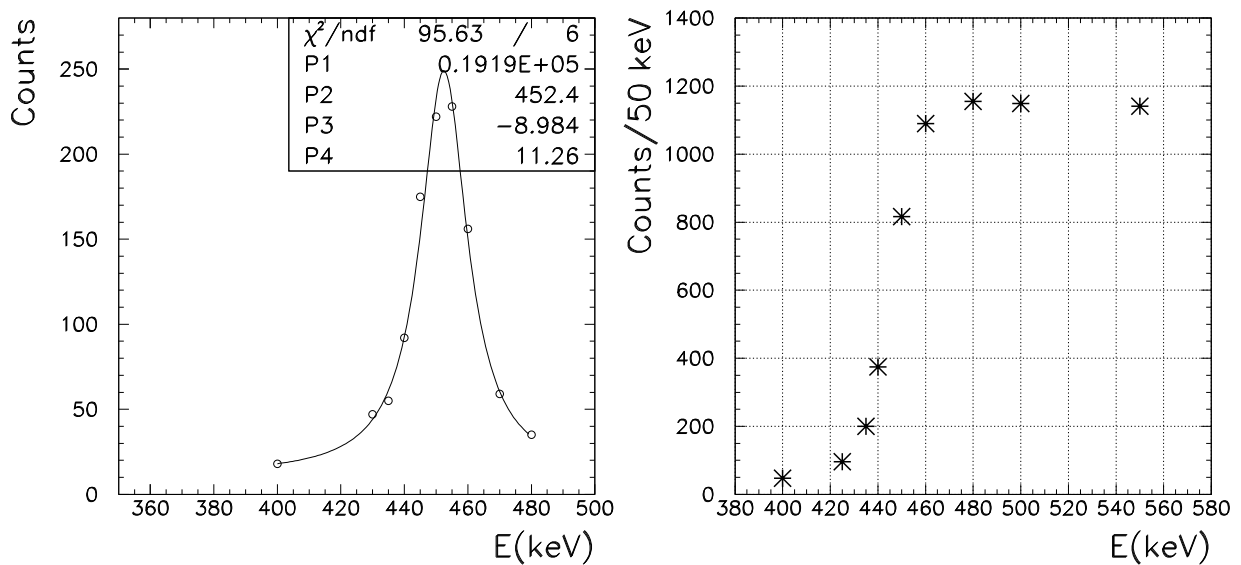


Figure 10.7: (Left) Thin target Li excitation curve; target thickness $0.11\mu\text{m} \approx 1\Gamma_R$. (Right) Thick target Li excitation curve; target thickness $1.41\mu\text{m} \approx 10\Gamma_R$. Both curves are shifted relative to nominal resonant energy of 441 keV.

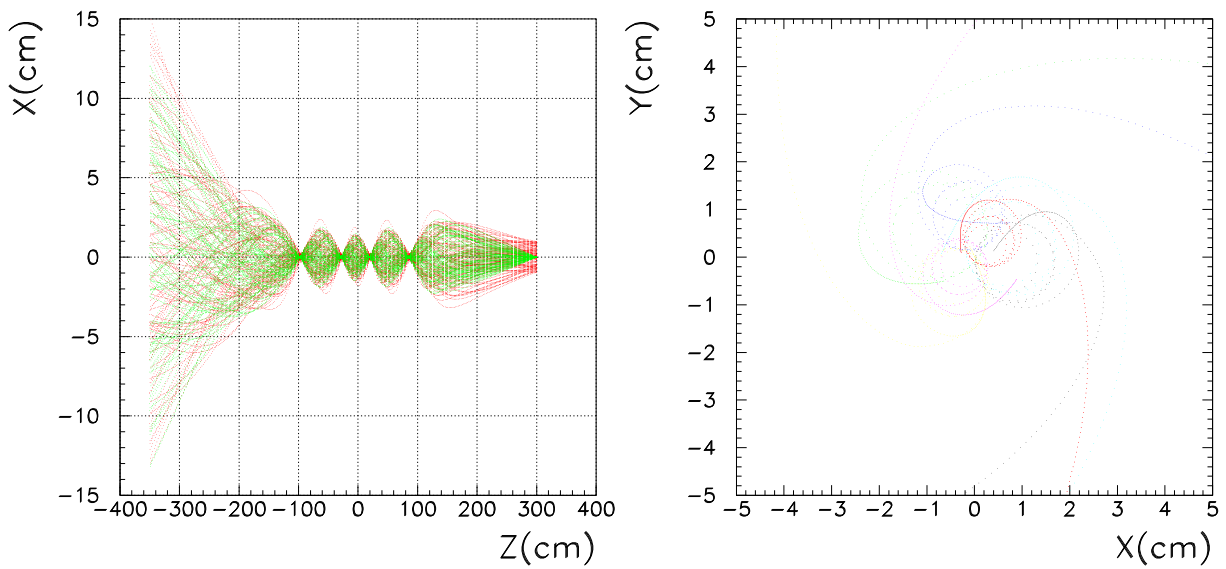


Figure 10.8: (Left) Proton trajectory envelope, at $T_p = 440$ keV inside the COBRA spectrometer. Beam entrance at 300 cm from the Cobra center. The green trajectories are associated with a point-like beam spot, the red trajectories with a 2 cm diameter circular beam spot. (Right) Detail of X - Y projection for 10 events. (right)

Table 10.3: Comparison between a C-W and a RFQ accelerator

| Feature | C-W | RFQ |
|---|---|------------------------|
| Beam Properties | | |
| Energy range (keV) | variable: 100-1000 | fixed: 500 |
| Energy spread (keV) | 0.2, no tails | 5 (± 20 keV tail) |
| Current range | 1-100 | - |
| Peak intensity (μA) | - | 250-5000 |
| Pulse repetition rate (Hz) | - | 100 |
| Pulse duration (μsec) | - | 100 |
| Duty cycle (%) | 100 | 1 |
| Average intensity (μA) | - | 2.5-50 |
| Average Li γ -flux on cal. (kHz) | 100, at 50 μA and at 440 keV | 5-100 |
| Peak Li γ -flux on cal. (kHz) | 100, at 50 μA and at 440 keV | 500-10000 |
| Max. flux on cal. (kHz) | 200 | 200 peak flux |
| γ 's per pulse | - | 50-1000 |
| Emittance ($(\text{mm} \cdot \text{mrad})^2$) | 3x10 | 7x10 |
| Beam spot at 3 m (cm^2) | <1x1 | 2x3 |
| Operational considerations | | |
| Automated operation | startup, conditioning, run | same |
| Startup time | 10 min | 15 min |
| Energy reproducibility (%) | 0.1 | 0.1 |
| Energy stability (%) | 0.1 | 0.1 |
| Current stability (%) | 2 | < 10% |
| Current reproducibility (%) | 10 | 10 |
| Stability when moved | good | good |
| Susceptibility to magnet fields | small for axial field | small, for axial field |
| Emitted radiation | < $2\mu\text{S/h}$ | low |
| Ferromagnetic materials | large tank is steel | small magnet in source |
| Movable on rails | yes | yes |
| Acc.physical properties | | |
| Exterior dimensions (m) | 2(l)x1(h)x1(w) | 1.35(l)x1.1(h)x0.5(w) |
| Minimum beam hight (m) | 1.2 | 1.0-1.5 |

The 4.4 MeV gamma-line, registered by the small NaI during the coincidence measurements is in Fig. 10.12 (right). At $T_p = 600$ keV and $I_p = 120$ nA the two NaI's measured two consistent rates: $R_{small} = 0.2 \pm 0.06$ Hz and $R_{big} = 0.17 \pm 0.04$.

10.1.3 Towards a proton accelerator

The studies of the lithium and boron reactions, discussed above, were entirely satisfactory. They also advise the integration of a proton accelerator into the MEG experiment. The accelerator must be sufficiently versatile to meet the different calibration requirements, like, for instance, a tunable beam energy and intensity.

Some effort was dedicated to studying and comparing the performances of different accelerators produced by various companies. We focussed on a Cockcroft-Walton accelerator (High Voltage Engineering) and a Radio Frequency Quadrupole (AccSys Technology) (see Tab. 10.1.3).

The following are the many relevant characteristics:

1. The proton energy range. The energy spread. The energy stability.
2. The current range and the current stability. The duty cycle.
3. The safety aspects and the emitted radiation (X-rays, neutrons, etc.)

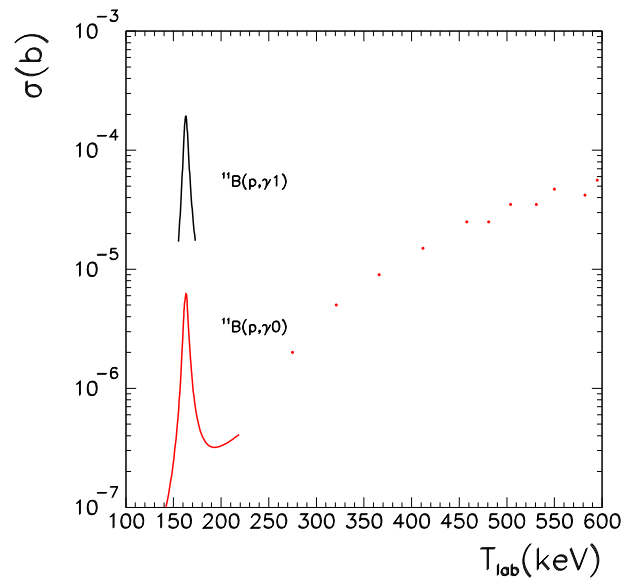


Figure 10.9: ${}^{11}\text{B}(p,\gamma){}^{12}\text{C}$ cross section as a function the proton energy.

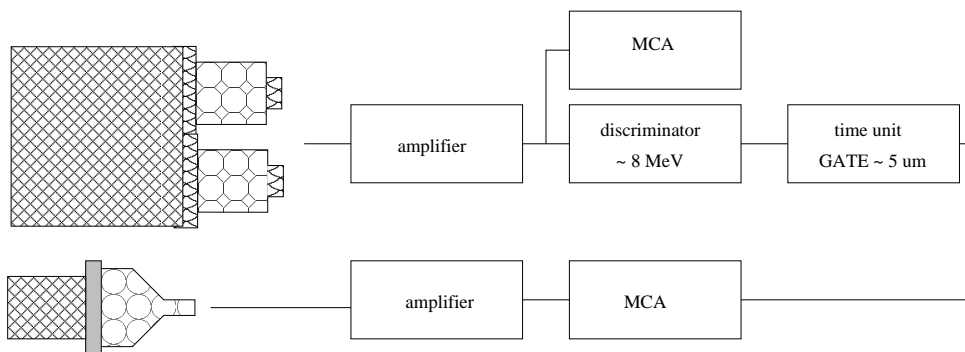


Figure 10.10: *Experimental set-up for measuring the coincidences between the 11.7 MeV and 4.4 MeV γ 's from the ${}^{11}\text{B}(p,\gamma){}^{12}\text{C}$ reaction.*

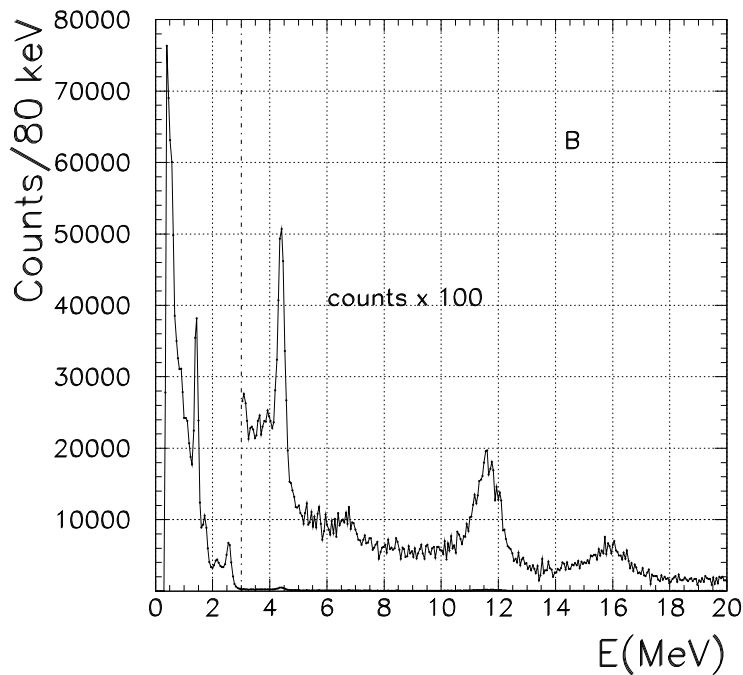


Figure 10.11: Boron γ -spectrum at $T_p = 600$ keV. The 16.1 MeV, 11.7 MeV and 4.4 MeV γ -lines are clearly visible. Natural radioactivity γ -lines appear at low energies.

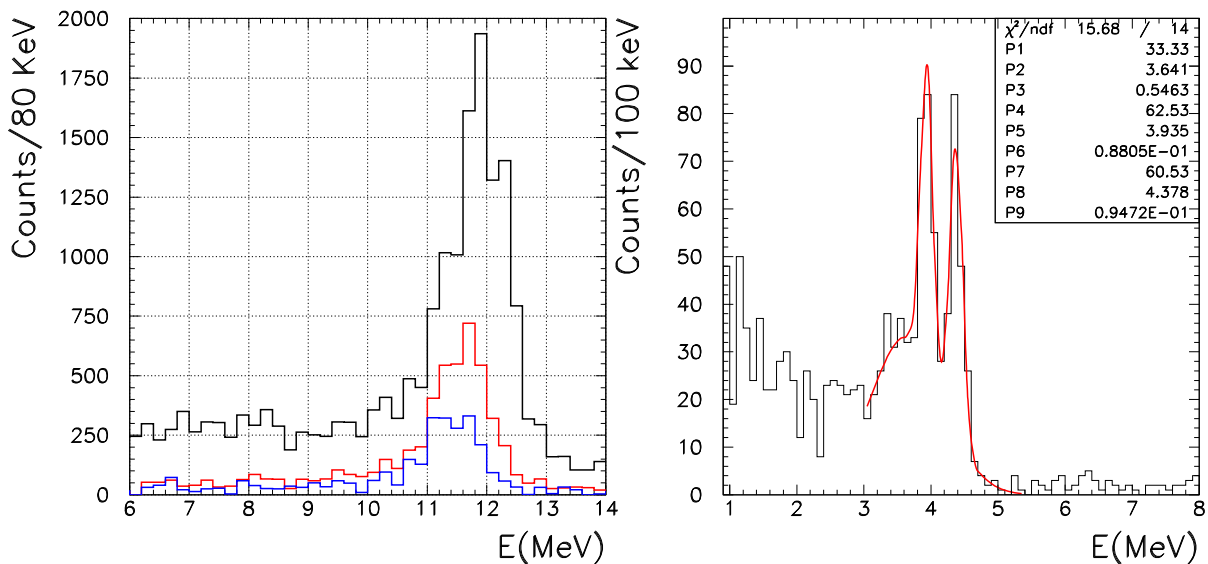


Figure 10.12: (Left) Histograms (normalized to the proton beam charge) presenting the 11.7 MeV integrated γ -rate at $T_p = 600$ keV (black), $T_p = 500$ keV (red) and $T_p = 400$ keV (blue). (Right) The 4.4 MeV γ -line measured by the small NaI detector (line and escape peak) (right). A 11.7 MeV and 4.4 MeV γ -coincidence is required.

4. The beam phase space. The beam optics. The beam monitoring.
5. The vacuum beam line. The special needs for the machine operation (machine cooling, insulating gas, power dissipation, etc.)

Our conclusions are as follows. The most important point is the possibility of proton energy tuning and the extent of its range, which is what allows the excitation in a variety of reactions. A sharp γ -line, as needed for precise energy calibration, is obtainable if the resonant nuclear reaction is excited exactly at the resonance energy. At higher proton energies the line is spoiled by straggling and kinematical effects. The excitation of a resonant reaction with a fixed energy machine is unadvisable. It makes optimization difficult and it constrains the target properties in type and thickness. A small energy spread and a good energy stability are always needed.

Another important point is the possibility of varying the beam intensity within a sufficiently large range. We normally use low beam currents (500 nA) since cross sections are rather high and high beam intensities mean extra heat and radiation background. Higher currents are used, from time to time, to study a detector behaviour at high rates or to improve the signal to noise ratio at a fixed acquisition rate against cosmic rays and natural radioactivity.

Some considerations regarding the beam duty cycle. The MEG experiment uses a continuous muon beam and has a limiting acquisition rate of ≈ 100 Hz. The PMT bases were, as a matter of fact, designed for such a 100% duty cycle operation. An accelerator with a low accelerator duty cycle might easily generate problems. Therefore the C-W, a versatile and reliable 100 % duty cycle machine, is well suited to MEG.

Machine experts prize the RFQ as a simple, high current, fixed energy device, very good as an injector, but the C-W is considered more appropriate for a physics experiment.

Once the accelerator is selected, the next problem is how to couple it to the experiment (accelerator hall, beam transport system, operational issues, safety issues, etc.). Before discussing these points, we present and discuss the C-W operation.

10.2 The Cockcroft-Walton accelerator

The use of a Cockcroft-Walton for an elementary particle experiment is rather exceptional. MEG needs a high and stable energy resolution; the quality of the experiment is based on the calibration and monitoring by the C-W.

A picture of the C-W is shown in the Fig. 10.13.

One can see, from left to right, the RF coil, the C-W support and its front-plate, the beam-pipe and the beginning of the beam-line. In more detail (Fig. 10.13), at the front-plate, one can observe the beam-pipe with its vacuum pumps and gate-valves, the motor which drives an internal voltage generator for the ion-source (kept at the HV of the terminal electrode), the cylindrical box housing the PMT which detects possible internal discharges, and two signal boxes. A red lamp, close to the gate-valve in the picture, signals the HV-On status. All the parameters of the C-W accelerator are controlled via an accelerator cabinet, by local or remote control.

The basic elements of an accelerator are the source (a RF ion source), the accelerator tube (made of electrodes which compose the electrode cascade), and the high voltage circuit (providing potentials to the source and to the electrodes). A discussion of the machine operation follows.

10.2.1 The RF ion source

Fig. 10.14 shows a simplified scheme of the accelerator and of its essential parts: the RF ion source and the electrodes (only two electrodes are represented).



Figure 10.13: *A view of the C-W accelerator (left). A detail of the C-W front-face (right).*

The RF ion source is a long life and heavy duty source for hydrogen and other ions. The source bottle contains a gas, which is excited by an RF (Radio Frequency). The plasma is confined by an axial magnetic field produced by permanent magnets symmetrically placed around the bottle.

Several variables affect the characteristics of the discharge and of the resulting beam: the gas pressure in the chamber, the RF field (its magnitude and its coupling to the plasma), the external magnetic field, and the extraction voltage. These variables are interdependent and have complex relations.

A system of electrodes, the extractor, is invested by a plasma flow. High voltages are applied to the various electrodes of the extractor and the corresponding beam optics generates an accelerated and focalized ion beam. The downstream vacuum chamber is at ground potential. The first electrode is in contact with the plasma and is maintained at the positive high voltage, the second electrode is fixed at the ground potential. The ion-accelerating electric field is therefore located between the electrodes of the extractor. Additional electrodes are often added to avoid possible H.V. breakdown, by introducing a gradual increase of the electric field.

10.2.2 The electrode cascade

The high voltage is generated by a circuit shown schematically in Fig. 10.16. The first voltage multiplier was proposed by Greinacher and Schenkel and was used by Cockcroft and Walton to build the accelerator with which the first artificial nuclear reactions were studied.

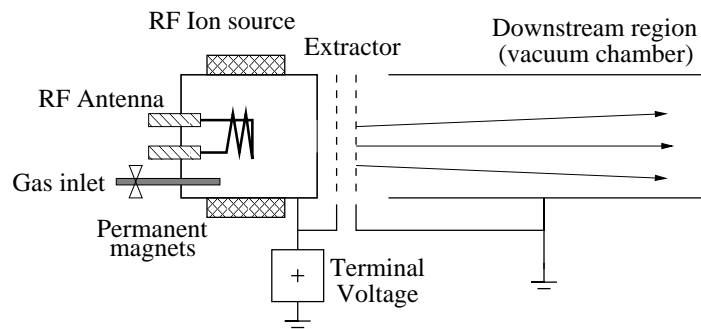


Figure 10.14: Scheme of the C-W accelerator. Visible: *i*) the extraction grid contained in the plasma chamber, *ii*) the downstream space at ground potential, and *iii*) the terminal voltage.



Figure 10.15: The RF ion source.

The basic element of this circuit is shown inside the dashed contour.

The generator at the base of the circuit is a transformer which produces an alternating high voltage.

The generator is connected to a column of capacitors (the pulsating column). Another capacitor column has its base at ground potential (the static column). During the first negative half-cycle, $D1$ will be forward biased. $C1$ charges up to a $\Delta V = U_0$. Note that, at this stage, the capacitor polarity is opposite to that of the generator. During the following positive half cycle, $D1$ is reverse biased and will not conduct, while $D2$ is forward biased and a current will charge $C2$ at the expense of the charge deposited on $C1$. After some cycles an equilibrium situation is reached in which $C2$ is permanently charged at $V = 2U_0$, while $C1$ will pulsate with $U = U_0 + U_0 \sin \omega t$. The process is repeated for all the other capacitors because of the pulsating column and of the presence of the diodes. If the number of stages in the columns is N , the final equilibrium voltage reached by the terminal of the static column is $U = 2NU_0$. The maximum high voltage reachable in such a multiplier depends on the H.V. breakdown in the gas insulating the system.

We described schematically the HV circuit on which the operation of a C-W is based. The MEG accelerator has some peculiarities. Fig. 10.17 shows the interior of the C-W accelerator. A scheme of the circuit is shown in Fig. 10.18. Two long semi-cylindrical electrodes, connected to the RF driver and to the RF oscillator coils, partially surround the diode/capacitor column. A set of capacitor coupling rings (visible in Fig. 10.17) transmits the voltage to the capacitors. The high

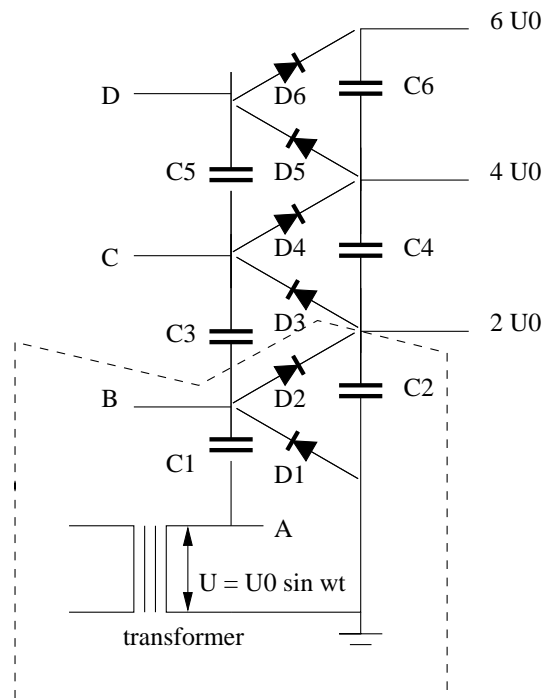


Figure 10.16: *Scheme of the C-W high voltage circuit.*

voltage multiplier is located in the main pressure tank. The RF resonance coils are located in a separate SF₆ filled tank, whereas the RF driver is located in a cabinet, close to the main pressure tank.

10.2.3 The accelerator driver

The C-W accelerator is remotely controlled by a dedicated industrial PC.

Once the control cabinet main power and the PC are switched on, the machine is ready to start. Fig. 10.19 shows the control panel.

The vacuum level along the beam line must first be checked. If the vacuum is sufficiently good ($< 5 \cdot 10^{-6}$ mbar), the C-W gate valve can be opened, and when vacuum level stabilizes, around $1 \cdot 10^{-6}$ mbar, the motor generator can be switched on and the gas for the ion source selected. The insertion of a value different from zero for the RF gas inlet variable activates the RF ion source. The plasma reaches stable conditions after about 2-3 minutes. At this point the beam parameters can be set, corresponding to the desired beam properties. The “RF voltage probe” mainly determines the beam current, since it controls the ion extraction from the source. The desired beam optical properties can be somewhat tuned by the “RF voltage extraction” and finally the ion energy is set by the “terminal voltage” value.

10.2.4 The acceptance test

We performed the machine acceptance test at High Voltage Engineering in Amersfoort before shipping the machine to Villigen. Not all the instruments used at Amersfoort will again be available at PSI. The tests followed the list specified in the contract (see Fig. 10.20). The results indicated a very satisfactory C-W performance. Many additional measurements were performed:

1. a study of the start-up time under manual or automatic operation;
2. a study of the beam optical properties, as a function of the current and of the terminal HV;

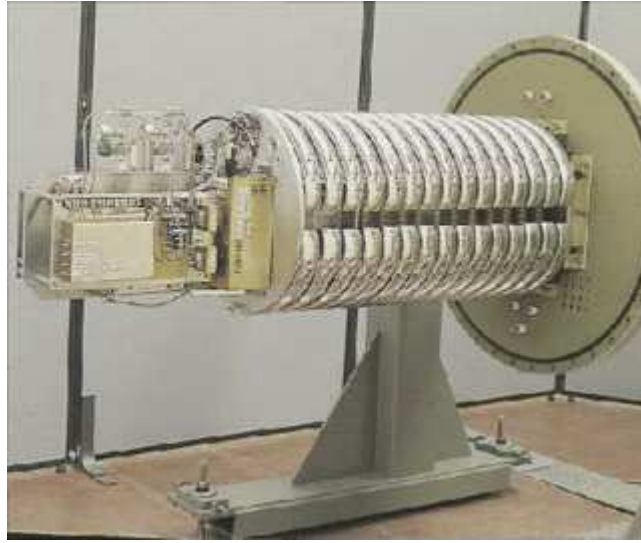


Figure 10.17: *The electrode cascade.*

3. a study of the X-ray radiation emitted by the C-W;
4. a study of the prompt and delayed nuclear radiation emitted by the target.

All this will be examined in separated sub-paragraphs.

The acceptance protocol

It is worth pointing out that some of the C-W performances were better than the contract specifications, particularly those relating to the terminal voltage ripple, the beam spot size and divergence, the start-up time and the X-ray radiation level.

The start-up time and the normal operation

The C-W can be turned on by using a manual or an automatic procedure. The latter can be programmed in advance and applied at a preset time. The manual operation is however faster and more precise. The machine reaches stable conditions after about 15 min.

The measured ripple, superimposed on the terminal voltage value, was $< 40 V_{\text{RMS}}$ at 50 kHz, against a specification of $< 500 V_{\text{RMS}}$. The ripple can be rather easily controlled by mechanically varying the coupling of the RF electrodes to the half-rings of the accelerating column. The nominal energy and beam current were stable, within specifications, for several hours. We changed the beam current in the interval $0.3 < I_p < 130 \mu\text{A}$ and the energy in the interval $400 < E_p < 750 \text{ keV}$.

The beam optics and the beam composition

The dimensions of the beam spot (gaussian shape) at two different positions, at a current $I_p = 50 \mu\text{A}$ and at an energy of $T_p = 500 \text{ keV}$ are shown in Tab. 10.4. The spot size was measured by

Table 10.4: Beam spot sizes along the beam line.

| distance(cm) | spot size FWHM (mm) |
|--------------|---------------------|
| 58 | 6.5 ± 1 |
| 340 | 17.5 ± 1 |

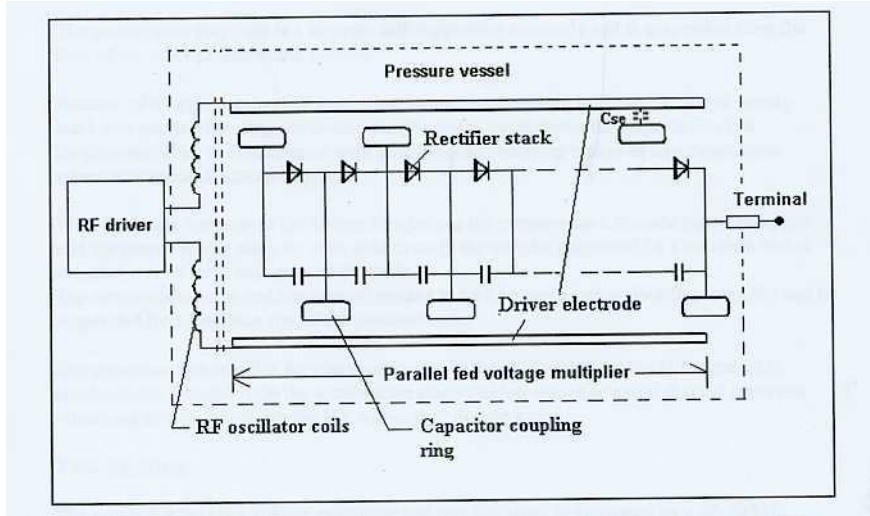


Figure 10.18: The HVVE electrode cascade for the C-W accelerator.

two HVVE wire scanners (Fig. 10.21). The scanner consists of two wires, at a relative angle of 90° , mounted on a vibrating support which makes the wires move in a plane orthogonal to the beam. The wires alternatively cross the beam. The wire signal is presented on an oscilloscope screen after being processed on-line (Fig. 10.22). An x - y profile is obtained. Using the measured spot sizes at two different positions, the divergence of the beam is derived: $\alpha(FWHM) = 3.9 \pm 0.3$ mrad. The beam size turned out to be largely independent of the beam current (Tab. 10.5).

Table 10.5: Spot size as a function of the current intensity at a distance of 58 cm from the C-W front plate.

| $I_p(\mu A)$ | spot size FWHM (mm) |
|------------------|---------------------|
| 0.35 ± 0.005 | 5.8 ± 1 |
| 50 ± 0.005 | 6.5 ± 1 |

When hydrogen is ionized in the ion source, one obtains H^+ ions, but also H_2^+ and H_3^+ ions. The beam composition was determined by measuring the current associated with each kind of ion. The ions were selected by a deflecting magnet mounted in the beam line. If we define n_k , m_k and i_k as the k -ion density, mass and current, we expect $n_k/n_l = (i_k/i_l) \cdot (\sqrt{m_k/m_l})$. The magnet currents scaled, as $1 : \sqrt{2} : \sqrt{3}$, as expected. The beam currents were measured by a Faraday cup at the end of the beam line. The beam centering was checked by the wire scanner. Tab. 10.6 and the histograms Fig. 10.23 (left) show the ion beam composition for several current values. It appears to be approximately constant. Other ion beam composition measurements were performed at $T_p = 750$ keV. The results are shown in Tab. 10.7 and in Fig. 10.23 (right).

Table 10.6: The beam ion composition at $T_p = 500$ keV for different current intensities.

| Ions | I_p (nA) | % | I_p (nA) | % | I_p (nA) | % |
|---------|--------------|------------------|--------------|----------------|-------------|------------|
| H_1^+ | 9700 ± 5 | 73.36 ± 0.08 | 1100 ± 5 | 75.4 ± 0.6 | 320 ± 5 | 74 ± 2 |
| H_2^+ | 2370 ± 5 | 25.05 ± 0.05 | 230 ± 5 | 22.3 ± 0.4 | 90 ± 5 | 21 ± 1 |
| H_3^+ | 200 ± 5 | 2.61 ± 0.07 | 24 ± 5 | 2.3 ± 0.5 | 13 ± 5 | 5 ± 2 |

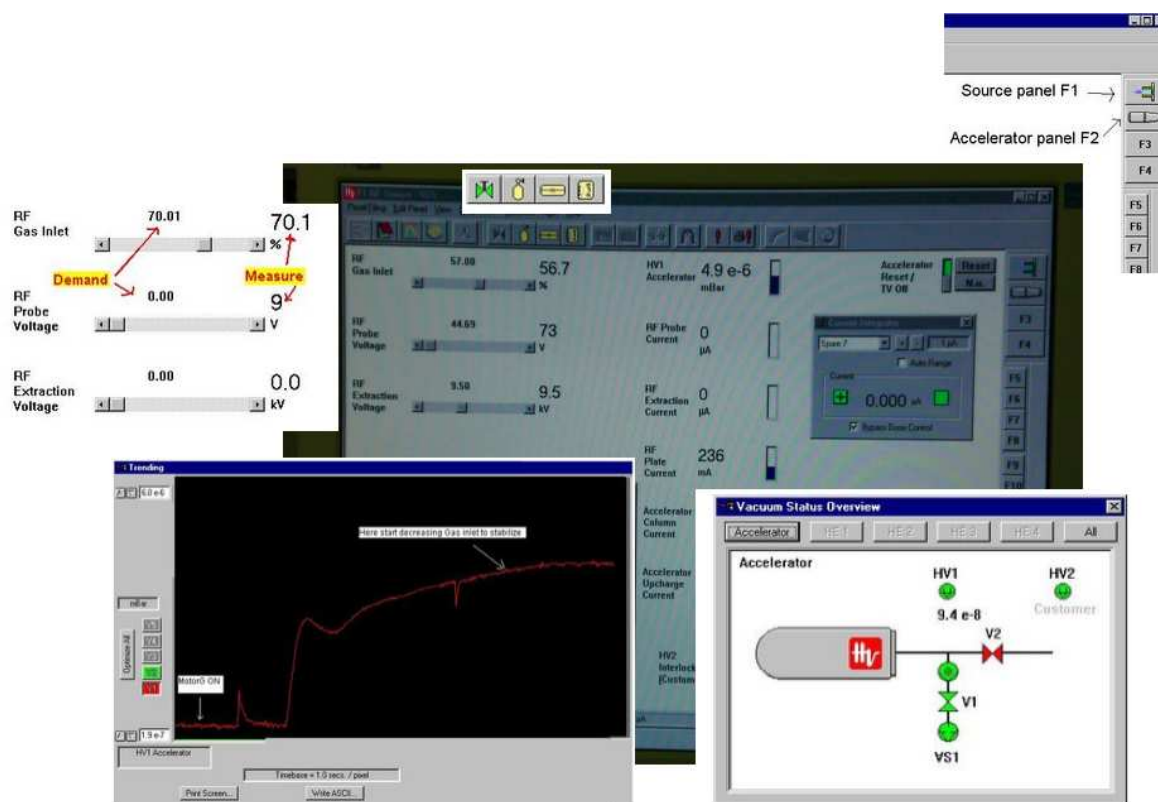


Figure 10.19: The monitor for the C-W remote control. The picture shows a detail of the vacuum level of the ion source (bottom, left); the vacuum system (bottom, right), the settings associated with the ion source (hydrogen level), the proton current (Probe voltage), the beam focusing (Extraction voltage) (top, left).

The emission of radiation from the accelerator and from the target

This aspect of the accelerator behaviour is important from the point of view of radiation safety. During all the tests we monitored and measured the emission of radiation from the accelerator.

The electromagnetic radiation potentially present around the C-W, its beam-line and the target region, has three possible origins:

1. X-ray bursts due to occasional anomalous accelerator HV discharges;
2. nuclear reactions;
3. proton induced X-ray production.

The radiation due to 2) and 3) can take place at various positions along the beam (target, beam shutter, beam slits, beam diagnostic elements or beam pipes in case of beam misalignment).

Since the C-W energy is always below the neutron production threshold, the neutron flux is expected to be negligible.

The radiation level, measured at $T_p = 500$ keV, by a soft X-ray radiation monitor around and close the accelerator, was always $< 1\mu\text{Sv/h}$, indistinguishable from the ambient background, even at a $I_p = 100\ \mu\text{A}$ C-W current. The neutron background at $I_p = 100\ \mu\text{A}$, was measured by a



HIGH VOLTAGE ENGINEERING EUROPA B.V.
 Amsterdamseweg 63, 3812 RR Amersfoort, P.O. Box 99, 3800 AD Amersfoort, The Netherlands
 Phone: +31-33-4619741 - Fax +31-33-4615291, Trade register Amersfoort nr. 51014544
 E-mail: info@highvolteng.com - Web: www.highvolteng.com

ACCEPTANCE PROTOCOL

1.0 MV SINGLETRON POSITIVE ION ACCELERATOR SYSTEM

Paul Scherrer Institute ref.: E 642950
INFN - Sez. di Pisa ref.: Pur. order n.110
HVEE ref. B6759 & B6760

We herewith declare that with the SINGLETRON system as described in above mentioned contracts the following tests are performed.

1. System function test
 During the system function test it is shown that the specified equipment is in operating condition by means of function checks on the major components and that the system can be set into operational mode within 20 min from cold start-up.

2. System performance test

2.1 Terminal voltage: 1000 kV during hours (spec. 1000kV - 4 hours)

2.2 During the verification test* the following specifications are demonstrated:

| Item | Specification | Remark | For approval at | |
|----------------------------------|---|--|-----------------|-----|
| | | | HVE | PSI |
| Base vacuum level | 10 ⁻⁶ mbar range | | | |
| Terminal voltage Range | 300 – 900 kV | | | |
| Terminal voltage ripple | 500 V _{RMS} | | | |
| Max. beam current H ⁺ | 100 μA – 1 hour | | | |
| Beam current dynamic range | 1 – 100 μA (total current ~ 125 μA) | At PSI only demonstration of total current. No mass-analysis possible. | | X |
| Spot size | 3 x 3 cms (FWHM) | No demonstration at PSI | | X |
| Angular divergence | 5 x 5 mrad (FWHM) | No demonstration at PSI | | X |
| Current stability | 10 % (4 hrs) | | | |
| Current reproducibility | 20 %, measured on two consecutive days | | | |
| Start-up time | < 20 min | | | |
| Software automatisaton | Ion source automatic start-up procedure | | | |
| X-ray level (1 m from tank) | < 2 μSv/hr @ 1 μA 500 keV H ⁺ | | | |
| | < 5 μSv/hr @ 100 μA 500 keV H ⁺ | | | |

* At HVE in Amersfoort running at 50 uA, 500 keV H⁺ at ~ 3 meters from the baseplate, unless otherwise noted.
 At PSI running at 50 uA, 500 keV H⁺ at ~ 1 meter from the baseplate, without mass analysis magnet, unless otherwise noted.

Figure 10.20: Tests required for the C-W acceptance. Part of them where be repeated at PSI.

neutron monitor and was always $< 10^{-4}$ $\mu\text{Sv/h}$.

The radiation emitted from a Tantalum target at $I_p = 100 \mu\text{A}$ and $T_p = 500 \text{ keV}$ was $> 5 \mu\text{Sv/h}$ at a 3 cm distance from the target, $0.1 \mu\text{Sv/h}$ at a 50 cm distance, $< 0.1 \mu\text{Sv/h}$ at other positions close to the C-W accelerator. This radiation, measured by the low-threshold monitor, could not be separated into components. Part of it is certainly of nuclear origin, but a large X-ray component might also be present.

We irradiated the target for about one hour, at $I_p = 58 \mu\text{A}$ and $T_p = 500 \text{ keV}$, and measured the radiation at the end of the beam line, at the back of the target, both before and after the C-W turn-off. The results are shown in the Tab. 10.8. The target activity decays with a $t_{1/2} \approx 15 \text{ m}$. After dismantling the Faraday cup holding the target, one could measure at the target surface, an activity $0.5 \mu\text{Sv/h}$, against $0.01 \mu\text{Sv/h}$ at the back of the Faraday cup. This difference is indicative of a certain amount of β -activation, only measurable at the target surface.

The radiation level was low, according to the safety requirements.

In chapter 14 we will discuss the possible utilization of the proton induced X-ray production for drift chamber calibrations and for beam current determinations.



Figure 10.21: *Closed and open wire scanner.*

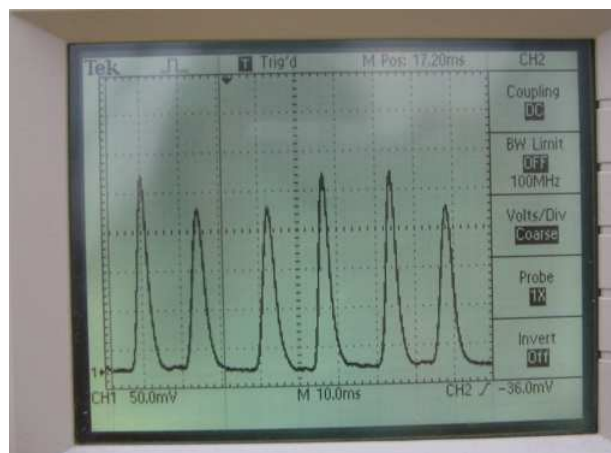


Figure 10.22: *Oscilloscope presentation of wire scanner signals.*

10.2.5 The C-W installation at PSI

The nuclear reactions for a MEG calibration must be produced at the center of COBRA. Originally we considered a C-W accelerator mounted on wheels and with a pipe, holding the target, which could be introduced into COBRA. A more appealing solution was adopted instead.

Prior to a calibration, the C-W accelerator must be turned-on, conditioned and tuned. If the accelerator is in a separate area, these operations can be conducted simultaneously with the normal MEG running. It is not advisable to move a C-W when tuned and in operation. It is more convenient to keep the accelerator at a fixed position, away from the COBRA fringing field, and insert into COBRA only the portion of the beam pipe holding the target.

The use of a special area for the C-W, separated from the main MEG experimental area, allows all the necessary maintenance service the accelerator might need (open and close the vessel, emptying and pressurizing the vessel, servicing the ion source, etc.) without affecting the running of MEG. The C-W area should have separate, safety-controlled access. This C-W area was localized directly at the back of the MEG experiment, allowing a simple proton beam insertion along the COBRA axis, opposite to the muon beam direction. It was necessary to slightly modify the shielding of the MEG area. The compatibility with the needs of other experiments was verified.

The C-W area is shown in Fig. 10.24. It has a width of 300 cm and a length of 550 cm along

Table 10.7: The beam ion composition at $T_p = 750$ keV.

| Ions | I_p (nA) | % | spot size FWHM (mm) | radioactivity($\mu\text{Sv/h}$) |
|----------------|--------------|----------------|---------------------|-----------------------------------|
| H_1^+ | 4450 ± 5 | 73.1 ± 0.2 | 12 ± 1 | 1 ± 0.1 |
| H_2^+ | 1070 ± 5 | 24.9 ± 0.4 | 10 ± 1 | 0.3 ± 0.1 |
| H_3^+ | 70 ± 5 | 2.0 ± 0.1 | 10 ± 1 | 0.05 ± 0.05 |

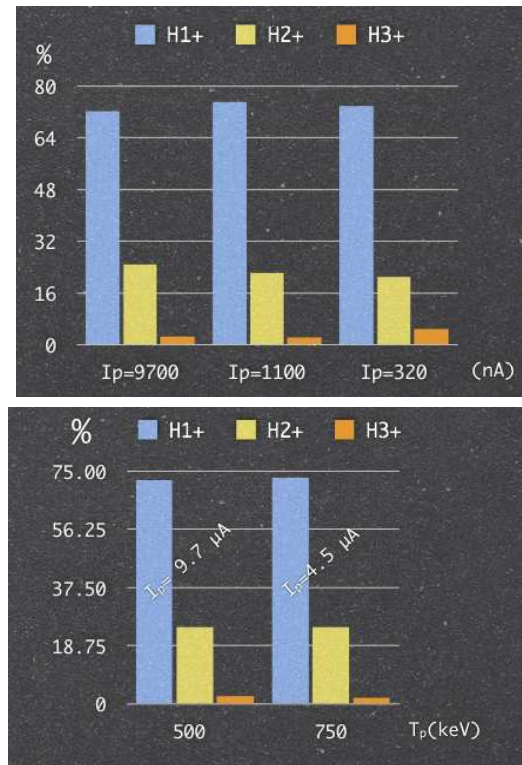


Figure 10.23: Measurement of the beam ion composition.

the beam direction.

10.2.6 The energy stability

Before starting the mounting of the proton beam line for the LXe calibration, we repeated the measurement of the LiF excitation curve, by using our machine. The good energy stability makes it possible to obtain a LiF thick target curve excitation as a function of the proton energy, in small energy steps. The γ 's are measured by using a small NaI. The result is reported in Fig. 10.25. The resonance is reconstructed at 443.4 ± 0.2 keV, with a $\Gamma_R = 9.2 \pm 0.2$ keV.

10.3 The proton beam line

A layout of the proton beam line is shown in Fig. 10.26. The C-W area is separated from the IIE5 area by a concrete wall where a beam shutter is positioned. The beam line is rather long (10.5 m from the C-W to COBRA center). The protons travelling along the line must be centered on the target after axially entering COBRA. It is worth pointing out that the experimental hall floor is made of ferroconcrete. The COBRA stray field and fields associated with the magnets of adjacent

Table 10.8: Target radioactivity as a function of time. The zero time value was measured with C-W still on.

| t(min) | radioactivity($\mu\text{Sv/h}$) |
|--------|-----------------------------------|
| 0 | 2.6 ± 0.1 |
| 3 | 0.6 ± 0.2 |
| 5 | 0.4 ± 0.1 |
| 10 | 0.4 ± 0.1 |
| 15 | 0.3 ± 0.1 |
| 20 | 0.15 ± 0.1 |
| 30 | 0.1 ± 0.05 |
| 35 | 0.05 ± 0.05 |

beam lines might influence the iron contained in the floor and influence the proton trajectories. Control of the beam along its path was assigned to a system of magnets and of diagnostic devices. It originally contained two x-deflecting and two y-deflecting magnets (parallel beam displacement) and a quadrupole pair for optimizing the beam focalization (Fig. 10.27). At the end of the beam line a bellows insertion system is used to insert the target into the spectrometer.

The mechanical details and the diagnostic system are described below.

10.3.1 Mechanics of the proton beam line

The right-hand MEG coordinate system has its origin at the target (and COBRA) center, the X -axis points away from the LXe calorimeter front face and the Z -axis is in the direction of the μ^+ -beam. The MEG experiment is symmetric with respect to the X - Y plane. The upstream region is defined as $Z < 0$ (the muon beam side), while the downstream region has $Z > 0$ (the proton beam side). The muon target is normally mounted at the Cobra center in the He atmosphere of a helium bag. The muon target is taken out of the way at the time of a C-W calibration. When MEG is in normal operation, the final portion of the proton beam line (the extensible “bellows system” and its rigid end section) is completely out of COBRA. At the moment of a C-W calibration, the bellows system extends and the nuclear target, supported by the last rigid portion of the beam line, reaches the COBRA center. Preliminary to this, one must create some air-filled free space in the helium bag which will be occupied by the rigid end section of the proton beam line. The so-called “insertion system” ensures that. It is a large rubber bellow which is pushed inside the helium bag (see Fig. 10.28). The bellows system and the insertion system are mechanically connected so that one (the bellows system) pushes the other (the insertion system). The movement is by hand or by motor.

The bellows system, composed of five ultra-high vacuum non-magnetic bellows, expands or contracts with a stroke corresponding to 2.2 m (Fig.10.29).

During the insertion of the rigid end section of the beam line into COBRA, the insertion velocity and the position of the nuclear target are continuously and remotely controlled by a precise absolute encoder ($\Delta Z < 1$ cm). The information associated with the absolute encoder is preserved even the event of power failure. The system contains several interlocks to protect the system and the experiment from possible damages. Some quantities: the supply voltage, the absorbed motor power, the proton target position and speed, the muon target position, the gas pressure in the helium bag, etc. are monitored and on-line displayed.

The time required to move the nuclear target from the parking position to the calibration position is about 10 min (at a speed $v \approx 3$ mm/s). The reason for such a low speed is the need to avoid dangerous extra pressures in the helium bag, where the delicate drift chamber system is contained. The pressure is kept under control and differences from a reference value can be compensated.

The required vacuum level in the proton beam line is about 10^{-6} mbar, reached by two pumping systems (each composed of a primary scroll pump and a turbo-molecular pump) mounted along the line. The pressure is read by a Pirani gauge. The C-W vacuum and beam line vacuum system

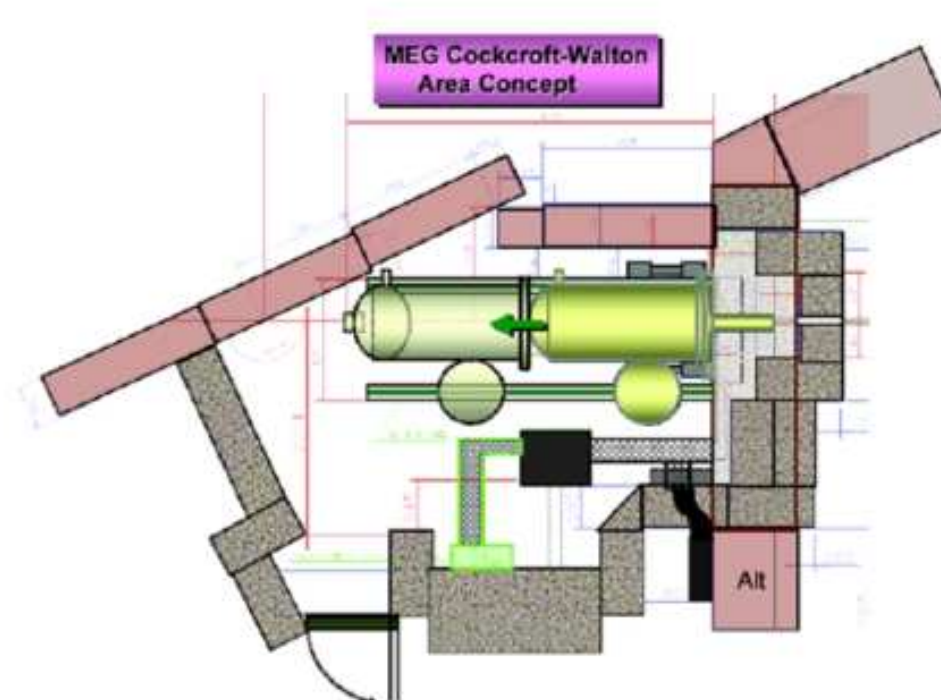


Figure 10.24: *The dedicated C-W area.*

are separated by a gate valve (close to the wall between the C-W and the MEG area) which can be opened when the two vacuum levels are compatible and correspond to a high vacuum. The gate valve automatically shuts in the event of accident. Another gate valve is mounted at the bellows system. It separates from the initial part the last section of the proton beam line during its movements in and out of COBRA.

10.3.2 The beam diagnostics

A schematic drawing of the items mounted along the proton beam is shown in Fig. 10.30.

The Faraday cup

The proton beam current and the integrated beam current (the total charge) reaching the nuclear target are directly measured at the target. These measurements are not accurate because of geometry and because of the influence of the intense COBRA magnetic field. A precise current reading is only possible with a well-designed Faraday cup. The cup must collect the charges carried by protons, but must also capture all secondary charges generated by the proton collisions against the Faraday cup material (the loss of part of the total current causes wrong beam current measurements). A good Faraday cup must have a length $L_{FC} > R$, where R is its radius. The electron losses due to the effects of the residual COBRA field is minimized by a guard ring, kept at a negative potential and mounted close to the cup entrance region.

The Faraday cup is inserted, when needed, into the beam line close to the bellows system, by a compressed air and remotely controlled system. Since rough current measurements are also possible on several elements of the beam line (nuclear target, beam shutter, diagnostic devices,

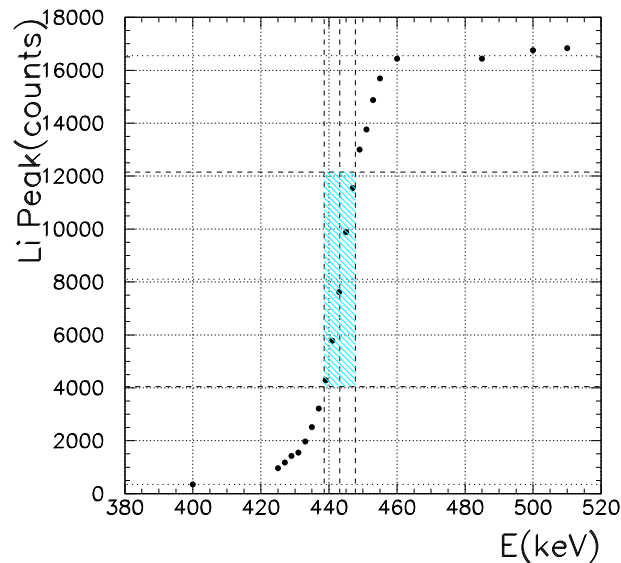


Figure 10.25: *The lithium thick target excitation curve.*

etc.) inter-calibrations between the Faraday cup and the other elements are often useful. An absolute calibration of beam current can be obtained by remeasuring a precisely known nuclear cross section, the best candidate being the process ${}^9\text{Be}(p,\gamma){}^{10}\text{B}$ whose cross section is shown in Fig. 10.31 [183].

The beam shutter

A beam shutter is mounted in the wall separating the C-W from the IIE5 area. It is remotely operated by a compressed air system and is an essential part of the safety system controlling the access to the experimental areas. It automatically blocks the proton beam in the event of emergency (i.e.: power off, compressed air off, etc.). When closed, it is possible to measure the current of the beam reaching it. As already said, a beam current measurement by the beam shutter is affected by systematic errors and depends on the proton energy and on the COBRA status, as visible in Fig. 10.32.

The beam diagnostic by proton induced fluorescence

A movable quartz crystal, operated by compressed air, is mounted in the first section of the proton beam line. The quartz emits an intense blue light, easily recorded by a TV camera, when irradiated by the proton beam. It is therefore possible to optimize the beam focalization and to center the beam, before entering the bellows system and COBRA (where a TV camera is not easily usable) (see Fig. 10.33 and Fig. 10.34).

The beam position and the beam focalization are measured on-line, by a fast data analysis of the CCD information. The beam position is determined with a precision of 1 mm (see Fig. 10.35). The crystal is covered by a very thin tungsten wire net which prevents electrostatic discharges at the crystal surface. It is possible to measure the beam current reaching the crystal and collected by the tungsten net.

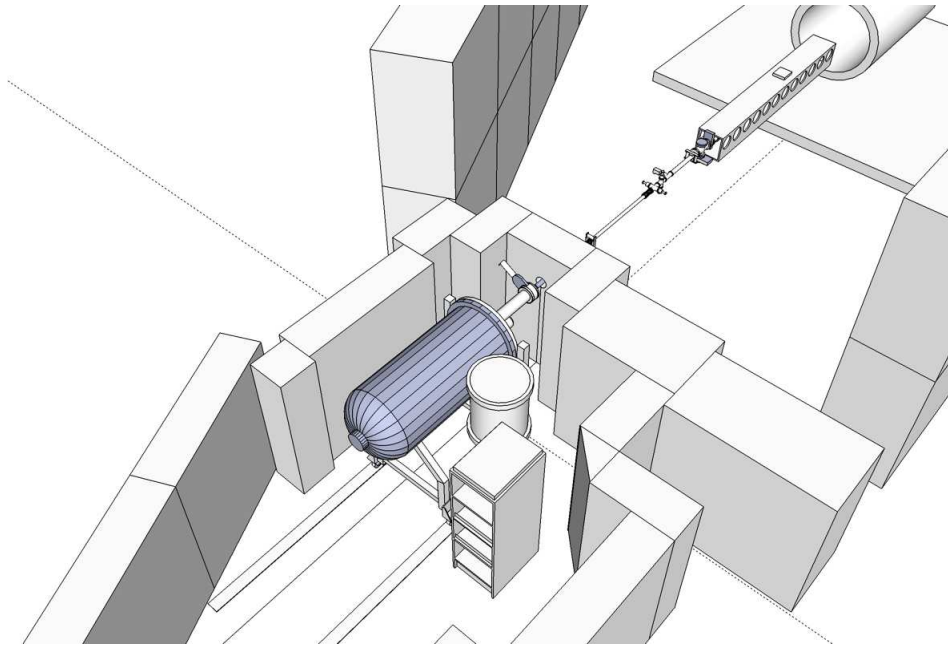


Figure 10.26: *The C-W area and the HIE5 area layouts. The proton beam line.*



Figure 10.27: *The proton beam line from the accelerator to the Cobra center.*

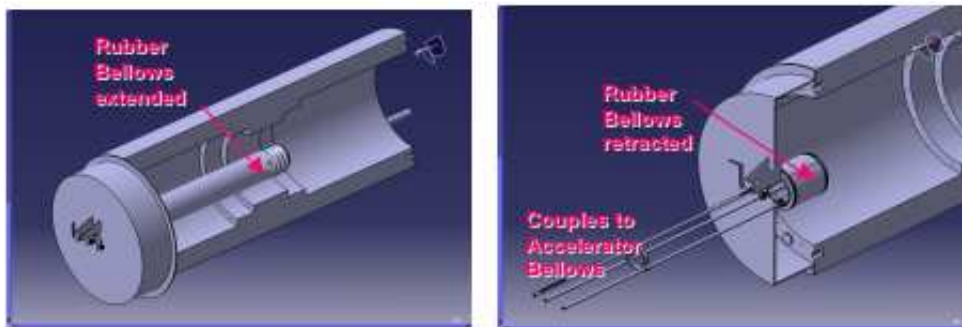


Figure 10.28: *The Insertion System layout. Fully inserted system (left). Fully retracted system (right).*



Figure 10.29: *The bellows system layout.*

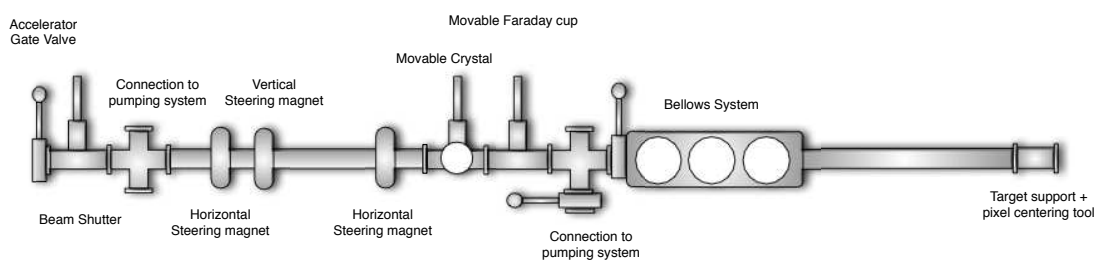


Figure 10.30: *The items mounted along the proton beam line. Side view (not to scale).*

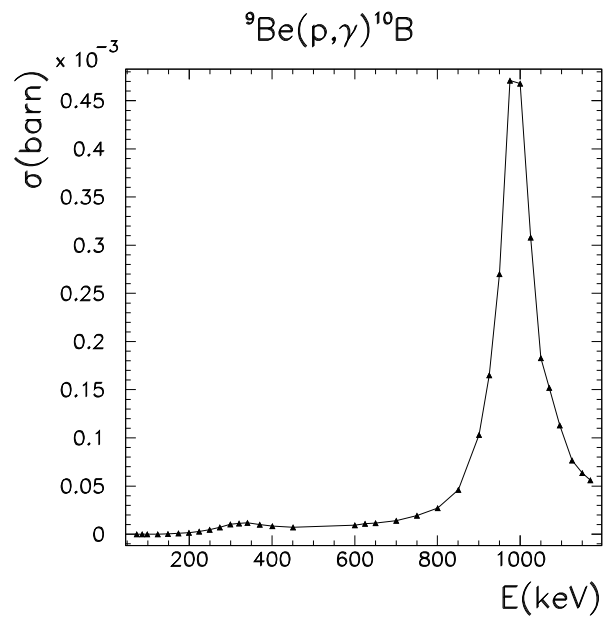


Figure 10.31: The ${}^9\text{Be}(p, \gamma){}^{10}\text{B}$ cross section as a function of the proton energy. Two broad resonances are visible [183].

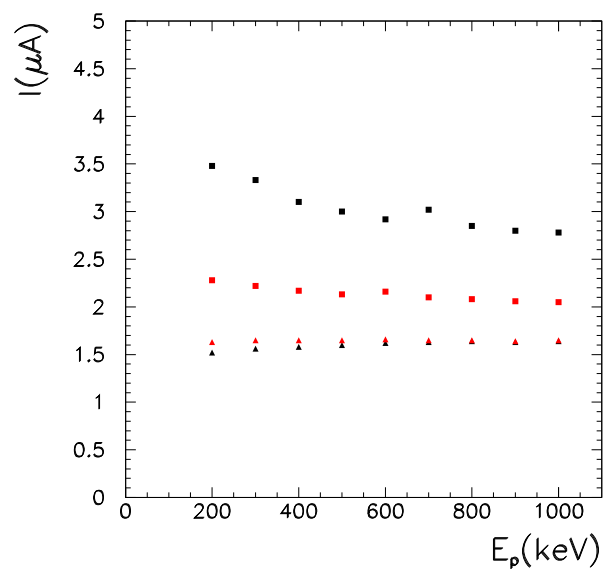


Figure 10.32: The beam current read on the Beam Shutter with COBRA ON (black square) and OFF (red square) and by the Faraday Cup with COBRA ON (black triangle) and OFF (red triangle), as a function of the proton energy. The beam shutter measurements strongly depend on the proton energy and on the COBRA status.

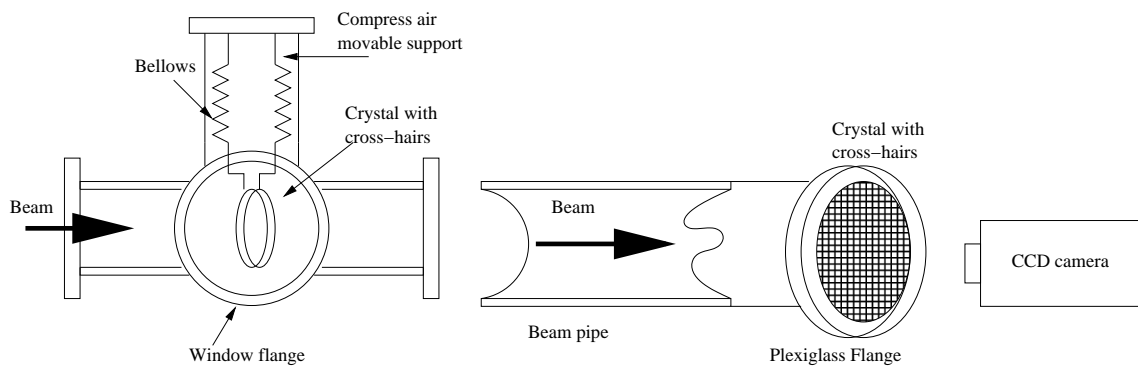


Figure 10.33: Scheme of the movable (left) and of the fixed (right) quartz crystals.

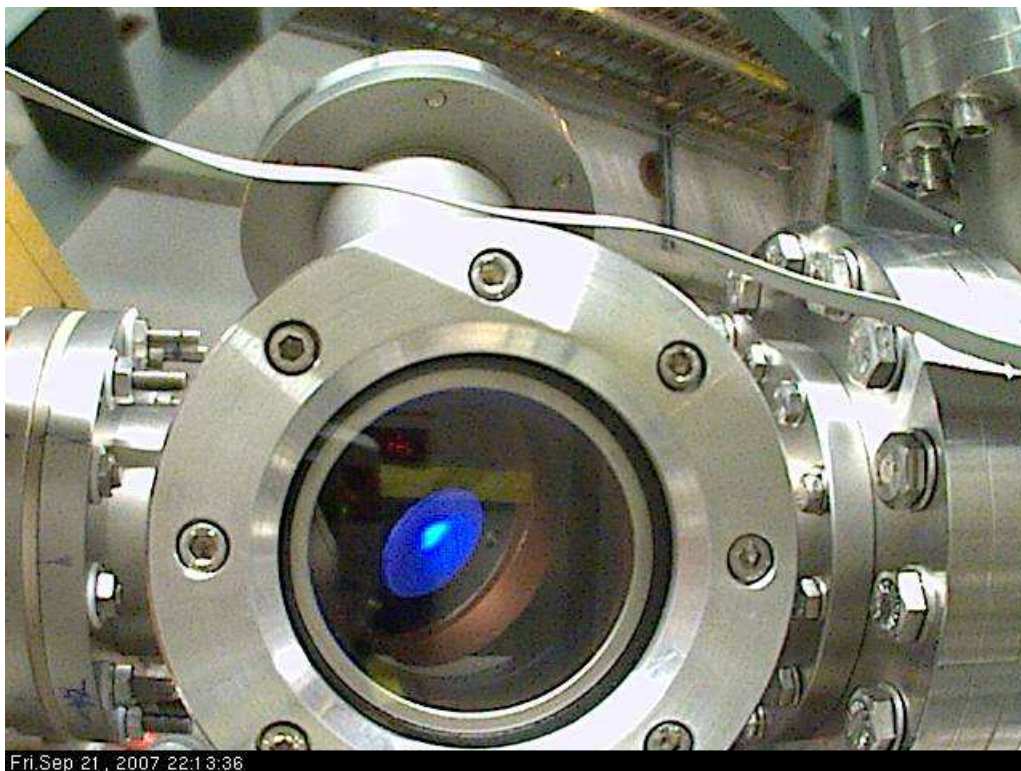


Figure 10.34: Fluorescence blue light emitted by a quartz crystal under proton bombardment.

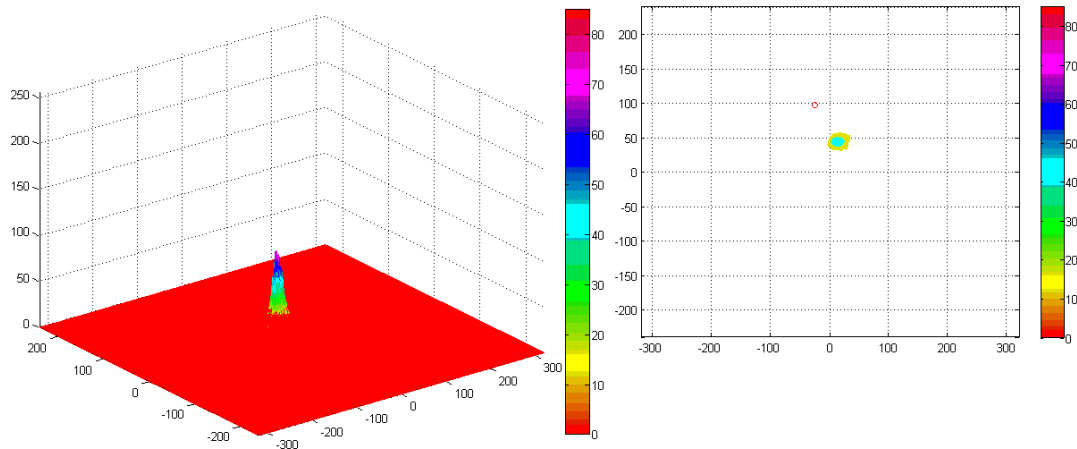


Figure 10.35: *Proton beam spot and beam position from the analysis of the CCD information.*

The movable target support and the Pixel centering device

A rotating target support and a pixel centering device are mounted at the end of the beam line. The target is normally kept at an angle of 45° relative to the beam direction. It moves toward a parking position out of the beam when one uses the pixel centering device. This is obtained by circulating a current in a coil mounted at the back of the target support. The current generates a magnetic moment producing a torque and the target rotation in the COBRA magnetic field (Fig. 10.36).

The pixel device has thin copper pixels deposited on vetronite. The beam position is reconstructed from the current readings of each independent pixel. The system is computer interfaced and an example of a pixel current pattern is shown in Fig. 10.37. The pixel system correctly operates in the COBRA magnetic field (≈ 1.3 T) and is essential in centering the beam on target at different C-W proton energies.

10.3.3 The proton beam optics and the beam alignment.

The proton beam line was mounted in successive steps, introducing additional elements, optimizing their positions and testing their effects. During this process, the beam characteristics were studied with the crystal fluorescence method. The quartz crystal was mounted on a plexiglass flange, at the end of the beam line. The fluorescence method proved to be reliable and simple.

The measurements were performed with COBRA off and on.

Only three optical elements (steering magnets) were required for the final configuration of the proton beam. The first image of the proton beam at the Cobra center is shown in Fig. 10.38. It is possible to distinguish the different hydrogen ions (H_1^+ and H_2^+), whose trajectories split in the COBRA magnetic field.

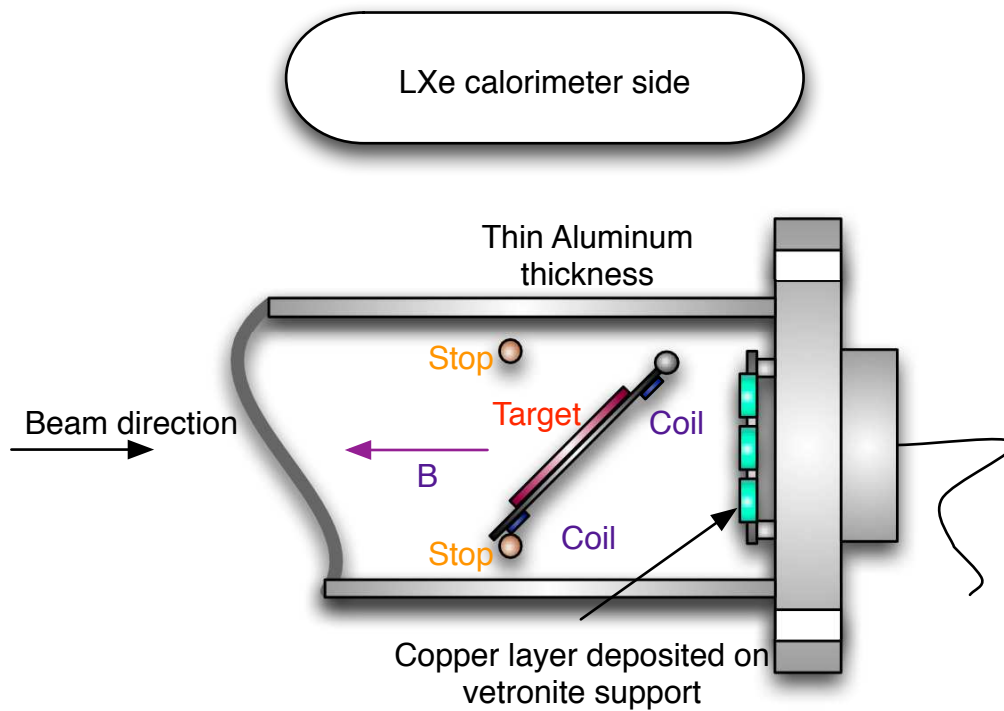


Figure 10.36: Scheme of the movable target and of the pixel centering device.

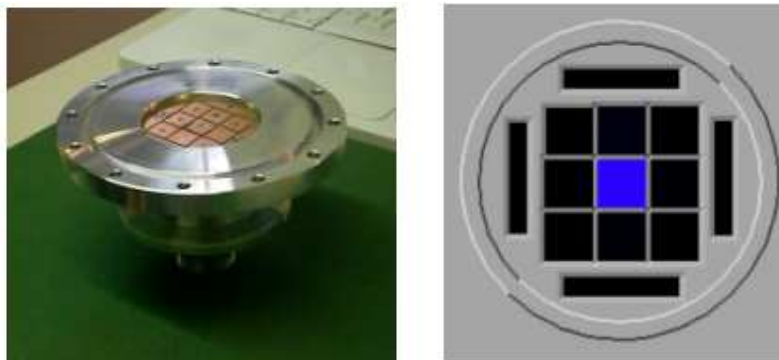


Figure 10.37: The pixel system mounted on a vacuum flange (left). Monitoring of the proton beam position by the pixel system (right).

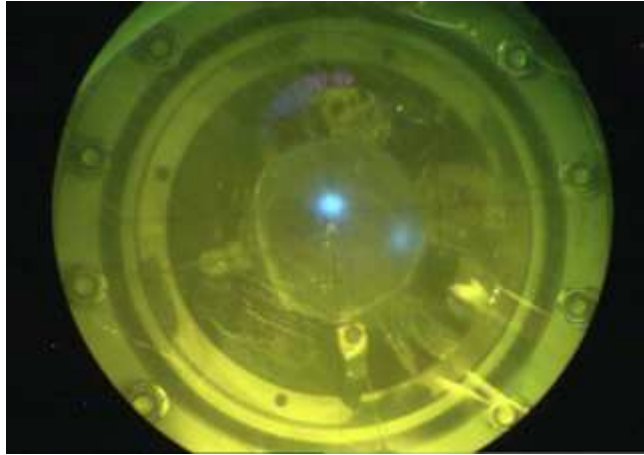


Figure 10.38: *The light spot associated with the beam. The picture was recorded by a CCD TV camera with the help of a theodolite focused on the target inside COBRA. Two of the hydrogen ions (H_1^+ and H_2^+) are separately seen.*

10.4 The target support; heat production and cooling; the targets

Table 10.9: The heat production

| \dot{A} | I_p (nA) | P (W) | R_γ | measurement condition |
|-----------|------------|---------|------------|-----------------------|
| | 200 | 0.1 | 360 | calibration |
| | 2000 | 1 | 3600 | high rate test |
| | 20000 | 10 | 36000 | high rate test |

The target support and the target, mounted under vacuum at the end of the proton beam line, are heated up by the proton beam and, being under vacuum, have a reduced heat dissipation. We studied this problem in the laboratory, under simulated conditions and trying to optimize the target thermal contact with its support and with the beam pipe. The information on the power levels is summarized in Tab. 10.4, which lists the typical heat production associated with different conditions of calorimeter calibration.

We verified that a water cooling system is not needed.

The final target for the experiment is a $Li_2B_4O_7$ crystal, which satisfies different calibration needs, as discussed in the chapter 13.

Chapter 11

The 54.9 MeV and 82.9 MeV γ -lines from the CEX reaction induced by negative pions

The production of π^0 's by the charge exchange reaction $\pi^- + p \rightarrow \pi^0 + n$, at rest, is an important physical process for MEG, since γ -rays are produced which match those from $\mu \rightarrow e\gamma$. The γ energy spectrum is flat in the interval $54.9 < E_\gamma < 82.9$ MeV. One can select a 54.9 MeV γ by detecting a coincident γ emitted in the opposite direction. An auxiliary detector, facing the LXe calorimeter, is therefore required, to select the higher energy γ ; the lower energy γ is the one normally used to calibrate the LXe calorimeter. The method allows the determination of the energy, position and time resolutions of the LXe calorimeter.

We present the first results obtained with the LXe Large Prototype. They confirmed that the resolutions had the desired values and proved the usefulness of the π^0 method.

At the end of the chapter, we discuss how the π^0 calibration set-up was integrated into MEG. In particular we present the two new components which were developed: the hydrogen target and the movable NaI detector.

The results of the most recent charge exchange calibration in MEG are discussed in chapter 16.

11.1 The kinematics of the π^- charge exchange reaction

The negative pions are captured by protons at rest. Two competitive reactions exist. The charge exchange reaction CEX:



and the radiative capture reaction RC:



The relative probability of these two processes was originally measured by Panofsky. The so called ‘‘Panofsky ratio’’ [184] is:

$$P = \frac{\Gamma(\pi^- + p \rightarrow \pi^0 + n)}{\Gamma(\pi^- + p \rightarrow n + \gamma)} = 1.533 \pm 0.021, \quad (11.3)$$

The branching ratios of these two processes are:

$$B_{CEX} = \frac{\Gamma(\pi^- + p \rightarrow \pi^0 + n)}{\Gamma_{tot}} = 0.605 \pm 0.013 \quad (11.4)$$

$$B_{RC} = \frac{\Gamma(\pi^- + p \rightarrow n + \gamma)}{\Gamma_{tot}} = 0.395 \pm 0.008. \quad (11.5)$$

We rely on the two γ 's π^0 -decay. The γ from the radiative capture reaction $\pi^- + p \rightarrow n + \gamma$ has too high an energy (129 MeV).

In the rest system of the π^0 (the CM starred system), the two γ 's have each energy $E^* = m_{\pi^0}/2 = 67.5$ MeV. The π^0 is produced with an energy $E_{\pi^0} = 137.8$ MeV, while its mass is $m_{\pi^0} = 135.0$ MeV. The CM-system is therefore boosted with respect to the LAB system ($\beta^* = 0.2$). In the LAB system the two γ 's have an energy in the interval:

$$E_{MIN} = \gamma \frac{m_0}{2} (1 - \beta^*) = \frac{m_0}{2} \sqrt{\frac{1 - \beta^*}{1 + \beta^*}} = 54.9 \text{ MeV} \quad (11.6)$$

$$E_{MAX} = \gamma \frac{m_0}{2} (1 + \beta^*) = \frac{m_0}{2} \sqrt{\frac{1 + \beta^*}{1 - \beta^*}} = 82.9 \text{ MeV}. \quad (11.7)$$

where E_{MIN} and E_{MAX} are the minimum and maximum energy of the γ 's in LAB.

The energy spectrum dN_γ/dE_γ is flat:

$$\frac{dN_\gamma}{dE_\gamma} = \frac{dN_\gamma}{d\Omega^*} \frac{d\Omega^*}{dE_\gamma} = \frac{dN_\gamma}{d\cos\theta^*} \frac{d\cos\theta^*}{dE_\gamma} \quad (11.8)$$

$$= N_0 \frac{1}{\gamma\beta^*E^*} = \frac{2N_0}{E_{MAX} - E_{MIN}} \quad (11.9)$$

where N_{π^0} is the π^0 rate. Note that the angular distribution is isotropic in the CM system.

The relative angle of the two γ 's $\Theta_{\gamma\gamma}$ as a function of the γ energy (one of the two energies) is:

$$\Theta_{\gamma\gamma} = \arccos \left(1 - \frac{m_0^2}{2E_\gamma(E_{\pi^0} - E_\gamma)} \right). \quad (11.10)$$

The selection of γ 's emitted around the opposite direction corresponds to a selection of the γ energy. In particular, the request $\Delta E/E < 1\%$ corresponds to $\Delta\Theta_{\gamma\gamma} < 5^\circ$. The γ -single rate is reduced by the "coincidence factor" f_{coin} :

$$\begin{aligned} f_{coin} &= \int_{\cos\Theta} \left| \frac{d\cos\theta^*}{d\cos\Theta} \right| d\cos\Theta \\ &= \int_{\cos\Theta} \left| \frac{1}{\beta\gamma^2(1 - \cos\Theta)^2 \sqrt{1 - \frac{2}{\gamma^2(1 - \cos\Theta)}}} \right| d\cos\Theta \end{aligned} \quad (11.11)$$

The request $\Delta\Theta < 5^\circ$ is equivalent to $\cos\Theta_{MIN} = -1$ and $\cos\Theta_{MAX} = -0.996$. Finally:

$$f_{coin} \approx \int_{\cos\Theta_{MIN}}^{\cos\Theta_{MAX}} (48 + 42\cos\Theta) d\Theta = 0.024. \quad (11.12)$$

This value is used to evaluate the expected γ -rate.

11.2 The π^- capture on hydrogen and hydrogenous compounds

A liquid hydrogen target is required for the $\pi^- + p \rightarrow \pi^0 + n$ reaction, because of the liquid higher density. A cryogenic set-up was developed, to keep the hydrogen in the liquid phase (< 20.39 K, at a

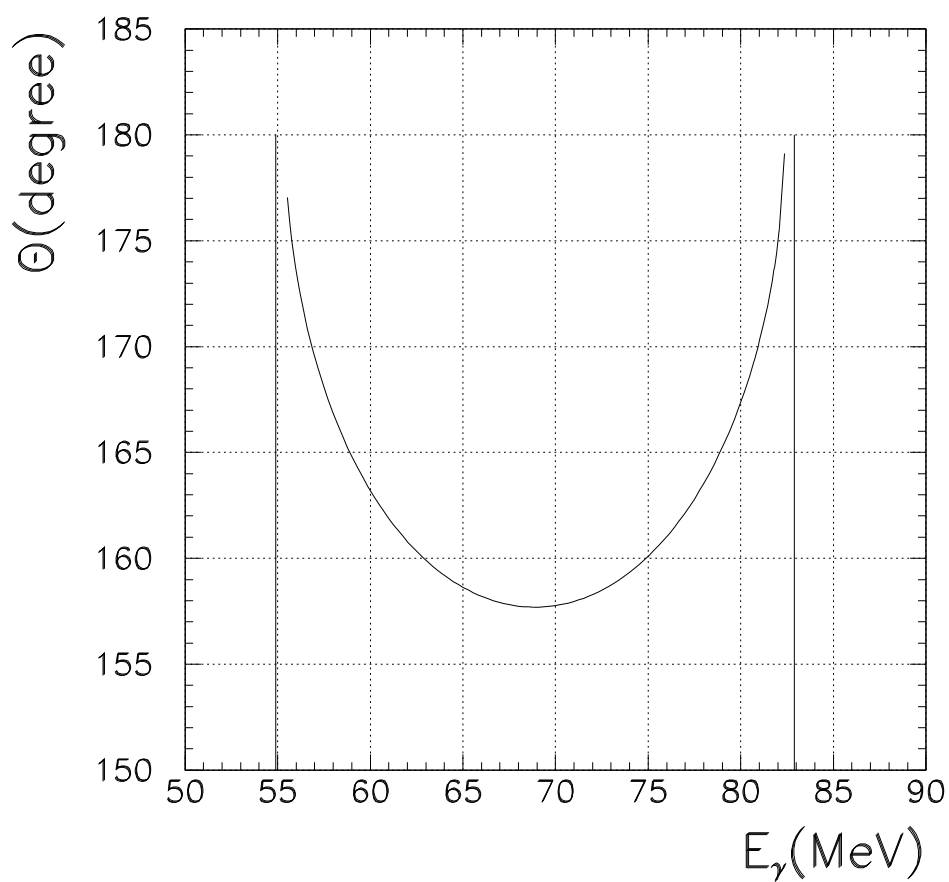


Figure 11.1: The relative angle of the γ 's from the reaction $\pi^0 \rightarrow \gamma \gamma$, in the LAB system, as a function of the energy.

pressure of 1 atm). The target must be positioned at the Cobra center. It was therefore necessary to design a mechanical structure for inserting the target from the region downstream of COBRA.

We also studied the possibility of using a hydrogen compound solid target, safer than a hydrogen target inside COBRA and simpler to use than a cryogenic system. We must therefore discuss the effects of the chemical bond on the π^- -capture probability.

The π^- -capture in matter can be schematically subdivided into a series of steps:

1. ionization energy loss;
2. π^- -capture in atomic orbits of high quantum number;
3. de-excitation of the initial highly excited state via Auger and radiative transitions;
4. (in case of a compound:) the transfer of the π^- to other atoms of the compound;
5. nuclear capture or decay of the π^- .

The time needed to go through all steps lies between 10^{-13} and 10^{-9} s; it depends on the chemical and physical properties of the compound. The π^- can be captured before decaying (π^- -mean life = $2.6 \cdot 10^{-8}$ s).

For chemically bound hydrogen atoms, the probability W that a π^- is captured by a proton is reduced compared to that of pure hydrogen (conventionally $W(\text{H}_2) = 1$). Let us consider a binary compounds of the type $Z_m\text{H}_n$ (Z denotes both the element and its atomic number). As a first approximation the probability W can be written ([186], [187], [188] and [189]):

$$W = PQR \quad (11.13)$$

where P is the compound capture probability, which corresponds to an orbit of the “mesomolecule”; mesomolecule is what is obtained when a pion replaces (via Auger capture) an electron of the bound Z -H system, so forming a large mesic molecule $ZH\pi^-$. Q is the probability that the pion is transferred from the mesomolecular to a hydrogen mesoatomic orbit, so forming a pionic hydrogen atom ($p\pi^-$). R is the probability of π^- capture by the hydrogen nucleus (assumed here to be equal to one).

The P probability follows the Fermi-Teller law, the “ Z -law” [185]: the π^- -atomic capture probability is a linear function of Z . For a $Z_m\text{H}_n$ molecule one obtains:

$$P = \frac{n}{mZ + n} \quad (11.14)$$

i.e.: the ratio of the number of the hydrogen electrons to the total number of electrons of the molecule.

The pionic hydrogen atoms are formed, via radiative transitions from the mesic molecular orbits, with a probability:

$$Q \approx Z^{-2} \quad (11.15)$$

Thus the pion capture probability by the protons of the compound $Z_m\text{H}_n$ is:

$$W = a_z \frac{1}{Z^2} \frac{n}{mZ + n}. \quad (11.16)$$

The empirical factor a_z takes into account all other possible smaller effects: the detailed properties of the Z -H bond, the possible deviations from the expressions (11.14) and (11.15).

In conclusion, the π^- -capture by a proton in a compound $Z_m\text{H}_n$ has a probability W which is proportional to $\approx Z^{-3}$. This prediction is experimentally verified.

If we apply eq. (11.16) to CH_2 , the most suitable material to replace the liquid hydrogen target, we obtain a π^- -capture by the hydrogen of the compound of about 1% of that by pure hydrogen.

This strongly suggests the use of a liquid hydrogen target, if one wants to reach a γ -rate of few Hz during a calorimeter calibration. Let us recall that the π^- -beam intensity is $\approx 10^6$ particles/s, the selection of the two back-to-back γ 's introduces a factor $\approx 10^{-2}$ and we expect to cover a fraction of the solid angle of $\approx 10^{-4} - 10^{-3}$.

11.3 The first CEX reaction measurement

In this section we present our first measurement of the CEX reaction.

11.3.1 The experimental set-up

A π^- -beam of $8 \cdot 10^5$ particles/s, with an initial momentum equal to $p_\pi \approx 110$ MeV/c and a final momentum of $p_\pi \approx 60$ MeV/c, is slowed down and brought to rest in a hydrogen target (length $L = 9$ cm, diameter $d = 4$ cm).

The reason for the choice of the initial beam momentum is motivated by the need to reject electrons. Electrons in the beam are more abundant than pions by a factor of 20. The e^- -contamination is strongly reduced by the combined use of a 4 mm (graphite) degrader and an electrostatic separation. The thickness of this first degrader is kept to a minimum to reduce multiple scattering and straggling. A second thicker graphite moderator (thickness ≈ 3 cm) is placed close

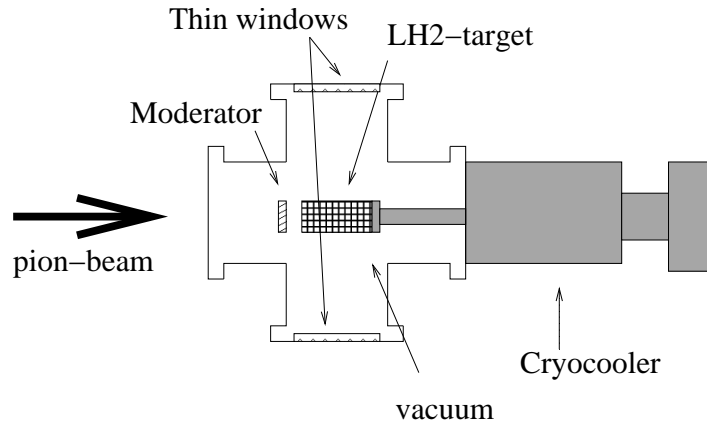


Figure 11.2: *The liquid hydrogen target. The moderator inside the vacuum chamber is visible.*

to the thin mylar window of the hydrogen target, inside the vacuum chamber (Fig. 11.2). Taking into account the thickness of a scintillation counter, mounted in front of the liquid hydrogen target (LHT), the pions reach the liquid hydrogen with a momentum of ≈ 60 MeV/c (π^- -range $R_\pi = 4.5$ cm at $p_\pi = 60$ MeV/c). A summary of the relevant parameters is presented in Tab. 11.1. The result is shown in Fig. 11.3. The fraction of pions stopped in the target is 83%.

The LXe calorimeter prototype and the NaI tagging detector were placed orthogonally to the beam direction (see Fig. 11.4). Two lead collimators were mounted in front of the detectors to select the back-to-back γ 's (with a relative angle $\Theta_{\gamma\gamma} > 175^\circ$). The equivalent angular acceptance was equal to $\Delta\Omega_{\gamma\gamma} \approx 5 \cdot 10^{-4}$ sr. The total acceptance, taking into account the coincidence factor f_{coin} , was $A_{\gamma\gamma} = \Delta\Omega_{\gamma\gamma} \cdot f_{coin} \approx 10^{-5}$.

The measured rate was a few Hz.

11.3.2 The results

The CEX reaction allowed, for the first time, the determination of the LXe LP energy resolution in the MEG region of interest. The correlation of the energies deposited in the LXe LP and in the NaI

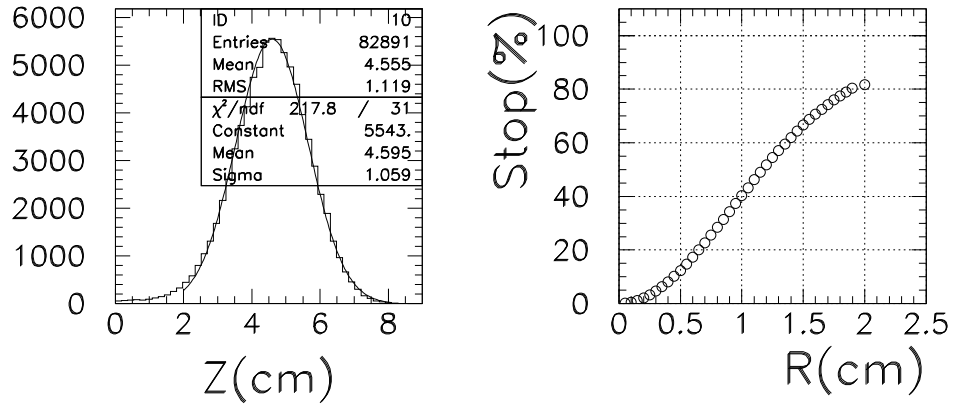


Figure 11.3: The longitudinal and radial distributions of negative pions stopped in the hydrogen target. The target dimensions: length = 9 cm and diameter = 4 cm.

Table 11.1: The parameters used in the Monte Carlo simulation.

| Parameter | Value& Unit |
|---------------------------------------|-------------|
| Generated events | 100000 |
| Target diameter | 4 cm |
| Target length | 9 cm |
| Target walls (Al) | 0.05 cm |
| Mylar window | 0.019 cm |
| Vacuum space along the beam direction | 10 cm |
| Graphite moderator thickness | 2.87 cm |
| Scintillation counter thickness | 0.5 cm |
| Beam Δx (FWHM) | 2.026 cm |
| Beam Δy (FWHM) | 0.576 cm |

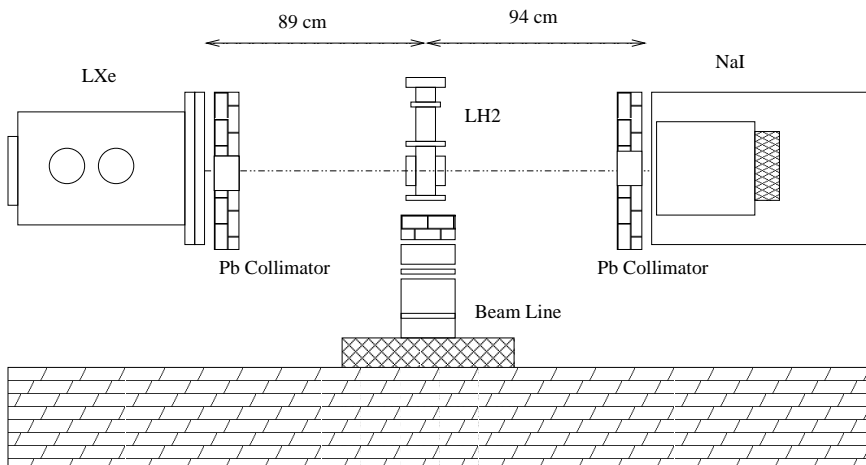


Figure 11.4: The experimental set-up for measuring the CEX reaction.

detector is shown in Fig. 11.5. The separate energy spectra of the two detectors, with no selection applied, are presented in Fig. 11.6. The energy peaks associated with the two back-to-back γ 's are clearly visible. After selecting the higher energy γ in the NaI detector, we were able to determine a LXe LP energy resolution $\Delta E/E$ ($FWHM$) = $5.15 \pm 0.64\%$ at a γ -ray energy of 54.9 MeV (see Fig. 11.7). We list all selections which were applied in this analysis:

1. π^- were separated from residual e^- by the use of the time-differences between the machine radio-frequency signal and the LHT scintillation counter signal;
2. 82.9 MeV γ 's were required to be detected in the NaI detector;
3. a *depth-cut* was applied to eliminate γ 's converting before the xenon active volume (the distance of the γ -conversion point from the calorimeter wall must be > 2.5 cm);

The measured energy resolution did not reach the better value predicted by the MC simulation ($\Delta E/E(FWHM) = 4\%$). We believe this to be due to an insufficient knowledge of the PMT quantum efficiencies and to the faulty behaviour of a few PMTs. These aspects were better taken care of in setting-up the final calorimeter.

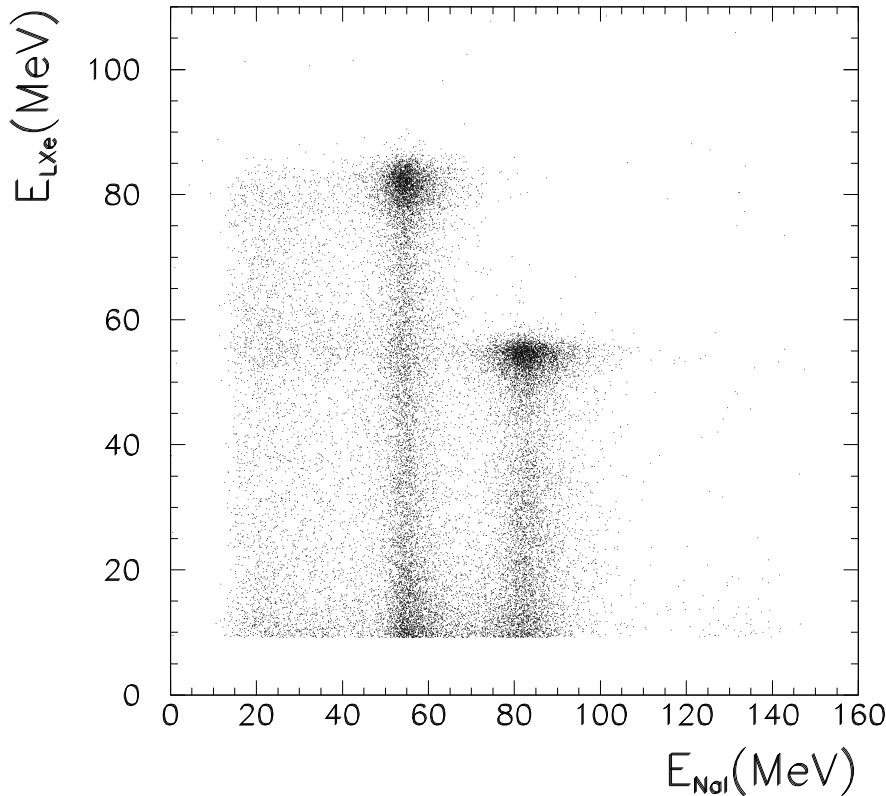


Figure 11.5: *The correlation between the energies deposited in the liquid xenon large prototype and in the sodium iodine detector.*

During the CEX data collection we also measured, for the first time, the “intrinsic” timing resolution of the LXe LP at γ energies close to those of the $\mu \rightarrow e\gamma$ decay.

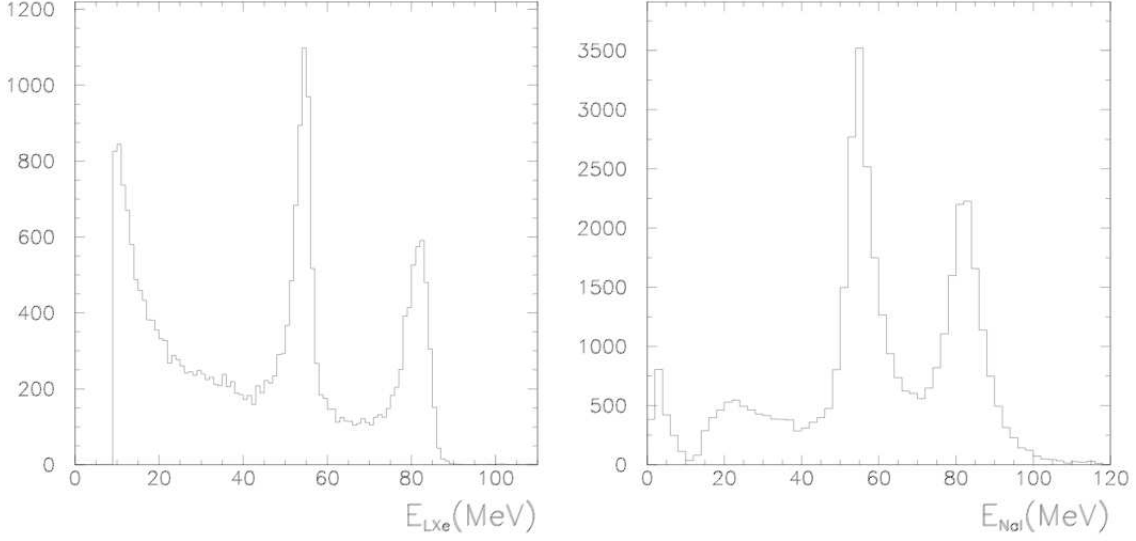


Figure 11.6: *The energy spectrum in the LP detector (left) and the energy spectrum in the NaI detector (right).*

The time T_0 in which a γ leaves the target is related to the time recorded by the PMT T_i by the following expression:

$$T_0 = T_i - T_f - T_{tt} - T_{dly} \quad (11.17)$$

where T_f is the sum of the γ time of flight, from the target to the conversion region, and of the γ time of flight from the conversion region to the i -PMT photocathode surface, T_{tt} is the electron transit time in the PMT and T_{dly} is a fixed delay due to cables, electronics etc. The time of flight T_f depends on the reconstructed event position inside the calorimeter. We can divide the LXe calorimeter timing resolution σ_t into two terms, one called the position contribution the other, the “intrinsic” resolution:

$$\sigma_t^2 = \sigma_{pos}^2 + \sigma_{intr}^2. \quad (11.18)$$

We measured σ_{intr} subdividing the LP PMTs into two groups, the “left” and the “right”. We measured the average timing given by each of the two groups T_L and T_R . The σ_{intr} is obtained from the distribution of the variable:

$$T_{intr} = \frac{T_L - T_R}{2}. \quad (11.19)$$

The σ_t as a function of the number of photoelectrons is shown in Fig. 11.8. Two examples of the $(t_L - t_R)/2$ distribution are also shown. The σ_t vs N_{phe} has a dependence given by the following expression:

$$\sigma_t = a + \frac{b}{\sqrt{N_{phe}}} \quad (11.20)$$

(superimposed on the plot, together with the effects of a one σ variation of the fitted parameters). Note that in the LP the typical QE of a PMT is $QE \approx 5\%$. In the final detector the PMT QE is $\approx 20\%$. We expect $N_{phe} \approx 100000$ for a 54.9 MeV γ -ray, corresponding to an “intrinsic” timing resolution $\sigma_{intr} \approx 25$ ps, similar to the predictions of MC simulation. Assuming $\sigma_{pos} = 25$ ps (see chapter 6) for each coordinate, σ_t is:

$$\sigma_t \approx 50 \text{ ps} \quad (11.21)$$

i.e. 115 ps FWHM. The LXe timing resolution is comparable with that of the TC; the relative timing of the two detectors can therefore be determined with a resolution of ≈ 150 ps (FWHM).

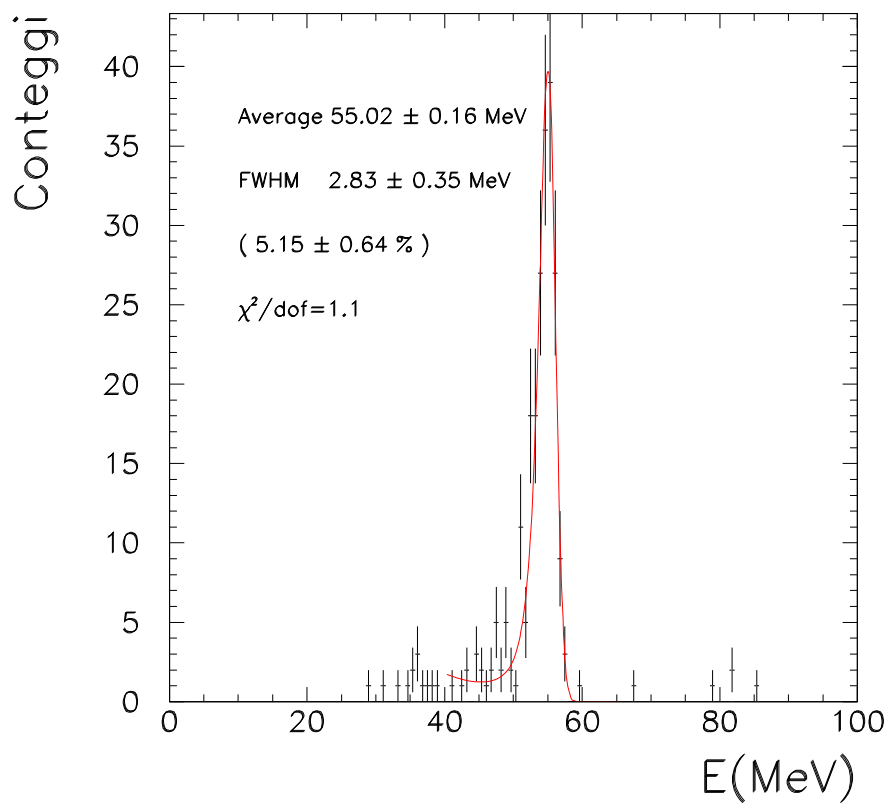


Figure 11.7: *The energy resolution determined with the LXe LP.*

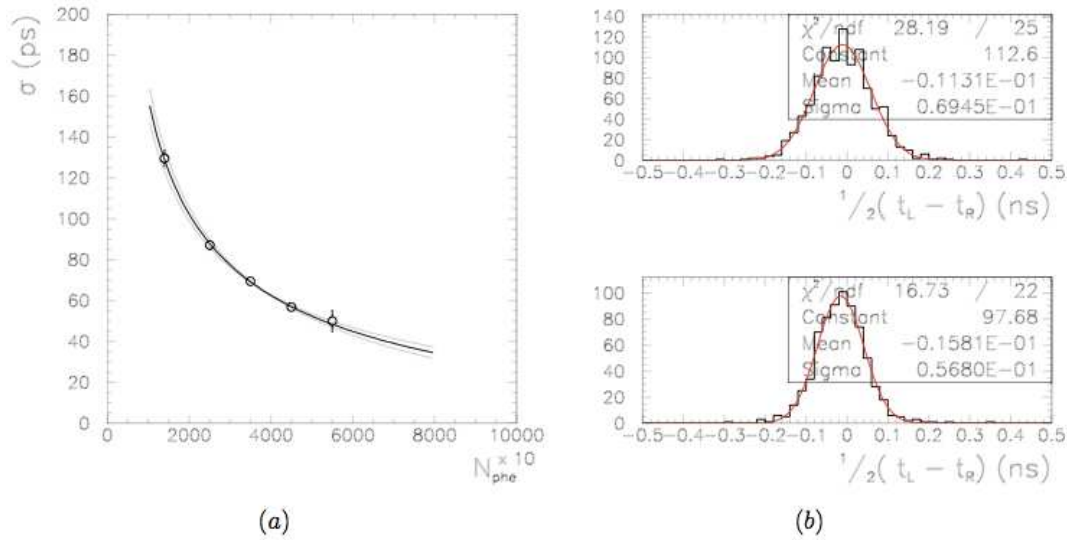


Figure 11.8: The intrinsic time resolution σ as a function of the number of photoelectrons (a). Two time spectra of the variable $(t_L - t_R)/2$ (b).

11.4 The experimental set-up for the CEX reaction in MEG

11.4.1 The liquid hydrogen target

During the first test of the CEX reaction in the LP, we used an LHT whose dimensions cannot fit into the final MEG set-up. A new *ad-hoc* liquid hydrogen target was therefore built to reach the Cobra center, while respecting the available space constraints. The LHT is inserted from the COBRA downstream region. Liquid helium, used as heat exchanger, flows in a 2 m long stainless steel pipe. The helium reaches a thick copper tube, wrapped around the LHT body, thus optimizing the cooling power. The helium is then recovered.

A schematic view of the cryogenic gas/liquid handling system is shown in Fig. 11.9. Three PT100s are present in the system to monitor its temperature. The first is mounted at the beginning of the He-inlet line. The second on the He-outlet line, at about 70 cm from the LHT. The last one is mounted on the LHT. Pressure gauges are used to check pressures at different locations.

In Fig. 11.10 we present the temperature (a.u.) reading of the PT100 at the H_2 target, and the pressure value in the buffer, from which the hydrogen gas is transferred to the target, during the first H_2 liquefaction. When the buffer pressure starts to decrease the H_2 liquefaction begins (Fig. 11.11).

11.4.2 The NaI tagging detector

A NaI positioning device was built (see Fig. 11.12 and Fig. 11.13) to move the NaI detector and to illuminate with tagged γ 's the various calorimeter regions. The positioning device can move the NaI in the z -direction (by ± 30 cm), in the ϕ -direction (by $\pm 60^\circ$) and around the axis supporting the detector (by $\pm 30^\circ$). The NaI is made up of 3×3 crystals, each of dimensions $(5 \times 5 \times 15 \text{ cm}^3)$. Each crystal is read by 2 avalanche photodiodes (APD Hamamatsu S8665-55), cooled by Peltier coolers.

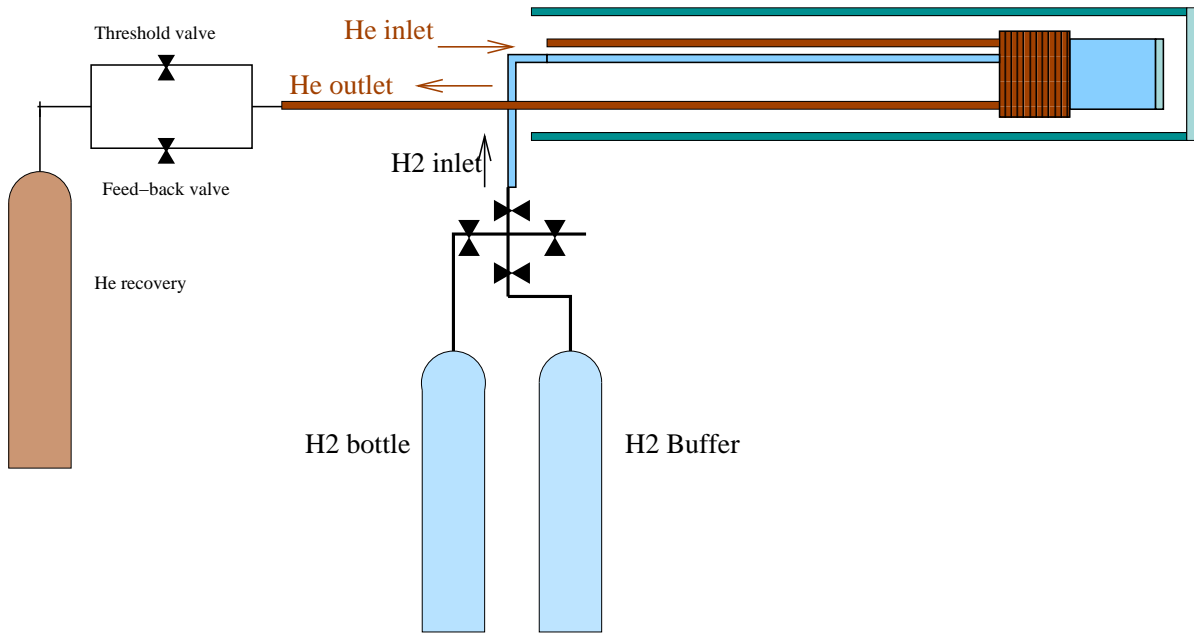


Figure 11.9: A scheme of the cryogenic gas/liquid handling system for liquid hydrogen target.

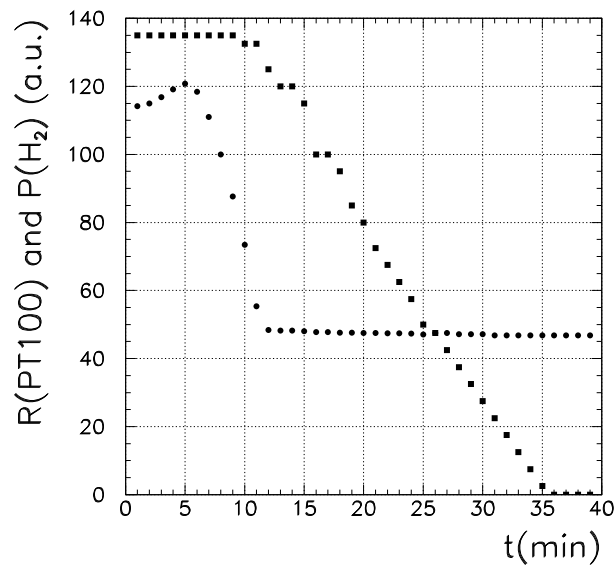


Figure 11.10: The reading of the PT100 resistance associated with the LHT (circle) and the reading of the buffer H₂ pressure (square) are plotted as a function of time.

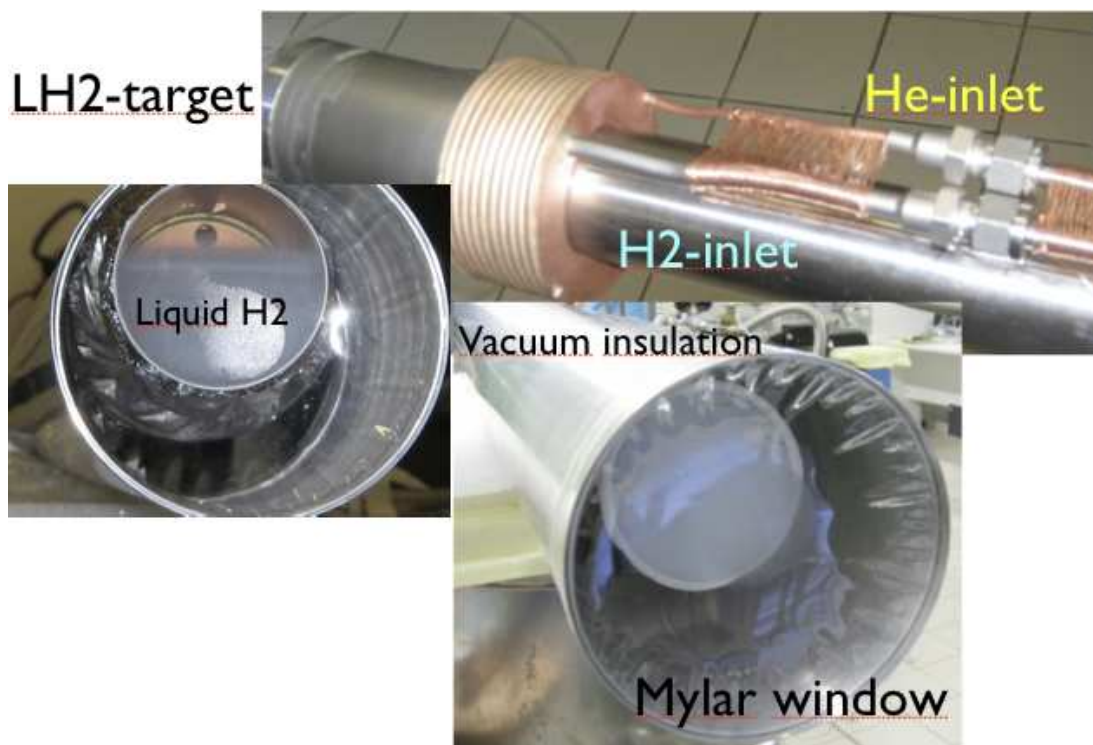


Figure 11.11: Some pictures of the liquid hydrogen target. The hydrogen liquefaction is visible in the picture at left.

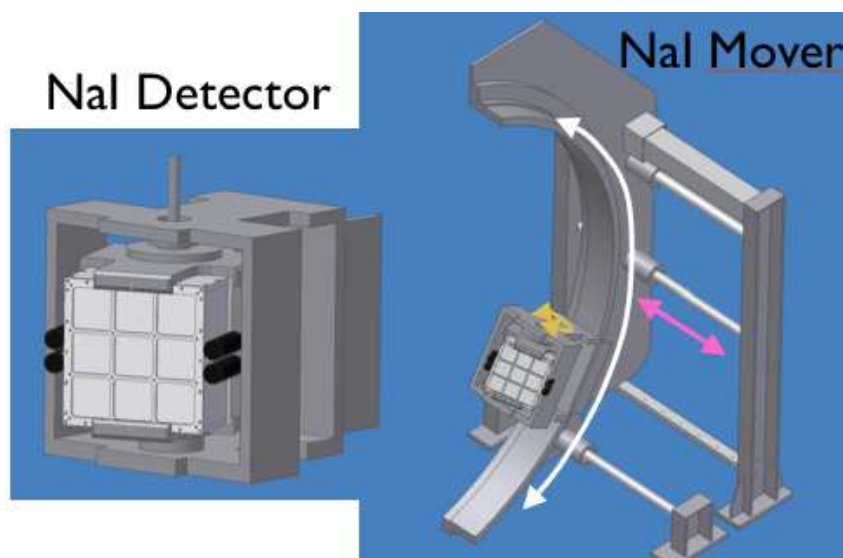


Figure 11.12: The NaI detector and its positioning device. The degrees of freedom of the motion are shown.

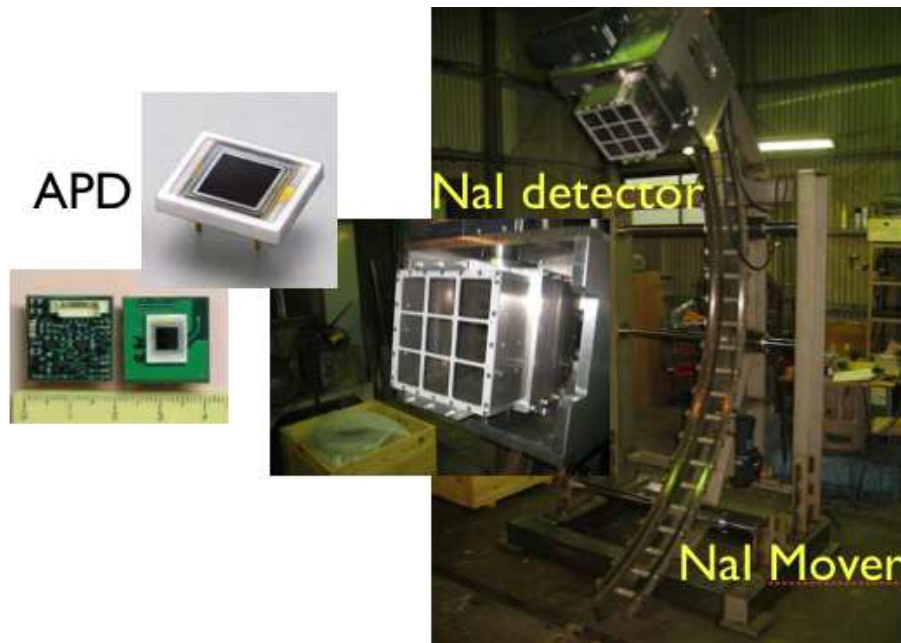


Figure 11.13: *The NaI detector, its positioning device and the APDs.*

11.5 Conclusions

The CEX reaction provides a very effective calibration method. A π^- -beam is required and consequently a change in the beam-polarity. The method is therefore associated with a time consuming preparation. A hydrogen target must be used and positioned at the COBRA center. A long running time is needed to scan the detector completely.

The method cannot be often applied. We plan to repeat it twice per year.

Chapter 12

Timing counter tuning with the proton accelerator

The proton reactions producing the γ 's used for the LXe calorimeter energy calibration and for monitoring its stability, uniformity and purity, can also be used to optimize the performance of the timing counter (TC) detector.

In this chapter we present the preliminary results obtained for the PMT charge and time equalization. We discuss the possible hardware improvements to obtain the most effective method for the absolute timing of the TC and of the LXe calorimeter.

12.1 Introduction

We mainly discuss the tuning of the TC detector (made of 30 scintillator bars and 60 PMTs; see section 3.3.3) associated with the use of the C-W accelerator.

The TC calibration follows a two-step procedure, dependent on the processing of the PMT information: (1) the charge calibration and (2) the timing calibration.

The first step deals with the PMT signal equalization of a particular bar (in other words: the relative gains of the PMTs of that bar are determined), and to equalize, for all bars, the signals corresponding to a defined particle energy loss. Energy and position information is then optimized (even if the TC is not a good calorimeter).

The second step repeats the previous scheme applying it to the PMT timing.

The parameters that are related to the light propagation in the scintillation bar, such as the effective velocity and the effective attenuation length, are also determined. Before presenting the relevant algorithms, we briefly discuss the measurement of the energy loss, interaction point and impact time of a ionizing particle crossing the TC.

One PMT is mounted at each end of all the plastic scintillator bars. Fig. 12.1 shows a simplified scheme. The intensity of the light measured at one end of the bar exponentially decreases as a function of the distance from the particle crossing point. If the length of the bar is L , the crossing point is z and the origin of our reference system is at the center of the bar, the amplitude A_L of the signal of the left PMT is:

$$A_L = a_L \cdot E_{dep} \cdot e^{-\frac{1}{\lambda_{eff}} \cdot (\frac{L}{2} + z)} \quad (12.1)$$

where a_L is a proportionality coefficient (which takes into account several effects like: the number of photons produced per MeV of deposited energy, the fraction of all photons which start propagating along the bar, the PMT characteristics: QE , g , etc.), E_{dep} is the energy deposited by the ionizing particle and λ_{eff} is the bar attenuation length. Similarly, for the right PMT, we write:

$$A_R = a_R \cdot E_{dep} \cdot e^{-\frac{1}{\lambda_{eff}} \cdot (\frac{L}{2} - z)}. \quad (12.2)$$

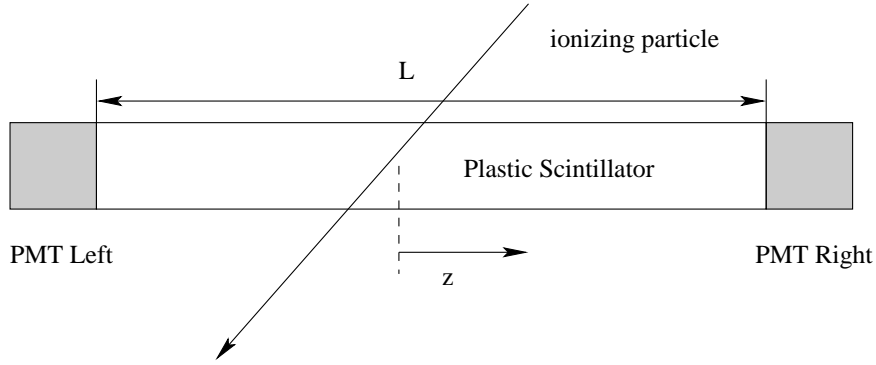


Figure 12.1: A scheme of the Timing Counter bar with its PMTs. A crossing particle is also shown.

Multiplying eq. (12.1) and eq. (12.2), we obtain:

$$A_L \cdot A_R = a_L \cdot a_R \cdot E_{dep}^2 \cdot e^{-\frac{L}{\lambda_{eff}}} \quad (12.3)$$

and then

$$E_{dep} \propto \sqrt{A_L \cdot A_R}. \quad (12.4)$$

The square root of the product of the two PMT signals is a measure of the total scintillation light, independent of its origin within the bar.

By dividing one signal by the other, we obtain:

$$\frac{A_L}{A_R} = \frac{a_L}{a_R} \cdot e^{-\frac{2z}{\lambda_{eff}}} \quad (12.5)$$

and then

$$\ln \frac{A_L}{A_R} = \ln \frac{a_L}{a_R} - \frac{2z}{\lambda_{eff}}, \quad (12.6)$$

or

$$z = \frac{\lambda_{eff}}{2} \left(\ln \frac{a_L}{a_R} - \ln \frac{A_L}{A_R} \right); \quad (12.7)$$

The logarithm of the ratio of the two PMT signals is therefore linearly connected with the position at which the scintillation occurs. On the other end, the impact point can also be determined by subtracting the two PMT signal times. The times measured by the two PMTs are t_R and t_L ; one can write the expressions:

$$\begin{aligned} t_L &= T_{TC} + \left(\frac{L}{2} + z \right) \cdot \frac{1}{v_{eff}} + b_L + \frac{c_L}{\sqrt{A_L}} \\ t_R &= T_{TC} + \left(\frac{L}{2} - z \right) \cdot \frac{1}{v_{eff}} + b_R + \frac{c_R}{\sqrt{A_R}} \end{aligned} \quad (12.8)$$

where T_{TC} is the particle crossing time on the TC, v_{eff} is the photon effective velocity along the bar, b_L and b_R are the time offsets (differences in cable length, PMT transit time, etc.) and c_L and c_R are the time walk correction distortion constants (time walk distortions are automatically present in measured times).

We are interested in a correct determination of the measured crossing times t_L^* and t_R^* ; we therefore purge t_L and t_R from the time walk effects (that is: we introduce time walk corrections) defining:

$$\begin{aligned} t_L^* &= t_L - \frac{c_L}{\sqrt{A_L}} = T_{TC} + \left(\frac{L}{2} + z \right) \cdot \frac{1}{v_{eff}} + b_L \\ t_R^* &= t_R - \frac{c_R}{\sqrt{A_R}} = T_{TC} + \left(\frac{L}{2} - z \right) \cdot \frac{1}{v_{eff}} + b_R \end{aligned} \quad (12.9)$$

where t^* is the corrected time. The difference between t_L^* and t_R^* is what is related to z :

$$\Delta t^* = t_L^* - t_R^* = \frac{2z}{v_{eff}} + (b_L - b_R); \quad (12.10)$$

z can be written in terms of Δt^* as the following:

$$z = \frac{v_{eff} \cdot \Delta t^*}{2} - \frac{v_{eff} \cdot (b_L - b_R)}{2}$$

$$C = -\frac{v_{eff} \cdot (b_L - b_R)}{2} = -\frac{v_{eff} \cdot (\Delta b)}{2} \quad (12.11)$$

where C contains the offsets between the two PMTs. Combining eq. (12.6) and eq. (12.11) we correlate $\ln(A_L/A_R)$ and $\Delta t^* = t_L^* - t_R^*$, and we obtain:

$$\ln \frac{A_L}{A_R} = \ln \frac{a_L}{a_R} - \frac{v_{eff}}{\lambda_{eff}} \cdot (\Delta t^* - \Delta b). \quad (12.12)$$

This expression allows the experimental determination of v_{eff}/λ_{eff} . It is worth noting that Δb is responsible of the fact that the Δt^* distribution is not centered to zero.

In conclusion: the energy deposited by the ionizing particle is proportional to the square root of the product of the two PMT charges; the coordinate of the interaction point is proportional to the logarithm of the ratio of the two PMT charges. The coordinate of the interaction point is also proportional to the time difference of the two PMT signals (as discussed in section 12.3).

12.2 The PMT gain equalization

In this section we develop the algorithm for the charge equalization between PMTs of the same bar (PMT equalization), and between the different bars (bar equalization). We present the results.

We start from the eq. (12.12):

$$\ln \frac{A_L}{A_R} = \ln \frac{a_L}{a_R} - \frac{v_{eff}}{\lambda_{eff}} \cdot (\Delta t^* - \Delta b) \quad (12.13)$$

and we plot the logarithm of the ratio of PMT signal amplitudes $\ln(A_L/A_R)$ against the time difference Δt^* of the PMT signals. We checked that in the region of interest $\Delta t^* \approx \Delta t$.

At present, the information from the Timing Counter optical fibers (z information) is still unavailable. The consequence is a certain arbitrariness in defining the limits of the accepted event region for the two variables $\ln(A_L/A_R)$ and $\Delta t = t_L - t_R$ (the fitted parameters weakly depend on this choice). The presently adopted method is to select events whose variables correspond to the region 5%-95% of the integral distribution. Note that if one changes these limits by $\pm 5\%$ the effective velocity changes by $\approx 5\%$, which gives a measure of the associated systematic error (the corresponding systematic error on the attenuation length is $\approx 10\%$). One hopes that, when the fiber information is available, the systematic error might be reduced.

From eq. (12.13) it follows that the (ordinate) intercept of this straight line is the charge equalization coefficients $g = \ln(a_L/a_R)$ and the slope m is the ratio of the bar effective light velocity and light attenuation length: $m = \frac{v_{eff}}{\lambda_{eff}}$. We evaluate the effective velocity by using the expression $v_{eff} = L/\Delta t$, where L is the bar length (we assume that the bar is wholly illuminated). We calculate λ_{eff} by the relation $\lambda_{eff} = v_{eff}/m$.

In conclusion we obtain, for each bar:

- the g coefficient (a measurement of the PMT relative gains);
- the v_{eff} effective velocity;
- the λ_{eff} attenuation length.

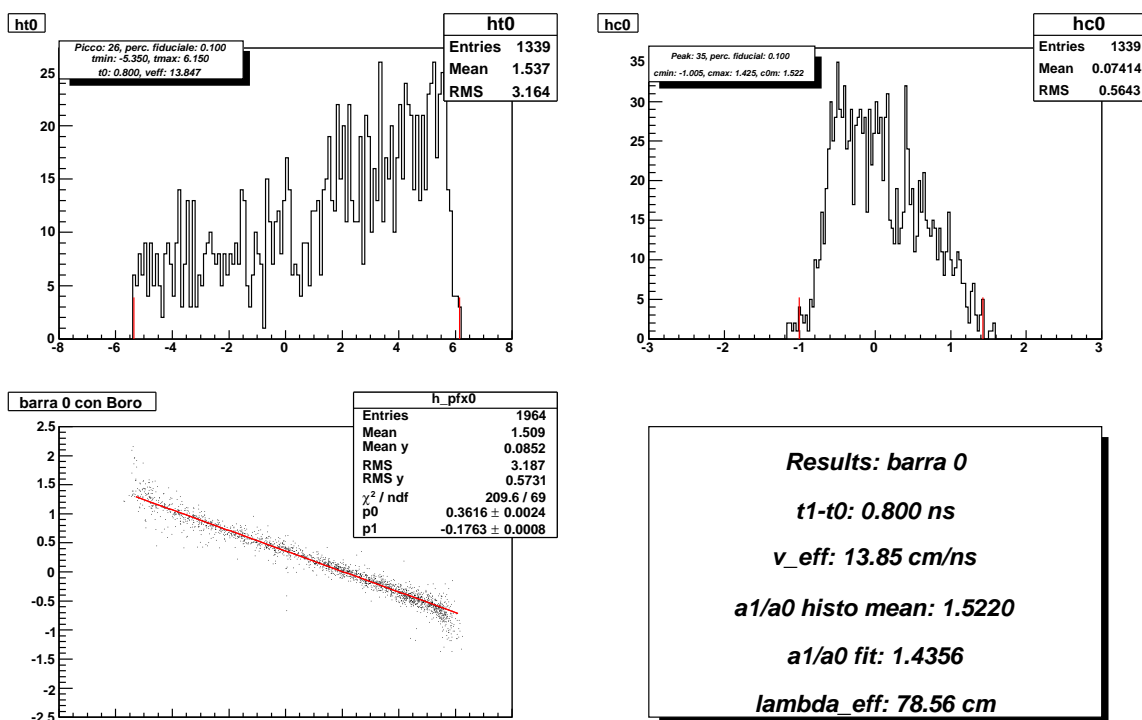


Figure 12.2: (Top, left) The distribution of the time differences (Δt in ns) relative to the two PMT signals of the same bar. (Top, right) The distribution of $\ln(A_L/A_R)$. (Bottom, left) The distribution $\ln(A_L/A_R)$ vs Δt^* . (Bottom, right) A linear fit results.

The results of the analysis on γ data produced by the Boron reaction are presented in Fig. 12.2. The first plot shows the distribution of the time difference Δt for one bar; the second plot shows the distribution of the logarithm of the charge ratio, $\ln(A_L/A_R)$; the third plot shows $\ln(A_L/A_R)$ versus Δt .

The results for the effective velocity of all bars are presented in Fig. 12.3. The data are those regarding Boron (B) and Lithium Fluoride (LiF) reactions, and from cosmic ray (CR) events. The distribution profiles are similar, thus confirming the consistency of the various methods (only statistical errors are shown).

Fig. 12.4 presents the attenuation length (cm) measured for each bar and the attenuation length distribution for all bars. The data are relative to B, LiF and CR events. Only statistical errors are shown.

To perform the charge calibration among bars we need distributions due to events depositing a fixed energy in the bars. Whatever the nature of the events, the corresponding distributions must be similar in shape (even if shifted in energy). Here we present the results obtained with the cosmic ray (high statistics) sample.

Fig. 12.5 shows the distribution of the energy deposited by cosmic rays in a single bar, using eq. (12.4). A Landau distribution, as expected.

Fig. 12.6 (top) and (middle) shows distributions from several bars (no charge equalization, top; with charge equalization, middle). The improvement due to the charge equalization can be appreciated in Fig. 12.6 where the deposited energy in all bars is plotted (bottom). The Landau distribution becomes sharper when the charge equalization correction is applied.

Cosmic rays are unfortunately associated with some problems:

- the bars are not uniformly illuminated; the outer bars are often associated with multiple hits;
- cosmic ray directions are different from those of beam generated events.

The bar orientation was optimized for beam generated events. Michel positrons, B and LiF events (coming from the target) would be more appropriate. The use of Michel positrons needs full tracking, while γ 's coming from a B or LiF target would be simpler to use. When interacting with the TC bars γ generate energy deposits due to the Compton effect, up to an energy corresponding to the Compton edge. The rate of such events is typically $R_B \approx 1\text{Hz}/\text{bar}$ and $R_{LiF} \approx 2\text{Hz}/\text{bar}$, but cosmic rays represent an important high energy background (cosmic ray rate is $R_{CR} \approx 1\text{Hz}/\text{bar}$).

In order to:

- operate in a background-free environment;
- obtain an absolute timing reference, useful for the TC and the LXe time calibration,

we proposed a small modification of the present experimental set-up, which is discussed at the end of this chapter.

12.3 The PMT time fine-tuning

The determination of the relative timing of the two PMT signals of each bar and then the determination of the relative timing among the signals of all bars is an important part of the MEG tuning.

In this section we present the strategy for the TC time calibration. We focus on the method associated with the use of the C-W accelerator.

We rewrite here the equations refer to t_L and t_R , the times measured by the two PMTs of each TC bar (Fig. 12.1):

$$\begin{aligned} t_L &= T_{TC} + \left(\frac{L}{2} + z\right) \cdot \frac{1}{v_{eff}} + b_L + \frac{c_L}{\sqrt{A_L}} \\ t_R &= T_{TC} + \left(\frac{L}{2} - z\right) \cdot \frac{1}{v_{eff}} + b_R + \frac{c_R}{\sqrt{A_R}} \end{aligned} \quad (12.14)$$

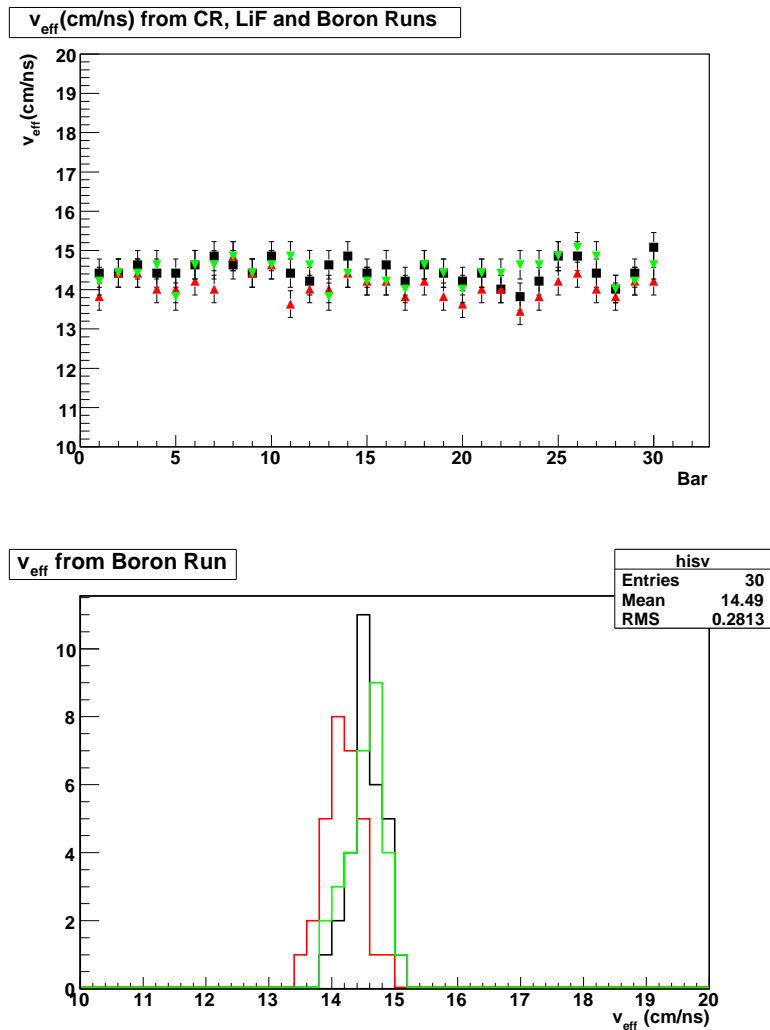


Figure 12.3: (Top) The effective velocity for each TC bar (statistical errors only). Boron (B, red triangle) and Lithium Fluoride (LiF, green triangle), Cosmic Rays (CR, black square). (Bottom) The velocity distribution for all bars and for each target (B: red, LiF: green and CR: black).

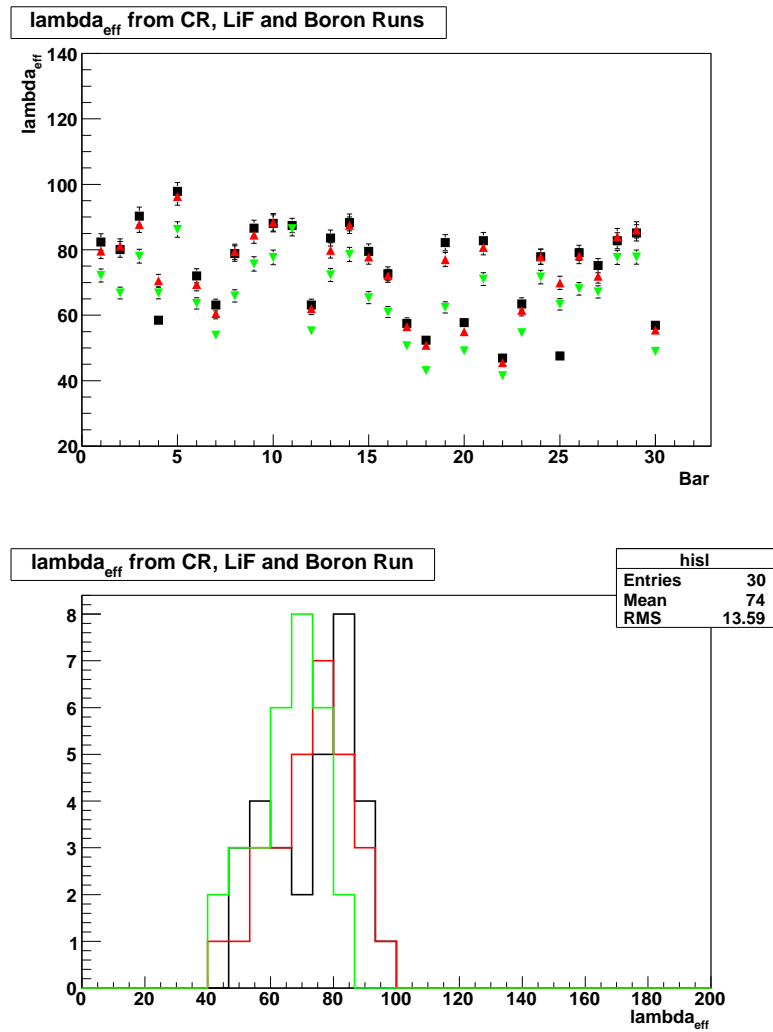


Figure 12.4: (Top) The measured attenuation length (cm) for each TC bar (statistical errors only). The data are relative to Boron (B, red triangle), Lithium Fluoride (LiF, green triangle) and Cosmic Ray events (CR, black square). (Bottom) The attenuation length distribution for all bars (B red, LiF green and CR black).

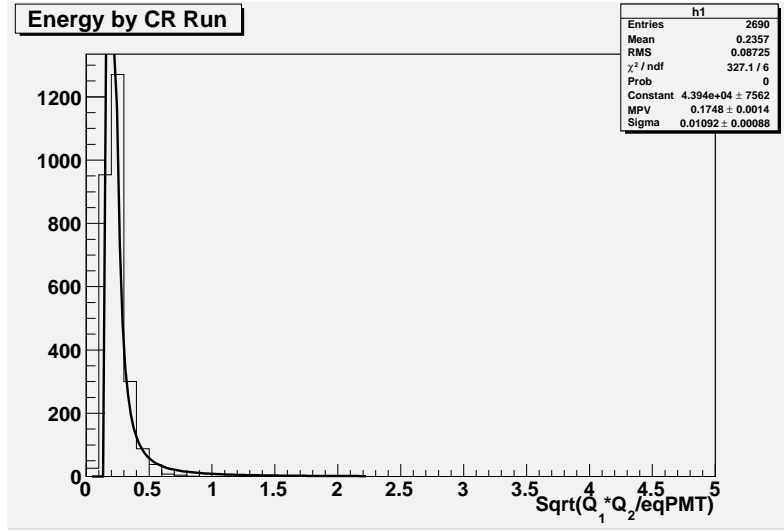


Figure 12.5: *The Landau distribution in one TC bar. Cosmic Ray events.*

where T_{TC} is the e^+ positron impact time on the TC, b_L and b_R are the time offsets and c_L and c_R are the time walk correction constants. The information that we want to extract is T_{TC} :

$$T_{TC} = \frac{t_L + t_R}{2} - \frac{L}{2v_{eff}} - \frac{b_L + b_R}{2} - \frac{1}{2} \cdot \left(\frac{c_L}{\sqrt{A_L}} + \frac{c_R}{\sqrt{A_R}} \right), \quad (12.15)$$

which is the arithmetic mean of the time measured by the two PMTs minus the constant terms, present in the eq. (12.15), which we need to know.

The bar offsets, defined as:

$$C_{offset} = \frac{L}{2v_{eff}} + \frac{b_L + b_R}{2}, \quad (12.16)$$

will be measured by using a laser system. A green light ($\lambda = 532$ nm), distributed by optical fibers, illuminates the center of each bar, allowing the precise evaluation of the (relative) C_{offset} in eq. (12.16). The laser system is presently not implemented.

As an alternative way for obtaining the relative timing between the two PMTs of each bar is based on events evenly distributed along the bar; the distribution of the two PMT time difference must be zero centered. This analysis can use Cosmic Ray or Boron data. In the first case one expects a zero centered flat distribution (any time shift from zero, represents a correction factor to be applied). In the second case the distribution is not flat because of the non-spherical symmetry of the TC relative to the target.

Fig. 12.7 shows the distribution of the time difference of two PMTs of one of the bars, by using cosmic ray data.

The time walk corrections are determined by using the available Michel data (we do not discuss this point here).

The last step of the calibration is the timing among bars.

The timing among bars must be based on coincident events. They occur for a fraction of the Michel positrons or of the LiF γ 's, when hits affect two adjacent bars. One can otherwise use the coincident γ 's from the Boron reaction. This method is applicable also to the timing of non-adjacent bars or of two TC sections (see Fig. 12.8). One γ is detected by the LXe calorimeter and the other by the TC detector. The mean of LXe-TC time difference for each bar $\Delta T_{\gamma\gamma}$ is

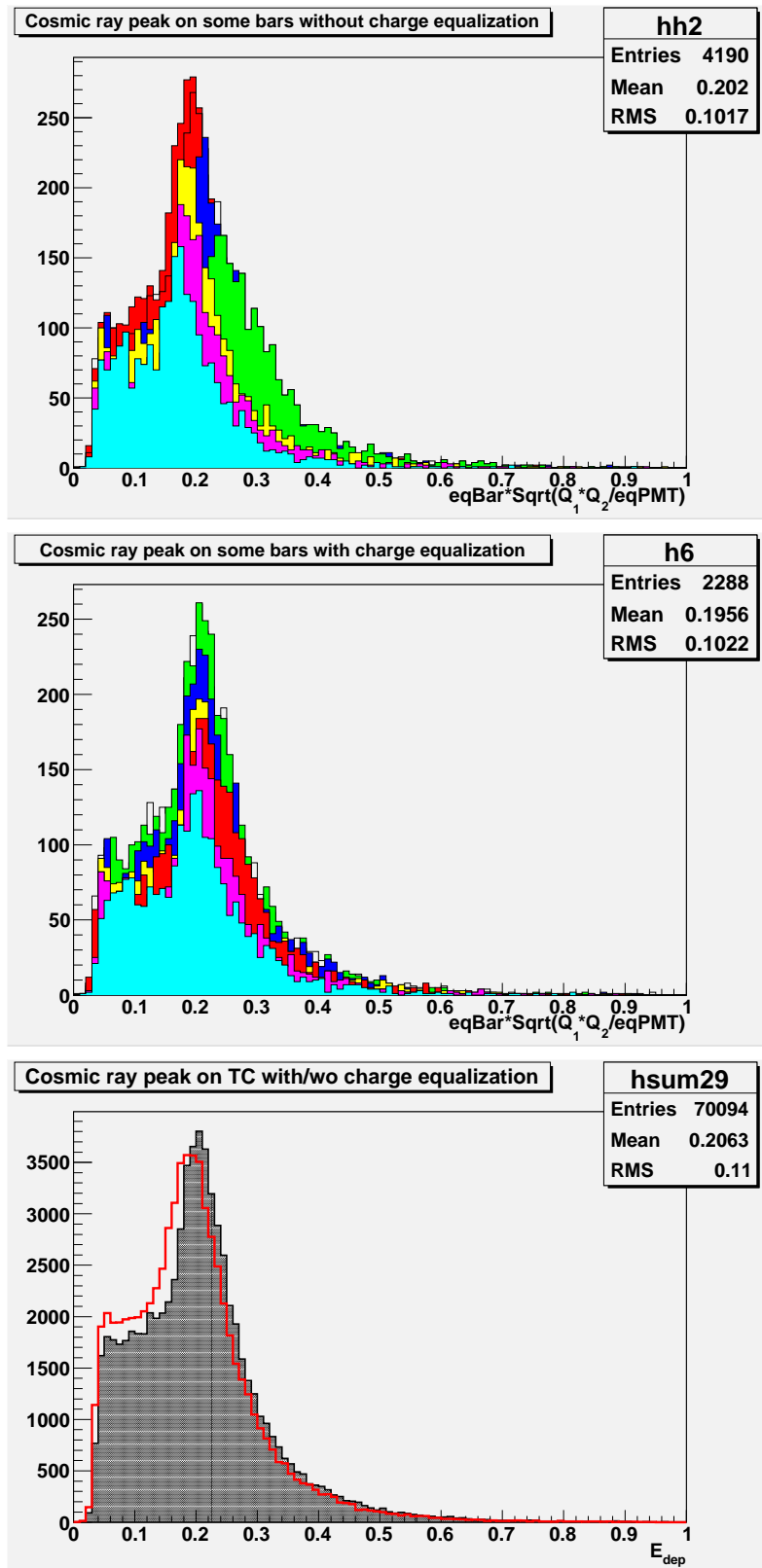


Figure 12.6: (Top) The deposited energy from cosmic ray events in several TC bars (no charge equalization). (Middle) The same (with charge equalization). (Bottom) The energy distribution for all bars: in red (no charge equalization), in black (with charge equalization).

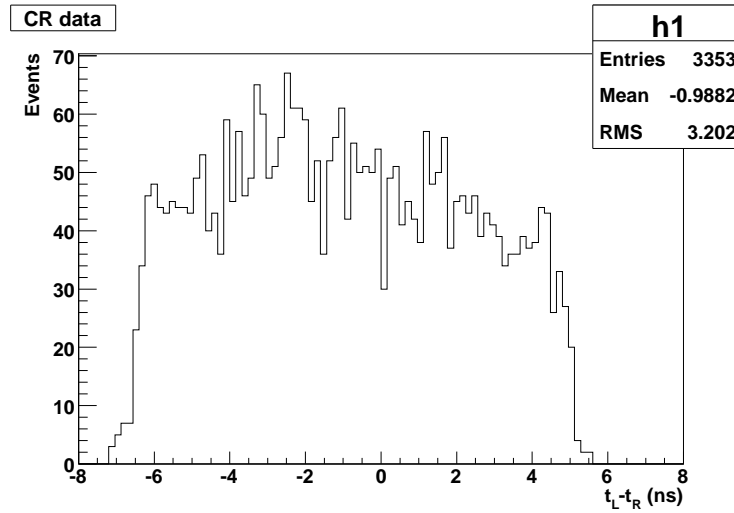


Figure 12.7: The distribution of the time difference between the two PMTs of the same bar. Cosmic ray data.

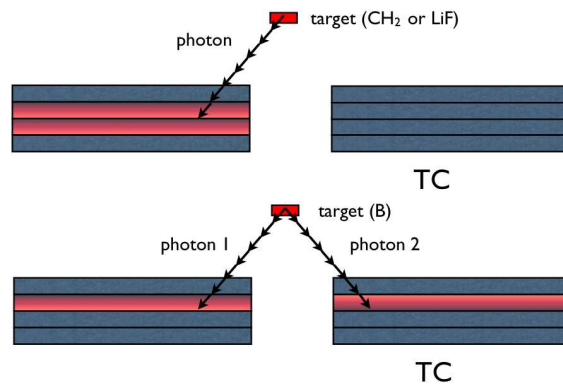


Figure 12.8: The LiF single γ 's or Michel positrons generating double hits in two adjacent bars of the TC (top). The two coincident γ 's from boron allow the timing also among non adjacent bars or between the two TC sections (bottom). The hit bars are highlighted in red.

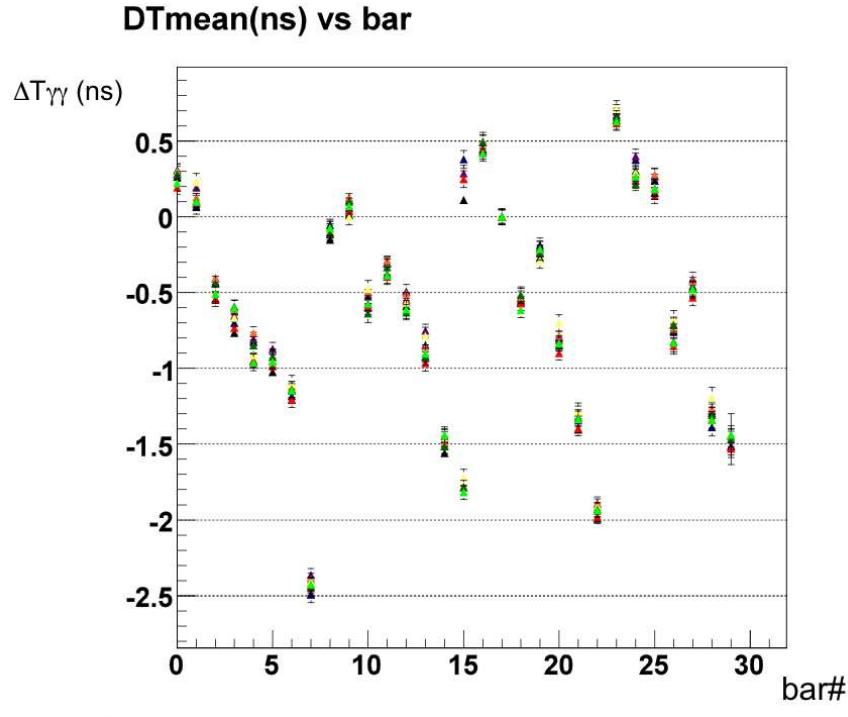


Figure 12.9: The ΔT between the two γ 's from the boron reaction, one detected by the LXe, the other by the TC, as a function of the bar number.

measured, from which the relative interbar timing is easily obtained (see Fig. 12.9). The different colors correspond to measurements in different periods (September: black \rightarrow December: green). The relative bar timing appears to be stable within 200-300 ps.

12.4 The timing of all MEG detector elements and plans for a new hardware

In the future, the boron reaction might be used for timing each MEG detector element. The low energy γ from boron would be detected by a fast scintillator and PMT assembly, mounted at the end of the proton beam line. The higher energy boron γ would be detected by the LXe calorimeter or would be converted and detected by a TC.

Table 12.1: YAP scintillator properties.

| | |
|-------------------------------|-------------------|
| Chemical formula | YAlO ₃ |
| Density (g/cm^3) | 5.37 |
| Emission (nm) | 350-360 |
| Decay constant (ns) | 28 |
| Light yield (ph/MeV) | 18000 |
| Refraction index | 1.95 |
| Hygroscopic | No |
| Melting point ($^{\circ}C$) | 1875 |

Fig. (12.10) presents the detailed set-up. A YAP crystal (a very fast scintillator, good for

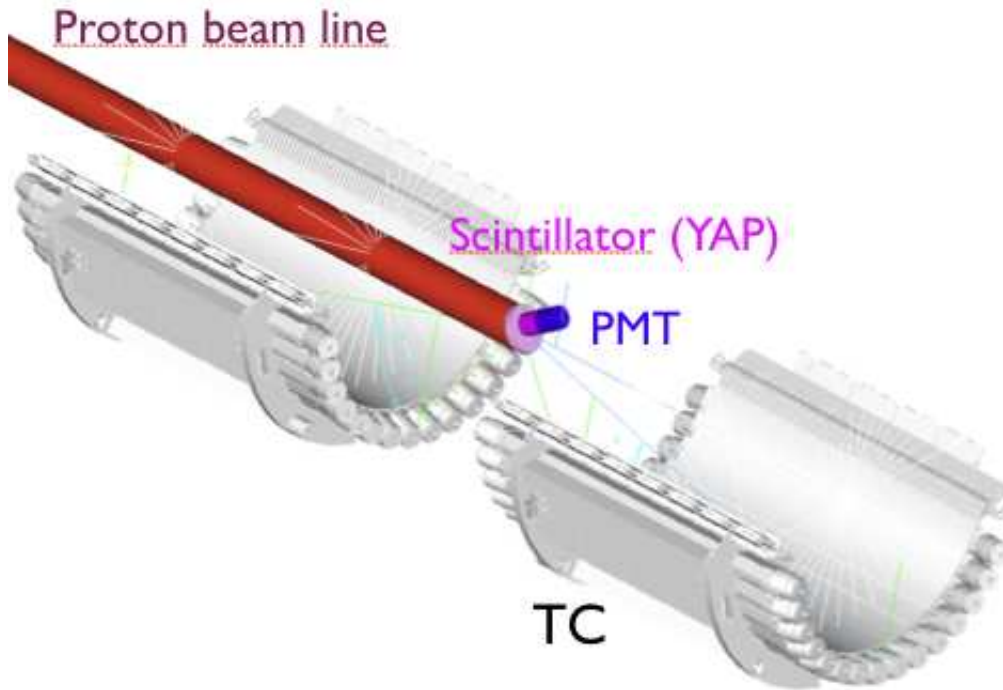


Figure 12.10: *Experimental set-up, to be mounted at the end of the proton beam line, for the absolute time calibration of each MEG detector element. The TC is shown together with the YAP scintillator and its PMT assembly.*

timing) with a high light yield (for a good energy spectroscopy), is mounted at the end of the beam line. Its characteristics are summarized in Tab. 12.1. The PMT must be carefully selected, since it is mounted at the COBRA centre, where the magnetic field intensity reaches 1.25 T. A fine mesh PMT (similar to the ones of the TC) should do the job if its axis is kept at 30° relative to the the magnetic field direction [66, 67]. The position of the YAP+PMT assembly is optimized to obtain:

- a TC completely illuminated by the high energy γ 's;
- the highest efficiency for detecting the low energy γ hitting the YAP crystal face.

The expected rate of γ -coincidences, at a proton current of $I_p = 1 \mu\text{A}$ and at a proton energy of $E_p = 1 \text{ MeV}$, is about 2 Hz/bar in a background-free situation.

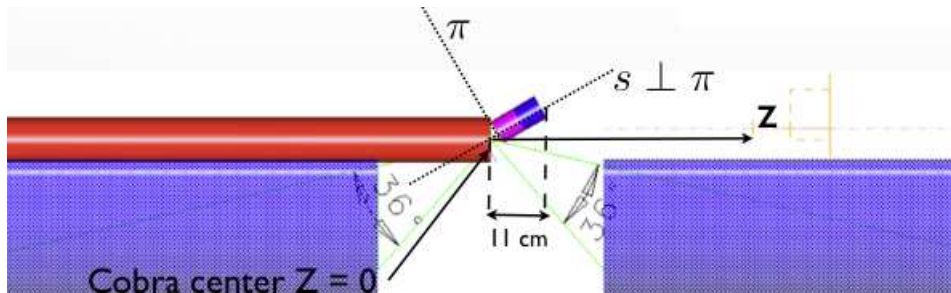


Figure 12.11: *The experimental set-up optimizing the TC absolute time calibration.*

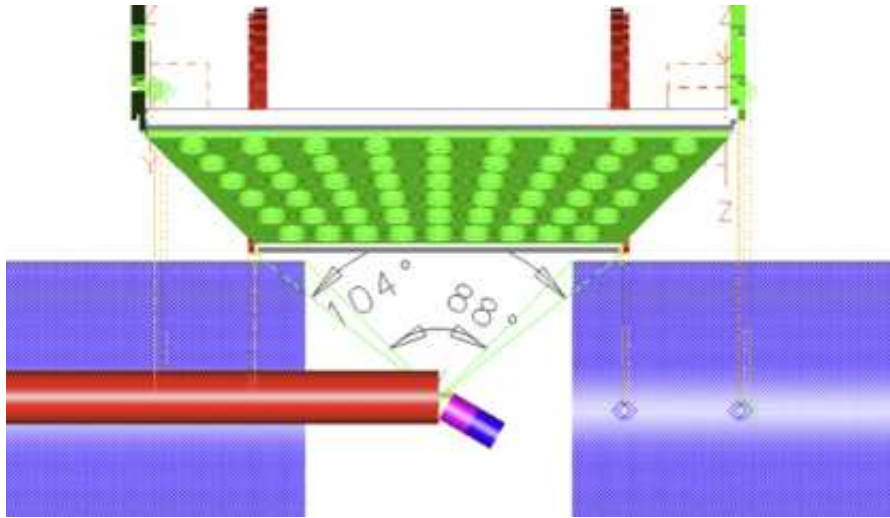


Figure 12.12: *The LXe absolute time calibration. The LXe detector, the TC, the YAP crystal and PMT assembly are shown. The experimental set-up is rotated relative to the one of the TC calibration to optimize the γ rate in the LXe calorimeter.*

During the timing of the LXe calorimeter the orientation of the YAP+PMT assembly must however be changed to optimize the γ -rate in the calorimeter (see Fig. 12.11). Since the YAP+PMT assembly is in air, its orientation can be varied without breaking the vacuum in the proton beam line (see Fig 12.12).

The expected rate of γ -coincidences in this configuration, at $I_p = 1 \mu A$ and at a proton energy of $E_p = 1 \text{ MeV}$, is about 500 Hz.

In conclusion: an absolute time calibration of all MEG detector elements can be performed using the C-W accelerator. We are planning to introduce the new necessary hardware during 2009.

Chapter 13

The time fine-tuning between the LXe calorimeter and the timing counter

The relative $e^+ - \gamma$ timing is one of the four variables used to identify the $\mu^+ \rightarrow e^+\gamma$ decay and it is essential in rejecting the accidental background. The e^+ is detected by the TC and the γ by the LXe calorimeter. We expect a time resolution of $\Delta t(\text{FWHM}) \approx 100$ ps for each of these devices. Note that the MEG timing resolution is a major improvement compared to that of previous $\mu^+ \rightarrow e^+\gamma$ searches.

A method based on the ${}^{11}_5\text{B}(p, \gamma){}^{12}_6\text{C}$ nuclear reaction induced by the MEG C-W accelerator was developed to precision timing between the LXe calorimeter and the TC.

This boron reaction is the only one, based on a natural element, that emits two time-coincident gamma-rays at MeV energies (4.44 MeV and 11.6 MeV). One of the γ 's is detected by the calorimeter, the other is converted and detected by the TC. They follow straight trajectories in reaching the two detectors, while the positron trajectory from $\mu^+ \rightarrow e^+\gamma$ or μ^+ radiative decays must be fully tracked in the COBRA spectrometer. The boron method stands out for its simplicity; it can moreover be used during periods of unavailable muon beam.

13.1 The boron thick-target excitation curve and the γ spectra

In the chapter 10 we discussed the ${}^{11}_5\text{B}(p, \gamma){}^{12}_6\text{C}$ nuclear reaction and we presented the results of the preliminary Legnaro measurements.

The reaction is resonant at 163 keV, with $\sigma_{\gamma 1} = 2$ mb and $\Gamma_{\gamma 1} = 5$ keV.

We are interested in the two γ 's coincidence rate. One must take into account the solid angles and the efficiencies of the two detectors and the probability that one of the γ 's converts in the TC.

Extrapolating from the Legnaro measurements one can estimate the expected rate of the calorimeter-TC coincidences in MEG. The result is: 0.25 Hz, a rather low value (corresponding to an overall detection efficiency $\epsilon_D \approx 0.002$).

The coincidence rate might be increased by increasing the C-W current, but this is presently limited to a maximum current $I_p = 1 \mu\text{A}$ by the Swiss ministry of health. Another possibility is to use the accelerator at the maximum energy $T_p = 1$ MeV (instead of $T_p \approx 200$ keV), in association with a thick target. At $T_p = 1$ MeV one integrates over a direct reaction contribution which is much greater than that corresponding to the resonance.

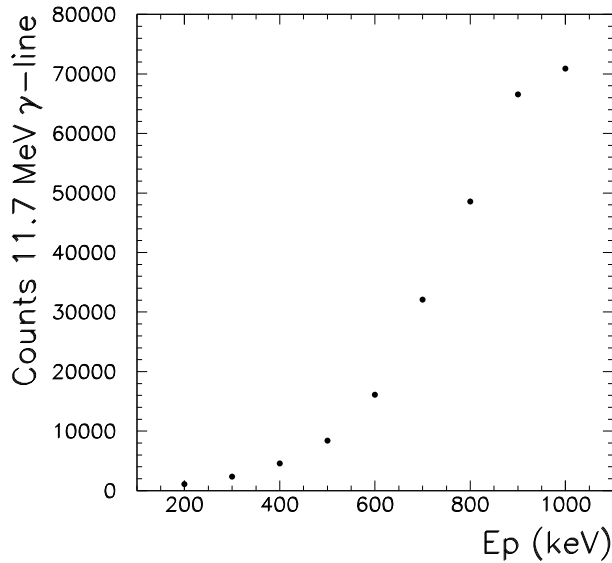


Figure 13.1: *Thick target excitation curve of the $^{11}\text{B}(p, \gamma)^{12}\text{C}$ reaction, as a function of the proton energy T_p . Rate of the 11.66 MeV γ_1 -line. Pure boron target.*

We performed a test with a thick pure boron target, to evaluate these different contributions.

The rate of the γ_1 -production as a function of the proton energy was measured by using a small NaI. Since the emission of the γ_1 -line is always associated with the emission of the 4.44 MeV-line, this measurement is also a determination of the number of potential coincidences.

Fig. 13.1 shows the B thick target excitation curve. It refers to the B γ_1 -line and clearly shows how important the direct production is. The B γ_1 -rate rate, or, in other words, the coincident rate, increases by a factor 80. As a consequence, at $I_p = 1 \mu\text{A}$ and $T_p = 1 \text{ MeV}$, we expect a γ -coincidence rate of 20 Hz between the LXe and the TC, reaching the maximal data acquisition capability.

The use of the C-W accelerator at energies higher than the one corresponding to the resonance spoils the quality of the γ -lines, with no consequence for the timing calibration. Fig. 13.2 shows the B γ -spectra, as a function of T_p , from 400 keV to 1000 keV. The Doppler shift (our detector is at $\approx 45^\circ$ relative to the beam line direction), and the γ_1 -line dependence on the proton energy can be appreciated. The different nature of the 4.44 MeV-line and of the γ_1 -line also appears: the first corresponds to the $^{12}\text{C}^*$ nuclear de-excitation, so its position is independent of the proton energy. We also notice that the relative branching ratio $\frac{\gamma_0}{\gamma_1 + \gamma_0}$ depends on T_p , increasing from 400 to 1000 keV.

13.2 Boron targets

One normally prepares boron targets by depositing a thin boron layer on a Cu disk with an electron beam evaporation technique (see section 10.1.1). However, if one is not interested in a thin film (thickness of a few μm) a convenient solution is to use pure boron, in the form of small chips glued together on a disk. Commercial boron compounds are also available, with well-defined shapes (i.e.: a cylindrical target). We studied, for instance, boron carbide B_4C behaviour. The pure B-target and the B_4C -target γ -spectra are compared in Fig. 13.3 (left, the two spectra are shifted because of

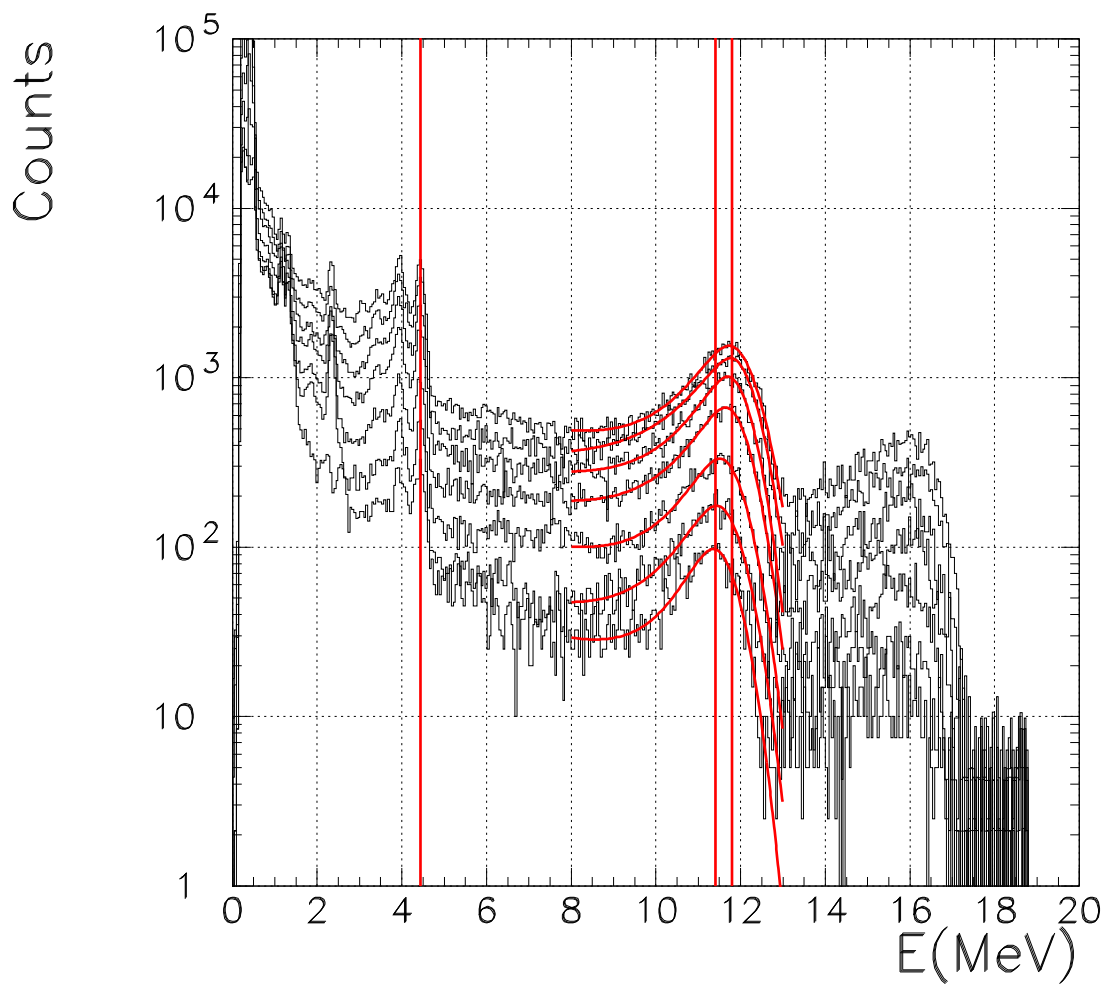


Figure 13.2: Boron γ -spectra as a function of T_p , from 400 keV to 1000 keV. The energy stability of the 4.44 MeV γ -line and the Doppler effect on the 11.66 MeV and 16.1 MeV lines are visible.

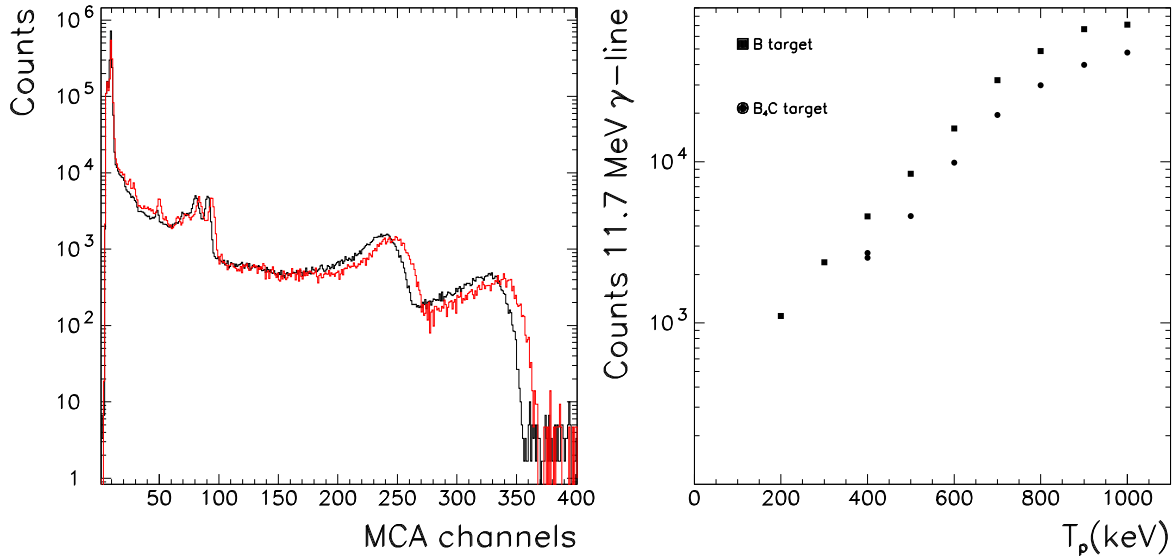


Figure 13.3: (Left) Boron-target and B_4C -target γ -spectra. The data were recorded at two different gains. (Right) Boron-target and B_4C -target γ production as a function of the proton energy. The data are with different solid angles.

the different PMT gains) and the γ -rate curves are compared in Fig. 13.3 (right, the two excitation curves are shifted because of the different solid angle used during the measurements). The carbon does not appreciably contribute to the γ -rate.

The pure B-target and the B_4C -target appear to be equivalent.

13.3 Lithium+boron targets

We investigated the possibility of carrying out both the LXe calorimeter energy calibration and the LXe calorimeter-TC timing calibration, with a single target (a boron and lithium compound), using the proper proton energy for each measurement.

One compound was $Li_2B_4O_7$, in the form of powder or crystal.

We prepared some tablets, by compressing the $Li_2B_4O_7$ powder at a pressure of 5000 Kg/cm². A mosaic of tablets was then assembled to form a target. The tablet production was further improved by sintering at a temperature of 950°. Harder tablets were obtained.

Another possibility for a boron and lithium compound target is the use of lithium triborate LiB_3O_5 small crystals, glued together on a Cu disk.

Fig. 13.4 shows the measured γ -spectra as a function of the proton energy.

We first checked the Li γ -line quality having in mind the LXe calorimeter energy calibration.

At an energy $T_p = 400$ keV, one can only see the B-lines, at 4.44 MeV and 11.66 MeV. The corresponding rate is rather low and the lines are therefore hardly visible. Nothing is seen at 16.1 MeV, since the corresponding rate is only ≈ 0.04 of the 11.66 MeV rate.

The Li γ -line is not visible because the proton energy is lower than the one of the Li resonance. At $T_p = 500$ keV the Li lines clearly emerge and dominate. The quality of the γ_0 Li-line, at 17.6 MeV, is preserved. In Fig. 13.5 we superimposed the γ -spectra obtained from the LiF-target (red line. γ -lines from the lithium and fluorine are visible) and from the $Li_2B_4O_7$ target (black line.

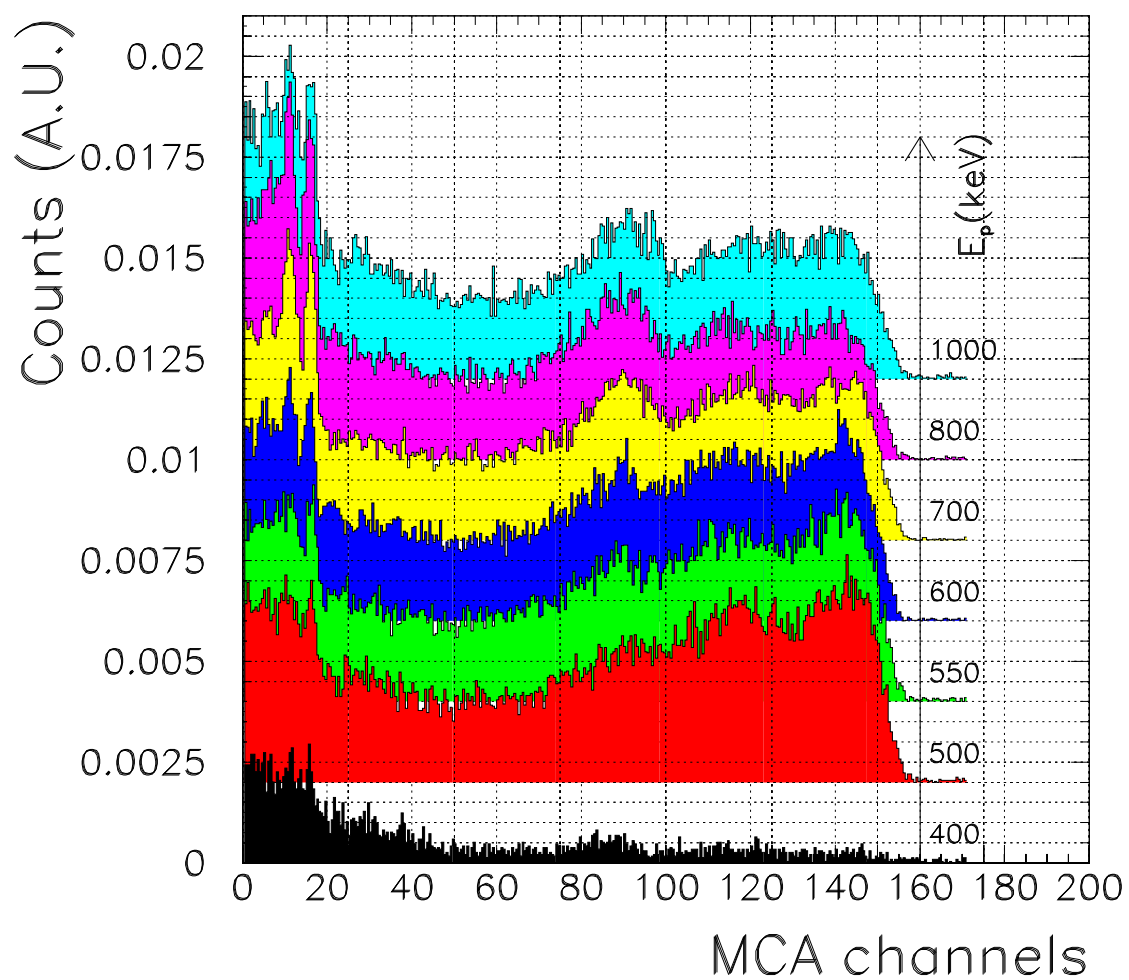


Figure 13.4: γ -ray spectra from the lithium tetraborate $\text{Li}_2\text{B}_4\text{O}_7$ -target, as a function of the proton energy.

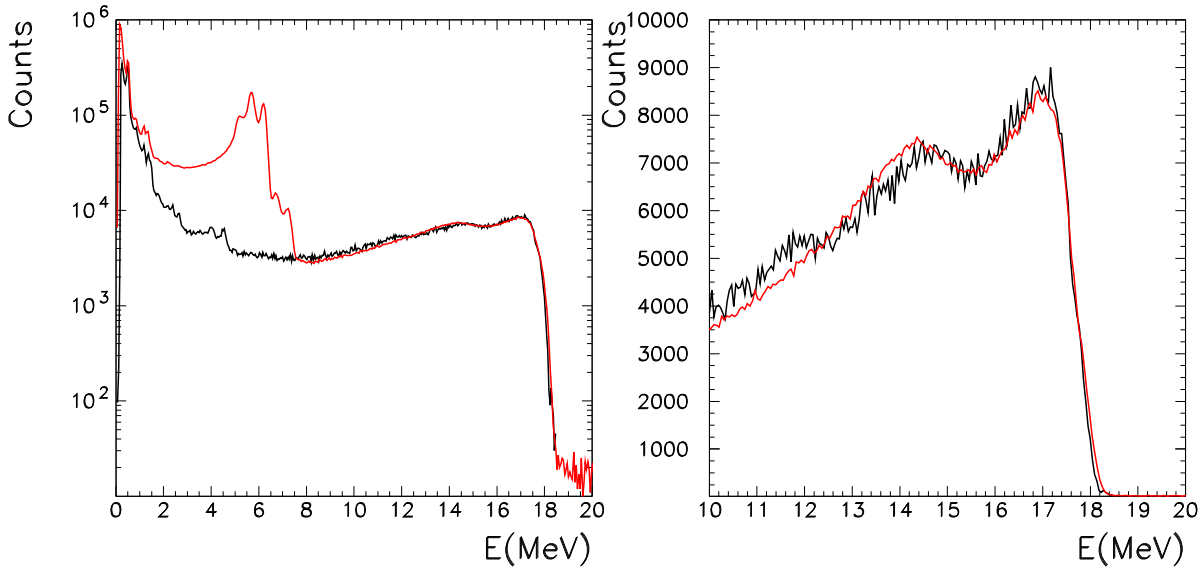


Figure 13.5: (Left) γ -spectra from the LiF-target (red) and the $\text{Li}_2\text{B}_4\text{O}_7$ -target (black). (Right) Zoom of the 17.6 MeV region.

The 4.44 MeV carbon γ -line is also visible).

At $T_p = 500$ keV the $\text{Li}_2\text{B}_4\text{O}_7$ and the LiF line qualities are equivalent, both acceptable for the LXe calorimeter energy calibration.

This results proved that a $\text{Li}_2\text{B}_4\text{O}_7$ target can be used in the MEG experiment. The Jinan Jinmaden Automation Technology Co. LTD provides us with $\text{Li}_2\text{B}_4\text{O}_7$ crystals.

The boron reaction study proved also that the γ -rate from boron increases, as expected, as a function of the proton energy.

Fig. 13.6 presents the different types of the boron-lithium compound targets.

13.4 The predictions of Monte Carlo method

The boron γ -coincidences between the LXe calorimeter and the timing-counter were simulated by the Monte Carlo method. Events were generated and “detected”. No attempt was yet made to fully reconstruct the events and to study the consequences of this procedure on the quality of the relative timing determination.

Fig. 13.7 shows the γ energy loss in the TC. Since the TC has no calorimetric properties, it was observed that only the two Compton edges corresponded to the ≈ 4.44 MeV and ≈ 11.66 MeV γ -rays, which are converted and detected in the TC. The overall efficiency for the detection of all the boron γ -coincidences, generated over the full solid angle and surviving all analysis selections, is $1.6 \cdot 10^{-3}$, corresponding to a possible acquisition rate of ≈ 20 Hz.

We studied how to increase this efficiency, by inserting thin converters close to the TC (up to $0.2 X_0$). Only marginal improvements were obtained. Such a difficult project was therefore abandoned.

Fig. 13.8 shows the distribution of the time difference between the TC and the LXe as a function



Figure 13.6: *The different boron targets. Upper target: pure boron. Lower targets, left: boron carbide B_4C , right: lithium tetraborate $Li_2B_4O_7$.*

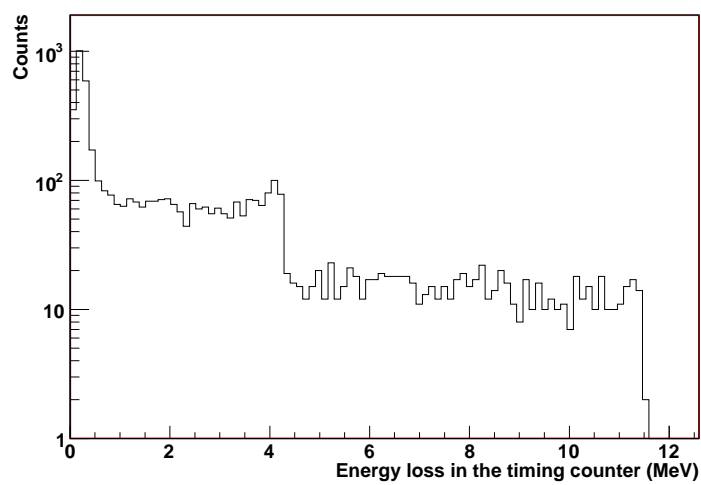


Figure 13.7: *The distribution of the energy loss in the timing counter.*

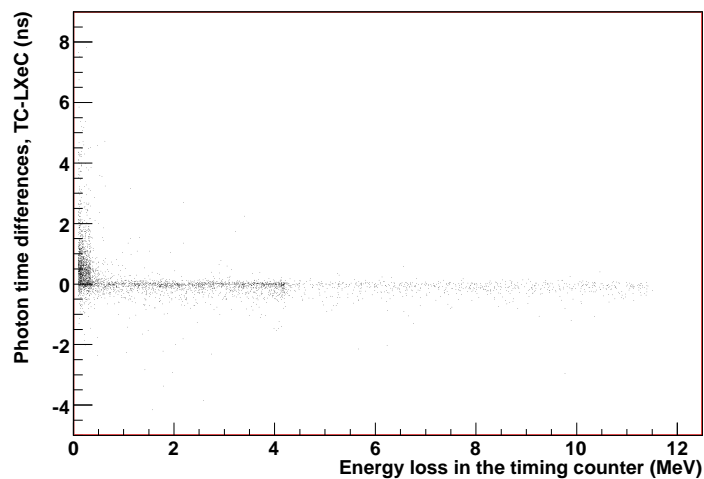


Figure 13.8: *The LXe-TC time difference as a function of the energy loss in the timing counter. No selection is applied.*

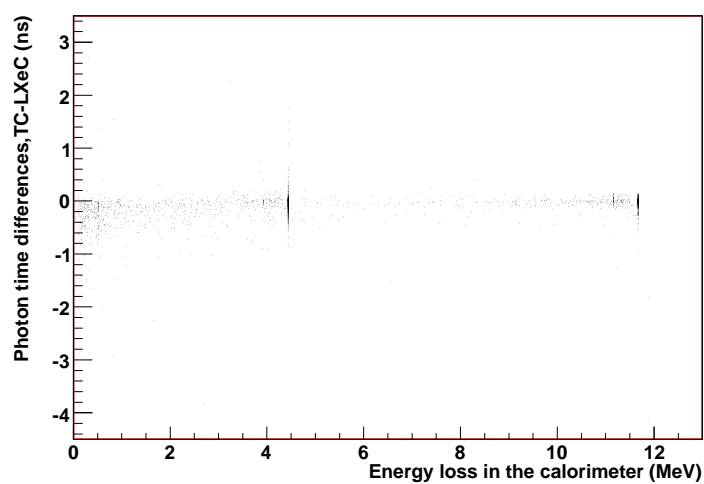


Figure 13.9: *The LXe-TC time difference as a function of the energy loss in LXe calorimeter. The selection $E_{loss}^{TC} > 1\text{MeV}$ is applied.*

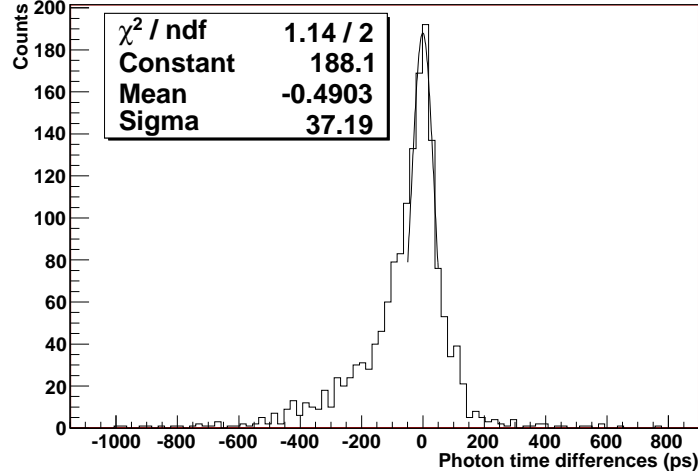


Figure 13.10: The LXe-TC time difference. The selections $E_{loss}^{TC} > 1 \text{ MeV}$ and $E_{loss}^{LXe} > 2 \text{ MeV}$ are applied.

of the energy loss in the TC. No selection was applied. At low energy, one has an accumulation of events due to γ 's that suffered early interactions and lost a large amount of their energy before reaching the TC. A selection $E_{loss}^{TC} > 1 \text{ MeV}$ eliminates such events.

Similar information for the LXe calorimeter is shown in Fig. 13.9 (the selection $E_{loss}^{TC} > 1 \text{ MeV}$ is applied). At low energy an event accumulation is also present, now visible at negative times, and due to the early interactions at the calorimeter side. Note that in the LXe calorimeter the B γ 's are seen as γ -lines.

The time-difference distribution is shown in Fig. 13.10. The selections $E_{loss}^{TC} > 1 \text{ MeV}$ and $E_{loss}^{LXe} > 2 \text{ MeV}$ are applied.

The limiting sensitivity of the boron method is $\sigma \approx 40 \text{ ps}$, as the result of the fit shows. Some small improvements, at the expense of a reduction of the number of events, are obtainable if one requires a greater energy-loss in the calorimeter.

Chapter 14

Calibration method based on PIXE

So far we have discussed the γ production, at a relatively high energy, by proton-induced nuclear reactions. Another electromagnetic radiation emission, at very low energy, is associated with the operation of the C-W accelerator: the Particle Induced X-ray Emission (PIXE) [190, 191, 192, 193].

It is worth remarking that electrostatic accelerators in the energy range 0-3 MeV are the machines most frequently used for PIXE, the rapidly developing X-ray spectroscopic technique used in medical physics, geology, environment, archeology, etc. An obvious advantage of PIXE, with respect to X-ray production by electromagnetic radiation, is that proton beams can be transported and focused, without loss of intensity, to small and even micrometer sizes. In addition to that, the X-ray signal dominates over a much smaller bremsstrahlung background.

X-ray production might be put to use for the MEG experiment. A variable intensity source of monochromatic and tunable X-rays at the center of COBRA might help in monitoring the efficiency and the behaviour of the Drift Chamber System. It is worth noting that a fraction of the X-ray events can be tagged in the case of multi-step transitions, although at the price of a strong reduction in intensity.

14.1 The particle induced X-ray emission

When a target is bombarded by protons an electron might be ejected from the atomic inner shells, creating a vacancy. We list possible different causes for vacancies:

1. bombardment by electrons;
2. bombardment by protons, deuterons, α -particles, or other ions from accelerators;
3. irradiation by primary X-rays from high- or low-power X-ray tubes;
4. irradiation by α -, β -, γ -, and/or X-rays from radioisotopes;
5. irradiation by secondary X-rays from a target element, following a primary irradiation.

The filling of the vacancy leads to the emission of X-rays which are characteristic of the excited element. They are labeled K, L, M etc. to denote the shells they originated from. Another label is added (α , β or γ) to mark the transition of electrons from higher shells. Since within a shell there are multiple orbits of higher and lower binding energy, the transitions are further labelled (α_1 , α_2 or β_1 , β_2 , etc.) (see Fig. 14.1).

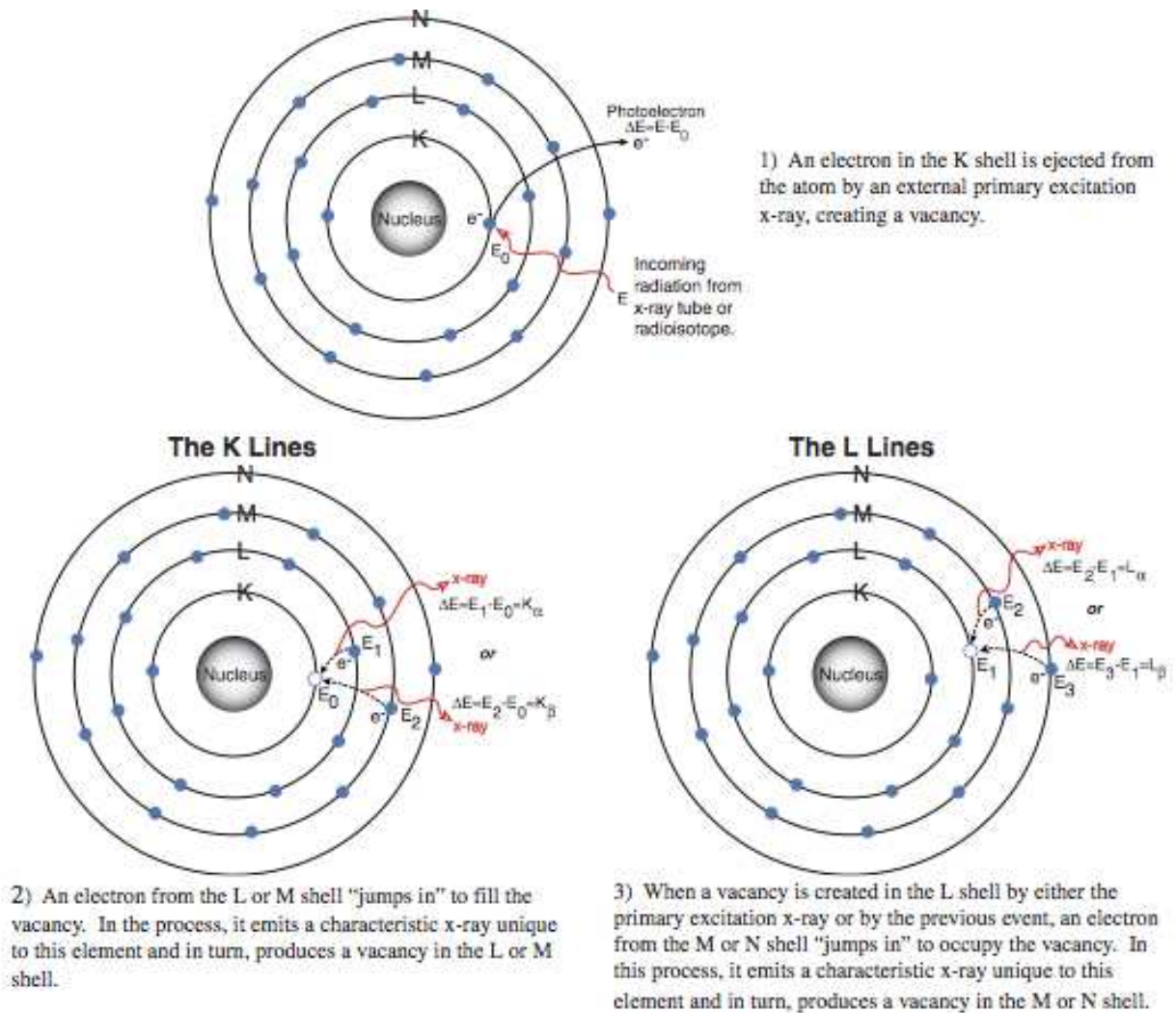


Figure 14.1: *The X-ray emission (titanium). The exciting radiation is also an X-ray.*

14.1.1 The ionization cross section

The ionization cross-section of an inner atomic shell by a charged particle, is given, as a first approximation, by [194], [195]:

$$\sigma_K \approx \frac{2^{20}}{45} \pi a_0^2 \frac{1}{Ry^4} \left(\frac{m}{M}\right)^4 \frac{T_p^4}{Z^{12}} \quad (14.1)$$

where a_0 is the first Bohr radius, Ry is the Rydberg constant, m is the free electron mass, M and T_p are the proton mass and kinetic energy and Z is the atomic number of the target.

This simple relation exhibits the qualitative behaviour of the cross section, in Born approximation, with some restrictions:

1. the binding energy I of the electron and the maximum energy T_{Max} , which a proton can transfer to the electron, must satisfy $I \geq T_{Max} = \frac{4Mm}{(M+m)^2} \cdot T_p$, where the proton mass is M , the electron mass is m and the proton energy is T_p ;
2. the incident particle velocity and the target atomic number must satisfy $Ze^2/\hbar \ll v$.

If the conditions 1) and 2) are met, the collision is near-adiabatic and the ionization cross-section increases as the fourth power of the incident energy and it is inversely proportional to the twelfth power of Z eq. (14.1). The cross-sections for the other shells have similar expressions.

A first modification to this simple evaluation comes from screening, i.e.: the fact that the ionization energy of any internal shell is modified by the presence of the more external shells. One can then introduce an effective Z_{eff} , which can be derived from the relation:

$$I_s = \frac{Z_{eff,s}^2 Ry}{s^2} \quad (14.2)$$

where s represents a particular shell and, this time, I_s is the experimentally determined ionization energy. We recall that, the Moseley relation for the position of the K X-ray lines, can be written, as a first approximation, as: $E_K \propto (Z - 1)^2$. The higher- Z elements emit therefore K X-rays of higher energy, but with rapidly decreasing cross sections. So L X-rays of increasing energy become more important, as Z increases.

Because of the PIXE technique, the cross sections for proton induced X-ray production were evaluated and experimentally measured for many elements in a wide energy range.

The computation is more difficult than in the case of X-ray emission induced by electrons and gammas mainly because of the very low proton velocity. The established models for the ionization cross section σ_i are the PWBA model and the ECPSSR model [196, 197]. The PWBA model is based on a Plane Wave Born Approximation. The ECPSSR model was introduced to improve the agreement between experiment and theory, particularly for low proton energies and for higher- Z targets. It takes into account several effects not considered in PWBA, like:

- Coulomb deflection of the projectile in the field of the target nucleus;
- binding energy effect due to the presence of the slow projectile near the atomic orbit during collision;
- relativistic corrections to the wave functions for orbital electrons;
- energy loss of the projectile especially at low velocity.

14.1.2 The X-ray production cross section

If these available models are used for the ionization cross section, the X-ray production cross-section is given by the following equation:

$$\sigma_n^X = \sigma_n^i \omega_n k, \quad (14.3)$$

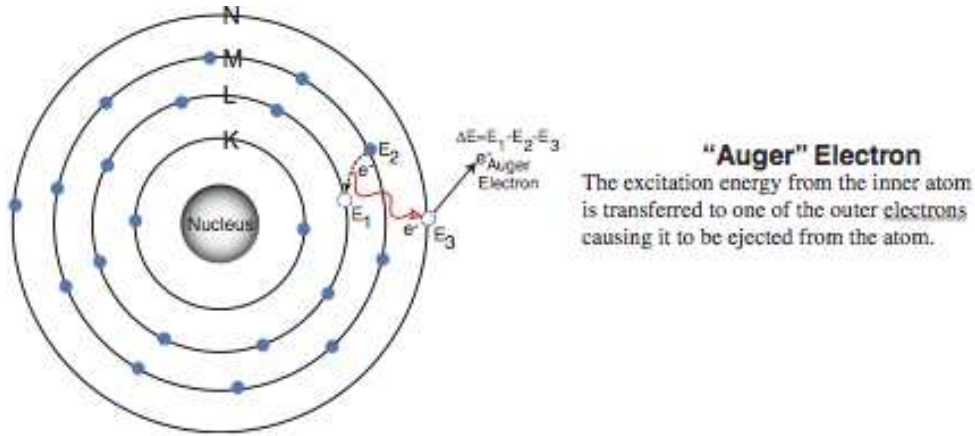


Figure 14.2: *The Auger effect. The excitation energy of an inner shell is transferred to one of the outer electrons, without radiation emission.*

where n indicates one particular X-ray line (K, L, M, N etc), σ_n^i is the ionization cross-section for the n -shell, ω_n is the fluorescent yield for the same shell and k is the relative X-ray transition probability.

The fluorescent yield is the probability that a vacancy in an atomic shell or subshell is filled through a radiative transition. An excited atom may return to a state of lower energy by ejecting one of its own electrons from a less tightly bound state. This transition is called Auger effect, and the ejected electrons are called Auger electrons (Fig. 14.2) [190].

Another X-ray radiationless process is the Coster-Kronig transition, which takes place through transitions between the subshells of an atomic shell having the same principal quantum number. Hence, a primary vacancy created in one of the subshells can shift to a higher subshell before the vacancy is filled by another transition.

Both of the above processes are taken into account by the ω_n factor.

The fraction of specific X-ray line emitted with respect to the total number of X-rays emitted from that shell refers to the k probability [192].

The computed K-line and L-line cross-sections for some elements, as a function of the proton kinetic energy, are shown in Fig. 14.3. We computed these σ_K^X and σ_L^X using the ISICS program, according to the ECPSSR model [196], [197], [198], [199], [200], [201]. This model corresponds to a good agreement between experiment and theory, particularly at low proton energies and for high-Z targets [202],[203]. The cross-section increases rapidly with increasing proton energy and decreasing target atomic number. At a fixed atomic number and proton energy, the L-line cross-section is higher than that of the K-line.

14.1.3 The X-ray rate emission

As a first approximation, the number of the emitted X-ray per second n_X can be written:

$$n_X = n_p \frac{N_A}{M} \int_{T_0}^0 \frac{-dT_p}{S(T_p)} \sigma_X(T_p), \quad (14.4)$$

where n_p is the number of the incident protons, N_A is the Avogadro's number, M is the target molecular weight, $\sigma^X(T_p)$ is the total X-ray cross-section and $S(T_p)$ is the target stopping power. This relation is only valid as a first approximation, since many effects, like: the energy straggling,

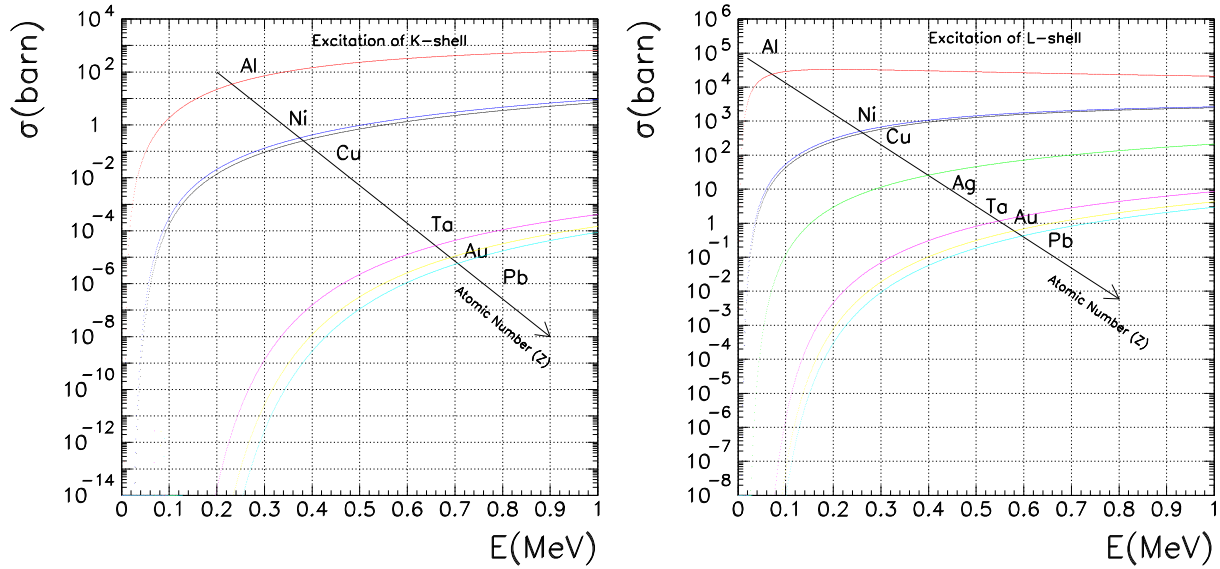


Figure 14.3: The K-shell (left) and L-shell (right) cross sections of some elements as a function of T_p . The L-shell cross-section is always greater than the one of the K-shell, at a fixed atomic number.

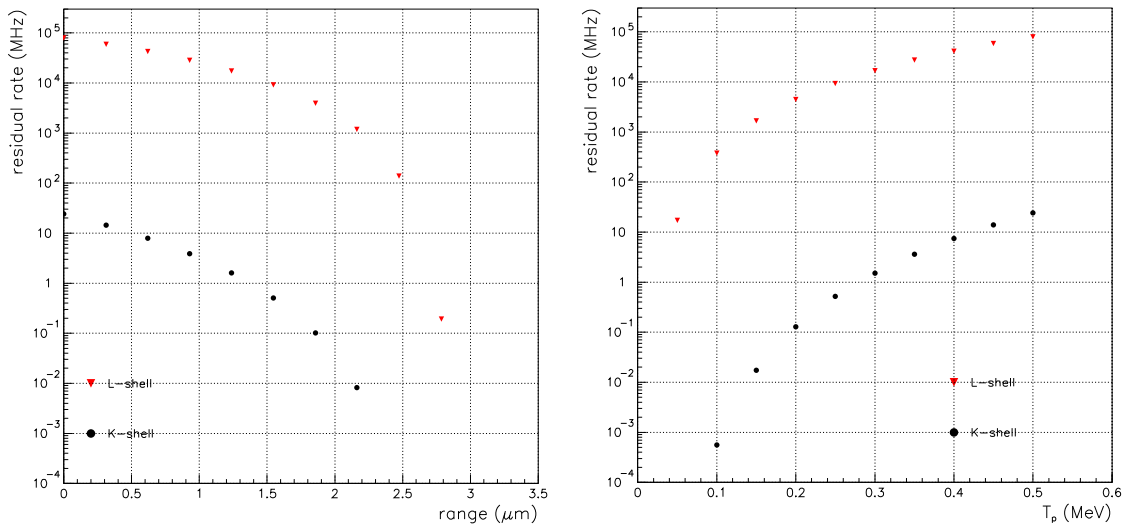


Figure 14.4: The L-shell (triangle) and K-shell (circle) residual rate for copper, as a function of the residual path in the target (left) and as a function of the residual energy (right). Residual rate means the number of X-rays emitted per second while the proton loses energy along its path (the proton absorption is neglected.)

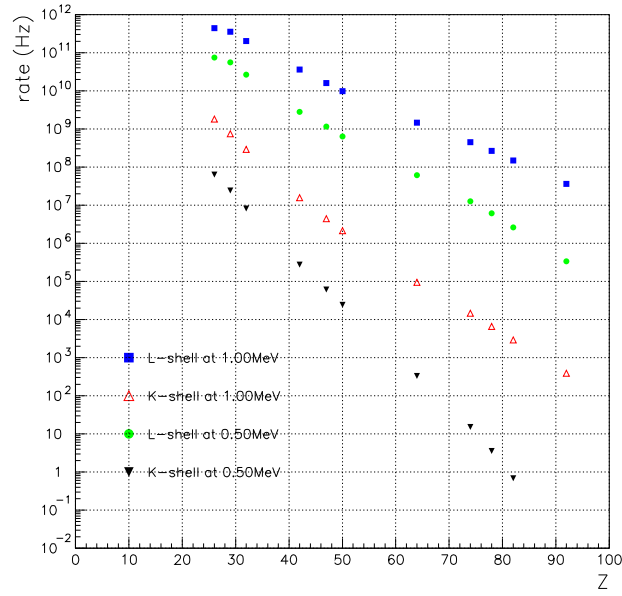


Figure 14.5: The rates for K and L X-ray production on different elements, as a function of Z , at $T_p = 0.5$ MeV and $T_p = 1$ MeV, $I_p = 1$ μ A.

the multiple scattering, etc. are not taken into account. A proper treatment would require a Monte Carlo calculation. $\sigma_X(T_p)$ and $S(T_p)$ strongly depend on energy, therefore we expect different contributions to the total X-ray production from the different target layers (as a function of the proton depth in the target or as a function of the residual energy T_p). This is shown in Fig. 14.4, for K and L X-rays from a copper target, in terms of the residual rate, as a function of residual path in the target and of the residual rate as a function of the residual energy T_p in the target. Residual rate means the number of X-rays emitted per second while the proton loses energy along its path. One can see that the X-ray production is essentially taking place at the target surface (unlike a resonant nuclear reaction).

The total rates for the K and L X-ray production at $T_p = 0.5$ MeV and $T_p = 1.0$ MeV, at a C-W current $I_p = 1$ μ A, as a function of Z are shown in Fig. 14.5. It can be seen that the rates reach rather high values at low Z .

Once computed the X-ray rates, one must take into account the attenuation of the X-rays produced, which also strongly depend on their energy, due to the amount of material they must cross (target, beam pipe, air, etc.), leading to the eq. (14.5). The X-ray self absorption by the target material must also be included.

$$n_X = n_p N/M \int_{T_0}^0 \frac{-dT_p''}{S(T_p'')} \sigma_X(T_p'') \exp\left(-\frac{\mu_i \cos\alpha}{\rho \cos\theta} \int_{T_{p0}}^{T_p''} \frac{dT_p'}{S(T_p')}\right) \quad (14.5)$$

Here μ_i and ρ stand for the absorption coefficient and the absorber density.

The X-rays must pass through different materials and thicknesses to spill out from the beam pipe. This strongly reduces the rates of the lower energy X-rays. Here we take into account this effect, but, to simplify the estimate, we consider an aluminum thickness of 1 mm for the beam pipe and we assume an orthogonal crossing of all surfaces. Only the rate corresponding to the target front face emission is considered. An interesting phenomenon takes place, which was first recognized by Livingston, Genevese and Konopinski in their beautiful historical paper [195]. This

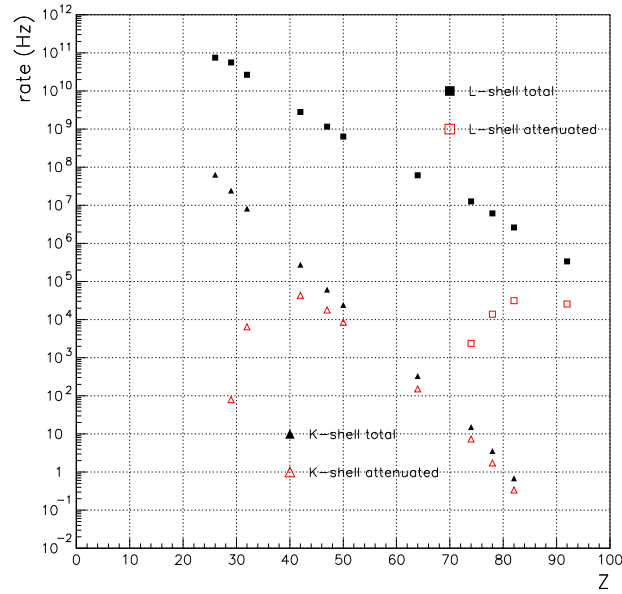


Figure 14.6: *Livingston-Konopinski plot for the MEG experimental conditions. $T_p = 0.5$ MeV and $I_p = 1 \mu\text{A}$.*

is illustrated in Fig. 14.6 where the X-ray rates from various elements are plotted as a function of Z . A double peak structure emerges. The rates are depressed at low- Z because of the low K X-ray energies and because of the absorption cut (≈ 8 keV); at greater Z , the K X-ray energy increases and the X-rays pass the absorption cut; at still higher Z , the rates drop to low values because of smaller K cross section; finally, L X-ray, whose initially low energies increase as a function of Z and which are copiously produced, pass the absorption cut and give rise to a second maximum as a function of Z , until the cross sections again reduce.

Finally Tab. 14.1 shows the thickness of different material which halves the incident flux, as a function of the X-ray energy. The X-ray rates, over the full solid angle for different materials and for a Be-window of 2 mm thickness, are summarized in Tab. 14.2, at a beam current of $I_p = 1 \mu\text{A}$. The window transmission efficiency is represented by ϵ_T . Note that the energy of the K and the L-lines, is an average of all lines corresponding to the same shell.

Table 14.1: The window thickness needed to halve the incident X-ray flux, as a function of the X-ray energy, for three different materials.

| X-ray energy (keV) | Window thickness (mm) | | |
|--------------------|-----------------------|----------------------|----------------------|
| | Mylar | Kapton | Berillium |
| 4 | $9.23 \cdot 10^{-2}$ | $9.86 \cdot 10^{-2}$ | $4.47 \cdot 10^{-1}$ |
| 6 | $3.19 \cdot 10^{-1}$ | $3.43 \cdot 10^{-1}$ | 1.66 |
| 8 | $7.83 \cdot 10^{-1}$ | $8.43 \cdot 10^{-1}$ | 4.25 |

14.2 The X-ray fluorescence measurements

We performed studies of X-ray emission, in controlled laboratory conditions, to familiarize ourselves with X-ray sources, X-ray detectors, X-ray fluorescence, calibrations, etc. All this was preliminary to the study of particle induced X-ray emission by protons from the Cockcroft-Walton accelerator

Table 14.2: The X-ray rate for different target elements. $I_p = 1\mu\text{A}$.

| Target | $T_p(\text{MeV})$ | $E_X^k(\text{keV})$ | $R(E_X^k)$ | ϵ_T | $E_X^l(\text{keV})$ | $R(E_X^l)$ | ϵ_T |
|--------|-------------------|---------------------|---------------------|--------------|---------------------|---------------------|---------------------|
| Ti | 0.35 | 4.65 | $4.5 \cdot 10^7$ | 0.15 | 0.454 | $4.3 \cdot 10^{10}$ | – |
| Cu | 0.40 | 8.32 | $7.4 \cdot 10^6$ | 0.75 | 0.937 | $4.1 \cdot 10^{10}$ | – |
| Mo | 0.60 | 18.2 | $8.6 \cdot 10^5$ | 0.98 | 2.422 | $7.6 \cdot 10^9$ | $2.7 \cdot 10^{-7}$ |
| Ag | 0.80 | 23.0 | $1.2 \cdot 10$ | 0.99 | 3.196 | $9.3 \cdot 10^9$ | $1.8 \cdot 10^{-3}$ |
| Gd | 0.30 | 44.7 | $4.5 \cdot 10^{-1}$ | 1.00 | 6.73 | $3.9 \cdot 10^6$ | 0.56 |
| Au | 0.45 | 71.3 | $4.4 \cdot 10^{-1}$ | 1.00 | 11.1 | $2.9 \cdot 10^6$ | 0.90 |

14.2.1 The experimental set-up

The X-ray detector characteristics are shown in Tab. 14.3.

The detector is a Si-pin photodiode (see Fig. 14.7). A X-ray interacting in silicon creates an

Table 14.3: The X-ray detector specifications.

| System performance | |
|---------------------|--|
| Energy resolution | FWHM@5.9keV: 174 eV |
| Energy range | Efficiency is > 25% from 1.5 to 25 keV |
| Maximum count rate | $1.2 \times 10^5 \text{s}^{-1}$ |
| Detector | |
| Detector type | Si-pin photodiode |
| Detector size | 7mm^2 |
| Silicon thickness | $300\mu\text{m}$ |
| Be window thickness | $25\mu\text{m}$ |

average of one electron/hole pair for an energy deposit of 3.62 eV. The detector is mounted on a thermoelectric cooler along with the input FET and is coupled to a charge sensitive preamplifier. The thermoelectric cooler reduces the electronic noise in the detector and preamplifier. The preamplifier output enters a pulse processor, a digital processor which replaces both a shaping amplifier and a multichannel analyser. The processed data are presented on a PC screen. The complete system is very compact and it is contained in an aluminum box of dimensions in $7 \times 10 \times 2.5 \text{cm}^3$.

The full energy detection efficiency for the XR-100 CR detectors is shown in Fig. 14.8. The curve for our detector is the one: 1 mil Be window and $300 \mu\text{m}$ Si PIN thickness.

This efficiency gives the probability that an X-ray entering the front of the detector deposits all of its energy in the detector by photoelectric effect.

14.2.2 The detector calibration

The X-ray detector was calibrated with several X-ray source: a ^{55}Fe - (activity $\approx 37 \text{MBq}$), ^{109}Cd - (activity $\approx 30 \text{kBq}$) and ^{241}Am -source (activity $\approx 360 \text{kBq}$). Their characteristics are summarized in the Tab. 14.4. In the table we also list the type of source nuclear decay and the range of elements which can be excited by that source (EC corresponds to “electron capture”).

The ^{55}Fe and the ^{109}Cd nuclides decay by electron capture. We assume that both the atom and the nucleus are at ground state. In principle, any of the atomic electrons is available for capture as long as the decay energy is great than the binding energy of the electron in the parent atom. K capture is by far the most probable process.

Regardless of the state of excitation of the nucleus, the direct result of the capture is the production of a vacancy in one of the inner electron shells, followed by the X-ray emission. In the



Figure 14.7: The X-ray Si-pin detector.

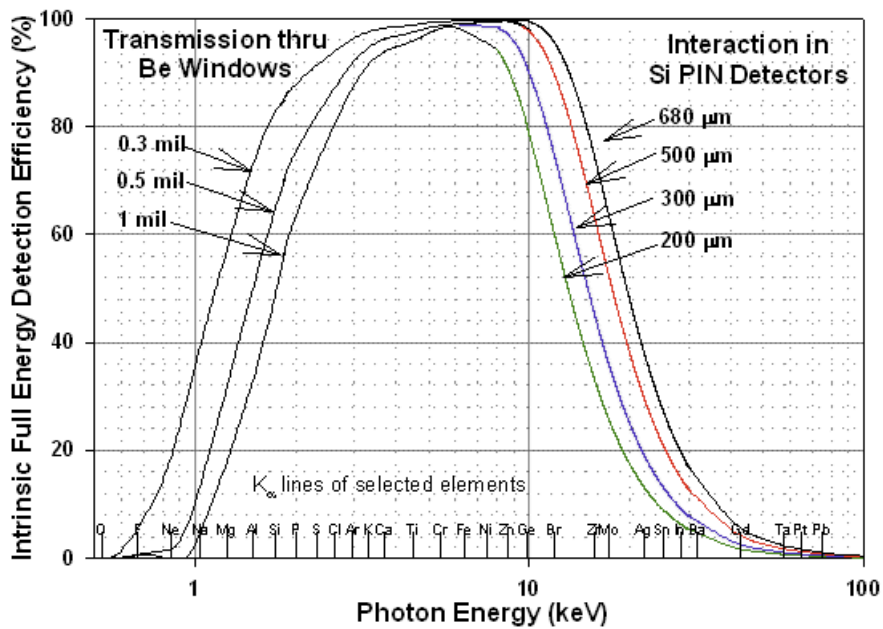


Figure 14.8: The full energy detection efficiency of the XR-100CR detector.

Table 14.4: Radioisotope γ and X-ray sources.

| Source | Half-life | Type of decay | Particle energy | Gamma rays | | Characteristics X-rays | | | Typical element range | |
|-------------------|-----------|---------------|-----------------|--------------|-------|------------------------|--------------|------|-----------------------|---------|
| | | | | Energy (keV) | (%) | Line | Energy (keV) | (%) | Yield | K-lines |
| ^{55}Fe | 2.73 y | EC | - | - | - | Mn $K_{\alpha 2}$ | 5.89 | 8.5 | Si-V | Zr-Ce |
| | | | | | | Mn $K_{\alpha 1}$ | 5.90 | 16.9 | | |
| | | | | | | Mn $K_{\beta 1}$ | 6.49 | 2.0 | | |
| | | | | | | Mn $K_{\beta 3}$ | 6.49 | 1.01 | | |
| ^{109}Cd | 426.6 d | EC | - | 88.04 | 3.61 | Ag $K_{\alpha 2}$ | 21.99 | 29.5 | Cr-Mo | Tb-U |
| | | | | | | Ag $K_{\alpha 1}$ | 22.16 | 55.7 | | |
| | | | | | | Ag $K_{\beta 3}$ | 24.91 | 4.8 | | |
| | | | | | | Ag $K_{\beta 1}$ | 24.94 | 9.2 | | |
| | | | | | | Ag $K_{\beta 2}$ | 25.46 | 2.3 | | |
| ^{241}Am | 432.2 y | α | 5.485 | 26.34 | 2.40 | Np $L_{\alpha 2}$ | 13.76 | 1.1 | Zn-Nd | W-U |
| | | | 5.422 | 33.40 | 0.13 | Np $L_{\alpha 1}$ | 13.95 | 9.6 | | |
| | | | 5.388 | 59.54 | 35.90 | Np $L_{\beta 2}$ | 16.82 | 2.5 | | |
| | | | | | | Np $L_{\beta 1}$ | 17.75 | 5.7 | | |
| | | | | | | Np $L_{\beta 3}$ | 17.99 | 1.4 | | |
| | | | | | | Np $L_{\gamma 1}$ | 20.78 | 1.4 | | |

particular case of the ^{109}Cd -source, the daughter nucleus is left in a excited state. The X-ray emission and the nuclear gamma emission are superimposed.

The ^{241}Am -source is an α -emitter. We expect nuclear gamma lines from the nuclear de-excitation and the X-ray spectrum from the daughter Np atom.

The results of the calibration are presented in Fig. 14.9. The X-ray lines from the Am- and Fe-source are shown (the spectrum from the Cd-source is not plotted because of its lower activity). Strictly speaking, it is not correct to indicate the X-ray lines by the source name, since they come from the daughter nuclides (Mn for Fe, Np for Am and Ag for Cd). Note that we must distinguish between the X-ray line and the gamma from the nuclear de-excitation. In Fig. 14.9 the Np-59.54 keV line is labelled as nuclear.

The detector response is linear as a function of the energy, as shown in Fig. 14.9

14.2.3 The results

X-ray fluorescence is a very convenient physical effect for studying the X-ray detector behaviour in background-free conditions. The initial target atomic vacancy is created by the absorption of a primary X-ray from a radioactive source. The secondary X-ray emission by the target, is called X-ray Fluorescence, or XRF.

We performed XRF measurements from different samples that we intend to excite also with protons. The X-ray emission was studied in an energy range of a few tens of keV. The experimental set-up is shown in the Fig. 14.10. The detector and the source are mounted in front of the sample, in such a way that they do not directly see each other, while they both see the sample.

The silver, lead and tantalum XRF spectra are shown in Fig. 14.11.

Silver is characterized by the $K_{\alpha 1} = 22.16$ keV and $K_{\alpha 2} = 24.94$ keV lines. The L-lines are not visible because of their low energy. The X-ray primary source is the ^{241}Am , whose lines are

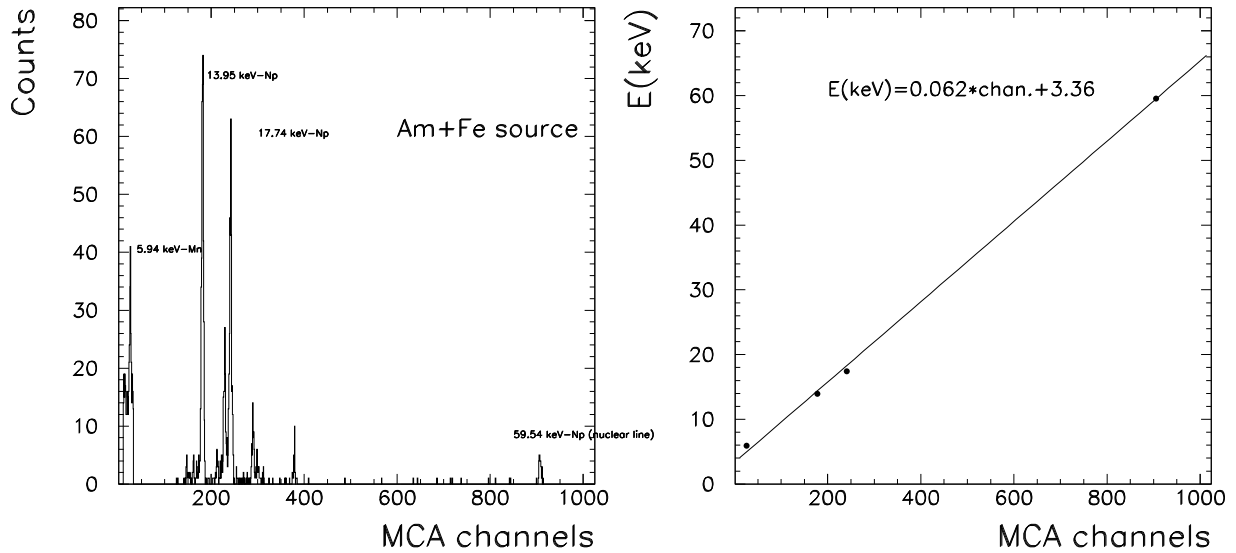


Figure 14.9: (Left) The X-ray line from the ^{55}Fe -source (activity ≈ 37 MBq) and ^{241}Am -source (activity ≈ 360 kBq). (Right) The linear response of the X-ray detector, as a function of energy.

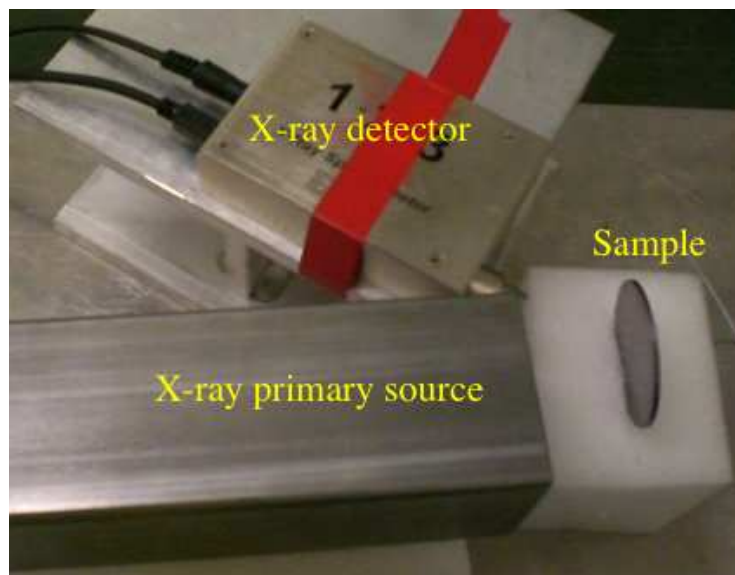


Figure 14.10: The experimental set-up for the XRF measurements.

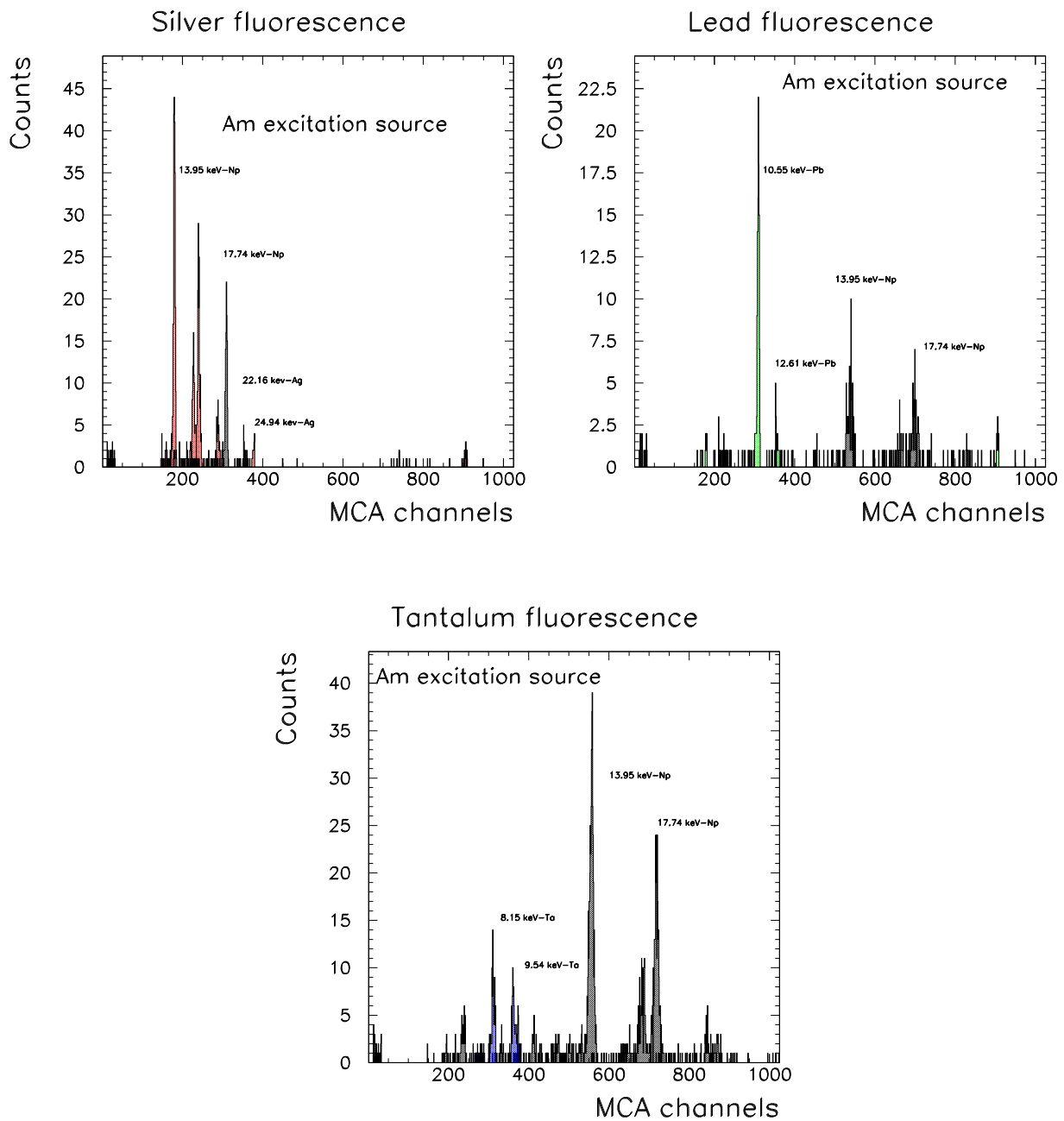


Figure 14.11: The XRF spectra line from ^{55}Fe -source (activity $\approx 37 \text{ MBq}$) and ^{241}Am -source (activity $\approx 360 \text{ kBq}$).

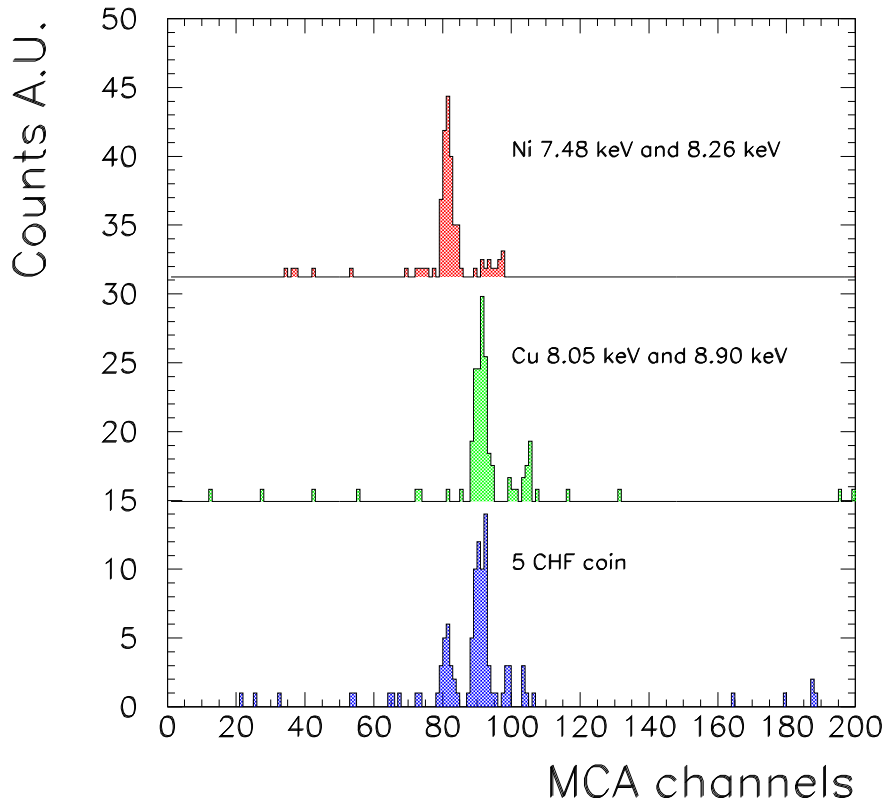


Figure 14.12: *The XRF spectrum from Ni and Cu. A qualitative composition analysis of a 5 CHF coin.*

superimposed on the Ag-spectrum.

The lead spectrum is shown, with the $L_{\alpha 1} = 10.55$ keV and $L_{\alpha 2} = 12.61$ keV lines for the same excitation source. Note that the K-lines energy is always greater than that of the L-lines. In this particular case the primary X-ray energy is not sufficient to excite K-lines ($\text{Ag} - K_{\alpha 1} = 74.96$ keV $>$ ^{241}Am -line = 54.94 keV).

Finally the tantalum XRF spectrum is presented. The $L_{\alpha 1} = 8.15$ keV and $L_{\alpha 2} = 9.34$ keV lines are visible. The X-ray primary energy is not sufficient to excite the K-lines.

The XRF is widely used to measure the elemental composition of materials, because it is a fast and non-destructive technique. We analysed, as an example, a 5 CHF coin. The qualitative results are presented in Fig. 14.12; the nickel and copper spectra are shown in the same picture. The Ni- $K_{\alpha 1} = 7.48$ keV and $K_{\alpha 2} = 8.26$ keV lines and the Cu- $K_{\alpha 1} = 8.05$ keV and $K_{\alpha 2} = 8.90$ keV lines are visible. The 5 CHF coin-spectrum proves the presence of these two elements only.

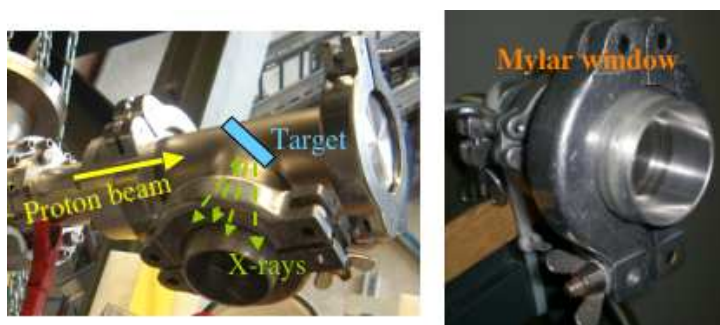


Figure 14.13: *The ad-hoc target support for the X-ray production by protons. A detail of the mylar window.*

14.3 The measurements of proton induced X-ray

We started the proton induced X-ray measurements, after acquiring sufficient knowledge of the properties of the X-ray detector and after performing some XRF analyses.

The protons from the accelerator travel along an aluminum vacuum beam-pipe, of about a 3 mm thickness. An *ad-hoc* target support, with a thin mylar window (thickness $\approx 200 \mu\text{m}$) was prepared (see Fig. 14.13) to allow the coming out of low energy X-rays, without drastically reducing their flux. The target was mounted at an angle of 45° with respect to the beam line. The complete experimental set-up is shown in Fig. 14.14.

We intended to study the X-ray emission from several targets as a function of the proton beam energy. The focusing and the centering of the beam were optimized by using the quartz crystal, mounted immediately before the target support. The beam current and the integrated charge were measured by a Faraday cup (the last portion of the beam pipe) electrically insulated from the rest.

The detector was calibrated by using the ^{55}Fe -source, at a distance of a few centimeter from the detector entrance window. The very clean X-ray line from the Cu-target is presented in the Fig. 14.15. The lines from the ^{55}Fe -source are superimposed. Note the good quality of X-ray line, with no bremsstrahlung background present (normally present when using X-ray tubes). Another impressive result is the high X-ray rate. We measured $\approx 200 \text{ Hz}$ over a small solid angle ($\Delta\Omega/2\pi \approx 8 \cdot 10^{-4}$, at $T_p = 500 \text{ keV}$ and $1 \mu\text{A}$).

The X-ray rate as a function of the beam energy is presented in Fig. 14.16 (left). The increase in rate, from $T_p = 500 \text{ keV}$ to $T_p = 1000 \text{ keV}$, is of about a factor of 10, see Fig. 14.5 (left). The X-ray rate is linear as a function of the beam current, see Fig. 14.16 (right).

We also present the X-ray lines from the Ag-target (see Fig. 14.17). This is an interesting measurement since the K-lines and the L-lines can be simultaneously monitored, at 2.98 keV and 3.15 keV, and at 22.16 keV and 24.94 keV. The two L-lines are not separated and appear as a single line in the plot. Note that the L-lines are, in reality, more intense than the K-lines (Fig. 14.3), if the energy dependent detector efficiency is taken into account.

The Ag X-ray K-line rate is lower than the Cu X-ray K-line rate at the same proton energy and with the same geometry, as expected for the X-ray emission as a function of the target atomic number (Fig. 14.3).

Our conclusion is that the proton induced X-ray emission gives very clean X-ray lines, whose energy can be varied by a choice of target and whose rate can be varied by a choice of proton energy.

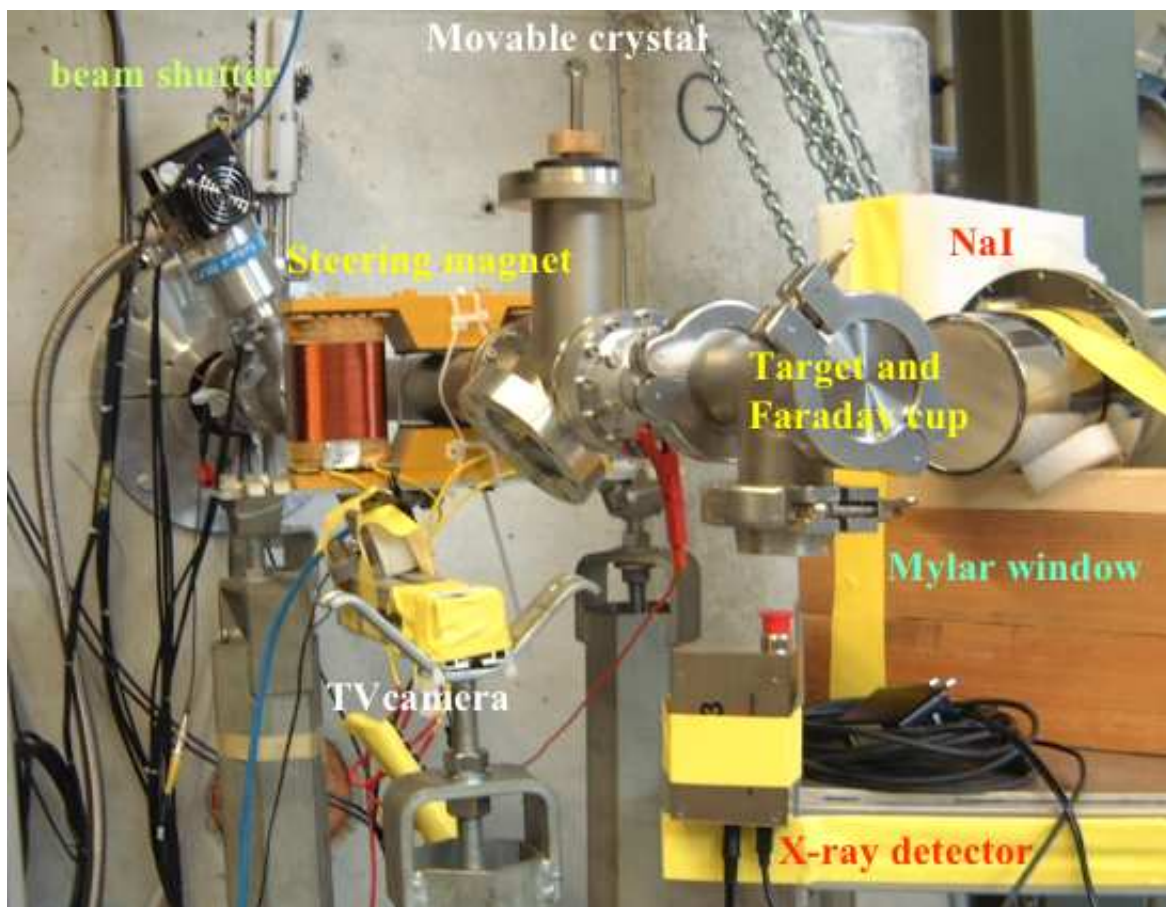


Figure 14.14: *The proton induced X-ray emission experimental set-up.*

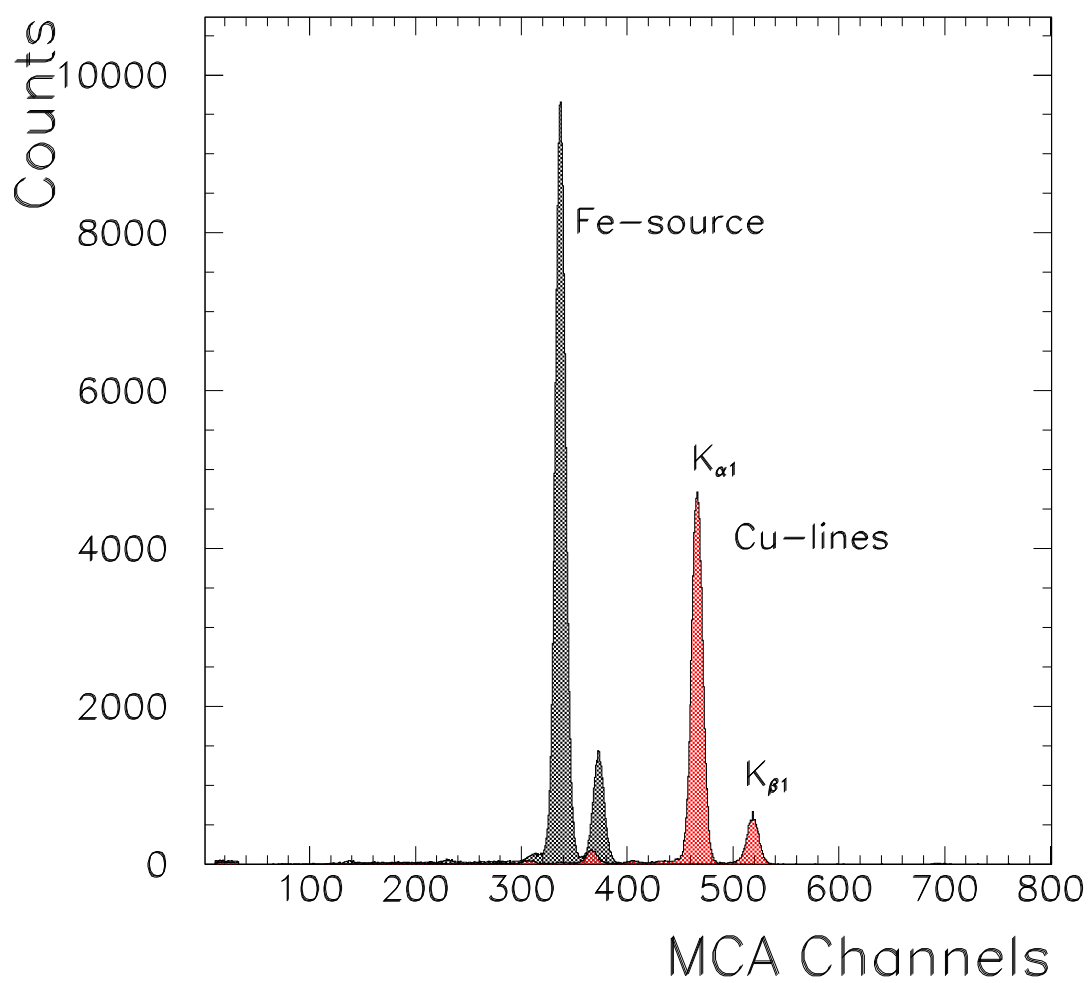


Figure 14.15: *The proton induced X-ray emission from a Cu-target. The X-ray lines from the ⁵⁵Fe-source are superimposed.*

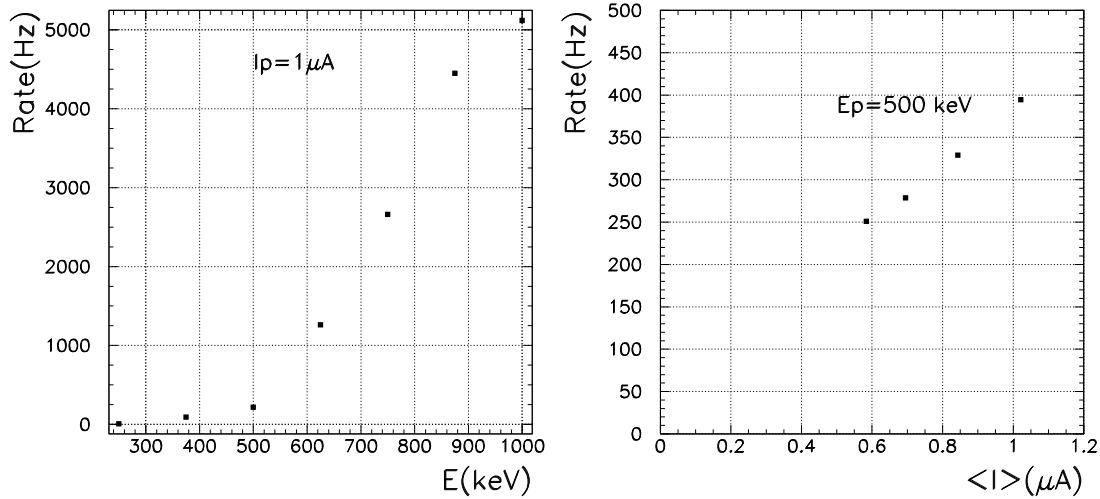


Figure 14.16: The proton induced X-ray emission from a Cu-target as a function of the proton energy at $I_p = 1 \mu A$ (left) and as a function of the beam current at $E_p = 500 \text{ keV}$ (right).

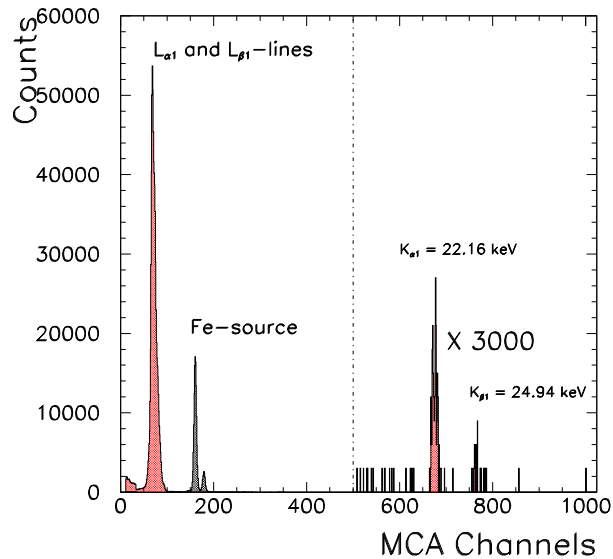


Figure 14.17: The proton induced X-ray emission from a Ag-target. The X-ray lines from the ^{55}Fe -source are superimposed. One can see both the K-lines and the L-lines.

Chapter 15

Muon Beam monitoring and diagnostics by luminescence

Two methods for continuously monitoring the muon beam intensity were studied: a muon induced X-ray production and a Helium ionization chamber [204].

In order to reach the planned unprecedented sensitivity of the MEG experiment, not only high precision innovative detectors are needed, but also a high intensity good quality muon beam.

The normalization of the experiment relies on knowledge of the number of muons stopped in the target, which is obtained from the measured number of secondary Michel positron tracks reconstructed in the drift chambers and timing counters. This method provides a self-normalization under the assumption of equivalent acceptances and efficiencies for positrons from Michel decays and those from a potential signal event. However, if this is not the case, a precise understanding of various efficiencies and acceptances is necessary.

Conversely, the muon stopping-rate obtained from a measurement of the muon beam intensity relies on knowledge of various factors (e.g. beam size, beam momentum bite, stopping efficiency etc.). Hence, in a precision experiment such as MEG it is advisable to measure important quantities with different methods, as for the calorimeter energy-scale and energy-resolution and for the timing of various sub-detectors. It is therefore convenient to have a continuous and independent measurement of the muon beam intensity.

We investigated the possibility of directly observing the μ -beam when it hits a suitable luminescent material. The light is collected by a TV camera and the introduction of the luminescent material in the beam is remotely controlled [205].

15.1 Introduction

During the set-up & commissioning phase of the beam line, the beam phase space, intensity and contamination were measured by a variety of techniques. The most commonly used in the COBRA field were: a scanning miniaturized PMT/pill-scintillator detector and a scanning avalanche photodiode/Geiger-mode APD-detector. These techniques are, when in use, muon beam “destructive”. It is interesting and possible to design a non-destructive device. In this case the location must be well chosen in order to preserve the beam optical properties. One has to consider that the beam propagates under vacuum (or in a Helium atmosphere) to reduce multiple scattering. We discuss two possible methods for precise and continuous monitoring of the beam intensity, while respecting the above constraints.

Table 15.1: Main properties of the MEG particle beams.

| Beam | Momentum | K.E. | Velocity | Intensity | Current |
|-------------|----------|------|----------|----------------------|---------------------|
| Units | MeV/c | MeV | Beta | Particles/s | μA |
| C-W | 43.3 | 1 | 0.046 | $6.25 \cdot 10^{12}$ | 1 |
| MEG μ^+ | 28.0 | 3.65 | 0.256 | $3.0 \cdot 10^7$ | $4.8 \cdot 10^{-6}$ |

15.2 Muon induced X-ray emission (MIXE)

Previously we discussed and measured the proton induced X-ray production using the MEG Cockcroft-Walton accelerator [191, 194]; we now turn to μ^+ -induced X-ray emission as a means of monitoring continuously the MEG muon beam intensity. While the X-ray emission following μ^- -capture and the formation of a muonic atom has a very extensive literature [206], dealing with fundamental issues or with applications to various condensed matter problems, very little is available on the μ^+ -induced X-ray emission and its measurement. We critically examined the theoretical models already applied to proton induced X-ray emission with a view to extending them to the positive muon case, at the MEG beam energy. We also performed a first measurement of μ^+ -induced X-ray production and compared it with predictions. It is worth recalling the typical parameters of the proton beam and of the MEG μ^+ -beam (see Tab. 15.2). Although the kinetic energies of the two particle beams are similar, their velocities are however very different, as is the intensity of the proton beam (number of particles per second), which is approximately five orders of magnitude larger than that of the muon beam. It is however remarkable that, even so, the X-ray emission (in particular for the K-lines) is rather similar. The compensation for this huge difference in intensity between the proton and the muon beam is mainly due to the difference in particle velocity.

15.2.1 MIXE simulation

The predictions for the μ^+ X-ray emission were obtained using the ECPSSR theory and by the use of the ISICS computer program previously used for protons [196, 197]. We computed the cross-sections and the X-ray production rates from different target elements and at different particle energies. We took into account the X-ray absorption and chose the target thickness to optimize the X-ray emission rates. For further details of the computation we refer to the previous MEG internal note [191]. The results for the proton and muon induced X-ray cross sections for tin (Sn) are presented in Fig. 15.1, as a function of the particle speed and for the K, L, M emission lines. The arrows indicate the particle speeds corresponding to 1 MeV protons and to 4.1 MeV muons. One can notice that the cross-sections are almost totally dependent on the particle speed and independent of particle type and superimpose over a wide speed interval. Differences mainly emerge at low particle speed (and at high-Z values), in the region where the ECPSSR theory gives a better approximation than the PWBA model (based on a Plane Wave Born Approximation). One also notices that, for our beams, the K X-ray cross-section is much larger for muons than for protons, while for L X-rays the cross-sections are almost equal and, for higher shells M, N X-rays, protons dominate over muons, as previously mentioned.

15.2.2 MIXE measurement

The measurement of the muon beam intensity is based on the detection of the X-rays emitted by a thin radiator crossed by the beam. The choice of material and thickness of the radiator should maximize the X-ray rates, while inducing minimal multiple scattering and muon energy loss. This also implies an appropriate choice for the radiator position, which should be, if possible, close to a beam focus. We intend to detect the X-rays emitted in the backward direction by the radiator. Since the radiator's X-ray self-absorption is high for X-ray energies of the order of 10 keV, there is no point in using a radiator of thickness much greater than one X-ray absorption

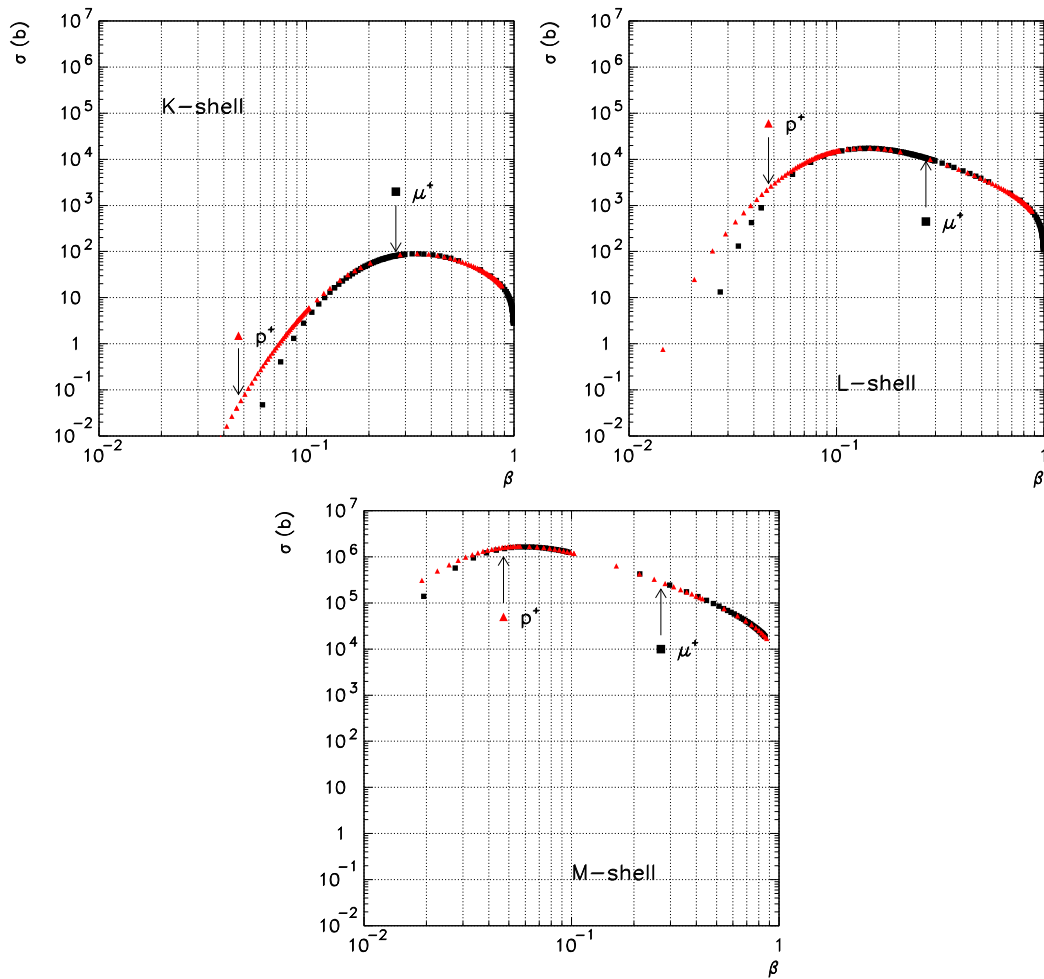


Figure 15.1: Cross-sections for the K- (top, left), L- (top, right), c) M-shell (bottom) emission as a function of β , for protons and muons on tin. The arrows indicate the speed for 1 MeV protons and for 4.01 MeV muons.

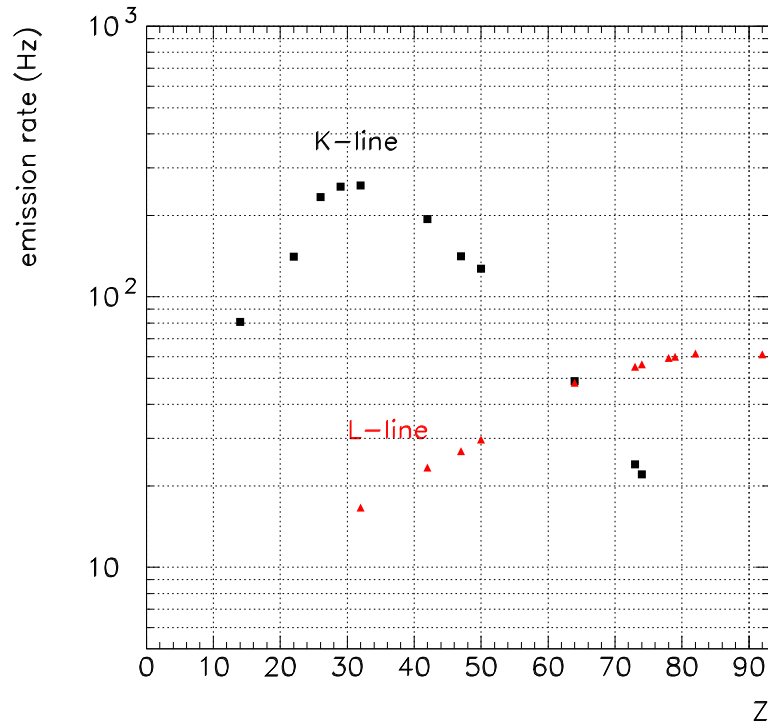


Figure 15.2: Rates for backward emitted X-rays, as a function of the radiator atomic number and for a radiator thickness equal to λ_X^{abs} .

length (λ_X^{abs} [207, 208]). The backward emitted X-ray rate is therefore evaluated for a radiator thickness corresponding to 1 absorption length. The K X-ray energy and the corresponding λ_X^{abs} are computed for each radiator atomic number and presented in Fig. 15.2 (X-ray Livingston's plot [195]), for the K and the L X-ray lines, as a function of the radiator atomic number Z . The detector is assumed to have a surface of 1 cm^2 and to be positioned at 20 cm distance from the radiators with a beam intensity assumed to be $2.5 \cdot 10^7 \mu^+/\text{s}$. As can be seen in Fig. 15.2, the X-ray rate is maximized and rather high for $Z \approx 30$, while the L-rate is much lower everywhere. The reasonable choice for the MEG radiator material and thickness is probably a $5 \mu\text{m}$ copper layer (about $0.2 \lambda_X^{abs}$ [207, 208]), a thickness much less than that of the present beam moderator. If one uses a NaI disk X-ray detector of diameter 2.5 cm at a distance of 30 cm from the radiator, a rate of $\approx 100 \text{ Hz}$ can be expected. The beam is therefore minimally perturbed while the X-ray rate is still adequate. The most likely position for such a radiator would probably be between the exit of the BTS and the entrance to COBRA. Since rather strong magnetic fields are present it is not yet clear which is the best choice for the final detector. The options lie between a low energy resolution, relatively large surface detector based on a thin NaI crystal coupled to a mesh-PMT, or a solid state detector with higher energy resolution, but smaller surface area. The X-ray production by muons was measured during a short preliminary test in which the beam was stopped in a copper target and the X-rays were detected with a AMPTEK X-123 detector. The rates were in reasonable agreement with expectations (better than 20%). The results are presented in Fig. 15.3. The Cu K-lines and the calibration ^{55}Fe -lines are visible over a very small background.

15.3 A He Ionization Chamber

The intensity measurement of high energy beams are often based on the use of ionization chambers [209, 210]. However the intense surface muon beams pose special problems because of their low momentum. Since the beam mostly travels in a vacuum, a thin-window gas-filled ionization

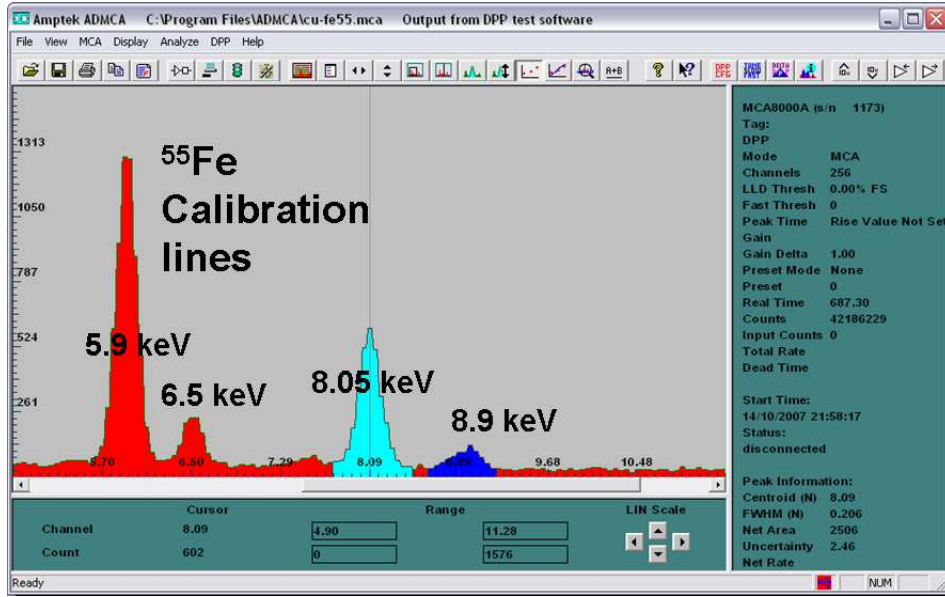


Figure 15.3: The X-ray K-lines produced by muons in copper (blue peak). The ^{55}Fe calibration lines are also visible (red peak).

chamber is difficult to build and operate. In the MEG case, the fact of having the central COBRA region filled with Helium might be put to use. One can measure the beam intensity with a parallel plate chamber ($10 \times 10 \times 10 \text{ cm}^3$) having plates parallel to the beam direction and using He as a filling gas see Fig. 15.4 (left). Apart from helium, the muon beam does not cross any material and it is only slightly perturbed by the chamber electric field, typically of the order of 200 V/cm (beam deflection $\approx 0.4 \text{ mrad}$). The amount of material associated with the chamber should be kept to a minimum. A study of possible re-interactions of background particles generated by muon-decays in the target region was performed, the result being that the presence of the chamber produces effects which are sufficiently small to escape detection. The prototype chamber was constructed with electrodes and guard rings as printed circuits on vetronite. A two-section chamber is also under study, in which one section is intended to measure the muon beam intensity, while the other measures the intensity of a reference α -source and hence is used to monitor the quality of the chamber gas, see Fig. 15.4 (right).

The chamber current can be evaluated as follows.
The number of pair n_{pairs} is given by:

$$n_{pairs} = n_{\mu} \cdot \frac{\Delta E}{E_{ion}} \quad (15.1)$$

where n_{μ} is the number of muons crossing the chamber, ΔE is the corresponding μ energy loss and E_{ion} is the ionization energy of the chamber gas (Helium in our case). For $n_{\mu} = 3 \cdot 10^7 \mu/s$, $\Delta E = 3.7 \cdot 10^{-2} \text{ MeV}$ (the chamber dimension along the beam is 10 cm , the μ momentum is $p_{\mu} = 22 \text{ MeV/c}$), and $E_{ion}(\text{He}) = 45 \text{ eV}$, the chamber current was evaluated and is 5 nA (≈ 1150 ion pairs/muon).

15.3.1 Ion motion in crossed E and H fields

A full study of the chamber behaviour under the influence of the crossed electric and COBRA magnetic field was performed [211, 212, 213]. The charge diffusion, the drift time of electrons and ions, the drift angle, the amount of space charge, as well as possible second order effects on the

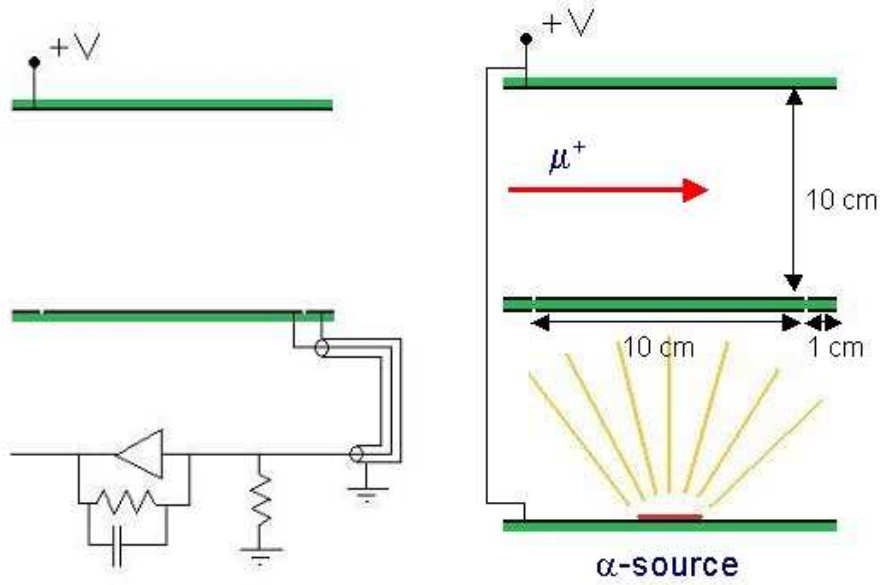


Figure 15.4: Scheme of the ionization chamber and electronics. Single-gap chamber (left). Double-gap chamber (right).

muon beam, etc. were investigated. The motion of ions in crossed electric and magnetic fields is different from that derived from the Lorentz force:

$$m\mathbf{v}' = q(\mathbf{E} + \mathbf{v} \times \mathbf{B}) \quad (15.2)$$

due to the frequent ion collisions with gas molecules and the corresponding shorter ion mean free path. The previous expression (15.2) must be substituted by:

$$\mathbf{v}_D = \mu(\mathbf{E} + \mathbf{v}_D \times \mathbf{B}) \quad (15.3)$$

where \mathbf{v}_D is the steady-state drift velocity, μ is the mobility (a function of the fields, negative or positive for electrons or positive ions) and $\omega = -qB/m$ is the electron cyclotron frequency. The spiral motion is substituted by a straight line motion. A solution to (15.3) is given by the Langevin equation:

$$\mathbf{v}_D = \frac{\mu}{1 + \mu^2 B^2} (\mathbf{E} + \mu \mathbf{E} \times \mathbf{B} + \mu^2 \mathbf{B}(\mathbf{E} \cdot \mathbf{B})). \quad (15.4)$$

In a right handed coordinate system we assume the fields to be oriented: \mathbf{E} in the negative z-direction; \mathbf{B} in the x-z plane, at an angle θ to \mathbf{E} , such that \mathbf{B} points in the negative x-direction if $\theta = \pi/2$. In such a system the \mathbf{v}_D projections are:

$$\mathbf{v}_D = \frac{\mu}{1 + \mu^2 B^2} \begin{pmatrix} \mu^2 B^2 \cos \theta \sin \theta \\ -\mu B \sin \theta \\ 1 + \mu^2 B^2 \cos^2 \theta \end{pmatrix} \quad (15.5)$$

The use of the Langevin equations gives the main information about the particle straight line trajectory. A more precise and complete view can be obtained with the MAGBOLTZ program [214, 215]. The angle between \mathbf{E} and \mathbf{B} was chosen to be 90° , while the value of \mathbf{B} depends on the exact position of the chamber. We assume a maximum field of 1 T. The angle α between the electric field and the drift velocity \mathbf{v}_D is given by the expression:

$$\tan \alpha = \omega \tau \quad (15.6)$$

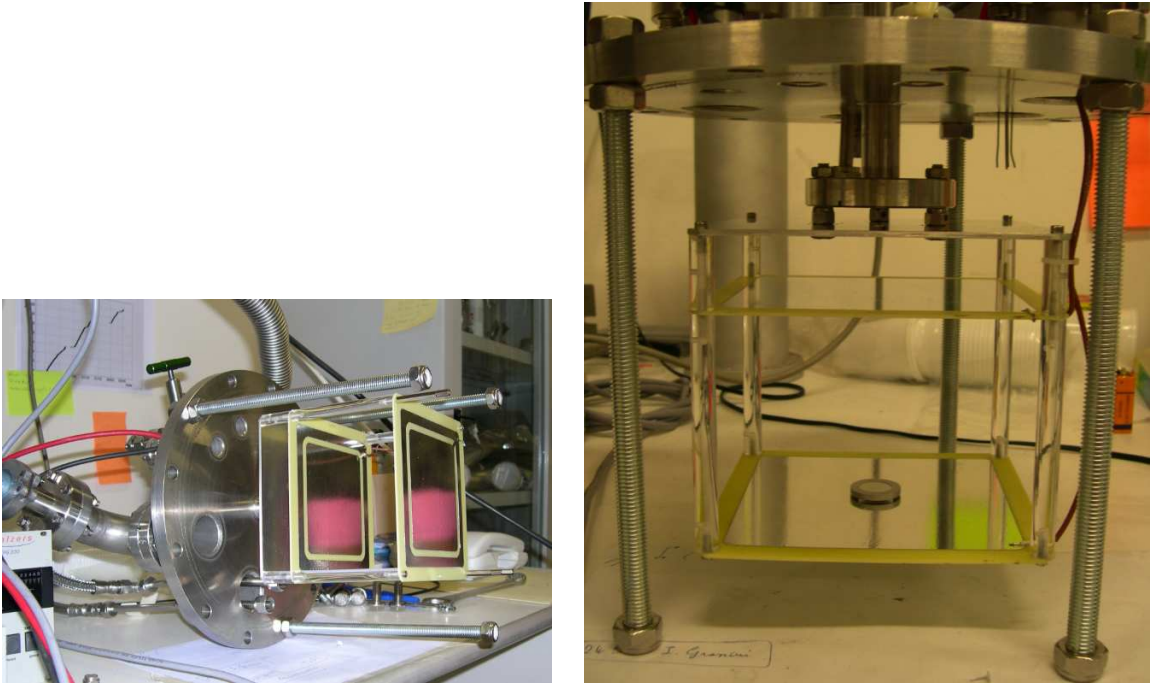


Figure 15.5: *The ionization chamber (left). The ^{241}Am -source mounted on the chamber bottom plate (right).*

where ω is the cyclotron frequency and τ is the time between two collisions. This gives for electrons $\alpha \approx 12^\circ$ for $E=200$ V/cm, an acceptable value which is compatible with the chamber dimensions (the value of α for the positive He ions is ≈ 0). The drift time for electrons is $\approx 2.3 \cdot 10^{-5}$ s, while it is ≈ 5 ms for the positive ions. The electron and ion diffusion during their drift produces effects ($\sigma = 0.5$ mm for electrons and $\sigma = 2$ mm for He ions) which are negligible with respect to the transverse muon beam size. The space charge does not significantly affect the positive and negative ion motions and alters the chamber applied field by $< 1\%$. A small contamination ($\approx 0.5\%$) by air in the He atmosphere is still compatible with a proper chamber performance.

15.3.2 Test of the first prototype

A first ionization chamber prototype (CH) was built and tested.

It is made up of two plates of vetronite (thickness 1.6 mm, surface 10×10 cm²) placed at a 10 cm distance (see Fig. 15.5, left). The chamber behaviour was tested with α -particles ($E_\alpha = 5.5$ MeV) emitted by an ^{241}Am -source (activity 71 kBq). The ^{241}Am -source was mounted on the chamber bottom plate (see Fig. 15.5, right).

An old cryostat (at room temperature), in which the chamber was placed, was re-used as a vessel in which to change gas type and pressure. The vessel was evacuated by a primary pump and the pressure was measured by a Pirani gauge. The system had valves allowing the input/output of gases.

HV is supplied to the chamber via a feedthrough and output currents are read by a picoamperometer (see Fig. 15.6).

The first test used He at different pressures as a chamber gas. Note that, in the final configuration, we intend to use a pressure of 1 atm.

Fig. 15.7 shows the chamber current as a function of the applied HV, for different He gas pressure.

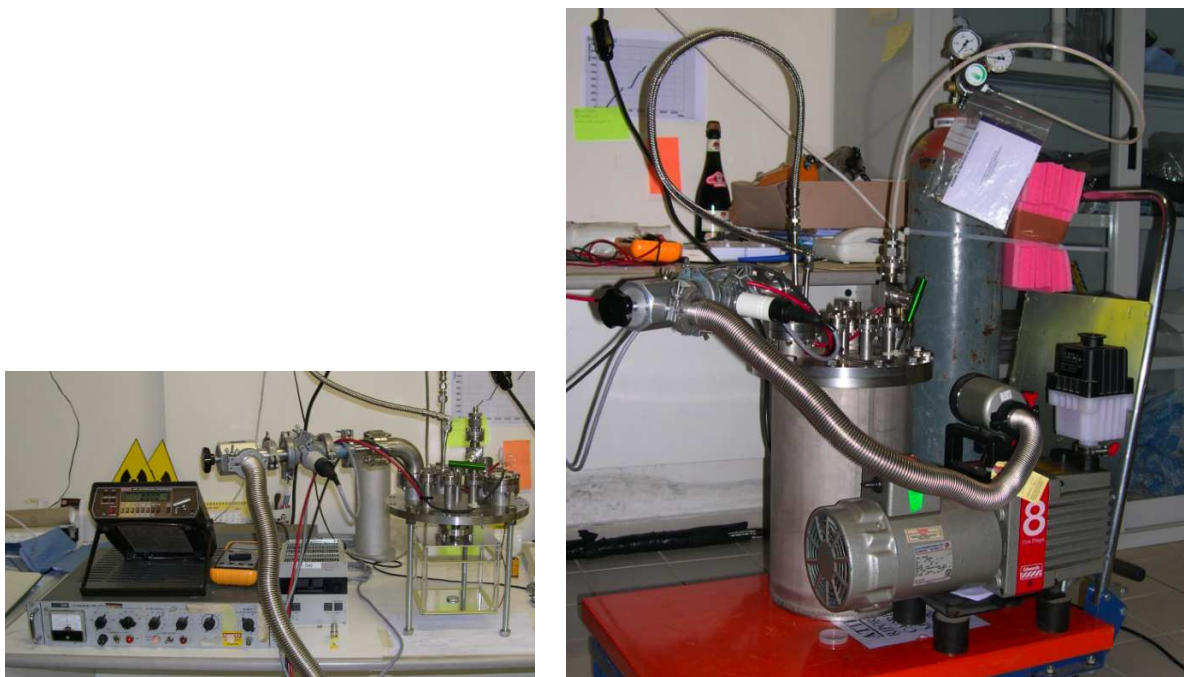


Figure 15.6: *The experimental set-up used for the preliminary test of the ionization chamber.*

At 1 atm the α range R_α is $R_\alpha = 22$ cm, more than the gas layer thickness. The energy deposited in the chamber is a fraction of the total, $E_{dep} \approx 2$ MeV. The expected current is about 250 pA. The measured value, for $HV > 200$ V is consistent with the prediction.

At pressure greater than 1 atm the R_α is smaller than the gas layer thickness: the α particles deposit their whole energy. The plateau associated with the curves at 2 atm and 3 atm are super-imposed. The measurement at 2 atm, for negative HV, is also plotted.

The measurements were repeated in argon.

Fig. 15.8 shows the measured current as a function of the applied HV, for two different gas pressures. The $R_\alpha = 4.2$ cm at 1 atm: the whole α energy is deposited in the chamber. If a HV value on the two curves (before reaching the plateau) is chosen, the current corresponding to the 1.5 atm curve is greater than the current corresponding to the 3 atm curve. This is due to the fact that the ion mobility is inversely proportional to the gas pressure.

The two curves reach the same plateau, as expected.

The tests were repeated in air, proving that the chamber works correctly also in this case. Fig. 15.9 shows the results.

15.4 Muon beam diagnostics by luminescence

We investigate the possibility of having good fluorescence emitters to allow the optical monitoring of a surface muon beam, in a similar way to the proton beam (see chapter 10). Quartz is ideal for protons, but not for the muon. The muon beam has an intensity which is five orders of magnitude smaller, one therefore needs a crystal emitter roughly 5 order of magnitude more efficient than quartz. The study to select such a crystal was performed both by UV light excitation and by the C-W proton energy loss. Previous measurements, at the CERN, suggest that a suitable material could be a CsI crystal. The measurements performed by both methods gave a ratio $I_{CsI}/I_{quartz} \approx 10^4$ [216]. We repeated the measurement by using our TV camera, but with the

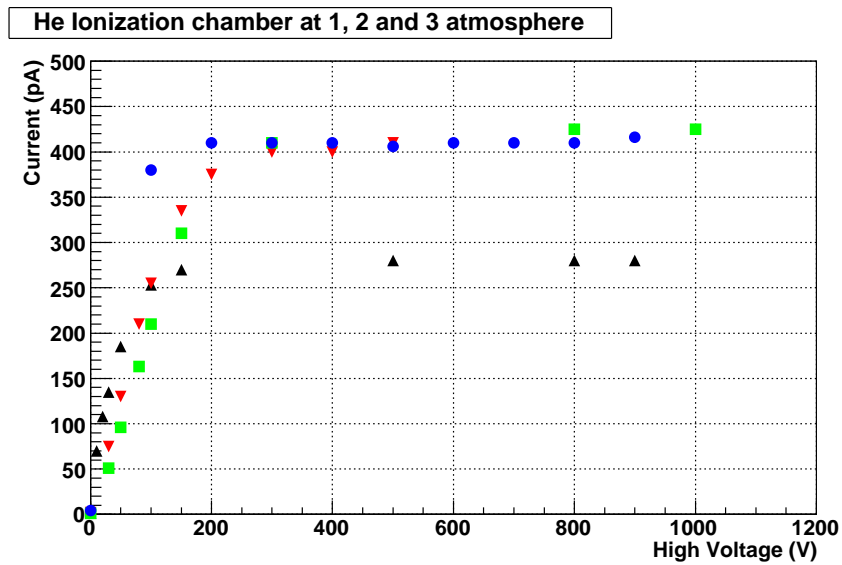


Figure 15.7: The measured current as a function of the applied HV (Helium). The different points correspond to different gas pressures: 1 atm (black triangle), 2 atm (red triangle and blue circle (negative HV)), 3 atm (green square).

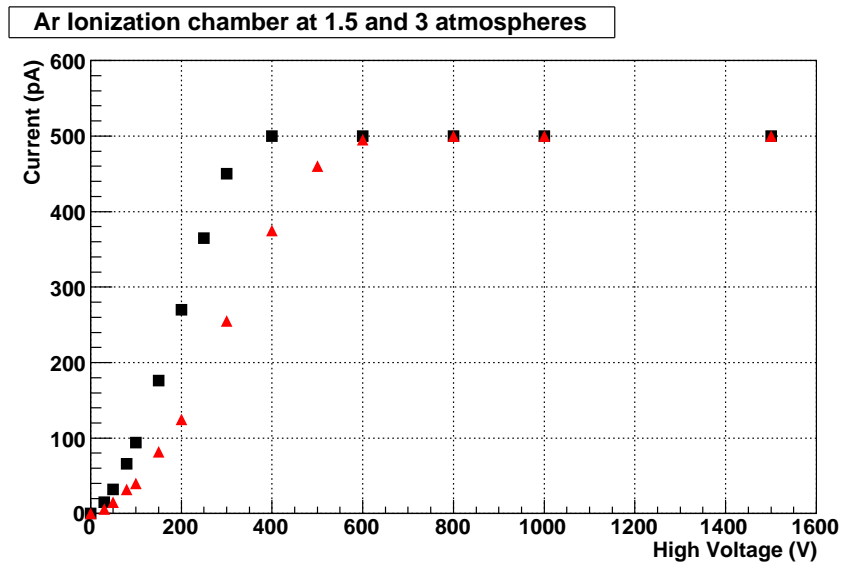


Figure 15.8: The measured current as a function of the applied HV (Argon). The different points correspond to different gas pressures: 1.5 atm (black square), 3 atm (red triangle).

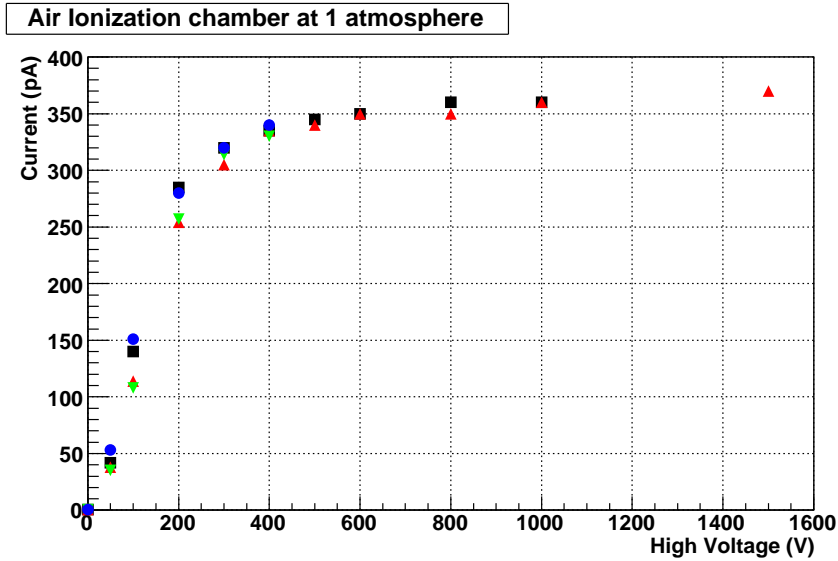


Figure 15.9: The measured current as a function of the applied HV (air) at 1 atm. The different points correspond to different HV polarity: HV+ (red and green triangle), HV- (black square and blue circle).

aid of a series of neutral optical filters of various transmissions, so as to bring the light, whatever its intensity, within the TV camera's dynamic range.

The total luminescence intensity was obtained by integrating over the TV image. The measured ratio is:

$$\frac{I_{CsI}}{I_{quartz}} = 16000 \pm 1500 \quad (15.7)$$

The comparison of the fluorescence intensity from the CsI(Tl) and quartz was also studied with the TV camera in the case of UV light crystal excitation. The ratio of the two responses varies greatly as a function of the radiation wavelength (in the case of the crystal excitation by protons, the fluorescence emission spectra corresponds to some kind of average over all the excitation wavelengths).

15.4.1 Muon beam diagnostics by CsI(Tl) light emission

The very intense CsI(Tl) fluorescence light emission, under UV light or proton excitation, and the high intensity of the MEG surface muon beam induced us to verify whether the MEG muon beam was observable using a CsI(Tl) crystal and a simple TV camera. We inserted a 40 mm diameter crystal and observed it with the TV camera while optimizing the camera parameters. Unfortunately, the beam was known to have a spot diameter larger than that of our crystal, therefore it was impossible to fully explore the diagnostic capabilities of this observational method. One can see in Fig. 15.10 (from top to bottom) the light due to muons+positrons (with the MEG positron separator off, with a beam intensity approximately eight times higher than that of the separated muon beam), the light due to the muon beam, and, as a comparison, the conditions of no-beam. The fluorescence light due to the muon beam is clearly visible. The test will be repeated, later on, with a larger crystal. It is worth pointing out that a higher sensitivity (by approx. a factor of 10) to the muon induced fluorescence light can be rather easily obtained (at a higher price, but without the need for image intensifiers) using a better optics and a higher performance commercial camera [65, 217, 218, 219]. The experience gained in the C-W optical beam diagnostics suggests the use of the same optical method (with CsI(Tl) crystals) for the study and monitoring of the MEG muon beam. The crystal could be introduced into the muon beam (travelling under

vacuum) also using a pneumatic system, similar to that of the C-W beam line. The use of two crystals, at two different positions along the beam, might provide fast and complete phase-space information.

15.5 Conclusion

A direct and continuous measurement of the intensity of the MEG surface muon beam can be based on a X-ray detector or on a windowless He ionization chamber. Both methods are promising and further tests are planned to evaluate a final system for the implementation in the experiment. At the moment it seems that the windowless He ionization chamber system is simpler to implement in the experiment than to the X-ray system.

Muon beam diagnostics by luminescence was investigated. The emission from CsI(Tl) is so high as to allow the optical monitoring of an intense muon beam by a TV camera.

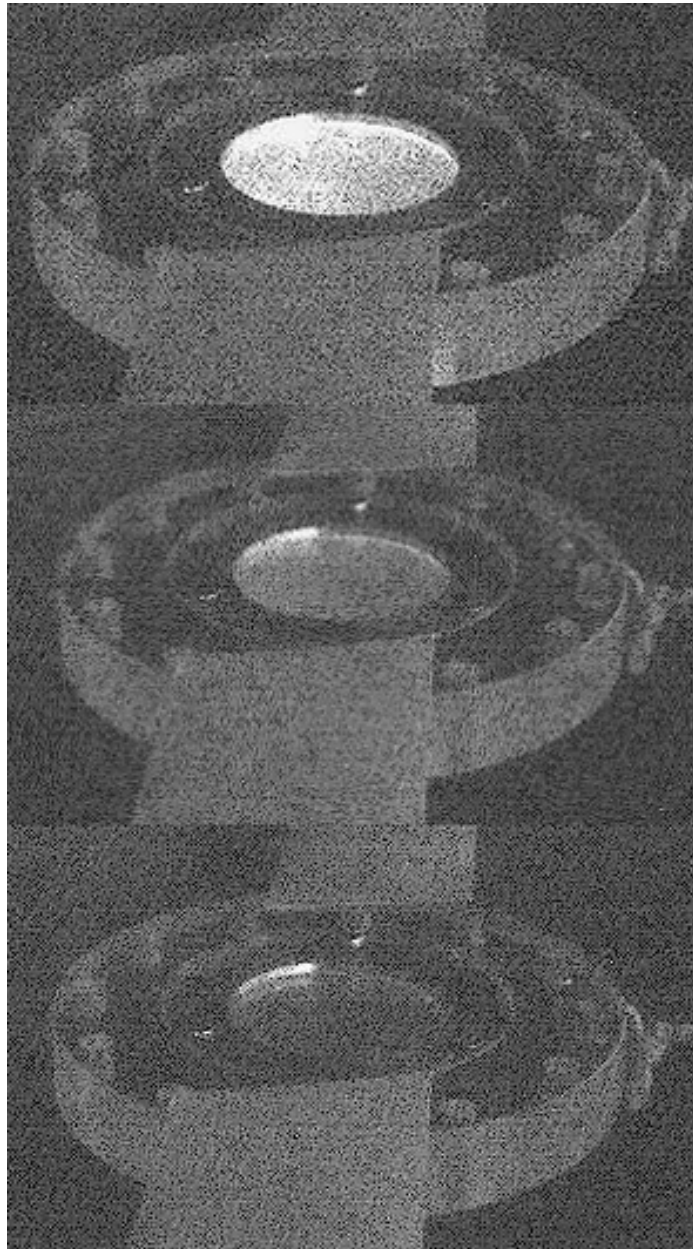


Figure 15.10: *Light emitted by the CsI(Tl) crystal under excitation by (from top to bottom) a muon+positron beam, a muon beam and no-beam.*

Part IV

MEG Run

Chapter 16

MEG Autumn 2008 Run

In this chapter we present the results of the calibration methods, showing the the quality of the performances reached by the MEG detectors.

We discuss the monitoring of the calorimeter LXe purity and the energy, position and time resolutions we obtained. We present the performances of the TC, the resolution in measuring the relative LXe calorimeter-TC timing. Finally we discuss the DC performances.

We estimate the sensitivity in determining the $B = \frac{\mu^+ \rightarrow e + \gamma}{\mu^+ \rightarrow \text{TOT}}$ by using the measured resolutions and efficiencies of the MEG detectors.

16.1 The LXe calorimeter

16.1.1 The monitoring of the LXe calorimeter

A pure LXe is required to reach the best calorimeter performance, as already discussed in chapter 4. Gaseous Xe was transferred from the storage dewar to the calorimeter in May. Fig. 16.1 clearly shows the level reached by LXe during the liquefaction process. α events from the Am-source on wire are reconstructed in the calorimeter. The blobs are associated with events in gas, while the rings are associated with events in LXe.

The Xe light yield LY, induced by γ s and α s was continuously monitored from the beginning of May to the end of December. During this period Xe was purified in the gas or in the liquid phase.

Fig. 16.2 shows the energy spectrum of γ events in the LXe calorimeter after 10 hours of purification in liquid phase. The γ -line, associated with the Li nuclear transition, from the excited state to the ground-state ($E_{\gamma 0} = 17.6$ MeV), and the γ -line, coming from intermediate state to ground-state ($E_{\gamma 1} = 14.7$ MeV) are both visible. The lower energy part of the spectrum is due to the overlapping of α -events and fluorine γ -lines ($E_{\gamma} = 6.1$ MeV, 6.9 MeV and 7.1 MeV). The data are not corrected for the PMT QEs; only the central part of the calorimeter ($|z| < 20$ cm and $|\phi| < 0.5$ rad) was selected. The two γ -lines are fitted with a double gaussian function. Fig. 16.3 shows the same energy spectrum after 126 hours of liquid phase purification (end of May); the two lines are better separated and the light yield increased.

The time evolution of the Li-line position (in number of photoelectrons) is shown in fig. 16.4. The total light yield has increased by a factor of 3, but the number of the photoelectrons N_{phe} expected at this energy has not been yet reached (26000 N_{phe} instead of 22000 N_{phe}). The Xe purification in liquid phase (blue) and in gas phase (blue light) are separately indicated. The errors in the plot result from the fit.

Two important observations emerge from the plot:

- the monitoring of the light yield allows a proper definition of the LXe calorimeter energy scale during the MEG run;

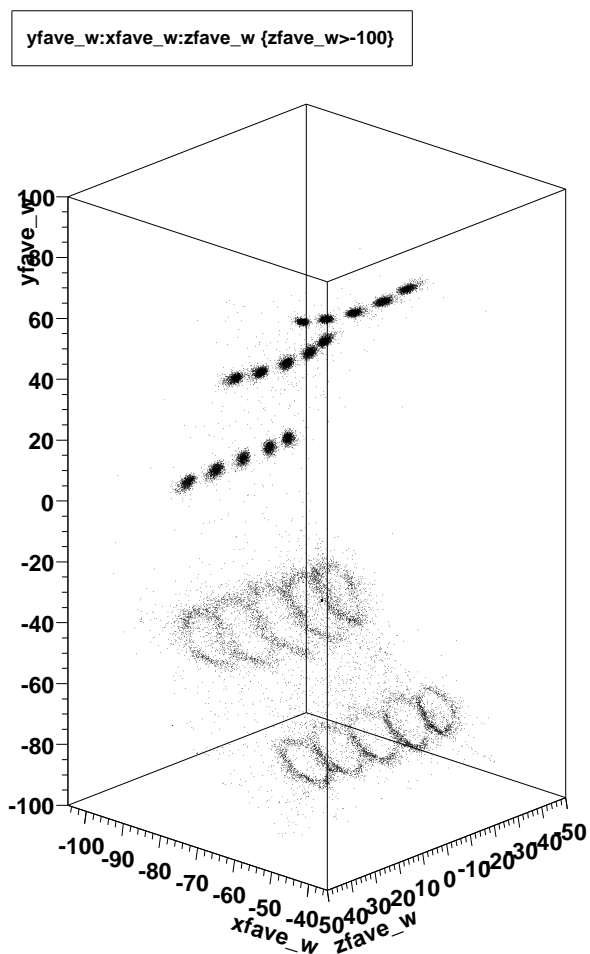


Figure 16.1: α events from the Am-sources on wire. The blobs and the rings are respectively associated with events in gas and in LXe.

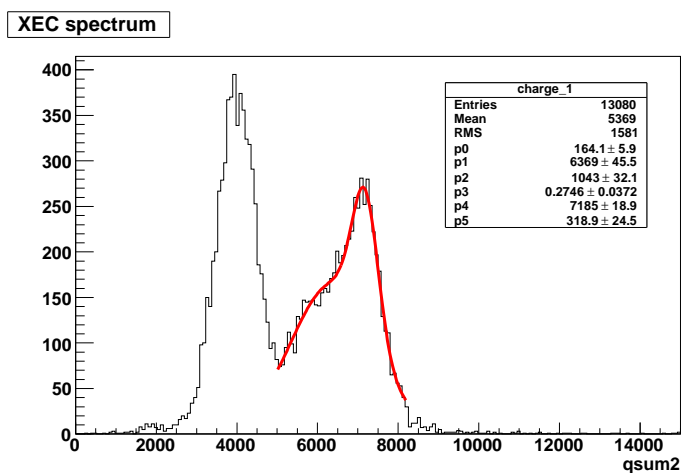


Figure 16.2: The γ -Lithium line at 17.6 MeV after 10 hours of Xe purification.

XEC spectrum

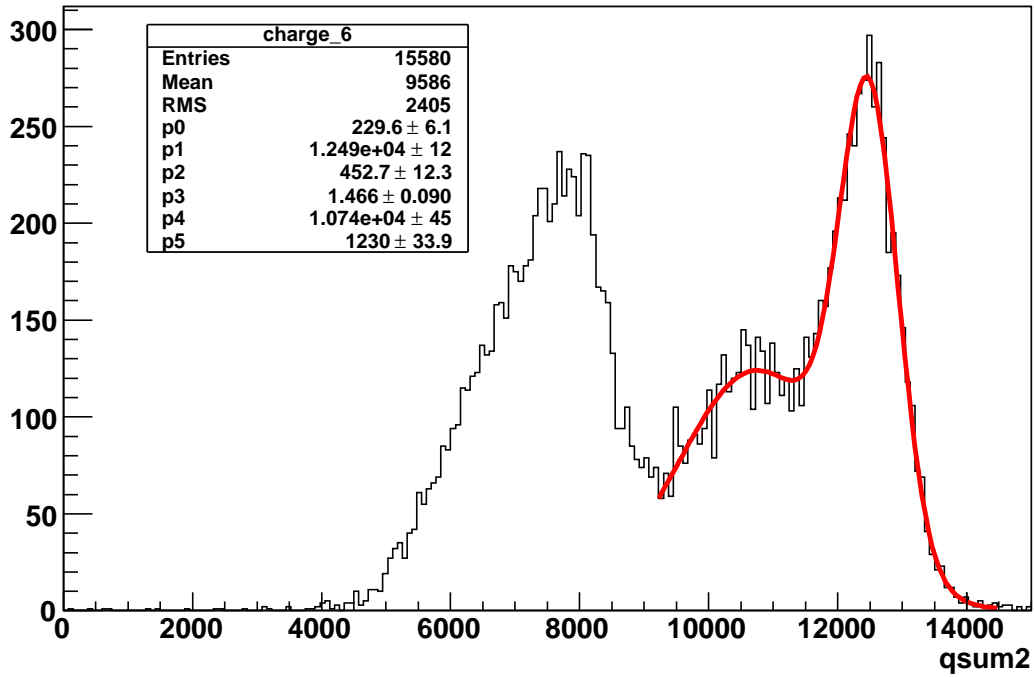


Figure 16.3: The γ -Lithium line at 17.6 MeV after 126 hours of Xe purification.

- the narrow γ -line allows the determination of the calorimeter energy resolution resulting from the LXe purification.

The relative energy resolution at 17.6 MeV improved from $\sigma_{E_\gamma}/E_\gamma = 5.62 \pm 0.15\%$ to $\sigma_{E_\gamma}/E_\gamma = 3.85 \pm 0.15\%$ (by a factor 1.5). If one assumes that the energy resolution of the LXe calorimeter scales as $1/\sqrt{N_{phe}}$, one obtains an extrapolated energy resolution at 52.8 MeV $\Delta E_\gamma/E_\gamma$ (FWHM) = 5 %, consistent with expectations.

The Xe LY was also monitored with the α wire sources. Fig. 16.5 shows the α LY evolution as a function of time. We selected one source mounted at the top (blue), one in the middle (red) and one at the bottom (green) of the calorimeter. The α LY initially increases and then stabilizes at the expected number of photoelectrons (about 9500). Fig. 16.6 shows the Li-line (black triangles) and the α -signal (red circles) superimposed. The α signal is here that of all sources together.

The results suggest the existence of two kinds of impurities: one affecting the transmission of the γ and α scintillation light in LXe, and the other, different for γ and α , affecting the Xe scintillation mechanism (see chapter 4). In accordance with this hypothesis one observes that the rise-time of the γ signal, after a long period of stability, has started to move towards longer values. One initially measured $\tau_\gamma = 27.99 \pm 0.01$ ns, while $\tau_\gamma = 29.31 \pm 0.01$ ns, at the end of December. It was verified that the time constant associated with the α signal is stable at approx. 22 ns.

The charge-to-amplitude ratio Q/A (fig. 16.7) is a way of keeping track of this effect.

The attenuation length λ_{att} , the λ_{Ray} and the absorption length λ_{abs} were also evaluated (see chapter 4 and chapter 8). Fig. 16.8 shows the results; we measured an attenuation length of $\lambda_{att} = 127 \pm 16$ cm, which corresponds to a Rayleigh scattering length of $\lambda_{Ray} = 94 \pm 10$ cm. Fig. 16.9 presents the result on the absorption length. The MC simulation uses the measured value of λ_{Ray} . We obtained $\lambda_{abs} \gg 500$ cm at 90% C.L.

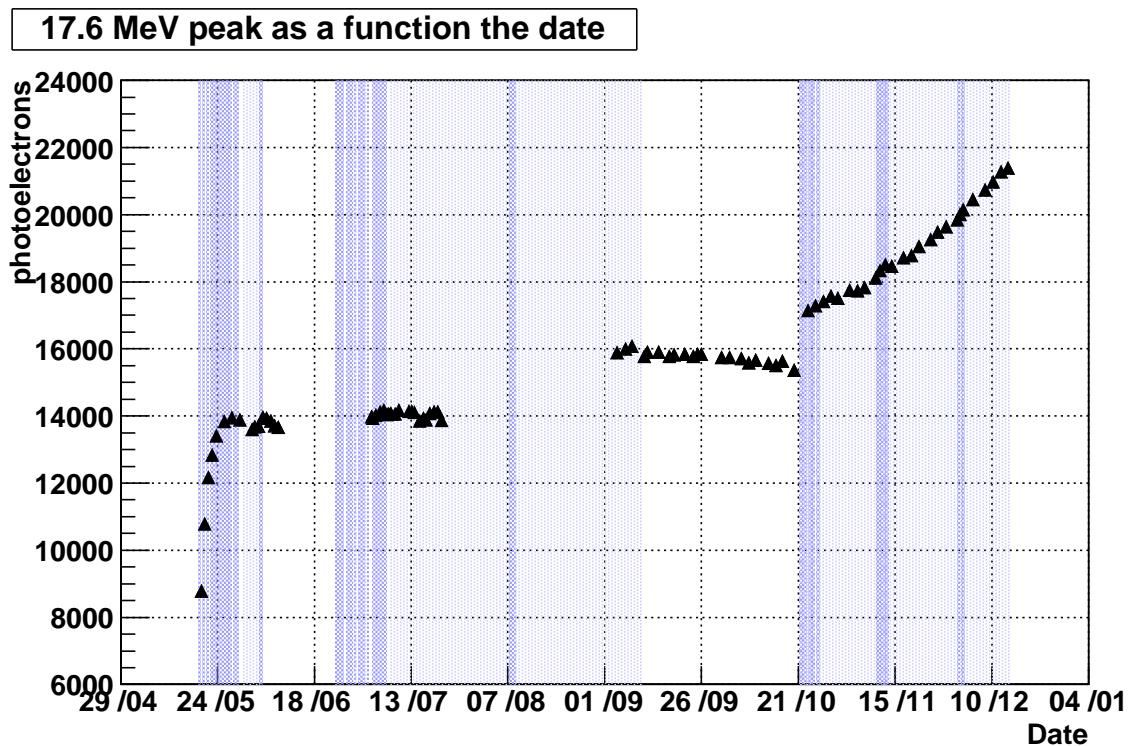


Figure 16.4: The 17.6 MeV γ -line as a function of time in the LXe calorimeter. The Xe purification periods in liquid phase (blue) and in gas phase (blue light) are also indicated.

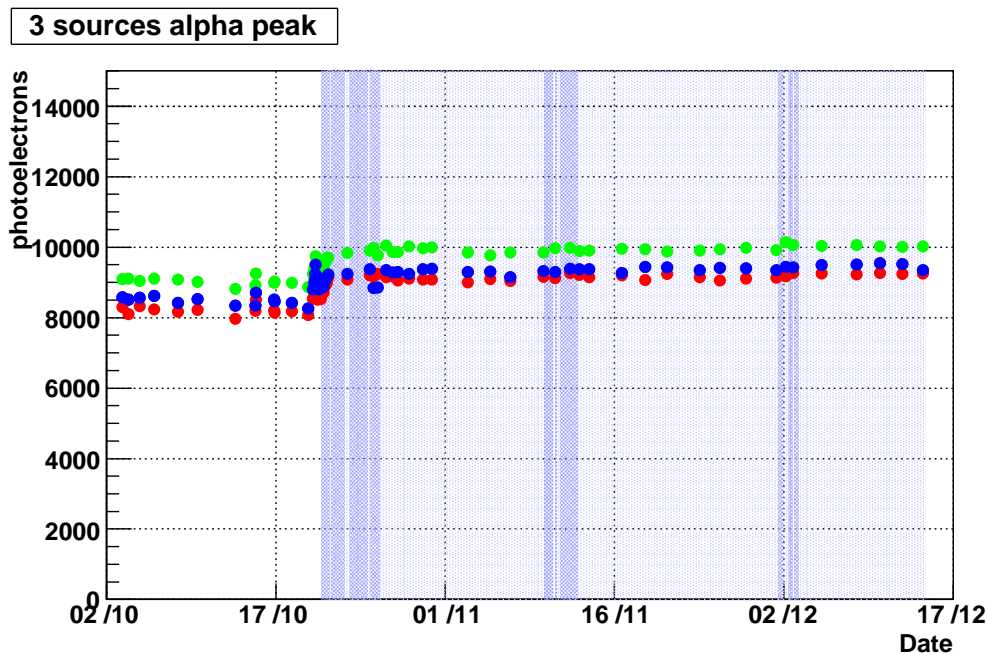


Figure 16.5: The α -signal as a function of time in the LXe calorimeter. Three sources were selected: one at the top (blue), one in the middle (red), one at the bottom (green) of the calorimeter. The Xe purification periods in liquid phase (blue) and in gas phase (blue light) are separately indicated.

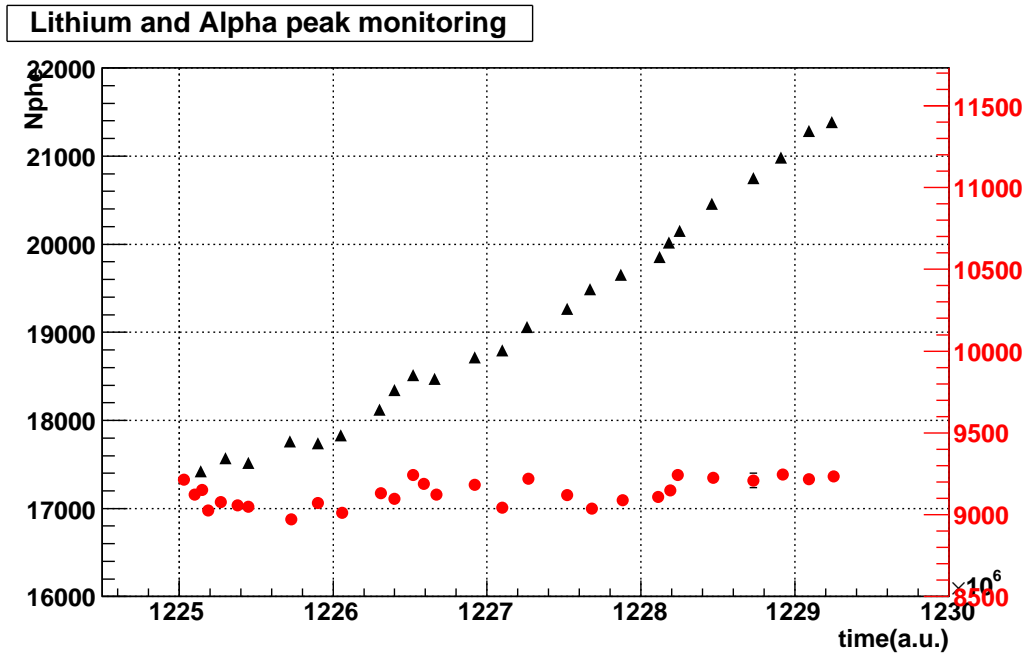


Figure 16.6: The γ -line (17.6 MeV) and the α -signal (5.5 MeV) in the calorimeter are plotted as a function of time.

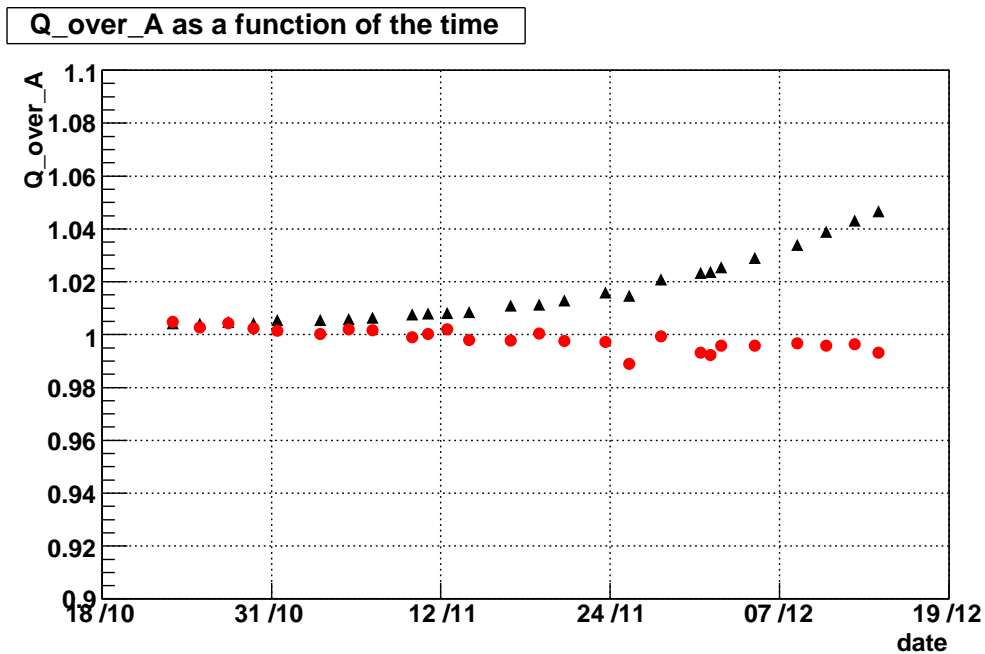


Figure 16.7: The charge-to-amplitude ratio Q/A as a function of time for the 17.6 MeV γ -line (black triangles) and for the α -particles (red circles).

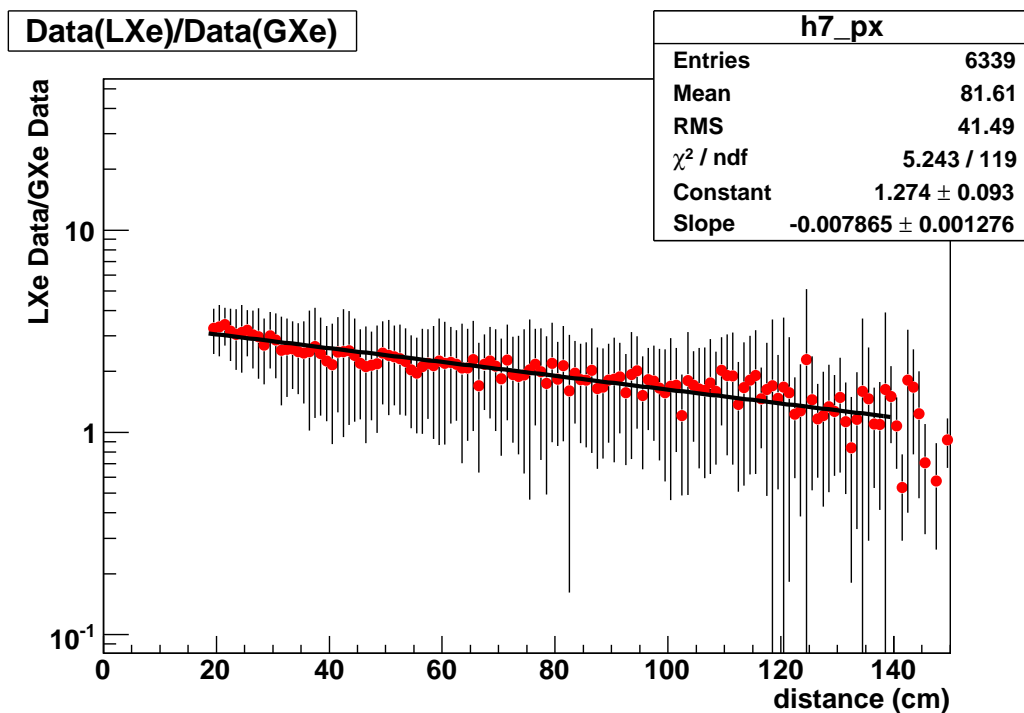


Figure 16.8: *The ratio of the number of photoelectrons in LXe and GXe, as a function of the alpha source-PMT distance.*

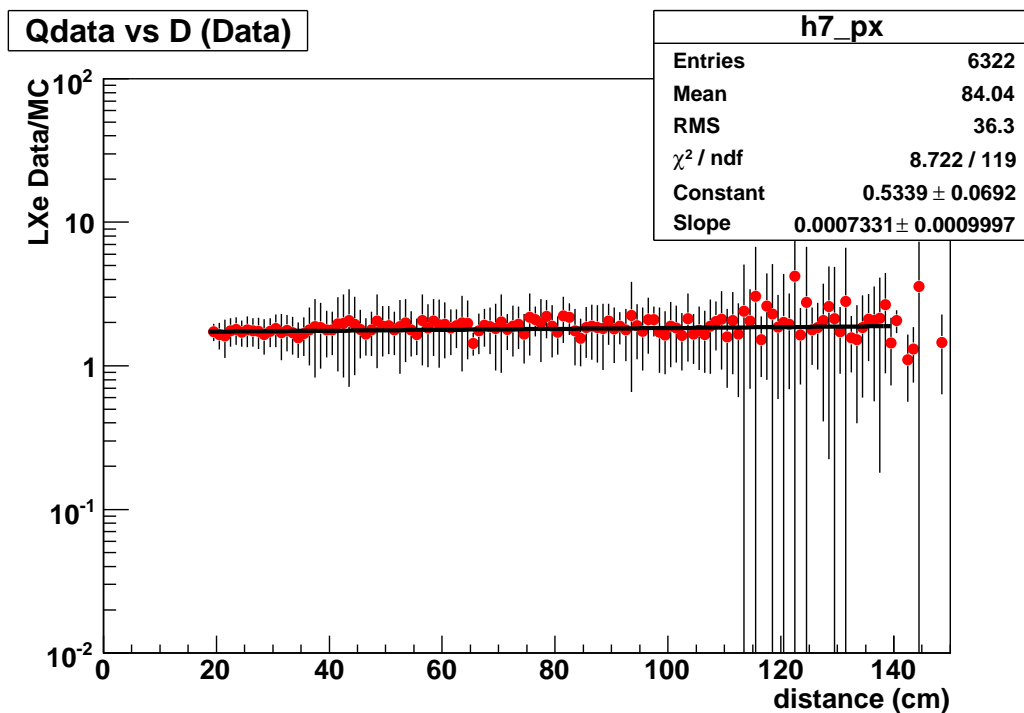


Figure 16.9: *The ratio of the experimental number of photoelectrons in LXe and the corresponding MC predictions, as a function of the distance alpha source-PMT.*

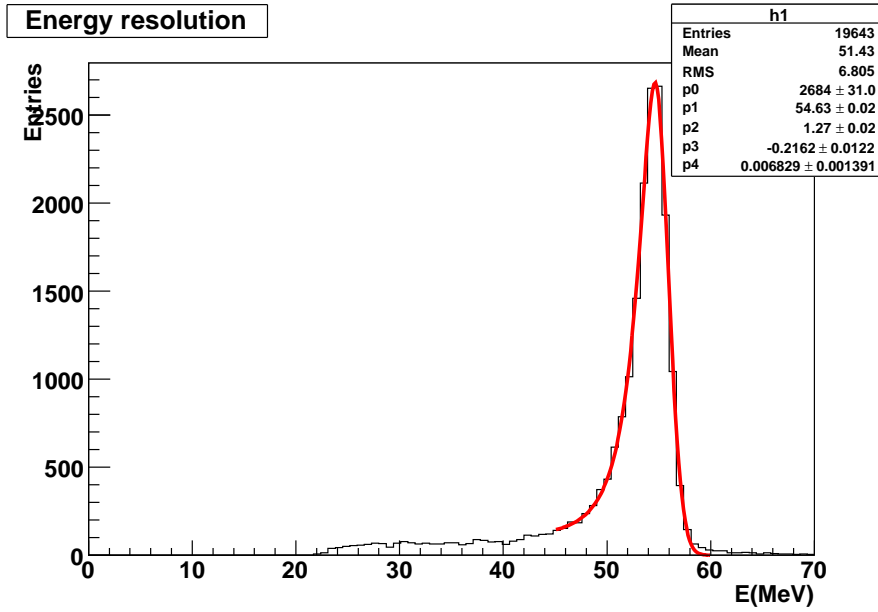


Figure 16.10: The LXe energy resolution ($\Delta E_\gamma/E_\gamma(FWHM) = 5.9 \pm 0.1\%$) at 54.9 MeV.

16.1.2 The LXe calorimeter linearity and energy resolution

The γ energy spectrum measured by the LXe calorimeter relative to the $E_{\gamma 1} = 54.9$ MeV from the π charge exchange reaction $p(\pi^-, \pi^0)n$ is shown in fig. 16.10. We required that the two gamma's be emitted in opposite directions by using the LXe calorimeter and the auxiliary NaI detector (see chapter 11). The applied selections were:

- the choice of the 54.9 MeV γ in the LXe calorimeter was obtained by requiring the $E_{\gamma 2} = 82.9$ MeV γ in the NaI detector;
- we only accepted events entering the calorimeter from the central part of the inner face;
- the saturated PMTs were excluded from the evaluation of the event energy.

The energy resolution (no QE correction applied) is $\Delta E_\gamma/E_\gamma(FWHM) = 5.9 \pm 0.1\%$. We are confident that the expected energy resolution ($\Delta E_\gamma/E_\gamma(FWHM) = 5\%$) can be reached, when the PMT QEs are available and implemented in the analysis.

Fig. 16.11 groups the measurements relative to several γ -lines used to study the energy linearity of the LXe detector. The calorimeter is linear in the range of interest.

16.1.3 The time resolution of the LXe calorimeter

We used events from π^0 decay, as previously described, to evaluate the time resolution of the LXe calorimeter at 54.9 MeV. The PMTs of the calorimeter were divided into two groups: even and odd PMTs. The LXe time resolution corresponds to the width of the distribution of the time differences between even and odd PMTs. $\sigma(t_\gamma)$ was studied as a function of the number of photoelectrons N_{phe} . Fig. 16.12 shows the results. The new data from the MEG calorimeter (black) are presented together with the old data from the Large Prototype (red). At $N_{phe} = 79000$ we measured a LXe calorimeter time resolution $\Delta t = 105 \pm 1$ ps (FWHM).

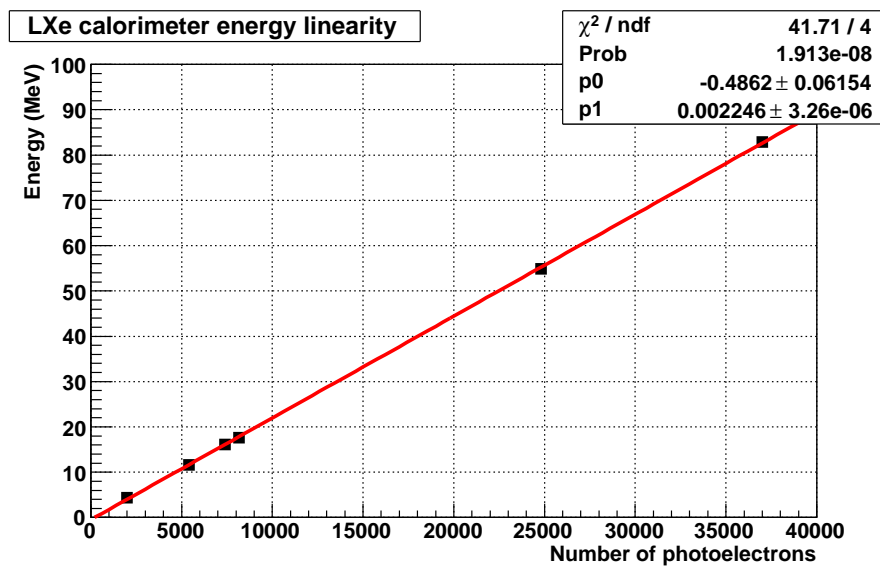


Figure 16.11: The measurements relative to several γ -lines (from Boron and Lithium reactions, and from π^0 -decay) are presented together. The LXe calorimeter is linear in energy.

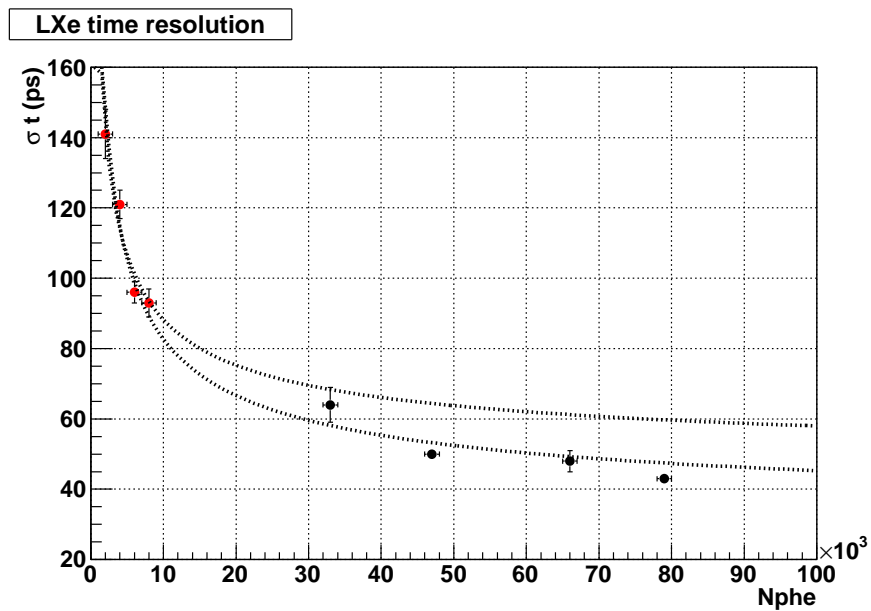


Figure 16.12: The LXe calorimeter time resolution as a function of the number of photoelectrons (π^0 -decay data). We measured $\Delta t = 105 \pm 1$ ps (FWHM) at $N_{phe} = 79000$.

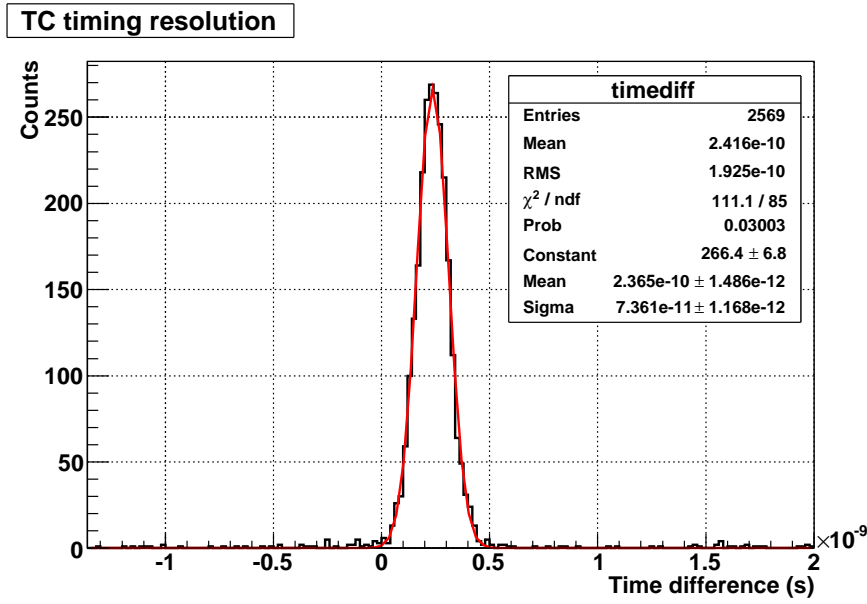


Figure 16.13: The TC time resolution. We measured $\Delta t(\text{FWHM}) = 123 \pm 2$ ps.

16.2 TC detector

16.2.1 The time resolution of the TC

Fig. 16.13 demonstrates the time resolution reached by the TC. The data are due to $E_e = 52.8$ MeV Michel positrons analysed by the spectrometer. We selected only the events simultaneously detected by two adjacent bars. The distribution of Fig. 16.13 is of their time differences. The measured time resolution is $\Delta t(\text{FWHM}) = 123 \pm 2$ ps, a little worse than expected ($\Delta t(\text{FWHM}) = 100$ ps).

16.2.2 LXe-TC timing

The π^0 run was also used to measure the absolute LXe-TC time offset. The events from the Dalitz process: $\pi \rightarrow e^+e^-\gamma$ were selected since the Dalitz π^0 events and the $\mu^+ \rightarrow e^+\gamma$ signal have similar topologies. The γ was detected by the LXe calorimeter and the e^+ by the TC. The trigger requirements were: a γ energy greater than 45 MeV, a time coincidence between the LXe calorimeter and the TC and a loose angular correlation between the two detectors (trigger 2). The selections introduced in the analysis are:

- the γ 's time and position must be measured by the the LXe calorimeter;
- the positron must be tracked by the DC system;
- a good matching DC system-TC is required;
- the positron time of flight is corrected by taking into account the length of the positron trajectory;
- the γ time of flight is corrected by taking into account the γ flight path from its origin, defined by the origin of the positron trajectory at the target;

The width of the distribution of the time differences is affected by the rather large dimensions of the liquid hydrogen target (used during the π^0 run, instead of the normal MEG small target. This contribution to the width is approx. 100 ps).

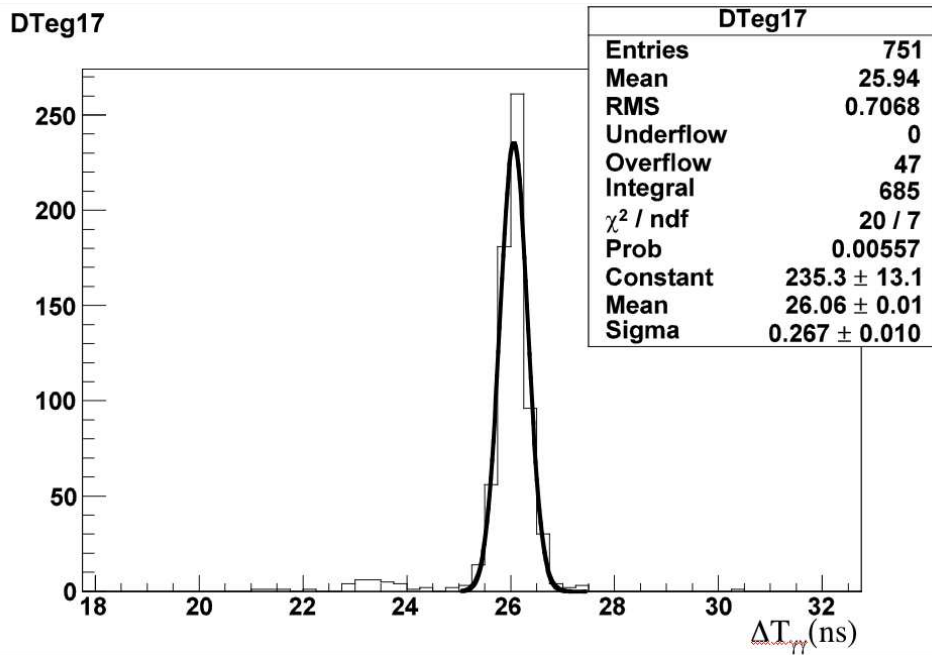


Figure 16.14: The LXe-TC time resolution from Dalitz events. $\sigma_{t_{e\gamma}} = 267 \pm 10$ ps.

Fig. 16.14 shows the distribution of the time differences for Dalitz events with positron and γ energies close to those of the MEG expected signal. $\sigma_{t_{e\gamma}} = 267 \pm 10$ ps (the contribution due to the target dimensions is still included).

16.3 The DC system

The performance of the Drift chamber system was studied by means of Michel positrons, during the 2007 engineering run. All the DC's were working at the nominal high voltage. Well tracked positrons were selected ($\chi^2 \leq 20$). Fig. 16.15 shows the positron spectrum. The spectrum edge appears at the expected momentum $p_e = 52.8$ MeV/c. The momentum resolution is $\Delta p_e/p_e$ (FWHM) = $2.2 \pm 0.1\%$, close to the expected value ($\Delta p_e/p_e$ (FWHM) = 0.9%). The DC performances deteriorated during the 2008 run (see next section). The positron momentum resolution further decreased to $\Delta p_e/p_e$ (FWHM) $\approx 3.5\%$.

16.4 The MEG detector efficiencies

In this section we make a preliminary evaluation of the MEG global detector efficiency.

16.4.1 The positron detection efficiency

One of the elements determining the MEG global efficiency is the measurement of the efficiency for positron detection. This efficiency $\epsilon(e^+)$ is defined as the probability of detecting a positron when it propagates within the geometrical acceptance A_G of the spectrometer (DC + TC):

$$\epsilon(e^+) = P(e^+ \in DC | e^+ \in A_G) \cdot P(e^+ \in TC | e^+ \in A_G, e^+ \in DC). \quad (16.1)$$

The first term of the product in the eq. (16.1) is what we call the DC efficiency $\epsilon(DC)$ (detection of the positron hits and its track reconstruction). The second term is what we call the DC-TC

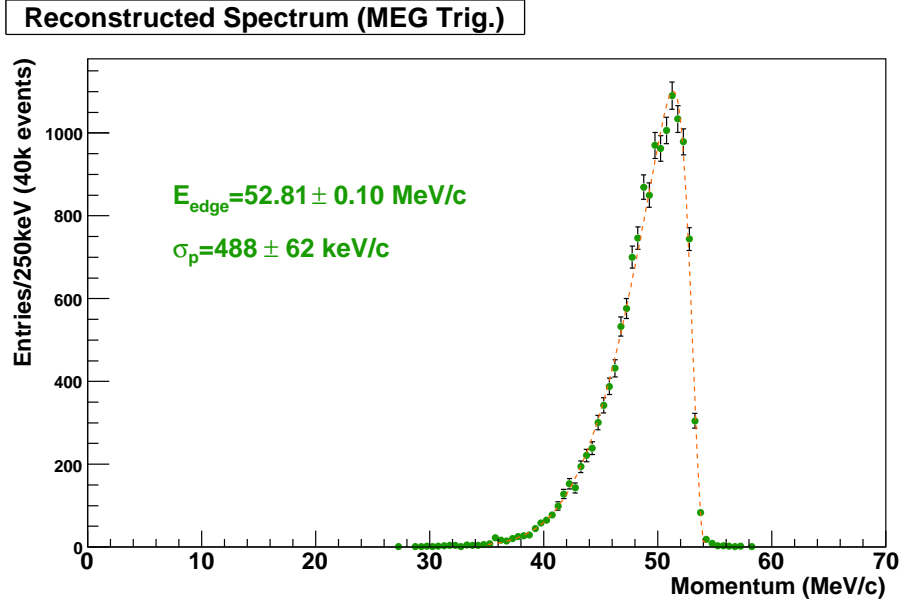


Figure 16.15: The Michel positron spectrum measured with the MEG spectrometer. The spectrum edge is at 52.8 MeV/c, as expected. We obtained a relative momentum resolution $\Delta p_e/p_e(\text{FWHM}) = 2.2 \pm 0.1\%$.

matching efficiency $\epsilon(\text{TC}/\text{DC})$.

The measurement of $\epsilon(\text{DC})$ was based on Michel events identified among the events accepted by a random trigger (pedestal trigger). The track multiplicity found in the Michel events is expected to follow a Poisson distribution:

$$p(n) = \pi(n|\mu) = \frac{\mu^n \cdot e^{-\mu}}{n!} \quad (16.2)$$

where n is the positron track multiplicity and μ is equal to:

$$\mu = R_e \cdot T, \quad (16.3)$$

where R_e is the positron rate (still to be determined) investing the DC system and $T = 500 \text{ ns}$ is the DRS time window.

The positron rate can be rewritten in terms of the rate of muons stopped in the target R_μ :

$$R_e = R_\mu \cdot A_G \cdot \bar{\epsilon}(\text{DC}), \quad (16.4)$$

where A_G is the geometrical acceptance for Michel positrons (evaluated by a MC simulation; $A_G = 12\%$), and $\bar{\epsilon}(\text{DC})$ is the DC average efficiency for Michel positrons, evaluated over the interval of positron momenta accepted by the DC system ($p_e \geq 35 \text{ MeV/c}$).

Eq. (16.3) becomes:

$$\mu = R_\mu \cdot A_G \cdot T \cdot \bar{\epsilon}(\text{DC}). \quad (16.5)$$

The performances of the individual chambers of the DC system were followed during the MEG run. This is the input information of a MC simulation which provides the DC efficiency $\epsilon(\text{DC})$ in the MEG signal region.

A comparison of the experimental results with the predictions of the MC simulation relies on two variables:

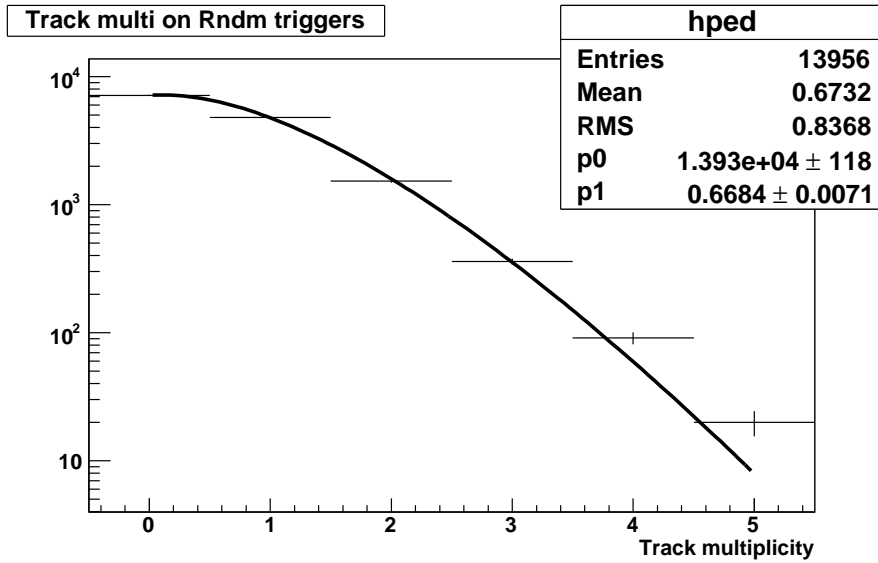


Figure 16.16: Drift chamber track multiplicity for a data sample at the beginning of the 2008 MEG Run.

- the positron rate R_e is derived from the measurement of μ and the application of eq. (16.3). R_e is also obtainable from the MC simulation of isotropically generated Michel events;
- $\bar{\epsilon}(DC)$ is derived from the measurement of μ and the application of eq. (16.5). $\bar{\epsilon}(DC)$ is also obtainable from the MC simulation of Michel positrons entering into the geometrical acceptance.

Fig. 16.16 shows the positron track multiplicity, for the runs from 24082 \rightarrow 24587 (14th – 16th Sept. 2008). The cyclotron proton current was stable at $2\mu\text{A}$ ($1950 \leq I_p \leq 2050 \mu\text{A}$) during this period. This current corresponds to a muon stopping rate $R_\mu = 2.8 \cdot 10^7 \mu/\text{s}$.

We determined a positron rate of $R_e = 1.34 \pm 0.01 \text{ MHz}$ and an average efficiency $\bar{\epsilon}(DC) = 40.7 \pm 0.5\%$. The corresponding MC predictions were $R_e = 1.09 \pm 0.17 \text{ MHz}$ and $\bar{\epsilon}(DC) = 38 \pm 0.5\%$.

Fig. 16.17 shows a partial result of the MC simulation: $\epsilon(DC)$ as a function of the e^+ momentum. $\epsilon(DC)$ at the MEG signal ($p_e = 52.8 \pm 1 \text{ MeV}/c$) is $\epsilon(DC) = 83 \pm 2\%$.

Unfortunately the DC performance degraded during the MEG run. Fig. 16.18 shows the DC performances (DCs correctly working: green box, DCs switched off: orange box) as a function of time and summarizes the results of this study. The table lists the experimental R_{e^+} , the expected (MC simulation) R_{e^+} , the experimental $\bar{\epsilon}(DC)$, expected (MC simulation) $\bar{\epsilon}(DC)$, $\epsilon(DC)$ extrapolated to the signal region (MC simulation). All these results were used to predict the single event sensitivity of our experiment.

The determination of $\epsilon(TC/DC)$ was based on events selected by the DC trigger. The trigger requires a minimum of 4 hits in 5 consecutive chambers; signals in the calorimeter or in the TC have no part in the trigger. This event sample is used to evaluate the probability that a positron reaches the TC, if there is a track in the DC system. The analysis was performed on 15 000 events associated with the DC trigger.

The analysis proceeds in two steps:

- the identification of a correctly tracked positron trajectory;
- the track matching to a TC hit.

The identification of a good track depends only on geometrical selections:

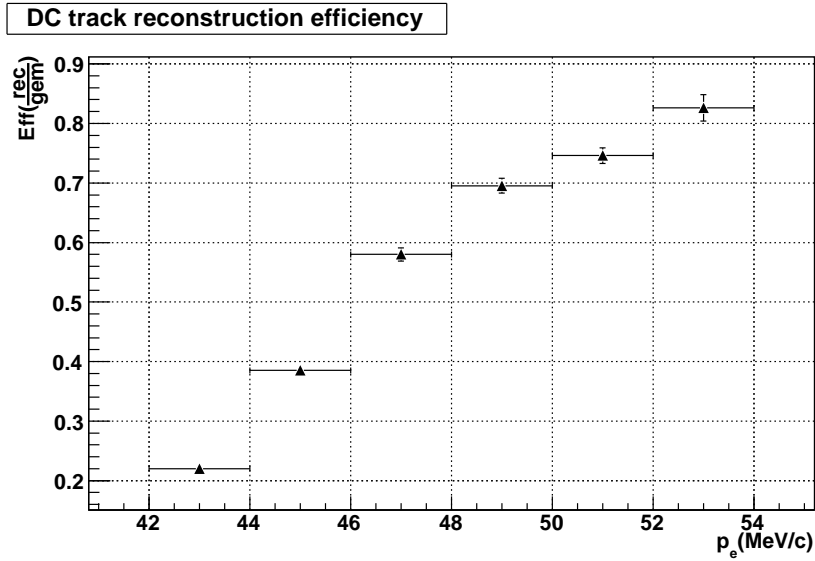


Figure 16.17: The MC simulated DC efficiency as a function of the Michel e^+ momentum. Some chambers were switched off in the simulation.

- the χ^2 associated with the tracked trajectory is lower than 20;
- the extrapolated trajectory matches has its origin in the target;
- the extrapolated trajectory reaches the TC.

An additional requirement is a positron momentum greater than 48 MeV. The distributions associated with these variables are shown in fig. 16.19.

Fig. 16.20 shows the distribution of the difference between the coordinates of the extrapolated positron trajectory and the coordinates of the TC hit.

No selection in timing has yet been applied. A time distribution relative to the DC and TC detectors is shown in fig 16.21; the difference between the DC and TC times is plotted. Apart from very loose selections on the DC and TC times, the important selection finally applied is $|\delta(t_{DC} - t_{TC})| \leq 50$ ns. All the matching criteria are intentionally made very loose. The measured matching efficiency is: $\epsilon_{TC/DC} = 37.4 \pm 0.3\%$.

The Monte Carlo simulations of Michel events predict a matching efficiency of $\epsilon_{TC/DC} = 55.5 \pm 0.4\%$. This number is obtained applying the same selections used for the data analysis. The TC PMT threshold is not implemented in the Monte Carlo simulation. This could be the reason for the discrepancies between them. We need to investigate this point further.

16.4.2 The efficiency of γ detection

We define the γ efficiency $\epsilon(\gamma)$ as the probability of detecting a γ at 52.8 MeV, which propagates into the geometrical acceptance of the calorimeter, given a positron of the same energy entering into the geometrical acceptance of the spectrometer:

$$\epsilon(\gamma) = P(\gamma \in LXe | e^+ \in A_G(\gamma), e^+ \in spectrometer). \quad (16.6)$$

A MC simulation was used to evaluate the LXe γ efficiency. The result is: $\epsilon(\gamma) \approx 40\%$.

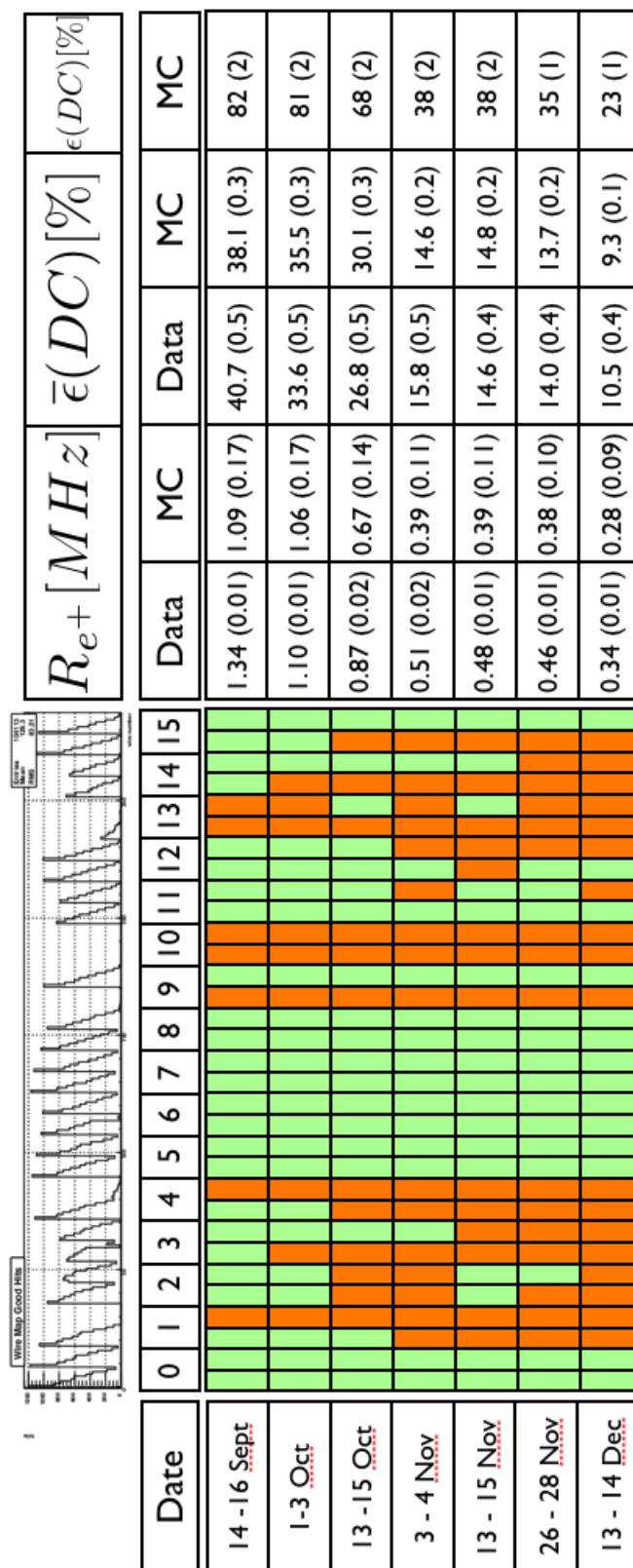


Figure 16.18: The DC performances as a function of time. The orange boxes correspond to DCs which were switched off.

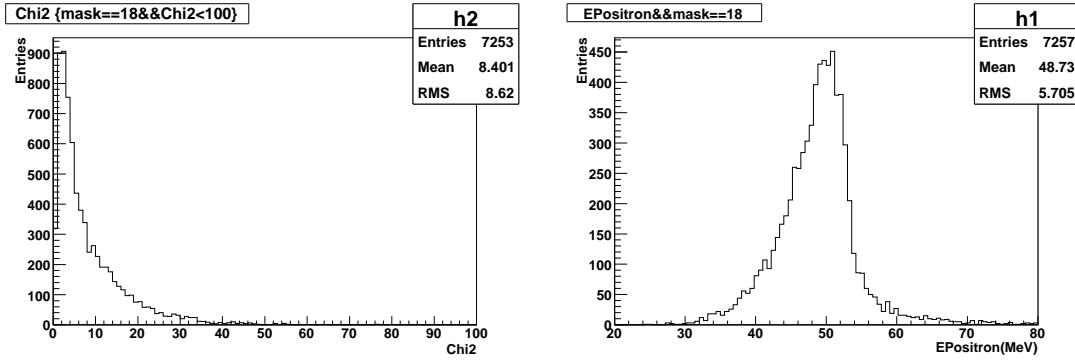


Figure 16.19: The χ^2 distribution of the tracked trajectories (left) and the e^+ momentum distribution (right).

16.5 The MEG sensitivity for the $\mu^+ \rightarrow e^+\gamma$ decay

We define the single event sensitivity of the MEG experiment as the branching ratio of the $\mu^+ \rightarrow e^+\gamma$ decay for which one event is observed:

$$SES_{\mu \rightarrow e\gamma} = \frac{1}{N_{TOT}} \quad (16.7)$$

where N_{TOT} is the number of Michel decays detected when subject to the same selection criteria as MEG events (among other criteria, a momentum threshold of ≈ 50 MeV will probably be applied). We can have:

$$N_{TOT} = R_\mu \cdot T \cdot A_G \cdot \epsilon(e^+) \cdot \epsilon(\gamma) \cdot \epsilon(TRG) \cdot \epsilon_{sel} \quad (16.8)$$

where $\epsilon(TRG)$ is the probability of trigger activation if the positron and the γ are detected:

$$\epsilon(TRG) = P(MEG \text{ trigger} | e^+ \in Spectrometer, \gamma \in LXe) = 0.63, \quad (16.9)$$

and ϵ_{sel} is the selection efficiency on the positron momentum, γ energy, γe^+ relative angle and relative time.

Fig. 16.22 shows the measured integrated proton current. This can be rescaled in terms of muon stops in the target (the muon rate, at a nominal 2 mA proton current, corresponds to $2.8 \cdot 10^7 \mu/s$). The total number of muons collected during the 2008 MEG run is computable from fig. 16.22 and is:

$$N_\mu = 9.1 \cdot 10^{13} \mu^+ \quad (16.10)$$

An estimate of the single event sensitivity is possible, if one uses the measured quantities R_μ , $\epsilon(e^+)$ and $\epsilon(TRG)$, and assumes an $\epsilon(\gamma) = 40\%$, (as obtained by the MC simulation), and a ϵ_{sel} corresponding to 90% of the signal for each variable ($\epsilon_{sel} = 0.9^4 = 0.66$).

Fig. 16.23 shows the single event sensitivity as a function of the run number, during the MEG run 2008. A value of $SES_{\mu \rightarrow e\gamma} = 3 \cdot 10^{-12}$ was reached, subject to likely modifications of the analysis methods in the course of time.

Other definitions of the MEG sensitivity can be introduced, starting from the previously computed $SES_{\mu \rightarrow e\gamma}$ value. We define, for instance, as MEG sensitivity, the upper limit (at the 90% confidence level) on the branching ratio of the $\mu^+ \rightarrow e^+\gamma$ decay, if no event is observed. Fig. 16.24 shows the contribution of the accidental background (from radiative decays annihilations in flight) to the branching ratio, as a function of the γ relative energy resolution and the positron relative momentum resolution (in terms of $\delta = 1.64\sigma$). The plot corresponds to a muon rate of $R_\mu = 2.8 \cdot 10^7 \mu/s$, a time resolution $\Delta t_{e\gamma} = 250\text{ps}$ (FWHM) and a $\theta_{\gamma e^+}$ angular resolution $\Delta\theta = 0.023$ mrad (FWHM). At $\delta E_\gamma = 4\%$ and $\delta p_{e^+} = 1.5\%$ we evaluate a $B_{acc} = 6 \cdot 10^{-13}$. Fig. 16.25 shows

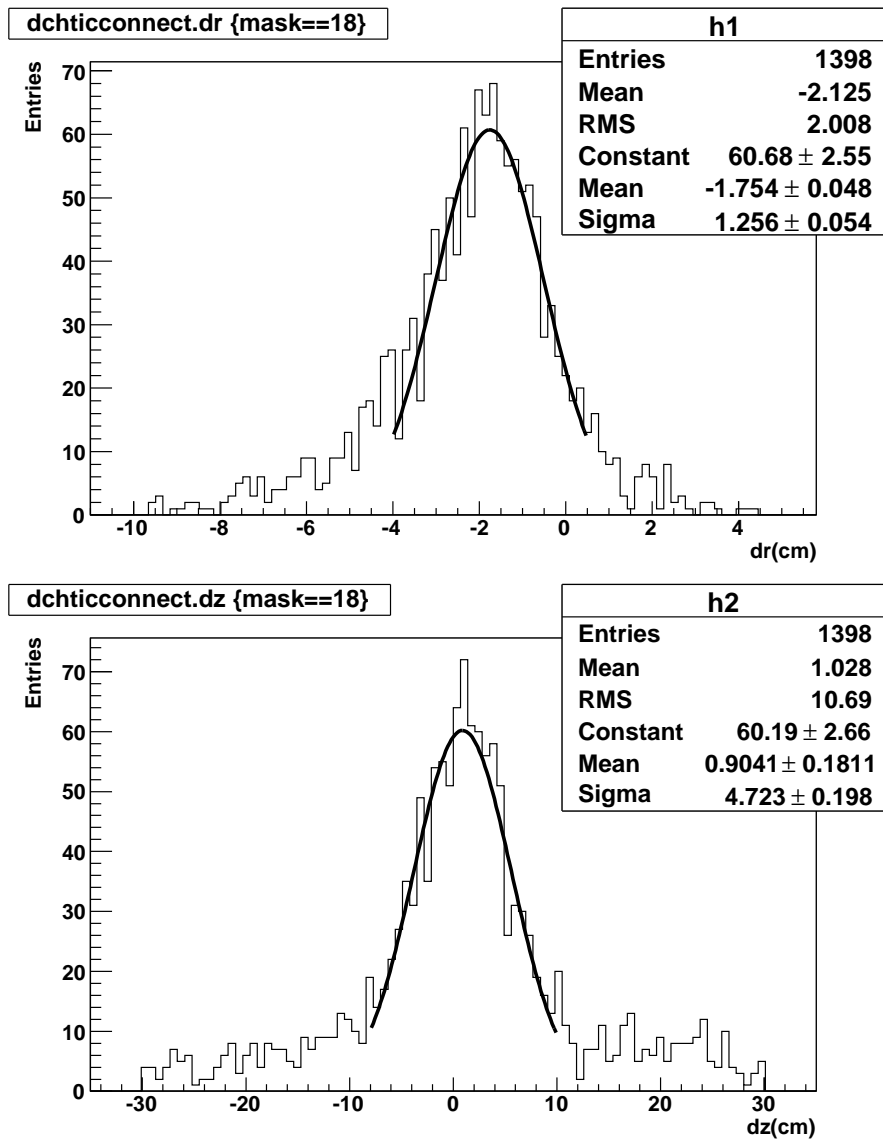
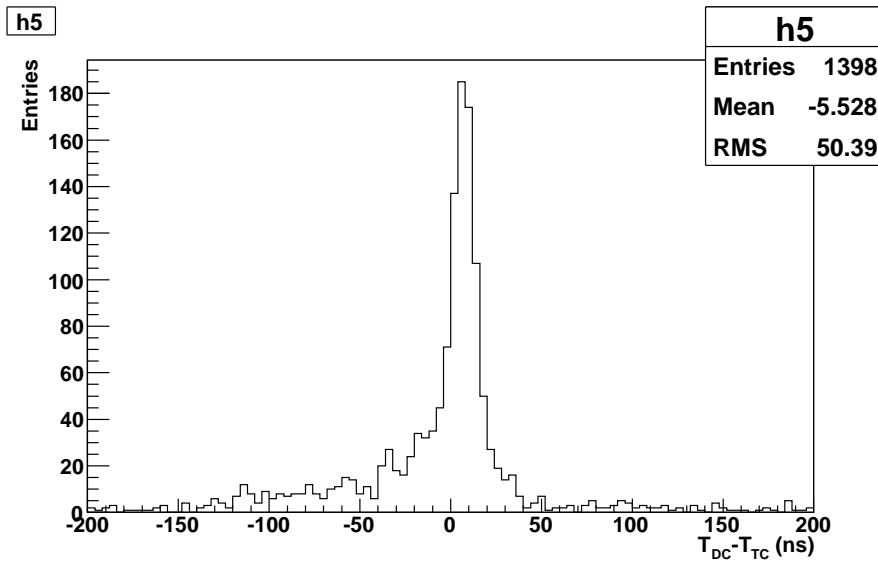
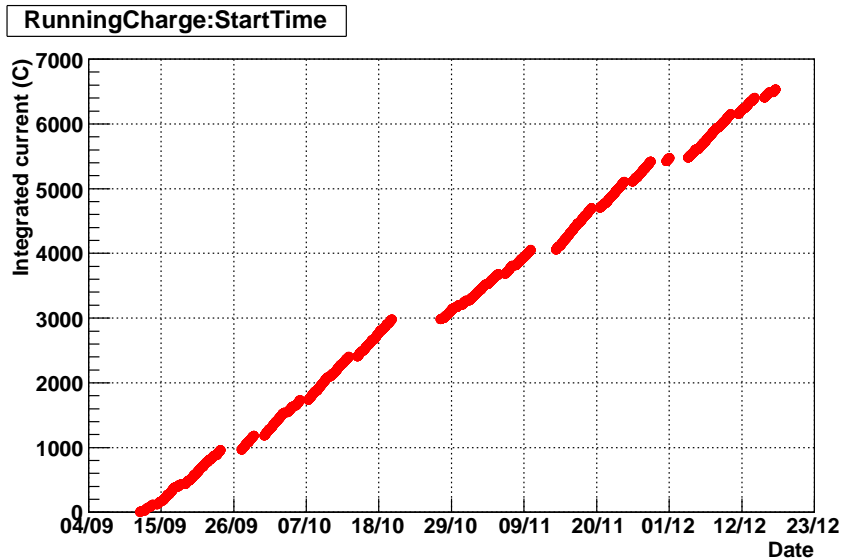


Figure 16.20: The distribution of the difference of the coordinates of the extrapolated trajectory and those of the TC hit ($\delta r = R_{DC} - R_{TC}$ (top) and $\delta z = Z_{DC} - Z_{TC}$ (bottom)).

Figure 16.21: *The distribution of the time difference $T_{DC} - T_{TC}$.*Figure 16.22: *The integrated proton current (Coulombs) as a function of time.*

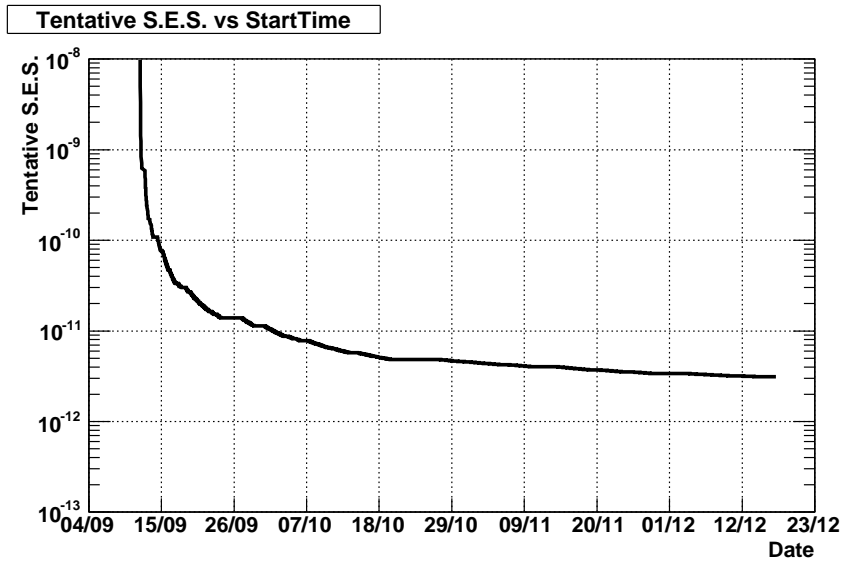


Figure 16.23: *The single event sensitivity as a function of time.*

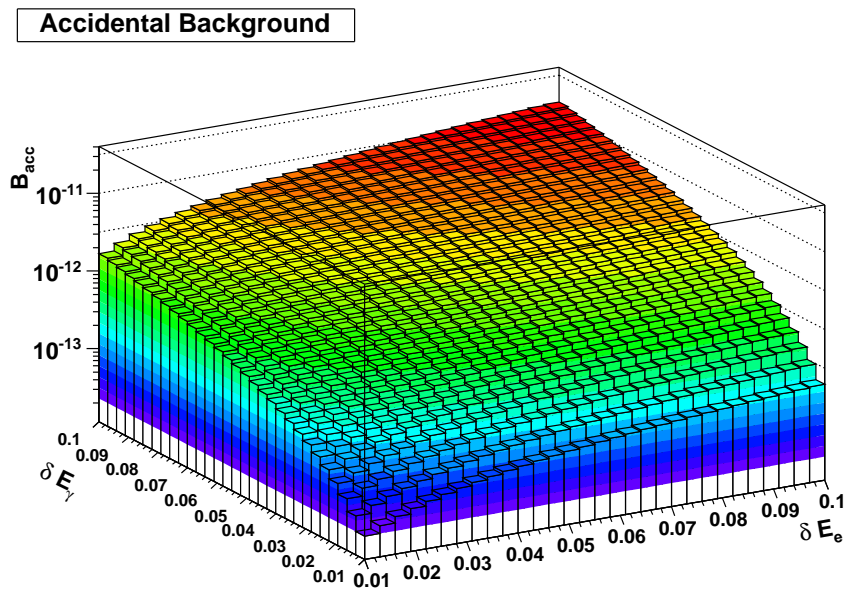


Figure 16.24: *The accidental background contribution to the branching ratio, as a function of the γ relative energy resolution and the positron relative momentum resolution.*

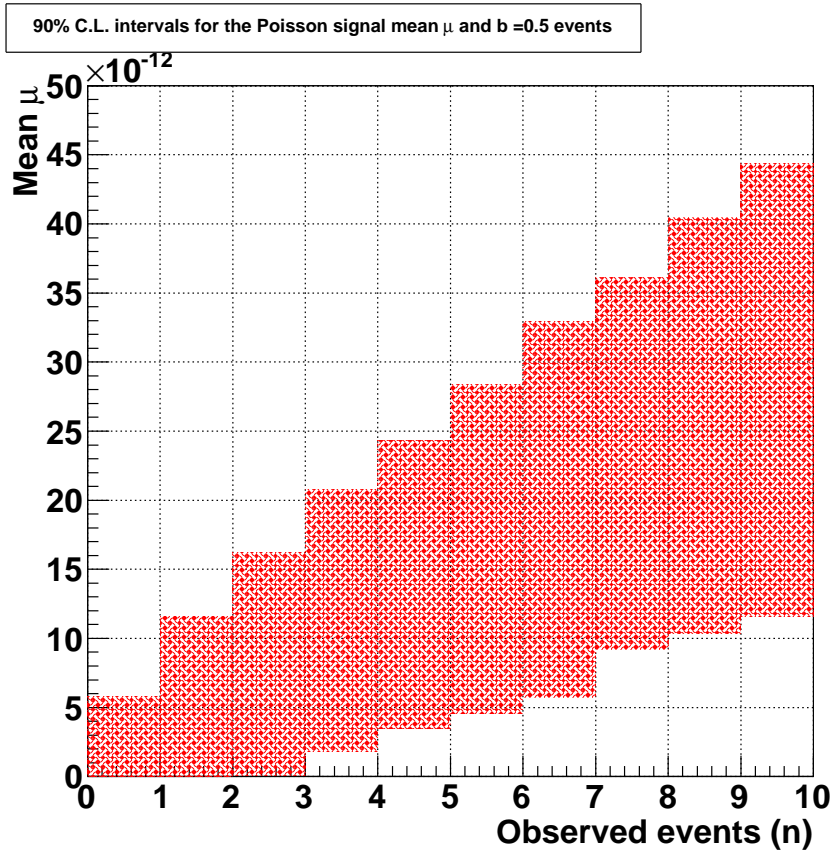


Figure 16.25: The 90 % C.L. intervals for the signal mean μ and a background $b = 0.5$ events, as a function of the observed number of events [220].

the confidence band calculated in a frequentist framework, using the Feldman-Cousins ordering prescription [220], for a Poisson-distributed signal over an expected background of 0.5 events (quoted as the ratio of B_{acc}/SES). In the case of no observed candidate ($k = 0$ on the x axis), the 90% C.L. region yields an upper limit on the branching ratio:

$$B.R.(\mu^+ \rightarrow e^+\gamma) < 5.8 \cdot 10^{-12} @ 90\% \text{C.L.} \quad (16.11)$$

If at least three $\mu^+ \rightarrow e^+\gamma$ candidates are observed, a discovery can be claimed and the branching ratio would have the limits:

$$1.8 \cdot 10^{-12} < B.R.(\mu^+ \rightarrow e^+\gamma) < 1.6 \cdot 10^{-11} @ 90\% \text{C.L.} \quad (16.12)$$

Note that the upper limit is comparable to that determined by the MEGA experiment (see chapter 2).

16.6 The muon radiative decay signal

We conclude this thesis with the presentation of an important physical result obtained in the MEG run 2008: a clear evidence of muon radiative decay $\mu^+ \rightarrow e^+\gamma\bar{\nu}_\mu\nu_e$.

The rare radiative decay events were identified rather easily. This is a demonstration of the quality of the MEG experiment, since those events are very similar to the ones of $\mu^+ \rightarrow e^+\gamma$ decay. They have:

- the same relative timing;
- relative angle $\Delta\theta_{e\gamma}$ and energies at the boundaries of the signal region.

The rarity of the radiative decay events is beneficial since otherwise they would represent a serious background for the experiment.

The data sample is made of dedicated runs, corresponding to a reduced muon intensity (stopping rate $\approx 1.2 \cdot 10^6 \mu/s$, total live time $\approx 4.5 \cdot 10^5$ s). The total number of triggers was $\approx 2 \cdot 10^6$ and the corresponding number of LXe-TC pairs was $\approx 2.8 \cdot 10^6$.

The events were selected by a dedicated trigger (RD trigger) based on a temporal coincidence between a Timing Counter hit and a Liquid Xenon hit (with respect to the normal MEG trigger, the RD trigger has a LXe lower energy threshold and the angular selection is also less stringent). The trigger rate is dominated by accidental coincidences; there are also two large correlated signals due to cosmic rays crossing the LXe (before) and the TC (after) or the TC (before) and the LXe (after).

The selection criteria were:

- a tracked trajectory in the DC system and at least one TC bar hit (this reduces the original sample to $\approx 3 \cdot 10^4$ events);
- a good time and spatial matching between the extrapolation of the positron trajectory to the TC and the TC hit ($|T_{DC} - T_{TC}| \leq 50$ ns $\sqrt{|Z_{DC} - Z_{TC}|^2 + |R_{DC} - R_{TC}|^2} \leq 20$ cm);
- a γ energy up to 60 MeV in the LXe calorimeter; a selection on the charge distribution was also applied, $Q_{out}/Q_{in} > 2$, to remove most of the cosmic rays crossing the calorimeter in accidental coincidence with a DC track (events coming from the target have small Q_{out}/Q_{in}); $\approx 2 \cdot 10^4$ events survive the selections;
- residual cosmic rays are further rejected by an angular selection ($\cos\theta_{e\gamma} < -0.7$);
- muons decaying at rest are selected by kinematics. The final sample is $\approx 8 \cdot 10^2$ events and the RD events are $\approx 5 \cdot 10^2$.

The kinematical selection is as follows. The invariant squared mass of the two neutrinos (neglecting the electron mass) is computed:

$$\begin{aligned}
m_{2\nu}^2 &= E_{2\nu}^2 - \vec{p}_{2\nu}^2 = (m_\mu - E_e - E_\gamma)^2 - (\vec{p}_e + \vec{p}_\gamma)^2 = \\
&\approx m_\mu^2 - 2(E_e + E_\gamma) \cdot m_\mu + 2 \cdot E_e \cdot E_\gamma \cdot (1 - \cos\theta) = \\
&= m_\mu^2 - 2(E_e + E_\gamma) \cdot m_\mu + 4 \cdot E_e \cdot E_\gamma \cdot \sin^2\left(\frac{\theta}{2}\right) \geq 0
\end{aligned} \tag{16.13}$$

Rearranging the terms of the eq. (16.13) and dividing them by m_μ^2 , one obtains:

$$\frac{4 \cdot E_e \cdot E_\gamma}{m_\mu^2} \cdot \sin^2 \frac{\theta}{2} \geq \frac{2 \cdot (E_e \cdot E_\gamma \cdot m_\mu)}{m_\mu^2} - 1. \tag{16.14}$$

Eq. (16.14) can be rewritten in terms of the variables $x = 2 \cdot E_e/m_\mu$ and $y = 2 \cdot E_\gamma/m_\mu$:

$$x \cdot y \cdot \sin^2 \frac{\theta}{2} \geq x + y - 1. \tag{16.15}$$

This inequality is the kinematic selection shown in fig. 16.26. Fig. 16.27 shows the $t_e - t_\gamma$ distribution. The clear peak at -25.5 ns is due to muon radiative decays. The TC-LXe timing resolution at the RD energies is $\sigma(t_{e\gamma}) = 160 \pm 5$ ps.

In conclusion: a radiative decay signal is identified in the MEG ultra-low intensity data. The measured TC-LXe timing resolution is about $\Delta t_{e\gamma}(FWHM) \approx 350$ ps, much worse than what stated in the proposal (100 ps). Since the time resolutions of the TC and of the LXe calorimeter

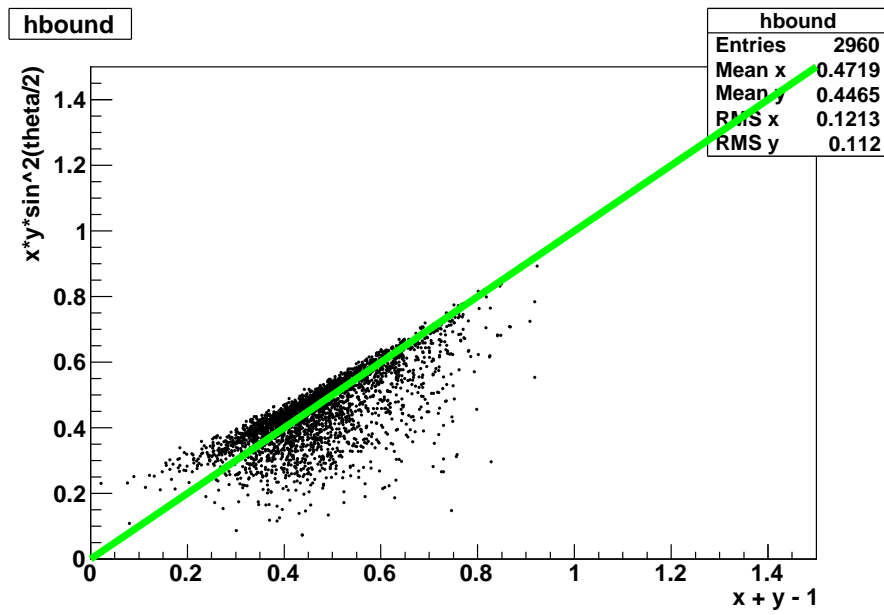


Figure 16.26: Kinematical selection for the muon radiative decays.

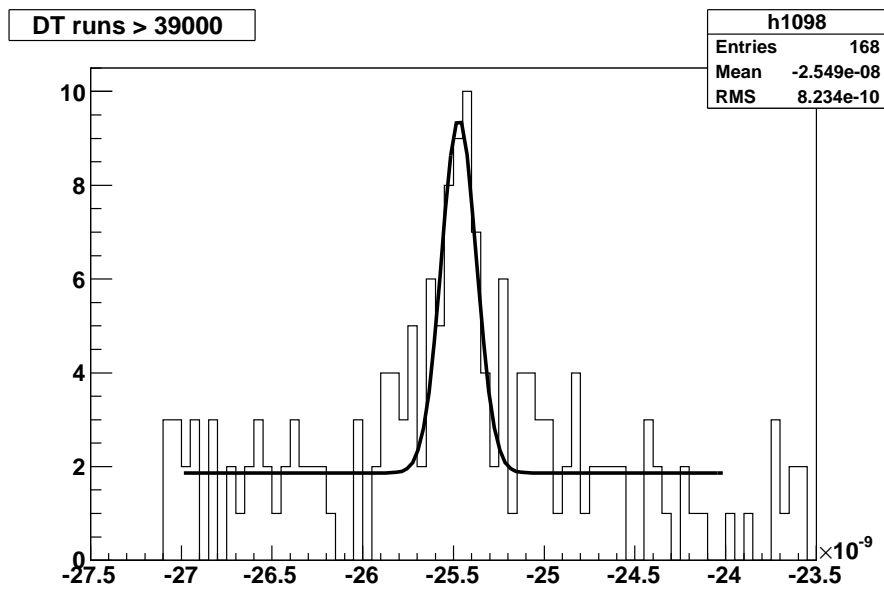


Figure 16.27: The $t_e - t_\gamma$ distribution in seconds (a RD event sub-sample). The radiative decay signal appears at -25.5 ns.

are rather close to the design values, most of the responsibility of the bad $\Delta t_{e\gamma}$ timing is due to the inadequate performances of the DC system during the 2008 run (see 16.3). A poorly tracked trajectory corresponds to uncertainties in the positron track length and to a degradation of the timing resolution on the positron time of flight. Once improved the DC system for the 2009 run, the timing resolution $\Delta t_{e\gamma}$ should improve by a factor of two.

Conclusions

The collaboration succeeded in having the “ first” MEG run at the end of 2008, with the whole apparatus installed and in operation. The muon beam intensity was the expected one. The stored data were associated with about 10^{14} μ^+ stopped in the target. We are hoping to reach a first MEG result during 2009. Although not all detectors reached the performances specified in the MEG proposal, we are confident of improvements in the near future.

The very clear observation of the radiative muon decay is an important achievement which proves the top quality of the experiment.

Abundant calibration data were obtained with α -sources, LEDs, the Cockcroft-Walton accelerator and with the π^- charge-exchange. These data were used to study the behaviour of all detectors during the experiment. At times it was possible to disclose malfunctionings and instabilities occurring in the apparatus.

All calibration methods were first tested for proving their effectiveness and then optimized for the MEG experiment (as described in detail in this thesis).

During 2009 the experiment will reach top performances and an improved stability, corresponding to the design sensitivity.

The great physics of MEG, the design, the assembling, the running of this experiment have been a great fun throughout !

Acknowledgements

The work discussed in this thesis is the result of a collaboration with many people, without whom the thesis would be no more than an ensemble of white sheets.

I am extremely grateful to Prof. Carlo Bemporad, my supervisor during these years. I think that it has been a great fortune to work with him, and in particular to benefit from his guidance and experience. I would like to express my gratitude to him for giving me the chance to experience the beauty and the difficulty of undertaking “scientific research”. He taught me to “first love and then do physics”. Fervor, passion, dedication, constancy, tenacity, competition, comparison, matching are the essential components in research. I have learnt from him a great deal of physics and in particular (I hope) the way to think as a physicist. I am grateful to him for his support and encouragement without which I would never have managed to finish this thesis.

Over the years I have enjoyed the aid and the support of the Pisa MEG group. Also in this case it is not simple to write words which are able to express my gratitude to them. Anyway I would like to associate to each one a particular aspect that “struck” me: Alessandro Baldini, for trusting me during these years and for teaching me that all things need to be understood deeply; Roberto Pazzi, for teaching me that the world can be correctly simulated if it is understood; Franco Sergiampietri, for introducing me to the beautiful world of the cryogenic; Marco Grassi, for teaching me that the foundations of a good scientific project are simplicity and logic; Fabrizio Cei, for his vast knowledge and the possibility of discussing any argument; Donato Nicolò, for his rigour and the extreme accuracy used in every circumstance and for his patience in transmitting his scientific background; Luca Galli and Giovanni Gallucci, who shared with me the status of PhD student (...and everything which is connected with this...). I wish also to thank Nicolino Curalli, Luca Perrozzi and Matteo Corbo, different parts of this thesis have overlapped with their work.

I would like to finish my “pisani” acknowledgements with Giovanni Signorelli. A lot of the work presented in this thesis was made together with him. It is difficult to find a unique attribute for him, probably because we have spent a lot of time together and I experienced that he incorporates all of the previously mentioned attributes.

It was for me a fortune to take advantage of the privilege of the immense scientific experience and wisdom of Prof. Bemporad, on the one hand, and the scientific freshness and vitality of Giovanni, on the other. We shared success and difficult moments, relax and hard work, gratification and bitterness.

It has been beautiful! I wish a similar experience to all PhD students.

Finally I would like to thank all the MEG collaboration. During these years a lot of effort has been put in by everyone in order to start the first data acquisition at the end of the last year. During this “tour de force” from each one I could take advantage of some aspects. I would like to thank Prof. Flavio Gatti, Riccardo Valle e Simeone Dussoni for sharing with us the first study on the nuclear reactions at the Legnaro National Laboratories; Prof. Satoshi Mihara, Wataru Ootani, Toshiyuki Iwamoto, Yasuko Hisamatsu for the discussion about the LXe calorimeter; Prof. Peter R. Kettle, with whom we shared the C-W accelerator installation to the PSI, the proton beam line design and installation, the X-ray emission induced from proton and muon, the study on beam monitoring by means of luminescent materials; Haijme Nishiguchi for the discussion about

the Drift Chamber (and for giving me Fig. 16.15); Malte Hildebrandt, for helping me during the MEG Run 2008; Ryu Sawada and Yusuke Uchiyama for suggestions about the MEG software; Stefan Ritt, for the collaboration and the support from the PSI; I would like to thank also people who did not work together with me directly, but who gave me useful suggestions (for example during the collaboration meeting); Prof. William Molzon, Ben Golden, Feng Xiao and the new entry Elisabetta Baracchini; Prof. Giancarlo Piredda, Prof. Dino Zanello, Alex Barchiesi, Gianluca Cavoto, Cecilia Voena (thanks also for giving me Fig. 12.9), Francesco Renga; Prof. Marco Panareo, Prof. Gianluigi Boca, Paolo Cattaneo, Massimo Rossella, Roberto Nardò and Antonio de Bari; Oleg Kiselev, Jeanine Adam; D. N. Grigoriev; and finally Prof. T. Mori (who, together with Alessandro Baldini, shares the experiment responsibility) for giving us the support which allowed us to believe in the experiment.

A particular thanks, different from the others, is for Alarico, who is neither a member of the MEG collaboration nor a physicist, even though it seems as if he had worked with me on every item discussed in this thesis. I shared with him the sensations and the emotions associated with this work. I am grateful to him for mediating the “strong” interaction between the physics and me in a way similar to the gluons, attenuating the interaction when I was strongly absorbed by the physics and increasing the interaction when I was depressed. He has been the glue which holds everything together.

I would also like to thank my parents, Vincenzo and Barbara for the support they provided me, even though it was not possible to spend time together because I was so busy with the experiment.

Bibliography

- [1] R. R. Crittenden et al., *Phys. Rev.* **121** (1961) 1823.
- [2] W. Bertl et al., *Phys. Lett.* **B140** (1984) 299.
W. Bertl et al., *Nucl. Phys.* **B260** (1985) 1.
- [3] S. J. Freedman et al., *Phys. Rev.* **D47** (1993) 811.
- [4] M. L. Brooks et al. (MEGA collaboration), *Phys. Rev. Lett.* **83** (1999) 1521.
- [5] U. Bellgardt et al., *Nucl. Phys.* **B299** (1988) 1.
- [6] R. D. Bolton et al., *Phys. Rev.* **D38** (1988) 2077.
- [7] Y. Fukuda et al. (Super-Kamiokande Collaboration), *Phys. Rev. Lett.* **85** (2000) 3999.
- [8] M. Ambrosio et al. (MACRO Collaboration), *Phys. Lett.* **B434** (1998) 451.
- [9] W. W. M. Allison et al. (Soudan Collaboration), *Phys. Lett.* **B391** (1997) 491.
- [10] Y. Fukuda et al. (Super-Kamiokande Collaboration), *Phys. Rev. Lett.* **86** (2001) 5656.
- [11] Q. R. Ahmad et al. (SNO Collaboration), *Phys. Rev. Lett.* **89** (2002) 011302.
- [12] B. Cleveland et al., *Ap. Jour.* **496** (1998) 505.
- [13] W. Hampel et al. (Gallex Collaboration), *Phys. Lett.* **B447** (1999) 127.
- [14] J. N. Abdurashitov et al. (SAGE Collaboration), *Phys. Rev. Lett.* **83** (1999) 4686.
- [15] M. Altmann et al. (GNO Collaboration), *Phys. Lett.* **B490** (2000) 16.
- [16] K. S. Hitara et al. (Kamiokande Collaboration), *Phys. Rev. Lett.* **65** (1990) 1297.
- [17] K. Eguchi et al. (KamLAND Collaboration), *Phys. Rev. Lett.* **90** (2003) 021802.
- [18] Particle Data Book.
- [19] C. Kraus et al., *Eur. Phys. J.* **C40** (2005) 447.
- [20] V. M. Lobashev et al., *Phys. Lett.* **460** (1999) 227.
- [21] K. A. Assamagan et al., *Phys Rev.* **D53** (1996) 6065.
- [22] R. Barate et al. (ALEPH Collaboration), *Eur. Phys. J.* **C2** (1998) 395.
- [23] H. Georgi and S. L. Glashow, *Phys. Rev. Lett.* **32** (1974) 438.
- [24] M. Gell-Mann, P. Ramond and R. Slansky, *Rev. Mod. Phys.* **50** (1978) 721.

-
- [25] D. I. Kazakov, “Beyond the Standard Model”, Lectures given at the European School on High Energy Physics, (2000), hep-ph/0012288.
- [26] H. E. Haber, “Introductory low-energy supersymmetry”, Lectures given at TASI 1992 (SCIPP 92/33, 1993), hep-ph/9306207.
- [27] W. de Boer, “Grand Unified Theories and Supersymmetry in Particle Physics and Cosmology”, *Progr. in Nucl. and Par. Phys.*, **33** (1994) 201, hep-ph/9402266.
- [28] H. Murayama, “Supersymmetry phenomenology”, Lectures given at ICPT Summer School 1999, hep-ph/0002232.
- [29] R. Barbieri and L.J. Hall, *Phys. Lett.* **B338** (1994) 212.
- [30] R. Barbieri, L.J. Hall and A. Strumia, *Nucl. Phys.* **B445** (1995) 219.
- [31] Y. Kuno and Y. Okada, *Rev. Mod. Phys.* **73** (2001) 151.
- [32] M. Raidal et al., “Flavour physics of leptons and dipole moments”, arXiv:0801.1826v1.
- [33] L. Calibbi et al., “Lepton flavour violation from SUSY-GUTs: where do we stand for MEG, PRISM/PRIME and a super flavour factory”, hep-ph/0605139.
- [34] S. H. Neddermeyer and C. D. Anderson, *Phys. Rev.* **52** (1937) 884.
- [35] M. Conversi, E. Pancini and O. Piccioni, *Phys. Rev.* **71** (1947) 209.
- [36] N. Nereson and B. Rossi, *Phys. Rev.* **64** (1943) 199.
- [37] M. Conversi and O. Piccioni, *Phys. Rev.* **70** (1945) 859.
- [38] B. Pontecorvo, *Phys. Rev.* **72** (1947) 246.
- [39] E. P. Hincks and B. Pontecorvo, *Phys. Rev.* **73** (1948) 257.
- [40] E. P. Hincks and B. Pontecorvo, *Phys. Rev.* **73** (1948) 1122.
- [41] E. P. Hincks and B. Pontecorvo, *Phys. Rev.* **77** (1950) 102.
- [42] E. J. Konopinski and H. M. Mahmoud, *Phys. Rev.* **92** (1953) 1045.
- [43] E. J. Konopinski, *Rev. Mod. Phys.* **27** (1955) 254.
- [44] L. Michel, *Phys. Rev.* **86** (1952) 814.
- [45] H. J. Bramson et al., *Phys. Rev.* **88** (1952) 304
- [46] S. Lokanathan and J. Steinberger, *Phys. Rev.* **98** (1955) 240.
- [47] G. Feinberg, *Phys. Rev.* **110** (1958) 1482.
- [48] R. Feynman and R. P. Gell-Mann, *Phys. Rev.* **109** (1958) 1482.
- [49] G. Feinberg and S. Weinberg, *Phys. Rev. Lett.* **6** (1961) 381.
- [50] D. Bartlett, S. Devons and A. M. Sachs, *Phys. Rev. Lett.* **8** (1962) 120.
- [51] G. Feinberg, P. Kabir and S. Weinberg, *Phys. Rev. Lett.* **3** (1959) 527.
- [52] G. Danby et al., *Phys. Rev. Lett.* **9** (1962) 36.
- [53] P. Depommier et al., *Phys. Rev. Lett.* **39** (1977) 1113.
- [54] A. Van der Schaaf et al., *Nucl. Phys.* **A340** (1979) 249.

- [55] W. W. Kinnison et al., *Phys. Rev.* **D25** (1982) 2846.
- [56] R. D. Bolton et al., *Phys. Rev.* **D38** (1988) 2077.
- [57] A. De Rújula, H. Georgi and S. L. Glashow, *Phys. Rev.* **D12** (1975) 147.
- [58] R. Pratt, *Phys. Rev.* **111** (1958) 646.
- [59] C. Fronsdal and H. Überall, *Phys. Rev.* **118** (1959) 654.
- [60] Proposal to PSI, Proposal to INFN at <http://meg.web.psi.ch/docs/index.html>.
- [61] A. E. Pifer et al., *Nucl. Instr. Meth.* **35** (1976) 39.
- [62] H. W. Reist et al., *Nucl. Instr. Meth.* **153** (1978) 61.
- [63] A. Badertscher et al., *Nucl. Instr. Meth.* **A238** (1985) 200.
- [64] B. Rossi, *High energy particles*, Prentice-Hall, New York (1952).
- [65] Hamamatsu Photonics, Hamamatsu City, Japan.
- [66] M. Bonesini et al., *Nucl. Instr. Meth.* **A567** (2006) 200.
- [67] M. Bonesini et al., *Nucl. Instr. Meth.* **A572** (2007) 465.
- [68] L. Galli IEEE NSS-MIC-RTSD Dresden, Germany 2008, N30-468, 2625.
- [69] C. Brönnimann et al., *Nucl. Instr. Meth.* **A420** (1999) 264.
- [70] S. Ritt, *Nucl. Instr. Meth.* **A494** (2002) 520.
- [71] S. Ritt, *Nucl. Scin. Symp. Conf. Record* 2004 IEEE.
available at http://ieeexplore.ieee.org/xpls/abs_all.jsp?arnumber=1462369
- [72] C. Rubbia, CERN EP Internal Report 77-8 (1977).
- [73] H. H. Chen and J. F. Lathrop, *Nucl. Instr. and Meth.* **150** (1978) 585.
- [74] E. Aprile et al., *Nucl. Instr. and Meth.* **A241** (1985) 62.
- [75] C. Rubbia, ICARUS-Proposal, INFN/AE-85/7(1985), ICARUS-I, LNF-89/005 (1988).
- [76] T. Doke et al., *Nucl. Instr. and Meth.* **A237** (1985) 475.
- [77] V. M. Aulchenko et al., *Nucl. Instr. and Meth.* **A289** (1990) 468.
- [78] A. Baranov et al., *Nucl. Instr. and Meth.* **A294** (1990) 439.
- [79] V. M. Aulchenko et al., *Nucl. Instr. and Meth.* **A327** (1993) 193.
- [80] M. Tanaka et al., *Nucl. Instr. Meth.* **A457** (2001) 454.
- [81] *Handbook of Chemistry & Physics*, The Chemical Rubber Company.
- [82] A. C. Sinnock and B. L. Smith, *Phys. Rev.* **181** (1969) 1297.
- [83] L'Air Liquide-Division Scientifique, *Encyclopédie des gaz*, Elsevier, Amsterdam (1976).
- [84] L. M. Barkov et al., *Nucl. Instr. and Meth.* **A379** (1996) 482.
- [85] J. L. Subtil et al., *Phys. Stat. Sol.* **B143** (1987) 783.

- [86] V. Chepel, *Transparencies, IDM2002* York (2002).
- [87] T. Doke, *Port. Phys.* **12** 9 (1981), reprinted in *Experimental Techniques in High Energy Physics*, T. Ferbel ed.(Addison Wesley, 1987).
- [88] T. Doke and K. Masuda, *Nucl. Instr. Meth.*, **A420** (1999) 62.
- [89] J. Jortner et al., *J. Chem. Phys.*, **42** (1965) 4250.
- [90] S. A. Rice and J. Jortner, *J. Chem. Phys.*, **44** (1966) 4470.
- [91] N. Schwenter, E. E. Koch and J. Jortner, "Electronic Excitations in Condensed Rare Gases", Springer-Verlag, Berlin 1985.
- [92] A. Baldini et al., *Nucl. Instr. Meth.* **A545** (2005) 753.
- [93] N. Ishida et al., *Nucl. Instr. and Meth.* **A384** (1997) 380.
- [94] S. F. Mughabghab, M. Divadenam and N.E. Holden, *Neutron Cross Sections*, Academic Press New York (1981).
- [95] T. Doke et al., *Nucl. Instr. Meth.* **A291** (1990) 617.
- [96] T. Doke, *Nucl. Instr. Meth.* **A327** (1993) 113.
- [97] E. Aprile et al., *IEEE Trans. Nucl. Scin.* **37**(2) (1990) 553.
- [98] M. Miyajima et al., *Nucl. Instr. Meth.* **B63** (1992) 297.
- [99] M. Suzuki et al., *Nucl. Instr. Meth.* **192** (1982) 565.
M. Suzuki et al., *Nucl. Instr. Meth.* **192** (1982) 623.
- [100] M. Suzuki, *Nucl. Instr. Meth.* **A215** (1983) 345.
- [101] V. Chepel et al., Proceedings of 13th ICDL, Nara, Japan, July 20-25, 1999.
- [102] V. Chepel et al., *Radiation Phys. Chem.*, **74** (2005) 160.
- [103] T. Takahashi et al., *Phys. Rev.* **A12** (1975) 1771.
- [104] L. Lavoie, *Medical Phys.*, **3** (1976) 283.
- [105] I. R. Barabanov et al., *Nucl. Instr. Meth.* **A254** (1987) 355.
- [106] A. Braem et al., *Nucl. Instr. Meth.* **A320** (1992) 228.
- [107] J. Seguinot et al., *Nucl. Instr. Meth.* **A323** (1992) 583.
- [108] P. Belli et al., *Nucl. Instr. Meth.* **A336** (1993) 336.
- [109] J. Seguinot et al., *Nucl. Instr. Meth.* **A354** (1995) 280.
- [110] R. Van Sonsbeek et al., *Nucl. Instr. Meth.* **A367** (1995) 362.
- [111] M. Yamashita et al., *Nucl. Instr. Meth.* **A535** (2004) 692.
- [112] K. Saito et al., *IEEE Trans. Nucl. Scin.* **49** (2002) 1674.
- [113] A. Hitachi et al., *Phys. Rev.* **B27** (1983) 5279.
- [114] A. Hitachi et al., *Phys. Rev.* **A35** (1987) 3956.
- [115] E. Shibamura et al., *Nucl. Instr. Meth.* **A260** (1987) 437.
- [116] K. Masuda et al., *Phys. Rev.* **A39** (1989) 4732.

- [117] S. Konno and T. Takahashi, *Nucl. Instr. Meth.* **150** (1978) 517.
- [118] D. E. Grosjean et al., *Phys. Rev. Lett.* **74** (1995) 1474.
- [119] D. E. Grosjean et al., *Phys. Rev.* **B56** (1997) 6975.
- [120] C. Amsler et al., *Eur. Jour., JINST* 2008 JINST 3 P02001.
- [121] E. Conti et al., *Phys. Rev.* **B68** (2003) 054201.
- [122] J. V. Dawson et al., *Nucl. Instr. Meth.* **A545** (2005) 690.
- [123] E. Aprile et al., *Phys. Rev. Lett.* **97** (2006) 081302.
- [124] A. Baldini et al., *Nucl. Instr. Meth.* **A565** (2006) 589.
- [125] L. D. Landau and E. M. Lifshitz, *Electrodynamics of continuous media*, Pergamon Press.
- [126] J. D. Jackson, *Classical Electrodynamics*, Wiley.
- [127] U. Hohm and K. Kerl, *Molecular Physics* **69** (1990) 803.
- [128] J. Hout and T. K. Bose, *J. Chem. Phys.* **95** (1991) 2683.
- [129] H. J. Achtermann et al., *J. Chem. Phys.* **98** (1993) 2308.
- [130] A. C. Sinnock, *J. Phys.* **C13** (1980) 2375.
- [131] U. Hohm, *Molecular Physics* **81** (1994) 157.
- [132] A. Bideau-Mehu et al., *J. Quant. Spectrosc. Transfer* **25** (1981) 395.
- [133] L. M. Barkov et al., *Nucl. Instr. and Meth.* **A379** (1996) 482.
- [134] P. Laporte and I. T. Steinberger, *Phys. Rev.* **A15** (1977) 2538.
- [135] J. L. Subtil et al., *Phys. Stat. Sol.* **B143** (1987) 783.
- [136] V. Chepel et al., *Physics/0307044*.
- [137] G. M. Seidel, R. E. Lanou and W. Yao, *Nucl. Instr. and Meth.* **A489** (2002) 189.
- [138] S. A. Rice and J. Jortner, *J. Chem. Phys.* **44** (1966) 4470.
- [139] I. T. Steinberger and U. Asaf, *Phys. Rev.* **B8** (1973) 914.
- [140] T. Haruyama et al., *Advanced in Cryogenic Engineering* **B49** (2004) 1495.
- [141] T. Haruyama et al., *Advanced in Cryogenic Engineering* **B51** (2006) 1695.
- [142] R. Sawada et al., *Cryogenic* **43** (2003) 449.
- [143] T. Haruyama et al., *KEK Preprint 2007-49 accepted for publication on Advanced in Cryogenic Engineering*.
- [144] S. Mihara et al., *Cryogenic* **46** (2006) 688.
- [145] Photomultiplier tubes, *Principles and applications*, September 2002, Photonics, France.
- [146] A. Baldini et al., *Nucl. Instr. and Meth.* **A566** (2006) 294.

- [147] S. Belforte et al., “SVT Technical design report” CDF note 3108 (1994); CERN EP report 81-12/Rev.
- [148] A. Baldini et al., MEG Internal note, Partial analysis of the february 2002 test data from the Xe Calorimeter Large Prototype.
- [149] J. Jortner et al., *J. Chem. Phys.* **42** (1965) 4250.
- [150] N. Schwenter, E.E. Koch and J. Jortner, “Electronic Excitations in Condensed Rare Gases”, Springer-Verlag, Berlin 1985.
- [151] E. Morikawa et al., *J. Chem. Phys.* **91** (1989) 1469.
- [152] A. S. Schlüssler, *Appl. Phys. Lett.* **77** (2000) 1.
- [153] SORAD LTD, <http://www.raz-dva.cz/sorad/>.
- [154] AEA Technology QSA GmbH, <http://www.aeat.co.uk>.
- [155] International Organization for Standardization, “Radiation protection-sealed radioactive sources-leakage test methods”. ISO 9978, Geneva, 1992.
- [156] S. Bazzarri, G. Cicoli, P. De Felice, G. Rossi and F. Sedda, *Nucl. Instr. Meth.* **A560** (2006) 640.
- [157] “The Super-Kamiokande Detector: First Data and Preliminary Results”, James E. Hill, for the Super-Kamiokande Collaboration, in (Proceedings of the XXXII nd RENCONTRES DE MORIOND), (Editions Frontieres) 1997.
- [158] NDS-IAEA; <http://www-nds-iaea.org> .
- [159] A. Baldini et al., MEG Internal note, “Neutron background measurements in the $\pi E5$ area”, February, 2007 .
- [160] J. W. Marsh et al., *Nucl. Instr. and Meth.* **A366** (1995) 340.
- [161] S. Croft, *Nucl. Instr. and Meth.* **A281** (1989) 103.
- [162] E. A. Lorch, *Int. J. Appl. Rad. and Isotop.* **24** (1973) 585.
- [163] K. H. Beckurts and K. Wirtz, Neutron Physics, Springer-Verlag.
- [164] O. Hæusser et al., *Nucl. Instr. and Meth.* **213** (1983) 301.
- [165] NACRE - European Compilation of Reactions Rates for Astrophysics; <http://pntpm.ulb.ac.be/nacre.htm>
- [166] W. A. Fowler et al., *Rev. Mod. Phys.* **20** (1948) 236.
- [167] R. L. Walker and B. D. McDaniel, *Phys. Rev.* **74** (1948) 315.
- [168] R. O. Bondelid and J. W. Butler, *Phys. Rev.* **139** (1963) 1078.
- [169] D. Zahnow et al., *Z. Phys.* **A315** (1995) 229.
- [170] F. E. Cecil et al., *Nucl. Phys.* **A539** (1992) 75.
- [171] K. I. Hahn et al., *Phys. Rev.* **C53** (1996) 1273.
- [172] T. Huus and R. B. Day, *Phys. Rev.* **91** (1953) 599.
- [173] B. D. Anderson et al., *Nucl. Phys.* **A233** (1974) 286.
- [174] F. Zijderhand and C. Van der Leun, *Nucl. Phys.* **A 460** (1986) 181.

- [175] <http://electrochem.cwru.edu/ed/encycl/art-m03-machining.htm>
- [176] D.A. Glocker and S.I. Shah (Eds.), Handbook of Thin film process technology, IoP (1995).
- [177] R. M. Sinclair, *Phys. Rev.* **93** (1954) 1082.
- [178] G. K. Farney et al., *Phys. Rev.* **97** (1955) 720.
- [179] L. Keszthely et al., *Nucl. Phys.* **29** (1961) 241.
- [180] I. Berkes et al., *Nucl. Phys.* **43** (1963) 103.
- [181] K. M. Subotic et al., *Nucl. Phys.* **A331** (1979) 491.
- [182] K. Spyrou et al., *Eur. Phys. Jour.* **A7** (2000) 79.
- [183] D. Zahnow et al., *Nucl. Phys.* **A589** (1995) 95.
- [184] J. Spuller et al., *Phys. Lett.* **B67** (1977) 479.
- [185] E. Fermi and E. Teller, *Phys. Rev.* **72** (1947) 399.
- [186] L. I. Ponomarev, *Sov. J. Nucl. Phys.* **2** (1966) 160.
- [187] Z. V. Krumshtein et al., *Sov. J. Nucl. Phys.* **26** (1968) 906.
- [188] J. A. Bistirlich et al., *Phys. Rev.* **C5** (1972) 1867.
- [189] D. Horvat, *Radiochimica Acta* **28** 241 (1981).
- [190] Handbook of X-ray Spectrometry, R. Van Grieken and A. Markovicz editors, Marcel Dekker, Inc.
- [191] PIXE, S. Johansson, Wiley (2001).
- [192] I. Govil, *Current Science* **80** (2001) 1542.
- [193] H. Paul and J. Muhr, *Physics Reports* **135** (1986) 47.
- [194] E. Merzbacher and H. W. Lewis, "Encyclopedia of Physics" Flugge ed. **34** (1958) 166.
- [195] M. S. Livingston et al., *Phys. Rev.* **51** (1937) 835.
- [196] W. Brandt and G. Lapicki, *Phys. Rev.* **A20** (1979) 465.
- [197] W. Brandt and G. Lapicki, *Phys. Rev.* **A23** (1981) 1717.
- [198] D. D. Cohen and M. Harrigan, *Atomic Data Nucl. Data Tables* **33** (1985) 255.
- [199] D. D. Cohen and M. Harrigan, *Atomic Data Nucl. Data Tables* **34** (1986) 393.
- [200] M. H. Chen and B. Crasemann, *Atomic Data Nucl. Data Tables* **33** (1985) 217.
- [201] M. H. Chen and B. Crasemann, *Atomic Data Nucl. Data Tables* **41** (1989) 257.
- [202] S. Ouziane et al., *Nucl. Instr. Meth.* **B161-163** (2000) 141.
- [203] D. Strivay and G. Weber *Nucl. Instr. Meth.* **B190** (2002) 112.
- [204] MEG Internal Technical Note, TN044.
- [205] MEG Internal Technical Note, TN046.

-
- [206] D. F. Measday, *Physics Reports* **354** (2001) 243.
- [207] Stopping-Power and Range Tables for Electrons, Protons, and Helium Ions at <http://physics.nist.gov/>
- [208] Tables of X-ray mass attenuation coefficient at <http://physics.nist.gov/>
- [209] B. Rossi and H. Staub, *Ionization Chambers and Counters*, McGraw-Hill, reprinted Reitel Press (2007).
- [210] J. McDonald et al., *Nucl. Instr. Meth.* **A496** (2003) 293.
- [211] A. Peiser and F. Sauli, “Drift and diffusion of electrons in gases: a compilation” CERN 84-08.
- [212] Transport properties of gaseous ions over a wide energy range, *Atomic data and nuclear data tables* **31** 113 (1984).
- [213] D. Green, *The physics of particle detectors*, Cambridge (2000).
- [214] S. Biagi, *Nucl. Instr. Meth.* **A421** (1999) 234.
- [215] <http://consult.cern.ch/writeup/magboltz/usage.html> and write-up on *drift velocity* at <http://consult.cern.ch/writeup/garfield/notes/>
- [216] R. Jung et al., “Single pass optical profile monitoring”, Proceedings DIPAC 2003, Mainz, Germany.
- [217] Hitachi Kokusai Electric Inc., Tokyo, Japan.
- [218] Apogee Instruments Inc., Roseville CA, USA.
- [219] Advanced Scientific Imaging Technology, DTA s.r.l., Pisa, Italy.
- [220] G. J. Feldman and R. D. Cousins, *Phys. Rev.* **D57** (1998) 3873.